ANALYTICAL AND EXPERIMENTAL ASSESSMENT OF STEEL TRUSS BRIDGE GUSSET PLATE CONNECTIONS

A Dissertation
Presented to
The Academic Faculty

by

Yavuz Mentes

In Partial Fulfillment
of the Requirements for the Degree
Doctor of Philosophy in the
School of Civil and Environmental Engineering

Georgia Institute of Technology
December 2011

ANALYTICAL AND EXPERIMENTAL ASSESSMENT OF STEEL TRUSS BRIDGE GUSSET PLATE CONNECTIONS

Approved by:

Dr. Donald W. White, Advisor
School of Civil and Environmental Engineering
Georgia Institute of Technology

Dr. Roberto T. Leon, Advisor
School of Civil and Environmental Engineering
Georgia Institute of Technology

Dr. Kenneth M. Will
School of Civil and Environmental Engineering
Georgia Institute of Technology

Dr. Lawrence F. Kahn
School of Civil and Environmental Engineering
Georgia Institute of Technology

Dr. Dewey H. Hodges
School of Aerospace Engineering
Georgia Institute of Technology

Date Approved: August 1, 2011

To my parents, Hava Mentes and Muzaffer Mentes, my sister Yeliz Mentes, and my wife Hilal Sevindik Mentes for their tremendous support, patience, and love

ACKNOWLEDGEMENTS

I would like to express my deep and sincere gratitude to the people who made this PhD dissertation possible. It would not have been accomplished without their unlimited support.

First and foremost, I would like to present my special thanks to my advisors Dr. Donald W. White and Dr. Roberto T. Leon for their enormous guidance, encouragement, and assistance. Their experience and suggestions motivated me from the beginning of this research until I finish writing my dissertation. My dream of getting the PhD degree would not be achieved without their trust and continuous support.

My gratitude also goes to my thesis committee members, Dr. Kenneth M. Will, Dr. Lawrence F. Kahn, and Dr. Dewey H. Hodges for their patience, encouragements and invaluable comments. Their recommendations on different aspects of my research helped me improve my dissertation.

Financial support by the Federal Highway Administration (FHWA) is greatly appreciated. The experimental part of this research was performed at Turner-Fairbank Highway Research Center (TFHRC) of FHWA. I would like to thank my advisors and Dr. Mohammad Khan from Professional Service Industries, Inc. for giving me the chance to spend four months at TFHRC as a graduate co-op employee.

I would also like to thank Dr. Justin M. Ocel from FHWA, Dr. Robert S. Zobel from PSI, Inc. and Dr. Mark Iadicola from National Institute of Standards and Technology (NIST) for their unlimited valuable feedback, guidance and support. They provided significant amount of experimental data as part of this dissertation.

Special thanks are due to Yoon Duk Kim and Towhid Bhuiyan for providing the parametric study models that I used for my dissertation. They were not only talented colleagues but also very good friends with their endless support. Yoon Duk was the first person who explored the development of the FEA models using the Abaqus software in the earlier stages of this research and she also provided great help on the design recommendations as part of this research.

I would like to thank my officemates Cagri Ozgur, Andres Sanchez, Juan Jimenez, Cliff Bishop, and Akhil Sharma for their support and the friendly working environment they provided. I would also like to thank my friends Mustafa Kara, Sibel Kara, Efe Guney, Ilker Kalkan, Kezban Sokat, and Gurkan Sokat for their help to overcome the stressful days throughout my studies. I would like to express my gratitude to Sharon Dempsey and William Swenson for their support since I came to the US.

I would also like to present my thanks to all of my colleagues in the School of Civil & Environmental Engineering, especially, Timothy Wright, Karthik Ramanathan, Robert Moser, Jonathan Hurff, Brett Holland, Ben Deaton, Abdollah Shafieezadeh, Jieun Hur, Amal Jayapalan.

I would like to thank my mother-in-law Ayse Sevindik, father-in-law Ali Sevindik, brother-in-law Muhammet Ali Sevindik, and sisters-in-law Hanim Sevindik Bac and Mukaddes Sevindik for their great support throughout my doctoral studies.

My deepest gratitude goes to my beloved parents, Hava Mentes and Muzaffer Mentes, and my dearest sister, Yeliz Mentes. This thesis would not be possible without their support and love.

Last but not least, words cannot express my appreciation and heartfelt gratitude to my precious wife, Hilal Sevindik Mentes. She has been a part of me ever since we met. She gave her love to make everything easier for me to complete this dissertation. Her support and encouragement was in the end what made this dissertation possible.

TABLE OF CONTENTS

LIST OF TABLES

LIST OF FIGURES

SUMMARY

The I-35W Bridge over the Mississippi River in Minneapolis, MN had a catastrophic failure in the main span of the deck truss in 2007. This collapse has brought significant attention on the gusset plate connections in steel truss bridges throughout the U.S. Steel truss bridge gusset plate design has not received much focus in the past 40 years, and there is a lack of consensus within the design profession on the procedures to evaluate, design, and rate these critical elements. In the short term, based on the best available information on the gusset plate design, the Federal Highway Administration (FHWA) has issued preliminary guidance. Although some experimental research has been conducted on the ultimate strength of gusset plates, much of this work has been directed toward the performance of tension members and their connections. There has been limited experimental work on the compression capacity and stability of gusset plates, but most of this work is relevant primarily to bracing connections common in building structures.

This research focuses on comprehensive experimental and analytical studies on steel truss bridge gusset plate behavior. The studies include comparisons of advanced analytical models with the responses from large-scale experimental tests using discrete and innovative full-field measurements. The calibrated finite element analysis models are then utilized to study a variety of gusset plate configurations. Improved mechanistic idealizations that better capture the observed behavior in the experiments and analytical studies are proposed as the result of this work. The design checks recommended in this thesis present a comprehensive methodology for determining the ultimate gusset plate resistance. This research provides a large database of original results that will be useful for future similar studies. In addition, this research provides modeling procedures that permit the study of steel truss bridge connections and their adjacent framing members using truss bridge sub-assemblies. Based on the comprehensive analytical studies, simple and accurate design calculation procedures to assess the nominal ultimate strength of steel truss gusset plate connections are recommended for steel truss bridge gusset plate connections.

CHAPTER I : INTRODUCTION

1.1. Problem Statement

Gusset plate connections can be extremely complex structural assemblies, and their appropriate idealization for analysis and design has received comparatively little attention in comparison to their structural importance. On August 1, 2007, the I-35W bridge over the Mississippi River in Minneapolis, Minnesota collapsed (Figure 1.1.1). The National Transportation Safety Board (NTSB) investigation determined that failure of inadequately-sized gusset plates at the U10 node was the triggering event in the collapse sequence. A recent design review also revealed that the gusset plates at the U10 nodes were grossly under-sized, clearly as the result of an error in the design process. These plates became overloaded due to a substantial increase in the weight of the bridge, resulting from previous bridge modifications along with traffic and construction loads present on the bridge on the day of collapse. The collapse of the I-35W bridge has brought significant attention to the reliability and safety of gusset plate connections in steel truss bridges throughout the U.S.

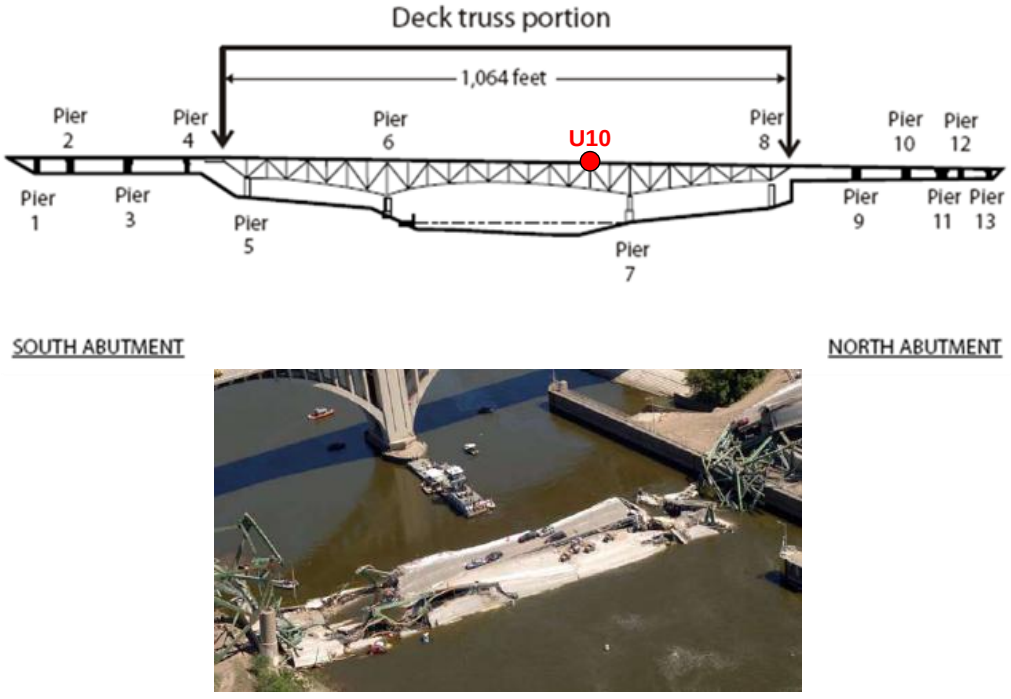

Figure 1.1.1: I-35W bridge east elevation view (top) and collapsed center section (bottom) (NTSB, 2008)(Adapted from Mn/DOT Graphic)

In Figure 1.1.2, a series of photos from an inspection in 2003, show that gusset plate U10 had already developed bowing during or prior to 2003, four years before the bridge collapsed in 2007. Before determining that the collapse of the bridge likely initiated with failure of the gusset plates at the U10 nodes, NTSB considered a number of potential other reasons, including corrosion damage in gusset plates at the L11 nodes, fracture of a floor truss, pre-existing cracking, temperature effects, and pier movement. These mechanisms were determined not to be the main causes of the collapse (Holt and Hartmann, 2008; NTSB, 2008).

Figure 1.1.2: U10 joint from the east and west trusses of the I-35W bridge (NTSB, 2008)(Source: University of Minnesotatop right photo; URS Corporation, other three photos)

Astaneh (2008) states that the additional considerable load due to construction materials and equipment caused the already over-stressed gusset plates U10 to reach their net section capacity. After fracture of the net section of gusset plate U10, the progressive collapse of the main trusses occurred quite rapidly and in a brittle manner. This rapid failure was due to lack of redundancy, since I-35W was unable to redistribute the large forces transmitted by the adjacent components.

Physical examination of the bridge structure concluded that the gusset plates at the east (U10 and L11) and west nodes (U10'and L11') fractured. Design methodologies in the past are believed to employ conservative assumptions for gusset plates with the result that a properly designed gusset plate should generally be stronger than the members it connects. Thus the collapse of the deck truss portion of the bridge was unusual in that it originated with the sudden failure of the U10 gusset plates.

Prior to the I-35W Bridge collapse, few cases of in-service truss bridge failure have been reported. There are several examples of partial bridge failures where gusset plates were considerably weakened by section loss due to corrosion. For example, four deteriorating corroded steel plates supporting the I-90 Grand River Bridge in Perry Township, Ohio, buckled in 1996 (Figure 1.1.3). The span dropped 3 inches and the bridge was closed for about six months for repairs costing $1.6 million.

c 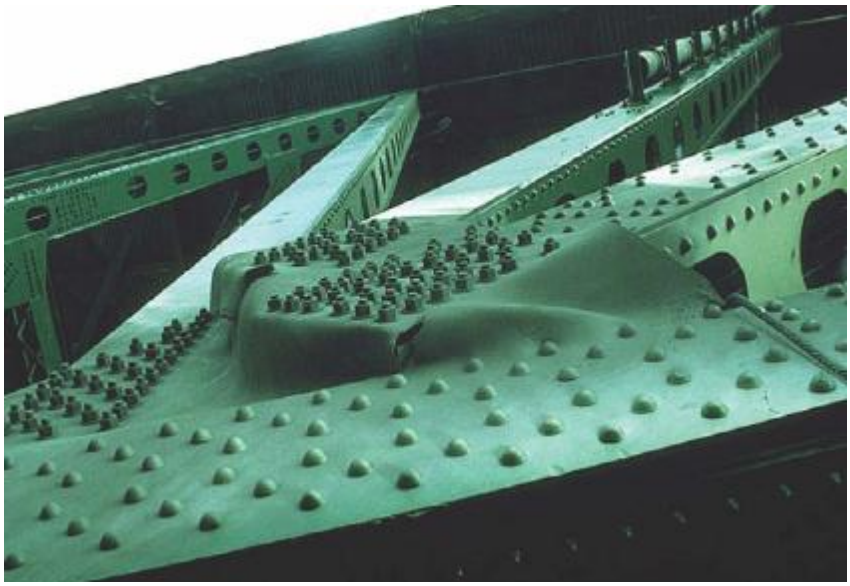

Figure 1.1.3: Buckled gusset plate in the I-90 bridge over Grand River (FHWA, 2010). (Photo from Firas Ibrahim, FHWA)

The I-35W collapse made it clear that (1) steel truss bridge gusset plate design has not received enough attention in the past 40 years, (2) there is limited information available to quantify the true ultimate strength of these components, and (3) there is a lack of uniformity or consensus among the design profession on the procedures to use for the design of these components. The Federal Highway Administration (FHWA) implemented a two-step approach to address the shortcomings listed above. In the short

term, based on the best available information on gusset plate design, FHWA issued a preliminary guide document (FHWA, 2009), which is referred to as the FHWA Guidance throughout this dissertation. This document has led to many discussions, since a significant number of truss bridges in service fail to meet the new FHWA Guidance.

In the longer term, FHWA and the Natiional Cooperative Highway Research Program (NCHRP) initiated a large experimental and analytical effort to verify and improve the provisions in the FHWA Guidance, since there is limited research available to support some of the provisions documented in the FHWA guide. Although some experimental research has been conducted on the ultimate strength of gusset plates, much of this work has been directed to performance of tension members and their connections. There has been limited experimental work on the compression capacity and stability of gusset plates, but most of this work has focused on bracing connections common in building structures. Similarly, there are no comprehensive analytical studies that leverage advanced finite element modeling and modern computational horsepower to address this problem.

1.2. Research Objectives

A large combined experimental and analytical study aimed at developing rational and consistent design criteria for large gusset plates is needed. This thesis reports on aspects of the long-term research sponsored by FHWA and the NCHRP, with the aim of providing: (a) the fundamental knowledge needed to develop robust analytical models and (b) design recommendations for steel truss bridge gusset plate connections. The analytical work reported herein is aimed at complementing and extending the large-scale experimental work being carried out at the FHWA laboratory (Ocel et al., 2010)

This thesis reports primarily on the ultimate strength capacity of gusset plate connections. The assessments of the structural capacity are conducted using full-nonlinear finite element analysis models implemented in the Abaqus software (Simulia 2009; Simulia 2010) and calibrated against full-scale experimental test results. Consideration of proper boundary conditions and initial geometric imperfections are addressed in the development of the finite element analysis procedures. The data collected from the experiments allows for a thorough calibration of the analytical finite

element models. After a refined finite element modeling strategy is reached through these calibrations, a wide variety of gusset plate configurations are investigated analytically.

The core objectives of this research are:

1. To develop advanced analytical models reflecting the potential failure modes and limit states for gusset plates.
2. To assess the validity of these analytical models through unique large-scale testing.
3. To propose improved mechanistic idealizations best matching the analysis results of these connections.
4. To provide recommendations for improved accuracy, and simplicity in the design of steel truss bridge gusset plate connections.

The major contributions of this research are in the development of fundamental knowledge related to:

1. Development of a large calibration database that can be used in the future for further investigations of design provisions.
2. Establishment of a sub-assemblage modeling approach that allows connection non-linear behavior to be studied without the need to model an entire structure. For structures such as long truss bridges, the savings in modeling and calculation time means that these models can be efficiently used for parametric studies and refined capacity assessments.
3. Clarification of the ultimate resistance mechanisms in both compression and tension for chord splices through the determination of the effective areas of the gusset and splice plates.
4. Development of methods to evaluate the stability of gusset plates under compression. Other than a free edge slenderness limit, currently there have been no comprehensive studies of steel truss gusset plates to identify their compressive resistance.
5. Clarification of the shear resistance of the gusset plates, including the identification of specific shear planes and the corresponding resistance checks for these planes.

6. Evaluation of techniques for retrofit and rehabilitation of existing truss bridges, including the use of stiffening angles.

1.3. Organization

This dissertation is organized into seven chapters. Chapter 2 presents a literature review of past research, along with a comprehensive study of plans of several representative large truss bridges. Selected joints from these bridges used in the earlier steps of this research are also discussed in detail. Chapter 3 discusses the implementation of test simulations for the representative bridge joints selected in the Chapter 2. Chapter 4 addresses the full-scale experimental tests, focusing primarily on a comparison between the tests and analytical results. It also provides information on how the analytical models are calibrated. Chapter 5 presents extensive analytical parametric studies performed using the robust finite element models developed in previous chapters. Chapter 6 provides proposed design recommendations and key contributions as the outcome of this research. Finally, Chapter 7 summarizes the findings and conclusions of this research and provides recommendations for future studies.

CHAPTER II : BACKGROUND

As a prelude to this research, a comprehensive literature review of existing research on gusset plates was conducted. The results of this review are described in Section 2.1. To focus the study on realistic gusset plate configurations, the plans of a large number of bridges considered to be representative of truss bridges built in the last 80 years were examined. This task and its conclusions are described in Section 2.2 and Section 2.3 respectively. Some of the information covered in this chapter is adapted from the project interim report (FHWA, 2010).

2.1. Review of Past Research

Since performance of gusset plate connections depends primarily on the behavior of the two major components, the fasteners (bolts or rivets) and the gusset plate itself, this literature review addresses previous studies on both gusset plate and connector elements. The first large scale test on riveted connections took place after the Quebec Bridge collapse in 1907 (Government, 1919). These riveted connections were subjected to shear in order to determine the fastener strength and ductility. These test results provide valuable data for assessment of older riveted steel truss bridge gusset plate connections.

One of important consideration in the evaluation of steel truss gusset plate connections is the difference in connection behavior between riveted and bolted connections (Leon, 1996; Munse 1956) and the understanding of the impact these differences have on the overall response. In riveted connections, the rivet shank expands and fills the hole completely during installation by repeated blows of the pneumatic hammer or other installation tools. This aspect of riveted connection decreases the possibility of slip which is common for bolted connections. The rivet shank contracts and the rivet head applies a clamping force on the connected plates during the cooling process (FHWA, 2010). The initial stress in rivets is found to be generally greater than 70% of the yield strength of the steel from which the rivets were made (Wilson and Oliver, 1930).

Early research on steel connections including the work of DeJonge (DeJonge, 1945) for riveted connections, Fisher and Beedle (Fisher and Beedle, 1964; Fisher et al.,

1966; ASCE, 1967) and Munse (Munse, 1976) for both bolted and riveted connections resulted in the common acceptance of bolted connections. Based on more recent detailed studies, Roeder et al. (1994) indicate that rivet behavior can be modeled experimentally by using A307 bolts, with initial non-linearities at about 20 ksi, ultimate strengths at 40 to 45 ksi and shear deformations of about 0.12 in. Only a few research efforts are cited here as a comprehensive description of rivet and bolt behavior can be found in the RCSC Guide (Kulak et al., 2001).

Whitmore performed the first comprehensive study to determine strain distribution in gusset plates (Whitmore, 1952). In this study, he conducted a test on a "Warren" type gusset plate connection (1:4 scale prototype) instrumented with strain gages (Figure 2.1.1). The need to capture large strain magnitudes in this study required a material with a low modulus of elasticity. In addition, the material needed to possess high strength and ductility similar to structural steel. Hence, a high strength aluminum alloy was selected as the most suitable material. The principal stress paths shown in Figure 2.1.1 were obtained using the strain readings from the strain gages. In this figure, the directions of the principal tension stresses are represented by solid lines (P stresses) and directionsn of the principal compression stresses are represented by dashed lines (Q stresses).

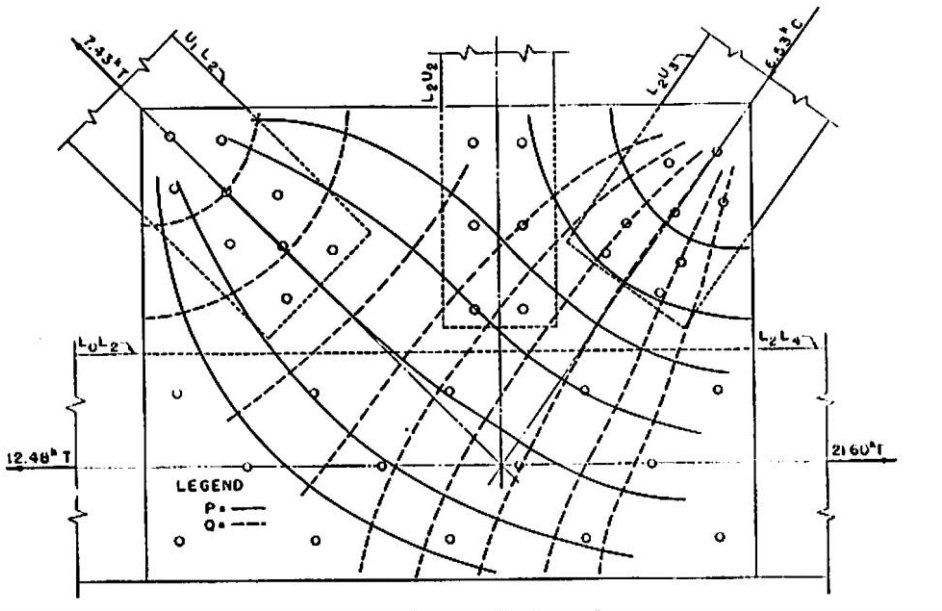

Figure 2.1.1: Stress trajectories in a warren truss gusset plate (Whitmore, 1952)

Based on these studies, Whitmore reached two main conclusions. First, he concluded that the most critical section of the gusset plate is the horizontal plane just above the chord members since large shear forces take place there. Second, he proposed an effective section which is known as "Whitmore width" today. The basic definition for Whitmore width is: "*Effective length normal to the member axis and obtained by intersecting two inclined lines making 30° with the member axis which originate at the outside fasteners in the first row and continue through the bottom row of rivets*." Whitmore states that the maximum tensile and compressive stresses can be calculated by assuming the force is uniformly distributed over an area obtained by multiplying Whitmore width with the plate thickness.

The work performed by Whitmore has three major limitations. First, the levels of stress applied are very low, so the results are valid only in the elastic range. Second, although the number of strain gages used is large for that time, the goal was to determine the main stress paths qualitatively without reaching quantitative results so no conclusion can be made about the values and locations of local stress concentrations. Finally, the number of fasteners is small and the main purpose is to check the behavior in tension, which is assumed to be the critical loading for assessment of the strength, without taking compression into account (FHWA, 2009). Plastic design methods have been developed for design of gusset plates common in building bracing connections to get rid of the first limitation that Whitmore's work encountered (Thornton and Kane, 1999). These design methods end up with very stiff and strong connections with thick gusset plates since they produce a safe design based on a lower-bound solution.

Recent work performed by Thornton and Muir (Thornton and Muir, 2008) on bracing connections in buildings discusses the buckling limit state including the gusset free edge buckling. However, this work is limited to corner bracing connections in buildings, which have only one member framing into the plate. These are substantially different from truss bridge connections where several members in tension or compression meet at a gusset plate. The key distinction relative to common building configurations is the use of two gusset plates, one on each side of the member. The compressive capacity of the gusset plates is usually assessed by evaluating the compression capacity of an idealized equivalent column at the base of the compression member by using the

Whitmore method. Experiments performed by Brown (Brown, 1988) on gusset plates typical to building construction and subjected to compression show that buckling of the free edge of the gusset always preceded the compression failure for the geometries tested. Brown investigated both plate and column buckling analogies and concluded that the column analogy works well based on the experimental data.

Dowswell (Dowswell, 2006) gathered 170 experimental test and finite element analysis cases where compressive loads were applied and selected 59 experimental test results and 56 finite element analysis results for statistical analysis in his study. Based on the statistical analysis results, he recommends the buckling lengths and the corresponding effective length factors for different types of gusset plate configurations. However, these studies still focus on gusset plate connections for building bracing connections. The history and variety of bridge gusset plate connections and behavior have been recently reviewed by Astaneh (Astaneh, 2010). He presents information on the failure modes and information on the concepts used in design of gusset plates in steel truss bridges. He also discusses procedures to design the steel truss bridge gusset plate connections consistent with the AASHTO LRFD Bridge Design Specifications (AASHTO, 2007).

The FHWA Guide recommends using the procedures in the AASHTO (2007) provisions (Sections 6.9.2.1 and 6.9.4.1) for axial resistance of compression members. The effective column slenderness ratio, KL/r_s, is used in resistance calculations. Calculation of the terms L and r_s involves determining the shape of an equivalent rectangular column in the gusset plate. The FHWA Guide recommends using the Whitmore section to set the column width. The unbraced length and the corresponding K value needs more research since current guidance in this area mostly depends on the engineer's judgment. The FHWA guide provides a very general guidance on K value to be applied in the resistance calculations. Gusset plate connections have substantial diversity in terms of geometry and applying a single methodology to all cases may not be possible. One key concern that has been voiced by numerous engineers is the applicability of the Whitmore method to "tight" gusset connections where there is little space between members. It is common for the Whitmore section to overlap other connecting members especially for the connections in which some of the web members are chamfered.

In the FHWA Guidance, the tension capacity of gusset plates is evaluated using the AASHTO provisions for tension capacity of members (Section 6.8.2). The gusset plate is checked for yielding on the gross section and fracture on the net section. Similar to the calculation of the compression resistance, the Whitmore method is used to determine both the gross and net section areas in these two checks. Richard (Richard et al, 1983) proposes the block shear rupture check as a suitable approach for gusset plate tension resistance The AASHTO code also requires a block shear rupture resistance check (Section 6.13.4). Cai and Driver (Cai and Driver, 2008) recommend to combine the block shear resistance calculation with other local limit state yielding and rupture checks. Kulak (Kulak et al, 2001) states that both Whitmore and block shear checks should be performed and the lowest resistance among these is taken as the controlling gusset plate resistance in tension.

The shear resistance of gusset plates in the AASHTO provisions (Section 6.13.5.3) is calculated using the equation:

$$R_r = \phi_v (0.58 F_y) A_g \Omega \qquad \text{(Eq. 2.1-1)}$$

where,

ϕ_v = LRFD resistance factor for gross-section yield resistance

F_y = Yield strength of the gusset plate (ksi)

A_g = Area of the gross-section for the shear plane (inch)

Ω = Reduction factor

If the shear stress distribution along the plane being checked is uniform, the reduction factor Ω is taken as 1.0. Ω value of 1.0 represents the ability of the gusset plate to fully plastify across the entire shear plane prior to shear buckling. Section 6.14.2.8 of the provisions states that $\Omega = 0.74$ is used for flexural shear. LRFD defines the shear resistance factor as $\phi_v = 1.0$ but the FHWA Guide recommends using $\phi_{vy} = 0.95$ to be consistent with the resistance factor for tension yielding. The FHWA Guide also recommends checking the ultimate shear rupture capacity along the net section using the equation:

$$R_r = \phi_{vu}(0.58F_u)A_n\Omega \quad \text{(Eq. 2.1-2)}$$

where,

ϕ_{vu} = LRFD resistance factor for net-section rupture resistance

F_u = Ultimate strength of the gusset plate (ksi)

A_n = Area of the net-section for the shear plane (inch)

Ω = Reduction factor

The resistance factor for this check is recommended as $\phi_{vu} = 0.80$ to be consistent with the block shear provisions. Many possible shear planes through gusset plates involve a significantly reduced net section. However, the AASHTO specification does not specifically require this check for shear in gusset plates. Since $\phi_{vu} = 0.80$ already provides factor of safety against failure, adding an additional reduction factor Ω may be overly conservative.

2.2. Comprehensive Study of Bridge Plans

In this section, existing truss bridge plans provided from state DOTs are summarized to investigate the diversity in design parameters such that representative connections can be selected for further study in this research. Twenty different bridge plans representative of the highway truss bridge inventory in the U.S. designed between 1929 and 1990 are reviewed. Eighteen of the bridge plans were provided by Idaho, Indiana, Minnesota, New York, Pennsylvania, and Tennessee DOTs. In addition, FHWA provided the plans for the I-275 Bridge in Kentucky and the original I-35W Bridge from Minnesota. A more detailed information on these truss bridges is provided by Wright (2009). Figure 2.2.1 shows the 20 bridge configurations drawn to the same scale.

In the 20 bridge plans, there are eight through-truss designs, nine deck truss designs, one combination deck and through truss, one trussed arch bridge, and one combination through-truss and trussed arch bridge. Five of the trusses are single span ranging from 114 to 420 ft., and two are large two-span truss bridges with span lengths of 720 and 725 ft. However, most of the bridges have three or more spans with main span

lengths ranging from 120 to 612 ft. The trussed-arch bridges have the longest main span lengths of 800 and 825 ft.

Table 2.2.1, from (Wright, 2009), provides a summary of the span and other relevant parameters for each of the truss bridges. Carbon steels (36 ksi or lower) are used in 11 of the bridges designed between 1929 and 1970. Low alloy steels (50 ksi or lower) are used for 11 bridges built between 1955 and 1990. High strength, quenched & tempered steel (100 ksi or T1) is used in four of the bridges fabricated from 1959 to 1976. In sixteen of the bridges built between 1929 and 1965 rivets are used to connect the gusset plates. A325 high strength bolts are used in five bridges built between 1959 and 1990. In general, trusses designed up to the late 1950's are riveted, those designed from the late 1950's to the late 1960's use either high strength bolts or rivets, and almost all of the bridges built after 1970 use high strength bolts. There is a trend from rivets to high strength bolts among the bridges investigated as part of the comprehensive study in this research (FHWA, 2009). Mostly 7/8" diameter fasteners are used in the selected bridge plans; seven of them use 1" diameter fasteners.

One of the key conclusions from this study is on the distribution of the gusset plate thicknesses. Plate thickness does not have any correlation with the size of the truss bridge itself. Some of the large bridges even utilize 3/8" gusset plates at certain joints. An example of how gusset plate thickness is distributed throughout some of the bridges can be seen in Figure 2.2.2 (Wright, 2009). Joints having secondary plates in addition to the main gusset plate are shown with double circles. Figure 2.2.3 shows a histogram of the gusset plate thicknesses used in 20 bridges. Gusset plate thicknesses less than 3/8" are not seen in any of the bridge plans.

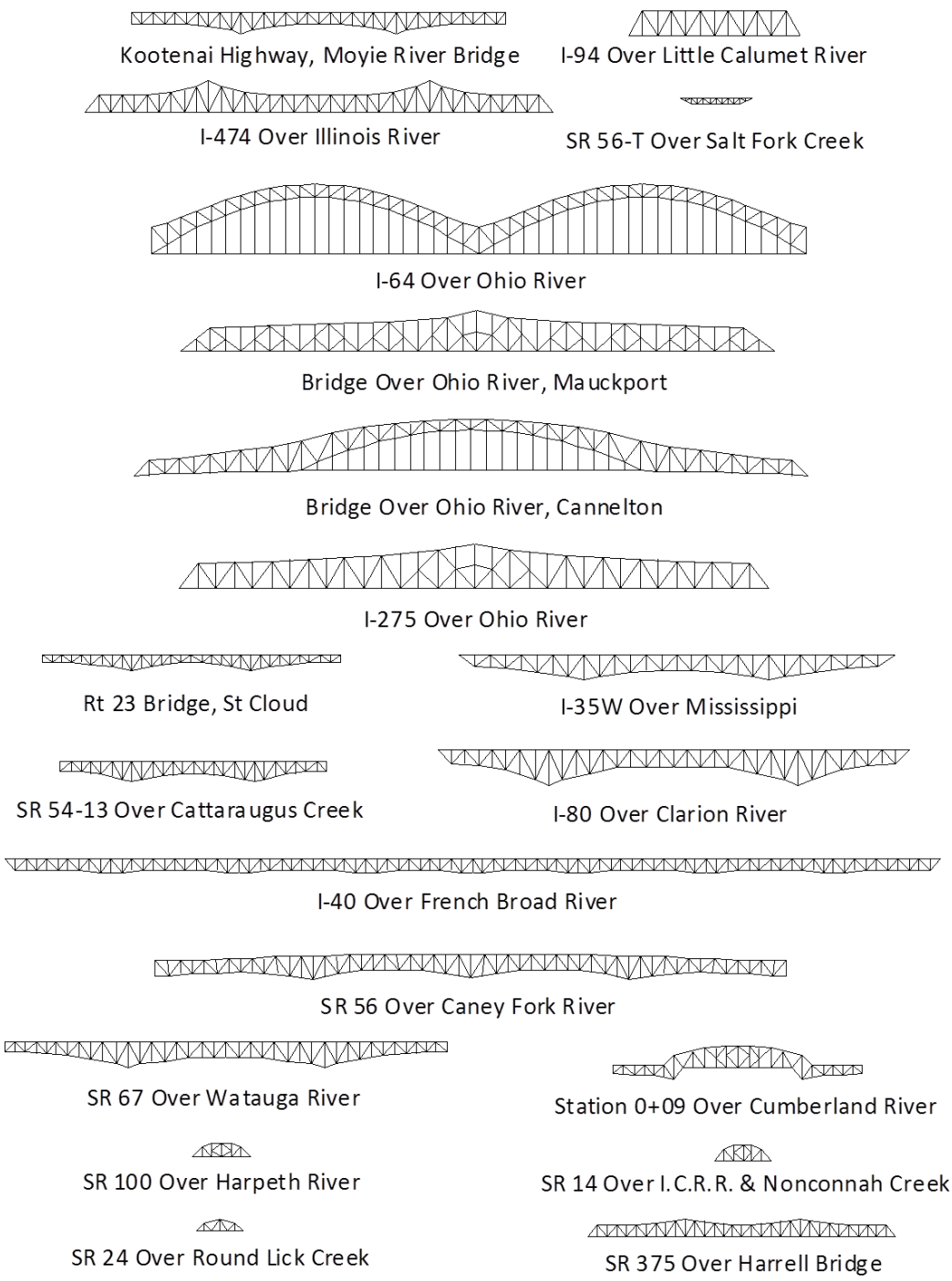

Figure 2.2.1: Configuration of the 20 bridges from various states. The bridges are drawn to same scale to illustrate the relative size (Wright, 2009).

Table 2.2.1: Overview of the 20 truss bridges (Wright, 2009)

BRIDGE	YEAR DESIGNED	STATE	TYPE	SPAN (ft)	GUSSET PLATE STEEL GRADE (ksi)	FASTENER TYPE
Kootenai Highway, Moyie River Bridge	1961	ID	Deck Truss	270-378-270	50	7/8” Rivets or 7/8” A325 bolts
I-94 Over Little Calumet River	1990	IL	Through Truss	420	50	7/8” A325
I-474 Over Illinois River	1970	IL	Through Truss	300 – 540 - 300	36 and 50	7/8” A325
SR 56-T Over Salt Fork Creek	1941	IN	Deck Truss	60 – 120 – 60	36	7/8” Rivets
I-64 Over Ohio River	1959	IN	Trussed Arch	800 – 800	50 and 100	1” A325
Bridge Over Ohio River, Mauckport	1964	IN	Through Truss	725 – 725	50 and 100	1” Rivets
Bridge Over Ohio River, Cannelton	1964	IN	Through-Truss & Trussed Arch	413 – 825 – 413	50 and 100	7/8” Rivets

Table 2.2.1 (continued): Overview of the 20 truss bridges (Wright, 2009)

BRIDGE	YEAR DESIGNED	STATE	TYPE	SPAN (ft)	GUSSET PLATE STEEL GRADE (ksi)	FASTENER TYPE
I-275 Over Ohio River	1976	KY	Through Truss	720 – 720	50 and 100	1” A325 Bolts
Rt 23 Bridge, St Cloud	1955	MN	Deck Truss	219 – 291 – 219	36 and 50	7/8” Rivets
I-35W Over Mississippi	1965	MN	Deck Truss	266 – 456 – 266	50	1” Rivets
SR 54-13 Over Cattaraugus Creek	1954	NY	Deck Truss	175 – 300 – 175	36	7/8” Rivets
I-80 Over Clarion River	1964	PA	Deck Truss	272 – 612 – 272	36 and 50	1” Rivets
I-40 Over French Broad River	1958	TN	Deck Truss	260 – 312 – 312 – 260	50	7/8” Rivets
SR 56 Over Caney Fork River	1947	TN	Deck Truss	387-384-384-387	36	7/8” Rivets

Table 2.2.1 (continued): Overview of the 20 truss bridges (Wright, 2009)

BRIDGE	YEAR DESIGNED	STATE	TYPE	SPAN (ft)	GUSSET PLATE STEEL GRADE (ksi)	FASTENER TYPE
SR 67 Over Watauga River	1946	TN	Deck Truss	300-492-300	36	1” Rivets
Station 0+09 Over Cumberland River	1934	TN	Deck – Through Truss	145-317-145	33	7/8” Rivets
SR 100 Over Harpeth River	1929	TN	Through Truss	100	30	7/8” Rivets
SR 14 Over I.C.R.R. & Nonconnah Creek	1929	TN	Through Truss	140	30	7/8” Rivets
SR 24 Over Round Lick Creek	1938	TN	Through Truss	114 Simple Span	33	7/8” Rivets
SR 375 – Harrell Bridge	1941	TN	Through Truss	235-282-235	36	7/8” Rivets

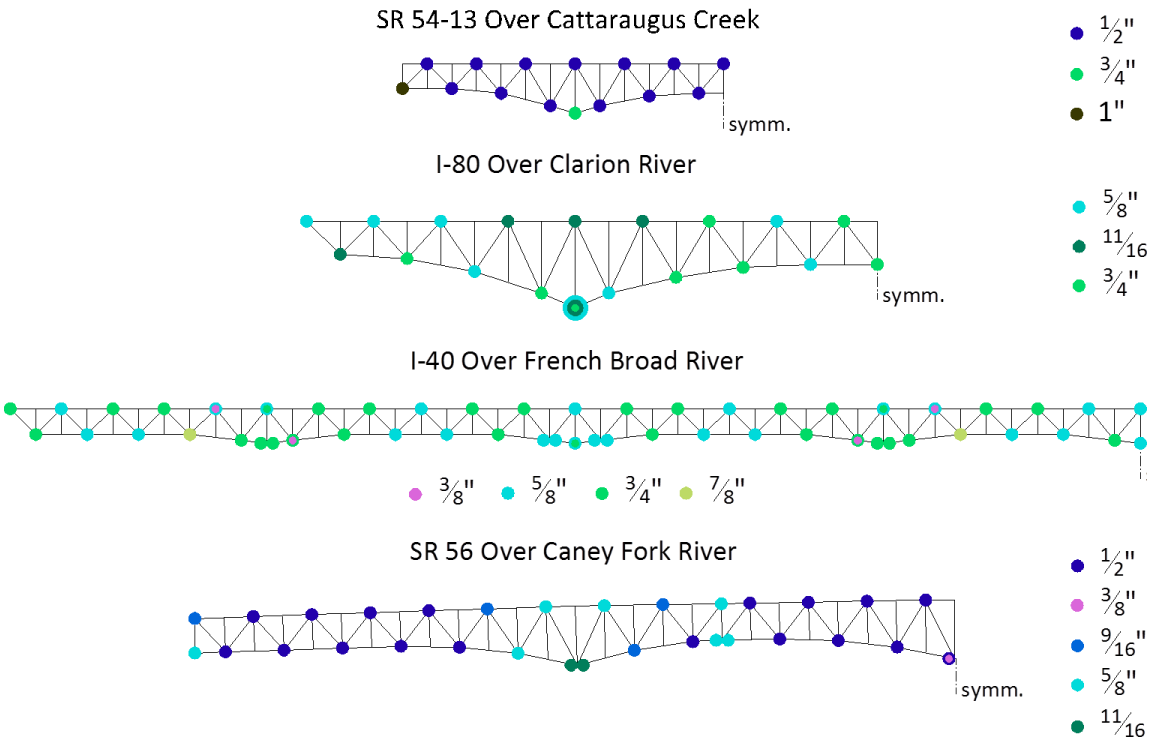

Figure 2.2.2: Gusset plate thicknesses used across four of the truss bridges (Wright, 2009)

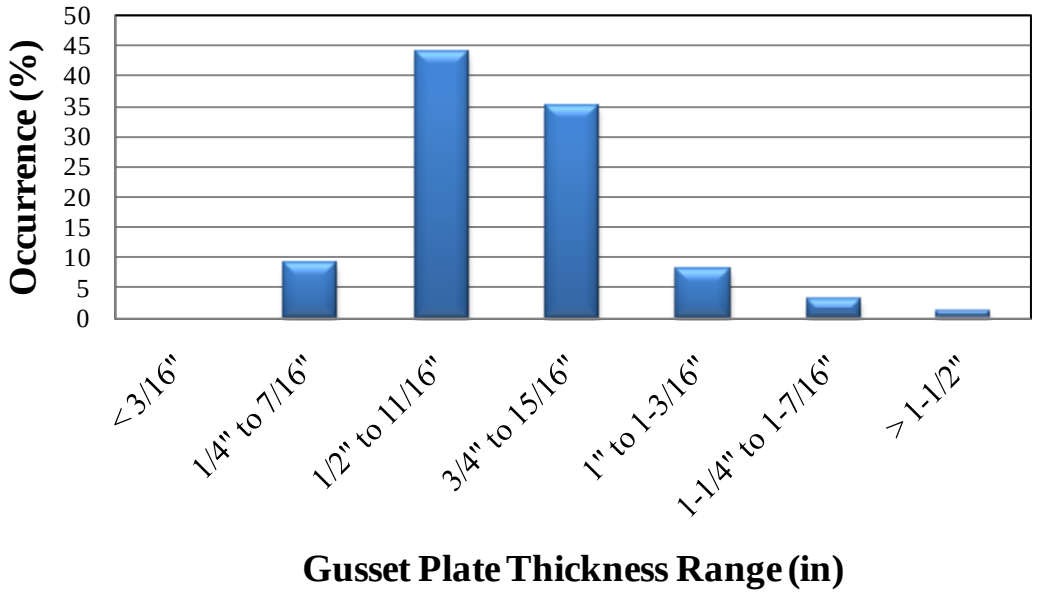

Figure 2.2.3: Histogram plot showing the overall gusset plate thickness distribution for the 20 bridges (smallest gusset plate thickness is 3/8 inch)

2.3. Selection of Representative Joints

From the bridges in Table 2.2.1, four example connections are selected for detailed FEA study (Figure 2.3.1). These four joints are all based on the original design drawings without considering any changes that occurred during the life of the bridge. The forces on some members are changed from the original design, which give only envelope values, to obtain equilibrium in the FEA truss model. In addition, assumptions for the material and fastener models that may not represent actual conditions are made when the information in the design drawings is missing (FHWA, 2009). Specific attributes of each selected connection are explained in detail below:

2.3.1. I-94 Bridge over the Little Calumet River (IL)

The L2 joint from the I-94 Bridge over the Little Calumet River Bridge in Cook County, Illinois is selected. This bridge is a deep truss with a substantially steep (60° from horizontal) angle for the diagonal members. The diagonals have a relatively large distance from the work point of the joint resulting in a relatively long gusset plate free-edge between the compression diagonal and the chord member. This joint is a relatively modern bridge design using high strength bolts (1990).

2.3.2. HW-23 Bridge over the Mississippi River (MN)

The U2 joint from the Highway 23 Bridge over the Mississippi River in St. Cloud, Minnesota is selected since it has relatively flat angles for the diagonal members (37° from horizontal), resulting in a relatively long gusset plate free edge between the diagonal members and the vertical member. The Minnesota Department of Transportation found "buckled" gusset plates in this bridge and it was decommissioned after rating calculations indicated a possible unsafe condition. This bridge is a representative design from the 1950s utilizing welded members and riveted gusset plate connections.

2.3.3. I-40 Bridge over the French Broad River (TN)

The U8 joint from the I-40 Bridge over the French Broad River in Jefferson County, Tennessee is selected since it provides an example with shingle (double) gusset

plates. Similar to the HW-23 Bridge, this bridge also represents a 1950s design with welded members and riveted gusset plate connections.

2.3.4. I-80 Bridge over the Clarion River (PA)

The last connection selected for the preliminary studies is a hypothetical joint used by FHWA to illustrate the guidance checks. The connection is a modification of the L3 joint in the I-80 Bridge over the Clarion River in Pennsylvania. FHWA made changes to the joint to facilitate the illustration of the guidance provisions. These changes include the angle of chord members, the reduction in gusset plate strength from 50 to 36 ksi, and an increase in member forces as compared to the original design.

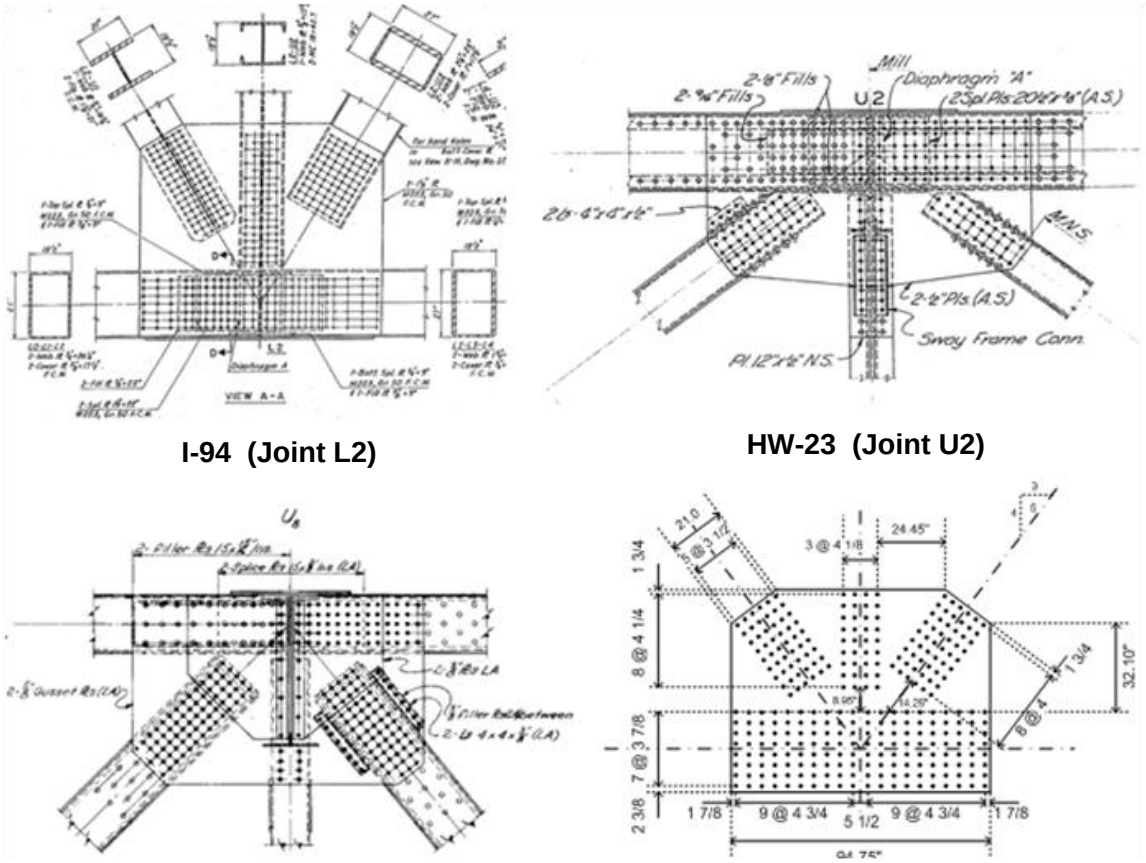

Figure 2.3.1: Four representative bridge joints selected for preliminary studies

CHAPTER III : TEST SIMULATION OF THE REPRESENTATIVE TRUSS JOINTS

3.1. Finite Element Methodology

In this chapter, the representative joints selected from the bridge plans in Section 2.3 are modeled using Abaqus FEA software (Simulia, 2009). Material and geometric nonlinearities are included in all the 3-D FEA studies. As noted in Chapter 2, equilibrium requires some modifications to the loads transferred to each joint. Each connection is modeled as a two-panel truss subassembly, with the joint located in the middle panel point of the subassembly. . Stable and statically-determinate boundary conditions are provided to the subassembly. In the models, the bolt/rivet holes are not modeled explicitly. However, the locations of the fasteners are determined from the bridge design drawings and members are connected using connector elements and corresponding fastener properties at these locations. Since the plates are modeled at their mid-thickness, the connector elements connect the centerlines of the plates (Figure 3.1.1).

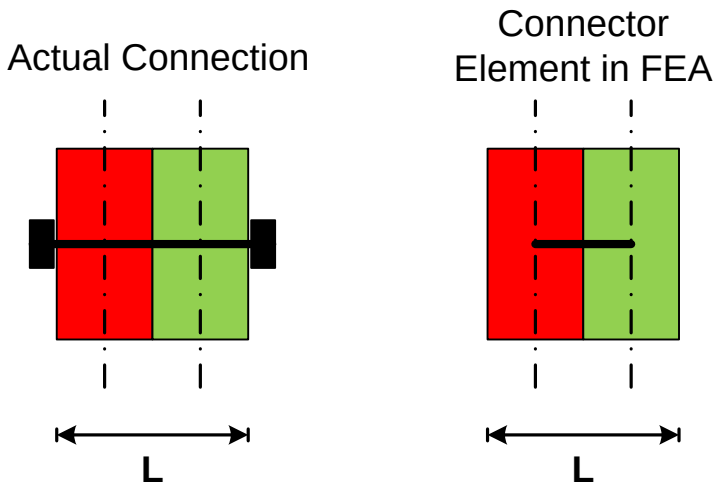

Figure 3.1.1: Connector element in the FEA models

By using connector elements, the nonlinear load-deformation and slip behavior of the fasteners can be modeled explicitly. When the fasteners connect three or more plates, these fasteners include two or more layers of connector elements. The fastener model used is the “CARTESIAN” plus “ALIGN” connector element in which three rotations are

restrained and thus only the three translational degrees of freedom are available (Figure 3.1.2).

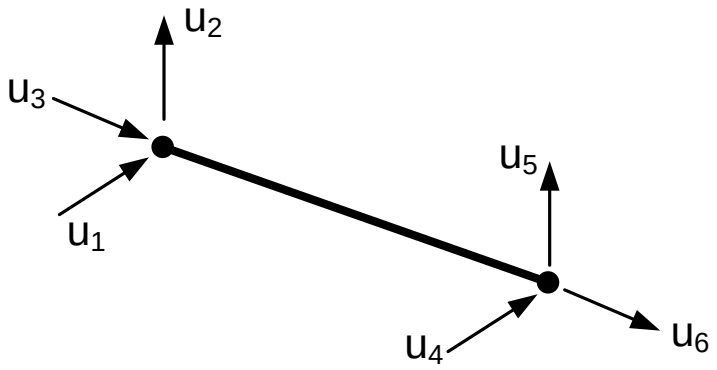

Figure 3.1.2: Degree of freedoms for the connector elements

For the in-plane fastener behavior, both the elastic and plastic properties of the bolts are modeled using the connector elements. Nonlinear load-deformation behavior of the bolt response is assigned to the two in-plane shear components of the connector elements. In the finite element model, a criterion is set which calculates the vector sum of the two in-plane components and when this absolute sum reaches the maximum fastener force, that fastener basically loses its ability to carry more load. The nonlinear bolt behavior is basically assigned to this derived component. For the out-of-plane component, elastic behavior is assumed with a stiffness of EA/L, where E is Young's modulus, A is the cross-section area of a fastener, and L is the total length of a fastener. This component does not become the dominant component of the fastener response as compared to the in-plane shear response in the direction of the applied loads. Hence, using the total length of the connected layers can be used as the "L" in this formula.

3.1.1. Geometry and Boundary Conditions

The gusset plates and splice plates in the joint under consideration are modeled using four-node shell elements. The truss members connected to the gusset plates are modeled using four-node shell elements up to a distance equal to *2d* from the edge of the gusset plate (*d* is the member depth). The rest of these members and all the other members that are not connected to the joint are modeled using two-node beam elements. The beam portion of each member is connected to the shell portion by using beam type

multi-point constraints (MPCs) in the Abaqus software. This approach improves the efficiency by reducing computation time of the finite element analysis. Figure 3.1.3 shows an example finite element subassembly created for the L2 joint from I-94 bridge. The applied forces are determined such that equilibrium is satisfied at the joint utilizing the design forces for the compression diagonal and chord closest to the compression diagonal. The design forces for the remaining three members are kept as close as possible to the design forces reported in the original plans of the selected bridges. Roller and/or hinge boundary conditions are assumed in the plane of the truss such that the sub-assembly is supported in a stable and statically-determinate fashion, and out-of-plane restraints are assigned at the truss nodes with the exception of the joint under consideration. These out-of-plane restraints are sufficient such that the failure by gross out-of-plane movement at the study joint does not occur.

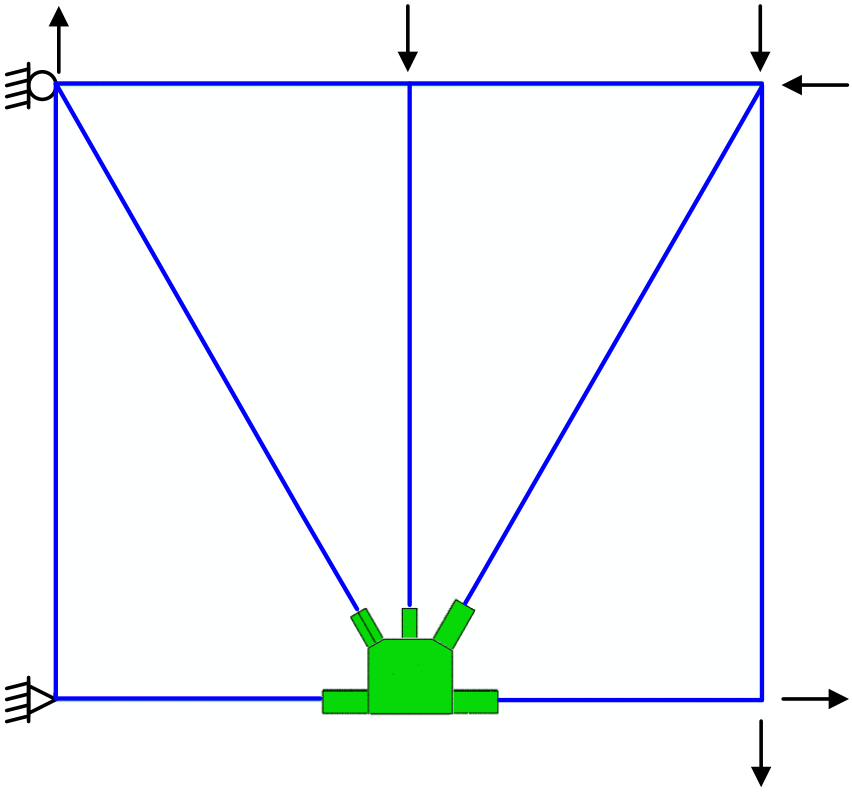

Figure 3.1.3: Finite element model of the two panel truss sub-assembly system for L2 joint of the I-94 bridge (elevation view)

3.1.2. Material Properties

Nonlinear material properties are assigned to the gusset plate, splice plate, and where applicable, the diaphragm plates. However, the members are assumed to be elastic in all cases. The main reason behind this choice is to focus on the gusset plate behavior and provide information on potential failure modes in the gusset plate itself. If the inelastic behavior of the members is considered in the trusses discussed in Section 2.3, several of the members typically fail before the strength limit of the gusset plates is reached. Any other failure modes possible in the connected members such as member local buckling, or in the truss subassembly due to global buckling in truss members are eliminated with the modeling approach used in this research. Figure 3.1.4 shows the true (Cauchy) stress vs. true (log) strain relationship created by the research team for Grade 36 and Grade 50 materials used in the finite element analysis of the representative bridge joints.

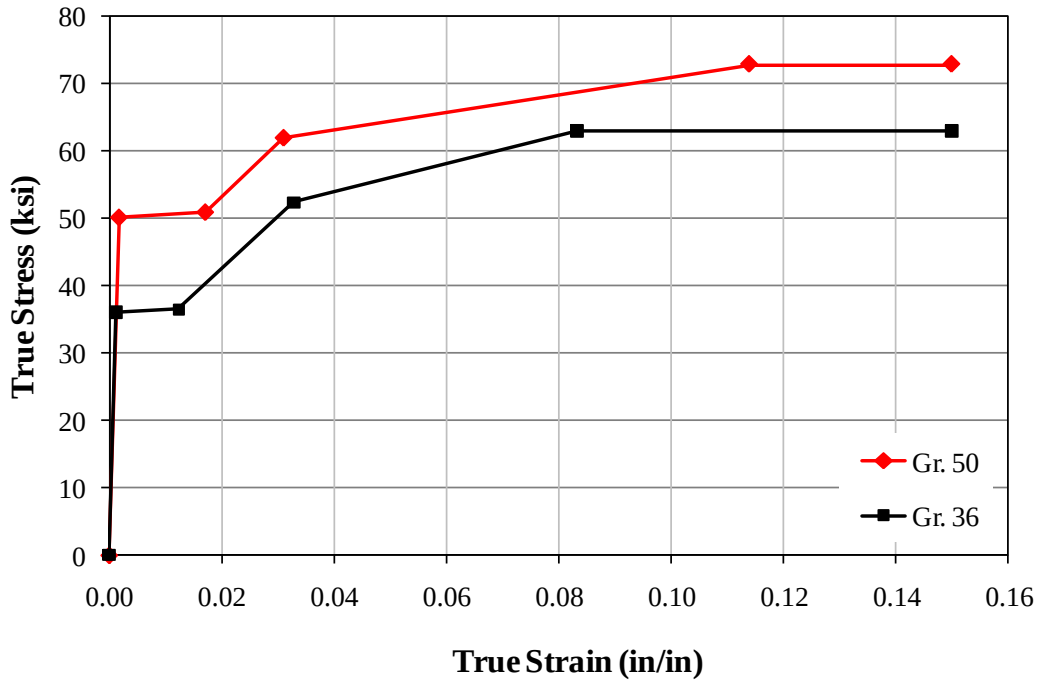

Figure 3.1.4: Grade 36 and Grade 50 steel material properties used in the finite element models of the four example joint

The finite element models simulate the physical bridge configuration in terms of connected members, gusset plates, splice plates and corresponding material properties.

The other major component of the connection is the fasteners (bolts or rivets) as discussed previously. Fastener properties are assigned to the connector elements, including a radius of influence, within which the displacements are constrained to those of the fastener elements. The radius of the bolt heads is used for the radius of influence in the finite element models in this study. Figure 3.1.5 shows the fastener force vs. displacement relationship for the four different fastener types used to model the representative bridge joints. These curves extended from the experimental tests performed in the past. Nonlinear fastener properties, which include the deformations due to both bolt hole ovalization and shear deformation of the fasteners, are assigned for the in-plane slip behavior. The axial stiffness of fasteners is assumed to be elastic.

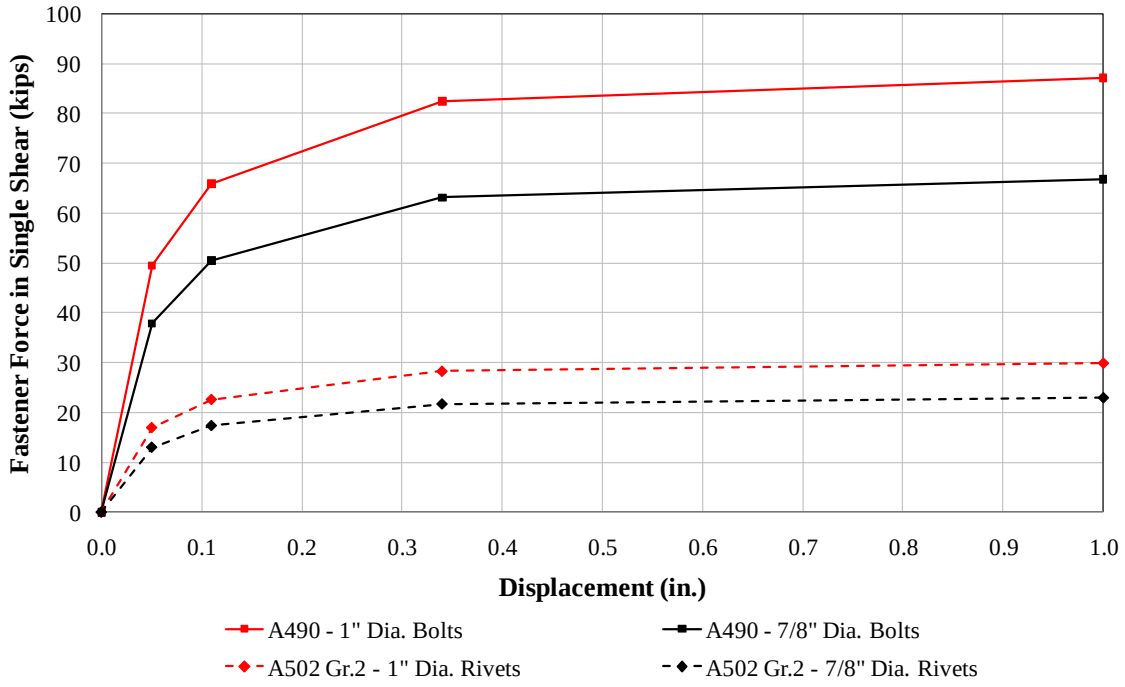

Figure 3.1.5: Fastener force vs. displacement relationship in single shear for the bolts and rivets used in the finite element models of the four example joints

3.1.3. Initial Imperfections

The resistance of structural components subjected to compression generally is affected to some degree by unavoidable initial geometric imperfections. In the studies of the four representative joints discussed in Section 2.3, several patterns and magnitudes of geometric imperfections are considered to study the impact of the geometric

imperfections on the gusset plate capacity. The largest reduction in the maximum joint capacity is observed when both gusset plates have an out-of-plane imperfection in the same direction on the compression diagonal side. When equal and opposite imperfections are applied in the two plates, plates fail in a symmetrical pattern and this provides a higher load capacity compared to the case with imperfections applied in the same direction. Effect of the maximum imperfection magnitude is also discussed in Section 3.1.5 where the analysis results for the four representative joints are explained in more detail.

To generate the geometric imperfections, corner nodes at the end of the chord members, tension diagonal, and vertical member along with the edges next to the vertical member and above the chord member on the compression diagonal side of the gusset plate are restrained out-of-plane in a pre-analysis. All the members except the compression diagonal are maintained in their ideal geometry by applying these boundary conditions. Figure 3.1.6 shows these additional boundary conditions. A uniform pressure load is then applied to the gusset plates on the side with the compression diagonal. The area of pressure application in the imperfection analysis models is shown in Figure 3.1.7.

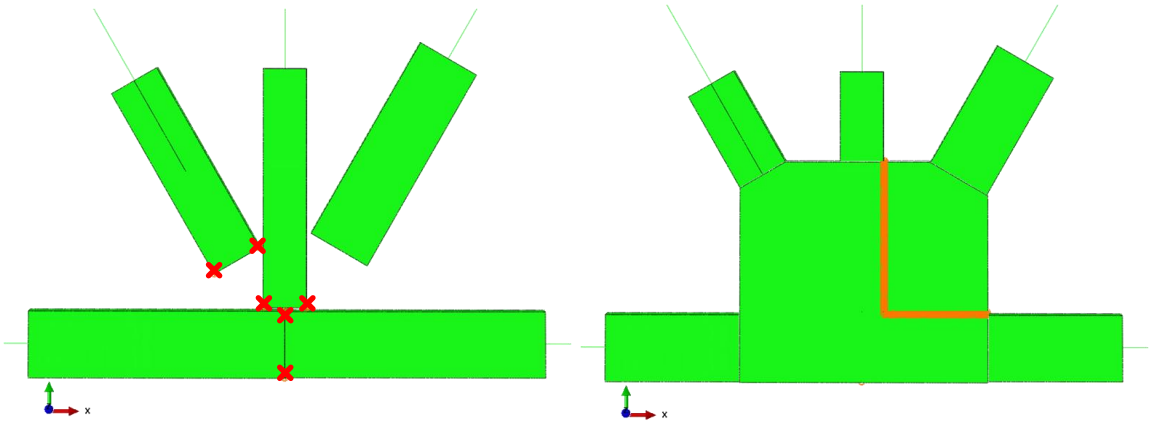

Figure 3.1.6: Boundary conditions applied in the imperfection model

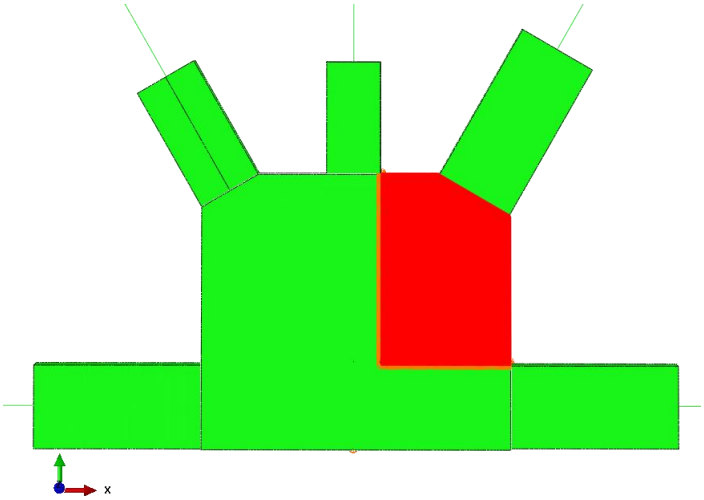

Figure 3.1.7: Area of applied pressure to create the initial out-of-plane imperfection in the gusset plates

A linear static pre-analysis is performed to obtain the initially imperfect shape and corresponding displacement field for all the assembly nodes. Out-of-plane displacement contours for the four example joints are shown in Figure 3.1.8 through Figure 3.1.11. The scale factor for the initial imperfections to be used in the nonlinear finite element analysis is selected so that the maximum imperfection in the gusset plates is limited to the selected imperfection magnitude when used in the main analysis. For example, the initial imperfection contours of the L2 joint from the I-94 Bridge in Figure 3.1.8 show that the maximum out-of-plane displacement in the pre-analysis is 5.309 inch. To match a target maximum out-of-flatness of 1/4" on the gusset plates, a scale factor of 0.0471 is used.

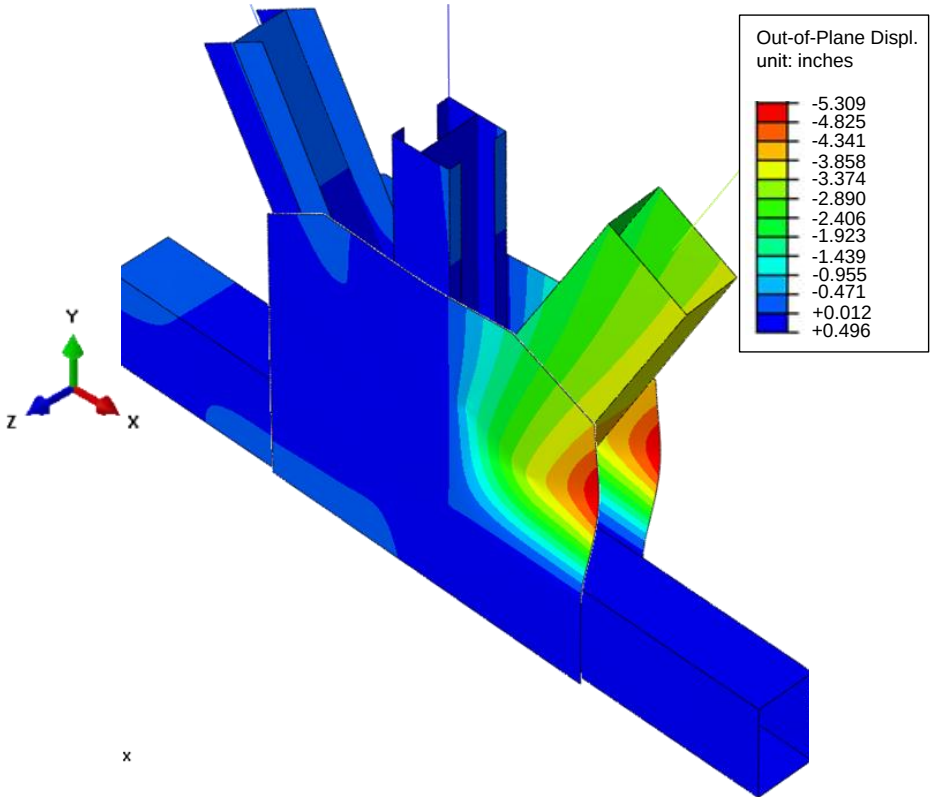

Figure 3.1.8: Initial imperfection shape applied in the nonlinear finite element analysis of the L2 joint from the I-94 bridge

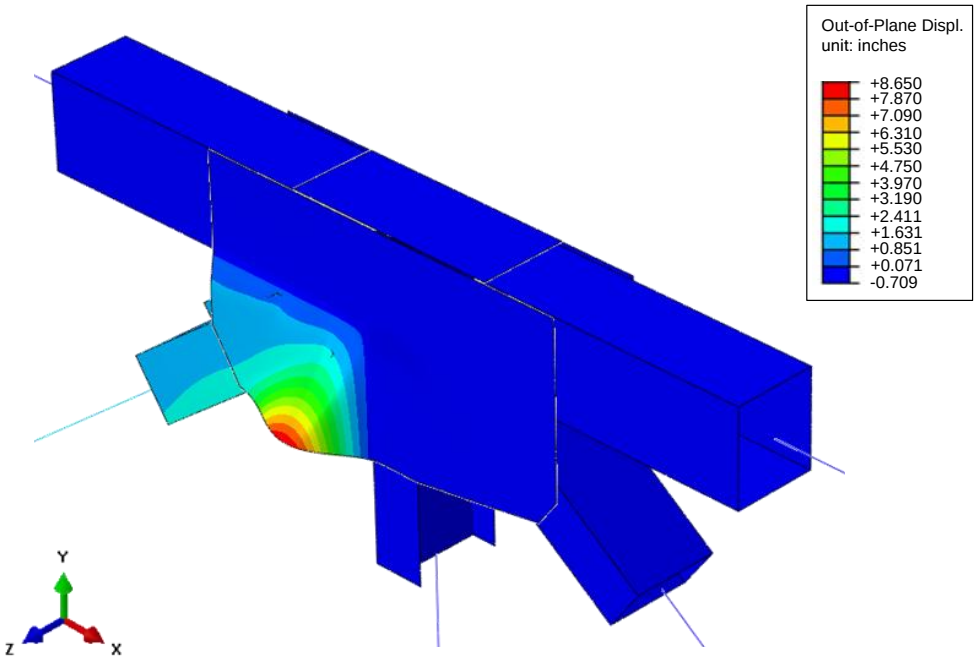

Figure 3.1.9: Initial imperfection shape applied in the nonlinear finite element analysis of the U2 joint from the HW-23 bridge

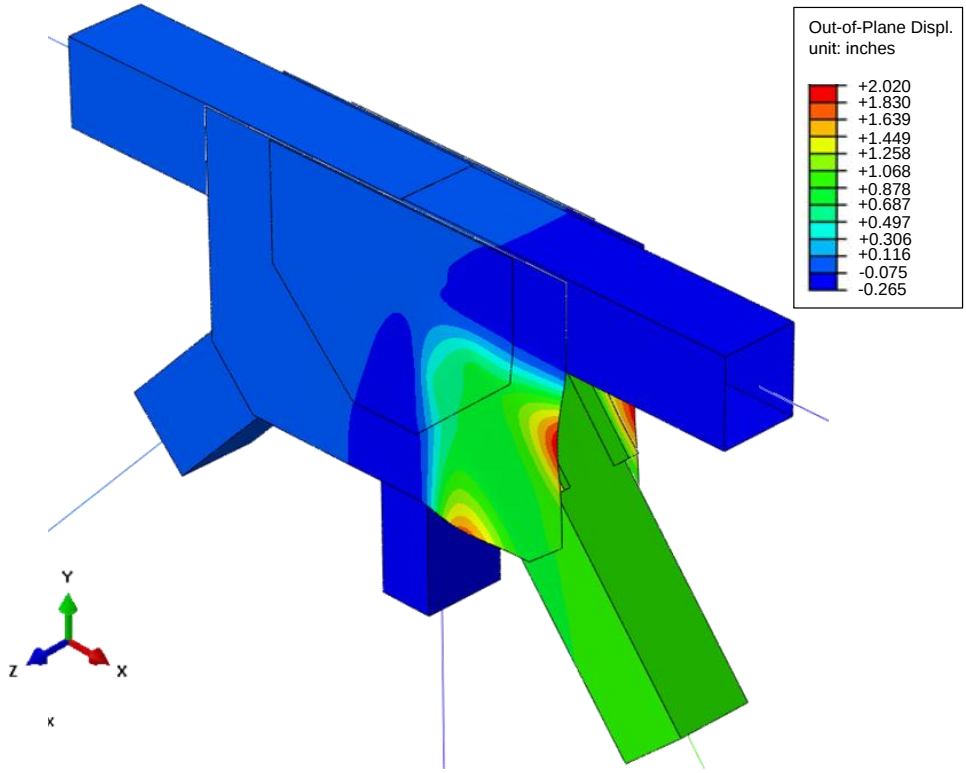

Figure 3.1.10: Initial imperfection shape applied in the nonlinear finite element analysis of the U8 joint from the I-40 bridge

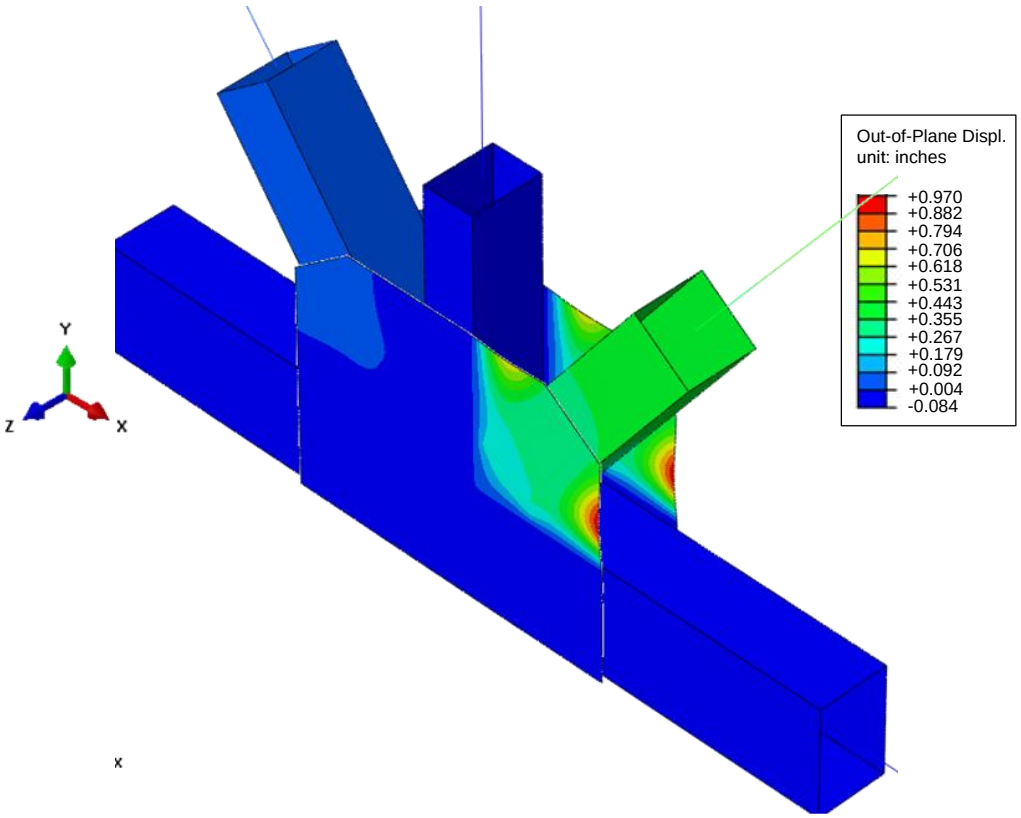

Figure 3.1.11: Initial imperfection shape applied in the nonlinear finite element analysis of the L3 joint from the I-80 bridge

3.1.4. Analysis Procedure

Nonlinear finite element analyses are performed of the four joints discussed in Section 2.3 using the nodal loads calculated from the original design drawings. Both dead load (D) and live load plus dynamic load allowance or impact (L+I) are imposed on the truss members using the appropriate load factors for LRFD STRENGTH I load combination. The member forces in the model are set so that the forces exactly match the envelope values for the compression diagonal and the chord member nearest to it. Adjustments are required for the forces in the remaining three members relative to the values on the engineering drawings to satisfy the joint equilibrium (the forces on the engineering drawings are envelope values). The main reason for the equilibrium mismatch is the force in the vertical member of the truss. For trusses with parallel top and bottom chords, this is ideally a zero force member or it is subjected to relatively small loads directly applied from the deck system of the bridge.

The analysis is implemented in two steps. First, the factored dead load is applied to the truss nodes. Second, the factored live load plus impact load is incrementally applied. For the L23 joint from I-80 bridge, there is an additional load (DW) integrated into the model based on the information obtained from the FHWA guide. From the analysis, the total factored load at any stage of the loading for the first three joint analyses can be calculated using the equation:

$$P_{FEA} = \gamma_D(D) + ALF\left[\gamma_{L+I}(L+I)\right] \quad \text{(Eq. 3.1-1)}$$

Similarly, the total factored load for the L3 joint from I-80 bridge can be calculated using the equation:

$$P_{FEA} = \gamma_D(D) + \gamma_{DW}(DW) + ALF\left[\gamma_{L+I}(L+I)\right] \quad \text{(Eq. 3.1-2)}$$

ALF is the Applied Load Fraction (i.e., the multiple) of the factored L+I loads applied at a given stage of the finite element analysis. The load factors are taken as γ_D = 1.25, γ_{DW} = 1.50 and γ_{L+I} =1.75 corresponding to the STRENGTH I limit state.

3.1.5. Limit of Maximum Useful Resistance

If the members are modeled with their actual material properties, the gusset plates can not be loaded to their maximum capacity. In that case, the members become the first components to fail. In the finite element analysis models, the intent is to focus on the gusset plate behavior by applying nonlinear material properties to the plate elements only. Thus, the members are kept in the elastic regime and joint is loaded up to their maximum resistance.

The primary mode of failure in the finite element model is difficult to define in most cases since multiple failure modes are often occurring simultaneously. However, the analyses show that a significant amount of the gusset plate material reaches the yield strength limit based on the von Mises yield criterion prior to the ultimate load. Four different load levels are determined on the load vs. displacement plots from each joint. It

is important to decide the load level at which the gusset plate reaches its maximum capacity. However, the gusset plate may reach a "limit of maximum useful resistance" prior to achieving a limit load in the analysis due to other factors such as significant plasticity or excessive fastener displacement. Therefore, the following four load levels are considered in assessing the joint response:

3.1.5.1. STRENGTH I Load Limit

This limit corresponds to the ALF (applied load fraction) of 1.0 which is basically the application of full live plus impact load on the joint, after the joint is subjected initially to the specified dead load.

3.1.5.2. 4% Equivalent Plastic Strain (PEEQ) at Mid-Thickness

In the finite element models, the actual bolt holes are not modeled and no fracture of the steel is not incorporated into the material models. Hence, the models can not capture the tension fracture, shear fracture or block shear tearout limit states. The gusset plates undergo significant amount of plasticity beyond the STRENGTH I limit. One criterion selected to indicate when ductile fracture may start to be of concern is the maximum equivalent plastic strain at the mid-thickness of the plates. This value is arbitrarily set at 4%, which is a common limit at which the strains may be considered as large.

3.1.5.3. 0.2 inch Fastener Shear Displacement

The fastener models used in the analyses are also nonlinear. The ALF value at a fastener shear displacement of 0.2" is decided to be a practical limit of fastener useful resistance. Fastener shear fracture may start to be of concern for shear displacements beyond this limit.

3.1.5.4. Peak of the Load vs. Displacement Curve

In general, the load vs. displacement curve from the analysis has a loading and a post-peak unloading path. The peak ALF value from this plot is another important limit for the joint response.

The smallest load level at which the limits described in 3.1.5.2 thru 3.1.5.4 are reached is defined as the maximum useful limit of resistance of the joints in this research.

3.2. Analysis Results

This section discusses the observations from the nonlinear finite element analysis performed on each of the joints described in Section 2.3. A brief summary on the initial imperfection sensitivity and stress and strain distributions within the gusset plates at the STRENGTH I and ultimate resistance levels are provided respectively. As the FEA model does not always create output exactly at ALF = 1.0 , the load step closest to 1.0 is chosen as the STRENGTH I load level for output of the stresses and strains. All stress contours in this section are presented as the von Mises stress to show the combined effect of all the stress components toward yielding. In addition, the equivalent plastic strain contours (PEEQ contours) are presented to show the plasticity patterns and degree of yielding in the gusset plates.

3.2.1. I-94 Bridge (Joint L2)

Figure 3.2.1 shows the factored dead loads (1.25D) applied in the first step of the finite element analysis for Joint L2 of the I-94 Bridge. The numbers in parentheses indicate the design loads for members L1L2 and L2U1 as shown on the original plans. For equilibrium of the joint L2, the forces in these members are changed to 1136 kips and 1266 kips respectively.

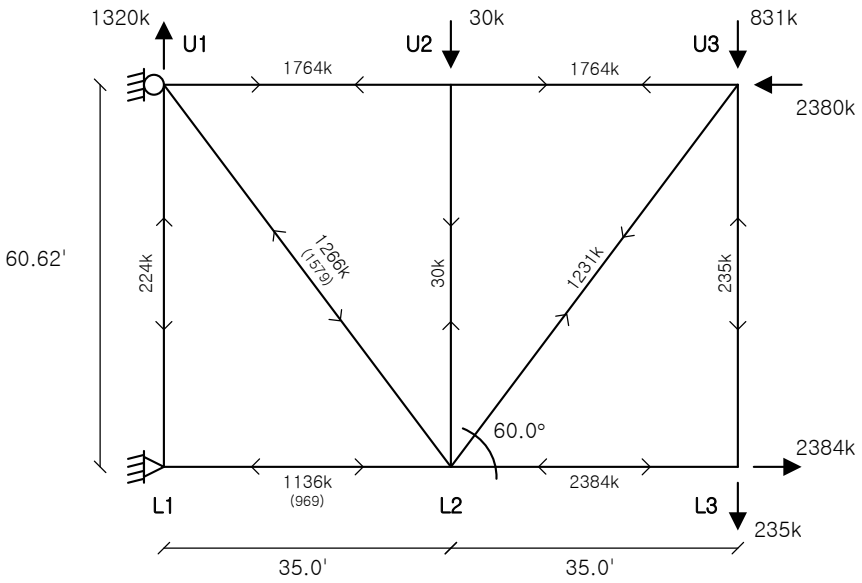

Figure 3.2.1: Factored dead loads (1.25D) for L2 joint

Similarly, Figure 3.2.2 shows the factored loads [1.75(L+I)] that are incrementally applied in the second step of the analysis. To satisfy joint equilibrium, the forces in members L1L2 and L2U1 are changed to 277 kips and 413 kips respectively.

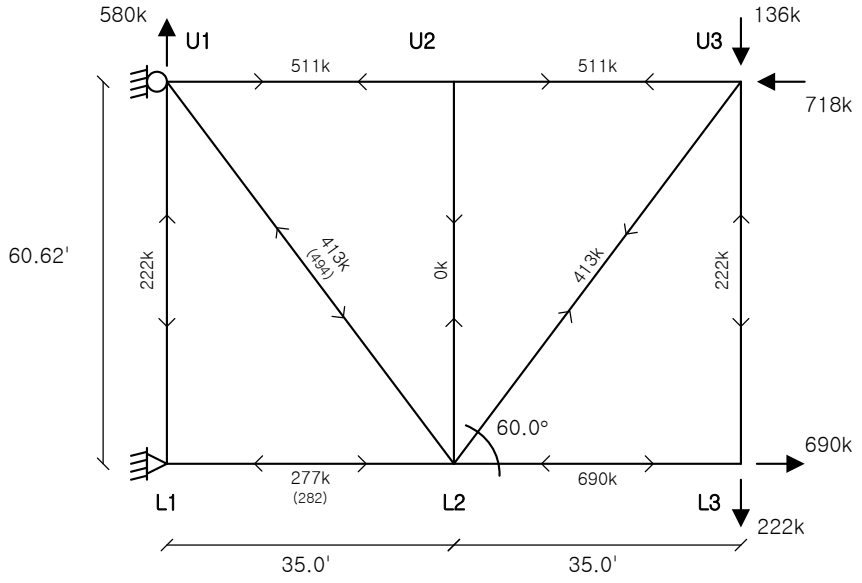

Figure 3.2.2: Factored live and impact loads [1.75(L+I)] for L2 joint

Since the initial imperfection applied to the model on the compression diagonal side of the plate pushes the compression diagonal and the free edges out-of-plane, the applied load fraction of the 1.75(L+I) vs. out-of-plane displacement relationship is investigated at three points (points 2,5,and 6) on the gusset plate as shown in Figure 3.2.3. The applied

load fraction vs. displacement plot shown in Figure 3.2.4 shows that out-of-plane displacement dramatically increases just after the peak of the curve. This result shows the out-of-plane nature of the failure.

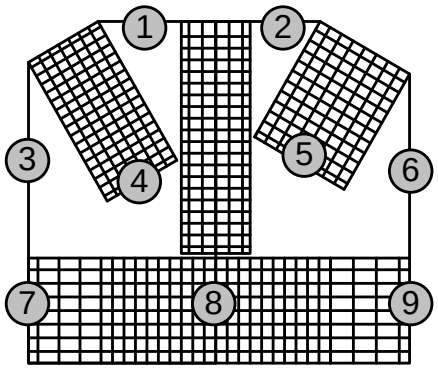

Figure 3.2.3: Node numbering used to get output from the L2 joint gusset plate

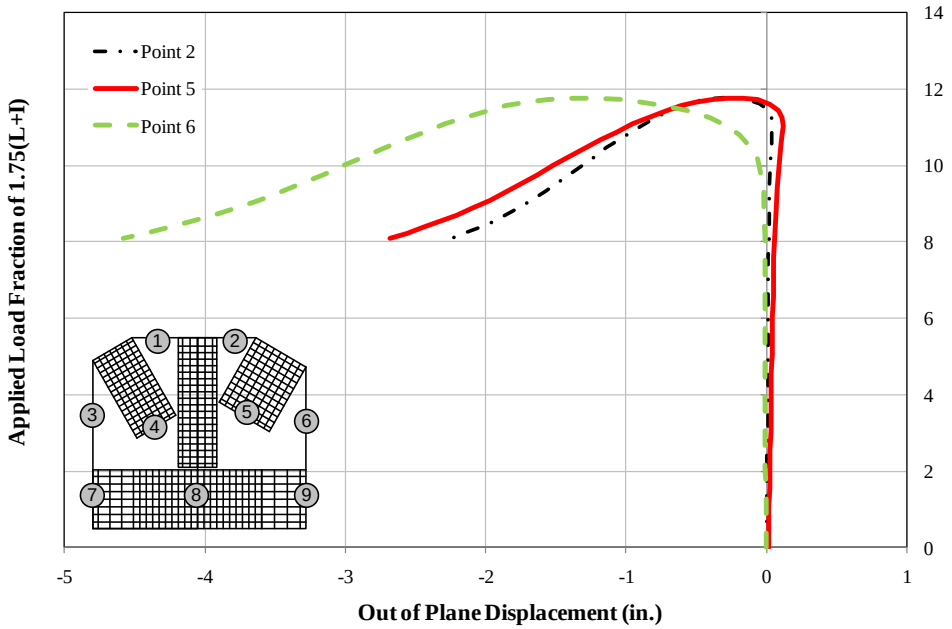

Figure 3.2.4: Applied load fraction of the factored live+impact loads [1.75(L+I)] vs. out-of-plane displacement relationship for L2 joint

To see the effect of initial imperfections on the joint capacity, 0", 1/8", and 1/4" maximum initial imperfection values are applied. Figure 3.2.5 shows how the peak load level decreases from 11.77 to 10.11 (-14%) with the application of the 1/8" maximum initial imperfection on the gusset plate. However, as the imperfection increases, the influence does not increase proportionally. When the imperfection is doubled to 1/4", the

peak load level reduces to 9.72 (-17%), only an additional -3 % change. The curves shown in Figure 3.2.5 correspond to Point 6 on the gusset plate.

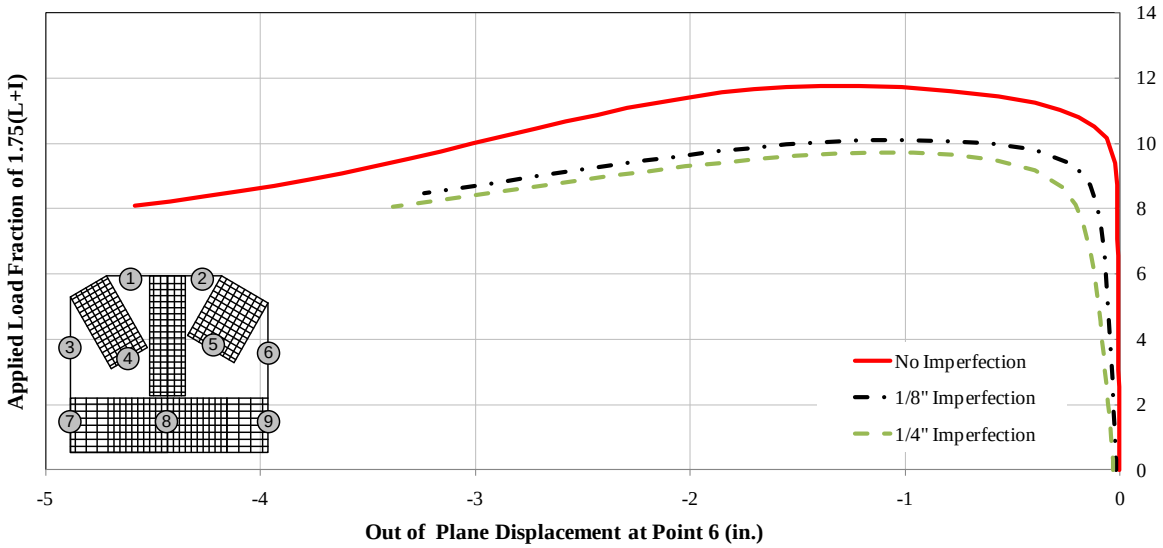

Figure 3.2.5: Effect of initial imperfection on the ultimate resistance of the L2 joint

The results for the model with the 1/4" maximum initial imperfection are discussed below. Based on the criteria defined at the beginning of this chapter, important load levels are identified on the ALF vs. out-of-plane displacement plot as shown in Figure 3.2.6. ALF=1.05 is taken as the STRENGTH I load level at which full dead and live loads are applied on the joint (i.e., this is the load level closest to ALF = 1.0). For this joint, the 4% PEEQ is reached just after the peak load. As shown in Figure 3.2.6, there is a considerable amount of reserve capacity beyond the STRENGTH I load level.

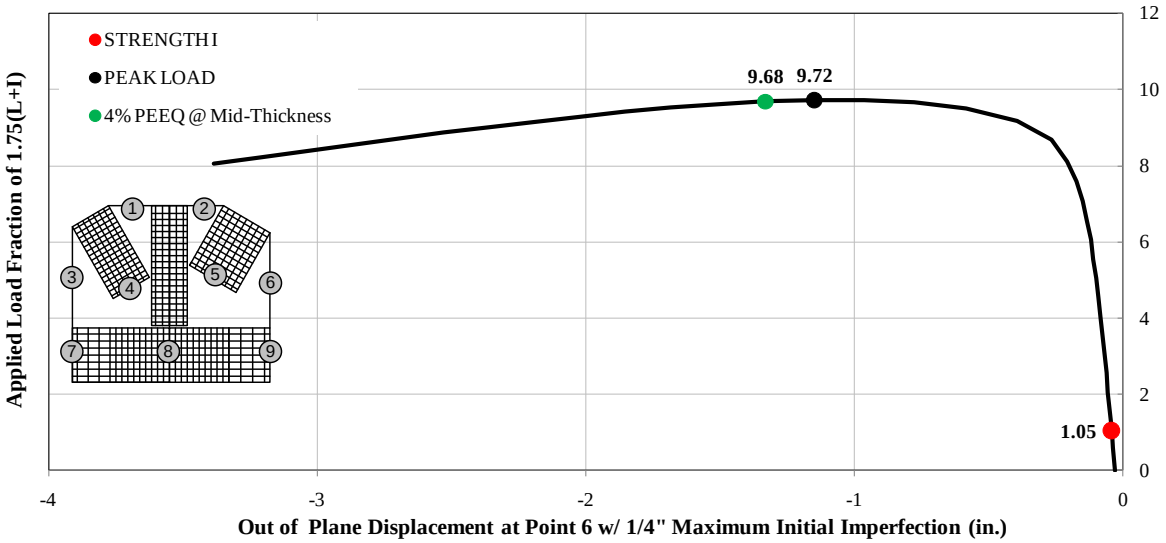

Figure 3.2.6: Different applied load fraction levels on the out-of-plane displacement behavior for point 6 on the gusset plate

Figure 3.2.7 shows the von Mises stresses in the connection when ALF = 1.05. This corresponds to the point labeled STRENGTH I in the ALF vs. displacement plot shown in Figure 3.2.6. The maximum stress in the gusset plate is approximately 25 ksi, or about half of its yield strength. Figure 3.2.8 confirms that the stress level is below yield and there is no plastic strain occurring in the gusset plate at this load level.

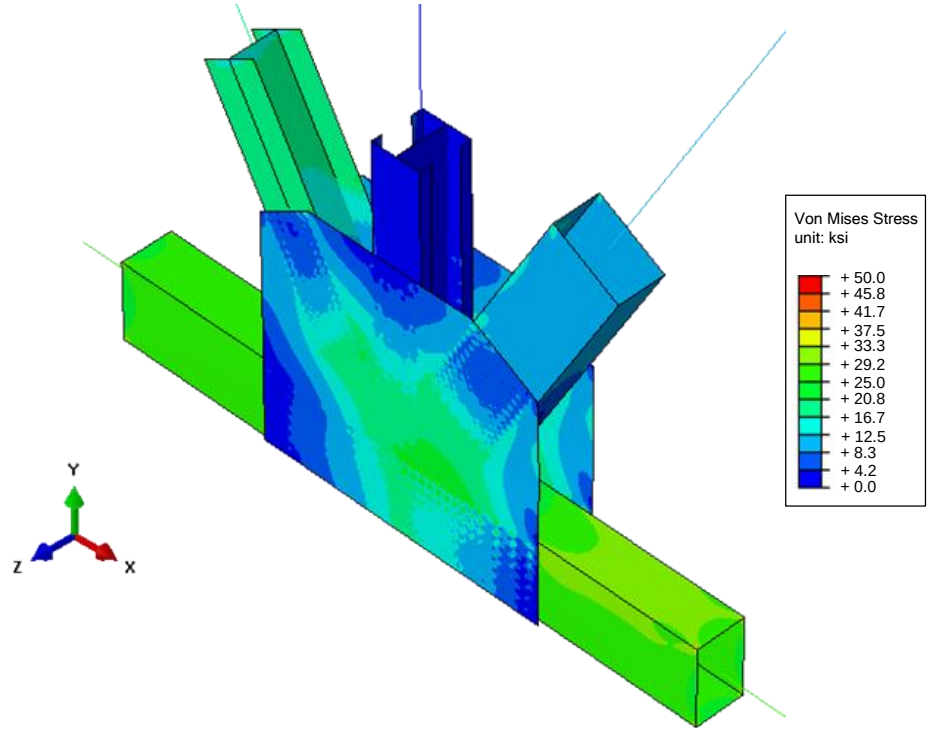

Figure 3.2.7: von Mises stress response contours at STRENGTH-1 level (ALF=1.05)

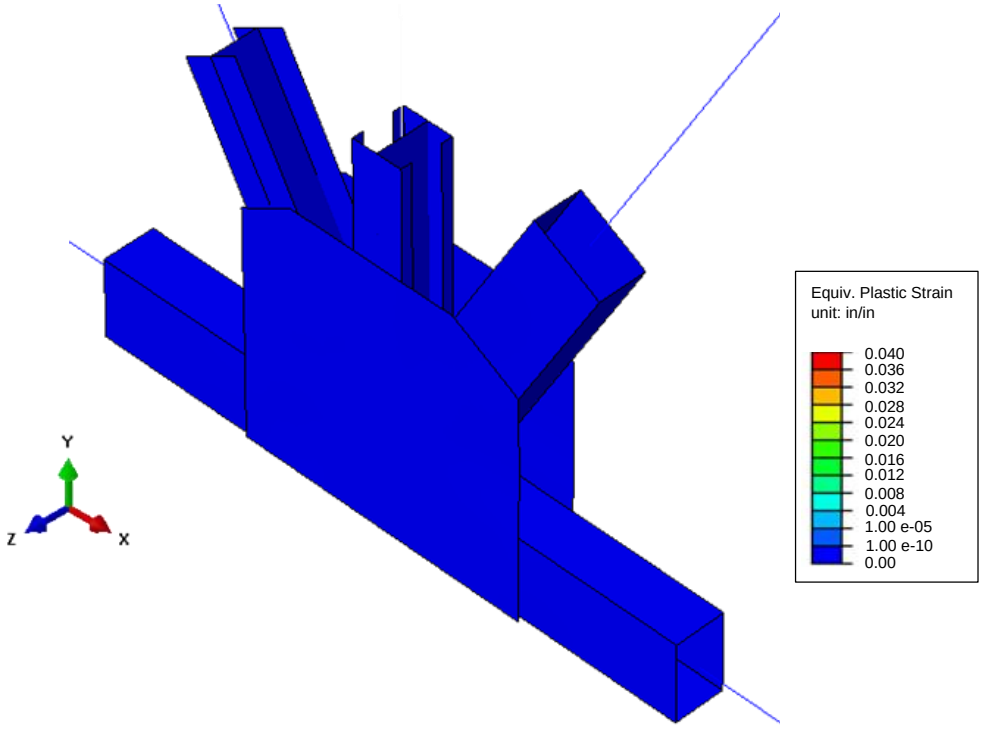

Figure 3.2.8: Equivalent plastic strain response contours at STRENGTH-1 level (ALF=1.05)

The von Mises stress state in the gusset plate corresponding to the limit load at ALF = 9.72 is shown in Figure 3.2.9. The plate has reached its yield strength at its mid-thickness at areas shown with the grey contours. Figure 3.2.10 shows the corresponding equivalent plastic strain contours. The material that is still elastic is shown as dark blue, while the light blue and green areas indicate the variation in magnitude of the plastic deformations. The largest amount of plastic deformation occurs in the region between the compression diagonal and the chord member. The displaced shape, shown in both figures with a deformation scale factor of 5.0, confirms that the final joint mode of failure is out-of-plane compression buckling of the gusset plate.

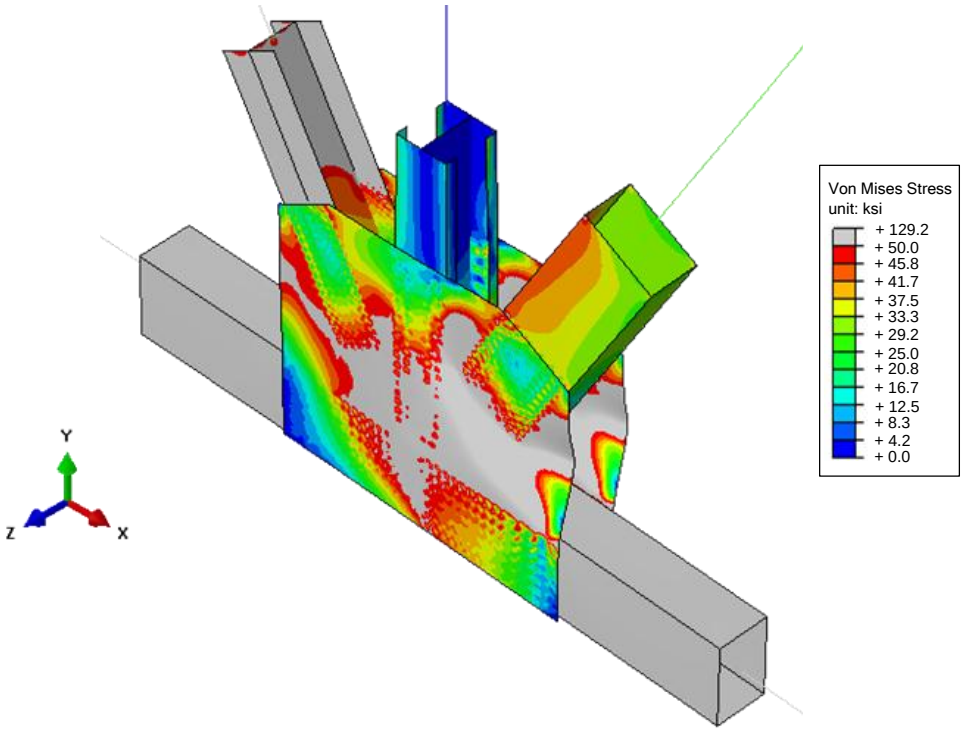

Figure 3.2.9: von Mises stress response contours at the limit load (ALF=9.72)

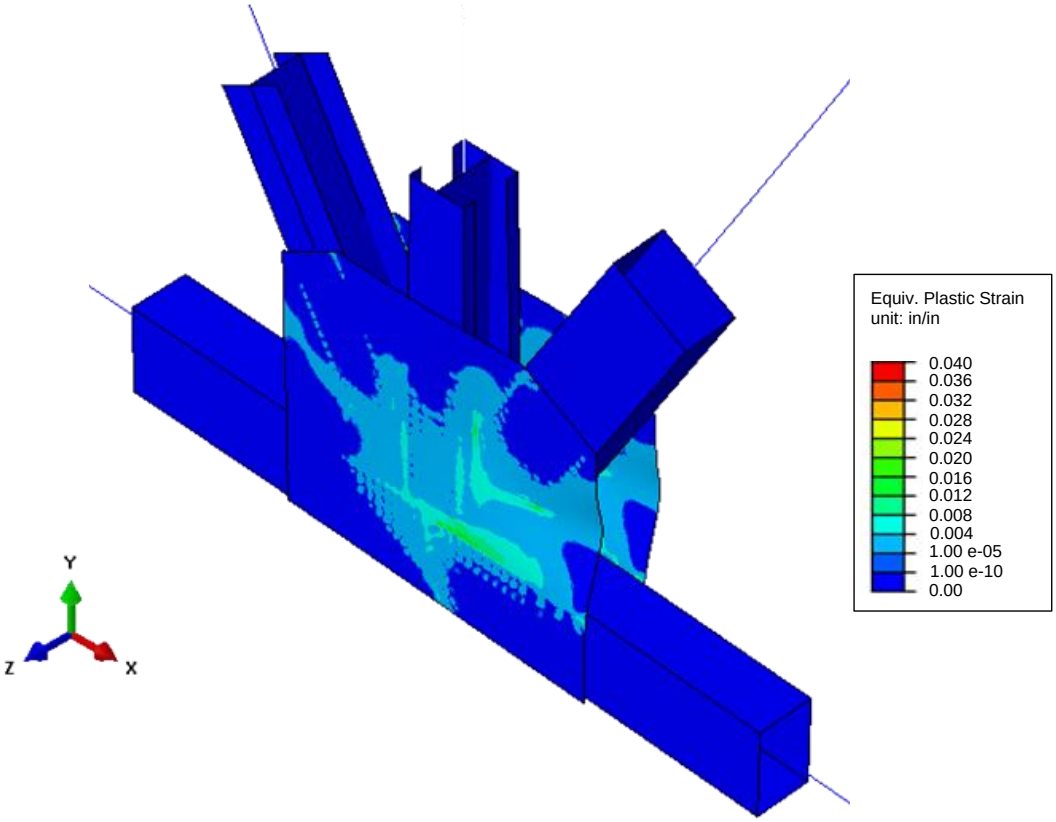

Figure 3.2.10: Equivalent plastic strain response contours at the limit load (ALF=9.72)

3.2.2. HW-23 Bridge (Joint U2)

Figure 3.2.11 and Figure 3.2.12 summarize the test configuration for Joint U2 of the HW-23 bridge and show the applied factored loads 1.25D and 1.75(L+I). For the joint equilibrium, the 1.25D force in member U2U3 is changed to 1070 kips and 1149 kips respectively.

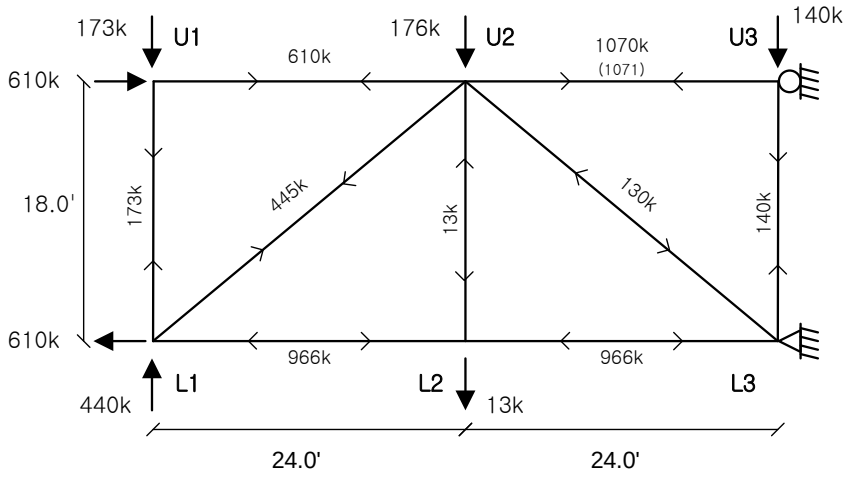

Figure 3.2.11: Factored dead loads (1.25D) for U2 joint

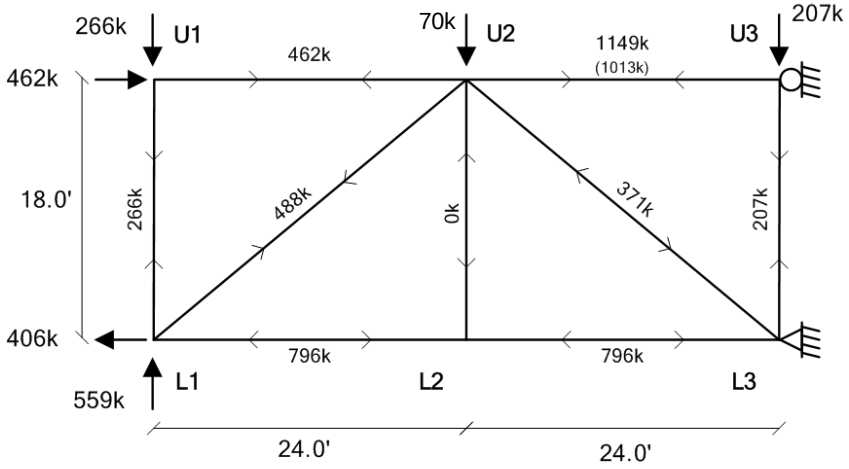

Figure 3.2.12: Factored live and impact loads [1.75(L+I)] for U2 joint

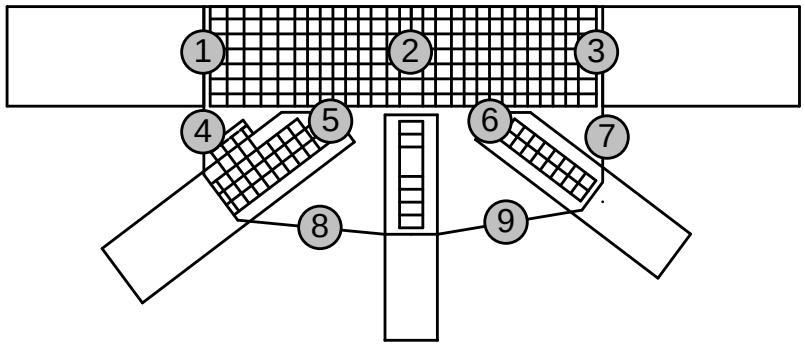

Figure 3.2.13: Node numbering used to get output from the U2 joint gusset plate

The applied load fraction of the 1.75(L+I) loads vs. the out-of-plane displacements of points 4, 5, and 8 on the gusset plate is shown in Figure 3.2.14. The out-of-plane displacement dramatically increases just after the peak of the curve. Similar to the previous case, this result shows the out-of-plane nature of the failure.

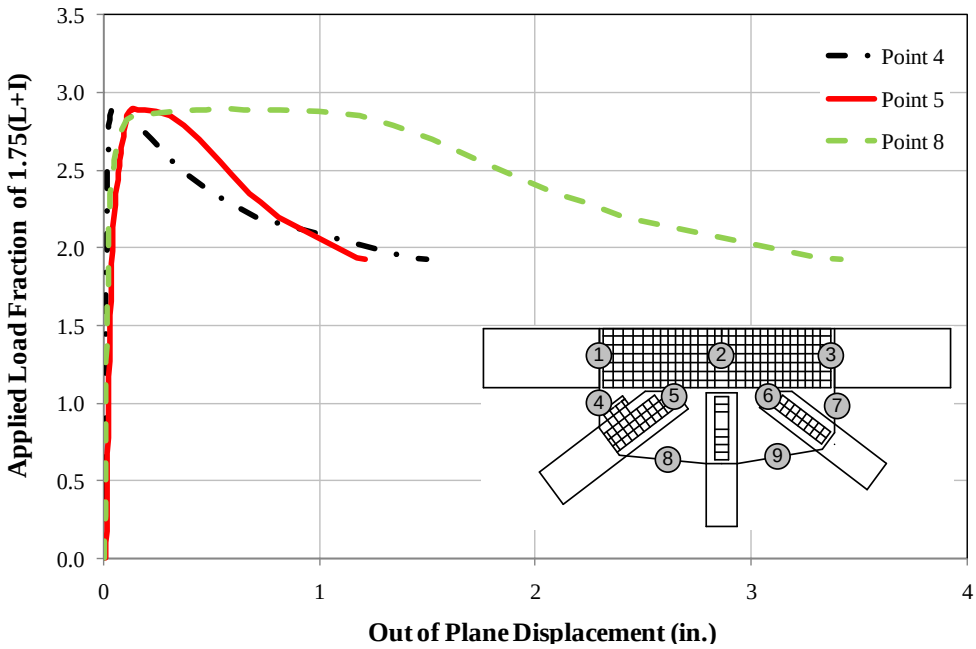

Figure 3.2.14: Applied load fraction of the factored live+impact loads [1.75(L+I)] vs. out-of-plane displacement relationship for U2 joint

Figure 3.2.15 shows how the peak value slightly decreases from 2.92 to 2.89, (-1%) with 1/8" maximum initial imperfection applied on the gusset plate. For a 1/4" initial imperfection, the sensitivity increases and peak value goes down to 2.70 (-8%). The curves in Figure 3.2.15 correspond to Point 8 on the free edge of the gusset plate.

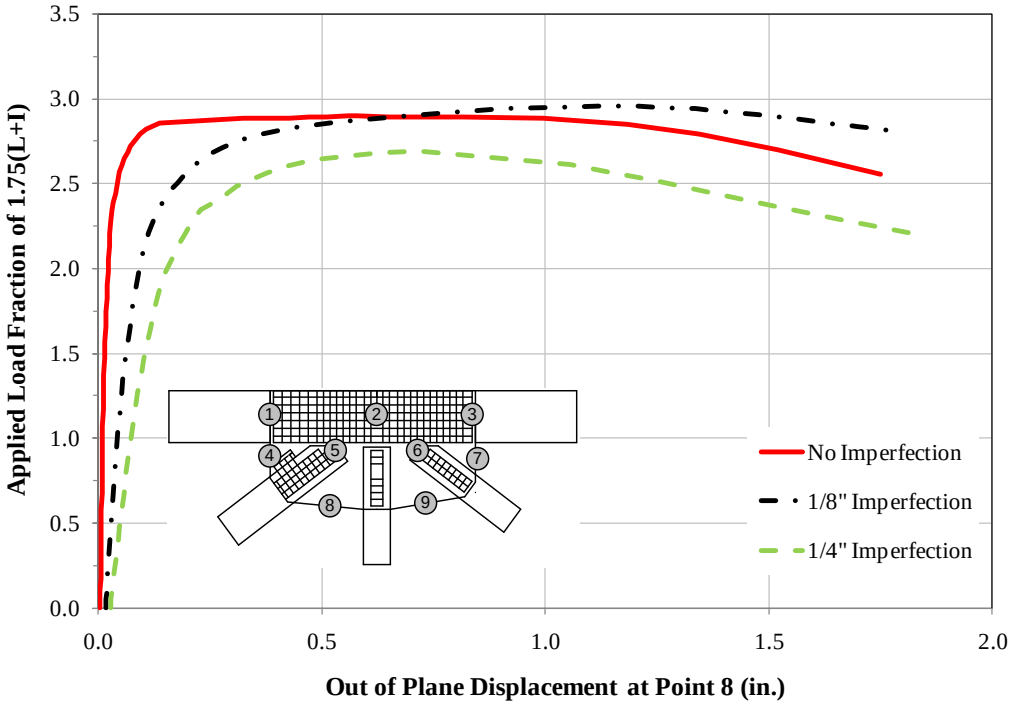

Figure 3.2.15: Effect of initial imperfection on the ultimate resistance of the U2 joint

Final analyses are performed based on the models with 1/4" maximum initial imperfection. Figure 3.2.16 shows the important load levels on the ALF vs. out-of-plane displacement plot. ALF=0.97 is the STRENGTH I load and the analysis continues until it reaches one of the other criteria to determine the limit of maximum useful resistance. Similar to the previous case, the 4% PEEQ is reached just after the peak load. The joint still has some reserve capacity beyond the STRENGTH I load level as shown in Figure 3.2.16.

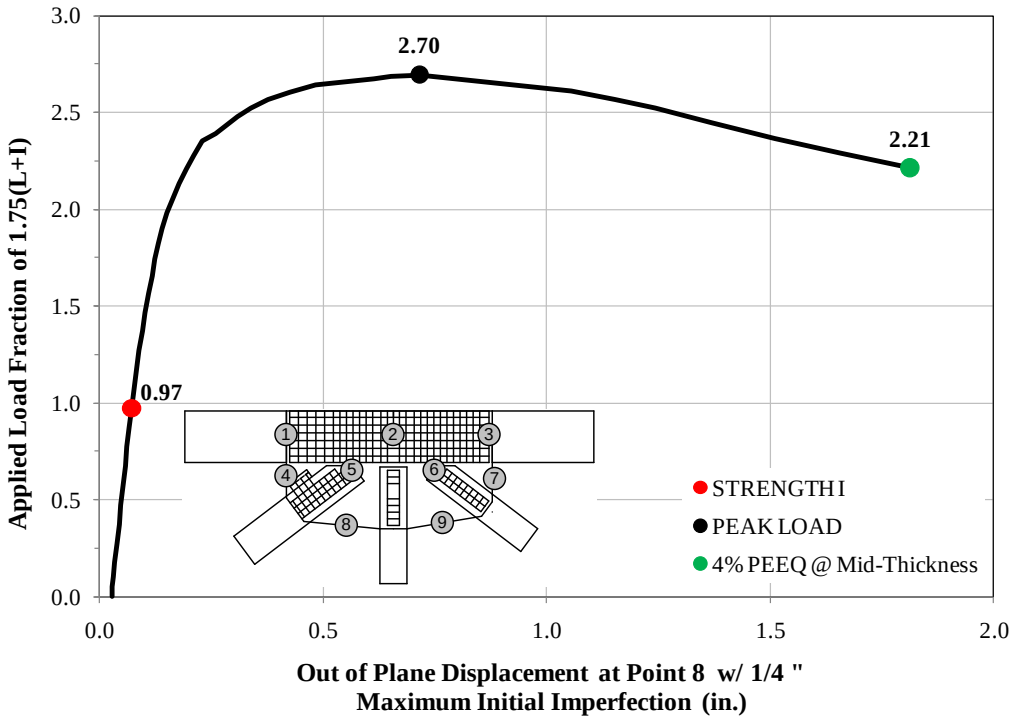

Figure 3.2.16: Different applied load fraction levels on the out-of-plane displacement behavior for point 8 on the gusset plate

Figure 3.2.17 shows the von Mises stresses in the connection when ALF = 0.97. This corresponds to the point labeled STRENGTH I in the ALF vs. displacement plot shown in Figure 3.2.16. The von Mises stress contour indicates the highest stress is occurring in the chord splice area and that the magnitude is about 90 percent of its yield strength. In addition, Figure 3.2.18 shows that no plastic strain is occurring at this load level.

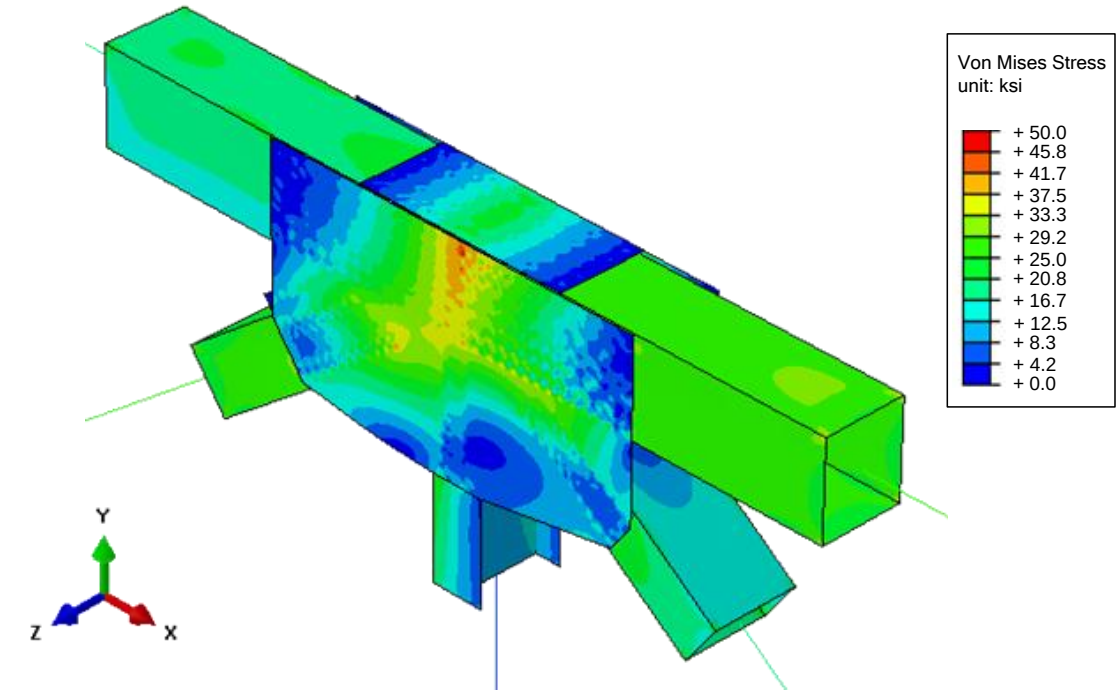

Figure 3.2.17: von Mises stress response contours at STRENGTH-1 level (ALF=0.97)

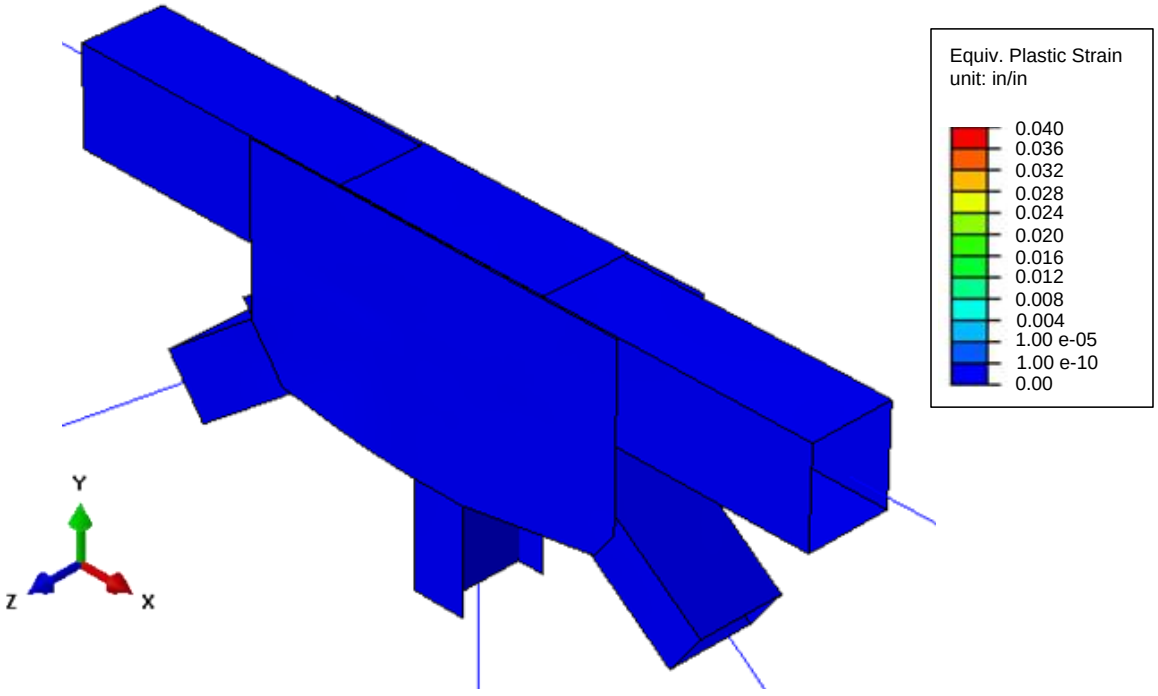

Figure 3.2.18: Equivalent plastic strain response contours at STRENGTH-1 level (ALF=0.97)

The von Mises stresses in the gusset plate corresponding to the limit load, in this case being the peak of the curve (ALF = 2.70) is shown in Figure 3.2.19. The plate reaches its yield strength at areas shown with grey contours. Figure 3.2.20 shows the corresponding equivalent plastic strain contours. The largest amount of plastic deformation is occurring in the splice region and the horizontal plane just below the chord members. The displaced shape observed in both contour plots with a deformation scale factor of 5.0 also confirms that out-of-plane compression buckling of the gusset plate takes place at the limit load. After extensive plastification and softening at the base of the compression diagonal, gusset plate kicks out-of-plane and undergoes considerable increase in the out-of-plane displacements.

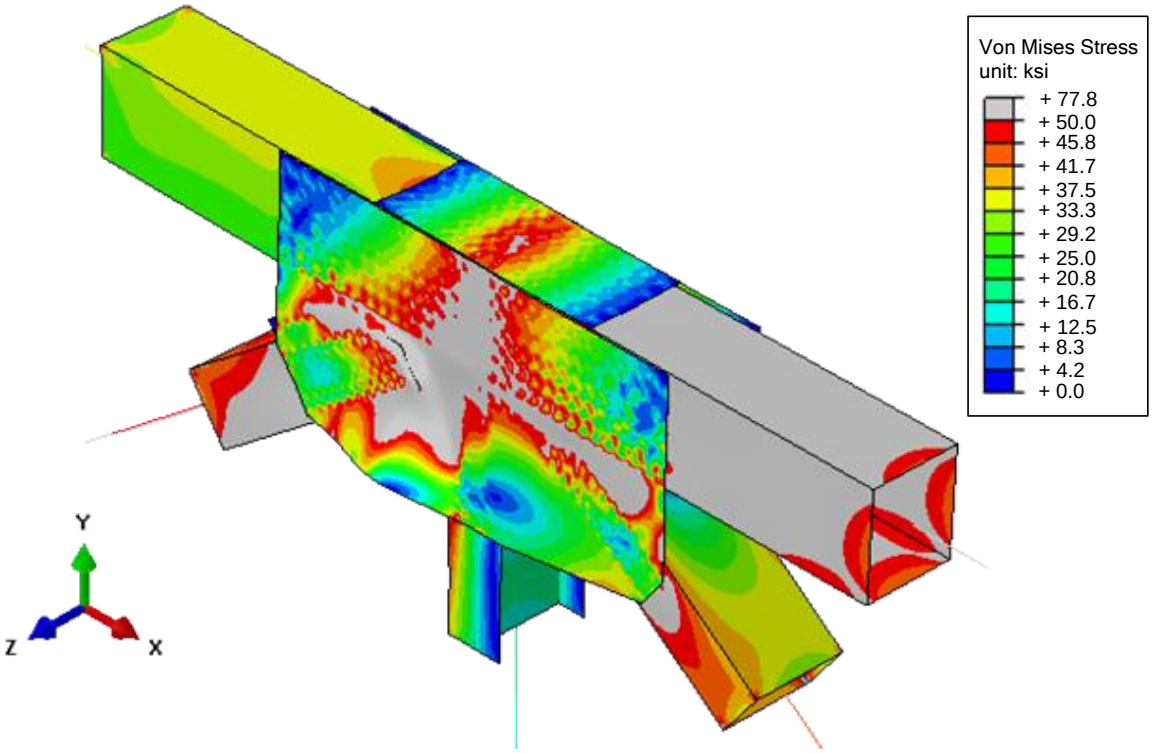

Figure 3.2.19: von Mises stress response contours at the limit load (ALF=2.70)

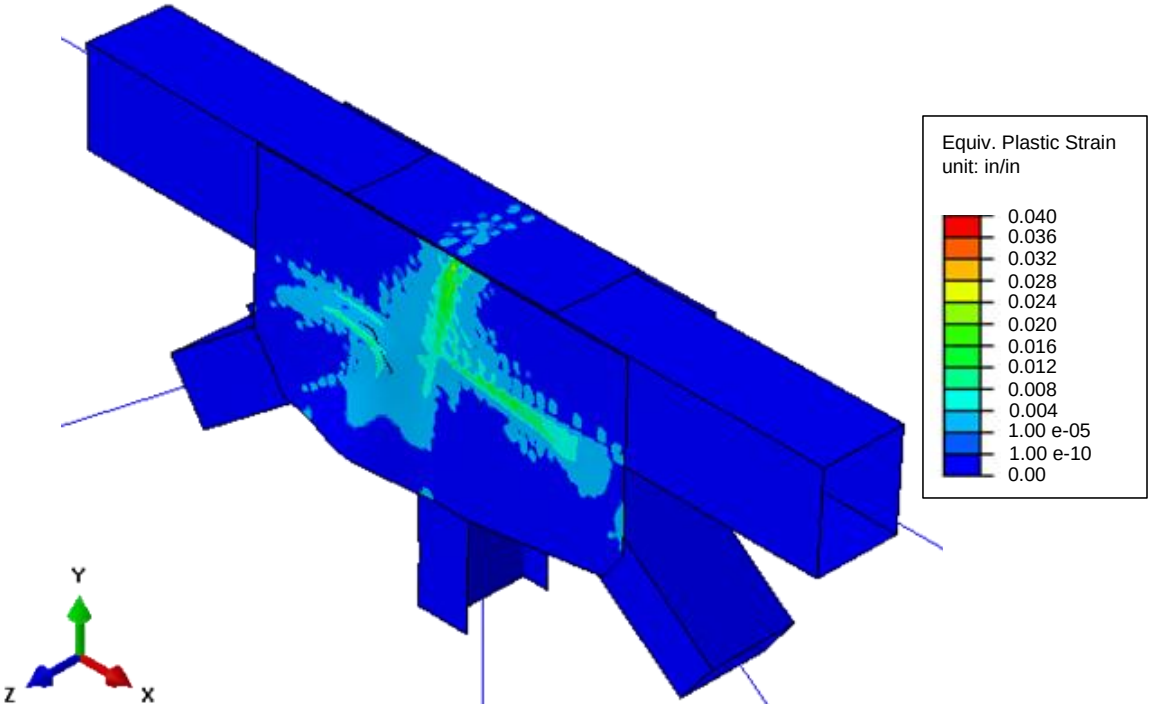

Figure 3.2.20: Equivalent plastic strain response contours at the limit load (ALF=2.70)

3.2.3. I-40 Bridge (Joint U8)

Member forces and factored loads applied at the truss nodes for the two load cases are shown in Figure 3.2.21 and Figure 3.2.22. For equilibrium of the joint U8, the forces in U7U8 and L7U8 members are updated.

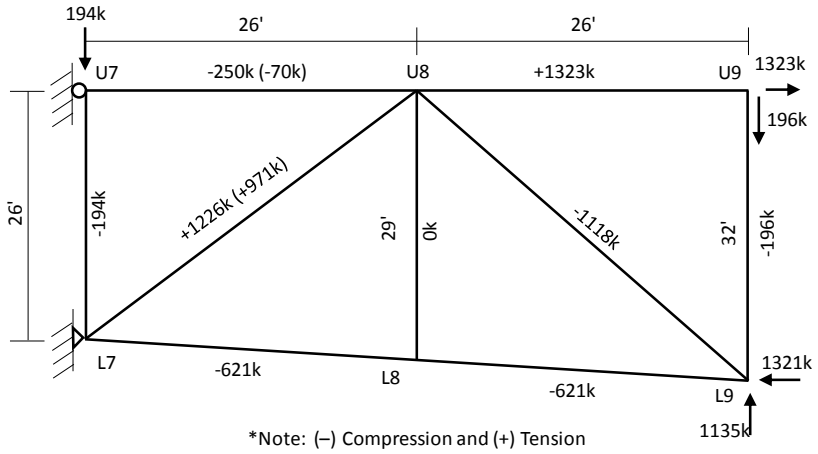

Figure 3.2.21: Factored dead loads (1.25D) for U8 joint

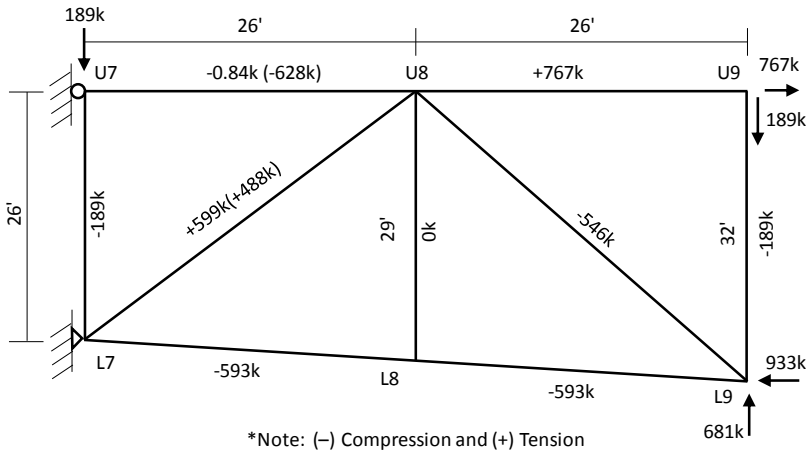

Figure 3.2.22: Factored live and impact loads [1.75(L+I)] for U8 joint

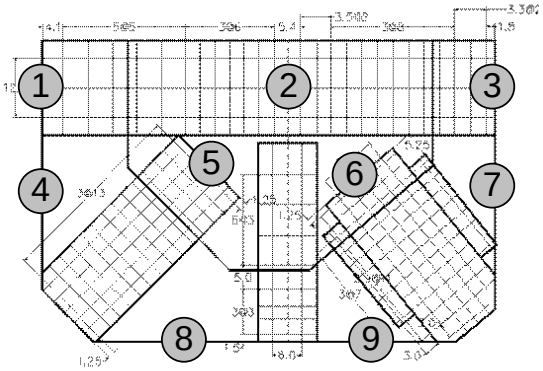

Figure 3.2.23: Node numbering used to get output from the U8 joint gusset plate

The applied load fraction of the 1.75(L+I) vs. the out-of-plane displacement relationship is investigated for points 6, 7, and 9 on the gusset plate as shown in Figure 3.2.24. The out-of-plane displacements remain very small and do not increase dramatically after the peak load as compared those seen in the joints from I-94 and HW-23 bridges discussed previously. This result shows the in -plane nature of the failure.

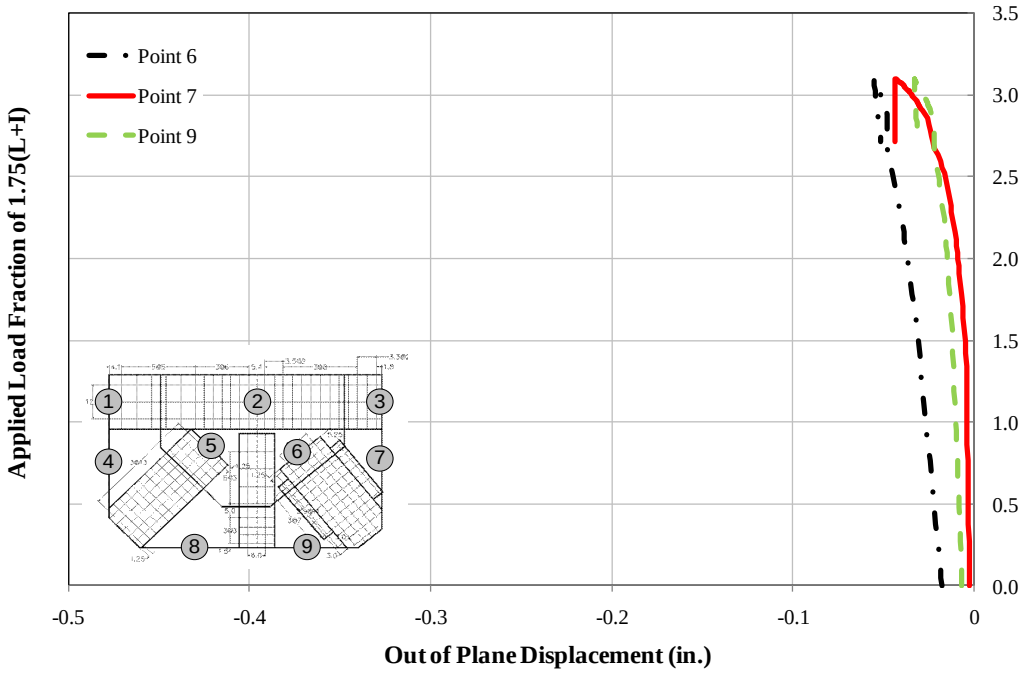

Figure 3.2.24: Applied load fraction of the factored live+impact loads [1.75(L+I)] vs. out-of-plane displacement relationship for U8 joint

Figure 3.2.25 shows how the peak value on the ALF vs. the out-of-plane displacement plot is not imperfection sensitive. The increase in the maximum initial imperfection only changes the magnitude of the displacement value. However, these values are much smaller than for the previous two joints since the failure is not driven by out-of-plane compression buckling in this case.

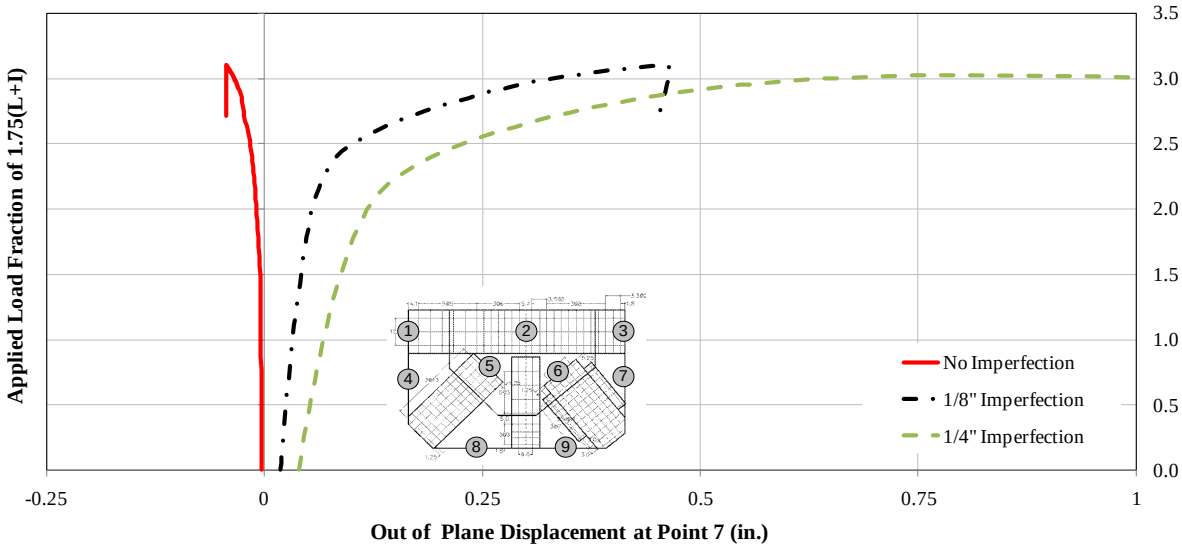

Figure 3.2.25: Effect of initial imperfection on the ultimate resistance of the U8 joint

Final analyses are performed based on the models with 1/4” maximum initial imperfection. Important load levels on the ALF vs. the out-of-plane displacement plot are shown in Figure 3.2.26. ALF = 1.04 is the STRENGTH I load and the analysis continues until the limit of maximum useful resistance. In this case, the 4% PEEQ is reached before the peak load.

One important analysis result is that fasteners connecting the chord member to the gusset plate reaches its 0.2” shear displacement limit at ALF = 2.16 which again confirms the in-plane failure mode of the joint. The shear rupture of the critical fastener is precipitated by extensive tension yielding of an inside web splice plate in the chord, resulting in redistribution of shear forces to the plane between the chord and the gusset.

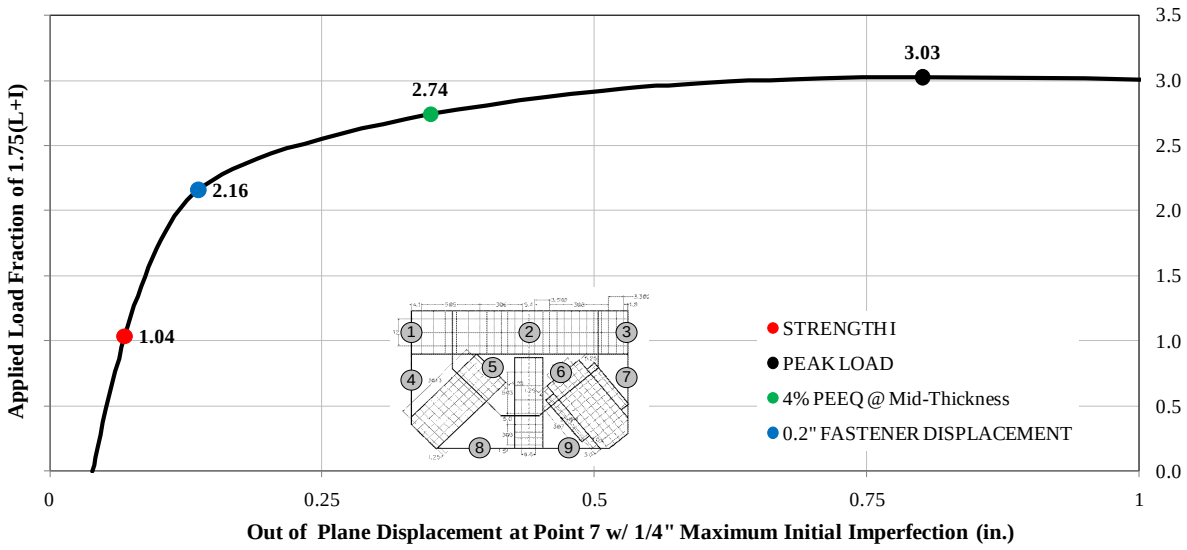

Figure 3.2.26: Different applied load fraction levels on the out-of-plane displacement behavior for point 7 on the gusset plate

Figure 3.2.27 shows the von Mises stresses in the connection when ALF = 1.04. This corresponds to the point labeled STRENGTH I in the ALF vs. displacement plot shown in Figure 3.2.26. The von Mises stress contour indicates the highest stress is occurring in the middle of the gusset plate and shingle plate areas and the peak stress is almost at the yield strength for the gusset plate. In addition, Figure 3.2.28 shows that no plastic strain is occurring at this load level. The joint still has reserve capacity to undergo additional plasticity until the proposed useful resistance level is reached.

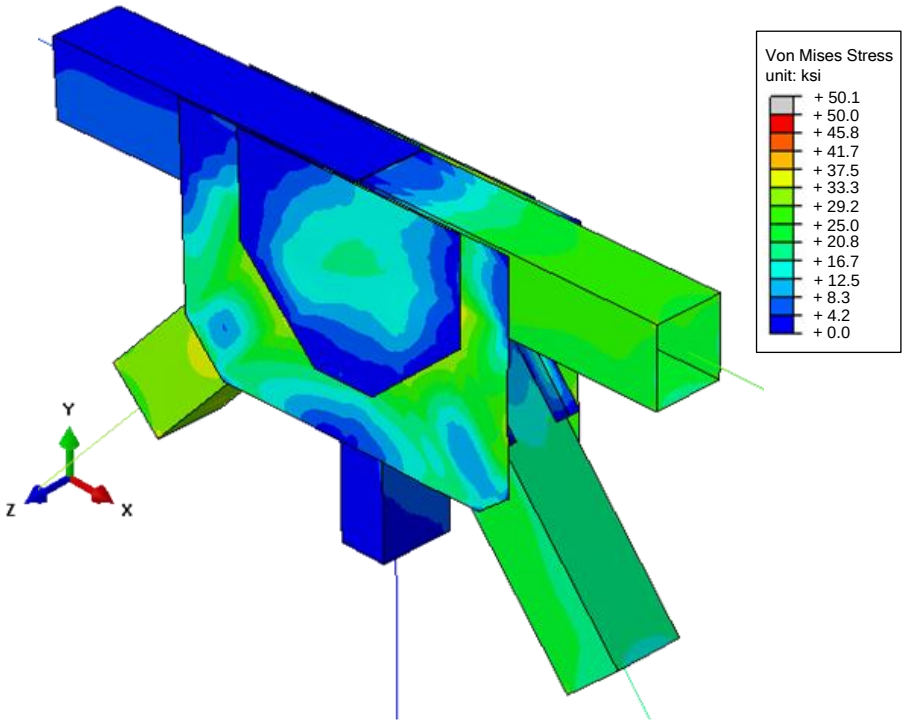

Figure 3.2.27: von Mises stress response contours at STRENGTH-1 level (ALF=1.04)

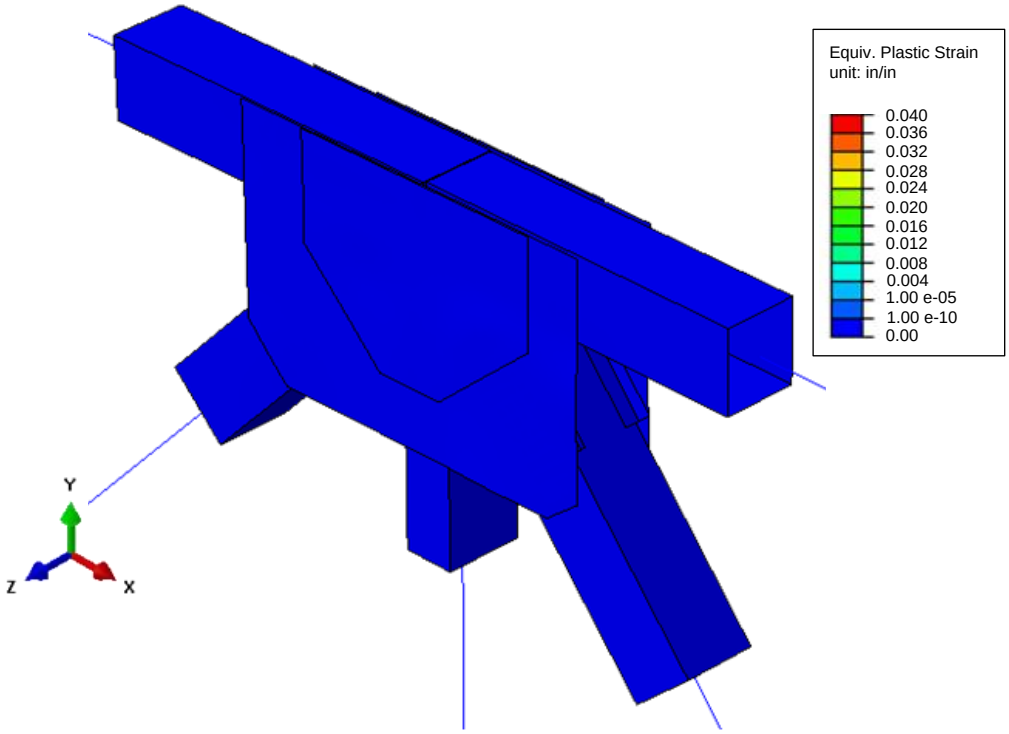

Figure 3.2.28: Equivalent plastic strain response contours at STRENGTH-1 level (ALF=1.04)

The von Mises stresses in the shingle plate corresponding to the limit load, in this case being the load level at which 0.2” fastener displacement is reached (ALF = 2.16), is shown in Figure 3.2.29. The gusset plate reaches its yield strength in areas shown with grey contours in Figure 3.2.30. Figure 3.2.31 and Figure 3.2.32 shows the corresponding equivalent plastic strain contours. The shingle plate does not have plastic strains although the plasticity is significant in the gusset plate at this load level. The displaced shape observed in the contour plots with a deformation scale factor of 5.0 also confirms that buckling of the gusset plate does not occur for this joint.

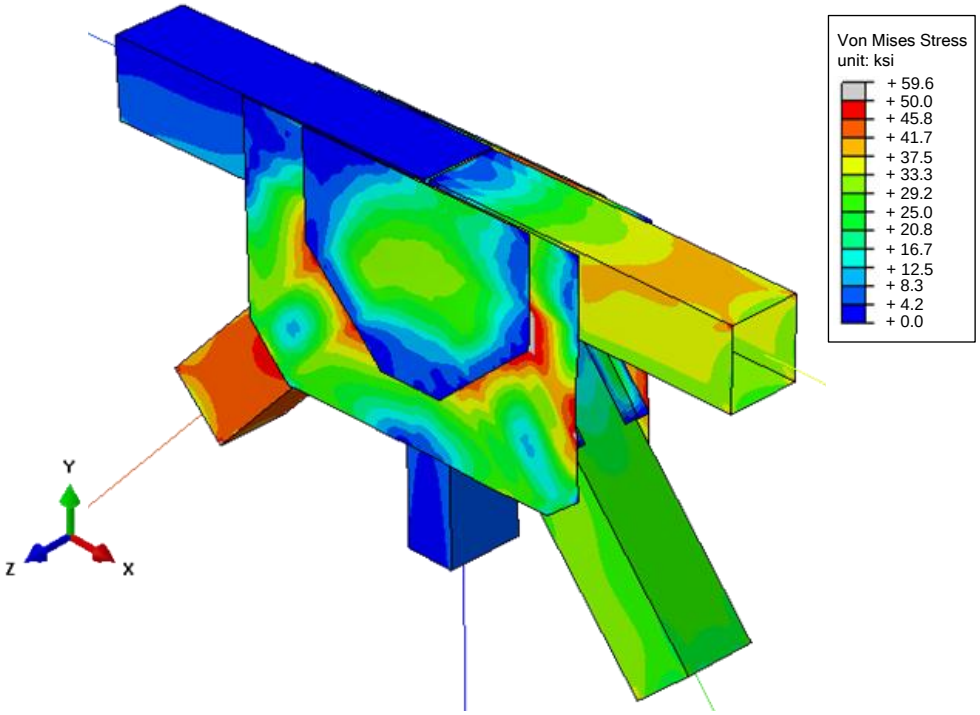

Figure 3.2.29: von Mises stress response contours at limit load (ALF=2.16)

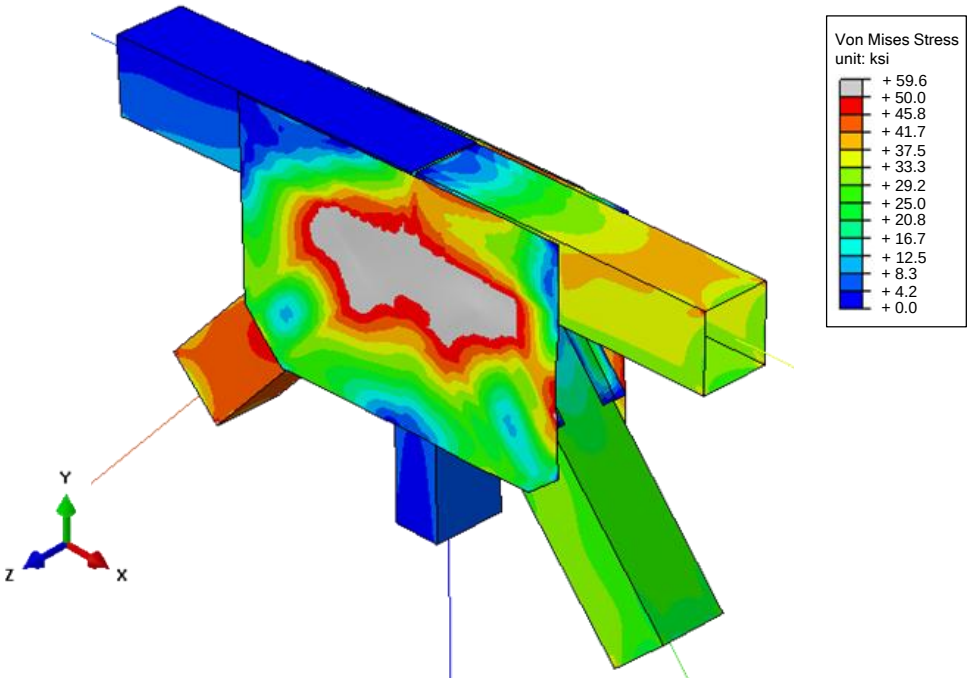

Figure 3.2.30: von Mises stress response contours at limit load (ALF=2.16). Shingle plates are not shown

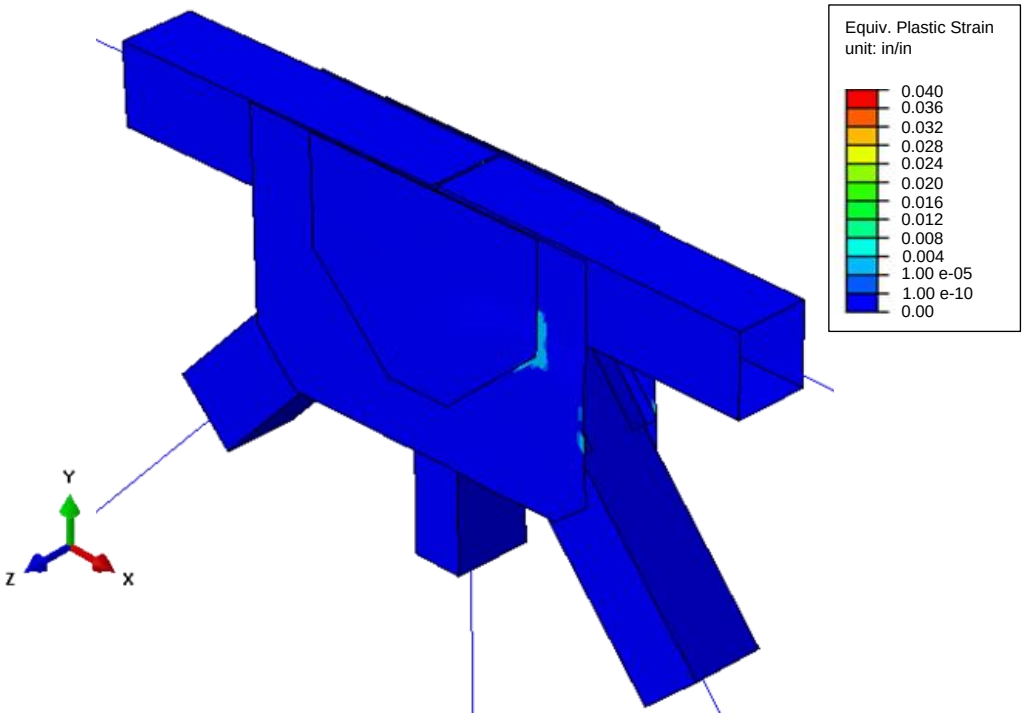

Figure 3.2.31: Equivalent plastic strain response contours at limit load (ALF=2.16)

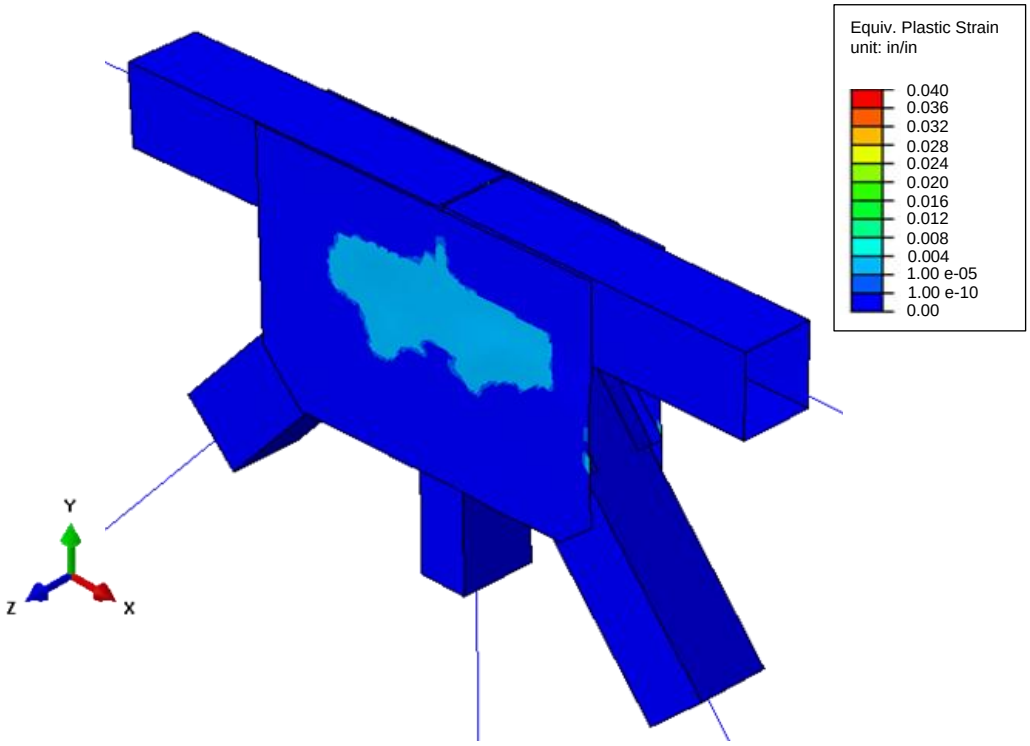

Figure 3.2.32: Equivalent plastic strain response contours at limit load (ALF=2.16). Shingle plates are not shown

3.2.4. I-80 Bridge (Joint L3)

As stated previously, joint L3 from the I-80 Bridge is an artificial example used in the FHWA guide. Factored loads, 1.25D+1.50DW, and 1.75(L+I) shown in Figure 3.2.33 and Figure 3.2.34 are calculated based on the unfactored envelope forces reported in the FHWA guide. The joint satisfies the equilibrium under 1.25D+1.50DW loads. However, forces in L2L3 and U2L3 are modified to reach the joint equilibrium under 1.75(L+I) loads.

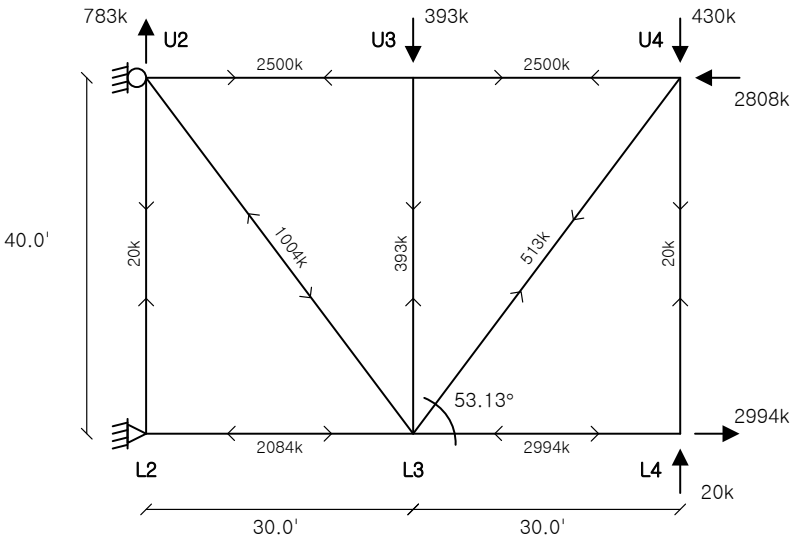

Figure 3.2.33: Factored dead loads (1.25D+1.50DW) for L3 joint

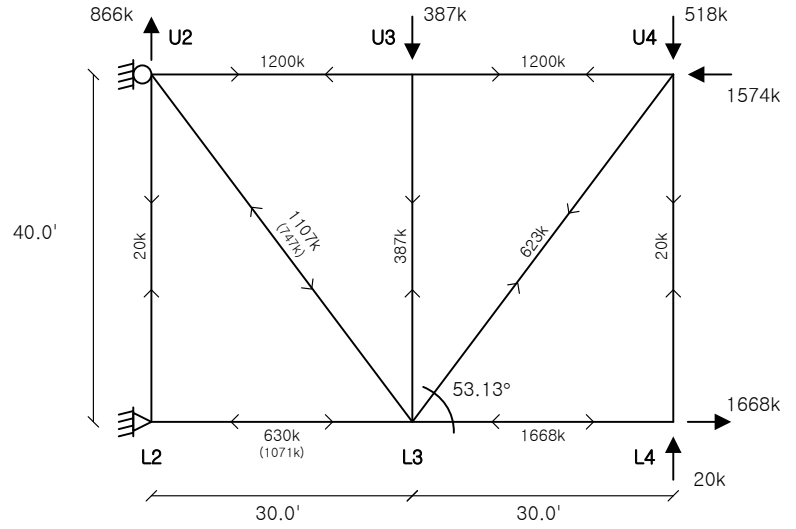

Figure 3.2.34: Factored live and impact loads [1.75(L+I)] for L3 joint

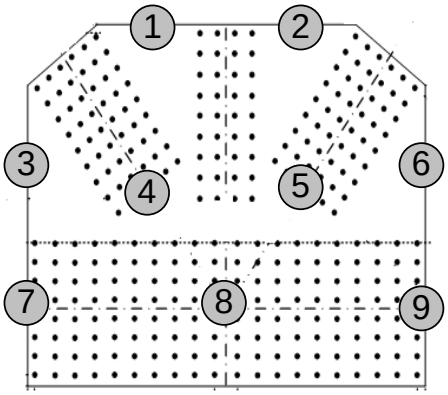

Figure 3.2.35: Node numbering used to get output from the L3 joint gusset plate

The applied load fraction of 1.75(L+I) vs. out-of-plane displacement relationship is investigated for points 2, 5, and 6 on the gusset plate as shown in Figure 3.2.36. The out-of-plane displacements remain very small and do not increase dramatically after the peak load as compared to the joints from I-94 and HW-23 bridges discussed previously. This result shows the in -plane nature of the failure similar to I-40 bridge.

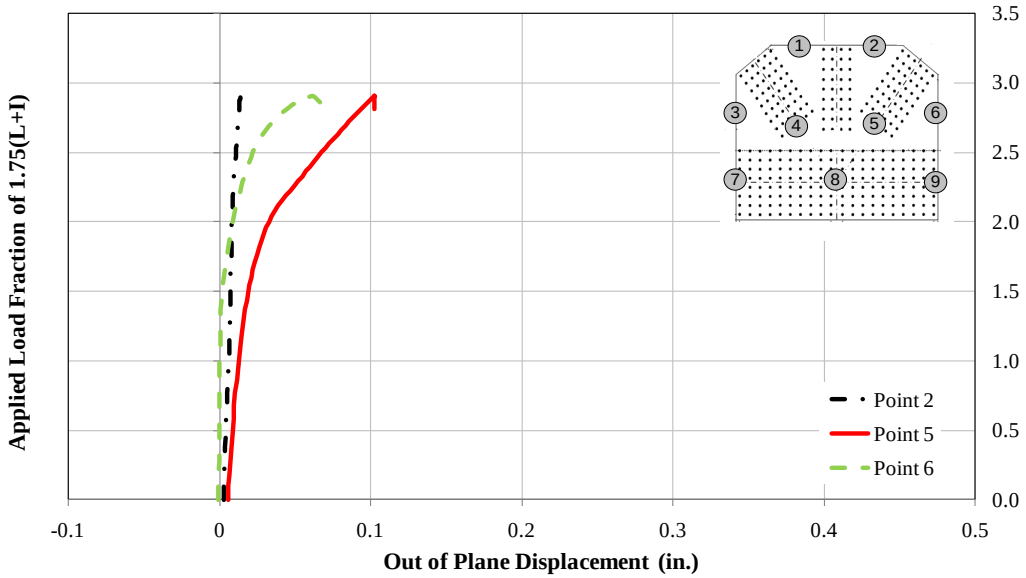

Figure 3.2.36: Applied load fraction of the factored live+impact loads [1.75(L+I)] vs. out-of-plane displacement relationship for L3 joint

Figure 3.2.37 shows how the peak value on the ALF vs. the out-of-plane displacement plot is not imperfection sensitive. The increase in the maximum initial imperfection only changes the magnitude of the displacements but these values are much smaller than the I-94 and HW-23 joints.

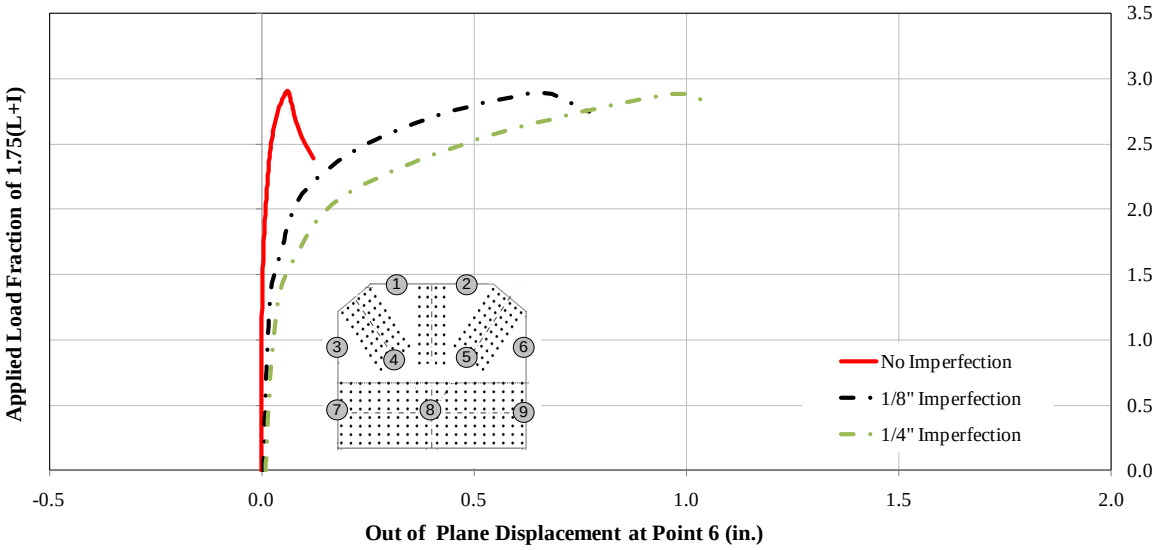

Figure 3.2.37: Effect of initial imperfection on the ultimate resistance of the L3 joint

Final analyses are performed based on the models with 1/4" maximum initial imperfection. Important load levels on the ALF vs. the out-of-plane displacement plot are shown in Figure 3.2.38. ALF = 1.03 is the STRENGTH I load and the analysis continues until the limit of maximum useful resistance. In this case, the 4% PEEQ is reached before the peak load and this limit determines the ultimate resistance of the joint.

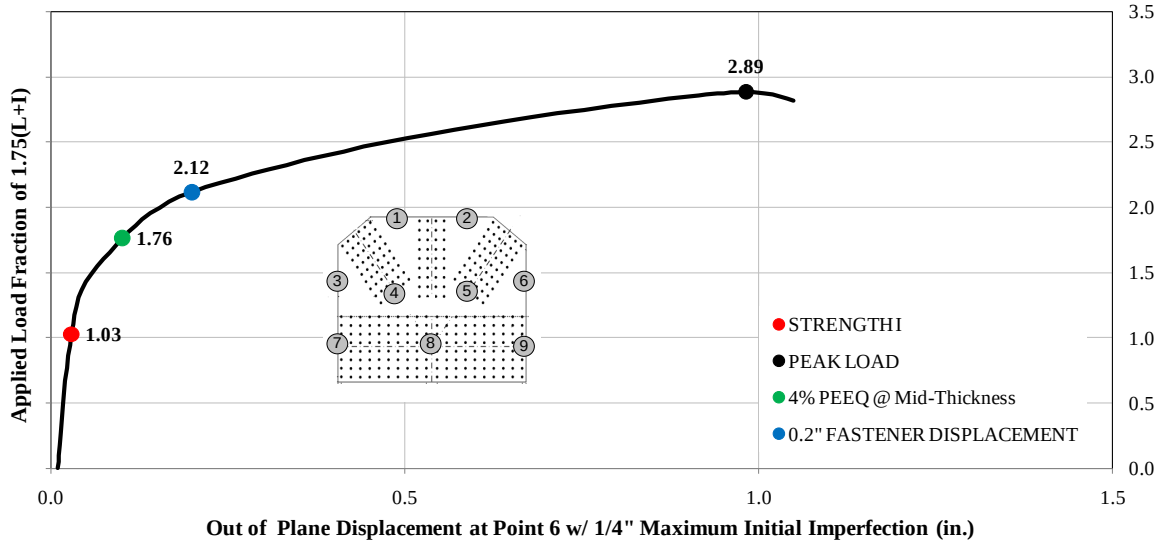

Figure 3.2.38: Different applied load fraction levels on the out-of-plane displacement behavior for point 6 on the gusset plate

The von Mises stress contour plot shown in Figure 3.2.39 at ALF = 1.03 indicates the highest stress is occurring in the chord splice area and the magnitude exceeds the

yield strength of the gusset plate. The area above the chord splice is also at the yield point almost all the way to the top of the gusset plate along the vertical plane. The equivalent plastic strain shown in Figure 3.2.40 indicates the highest plastic strain is occurring in the chord splice area. Unlike the previous joints, this gusset plate underwent significant plasticity even at the STRENGTH I load limit.

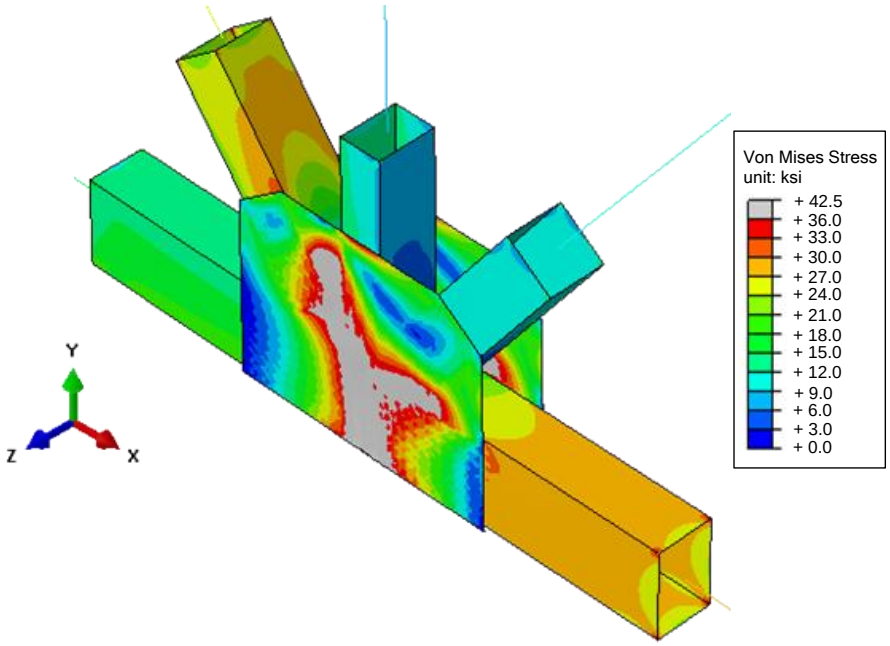

Figure 3.2.39: von Mises stress response contours at STRENGTH-1 level (ALF=1.03)

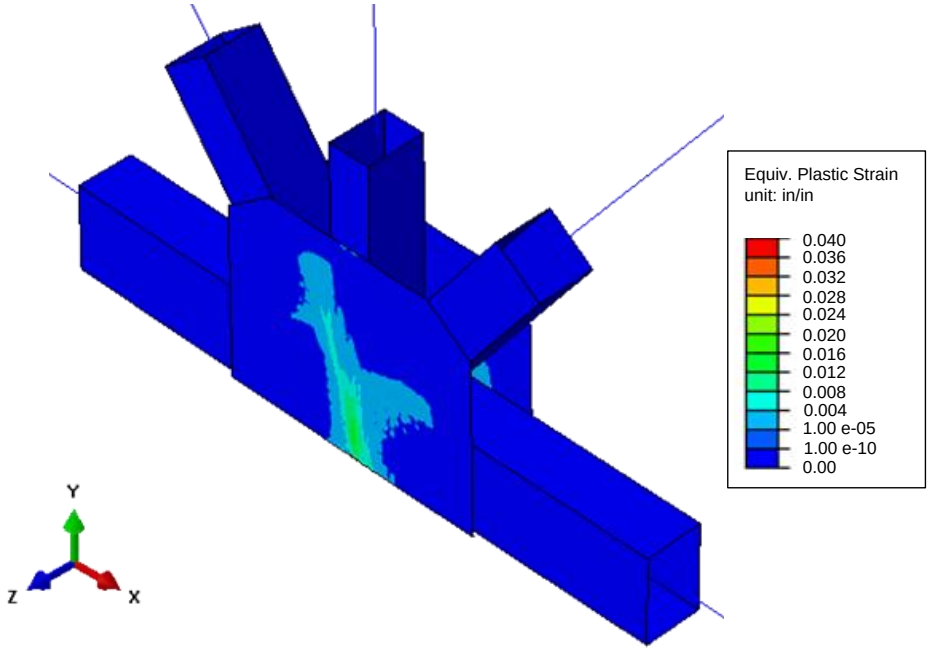

Figure 3.2.40: Equivalent plastic strain response contours at STRENGTH-1 level (ALF=1.03)

The von Mises stress and equivalent plastic strain contours at the proposed ultimate ALF of 1.76 are shown in Figure 3.2.41 and Figure 3.2.42, respectively. The gusset plate reaches its yield point over most of the free area outside of the fastener patterns. Yielding also progresses across both the horizontal and vertical planes through the gusset plate.

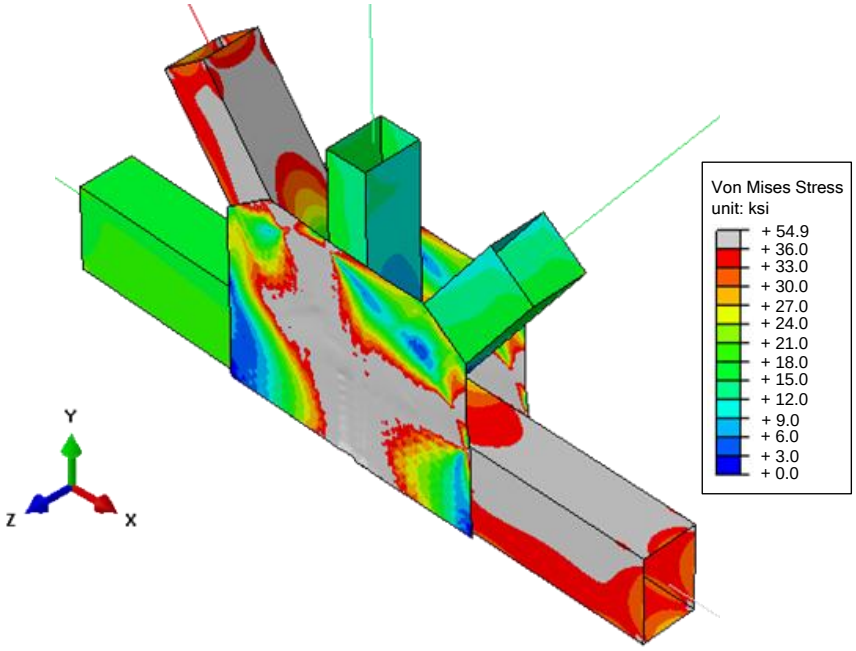

Figure 3.2.41: von Mises stress response contours at limit load (ALF=1.76)

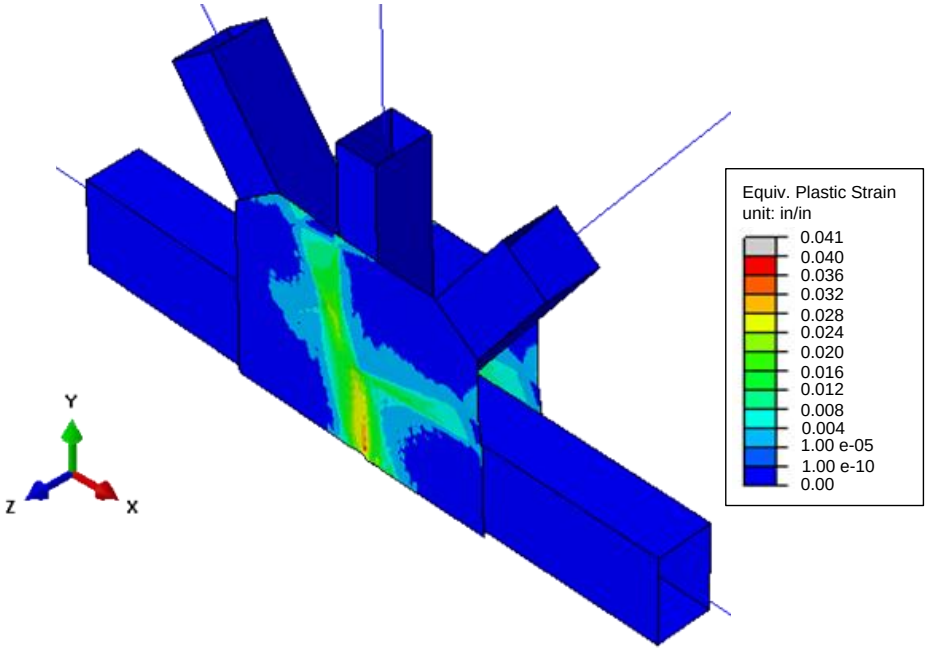

Figure 3.2.42: Equivalent plastic strain response contours at limit load (ALF=1.76)

3.3. Summary of the Results

These studies show that the gusset plate behavior can be investigated using advanced computational models by creating the connection in advanced finite element models. These models are calibrated based on the experimental results. Certain limits that are set to define the failure loads are also validated using the test results from different specimens. The preliminary finite element analyses performed on the representative four joints provide valuable information on the finite element methodology to be applied in the modeling of the test specimens and parametric study cases which will be discussed in more detail in Chapter 4 and Chapter 5.

CHAPTER IV : FULL-SCALE EXPERIMENTS AND VALIDATION OF THE ANALYTICAL MODELS

Experimental studies conducted as part of this research were performed at the FHWA Turner-Fairbank Highway Research Center in McLean, VA. Information on the test setup, member design and instrumentation is given next; more details are discussed in the project interim report (FHWA, 2010). Figures and photos representing the experimental effort have been provided by FHWA. The author was also present at the first test and assisted with the tests and data reduction, having spent four months at the FHWA facility as part of his research. Finite element analyses were performed by the author before and after the tests.

4.1. Load Frame

Plan and elevation views of the load frame with a specimen installed are shown in Figure 4.1.1. In this figure, elements in yellow correspond to actuators, those in purple to steel reaction beams, and those in green to the connected members in the joint. The experimental setup utilizes a five member configuration since connections in steel truss bridges typically have five members connected to two gusset plates. These members are a compression diagonal (West), a tension diagonal (East), a vertical member, and two chord members (West and East). Parametric studies cover different configurations including four member configurations (i.e., a joint without a vertical member).

Four reaction walls are used to create the axial loads on the diagonal and vertical members. The height of the walls is constrained by the 23.5 feet of clearance between the strong floor and the crane hook of the laboratory. The weight of the walls is constrained by the capacity of the two Structures Lab 20-ton overhead cranes. Each of the shear walls is post-tensioned to the strong floor to resist the loads being applied to the diagonal connection members.

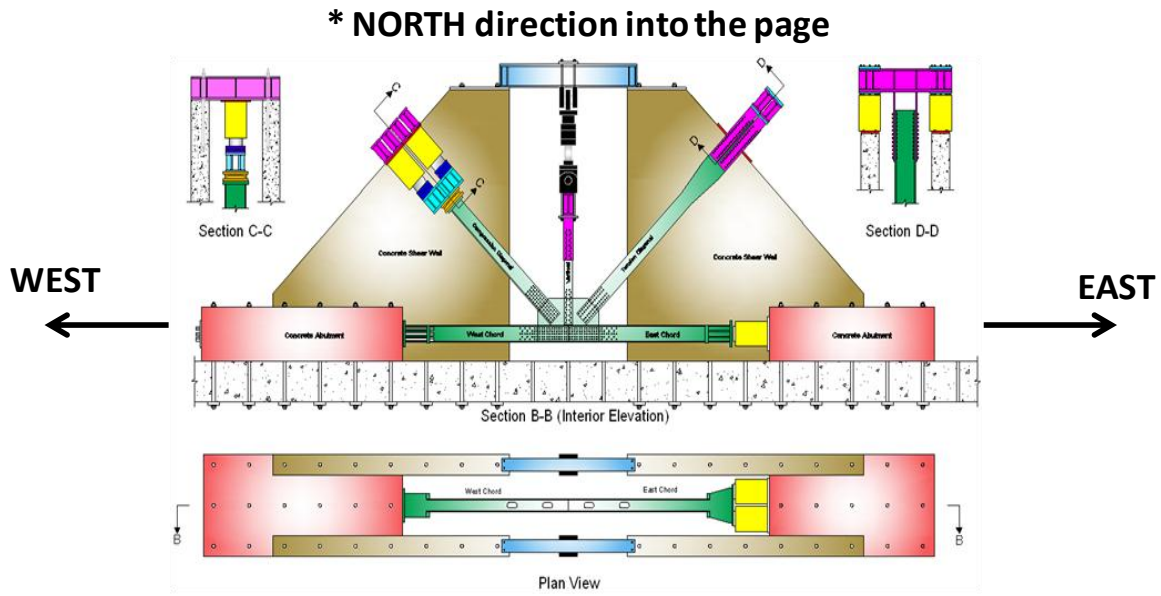

Figure 4.1.1: Plan and elevation views of the load frame with the installed specimen

Two concrete abutments are placed between the reaction walls on each side to provide a reaction point for the axial loads on the chord members. Figure 4.1.2 shows a perspective view of the west reaction wall (on the left), and the concrete abutment between the west reaction walls (on the right). The west chord in Figure 4.1.1 is the fixed or reaction chord and it is pretensioned to the abutment with six DYWIDAG bars to transfer tension and compression loads. The abutment on the East side of the frame in Figure 4.1.1 resists forces from the two jacks that provide loads to the chord. In the configuration shown, the jacks can only apply compression loads to the chord. However, ducts cast into this abutment provide the ability to reposition the jacks to the opposite side of the abutment in order to apply tension load in the East chord. This alternative configuration of the East chord jacks is shown in Figure 4.1.3.

Figure 4.1.2: Reaction walls (left) and the concrete abutment between them (right)

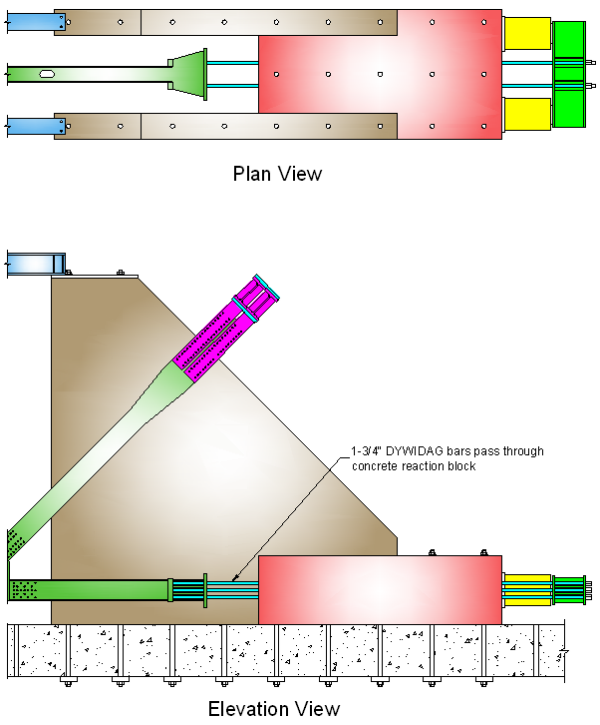

Figure 4.1.3: Alternate jack positioning to apply tensile load on the east chord

A total of six 1000-ton Enerpac hydraulic jacks are used to apply the member loads on the diagonals and East chord. For each diagonal and the East chord, the two jacks provide a maximum applied load of 1340 kips in each of those members, but a maximum capacity of 1200 kips is used in the design of the experiments. Four W18x192 sections transfer the forces from the compression diagonal to the reaction walls as shown in Figure 4.1.4. These four steel sections are attached to each shear wall with eight DYWIDAG bars. Enerpac jacks are placed directly on the diagonal edges of the reaction walls on the tension diagonal side and two W18x192 sections transfer the jack loads to the tension diagonal as shown in section D-D of Figure 4.1.1.

Figure 4.1.4: 1000-ton Enerpac jack before (left) and after installation (right)

Two double acting MTS jacks, each capable of applying 220 kips of tension or compression, are attached to W18x192 steel sections that span longitudinally between the two reaction walls. The steel sections are post-tensioned to the walls with DYWIDAG bars connected to embedded couplers within the wall. This enables the actuators to apply a maximum of 440 kips tension or compression load on the vertical member.

4.2. Member Design

The five load carrying members connected to the gusset plates are designed so that they can be reused throughout the experimental program. The steel used to fabricate these members is A514 Grade 100 material. The member design was carried out by FHWA personnel. The members were designed to ensure that they remain elastic up to the peak jack loads. The chord members and compression diagonal are welded box sections, while the tension diagonal and vertical member are built-up I-sections. Access holes on the box members are provided to expedite bolt installation.

The bolt holes on the box members are 15/16” diameter on a 2.5” gage and pitch. The I-sections also have bolt holes of 15/16” diameter on a 2.5” pitch. However, the bolt gage on those members is variable to eliminate any interference with the web. The number of bolt holes drilled on the members is such that all different gusset plate configurations and bolt patterns can be accommodated by the test setup. The overall width of the fastener pattern is 11”.

The chord member box sections are 14.5” deep but the member lengths are different from each other as shown in Figure 4.2.1 and Figure 4.2.2 respectively. The flanges are 3/4" thick and web plates are 1” thick. The compression diagonal box section is 14” deep with a flange thickness of 1/2” and web thickness of 1” (Figure 4.2.3). The tension diagonal has a 14” flange width with a 1” thickness (Figure 4.2.4). The vertical member flange has a 8” width and a 1/2” thickness as shown in Figure 4.2.5.

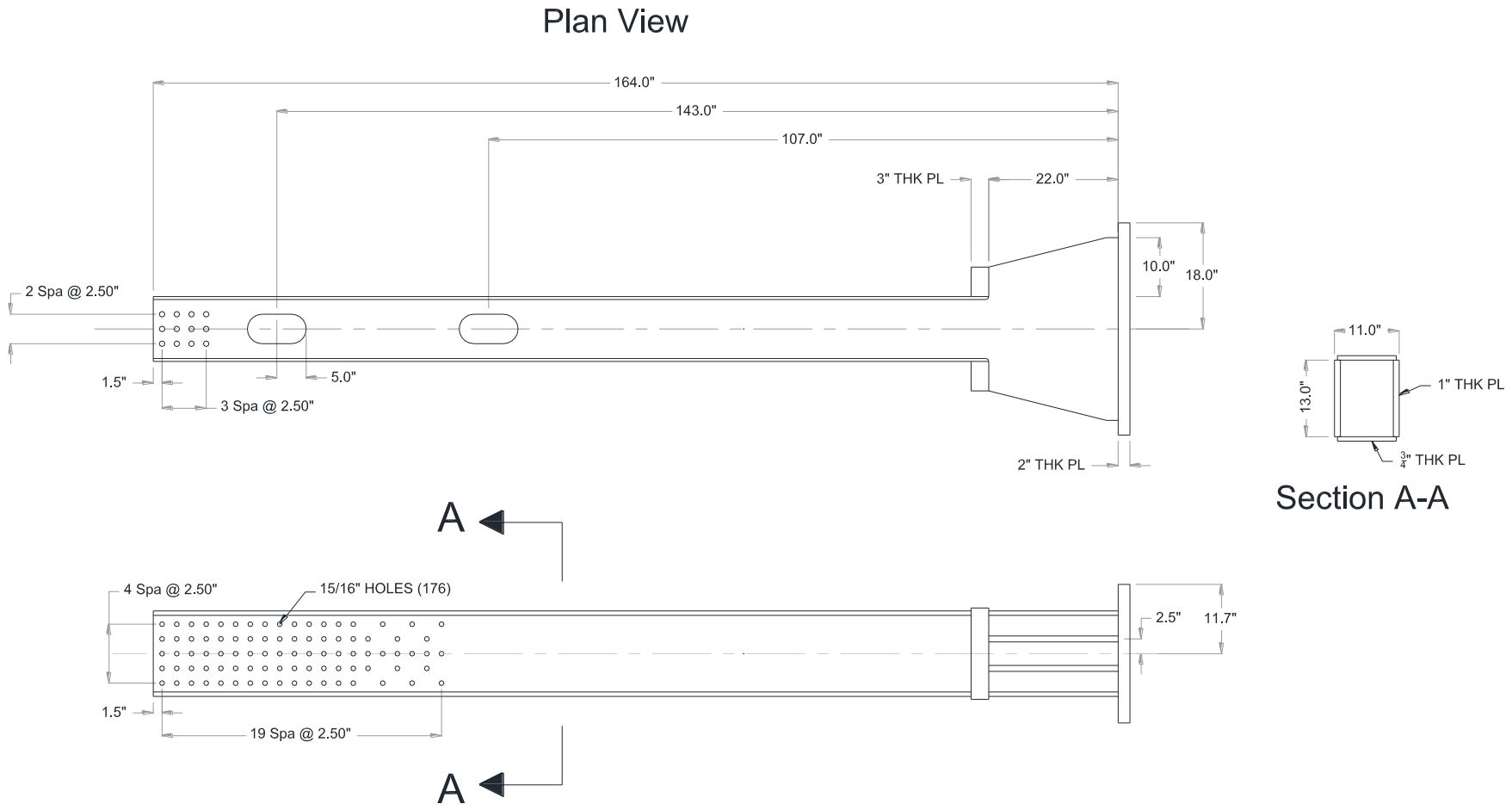

Figure 4.2.1: East chord plan/elevation views and cross-section properties

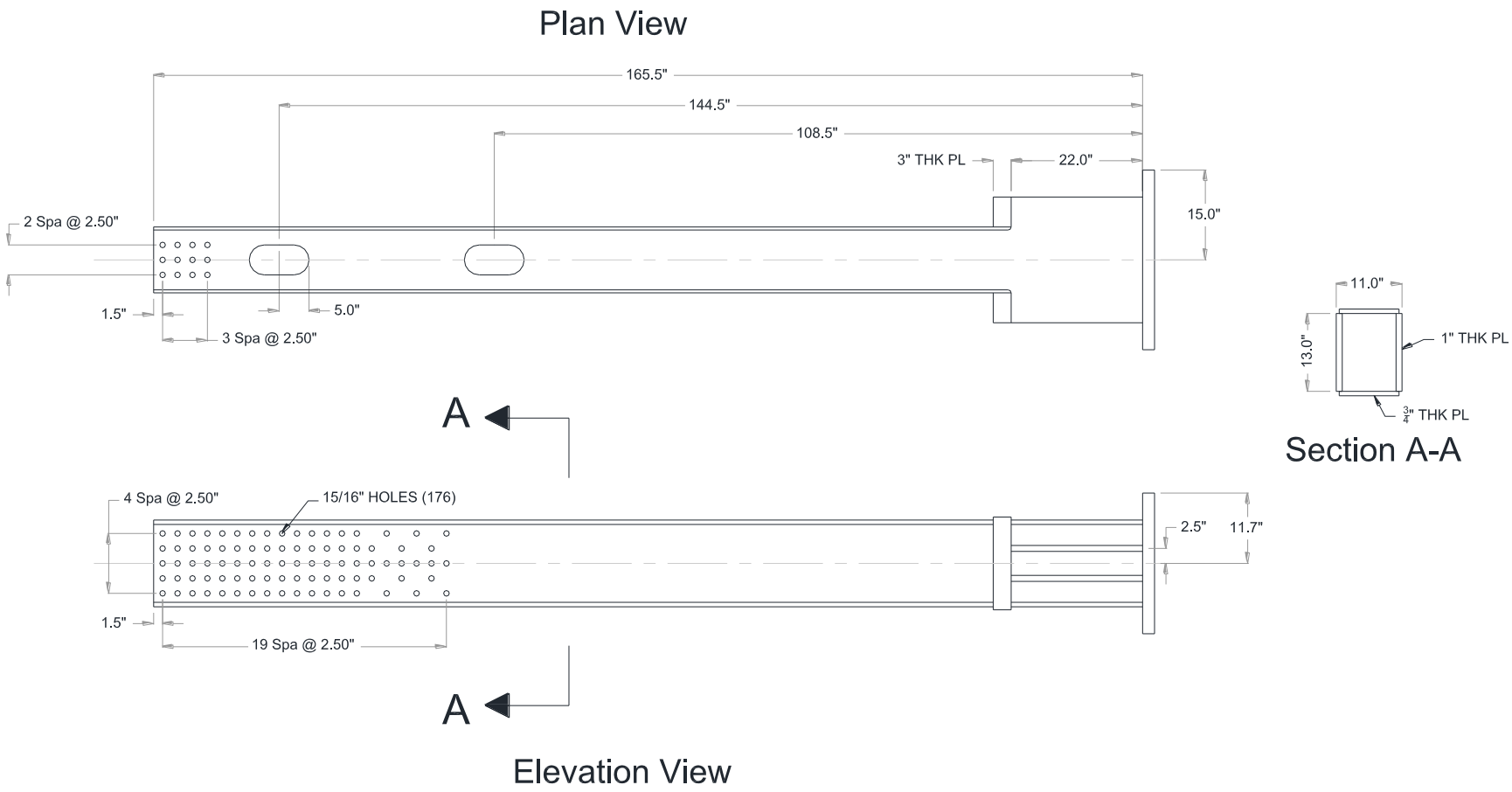

Figure 4.2.2: West chord plan/elevation views and cross-section properties

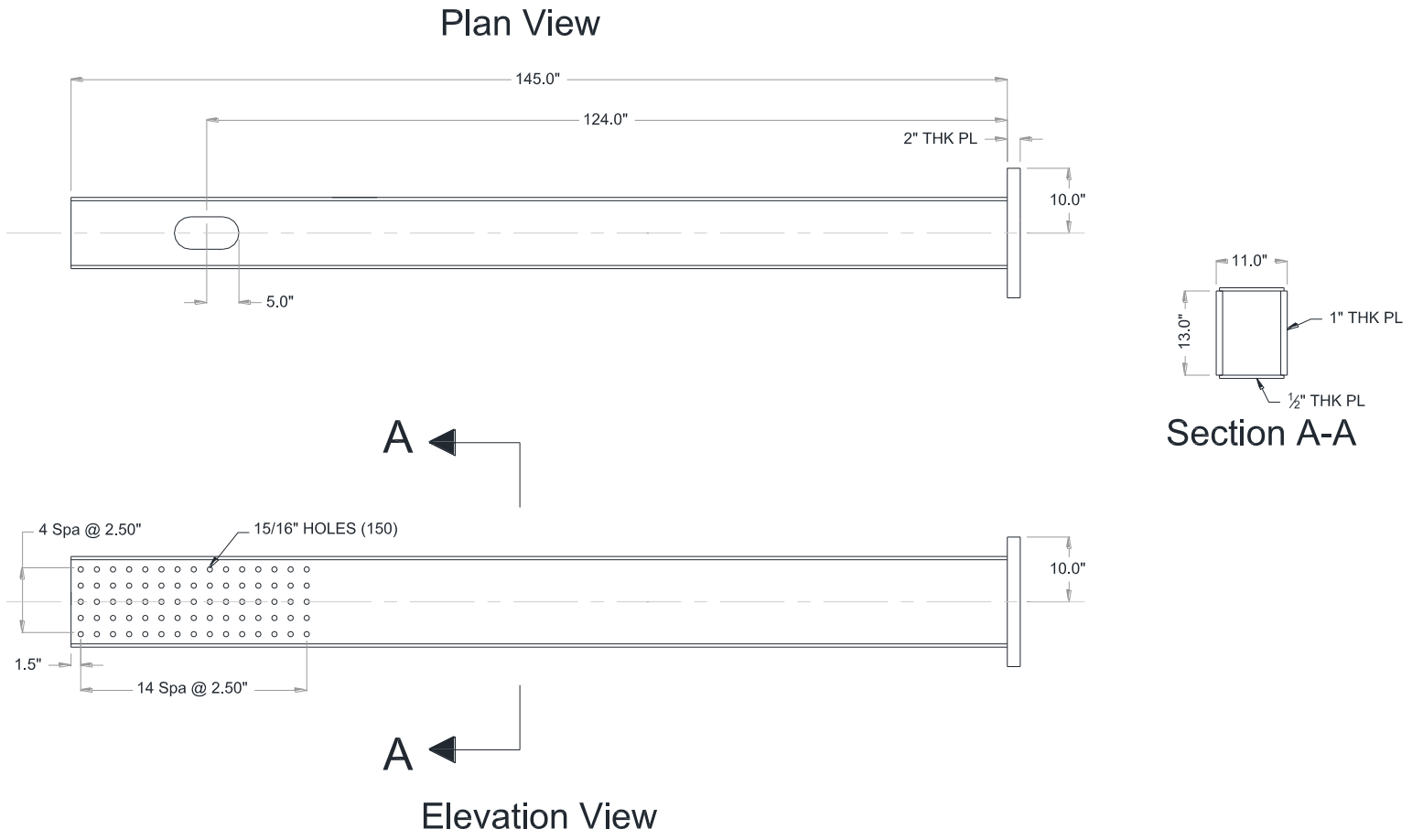

Figure 4.2.3: Compression diagonal plan/elevation views and cross-section properties

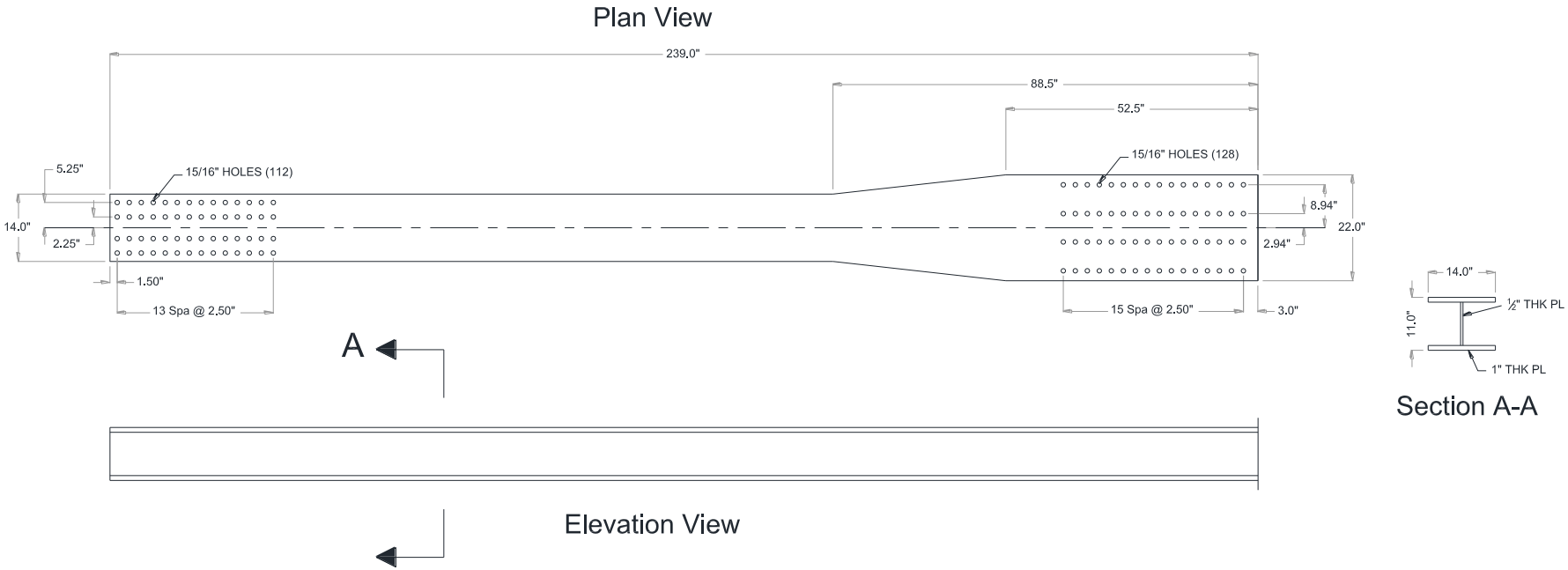

Figure 4.2.4: Tension diagonal plan/elevation views and cross-section properties

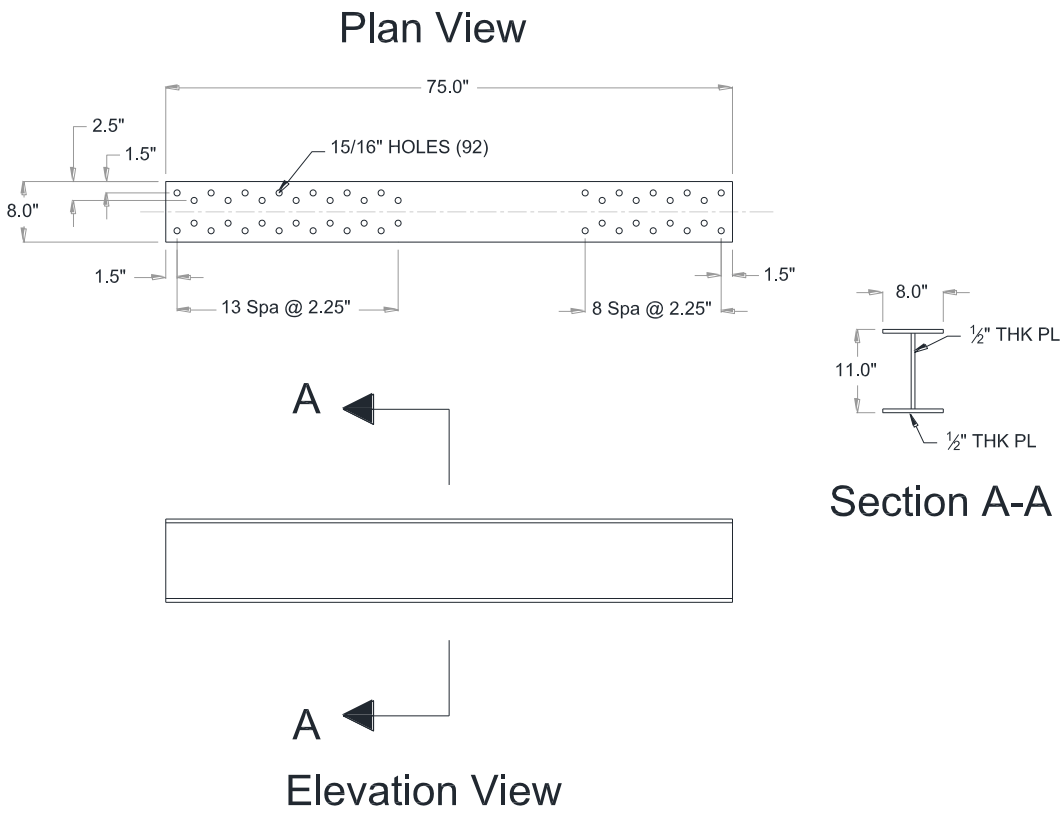

Figure 4.2.5: Vertical member plan/elevation views and cross-section properties

4.3. Test Specimens

The main conclusion from the study on the bridge plans discussed in Section 2.2 is that there is a considerable variation in gusset plate geometry, material properties, and loads applied to the joints. Thus, it is difficult to define a typical gusset plate representing several of the connections in steel truss bridges. The variations in the connections present in constructed bridges make it impossible to define gusset plate resistance based only on physical experiments. The number of tests to reach solid conclusions would be too expensive in terms of both cost and time considerations. The best alternative is to develop refined analytical models and use full-scale experimental results to validate the analytical models. The validated analytical models can be used both to simulate many different configurations representative of actual truss bridge connections and to conduct additional parametric studies on variables of interest for a given connection.

The primary goal of the FHWA full-scale experiments is to provide data to develop and verify refined finite element models and to test specimens that failed in as many modes as possible. Desired failure modes include both compression buckling and shear failure along either the horizontal or vertical critical planes of load transfer in the gusset plates. Research on the bridge plans shows that both rivets and bolts are utilized in steel truss bridges. For the experiments, A502 rivets would be very difficult and expensive to install. Taking the time and practicality into consideration, an alternative approach is used. Based on the studies by Roeder et al. (1994), rivets are modeled using A307 bolts inserted to fill the holes such that they are initially in bearing.

The first five test specimens to be used to validate the finite element models utilize both A307 bolts, providing relatively low strength and large fastener deformations, and A490 bolts, providing relatively high strength, little fastener deformation, high slip resistance and little to no slip displacements respectively. In the test specimens, four important parameters are explored,which lead to the following naming convention. Each specimen is labeled as ***GPwww-xyz***, where ***"www"*** represents the bolt type (A307 or A490 bolts), ***"x"*** refers to the gap between the corner of the compression diagonal and the chord member (S for short, L for long), ***"y"*** refers to the free edge length or member connection length (S for short, L for long), and ***"z"*** is the gusset plate thickness in eighths of an inch (i.e. 3 represents a 3/8 inch thick gusset plate). One exception is the GP490-

LS3 specimen which was re-tested because the initial specimen failed due to a control malfunction during the test to failure and it was renamed as GP490-LS3-1.

All five specimens utilize 3/8 inch thick gusset plates and additional parametric studies are performed on each specimen by changing the gusset plate thickness and removing the vertical member to represent the Warren truss without vertical members common in steel truss bridges. The framing angle of the diagonal members in the test specimens is 45° in all of the tests, although the test frame was designed initially to accommodate a small range of angles.

4.3.1. GP307-SS3 Specimen

Gusset plate dimensions for the GP307-SS3 specimen are shown in Figure 4.3.1. All the bolts in this connection are 7/8 inch diameter A307 bolts. The gap between the corner of the compression diagonal and the west chord is 1 inch, a value considered to be a practical lower bound for fabrication. The connection between the gusset plate and compression diagonal has only six rows of fasteners. This results in relatively shorter free edge lengths (11.3” & 14.1”) on the compression diagonal side compared to other two specimens utilizing A307 bolts.

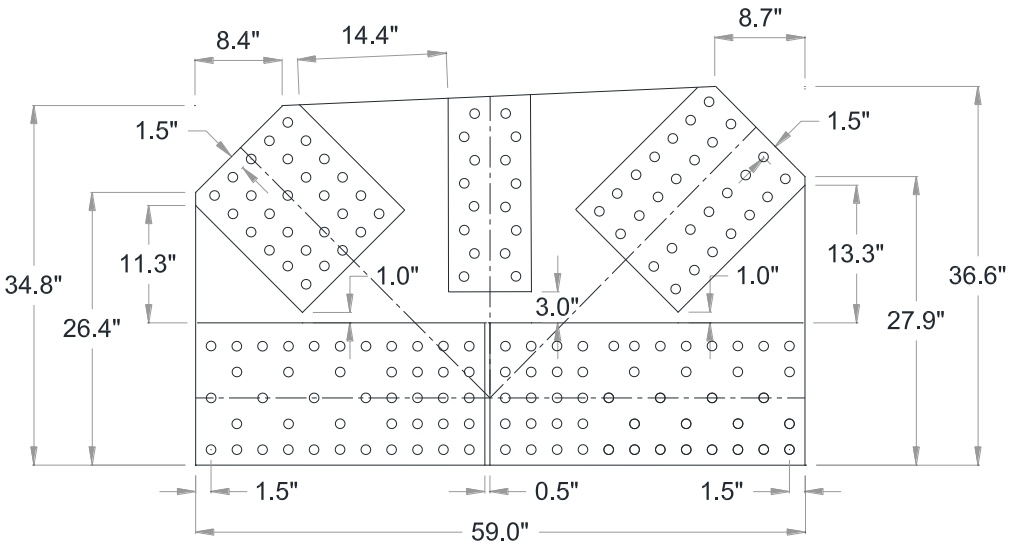

Figure 4.3.1: GP307-SS3 specimen gusset plate dimensions

4.3.2. GP307-LS3 Specimen

Figure 4.3.2 shows detailed dimensions for the gusset plate from the GP307-LS3 specimen. In this second specimen, the connection utilizes A307 bolts. In this case, the gap between the compression diagonal corner and the west chord is increased to 4.5 inches, a value considered as a practical upper limit from the available plans, as larger values would result in very large gusset plates. The number of fastener rows on the compression diagonal side is increased to seven rows to accommodate the new geometry. This results in longer free edges (16.9” and 19.7”) compared to GP307-SS3 specimen (11.3” & 14.1”). A major change in this specimen is the increase in the triangular area at the base of the compression diagonal and the corresponding equivalent column length used in the buckling resistance calculations. This is mainly due to the increase of the gap from 1 inch to 4.5 inches.

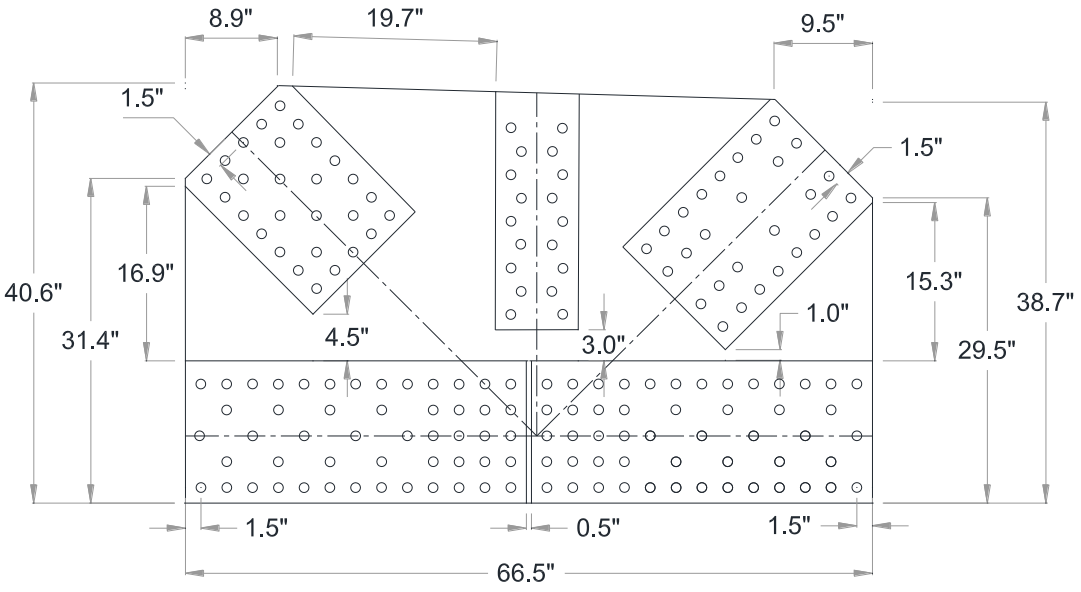

Figure 4.3.2: GP307-LS3 specimen gusset plate dimensions

4.3.3. GP307-SL3 Specimen

The third specimen with A307 bolts is the GP307-SL3 specimen, for which the dimensions are shown in Figure 4.3.3. Similar to the GP307-SS3 specimen, the gap between the compression diagonal corner and chord member is kept at 1 inch. However, connection length along the compression diagonal is longer than for the GP307-SS3

specimen. The number of rows increases from six to nine in this case. The intent is to keep the gap at 1 inch as in GP307-SS3 connection but increasing the free edge lengths on the compression diagonal side by changing the number of rows of fasteners.

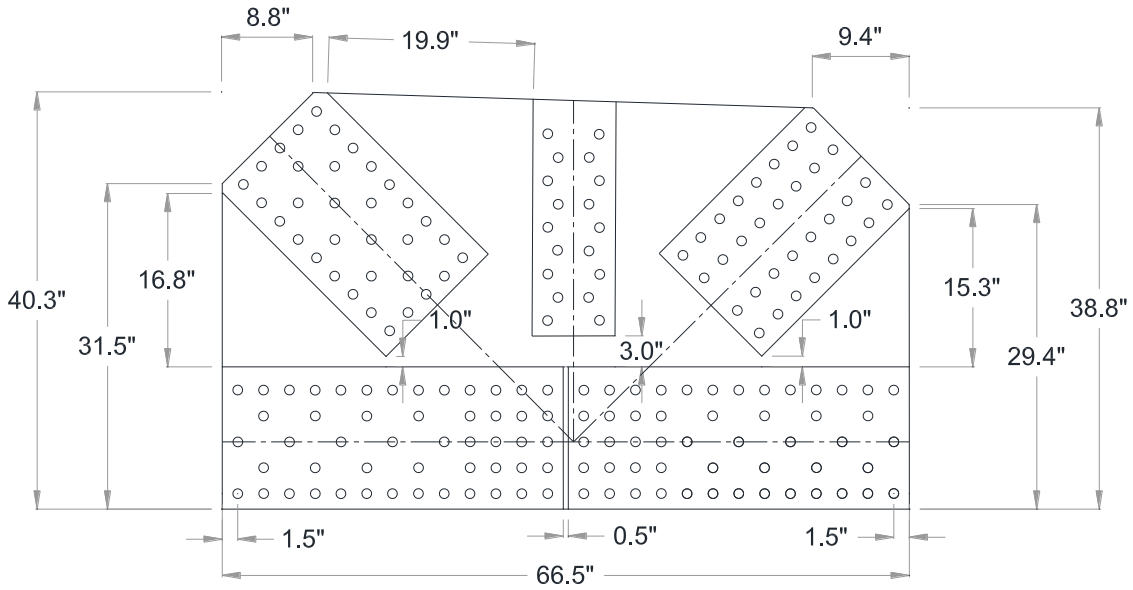

Figure 4.3.3: GP307-SL3 specimen gusset plate dimensions

4.3.4. GP490-SS3 Specimen

High strength A490 bolts are utilized for the GP490-SS3 specimen. Detailed dimensions for the gusset plate are shown in Figure 4.3.4. The gap between the compression diagonal corner and the chord member is 1 inch. Similar to the GP307-SS3 specimen, the connection length is relatively short and has only five rows of fasteners along the compression diagonal. This results in fairly short free edge lengths (9.2” and 12.7”).

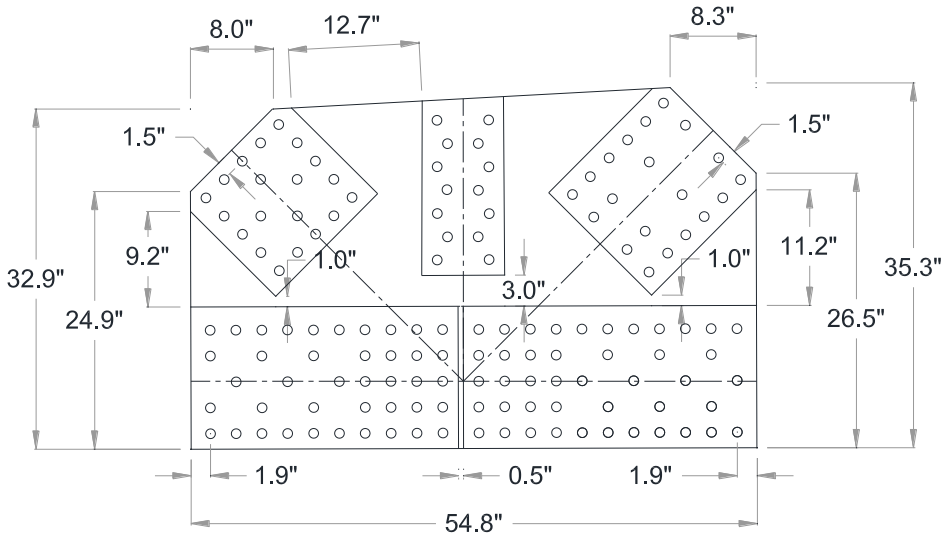

Figure 4.3.4: GP490-SS3 specimen gusset plate dimensions

4.3.5. GP490-LS3 (GP490-LS3-1) Specimen

The second specimen to utilize A490 bolts is the GP490-LS3-1 specimen. This is a repeat specimen of the original GP490-LS3 specimen. Elastic stages are performed on the original specimen before its failure due to loss of load control; those results are used to compare test results with analytical models. Parametric studies are performed on the analytical model using the initial imperfection data provided by FHWA. However, since it is the ultimate strength that is of primary interest in this research, final test comparisons are done using the data from the GP490-LS3-1 specimen. Detailed dimensions for the gusset plate are shown in Figure 4.3.5. Compared to the GP490-SS3 specimen, the gap between the compression diagonal corner and the West chord is increased to 4.5 inches. Due to this increase, the free edge lengths slightly increase (12.9” and 16.0”) compared to the GP490-SS3 specimen (9.2” and 12.7”). However, the main change is the increase in the equivalent column length used in the buckling resistance calculations.

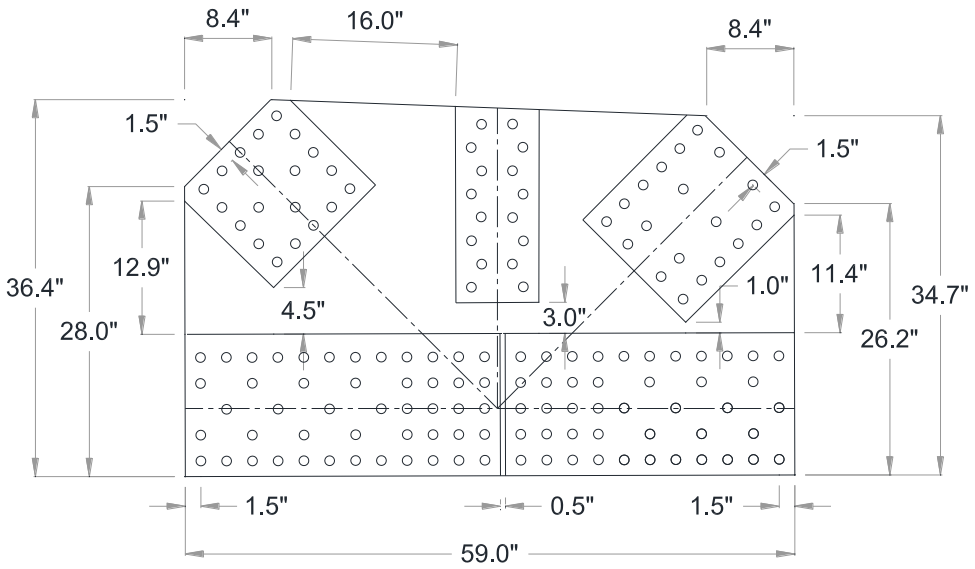

Figure 4.3.5: GP490-LS3 specimen gusset plate dimensions

4.4. Instrumentation

LVDTs and strain gauges (single-axis or rosettes) are used extensively for large scale experiments in structural engineering. This would be an effective combination to gather data if the principal strain directions and locations of maximum deformations can be predicted correctly a priori. However, steel bridge truss gusset plate connections differ from many other common structural components because they have complex strain fields. Thus a large number of strain gauges would need to be installed to reliably capture the strain distribution within the gusset plate. Another important attribute is that the gusset plate displacement field becomes three dimensional as the gusset plates undergo a buckling failure. To follow this three dimensional displacement field would also require a large number of sensors. In this research, a combination of conventional instrumentation (strain gauges) and three full field measurement techniques are employed. Two of the three full field measurement techniques represent significant innovations as this is the first time they are used in tests of this kind.

4.4.1. Strain Gauges

Conventional single-axis strain gauges and rosettes are used on the back of the gusset plates and splice plates. They are also utilized at key locations on the five

connected members to determine member forces and make sure the loading system works properly during each test. Discrete strain gauge data provides a limited additional set of output to compare with the analytical models and data from the imaging systems.

More importantly, however, the strain gauges provide valuable data to check and calibrate the output of the innovative instrumentation used to capture the full field strains.

Figure 4.4.1 shows the strain gauge and rosette pattern used on the gusset plate of the GP307-SS3 specimen. Despite the changes in gusset plate geometry of each specimen, a similar pattern and number of gauges are utilized in all the specimens. Figure 4.4.2 shows the top/bottom splice plates along with the web splice plates used in the tests. For each specimen, 3/8 inch splice plates are fabricated from the same plate material as the gusset plates. Figure 4.4.3 through Figure 4.4.7 shows the strain gauge pattern applied on each member connecting to the gusset plates.

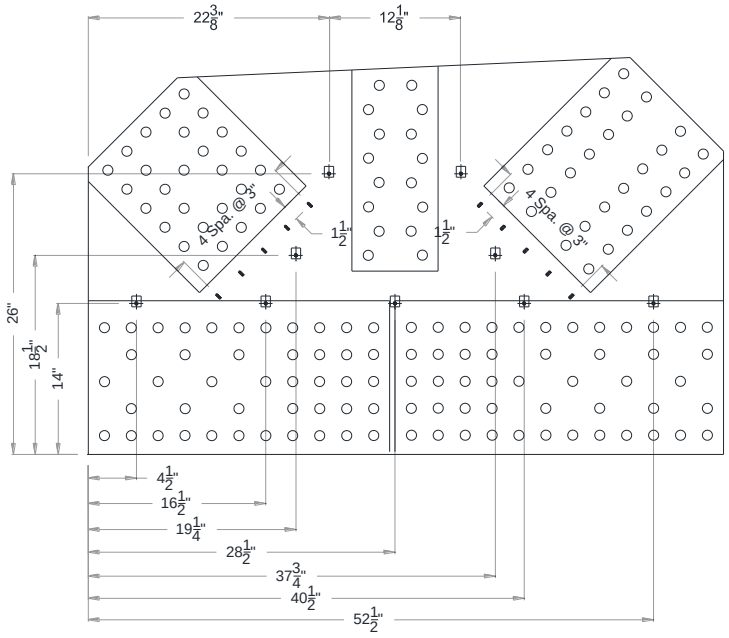

Figure 4.4.1: Strain gauge and rosette pattern for the GP307-SS3 gusset plate

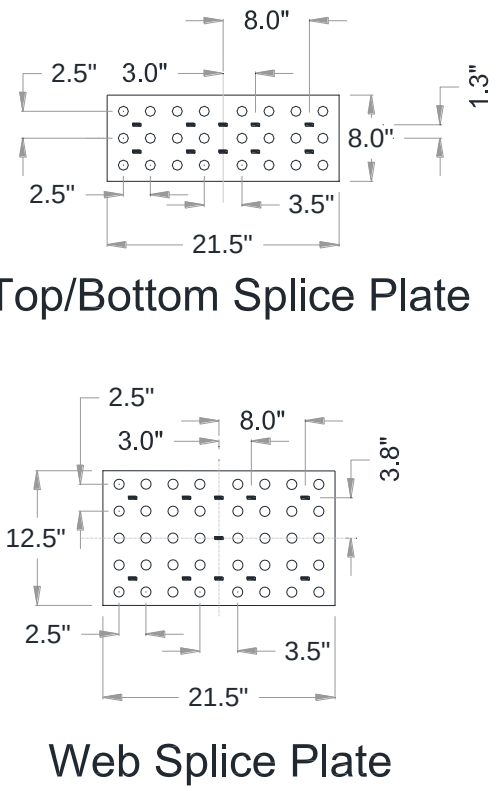

Figure 4.4.2: Strain gauge locations on the web splice plates and top/bottom splice plates

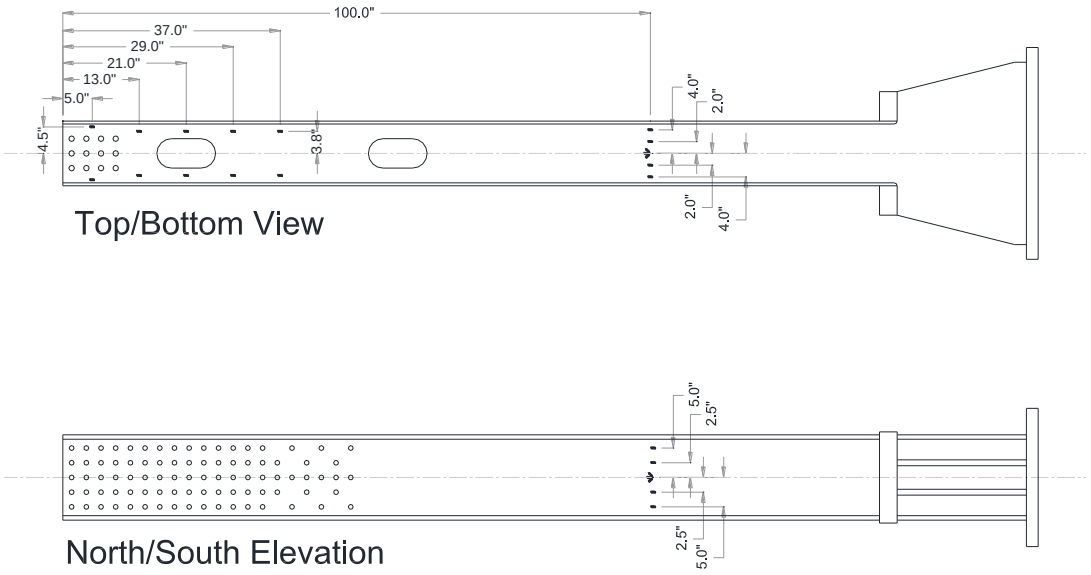

Figure 4.4.3: Strain gauge and rosette locations on the east chord

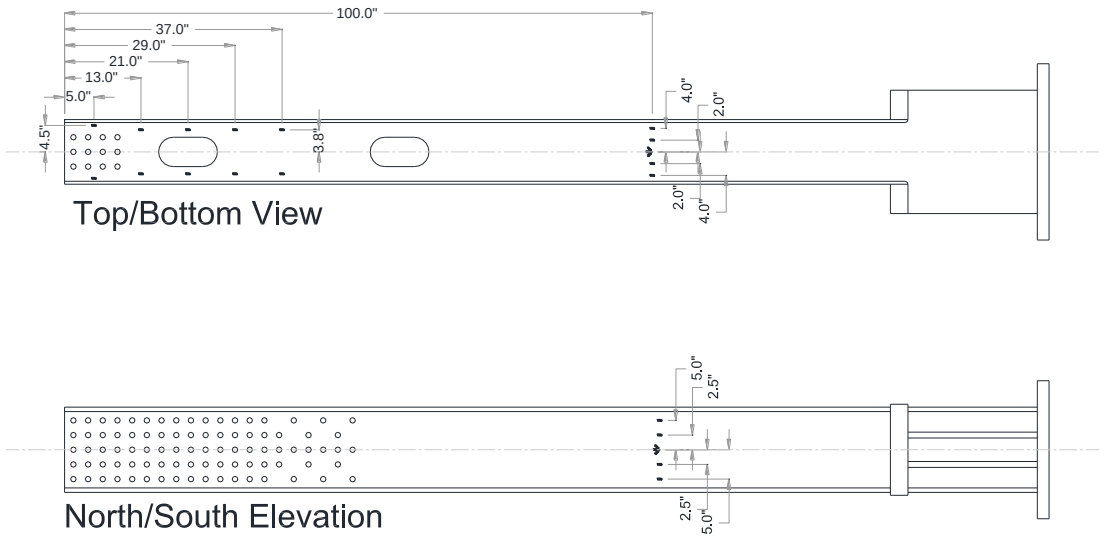

Figure 4.4.4: Strain gauge and rosette locations on the west chord

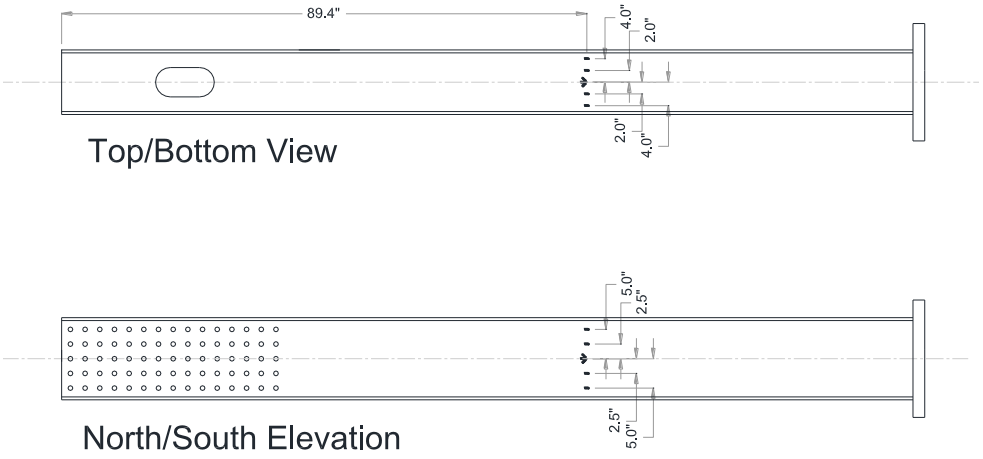

Figure 4.4.5: Strain gauge and rosette locations on the compression diagonal

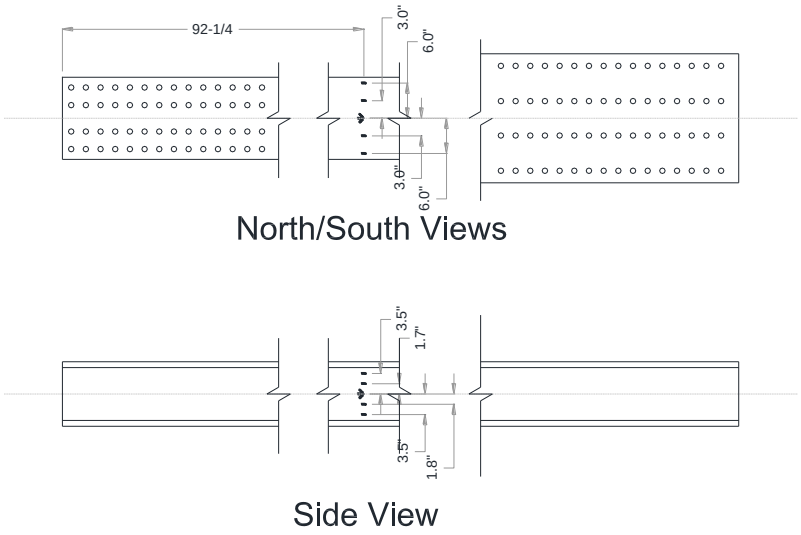

Figure 4.4.6: Strain gauge and rosette locations on the tension diagonal

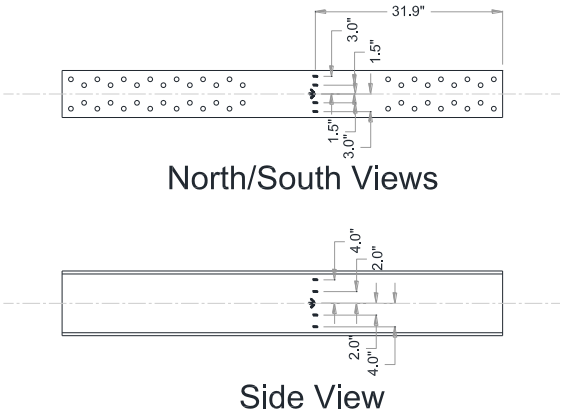

Figure 4.4.7: Strain gauge and rosette locations on the vertical member

4.4.2. Photo-elastic Strain Measurement System

For each specimen, the full strain field of the external face of the South gusset plate is monitored using a photo-elastic strain measurement system. The system involves coating the gusset with a substance that has certain birefringent characteristics. Figure 4.4.8 shows the coated gusset plate for the GP307-SS3 specimen. All the calibration and preliminary testing for this system was performed by FHWA personnel before the test of each specimen. This system is utilized during the elastic stages since it works best up to approximately 1500 με. It is able to determine the diameter of the Mohr's Circle of strain

and the direction of the first principal strain at any location, but it does not indicate the center location of the circle. The most reliable data from the system is the diameter of Mohr's Circle which is called the "Maximum Shear Strain" throughout this research. This output is used to compare experimental results with the finite element analyses from Abaqus.

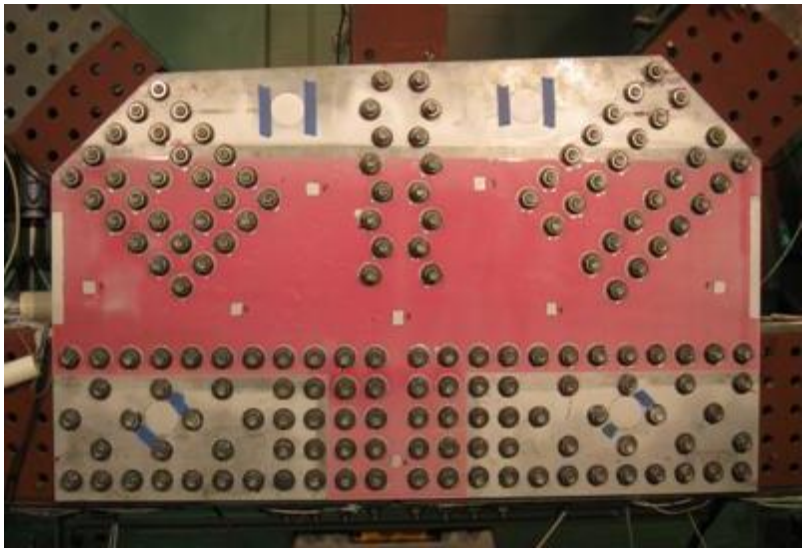

Figure 4.4.8: Epoxy coating applied on the south gusset plate of the GP307-SS3 specimen for photo-elastic strain measurement system

4.4.3. Digital Image Correlation (DIC)

This system uses two digital cameras in a stereoscopic arrangement (Figure 4.4.9). The external face of the north gusset plate is monitored using DIC techniques during the test to failure of each specimen. It provides full three dimensional displacement fields in addition to the complete in-plane strain field for the gusset plate. The output from this system is the radius of the Mohr's Circle of strain (referred to as the Tresca Strain). The uncertainty in this measurement is approximately +/- 150 με, which makes this system more reliable when strains become significantly large. Hence, this system is used to provide data for the final tests to failure.

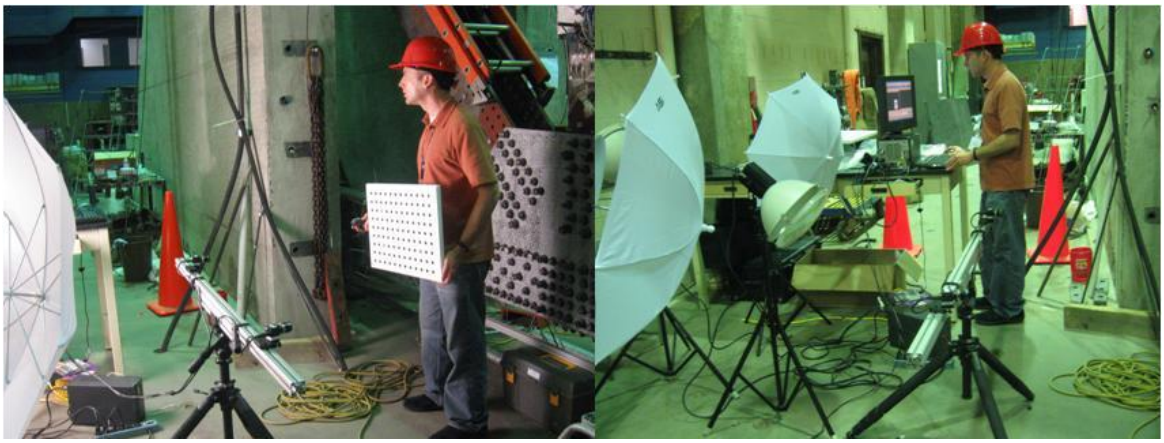

Figure 4.4.9: Digital Image Correlation (DIC) system calibration to monitor the north gusset plate of the GP307-SS3 specimen (performed by Dr. Mark Iadicola from NIST)

4.4.4. FARO ION Laser Tracker

This system is used to obtain discrete displacement measurements on gusset plate and connected members. These targets are shown in Figure 4.4.10. One major use of this system is to determine accurate (+/- 0.0004") initial positions of the members and the shape of the gusset plates as installed in the joint configuration at the start of the tests. It is very important to have this data so that initial imperfections can be integrated into the finite element models as accurately as possible. The standard Spherical Mounted Reflector (SMR) is a 1.5 inch diameter steel ball with a prism precisely mounted at the center of the sphere. During the tests to failure, the SMR is located on each discrete target and is used to determine the three dimensional displacements at the target locations on the gusset plate during each load step (Figure 4.4.11).

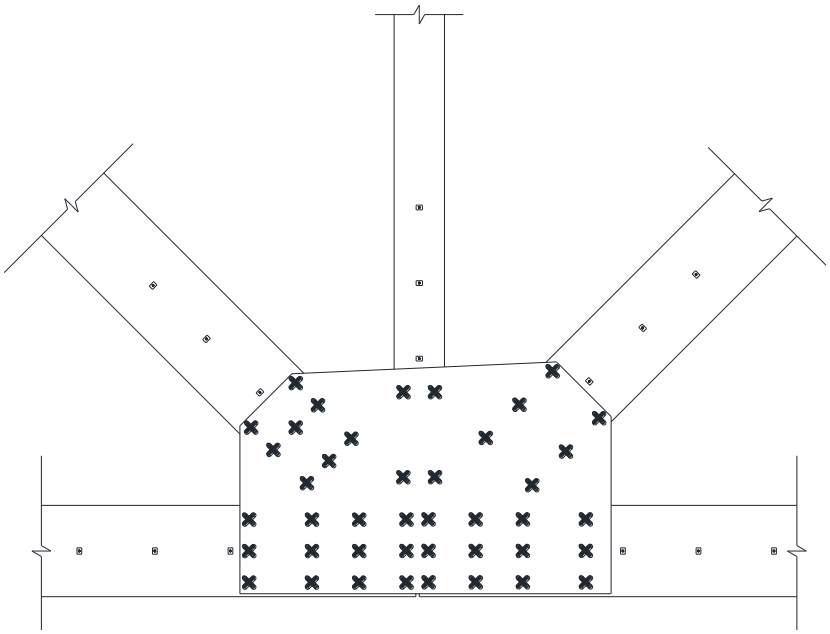

Figure 4.4.10: Target locations on the north gusset plates for FARO ION laser tracking system

Figure 4.4.11: FARO ION laser tracker (left) is being operated to get the displacement measurements from target locations during the test (right)

4.5. Data Acquisition

All sensor data including the strain gauges and conditioned voltages from the MTS FlexTest GT controller (i.e. the load and stroke of each jack) are collected by a Hewlett-Packard (HP) VXI CT100B mainframe. All strain gauge and rosette data are converted to usable data formats such as forces, moments, and principal strains. The data sets include the calculations of the diameter of the Mohr's Circle to make comparisons between experimental results and finite element analyses. The photo-elastic strain measurement system, Digital Image Correlation (DIC) system, and FARO ION Laser Tracker system have their own stand-alone computers to collect and store their data. Post-processing is performed on each set of data to obtain the required experimental data.

4.6. Analytical Test Simulation Models

Each test specimen is modeled using the Abaqus finite element analysis (FEA) software (Simulia, 2009; Simulia, 2010). Material and geometric nonlinearities are included in each analysis representing the test to failure. Actual equilibrium loads from the physical test are integrated into the analytical models for the full nonlinear 3-D finite element analysis.

4.6.1. Geometry and Boundary Conditions

Gusset plates and splice plates are modeled using four-node shell elements (S4R elements in Abaqus). The members connected to the gusset plates are modeled using four-node shell elements up to a length of approximately 2d from the edge of the gusset plate where d is the member depth. The intent is to keep the size of the model as small as possible to increase the feasibility of conducting a large number of parametric studies, while also aiming to provide highly refined solutions of the gusset plate response. In the test specimen models, the shell element size is around 0.5 in. This provided essentially a converged numerical solution for the response contours.

Figure 4.6.1 shows the assembly with the shell elements applied to all plates and members. The rest of the members are modeled using two-node linear-order beam elements (B31 elements in Abaqus). Sixteen elements are used throughout the portion of each member represented by the beam elements. This portion is then connected to the

shell portion by using a beam type multipoint constraint (MPC) in the Abaqus software (Figure 4.6.2).

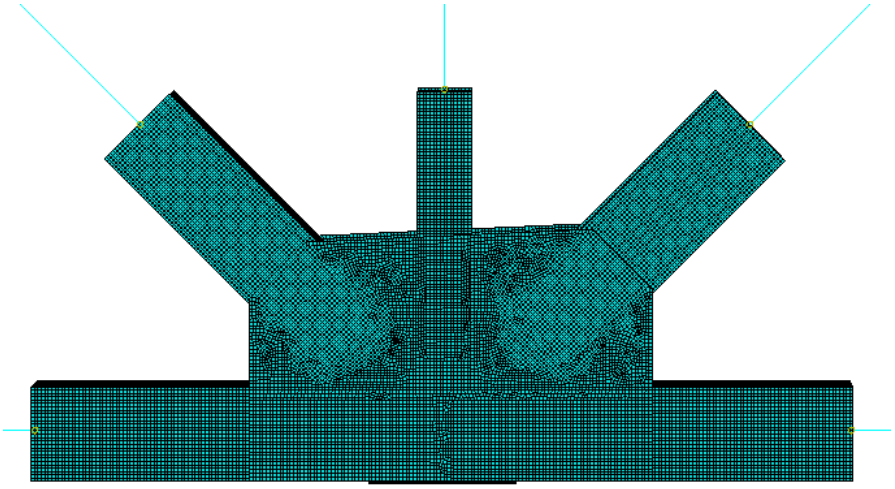

Figure 4.6.1: Finite element mesh showing the shell elements of the plates and connected members

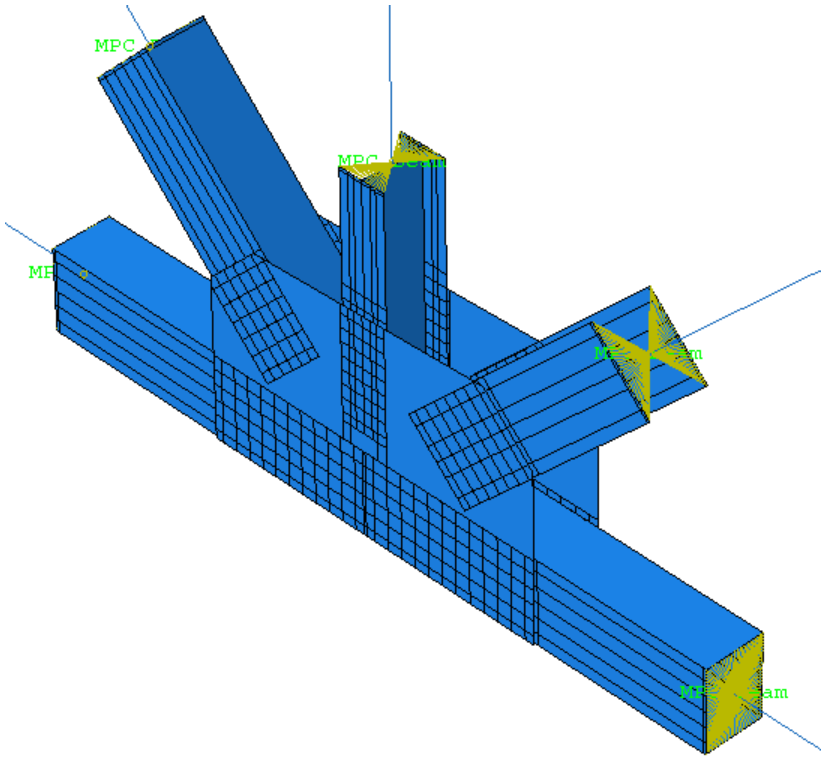

Figure 4.6.2: Beam type multi-point constraints (MPCs) connecting the beam portion to the shell portion of the members

The in-plane boundary conditions applied in the FEA model are shown in Figure 4.6.3. The West chord is a reaction chord and all six degrees of freedoms for displacement and rotation are fixed. For the remaining four members, translation along the length of the member is allowed, as represented by a roller at the ends.

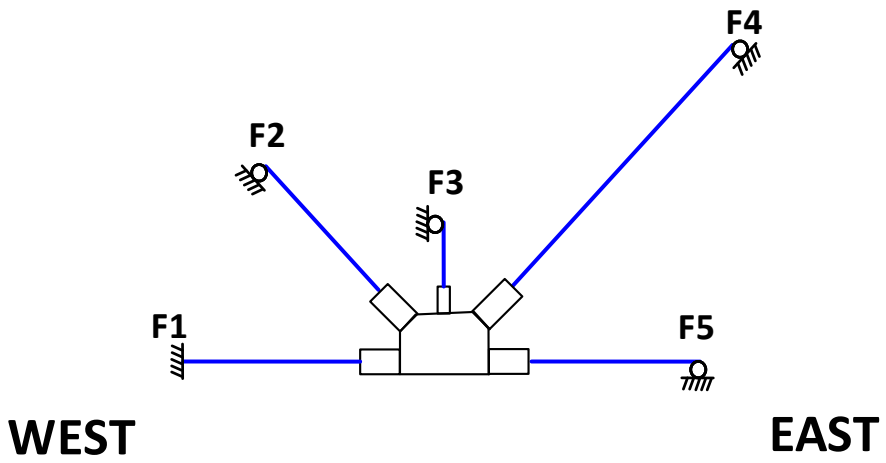

Figure 4.6.3: In-plane boundary conditions applied in the finite element models of the test specimens

In addition to the in-plane boundary conditions, torsional rotation and out-of-plane displacement are restrained at the opposite ends of all the member from the test joint. Figure 4.6.4 shows a perspective view with all boundary conditions. In this figure, orange shapes represent the displacement restraints and blue shapes represent the rotational restraints respectively.

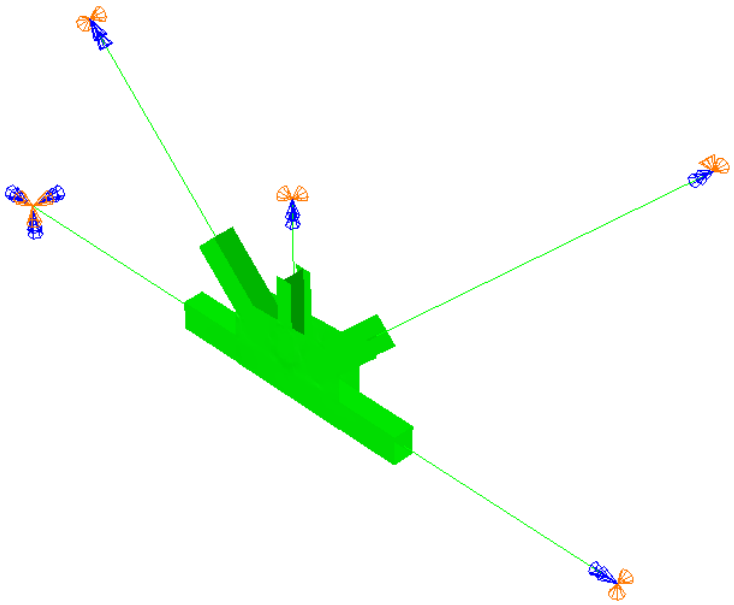

Figure 4.6.4: 3-dimensional displacement and rotation restraints applied at the member ends

4.6.2. Material Properties

For each specimen, the gusset plates and splice plates are taken from the same plate by cutting a single 48” x 240” plate using a CNC machine. In addition, FHWA performed extensive coupon tests from these plates to provide the physical material properties to be used in the analytical models. Coupons are cut from the plate in both the parallel and perpendicular direction to the cutting direction to measure both longitudinal and transverse material properties. The main conclusion from the coupon tests is that there was no substantial anisotropy between these two directions as expected.

In an effort such as this, it is essential to obtain the correct material properties to apply in the finite element models. The yield strength is determined as the static yield stress. Using the coupon test results, nonlinear material properties are back-calculated in terms of true stress and corresponding true plastic strain (not engineering stress and strain), as these are the properties needed by the software. The true stress versus plastic strain relationship to be used as the input for the five specimen models is shown in Figure 4.6.5. The GP307-SS3 specimen has a static yield of 36.4 ksi. The other specimens have static yield strengths varying from 45.9 to 48.2 ksi. The connected members are designed to remain elastic throughout the test. Hence, they are assigned elastic material properties

since the studies focus on the gusset plate behavior and the failure modes in the gusset plates without failing the connected members.

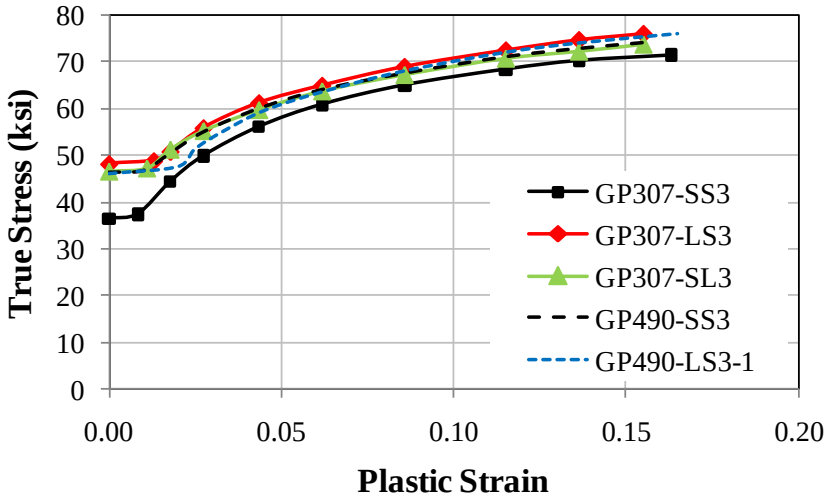

Figure 4.6.5: True stress vs. true strain relationship for the plate materials used in the finite element models of the five test specimens

Two different bolt shear force – shear displacement curves are used in the analytical models to represent the two types of fasteners employeds in the tests, the A307 and A490 bolts as discussed previously in Section 4.3. Lap-splice experimental tests were performed by FHWA for the bolts utilized in the tests, to define the single shear response for input into the connector element model of the analytical studies.

The connector element utilized in the studies is described in Section 3.1. The bolt holes are not explicitly modeled. Instead, bolts are modeled using the connector elements and corresponding nonlinear fastener properties are assigned to these elements (Figure 4.6.6). Within the interaction module of Abaqus, the number of layers can be defined and for each layer a single fastener element is created to connect the two surfaces.

The fastener model includes a "radius of influence" within which the displacements are constrained to the fastener element. This surface constraint forces the nodes to deform together and represents the extra stiffness that the bolt head or nut provides on two connected surfaces.

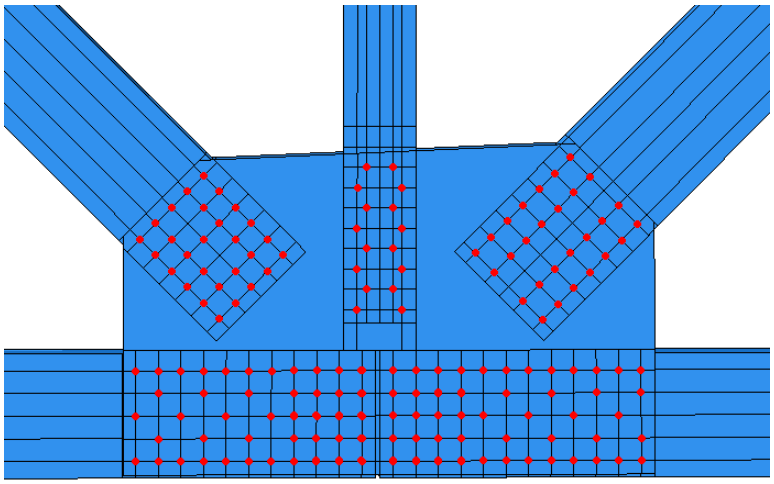

Figure 4.6.6: Connector elements in the finite element model (in-plane view showing the discrete fastener locations)

All the bolts used in the experiments are 7/8" diameter. The radius of influence in the models is taken as 7/8". The fastener experiments were calibrated through finite element modeling of the single-shear lap splice tests run at FHWA. Figure 4.6.7 shows the fastener force versus displacement relationship for the A307 and A490 bolts (Ocel et al., 2010). The shear displacements are predominantly due to fastener deformation for the A307 fasteners, where they are predominantly due to plate bearing deformations in the vicinity of the bolt for the A490 fasteners.

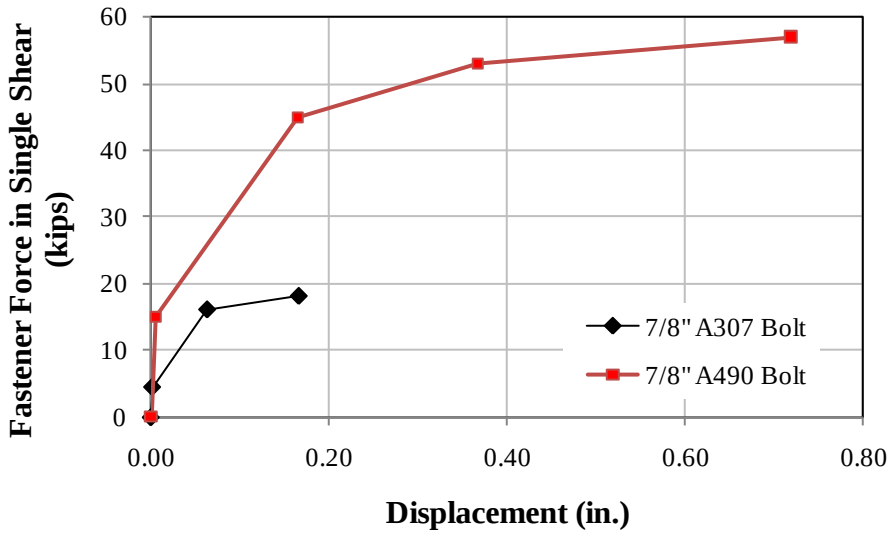

Figure 4.6.7: Fastener force vs. displacement relationship for 7/8 inch A307 and A490 bolts in single shear

4.6.3. Initial Imperfections

The effect of the initial imperfections on the gusset plate resistance is discussed in the previous chapter.. The best option for a refined finite element analysis of the physical specimens is to input the measured initial imperfections into the analytical models. For each of the tests, the nodes close to the member corners and along the free edges are selected and values from the measured initial imperfection contours are applied as the initial out-of-plane displacements at these positions in the finite element model. A representative example from GP490-SS3 specimen with the picked node numbers in the finite element model is shown in Figure 4.6.8.

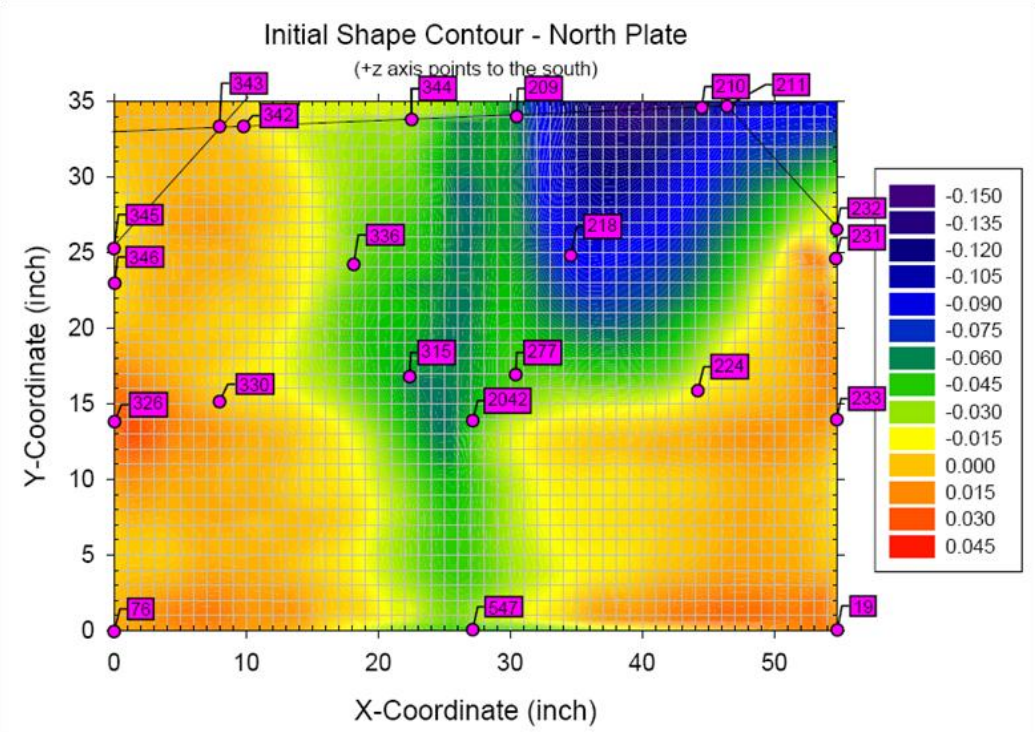

Figure 4.6.8: Example of the selected nodes for initial imperfection application

The physical gusset plates have initial imperfections when they are fabricated and before they are installed into the test setup. However, only the initially imperfect shape when the gusset plate is in-place just prior to testing is considered in this research. The induced stresses due to installation are neglected in the finite element models.

4.6.3.1. GP307-SS3 Specimen

The GP307-SS3 specimen was the first to be tested in the experimental phase of the research. Initial imperfection data was not obtained using the FARO laser scanner in this case. This test provides information on the future methods to apply during the test including the application of laser scanning to get initial imperfections but also about the photoelastic strain measurement system and coating applied on the gusset plate to gather that data. The initial imperfection data was provided using the Digital Image Correlation (DIC) set on one side of the connection. Since the DIC provides data only for one gusset, the same imperfection was applied for both gussets in the finite element model.

Figure 4.6.9 shows perspective view with the initial imperfection contours for the north gusset plate; the tension diagonal is on the left and the compression diagonal is on the right in this figure. In the finite element models, the +z direction was towards the South direction.

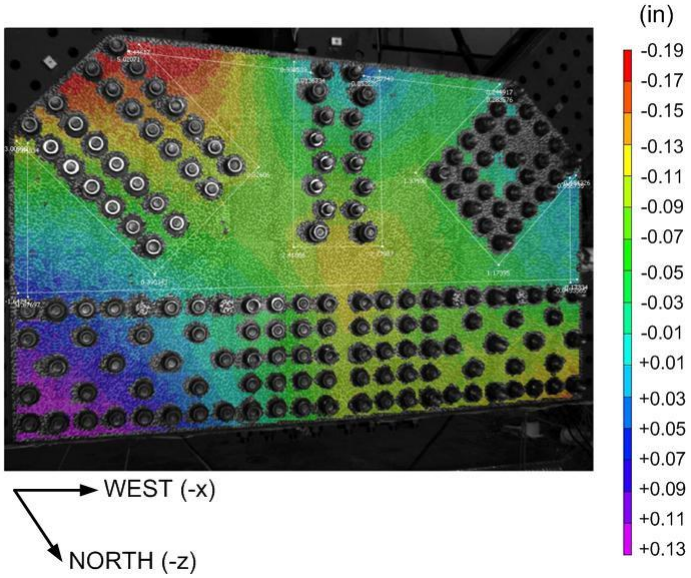

Figure 4.6.9: Initial imperfection data for the south and north gusset plates of the GP307-SS3 specimen

For the subsequent tests, a better approach was used to determine the initial imperfection data. An initial scan of both gusset plates in the connection was done using the FARO laser tracker and corresponding contours were created by FHWA. The contour plots obtained from the FARO system are discussed below.

4.6.3.2. GP307-LS3 Specimen

Figure 4.6.10 and Figure 4.6.11 show the initial imperfection contours for the south and north gusset plates of GP307-LS3 respectively.

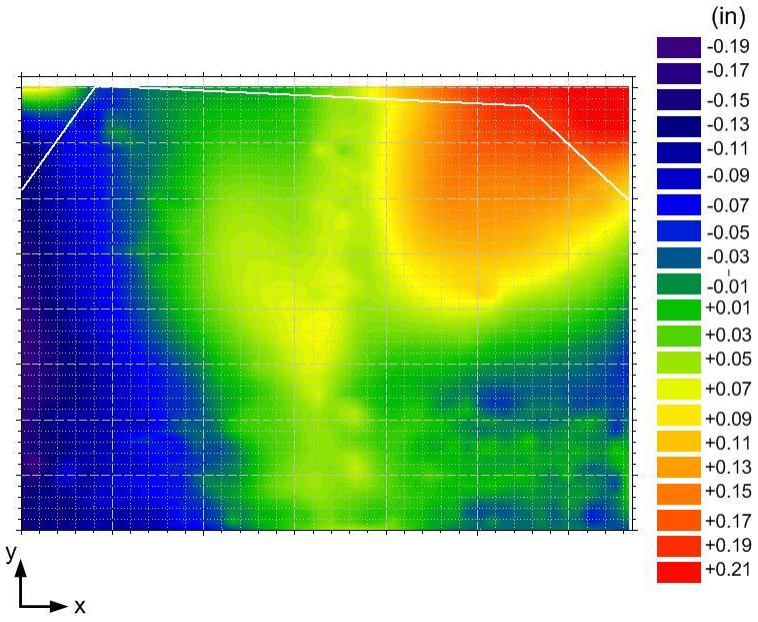

Figure 4.6.10: Initial imperfection data for the south gusset plate of the GP307-LS3 specimen

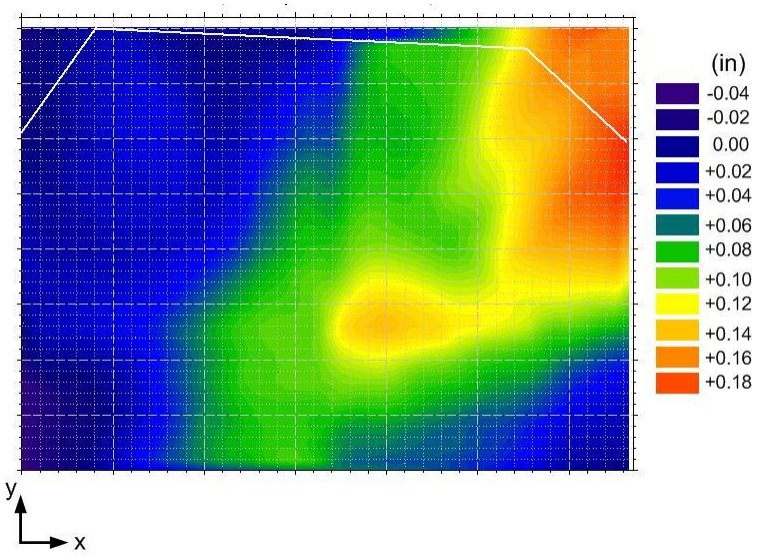

Figure 4.6.11: Initial imperfection data for the north gusset plate of the GP307-LS3 specimen

4.6.3.3. GP307-SL3 Specimen

The GP307-SL3 specimen has slightly smaller imperfection values for the North gusset plate as compared to the South gusset plate. The imperfection contours are shown in Figure 4.6.12 and Figure 4.6.13 for the two gusset plates of the connection.

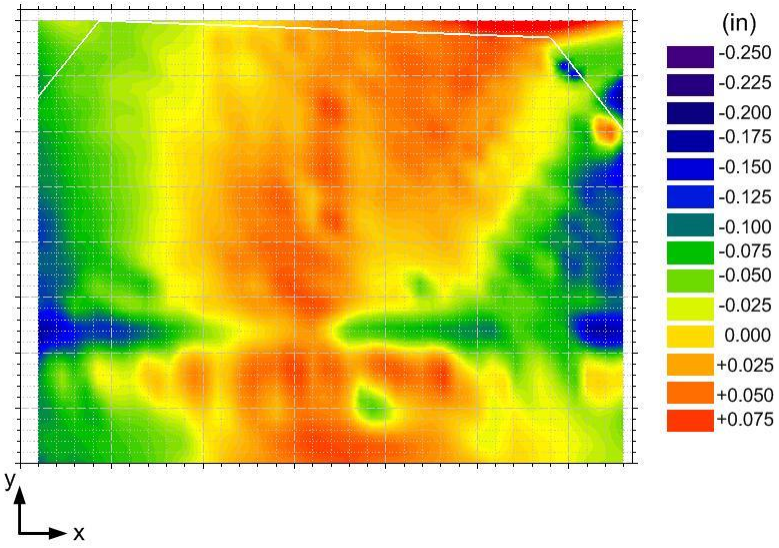

Figure 4.6.12: Initial imperfection data for the south gusset plate of the GP307-SL3 specimen

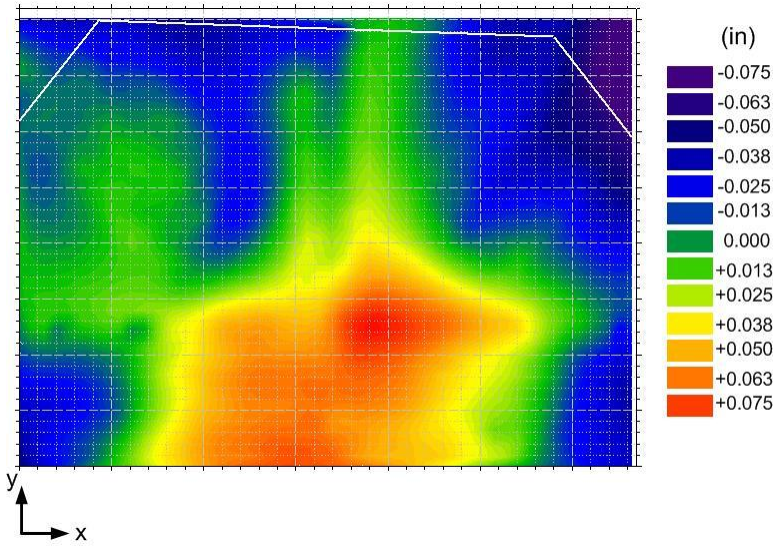

Figure 4.6.13: Initial imperfection data for the north gusset plate of the GP307-SL3 specimen

4.6.3.4. GP490-SS3 Specimen

The GP490-SS3 specimen imperfection contours are shown in Figure 4.6.14 and Figure 4.6.15.

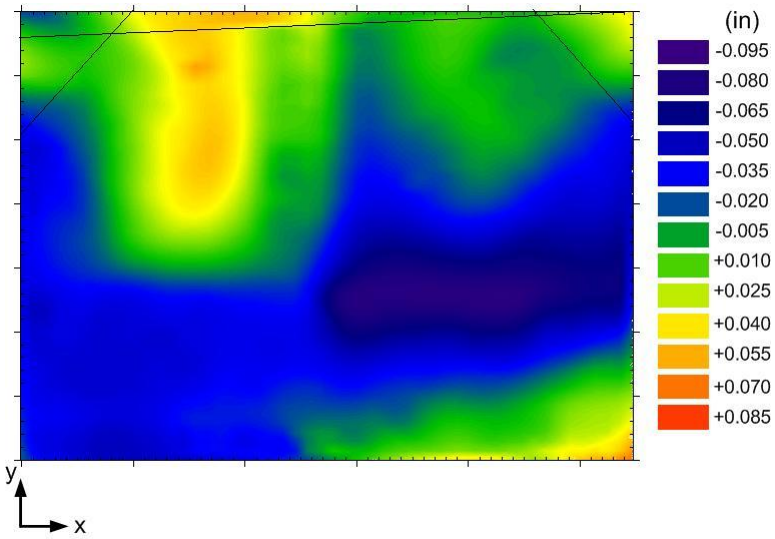

Figure 4.6.14: Initial imperfection data for the south gusset plate of the GP490-SS3 specimen

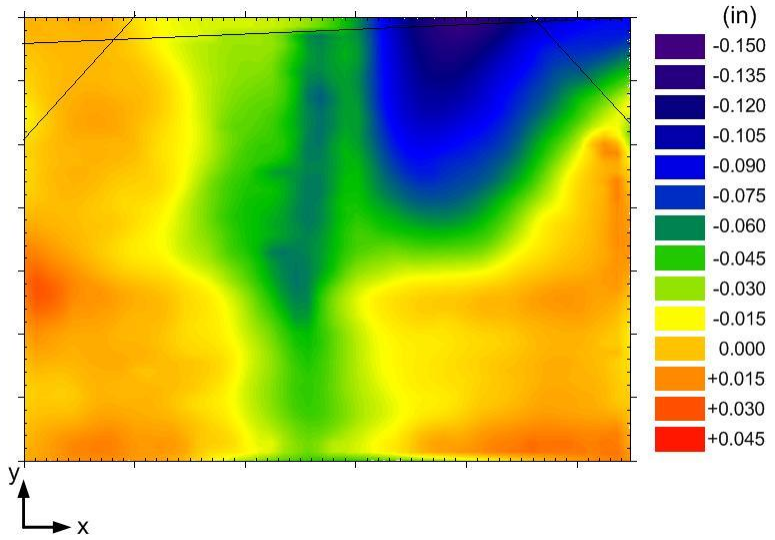

Figure 4.6.15: Initial imperfection data for the north gusset plate of the GP490-SS3 specimen

4.6.3.5. GP490-LS3 (GP490-LS3-1) Specimen

This test involved two separate replicate specimens. . Only elastic load histories were considered for the original GP490-LS3 specimen The imperfection data for the gusset plates in this specimen is shown in Figure 4.6.16 and Figure 4.6.17 respectively.

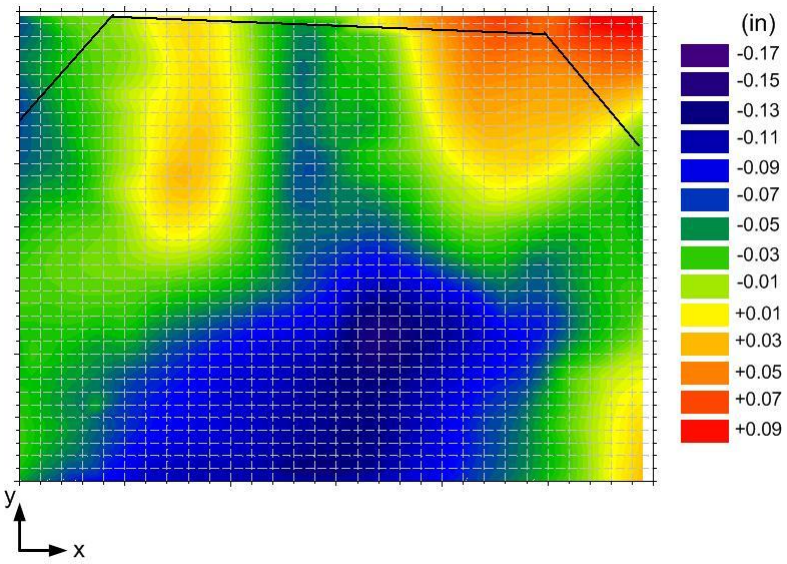

Figure 4.6.16: Initial imperfection data for the south gusset plate of the GP490-LS3 specimen

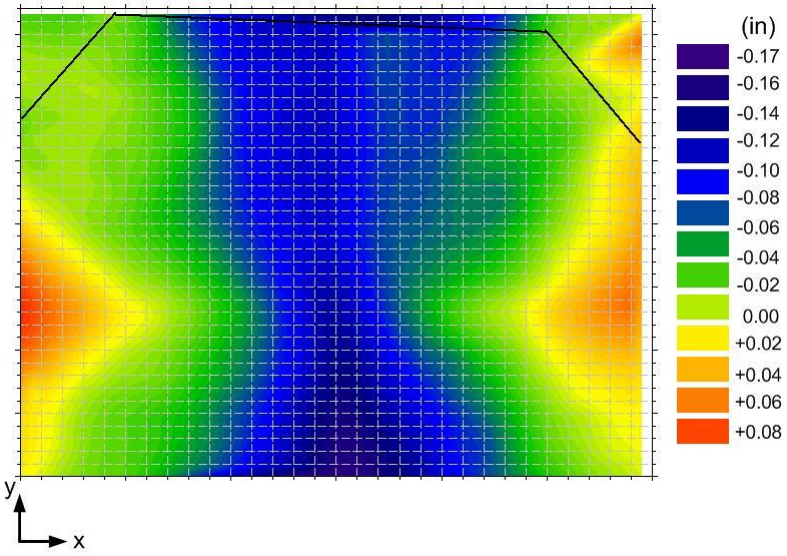

Figure 4.6.17: Initial imperfection data for the north gusset plate of the GP490-LS3 specimen

The replicate specimen, GP490-LS3-1 was tested to failure without considering any elastic load histories. The corresponding initial imperfection data for this specimen is shown in Figure 4.6.18 and Figure 4.6.19

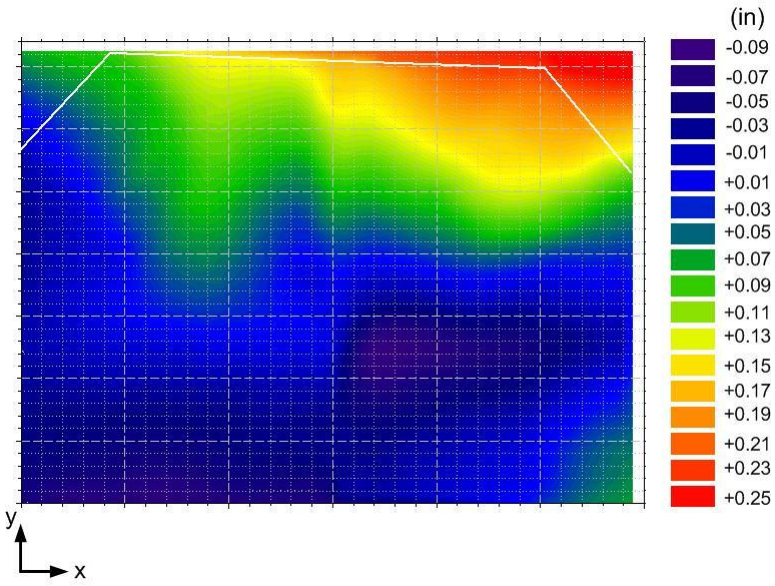

Figure 4.6.18: Initial imperfection data for the south gusset plate of the GP490-LS3-1 specimen

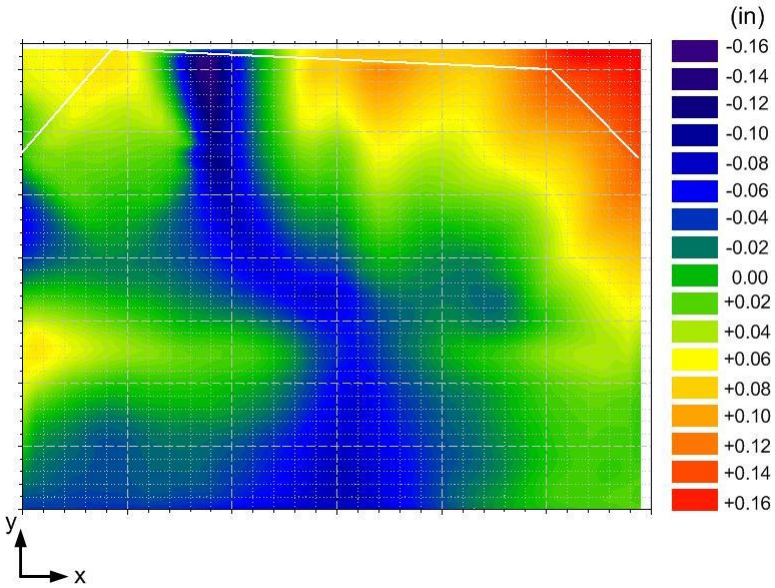

Figure 4.6.19: Initial imperfection data for the north gusset plate of the GP490-LS3-1 specimen

4.6.4. Load Histories

Generally, a large number of elastic experimental loading scenarios were applied to each of the gusset plates to calibrate and validate the analytical finite element models. The loads were applied in such a way that the maximum stress in the plate does not exceed the nominal yield strength. Based on the initial finite element analyses, the applied load fraction and corresponding member loads were provided to research team at the lab. These tests were conducted with and without splice plates between the two chord members. After the two elastic stages were completed, one load combination was selected and applied to test each specimen up to failure.

The total number of load combinations was varied from one specimen to another. GP307-SS3, GP307-SL3, and GP490-LS3 were subjected to 14 load combinations, and GP307-LS3 and GP490-SS3 were subjected to 8 and 13 load combinations respectively. A total of 126 sets of elastic comparison data were obtained from these studies considering cases with and without splice plates. The sign convention for the reference load combinations is shown in Figure 4.6.20. Forces in compression are taken as positive. The West chord is a reaction chord, and forces are applied on the remaining four members.

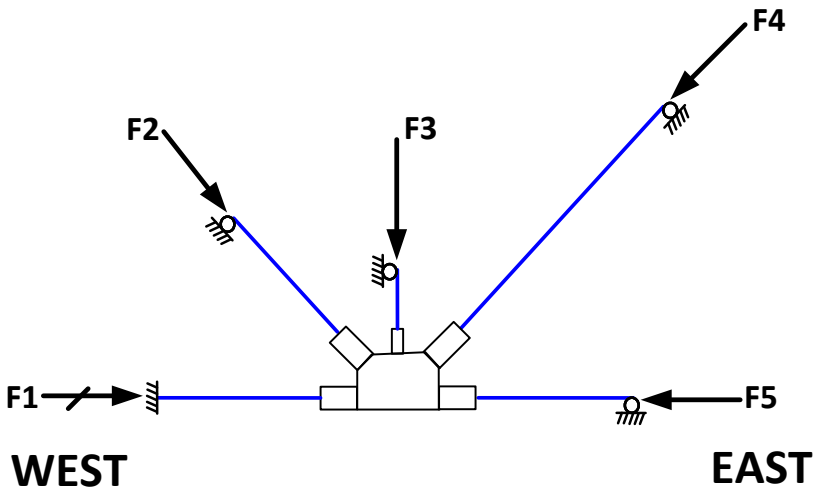

Figure 4.6.20: Sign convention for the load combinations applied on the test specimens. Compression is shown with positive (+) sign

4.6.4.1. GP307-SS3 Specimen

The fourteen reference load combinations used for the GP307-SS3 specimen are shown in Table 4.6.1. For this connection, the East chord is in compression.

Table 4.6.1: Reference load combinations for the load histories of the GP307-SS3 specimen

Load Combination	F1 (kip)	F2 (kip)	F3 (kip)	F4 (kip)	F5 (kip)
1	-1000	707	0	-707	0
2	0	707	0	-707	1000
3	-707	1000	0	-1000	707
4	-500	1000	-207	-707	707
5	-500	707	207	-1000	707
6	-707	1000	-207	-707	500
7	-707	707	207	-1000	500
8	-1000	707	207	-1000	0
9	-207	707	207	-1000	1000
10	-1000	1000	-207	-707	207
11	-207	1000	-207	-707	1000
12	431	322	117	-483	1000
13	-597	1000	-90	-874	728
14	-446	482	365	-1000	602

4.6.4.2. GP307-LS3 Specimen

Table 4.6.2 summarizes the eight reference load combination utilized for the GP307-LS3 specimen. These Load combinations put the East chord in tension.

Table 4.6.2: Reference load combinations for the load histories of the GP307-LS3 specimen

Load Combination	F1 (kip)	F2 (kip)	F3 (kip)	F4 (kip)	F5 (kip)
1	-1000	330	117	-496	-416
2	-1000	650	0	-650	-81
3	-1000	375	0	-375	-469
4	-1000	88	0	-88	-876
5	-1000	672	-119	-504	-168
6	-1000	504	119	-672	-168
7	-1000	697	-246	-348	-261
8	-1000	348	246	-697	-261

4.6.4.3. GP307-SL3 Specimen

The load combinations used for the GP307-SL3 specimen are the same as for the GP307-SS3 specimen. The East chord is in compression for this specimen.

4.6.4.4. GP490-SS3 Specimen

Thirteen load combinations are utilized for the GP490-SS3 specimen as shown in Table 4.6.3. The East chord is kept in compression for this specimen.

Table 4.6.3: Reference load combinations for the load histories of the GP490-SS3 specimen

Load Combination	F1 (kip)	F2 (kip)	F3 (kip)	F4 (kip)	F5 (kip)
1	-1000	707	0	-707	0
2	0	707	0	-707	1000
3	-707	1000	0	-1000	707
4	-500	1000	-207	-707	707
5	-500	707	207	-1000	707
6	-707	1000	-207	-707	500
7	-707	707	207	-1000	500
8	-1000	707	207	-1000	0
9	-207	707	207	-1000	1000
10	-1000	1000	-207	-707	207
11	-207	1000	-207	-707	1000
12	431	322	117	-483	1000
13	-597	1000	-90	-874	728

4.6.4.5. GP490-LS3 Specimen

The last specimen for which the fourteen reference load combinations were used is the GP490-LS3 specimen. Load combinations 1 through 13 are the same as for the GP307-SS3 and GP307-SL3 specimens. Load combination 14 is shown in Table 4.6.4.

Table 4.6.4: Reference load combinations for the load histories of the GP490-LS3 specimen

Load Combination	F1 (kip)	F2 (kip)	F3 (kip)	F4 (kip)	F5 (kip)
14	-531	600	282	-1000	600

4.7. Results and Validation of the Analytical Models

The actual member loads from the tests, provided by FHWA after each test,are applied statically in the finite element models.

As discussed before, one of the gusset plates was monitored using the photoelastic strain measurement system during the elastic stages. This system is able to determine the diameter of the Mohr's circle of strains, i.e. magnitude of the principal strains but not the center of the Mohr's circle. Hence, the system output used to compare with the finite element models and strain gauge data is chosen as the difference between the two principal strains which gives the diameter of the Mohr's circle of strains. This bulk strain output is called "Maximum Shear Strain" throughout the validation and comparison process of the results. The uncertainty of the photoelastic data is approximately +/- 30 microstrain.

There are five strain gauges located just above the chord members along the horizontal plane of the gusset plate as shown in Figure 4.4.1. Discrete strain gauge data along with the Abaqus FEA and Photoelastic data are plotted together in the following section to assess the correlation between the FEA and measured results. For three of the specimens, maximum shear strain contours were provided by FHWA. This is an additional qualitative validation for the analytical models. The response contours are compared with the finite element analysis results.

The second gusset plate was monitored using the Digital Image Correlation (DIC) system during the final test to failure of each specimen. In this case, the output used to obtain the response contours to compare with finite element models is the radius of the Mohr's circle of strains which is called the "Tresca strain". The uncertainty of the Tresca strains is approximately +/- 150 microstrain.

4.7.1. Elastic Stages without Splice Plates

4.7.1.1. GP307-SS3 Specimen

Member forces on four loaded members to be applied in the finite element analysis determined from the elastic stage tests are shown in Table 4.7.1.

Table 4.7.1: Member loads from the elastic load histories of the GP307-SS3 specimen without splice plates

Load Combination	F2 (kip)	F3 (kip)	F4 (kip)	F5 (kip)
1	196	2	-196	-5
2	196	4	-194	267
3	201	0	-205	164
4	232	-48	-192	181
5	239	56	-339	238
6	254	-48	-206	160
7	215	56	-326	186
8	163	44	-263	25
9	235	56	-304	301
10	214	-48	-172	42
11	270	-48	-219	278
12	90	28	-157	278
13	239	-20	-219	189
14	159	92	-348	215

This was the first test performed during the experimental phase. Hence, some of the efforts including the photoelastic system were at their developmental stage and maximum shear strain response contour images from photoelastic data are not available for the GP307-SS3 specimen. However, the test provides quantitative data along the horizontal plane above the chords. Figure 4.7.1 through Figure 4.7.14 shows that the analytical results, the discrete strain gauge data and continuous photoelastic system data match well except for a few localized differences.

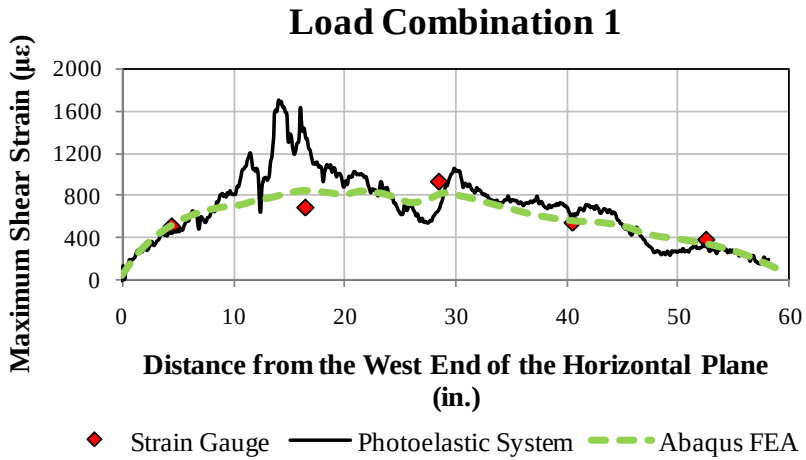

Figure 4.7.1: Comparison between the finite element analysis and experimental data (GP307-SS3 specimen - Load Combination 1)

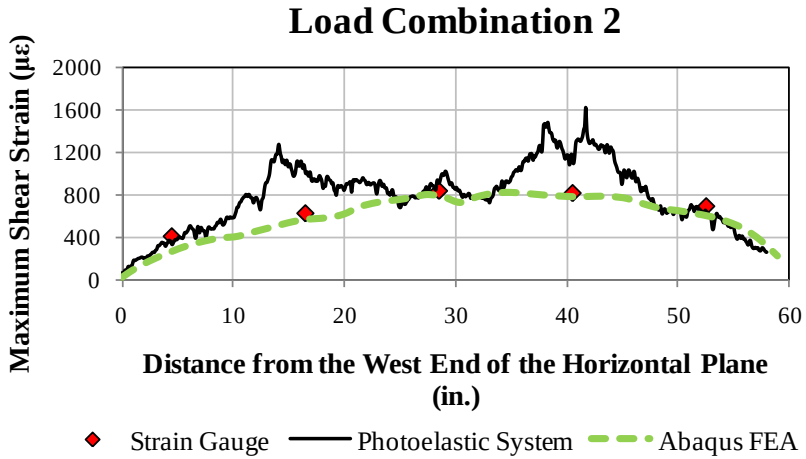

Figure 4.7.2: Comparison between the finite element analysis and experimental data (GP307-SS3 specimen - Load Combination 2)

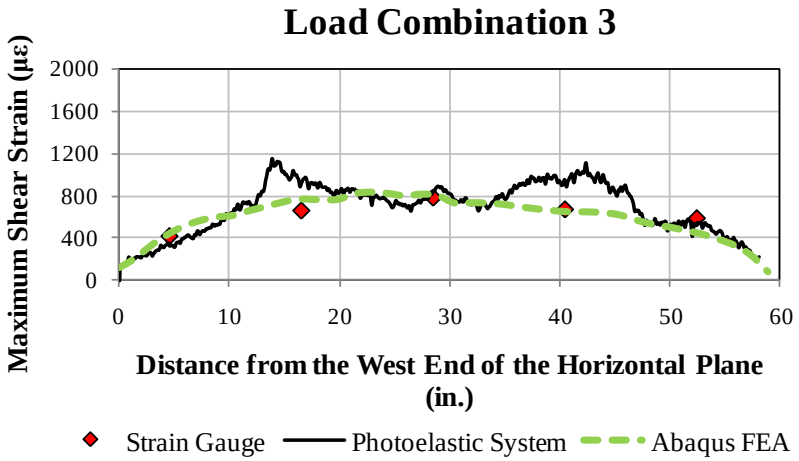

Figure 4.7.3: Comparison between the finite element analysis and experimental data (GP307-SS3 specimen - Load Combination 3)

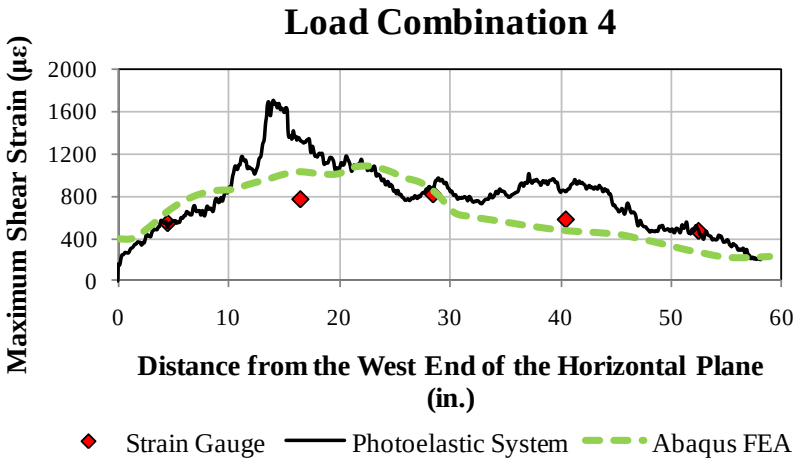

Figure 4.7.4: Comparison between the finite element analysis and experimental data (GP307-SS3 specimen - Load Combination 4)

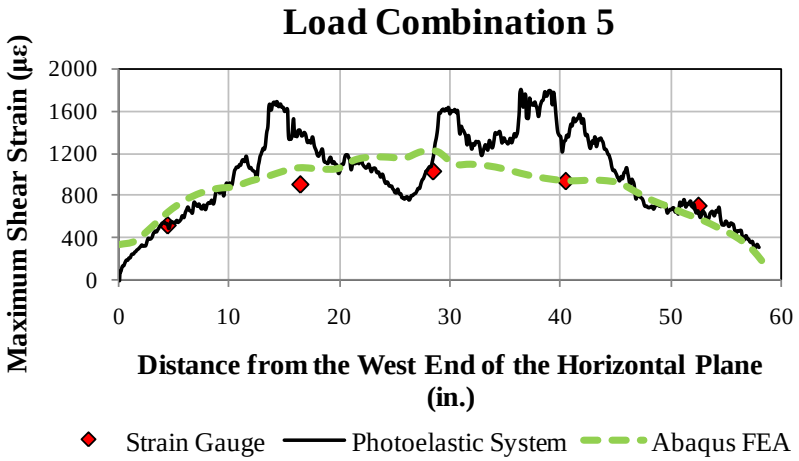

Figure 4.7.5: Comparison between the finite element analysis and experimental data (GP307-SS3 specimen - Load Combination 5)

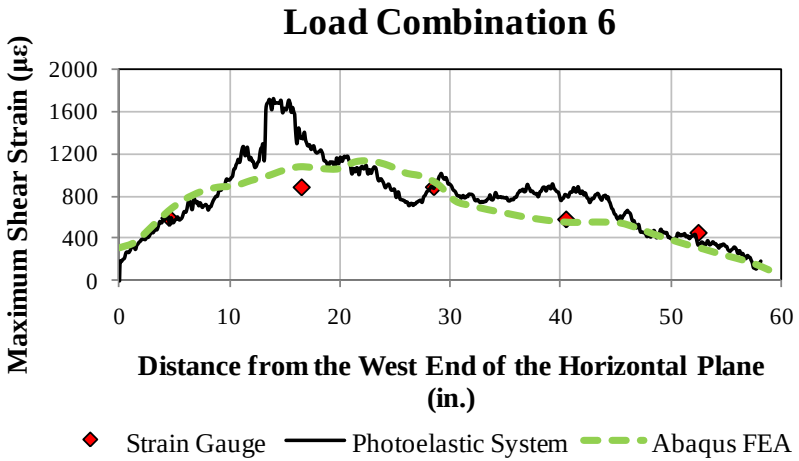

Figure 4.7.6: Comparison between the finite element analysis and experimental data (GP307-SS3 specimen - Load Combination 6)

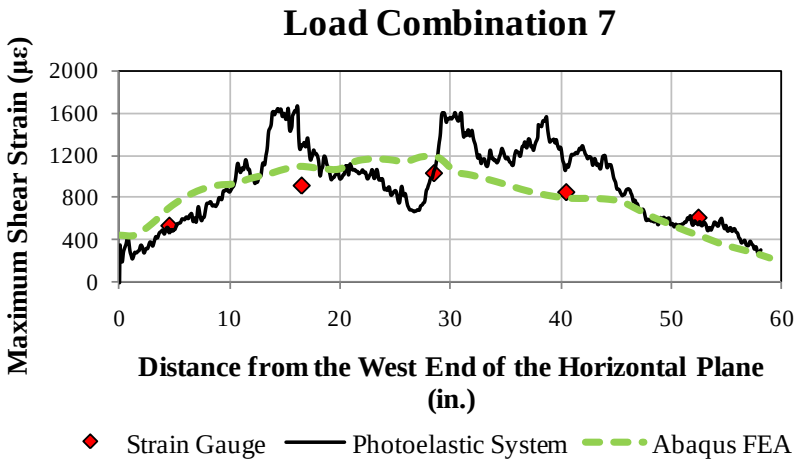

Figure 4.7.7: Comparison between the finite element analysis and experimental data (GP307-SS3 specimen - Load Combination 7)

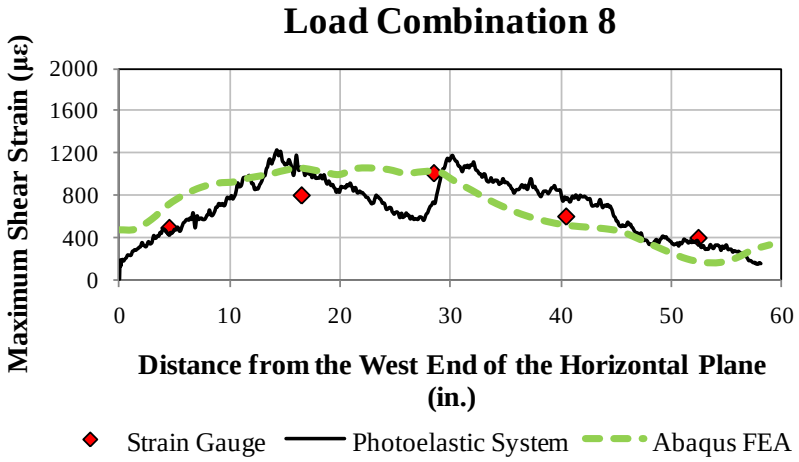

Figure 4.7.8: Comparison between the finite element analysis and experimental data (GP307-SS3 specimen - Load Combination 8)

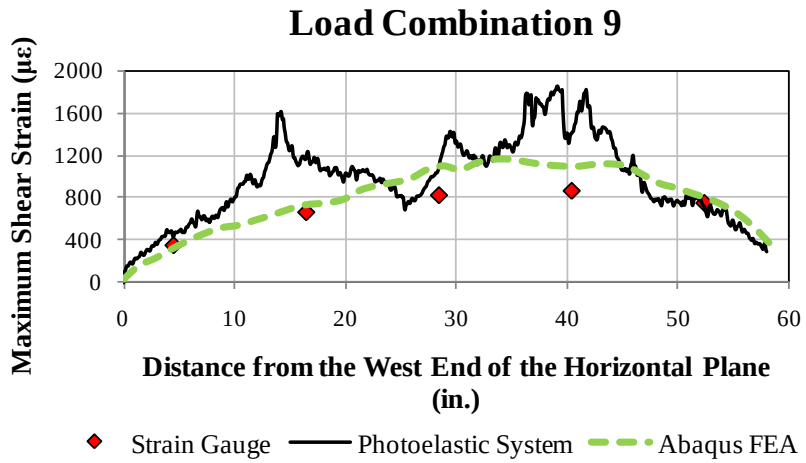

Figure 4.7.9: Comparison between the finite element analysis and experimental data (GP307-SS3 specimen - Load Combination 9)

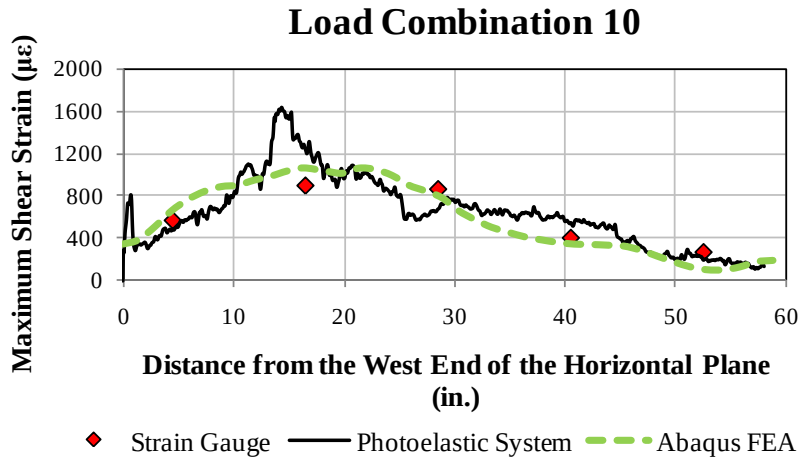

Figure 4.7.10: Comparison between the finite element analysis and experimental data (GP307-SS3 specimen - Load Combination 10)

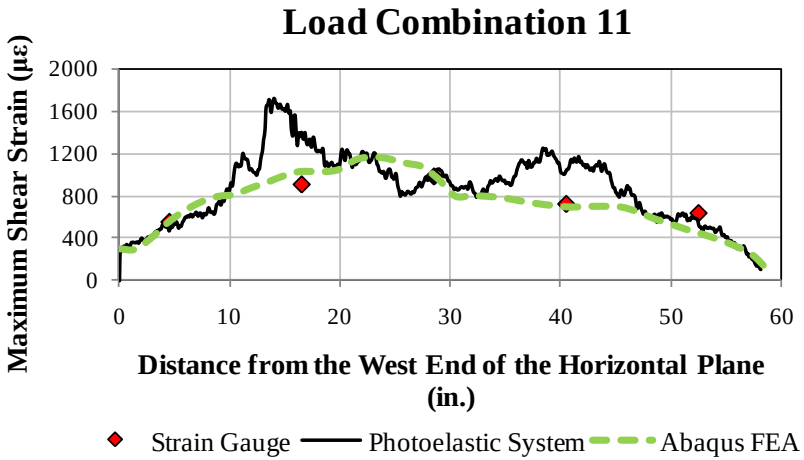

Figure 4.7.11: Comparison between the finite element analysis and experimental data (GP307-SS3 specimen - Load Combination 11)

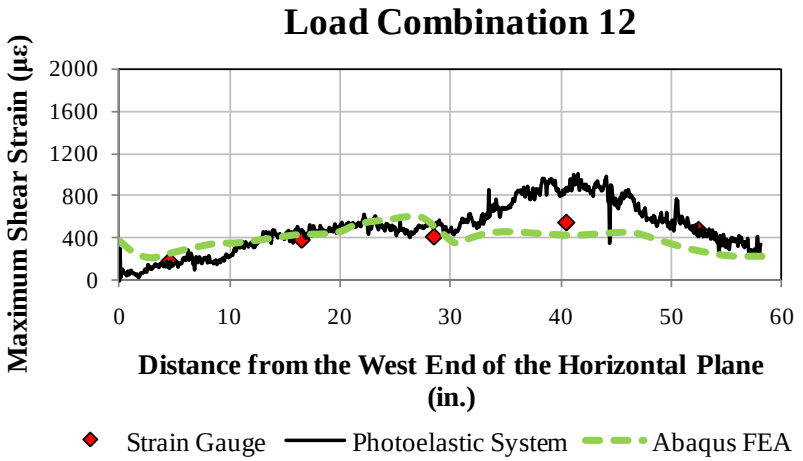

Figure 4.7.12: Comparison between the finite element analysis and experimental data (GP307-SS3 specimen - Load Combination 12)

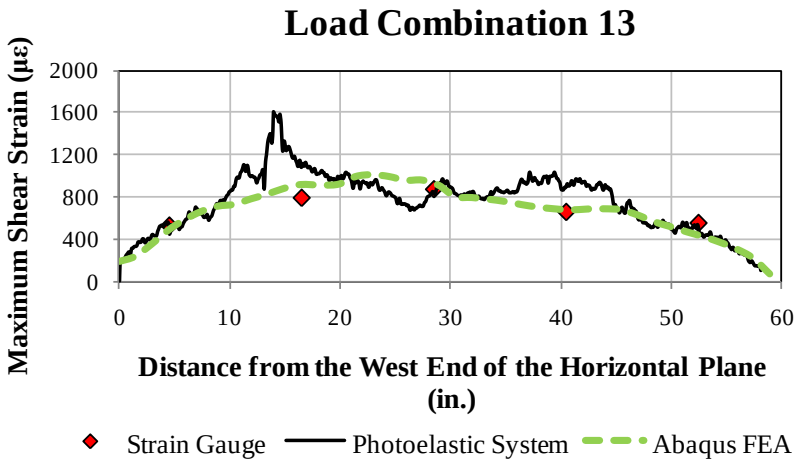

Figure 4.7.13: Comparison between the finite element analysis and experimental data (GP307-SS3 specimen - Load Combination 13)

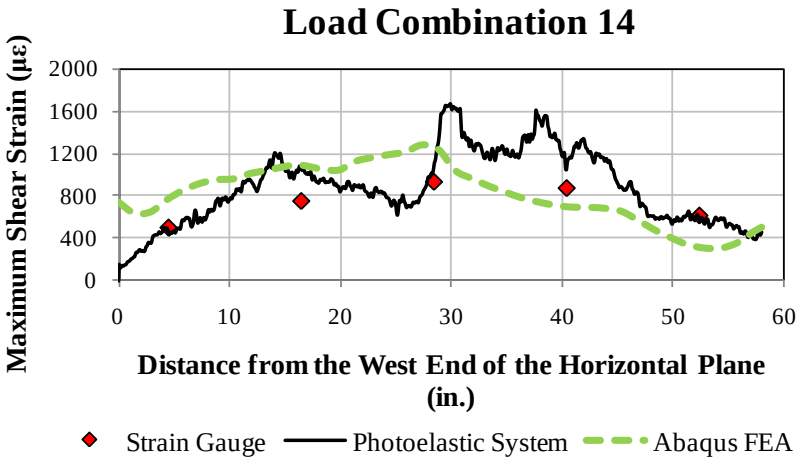

Figure 4.7.14: Comparison between the finite element analysis and experimental data (GP307-SS3 specimen - Load Combination 14)

4.7.1.2. GP307-LS3 Specimen

Table 4.7.2 summarizes the loads obtained from the tests and utilized in the finite element model of the GP307-LS3 specimen without splice plates installed.

Table 4.7.2: Member loads from the elastic load histories of the GP307-LS3 specimen without splice plates

Load Combination	F2 (kip)	F3 (kip)	F4 (kip)	F5 (kip)
1	47	17	-76	-74
2	120	0	-116	-10
3	53	0	-66	-74
4	16	0	-14	-113
5	116	-22	-98	-31
6	86	23	-123	-24
7	131	-51	-70	-48
8	49	43	-102	-34

For the GP307-LS3 specimen, maximum shear strain response contour images from photoelastic data were not available. The maximum shear strain versus the distance along the horizontal plane relationships are shown in Figure 4.7.15 through Figure 4.7.22. Finite element analysis matches the experimental data well in almost all load combinations. In some cases such as load combinations 2, and 6, deviations are observed for the photoelastic system data in certain regions. However, taking the testing conditions and uncertainty of the data acquisition into account along with the uncertainties such as initial imperfections and material properties applied in the finite element models, these differences can be considered to be acceptable. Even in those cases, the FEA results have reasonably well agreement with the discrete strain gauge measurements.

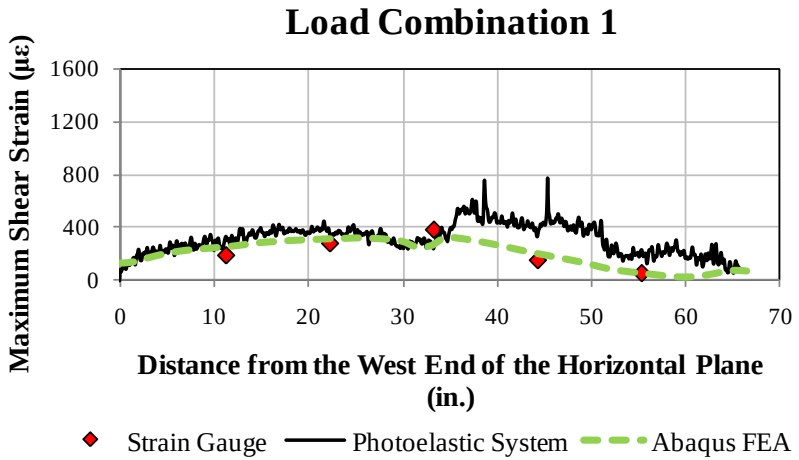

Figure 4.7.15: Comparison between the finite element analysis and experimental data (GP307-LS3 specimen - Load Combination 1)

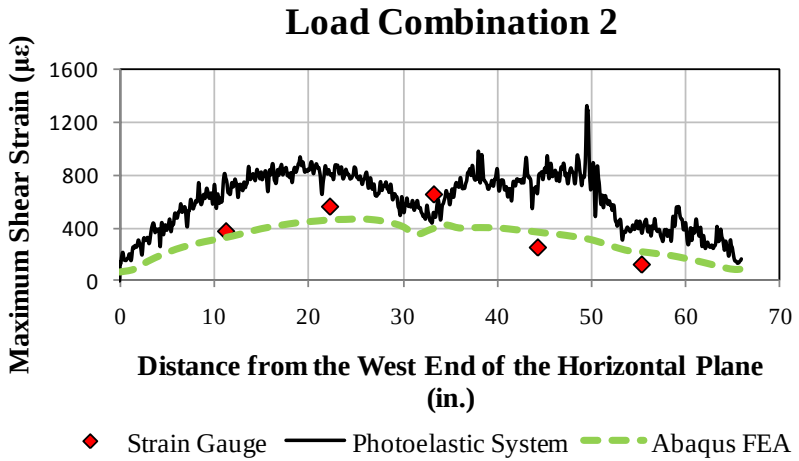

Figure 4.7.16: Comparison between the finite element analysis and experimental data (GP307-LS3 specimen - Load Combination 2)

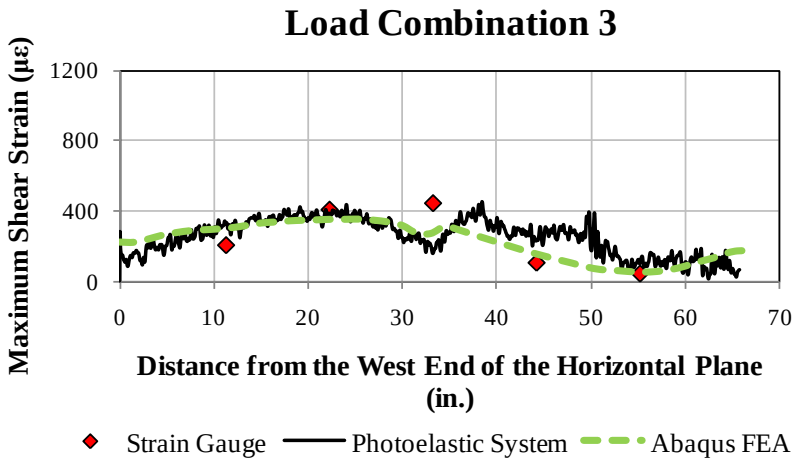

Figure 4.7.17: Comparison between the finite element analysis and experimental data. GP307-LS3 specimen - Load Combination 3

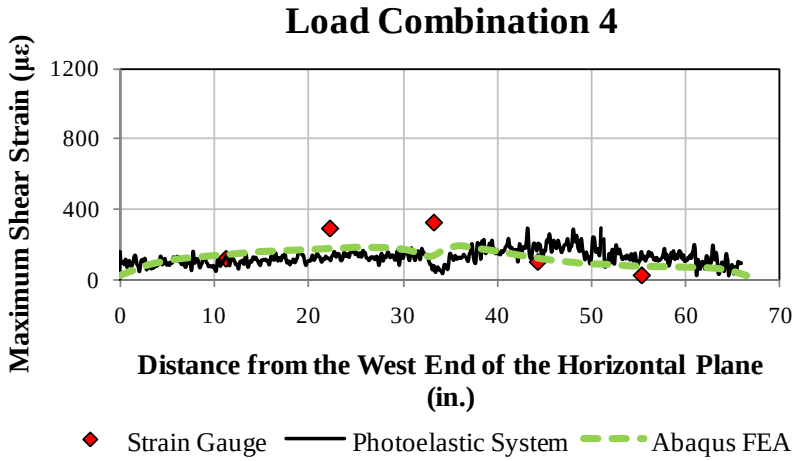

Figure 4.7.18: Comparison between the finite element analysis and experimental data (GP307-LS3 specimen - Load Combination 4)

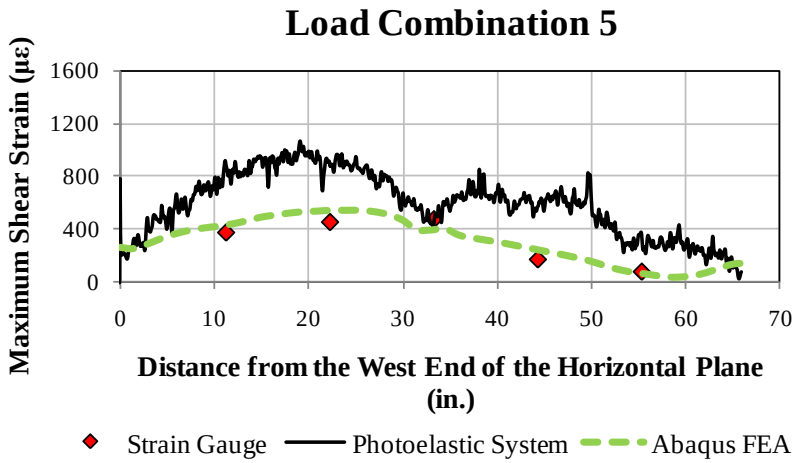

Figure 4.7.19: Comparison between the finite element analysis and experimental data (GP307-LS3 specimen - Load Combination 5)

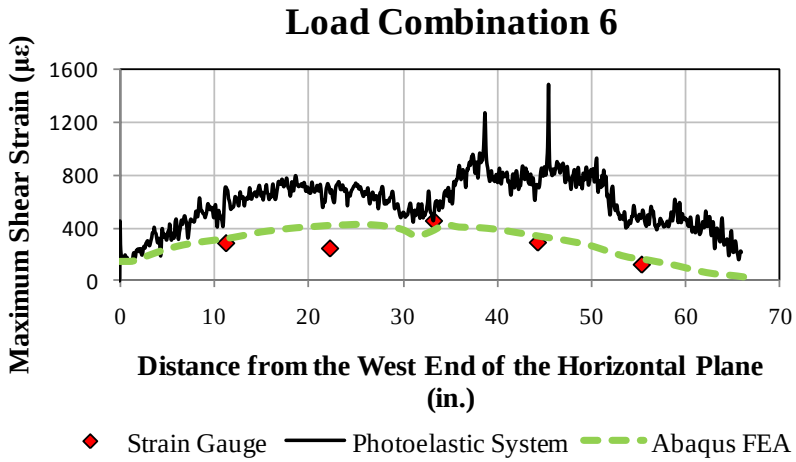

Figure 4.7.20: Comparison between the finite element analysis and experimental data (GP307-LS3 specimen - Load Combination 6)

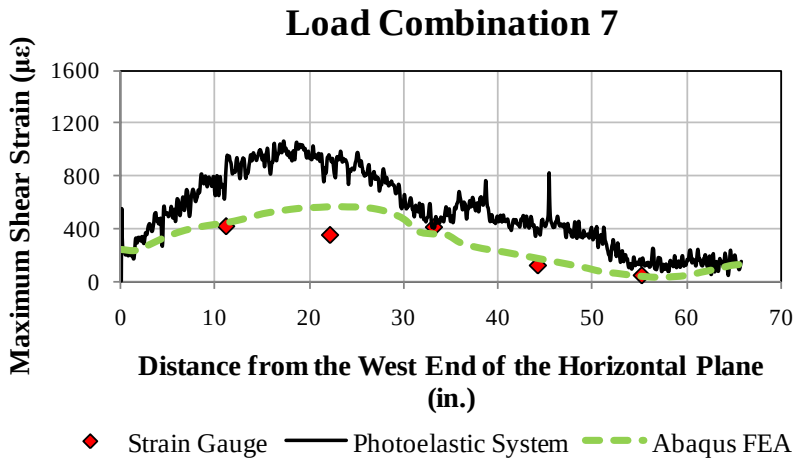

Figure 4.7.21: Comparison between the finite element analysis and experimental data (GP307-LS3 specimen - Load Combination 7)

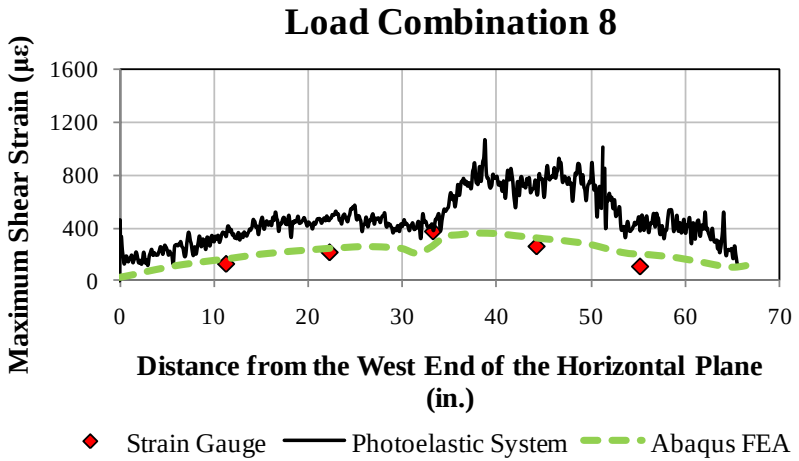

Figure 4.7.22: Comparison between the finite element analysis and experimental data (GP307-LS3 specimen - Load Combination 8)

4.7.1.3. GP307-SL3 Specimen

Load combinations and applied member loads for GP307-SL3 specimen are shown in Table 4.7.3.

Table 4.7.3: Member loads from the elastic load histories of the GP307-SL3 specimen without splice plates

Load Combination	F2 (kip)	F3 (kip)	F4 (kip)	F5 (kip)
1	274	-1	-261	38
2	276	0	-255	410
3	337	0	-348	267
4	365	-78	-273	273
5	286	83	-384	288
6	356	-76	-238	181
7	263	82	-396	206
8	201	65	-312	24
9	282	77	-375	372
10	350	-71	-241	66
11	378	-80	-274	368
12	116	43	-180	354
13	346	-32	-271	277
14	197	146	-378	226

GP307-SL3 specimen wass one of the specimens for which the qualitative contour plots were provided. The contours can be compared with the finite element analysis results. In addition, maximum shear strain versus the distance along the horizontal plane relationships are plotted and contours along with the corresponding plot for each load combination are shown in Figure 4.7.23 through Figure 4.7.50. The finite element analysis results well match the photoelastic system data except few load combinations. In addition, the second strain gauge from the left side provides results deviating from the two data sets.

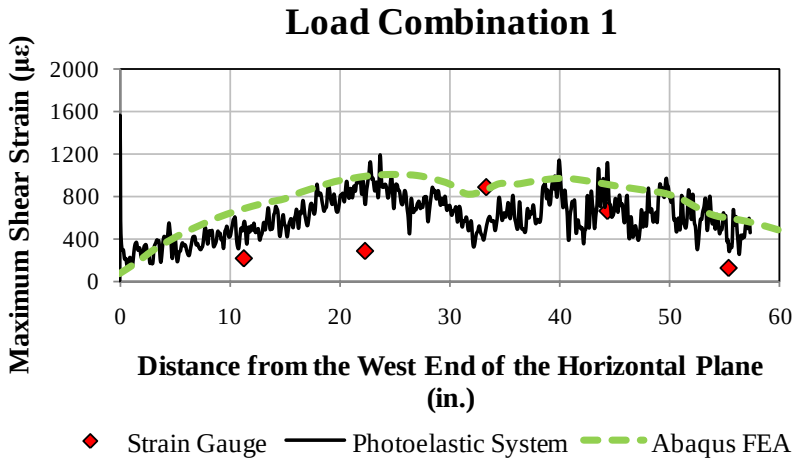

Figure 4.7.23: Comparison between the finite element analysis and experimental data (GP307-SL3 specimen - Load Combination 1)

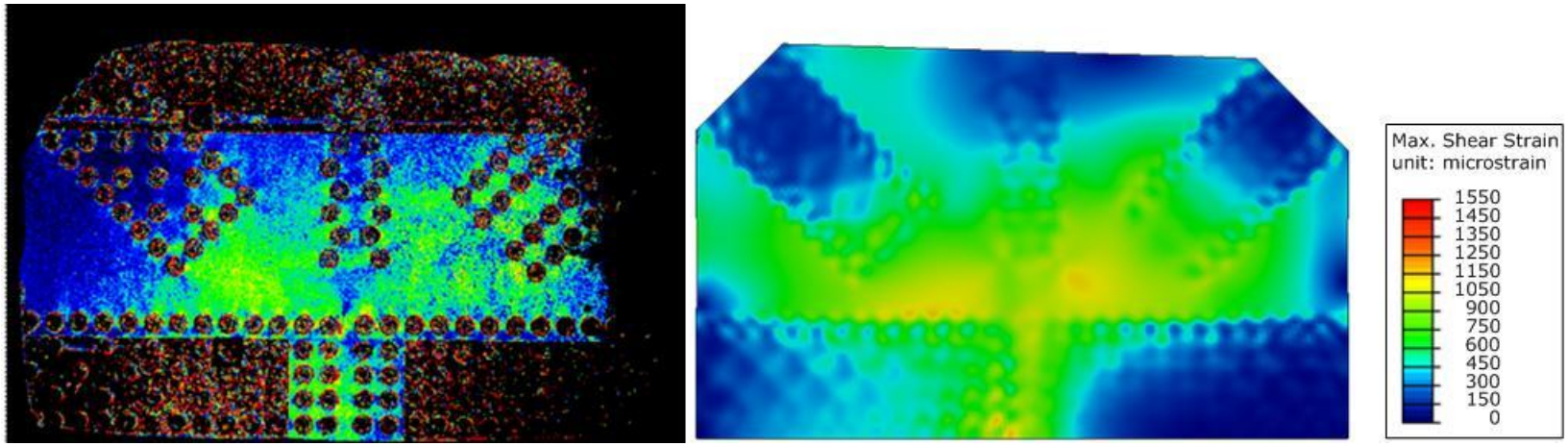

Figure 4.7.24: Comparison between the photo-elastic measurement system (left) and FEA (right) for Load Combination 1

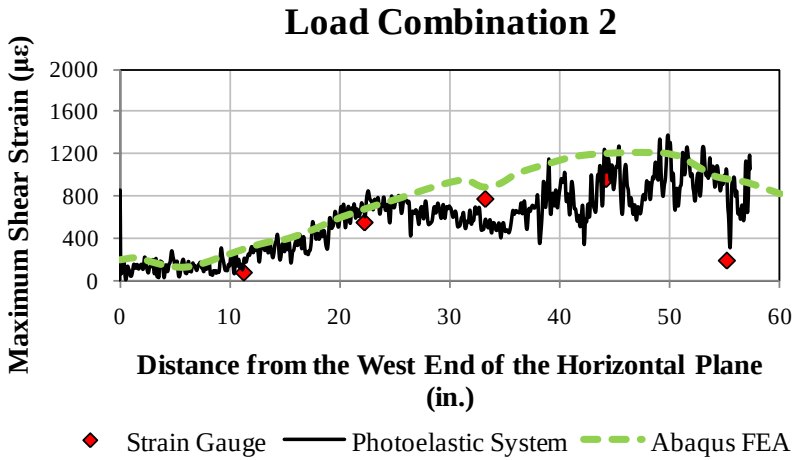

Figure 4.7.25: Comparison between the finite element analysis and experimental data (GP307-SL3 specimen - Load Combination 2)

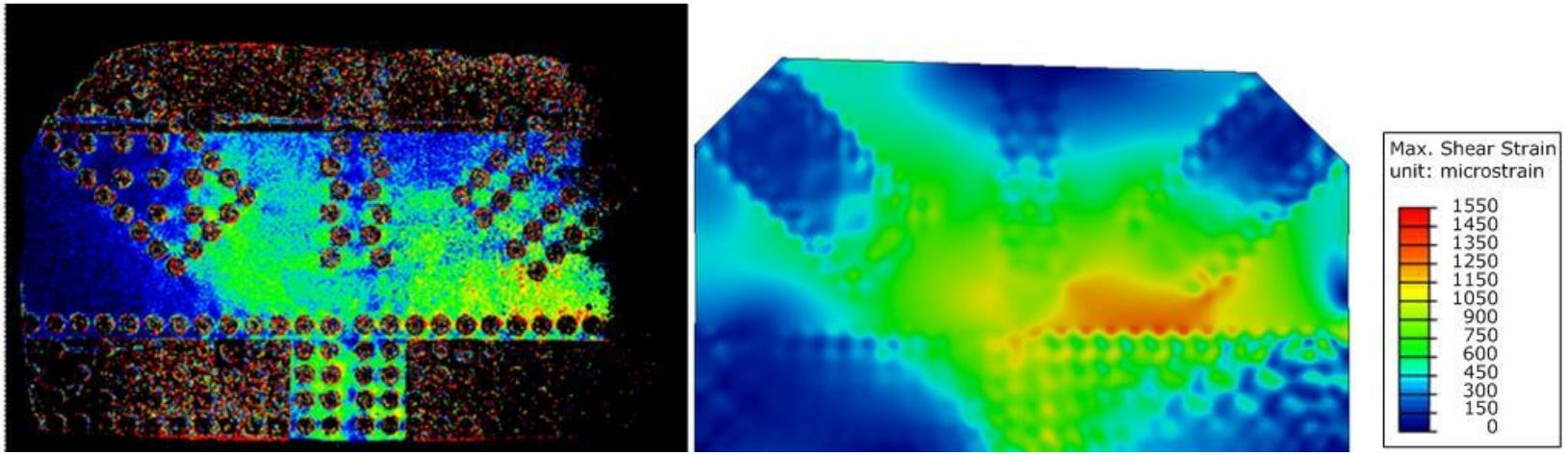

Figure 4.7.26: Comparison between the photo-elastic measurement system (left) and FEA (right) for Load Combination 2

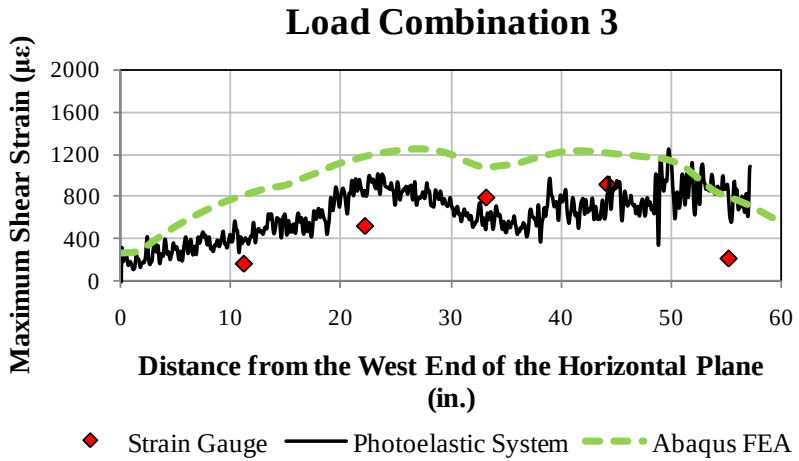

Figure 4.7.27: Comparison between the finite element analysis and experimental data (GP307-SL3 specimen - Load Combination 3)

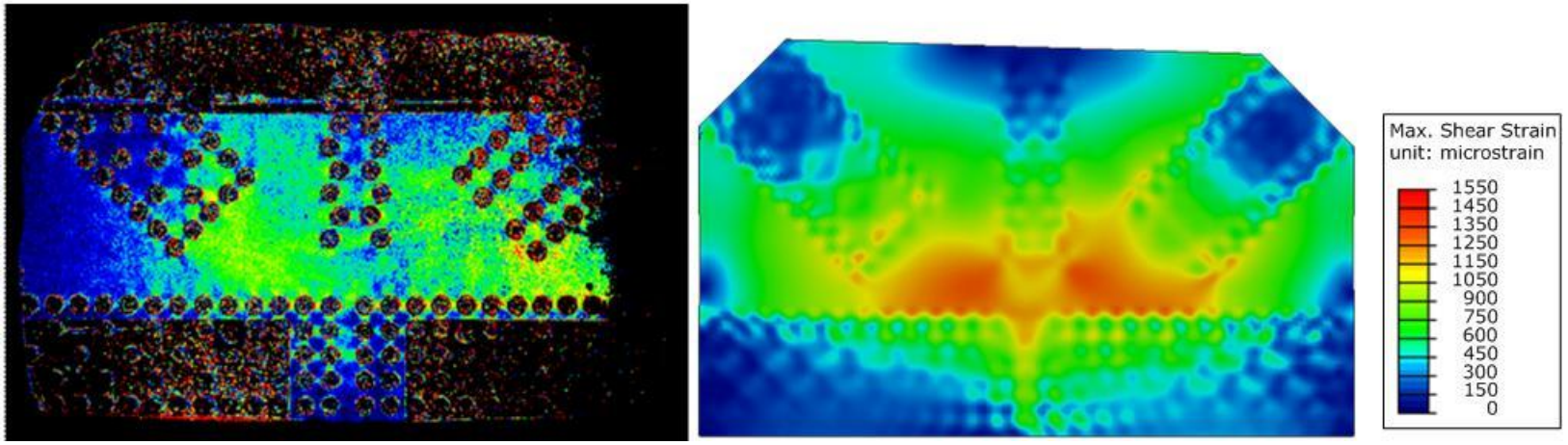

Figure 4.7.28: Comparison between the photo-elastic measurement system (left) and FEA (right) for Load Combination 3

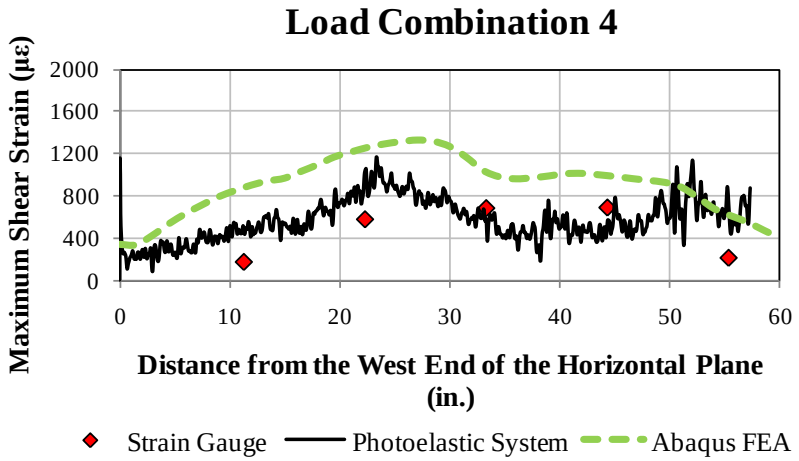

Figure 4.7.29: Comparison between the finite element analysis and experimental data (GP307-SL3 specimen - Load Combination 4)

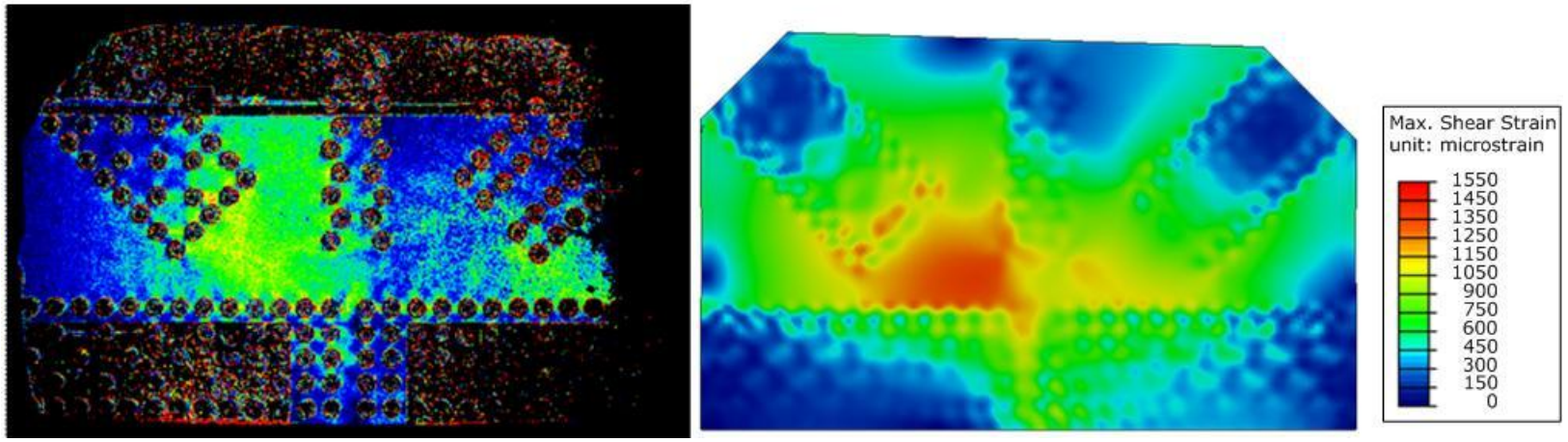

Figure 4.7.30: Comparison between the photo-elastic measurement system (left) and FEA (right) for Load Combination 4

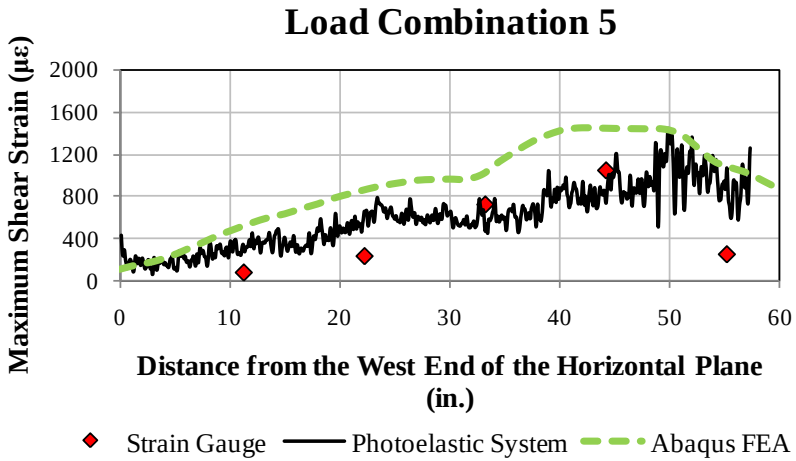

Figure 4.7.31: Comparison between the finite element analysis and experimental data (GP307-SL3 specimen - Load Combination 5)

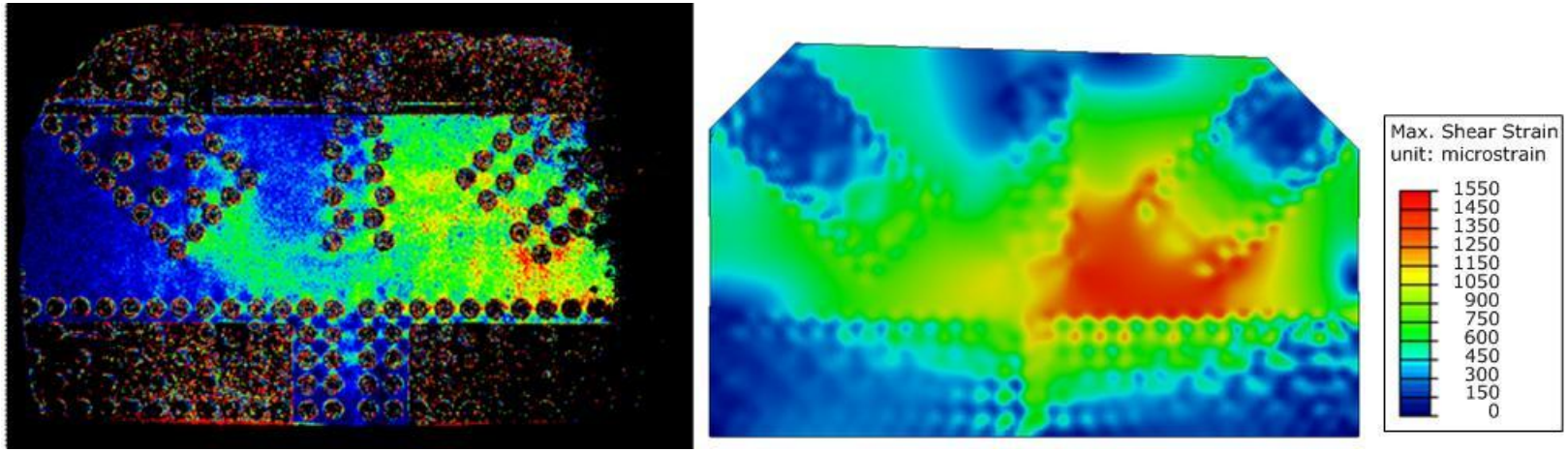

Figure 4.7.32: Comparison between the photo-elastic measurement system (left) and FEA (right) for Load Combination 5

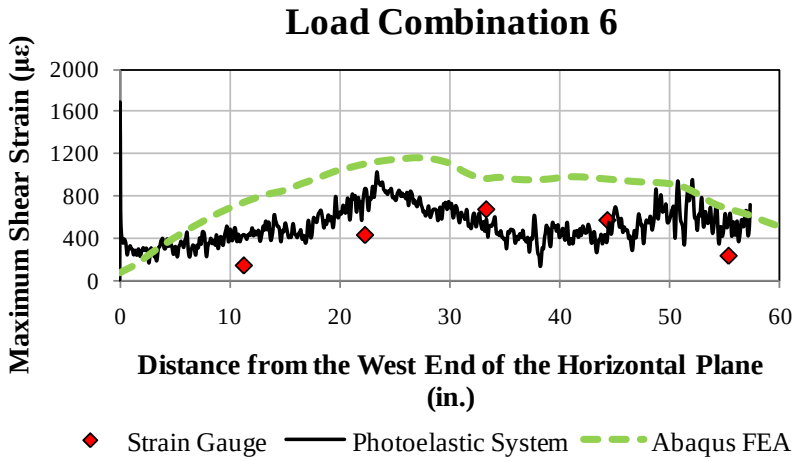

Figure 4.7.33: Comparison between the finite element analysis and experimental data (GP307-SL3 specimen - Load Combination 6)

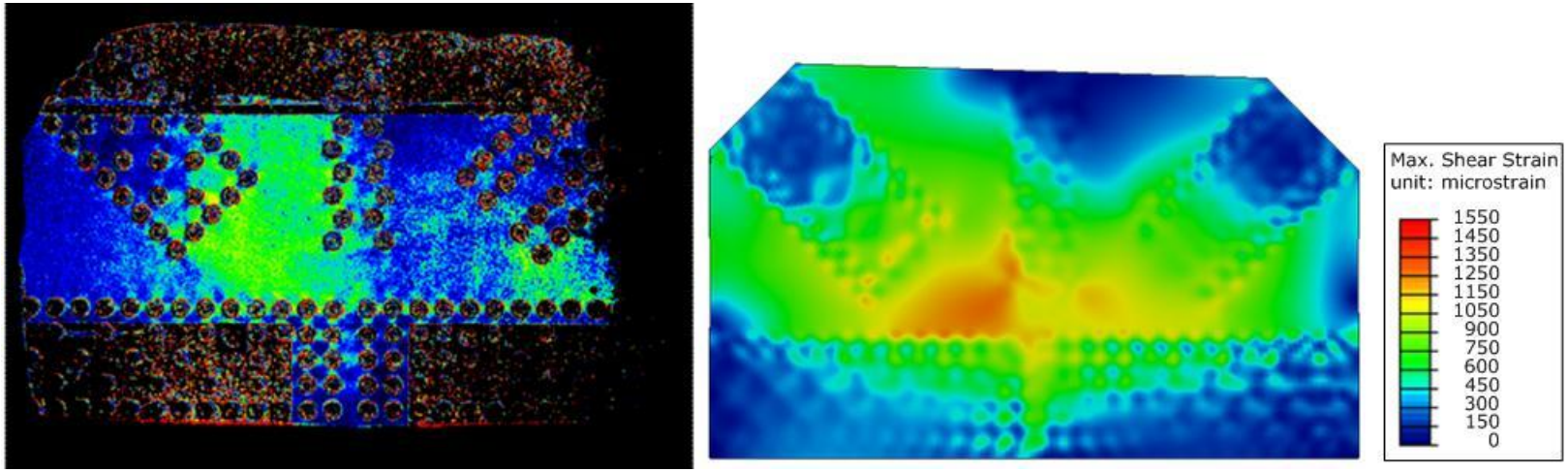

Figure 4.7.34: Comparison between the photo-elastic measurement system (left) and FEA (right) for Load Combination 6

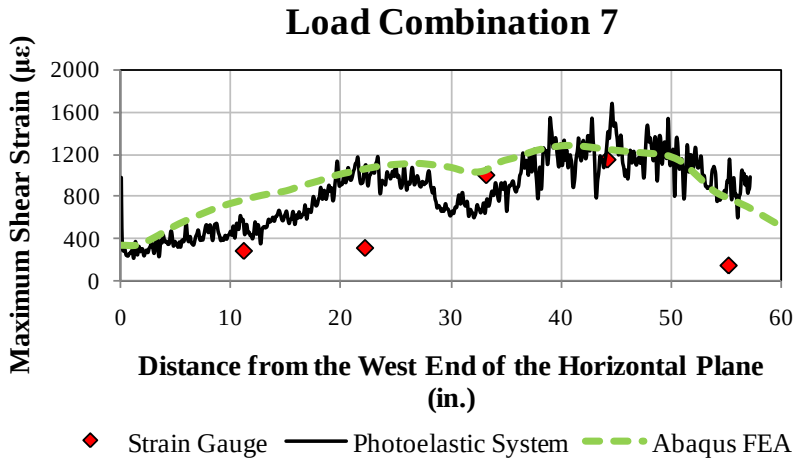

Figure 4.7.35: Comparison between the finite element analysis and experimental data (GP307-SL3 specimen - Load Combination 7)

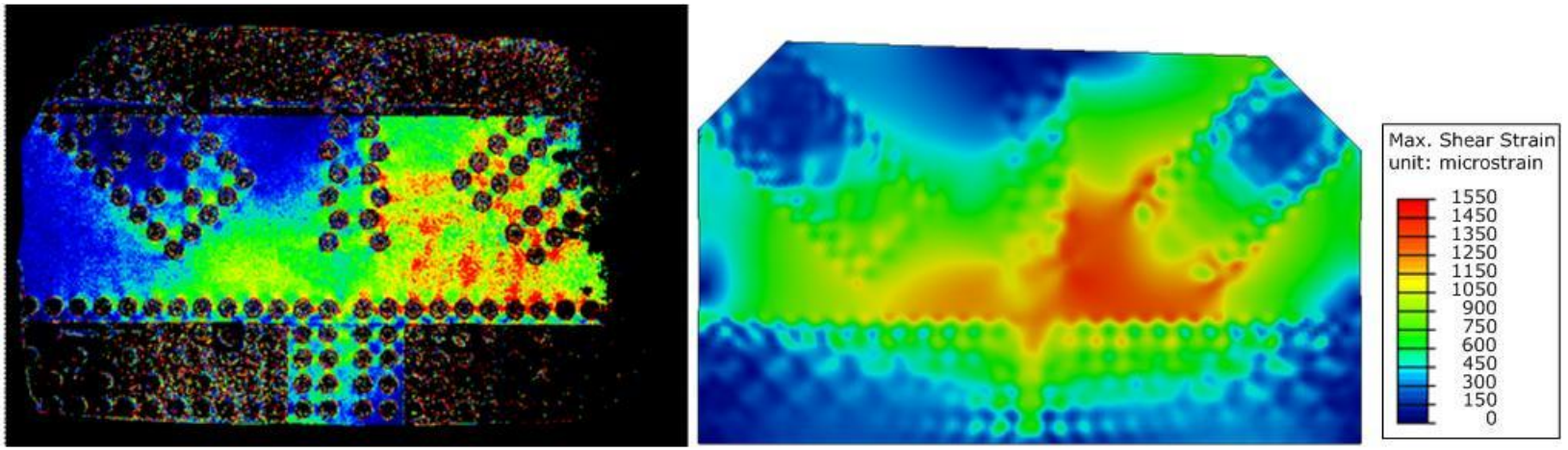

Figure 4.7.36: Comparison between the photo-elastic measurement system (left) and FEA (right) for Load Combination 7

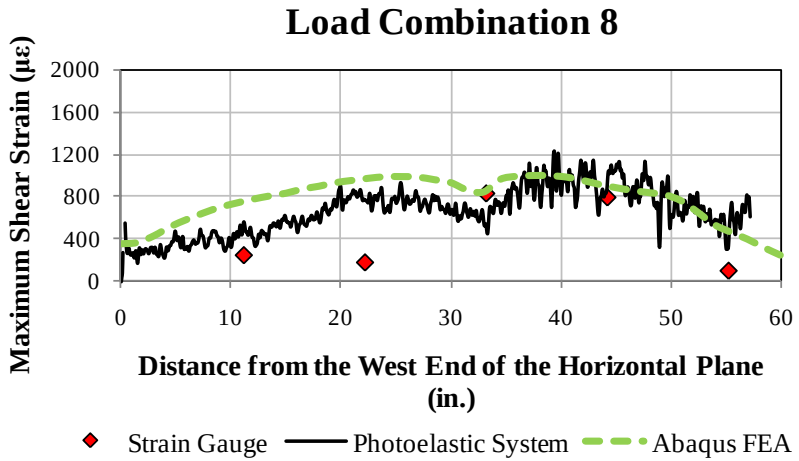

Figure 4.7.37: Comparison between the finite element analysis and experimental data (GP307-SL3 specimen - Load Combination 8)

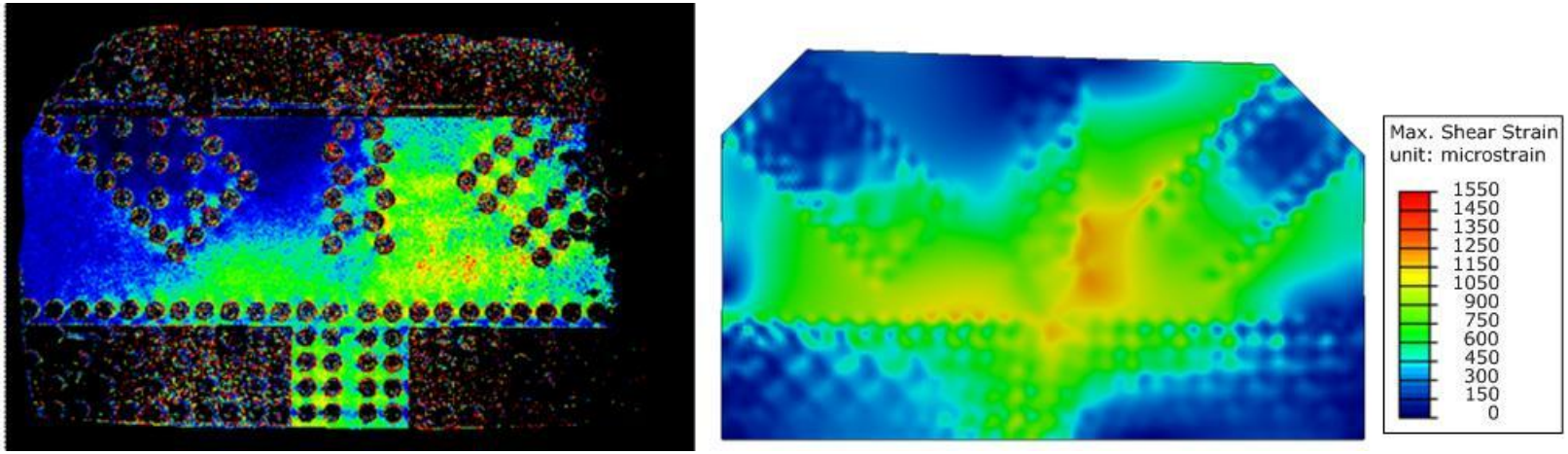

Figure 4.7.38: Comparison between the photo-elastic measurement system (left) and FEA (right) for Load Combination 8

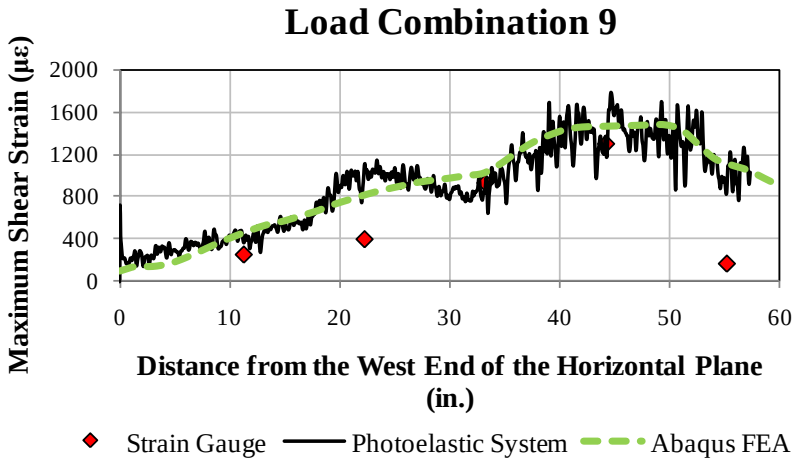

Figure 4.7.39: Comparison between the finite element analysis and experimental data (GP307-SL3 specimen - Load Combination 9)

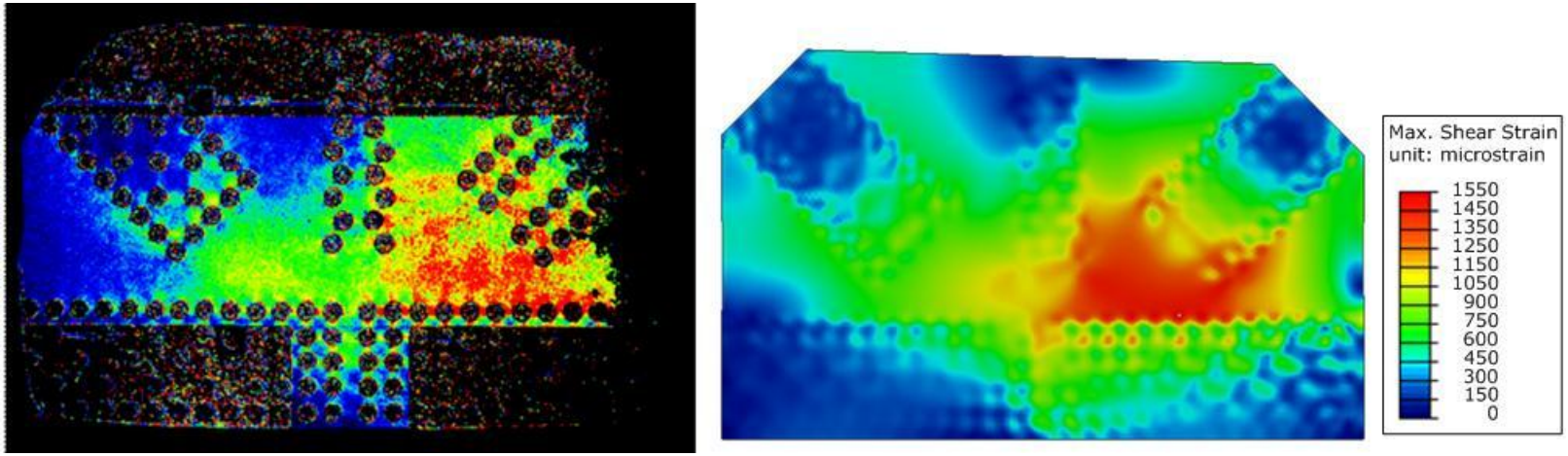

Figure 4.7.40: Comparison between the photo-elastic measurement system (left) and FEA (right) for Load Combination 9

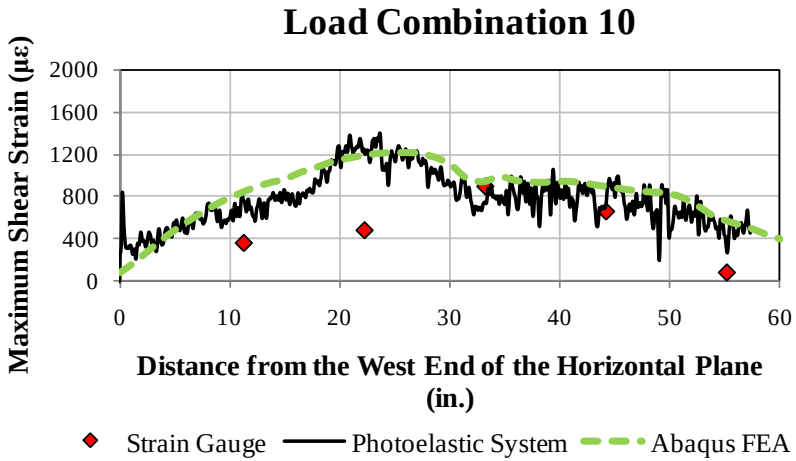

Figure 4.7.41: Comparison between the finite element analysis and experimental data (GP307-SL3 specimen - Load Combination 10)

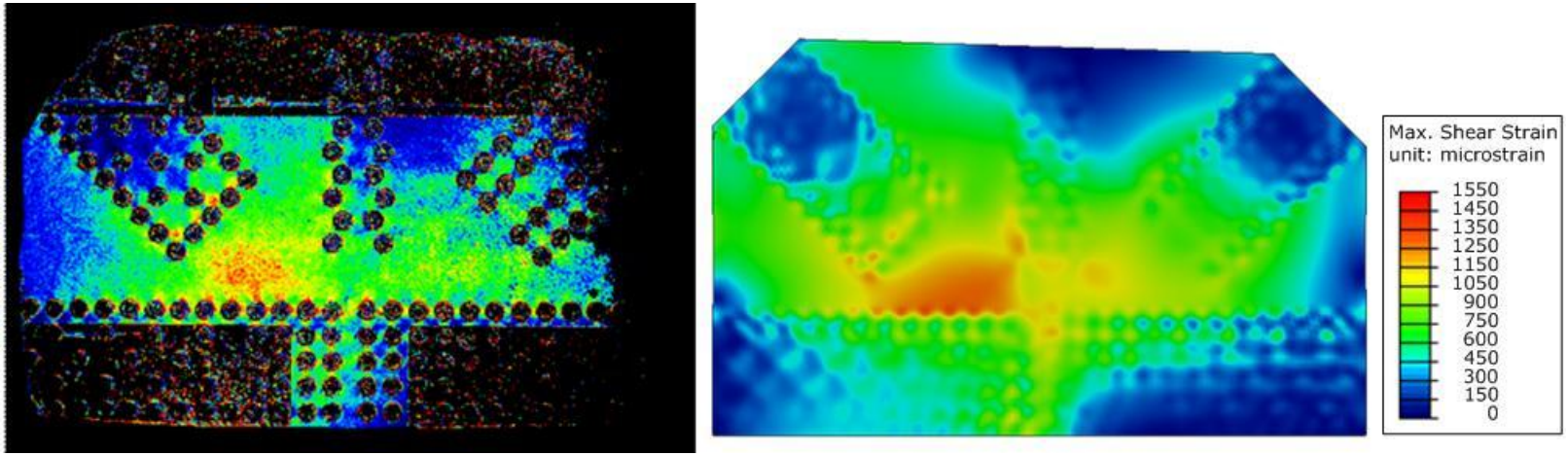

Figure 4.7.42: Comparison between the photo-elastic measurement system (left) and FEA (right) for Load Combination 10

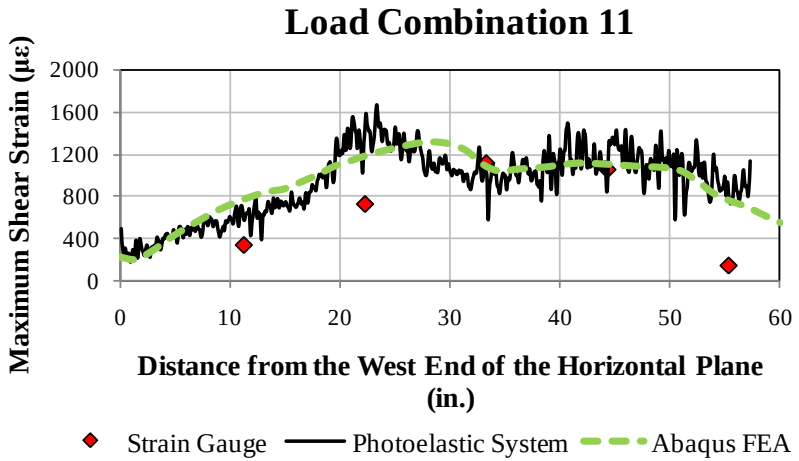

Figure 4.7.43: Comparison between the finite element analysis and experimental data (GP307-SL3 specimen - Load Combination 11)

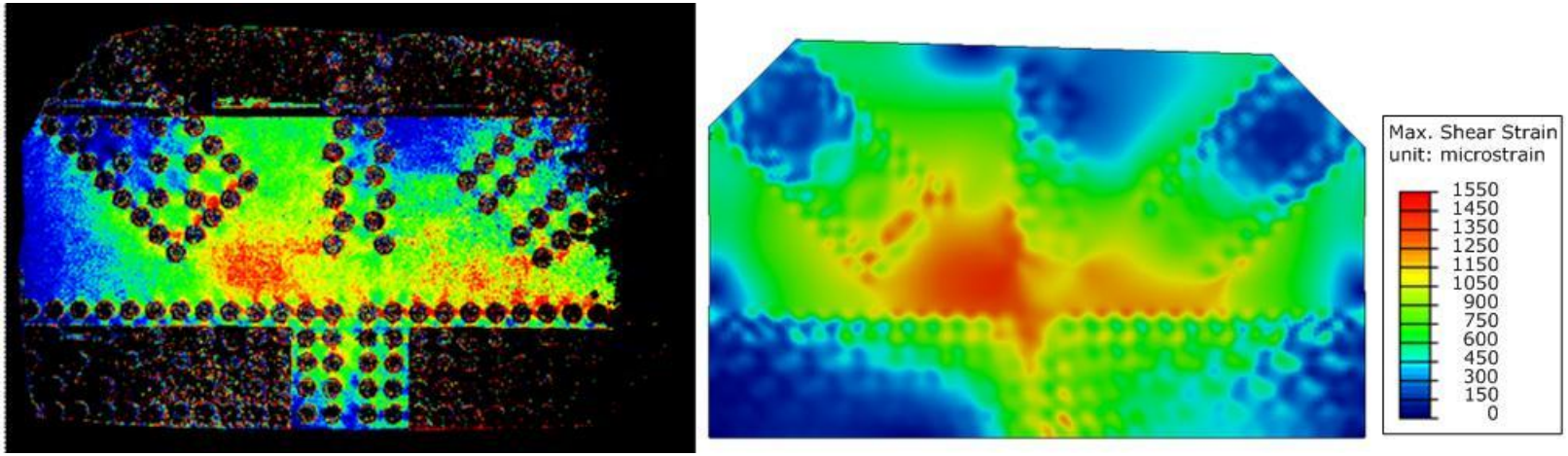

Figure 4.7.44: Comparison between the photo-elastic measurement system (left) and FEA (right) for Load Combination 11

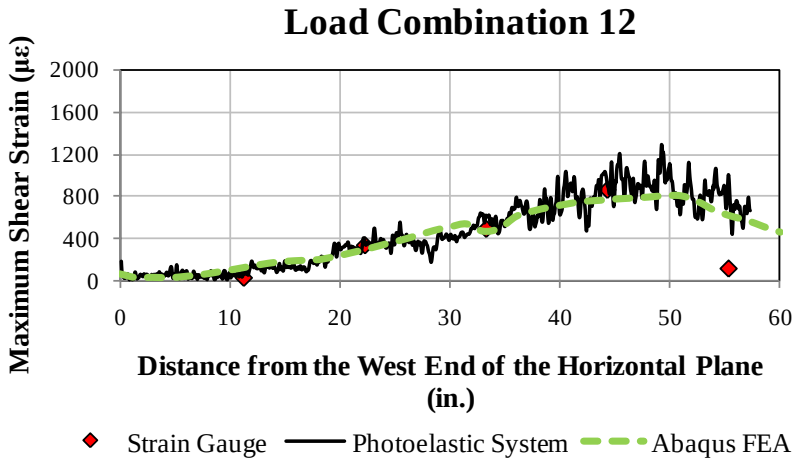

Figure 4.7.45: Comparison between the finite element analysis and experimental data (GP307-SL3 specimen - Load Combination 12)

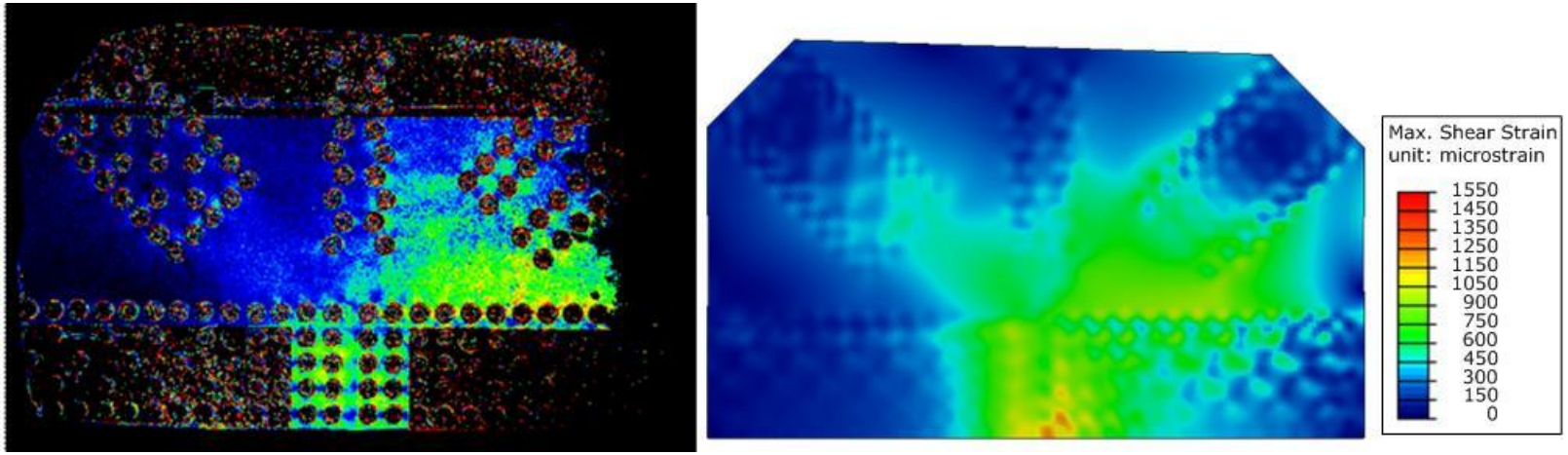

Figure 4.7.46: Comparison between the photo-elastic measurement system (left) and FEA (right) for Load Combination 12

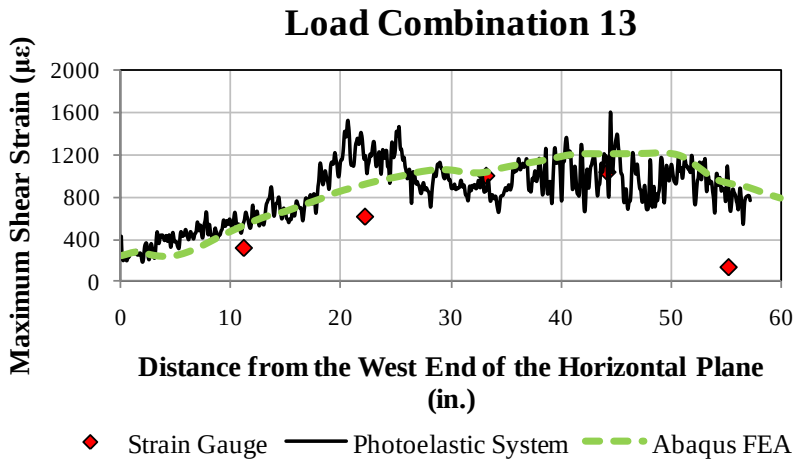

Figure 4.7.47: Comparison between the finite element analysis and experimental data (GP307-SL3 specimen - Load Combination 13)

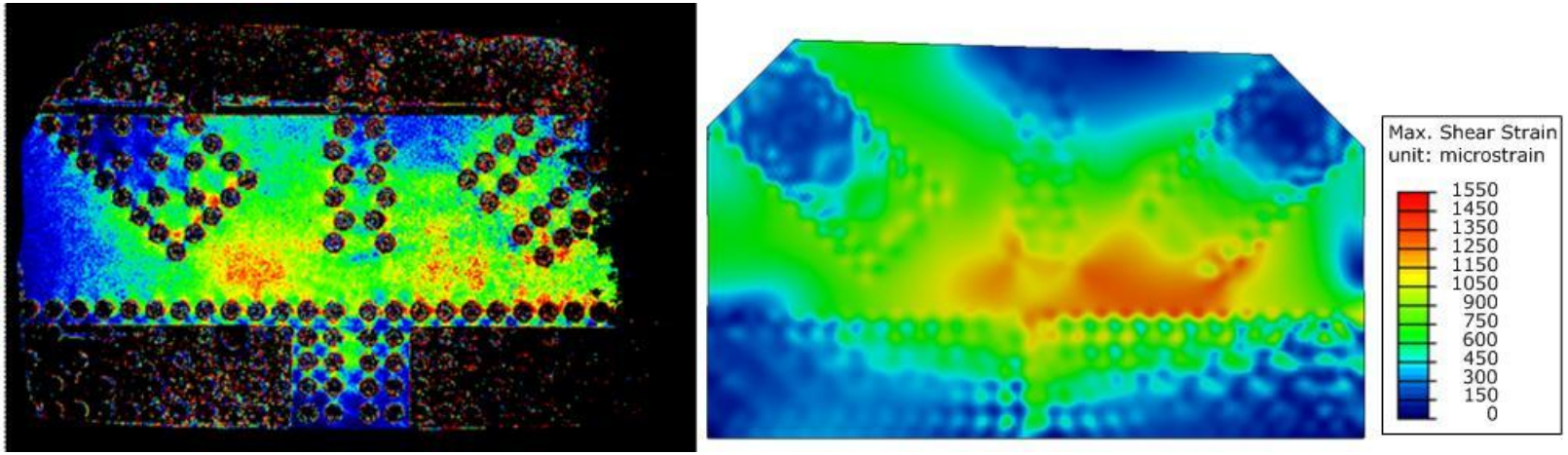

Figure 4.7.48: Comparison between the photo-elastic measurement system (left) and FEA (right) for Load Combination 13

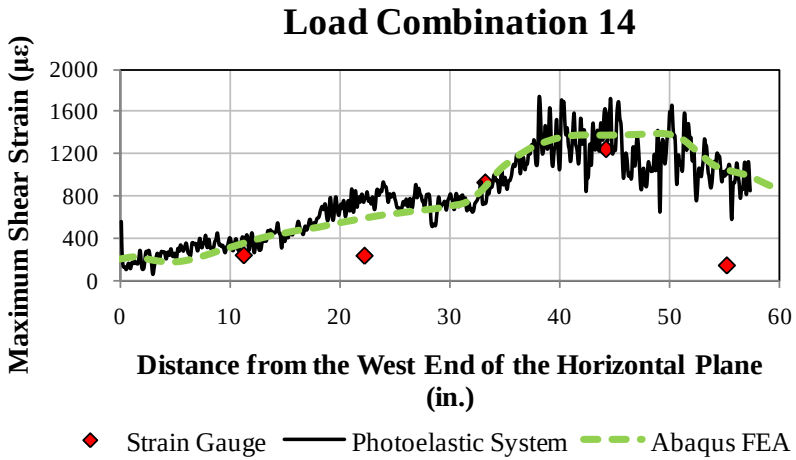

Figure 4.7.49: Comparison between the finite element analysis and experimental data (GP307-SL3 specimen - Load Combination 14)

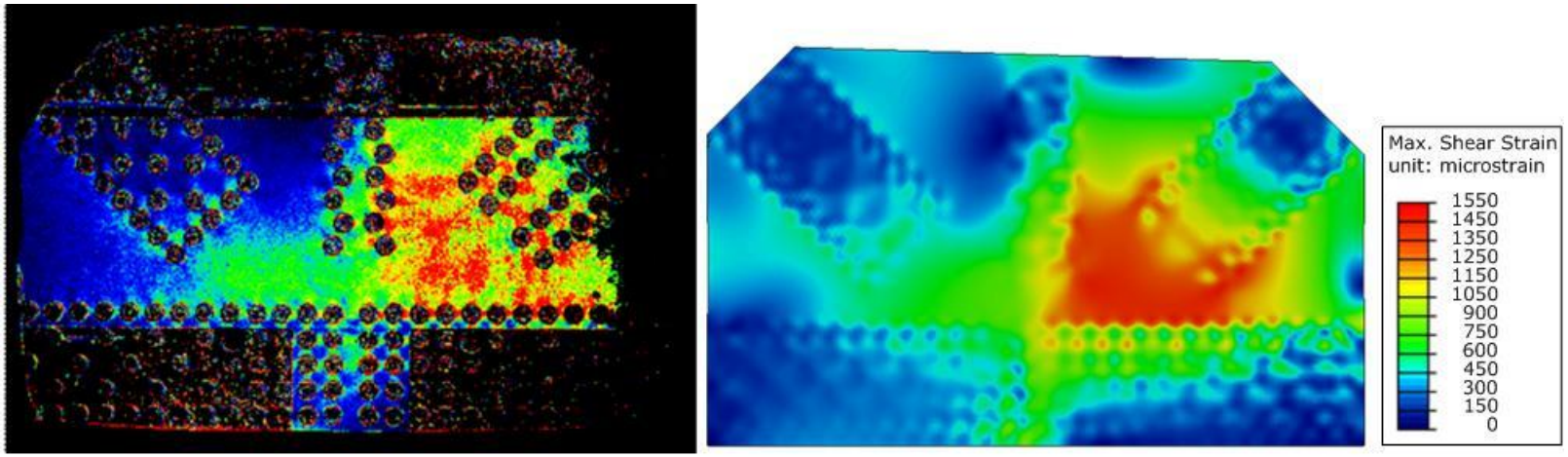

Figure 4.7.50: Comparison between the photo-elastic measurement system (left) and FEA (right) for Load Combination 14

4.7.1.4. GP490-SS3 Specimen

Table 4.7.4 summarizes the member loads for each load combination in GP490-SS3 without splice plate model.

Table 4.7.4: Member loads from the elastic load histories of the GP490-SS3 specimen without splice plates

Load Combination	F2 (kip)	F3 (kip)	F4 (kip)	F5 (kip)
1	239	0	-259	40
2	259	-1	-244	349
3	295	1	-303	178
4	281	-56	-210	219
5	236	69	-330	242
6	269	-53	-184	143
7	234	69	-327	165
8	193	58	-293	37
9	238	63	-337	317
10	266	-54	-198	75
11	281	-56	-190	251
12	109	41	-167	313
13	270	-22	-242	215

Both qualitative comparisons based on the contours from photoelastic data and quantitative comparisons similar to previous specimens were performed for the GP490-SS3 specimen. The finite element model captures not only the trend of the photoelastic data along the horizontal plane but also provided very close results to the discrete strain gauge measurements. Figure 4.7.51 through Figure 4.7.76 show the comparisons for all the load combinations.

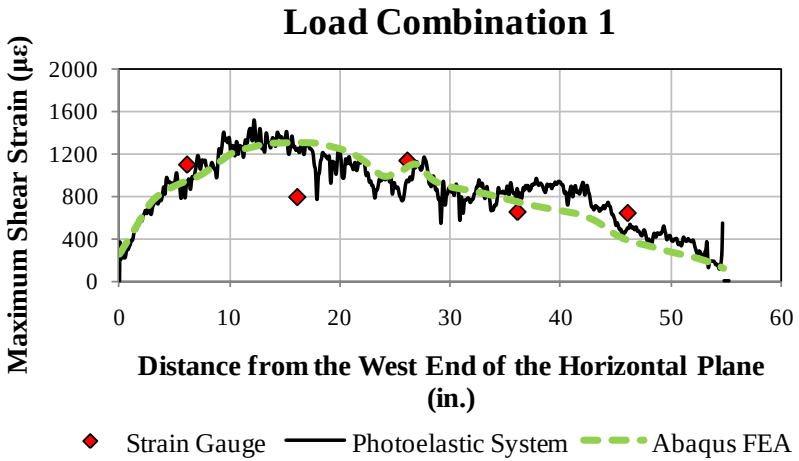

Figure 4.7.51: Comparison between the finite element analysis and experimental data (GP490-SS3 specimen - Load Combination 1)

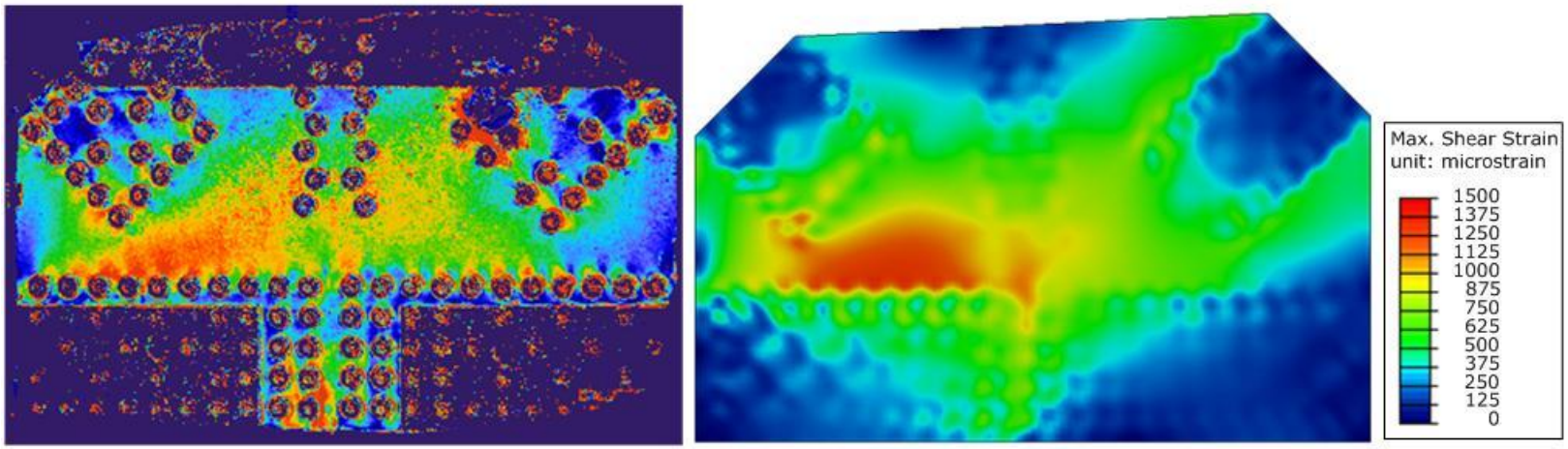

Figure 4.7.52: Comparison between the photo-elastic measurement system (left) and FEA (right) for Load Combination 1

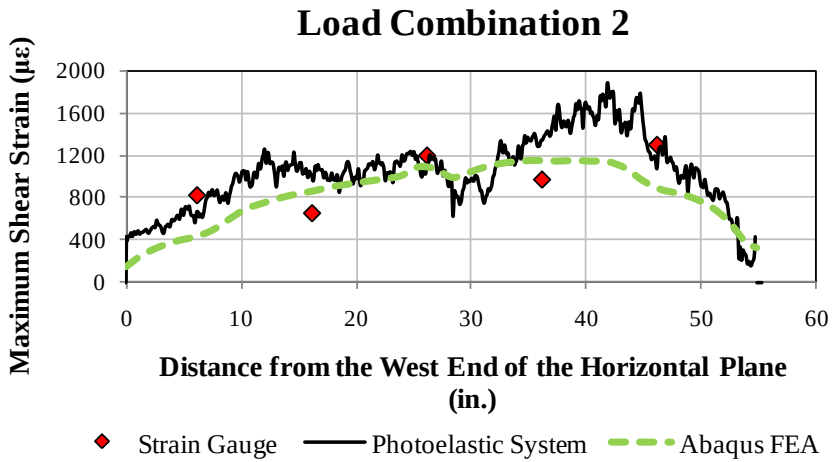

Figure 4.7.53: Comparison between the finite element analysis and experimental data (GP490-SS3 specimen - Load Combination 2)

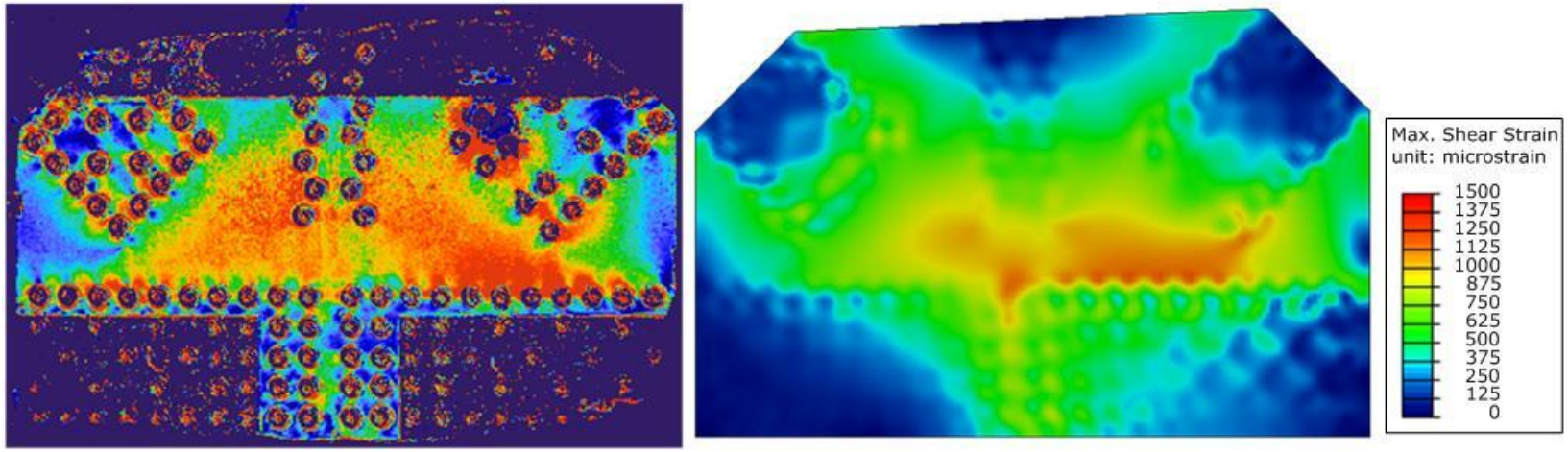

Figure 4.7.54: Comparison between the photo-elastic measurement system (left) and FEA (right) for Load Combination 2

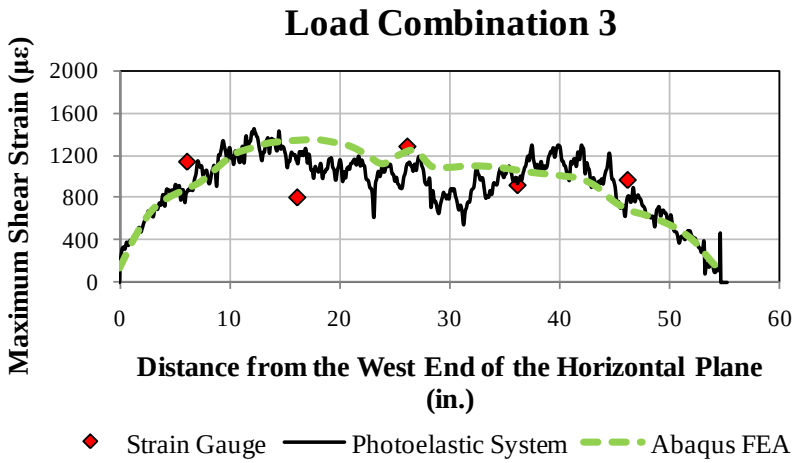

Figure 4.7.55: Comparison between the finite element analysis and experimental data (GP490-SS3 specimen - Load Combination 3)

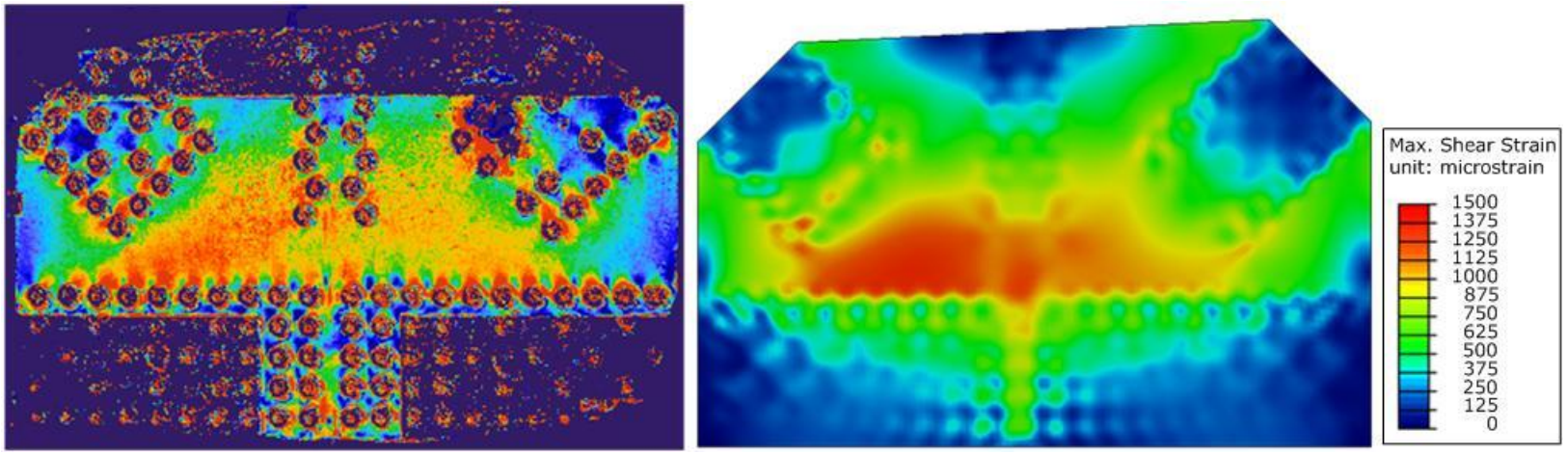

Figure 4.7.56: Comparison between the photo-elastic measurement system (left) and FEA (right) for Load Combination 3

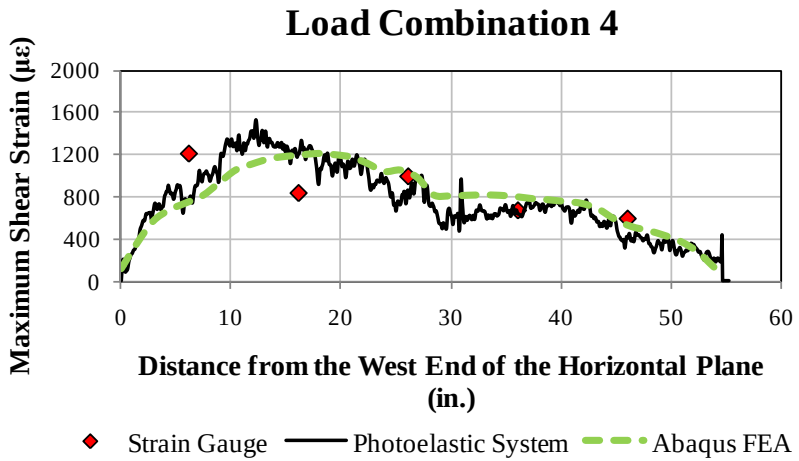

Figure 4.7.57: Comparison between the finite element analysis and experimental data (GP490-SS3 specimen - Load Combination 4)

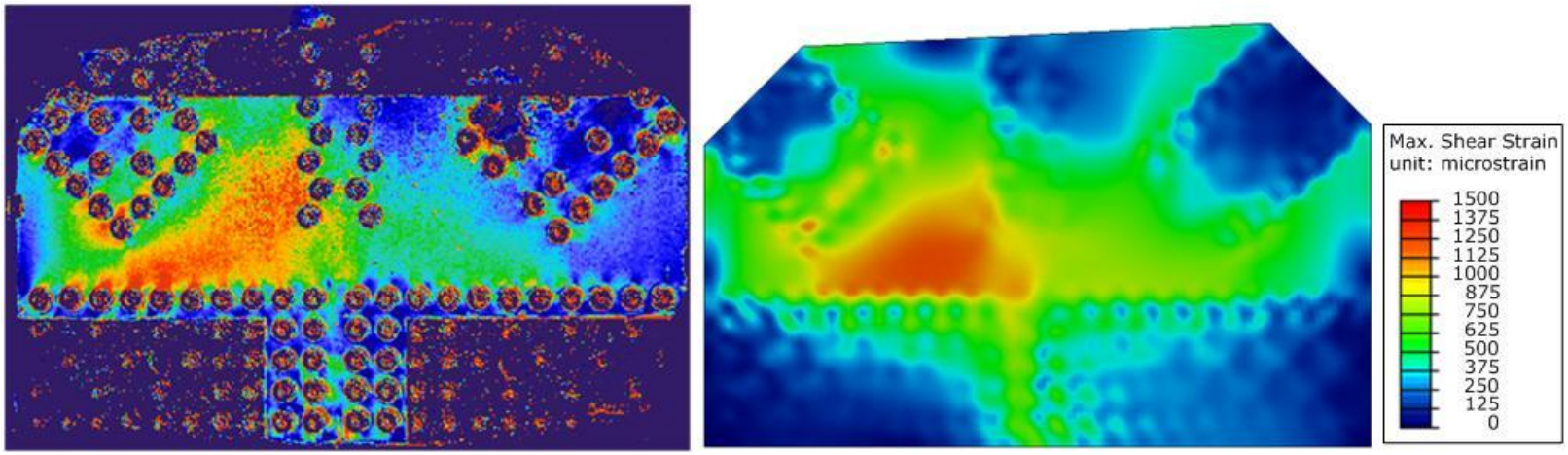

Figure 4.7.58: Comparison between the photo-elastic measurement system (left) and FEA (right) for Load Combination 4

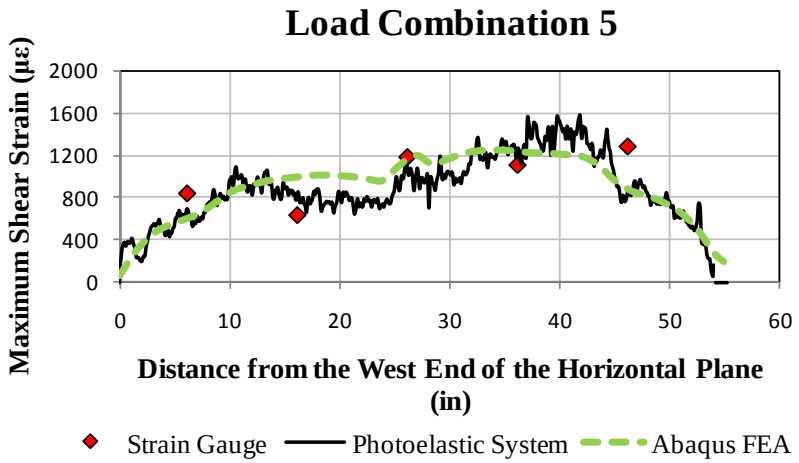

Figure 4.7.59: Comparison between the finite element analysis and experimental data (GP490-SS3 specimen - Load Combination 5)

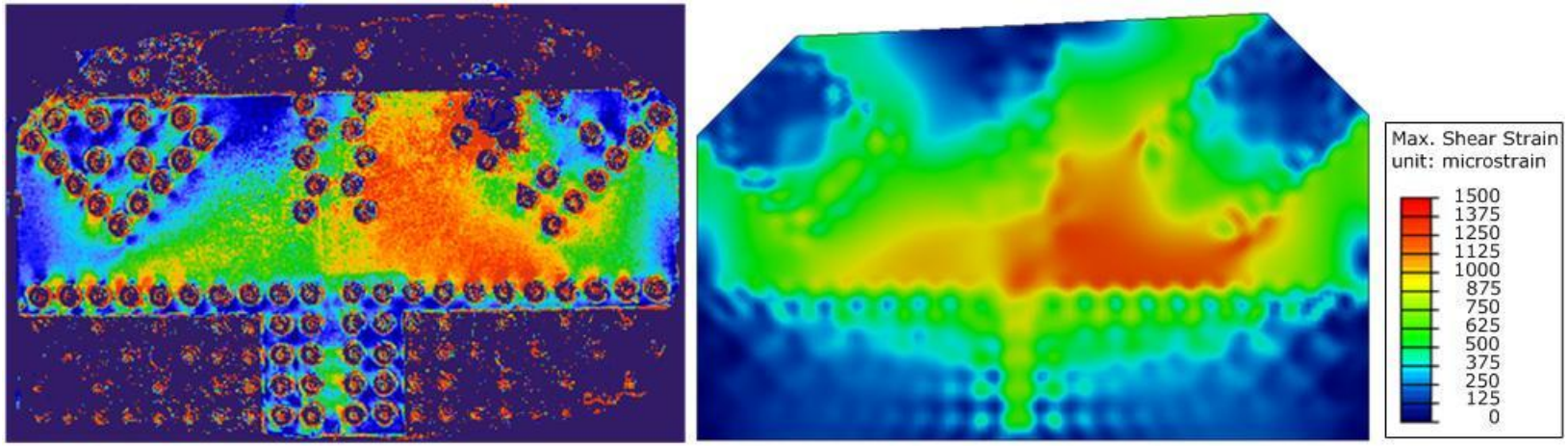

Figure 4.7.60: Comparison between the photo-elastic measurement system (left) and FEA (right) for Load Combination 5

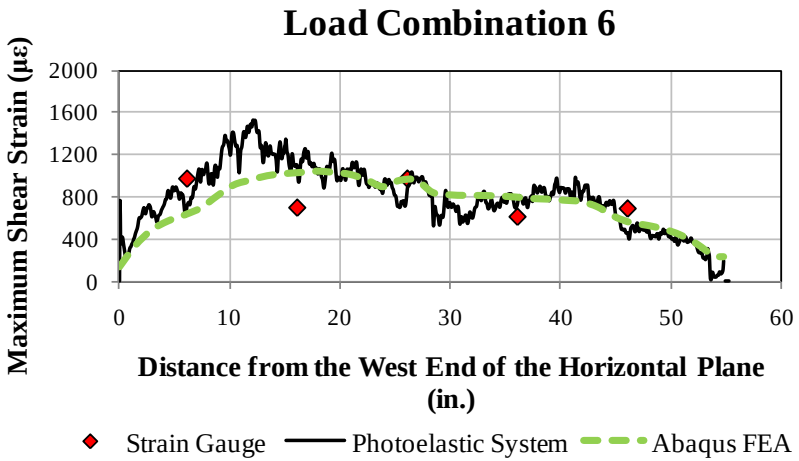

Figure 4.7.61: Comparison between the finite element analysis and experimental data (GP490-SS3 specimen - Load Combination 6)

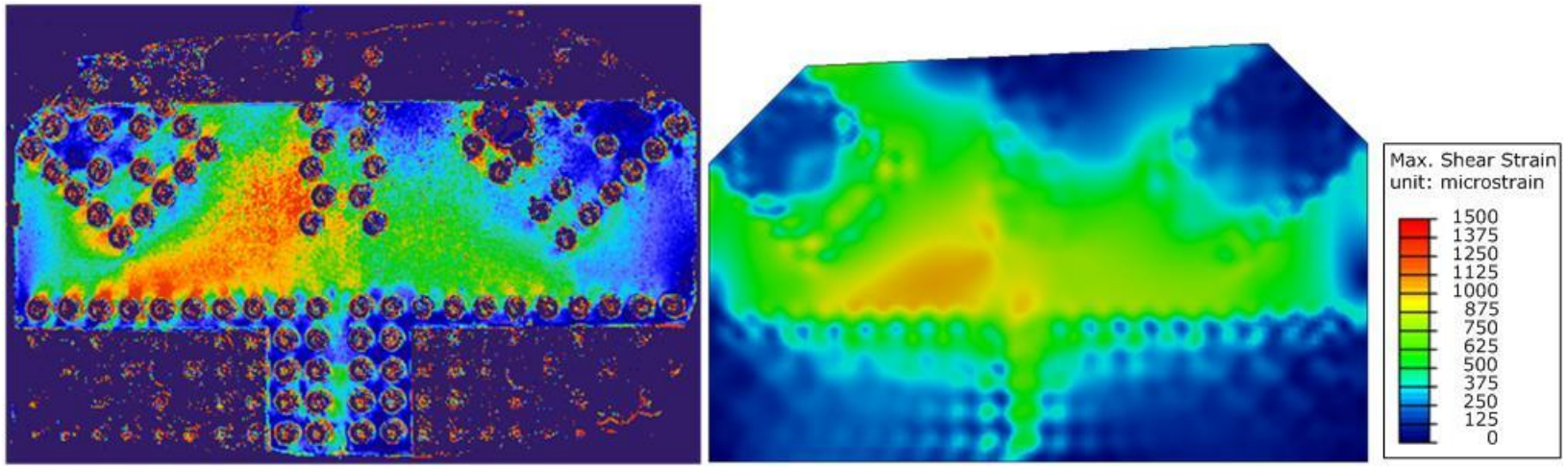

Figure 4.7.62: Comparison between the photo-elastic measurement system (left) and FEA (right) for Load Combination 6

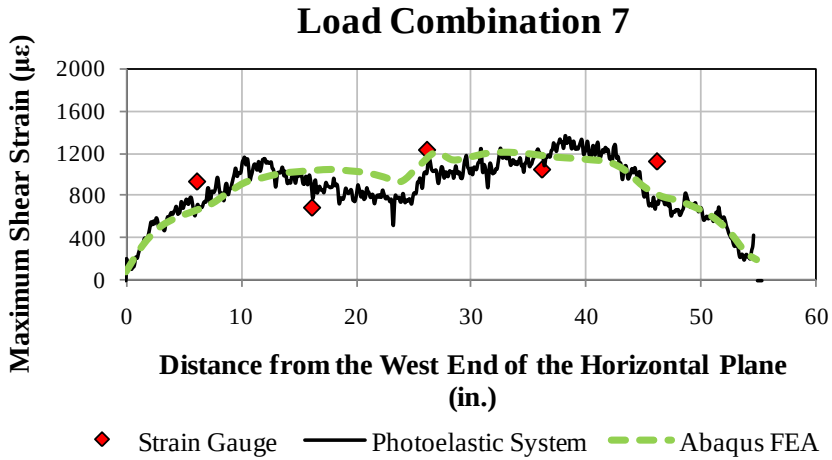

Figure 4.7.63: Comparison between the finite element analysis and experimental data (GP490-SS3 specimen - Load Combination 7)

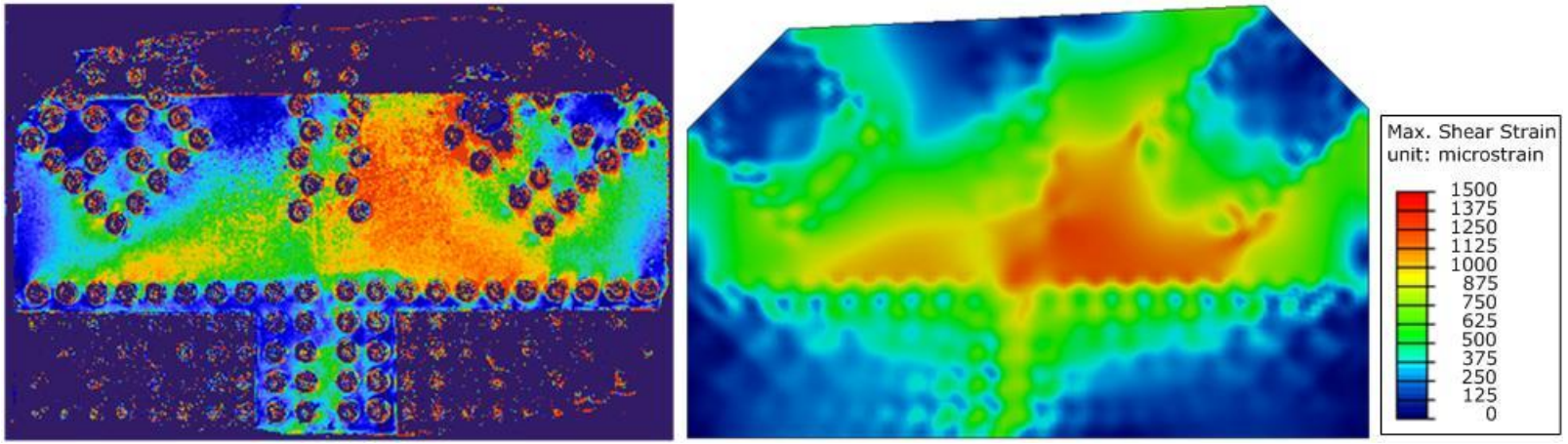

Figure 4.7.64: Comparison between the photo-elastic measurement system (left) and FEA (right) for Load Combination 7

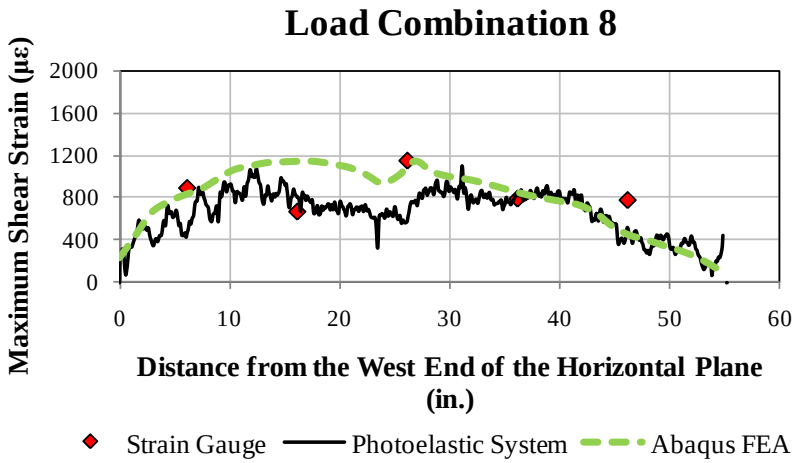

Figure 4.7.65: Comparison between the finite element analysis and experimental data (GP490-SS3 specimen - Load Combination 8)

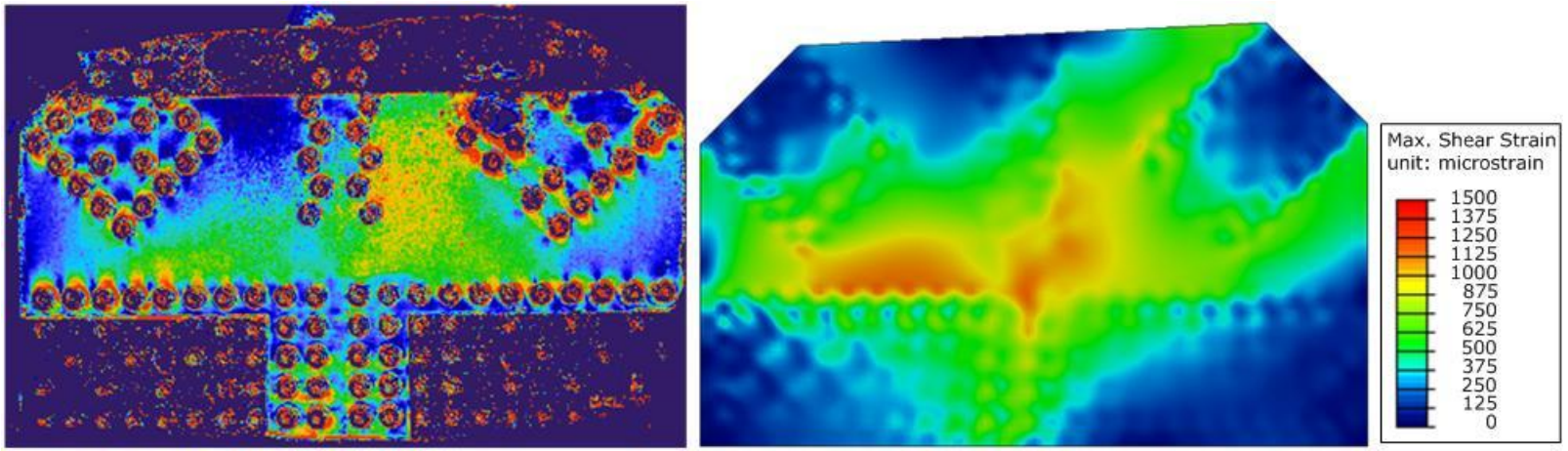

Figure 4.7.66: Comparison between the photo-elastic measurement system (left) and FEA (right) for Load Combination 8

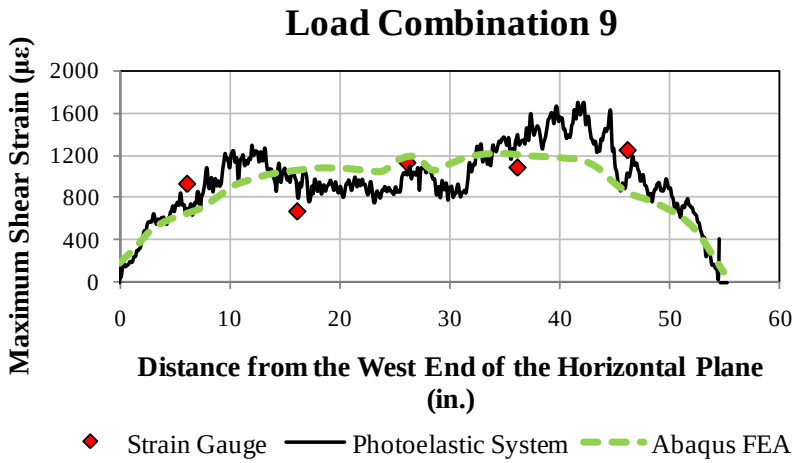

Figure 4.7.67: Comparison between the finite element analysis and experimental data (GP490-SS3 specimen - Load Combination 9)

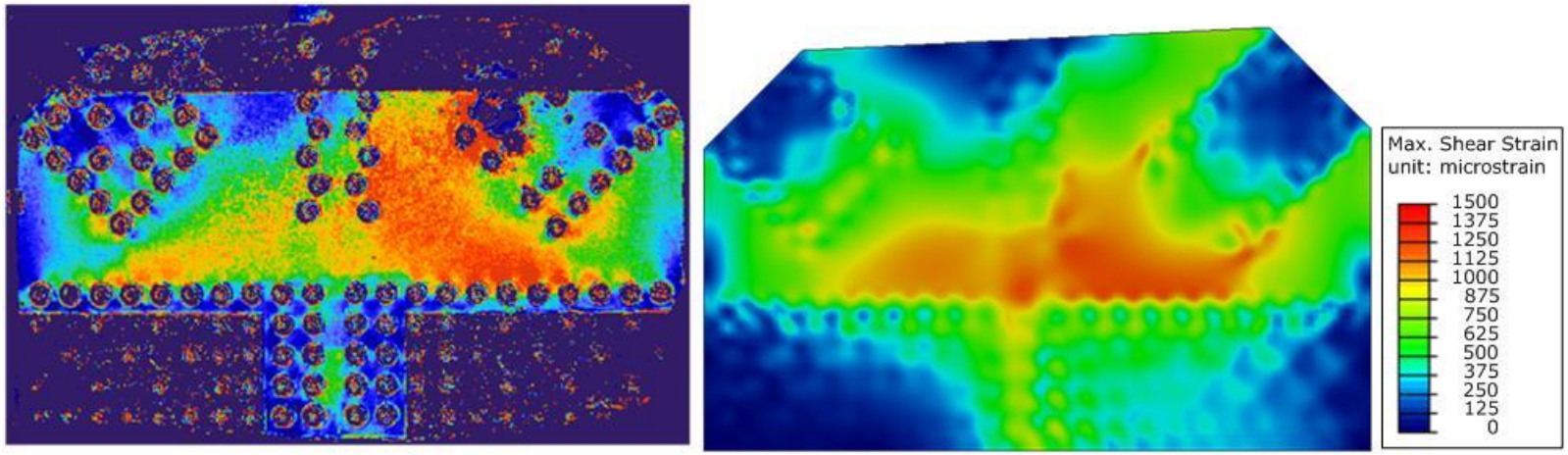

Figure 4.7.68: Comparison between the photo-elastic measurement system (left) and FEA (right) for Load Combination 9

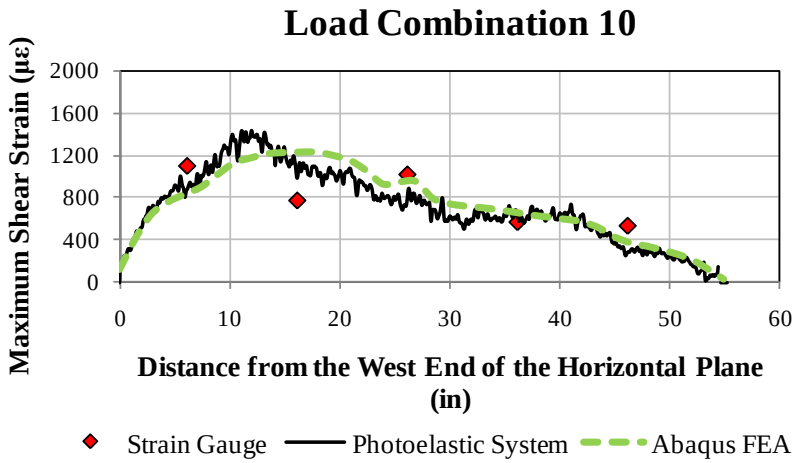

Figure 4.7.69: Comparison between the finite element analysis and experimental data (GP490-SS3 specimen - Load Combination 10)

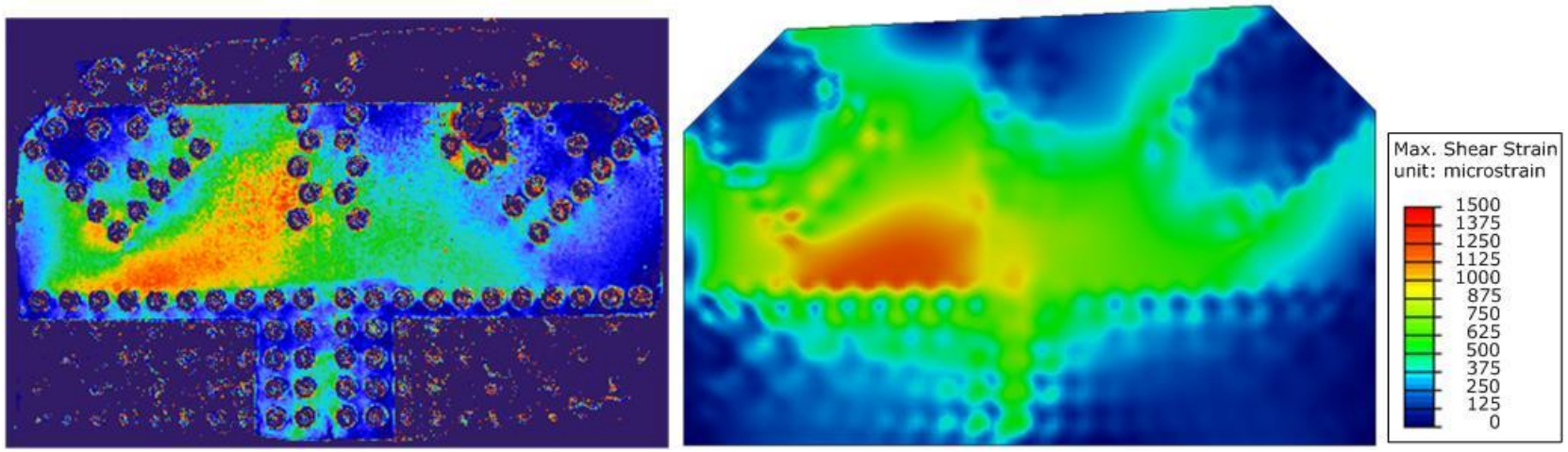

Figure 4.7.70: Comparison between the photo-elastic measurement system (left) and FEA (right) for Load Combination 10

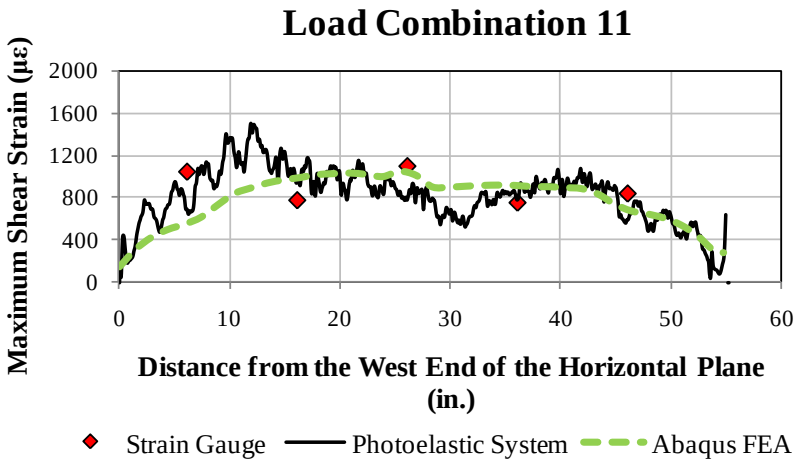

Figure 4.7.71: Comparison between the finite element analysis and experimental data (GP490-SS3 specimen - Load Combination 11)

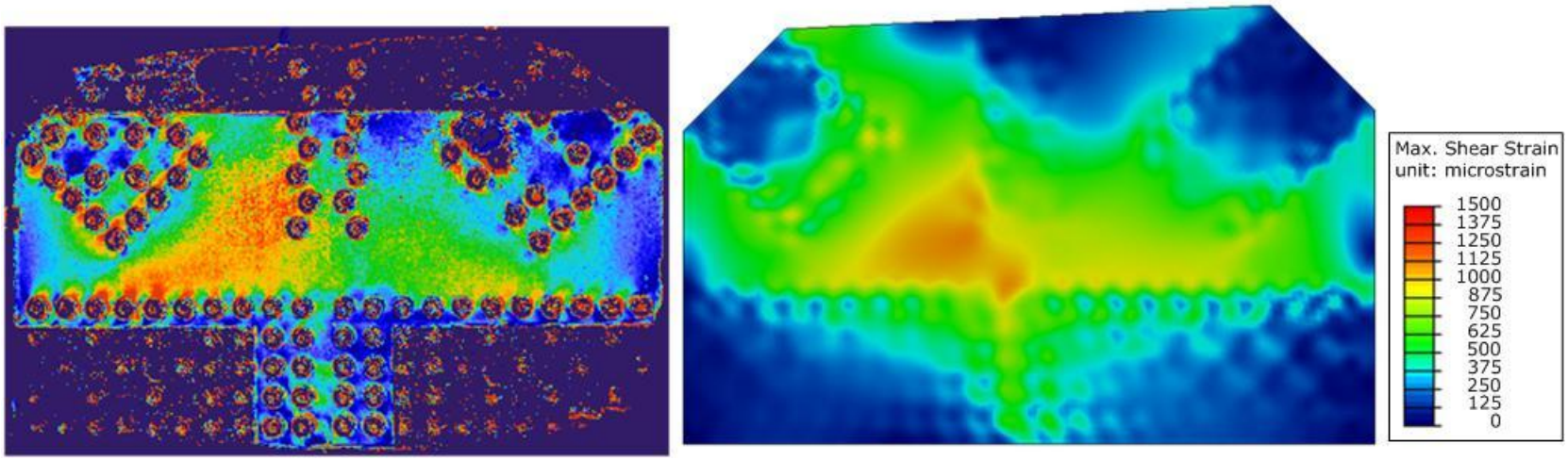

Figure 4.7.72: Comparison between the photo-elastic measurement system (left) and FEA (right) for Load Combination 11

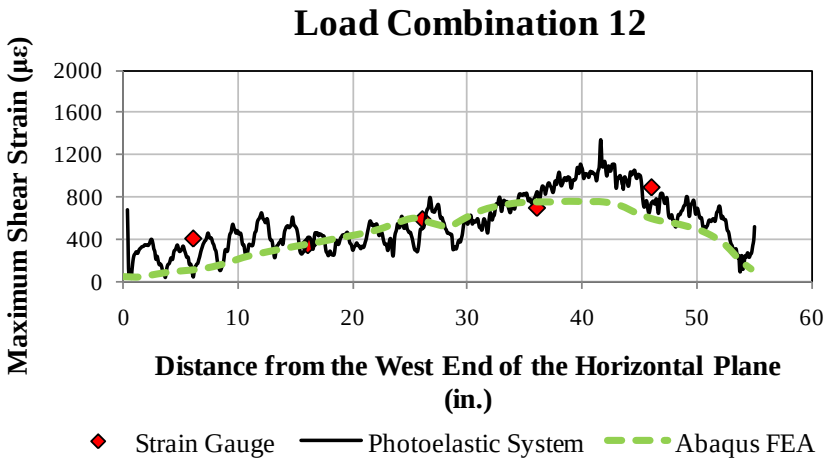

Figure 4.7.73: Comparison between the finite element analysis and experimental data (GP490-SS3 specimen - Load Combination 12)

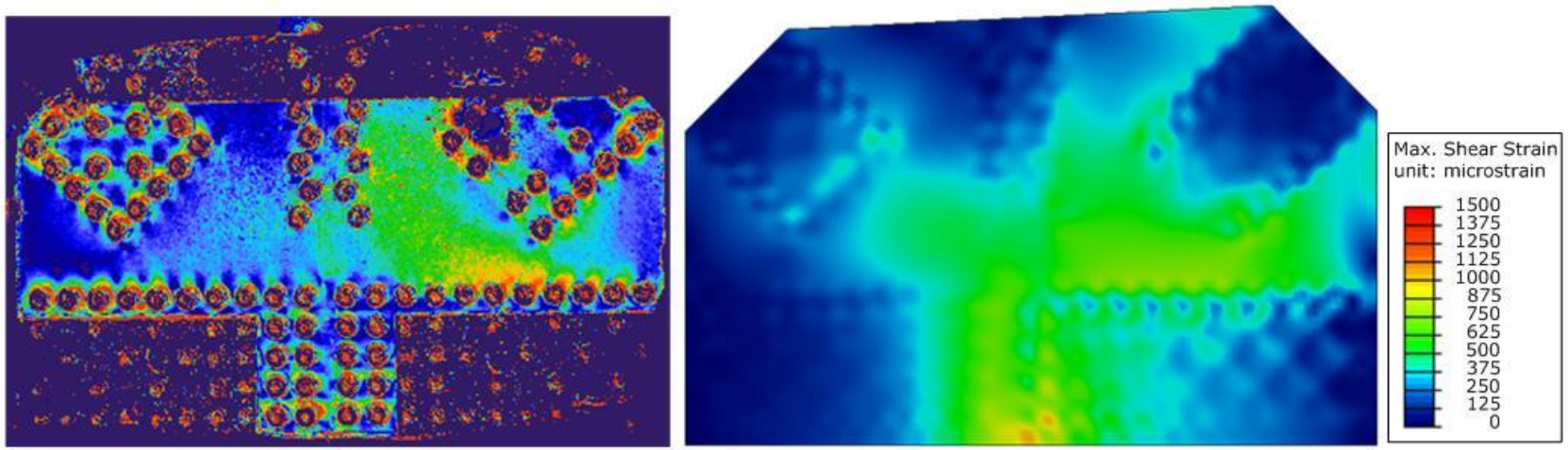

Figure 4.7.74: Comparison between the photo-elastic measurement system (left) and FEA (right) for Load Combination 12

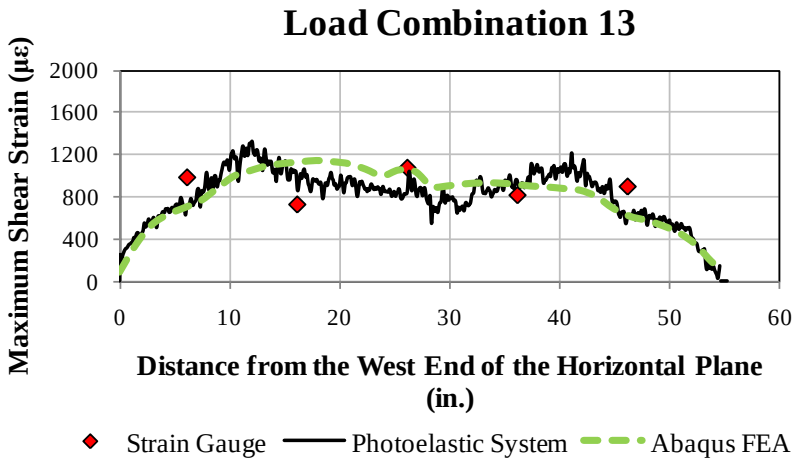

Figure 4.7.75: Comparison between the finite element analysis and experimental data (GP490-SS3 specimen - Load Combination 13)

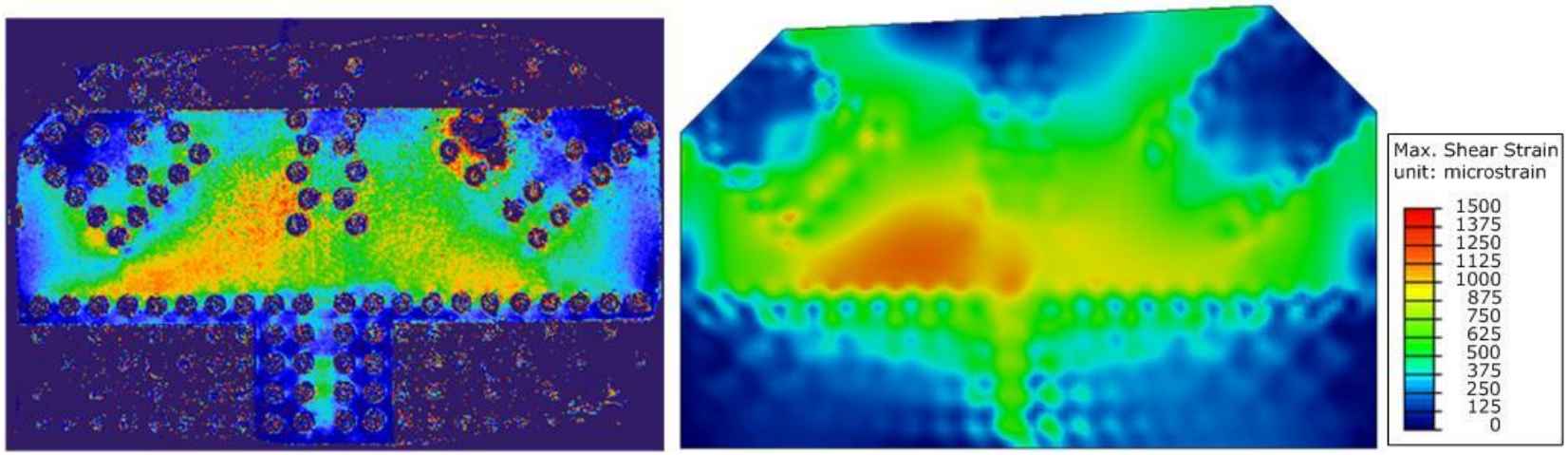

Figure 4.7.76: Comparison between the photo-elastic measurement system (left) and FEA (right) for Load Combination 13

4.7.1.5. GP490-LS3 Specimen

Each load combination, along with the actual member loads obtained from the tests are shown in Table 4.7.5 for the GP490-LS3 specimen. This specimen was the initial specimen for which the elastic stages were performed without any problem.

Table 4.7.5: Member loads from the elastic load histories of the GP490-LS3 specimen without splice plates

Load Combination	F2 (kip)	F3 (kip)	F4 (kip)	F5 (kip)
1	206	0	-200	29
2	224	0	-217	256
3	262	0	-264	207
4	272	-54	-203	167
5	235	66	-327	242
6	251	-52	-195	146
7	226	66	-310	158
8	162	48	-233	26
9	204	58	-279	279
10	231	-46	-162	57
11	279	-57	-221	270
12	108	32	-170	278
13	262	-23	-201	182
14	183	93	-347	209

The initial GP490-LS3 specimen failed due to a malfunction of the controls during the test. Hence only elastic stage data was gathered from this specimen. Both qualitative comparisons based on the contours from photoelastic data and quantitative comparisons similar to previous specimens were performed for the GP490-LS3 specimen. However, the quantitative data from the photoelastic system was not available so the plots only compare the finite element analysis results to the discrete strain gauge measurements. Figure 4.7.77 through Figure 4.7.104 show the comparisons for all the load combinations.

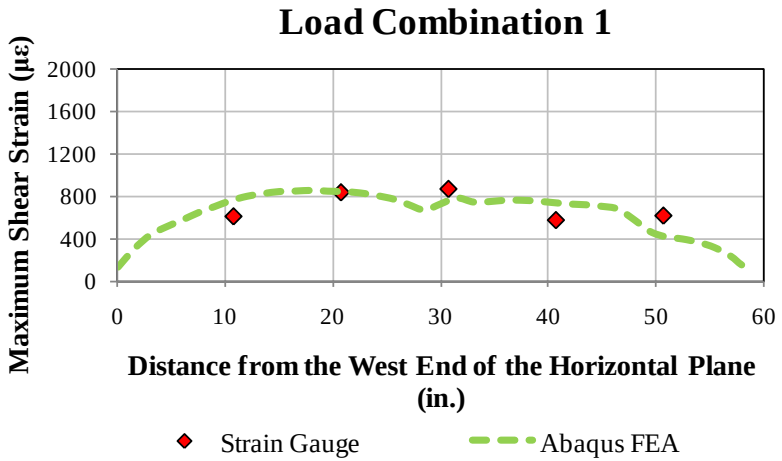

Figure 4.7.77: Comparison between the finite element analysis and experimental data (GP490-LS3 specimen - Load Combination 1)

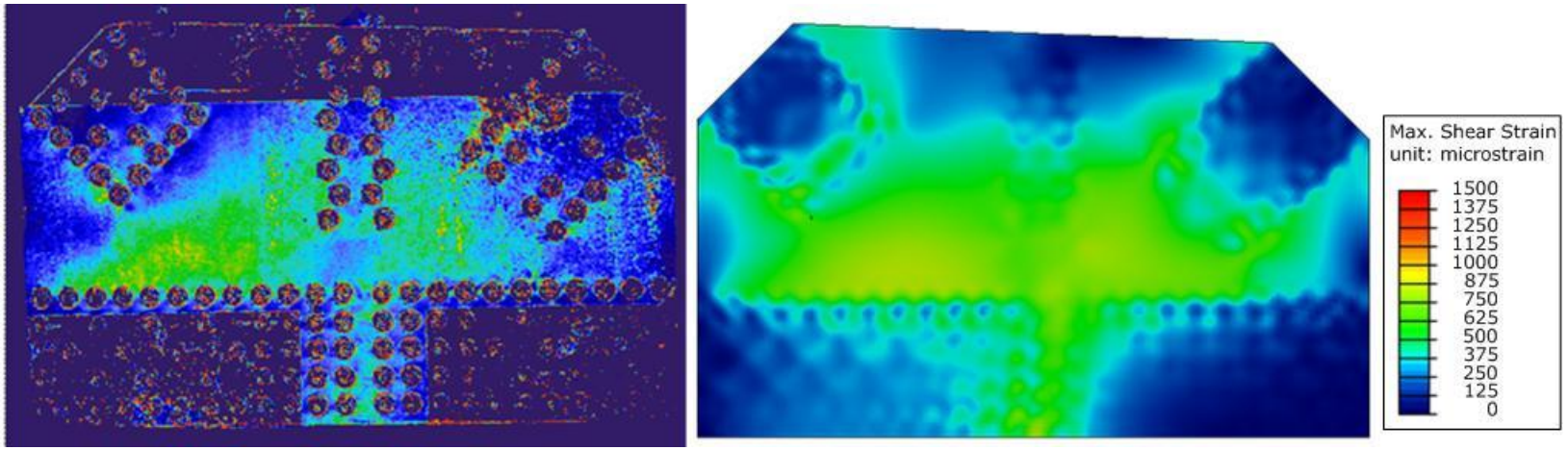

Figure 4.7.78: Comparison between the photo-elastic measurement system (left) and FEA (right) for Load Combination 1

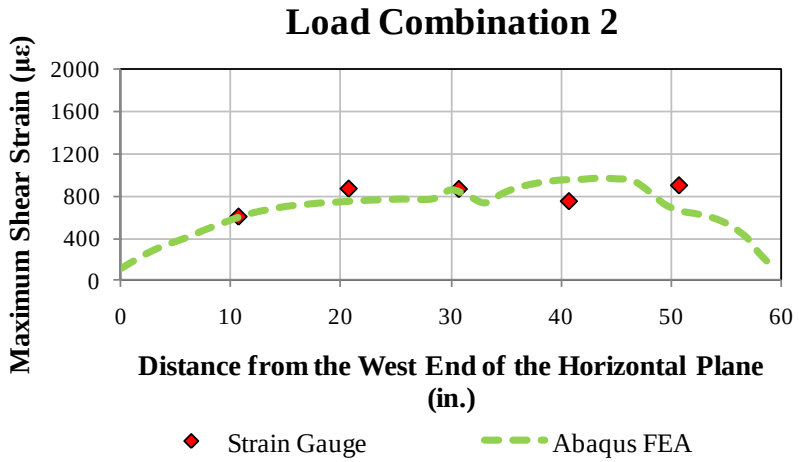

Figure 4.7.79: Comparison between the finite element analysis and experimental data (GP490-LS3 specimen - Load Combination 2)

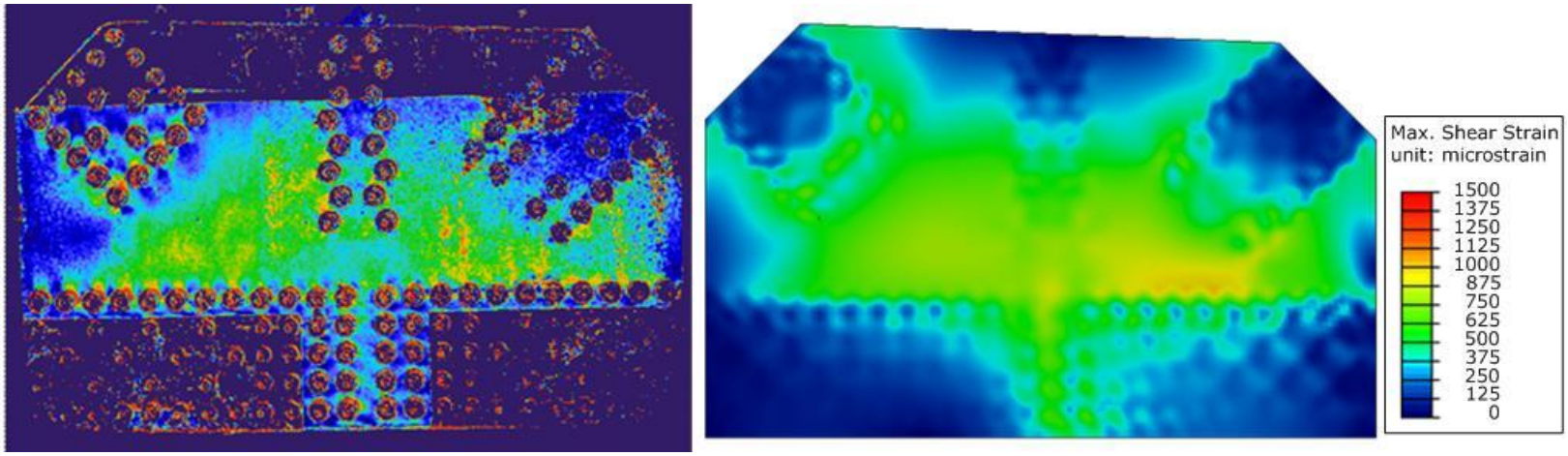

Figure 4.7.80: Comparison between the photo-elastic measurement system (left) and FEA (right) for Load Combination 2

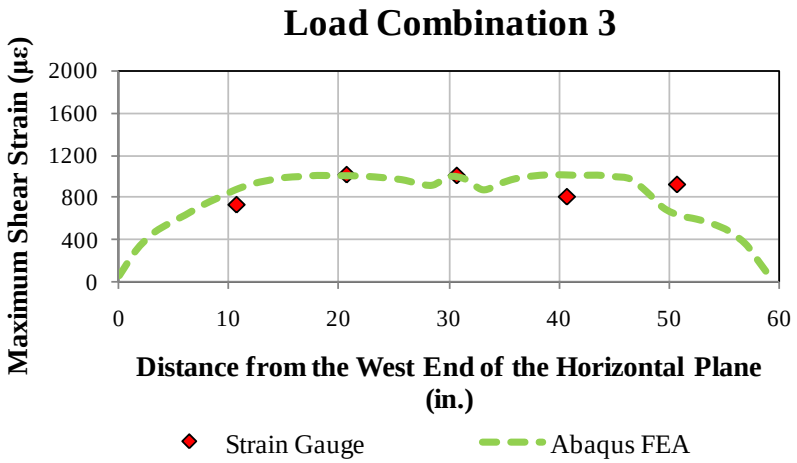

Figure 4.7.81: Comparison between the finite element analysis and experimental data (GP490-LS3 specimen - Load Combination 3)

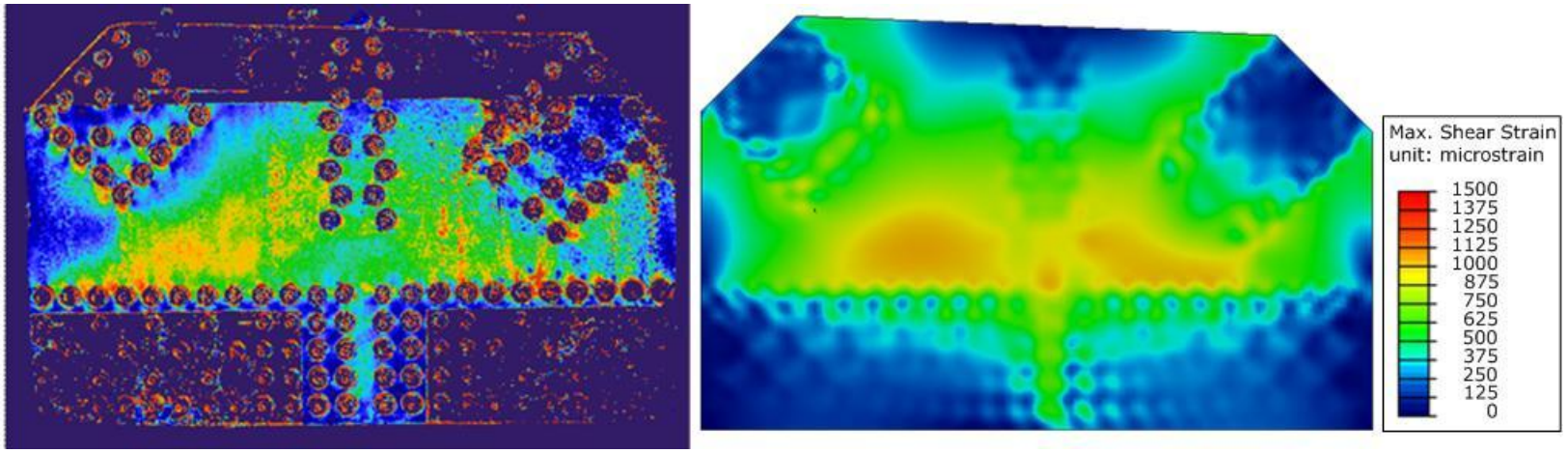

Figure 4.7.82: Comparison between the photo-elastic measurement system (left) and FEA (right) for Load Combination 3

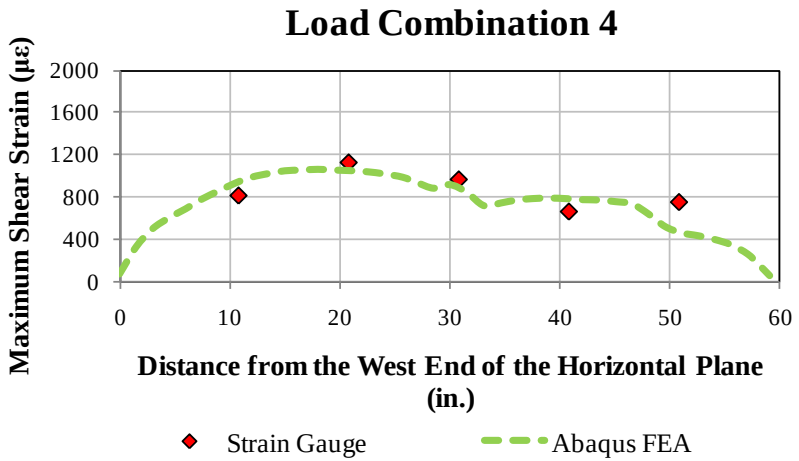

Figure 4.7.83: Comparison between the finite element analysis and experimental data (GP490-LS3 specimen - Load Combination 4)

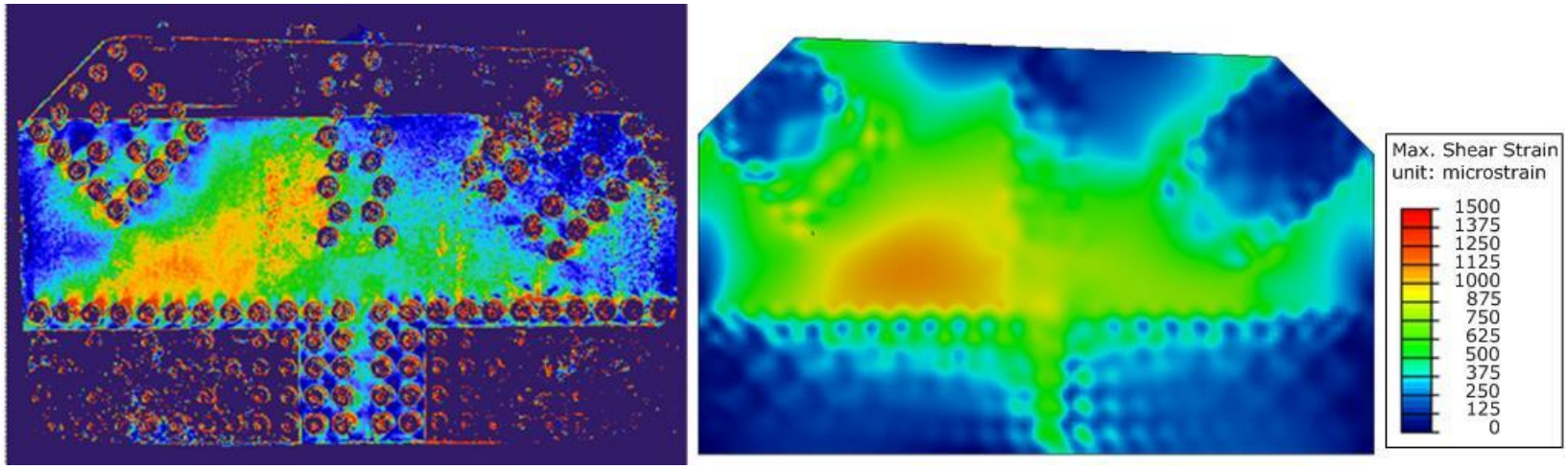

Figure 4.7.84: Comparison between the photo-elastic measurement system (left) and FEA (right) for Load Combination 4

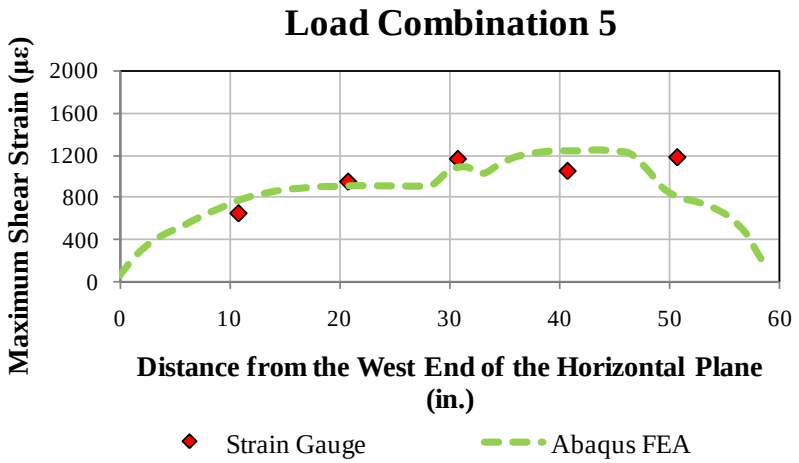

Figure 4.7.85: Comparison between the finite element analysis and experimental data (GP490-LS3 specimen - Load Combination 5)

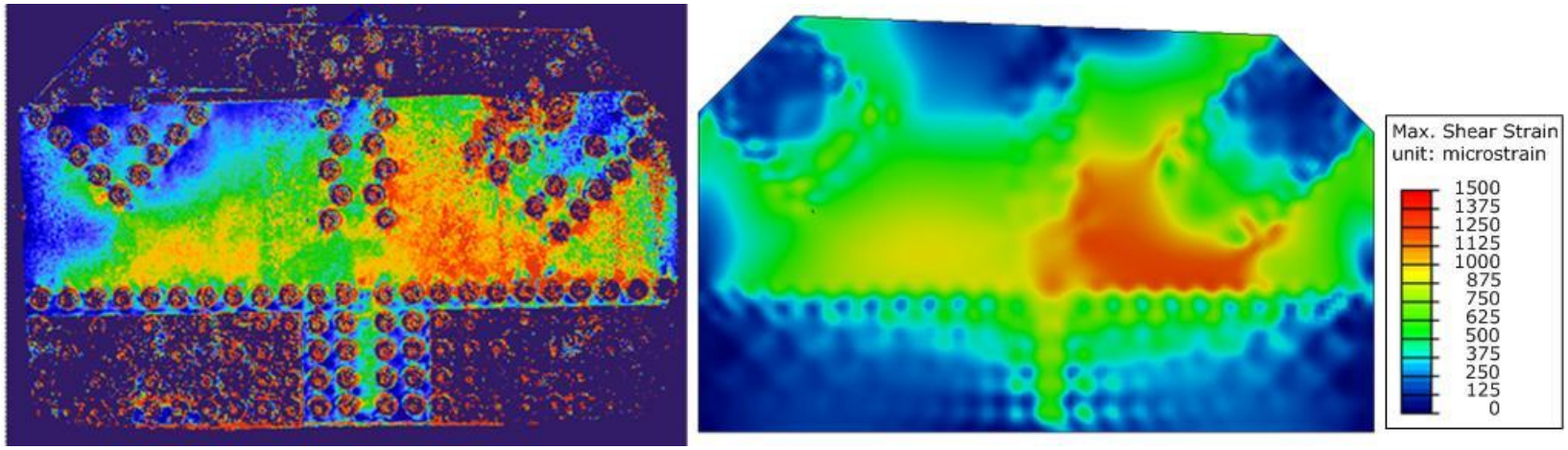

Figure 4.7.86: Comparison between the photo-elastic measurement system (left) and FEA (right) for Load Combination 5

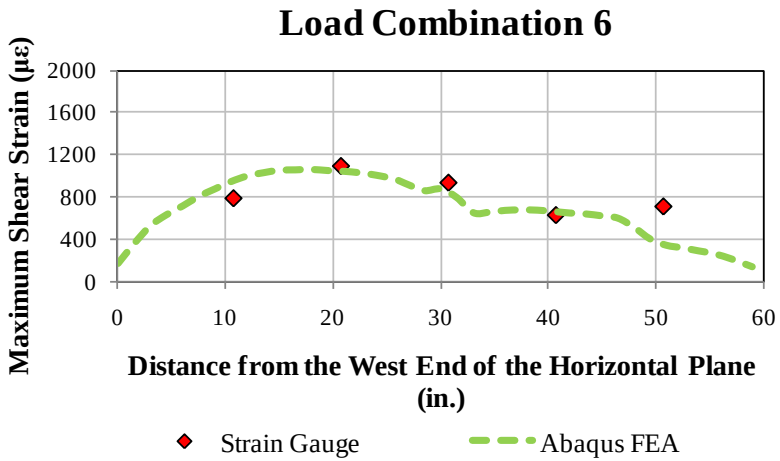

Figure 4.7.87: Comparison between the finite element analysis and experimental data (GP490-LS3 specimen - Load Combination 6)

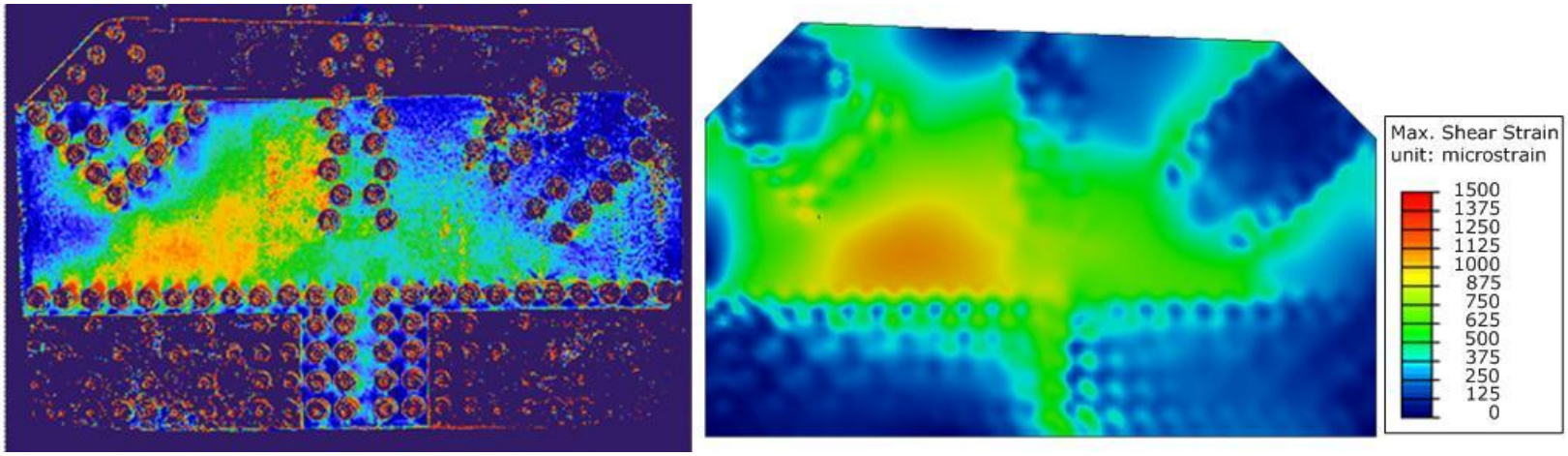

Figure 4.7.88: Comparison between the photo-elastic measurement system (left) and FEA (right) for Load Combination 6

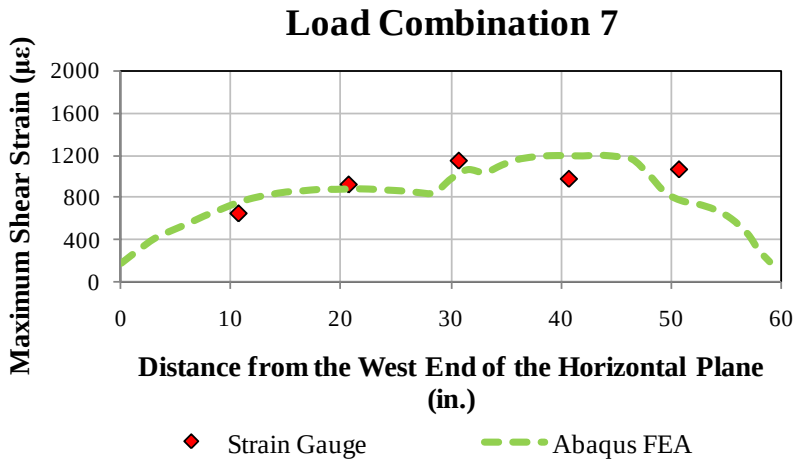

Figure 4.7.89: Comparison between the finite element analysis and experimental data (GP490-LS3 specimen - Load Combination 7)

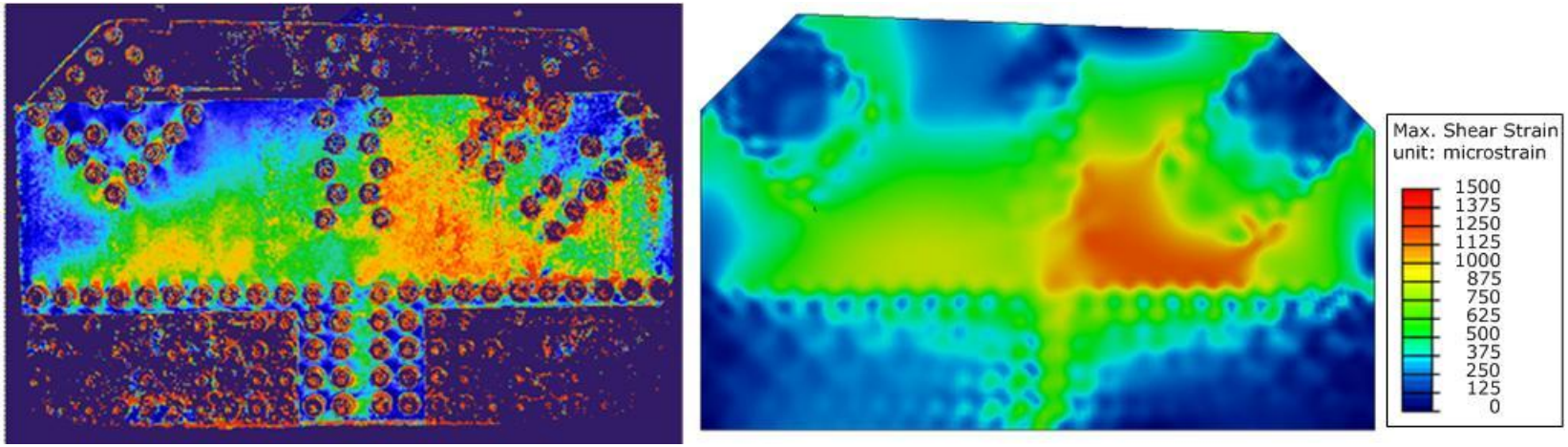

Figure 4.7.90: Comparison between the photo-elastic measurement system (left) and FEA (right) for Load Combination 7

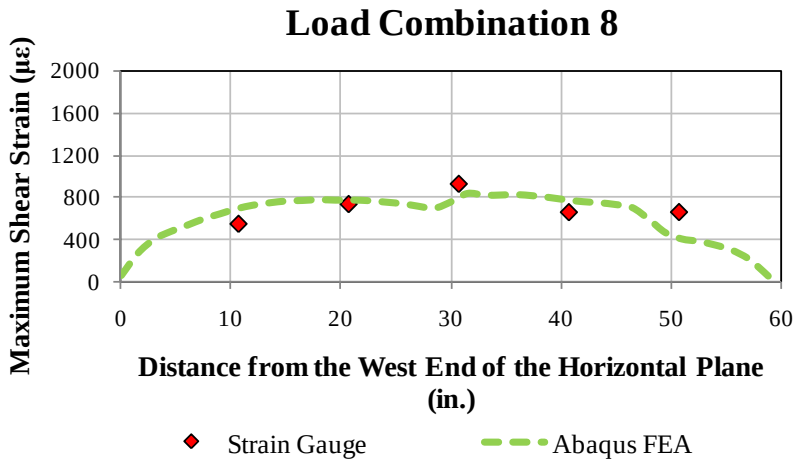

Figure 4.7.91: Comparison between the finite element analysis and experimental data (GP490-LS3 specimen - Load Combination 8)

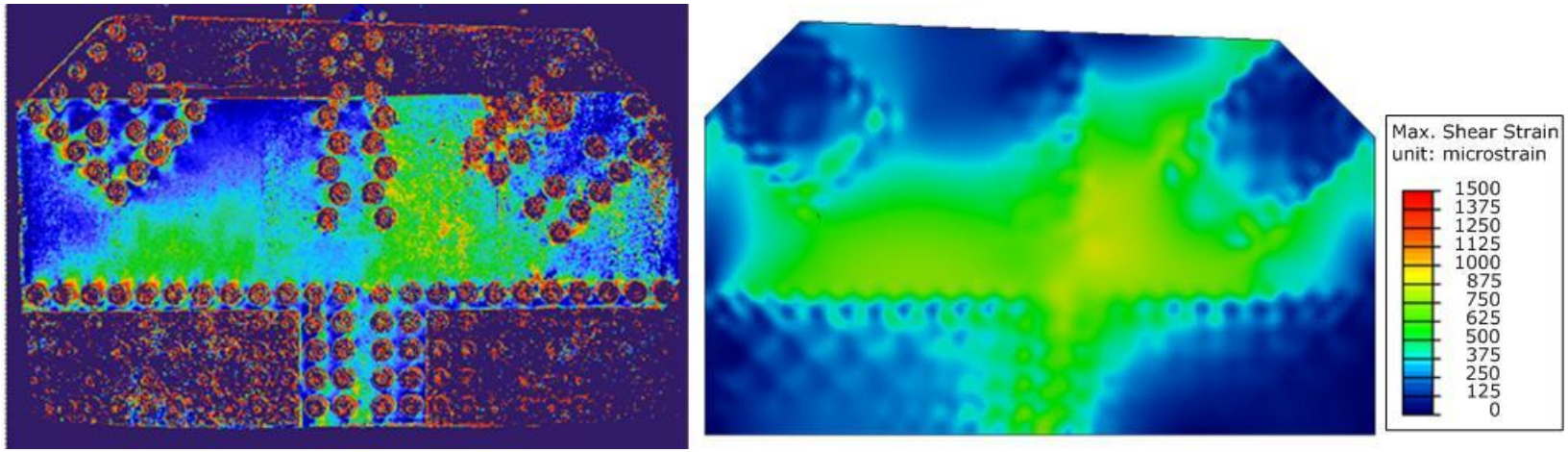

Figure 4.7.92: Comparison between the photo-elastic measurement system (left) and FEA (right) for Load Combination 8

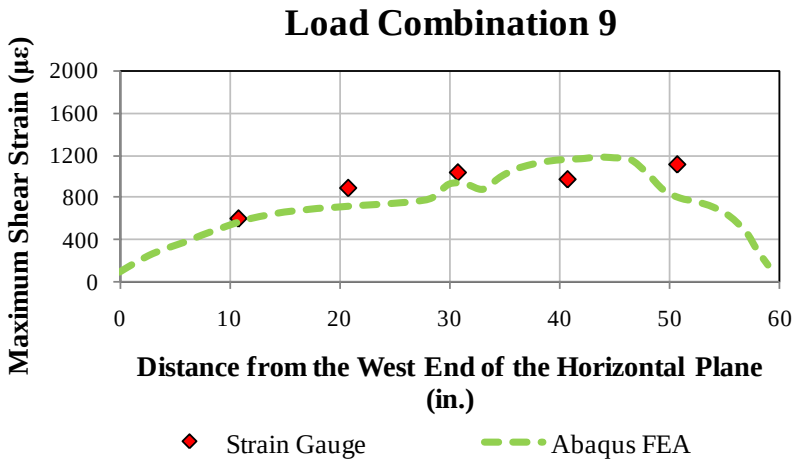

Figure 4.7.93: Comparison between the finite element analysis and experimental data (GP490-LS3 specimen - Load Combination 9)

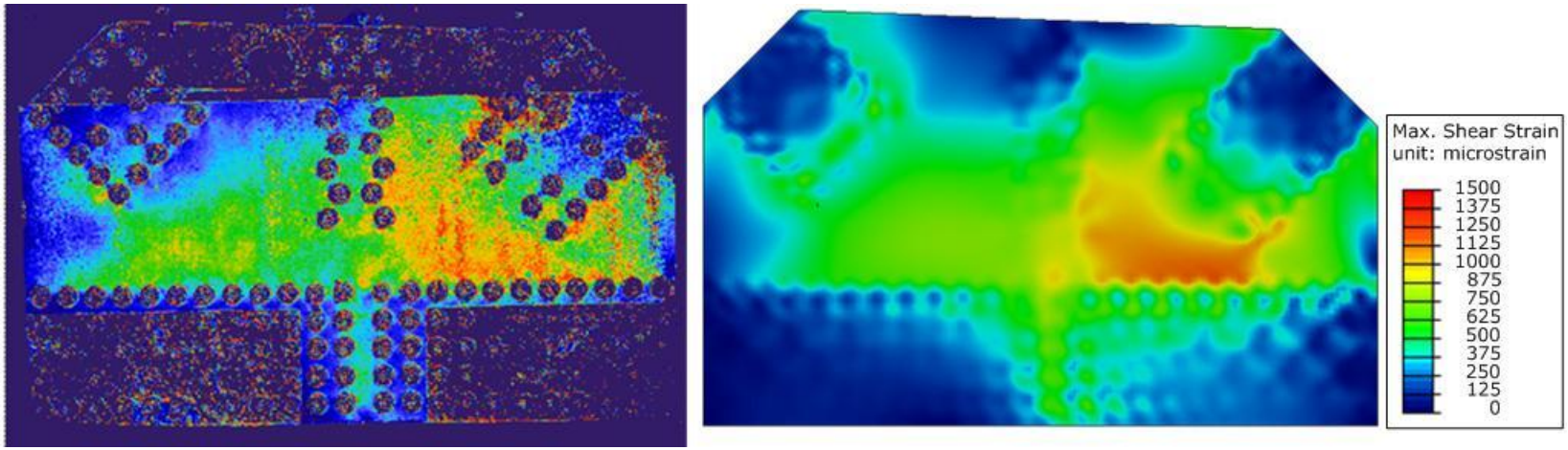

Figure 4.7.94: Comparison between the photo-elastic measurement system (left) and FEA (right) for Load Combination 9

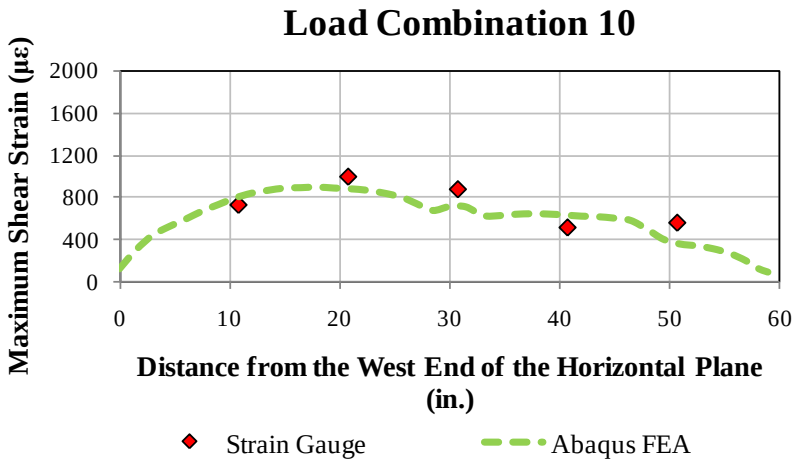

Figure 4.7.95: Comparison between the finite element analysis and experimental data (GP490-LS3 specimen - Load Combination 10)

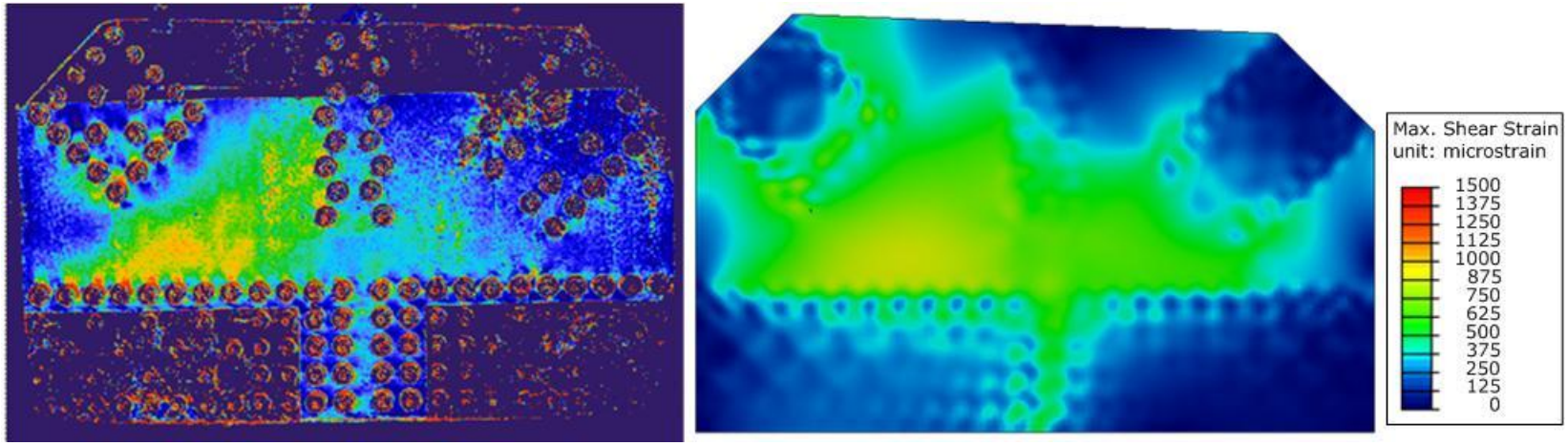

Figure 4.7.96: Comparison between the photo-elastic measurement system (left) and FEA (right) for Load Combination 10

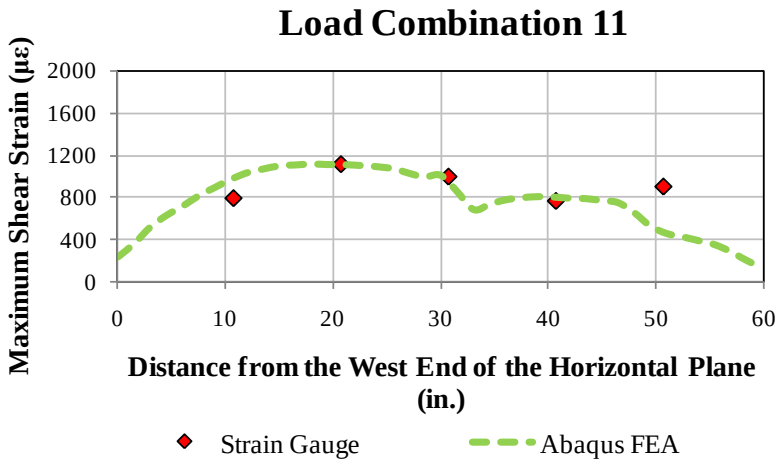

Figure 4.7.97: Comparison between the finite element analysis and experimental data (GP490-LS3 specimen - Load Combination 11)

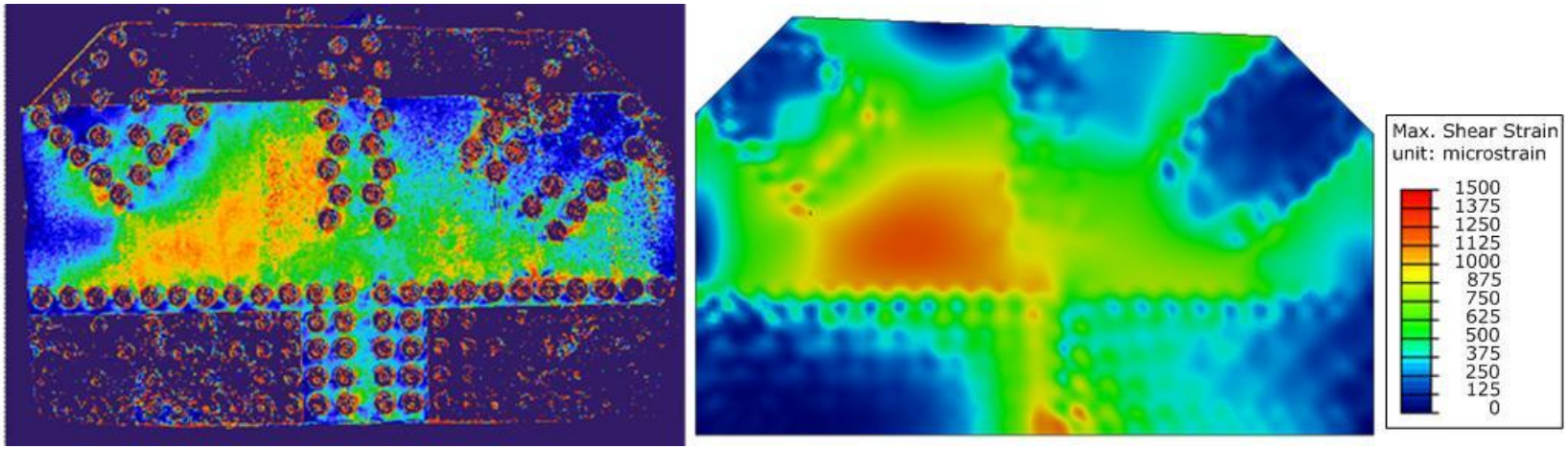

Figure 4.7.98: Comparison between the photo-elastic measurement system (left) and FEA (right) for Load Combination 11

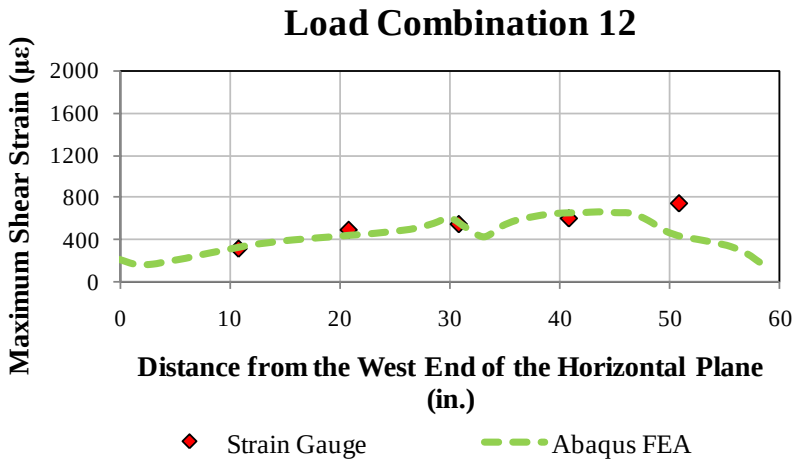

Figure 4.7.99: Comparison between the finite element analysis and experimental data (GP490-LS3 specimen - Load Combination 12)

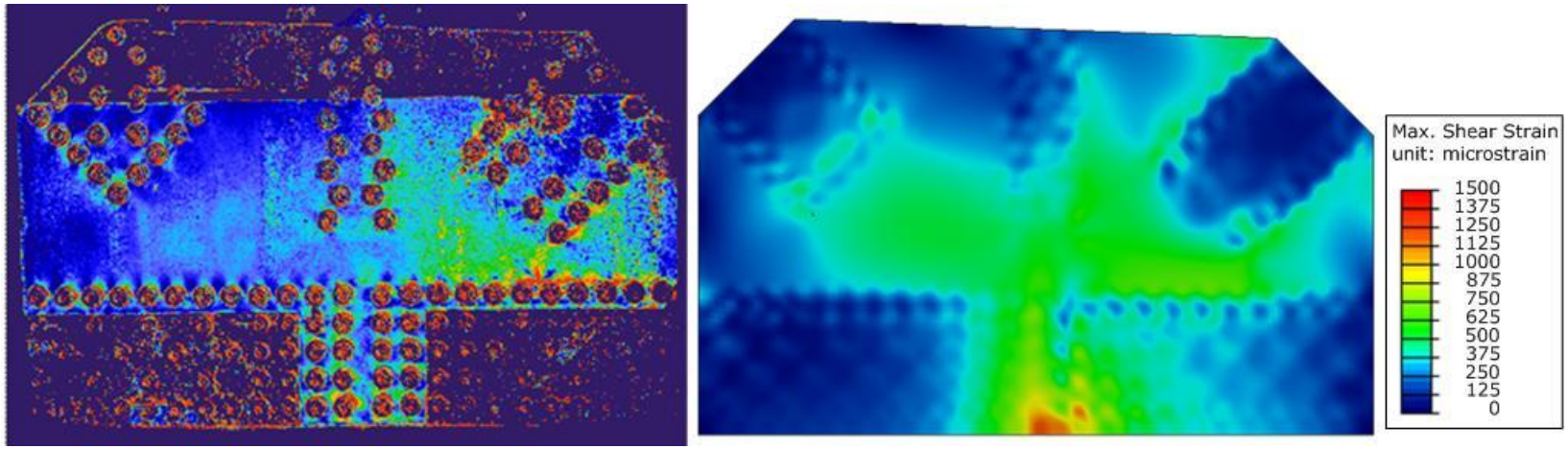

Figure 4.7.100: Comparison between the photo-elastic measurement system (left) and FEA (right) for Load Combination 12

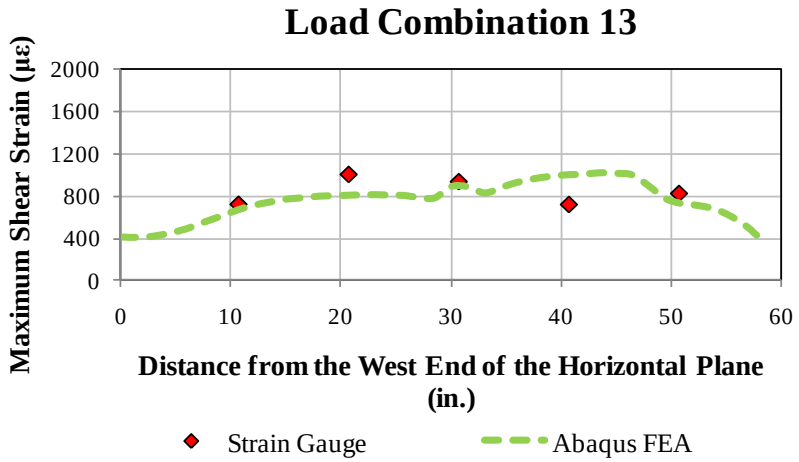

Figure 4.7.101: Comparison between the finite element analysis and experimental data (GP490-LS3 specimen-Load Combination 13)

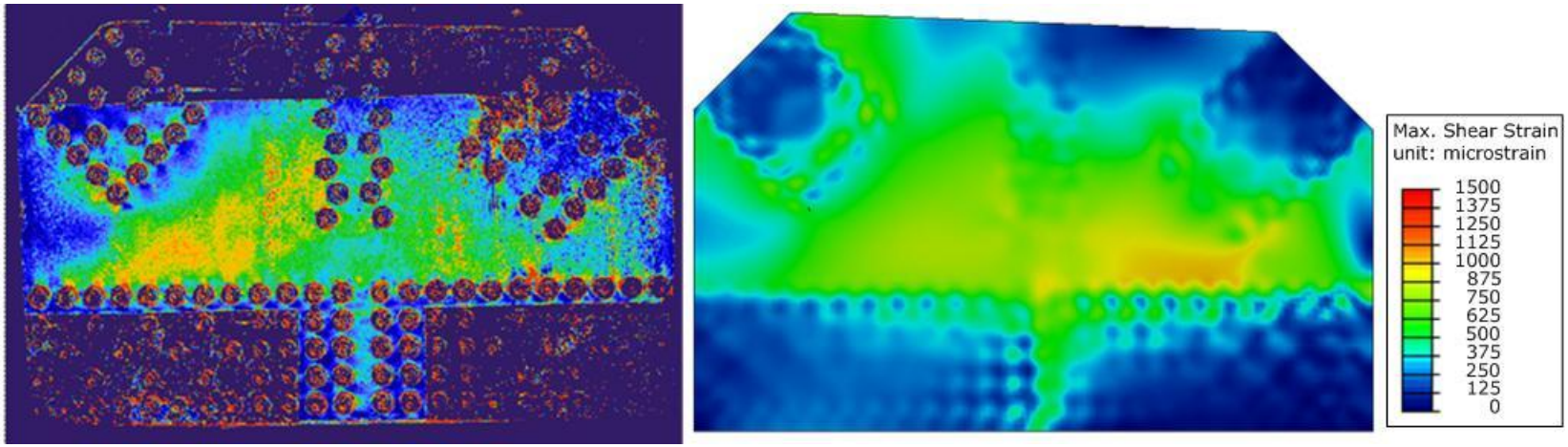

Figure 4.7.102: Comparison between the photo-elastic measurement system (left) and FEA (right) for Load Combination 13

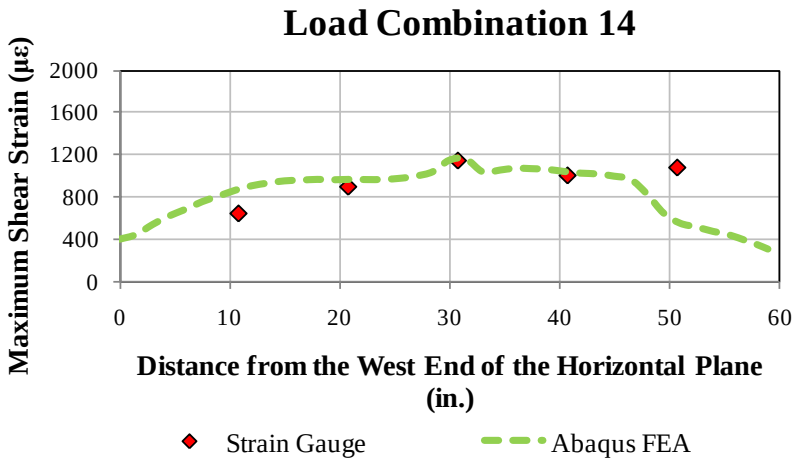

Figure 4.7.103: Comparison between the finite element analysis and experimental data (GP490-LS3 specimen-Load Combination 14)

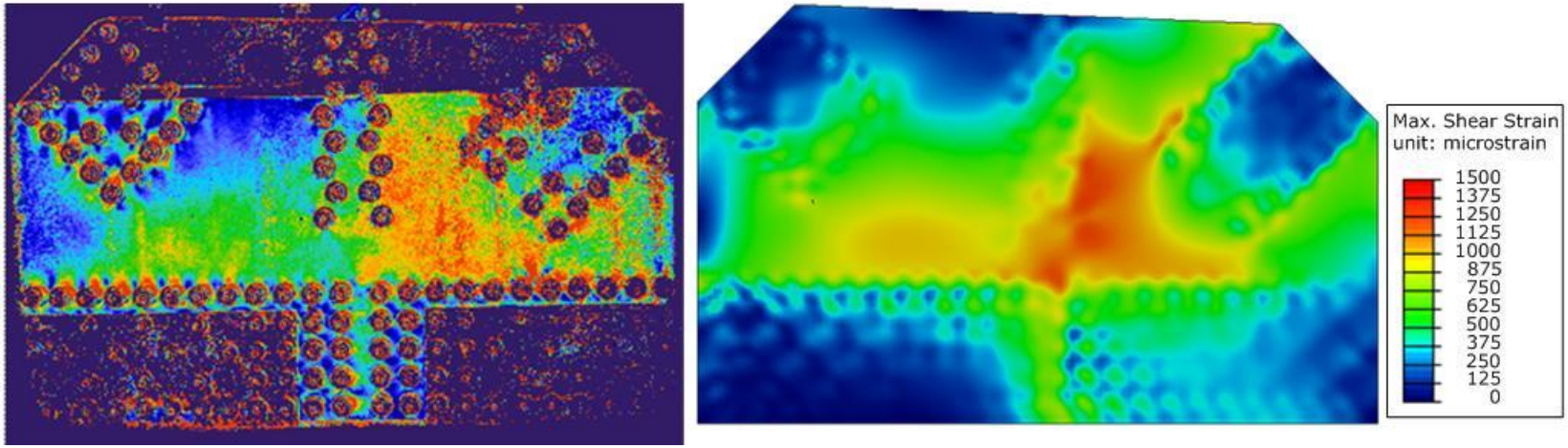

Figure 4.7.104: Comparison between the photo-elastic measurement system (left) and FEA (right) for Load Combination 14

4.7.2. Elastic Stages with Splice Plates

4.7.2.1. GP307-SS3 Specimen

Member forces on the four loaded members to be applied in the finite element analysis as determined from the elastic stage tests are shown in Table 4.7.6.

Table 4.7.6: Member loads from the elastic load histories of the GP307-SS3 specimen with splice plates

Load Combination	F2 (kip)	F3 (kip)	F4 (kip)	F5 (kip)
1	250	0	-265	40
2	230	2	-226	307
3	237	0	-238	189
4	256	-52	-183	179
5	239	64	-338	251
6	252	-52	-183	124
7	257	63	-324	164
8	175	48	-252	14
9	222	64	-285	292
10	231	-48	-171	53
11	256	-52	-197	255
12	81	36	-142	276
13	258	-20	-234	198
14	163	116	-313	190

Figure 4.7.105 through Figure 4.7.118 show that the analysis results performed on the GP307-SS3 specimen without splice plates match well the discrete strain gauge and photoelastic system data.

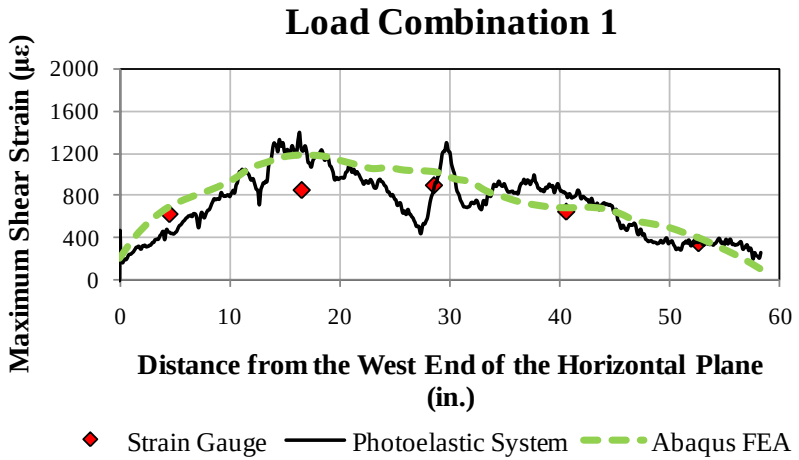

Figure 4.7.105: Comparison between the finite element analysis and experimental data (GP307-SS3 specimen - Load Combination 1)

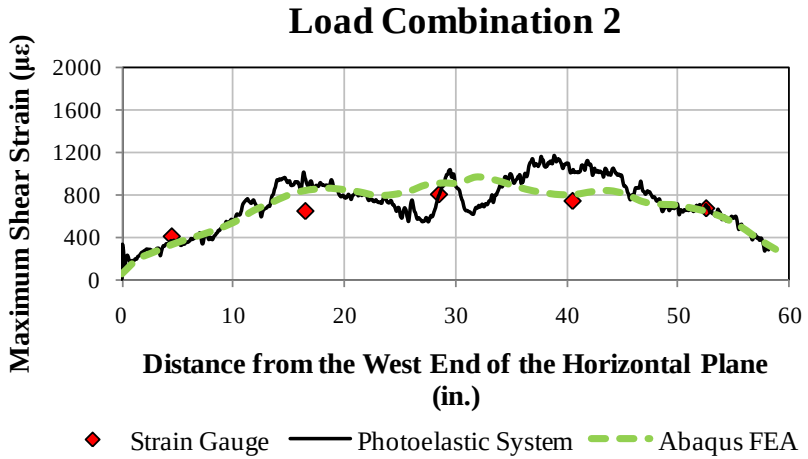

Figure 4.7.106: Comparison between the finite element analysis and experimental data (GP307-SS3 specimen - Load Combination 2)

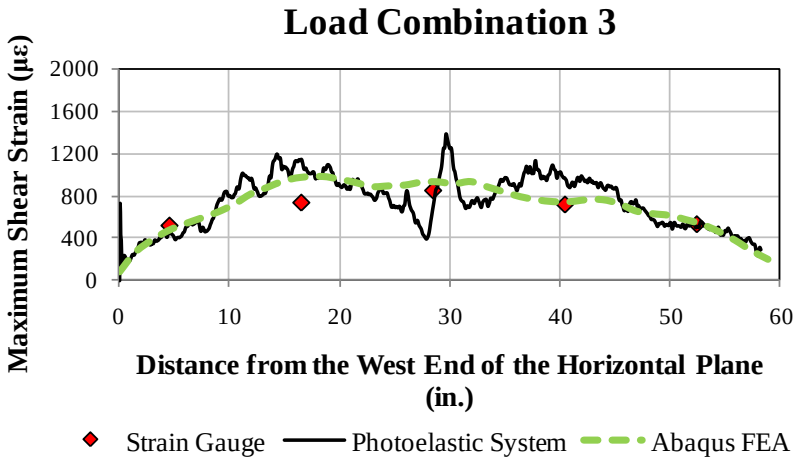

Figure 4.7.107: Comparison between the finite element analysis and experimental data (GP307-SS3 specimen - Load Combination 3)

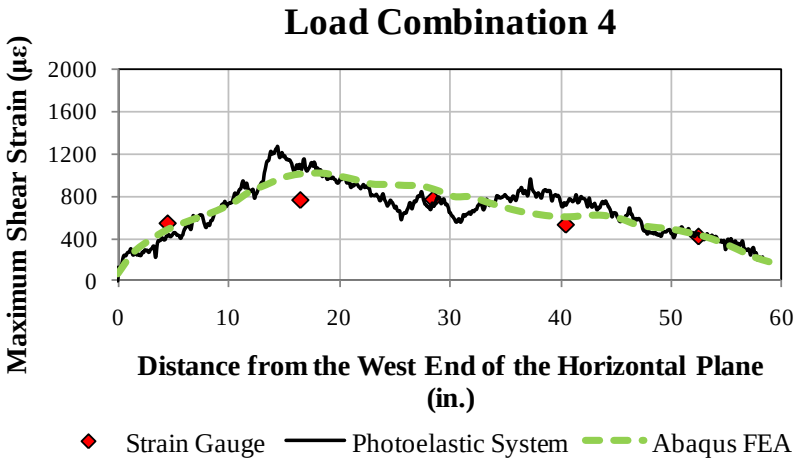

Figure 4.7.108: Comparison between the finite element analysis and experimental data (GP307-SS3 specimen - Load Combination 4)

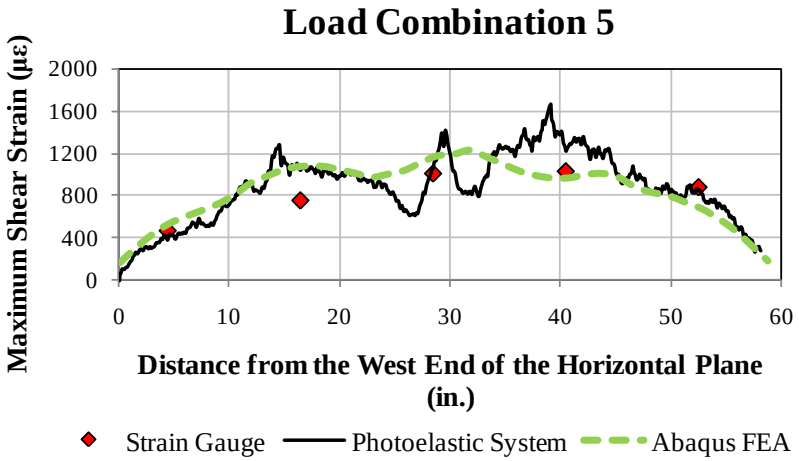

Figure 4.7.109: Comparison between the finite element analysis and experimental data (GP307-SS3 specimen - Load Combination 5)

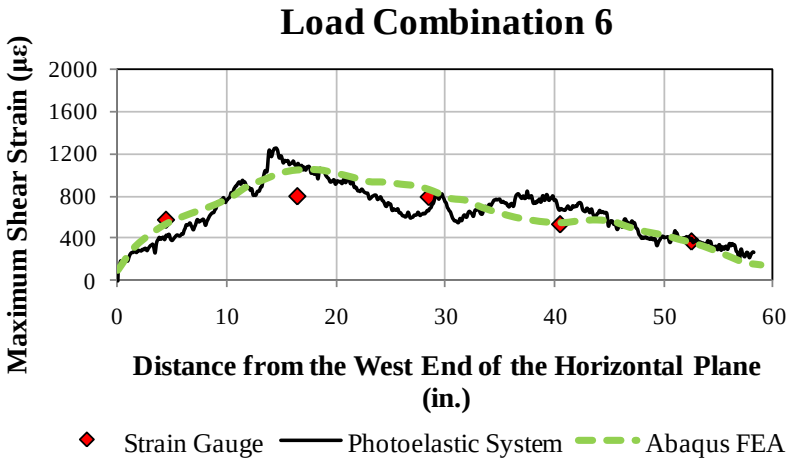

Figure 4.7.110: Comparison between the finite element analysis and experimental data (GP307-SS3 specimen - Load Combination 6)

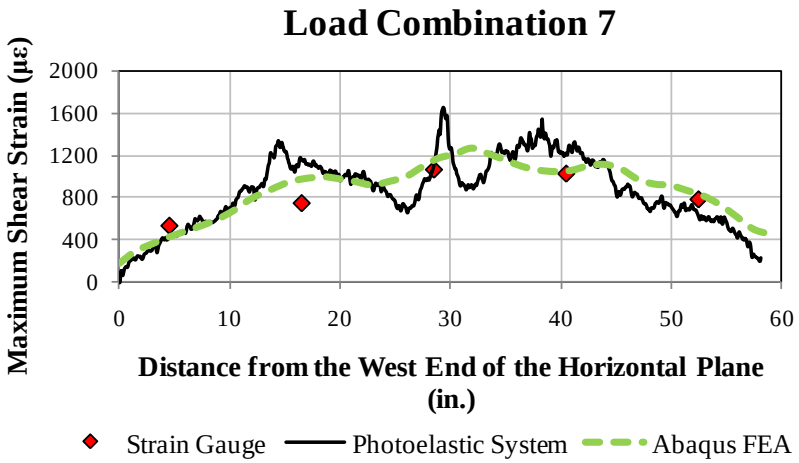

Figure 4.7.111: Comparison between the finite element analysis and experimental data (GP307-SS3 specimen - Load Combination 7)

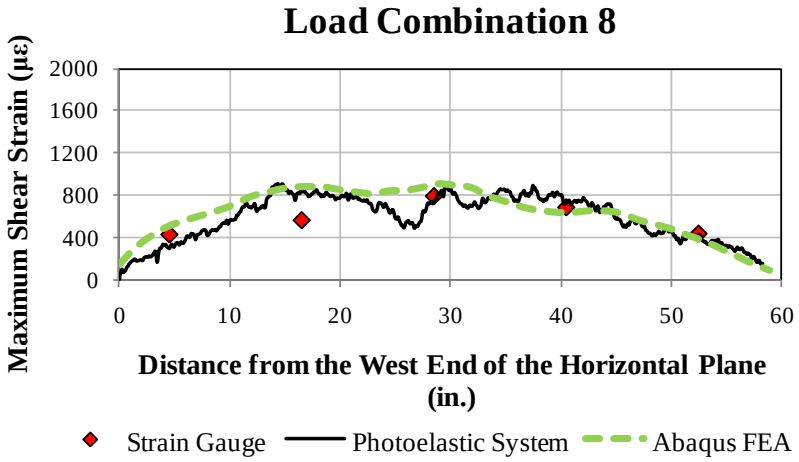

Figure 4.7.112: Comparison between the finite element analysis and experimental data (GP307-SS3 specimen - Load Combination 8)

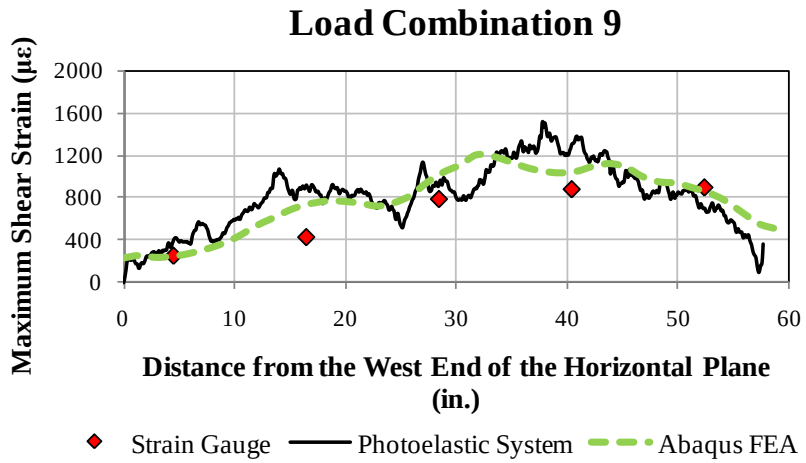

Figure 4.7.113: Comparison between the finite element analysis and experimental data (GP307-SS3 specimen - Load Combination 9)

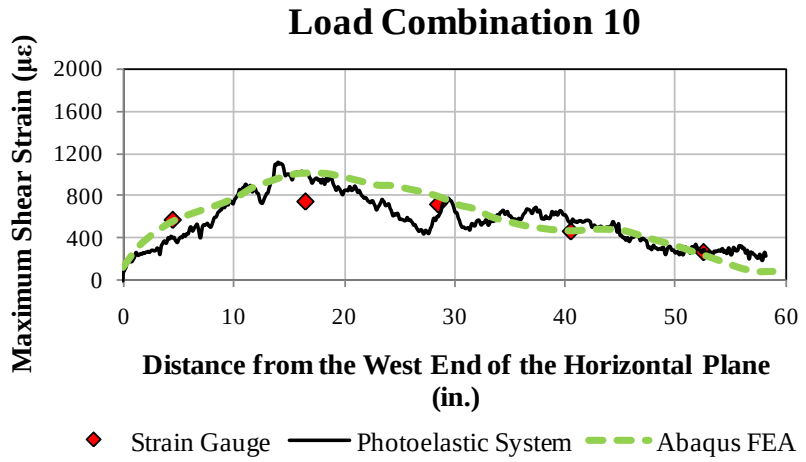

Figure 4.7.114: Comparison between the finite element analysis and experimental data (GP307-SS3 specimen-Load Combination 10)

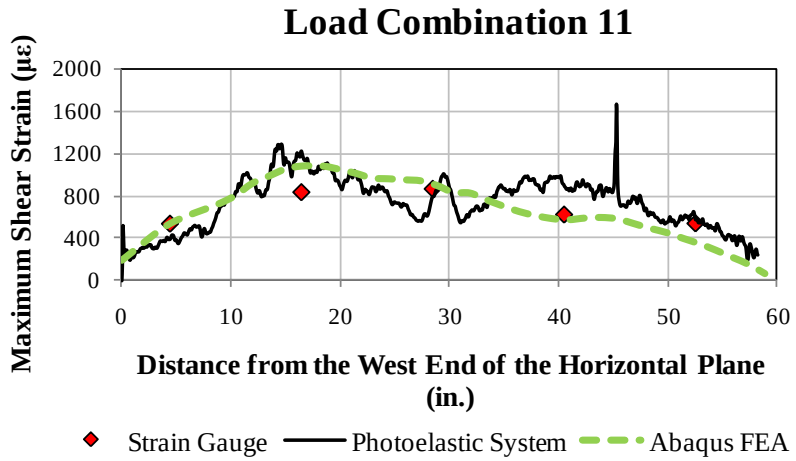

Figure 4.7.115: Comparison between the finite element analysis and experimental data (GP307-SS3 specimen-Load Combination 11)

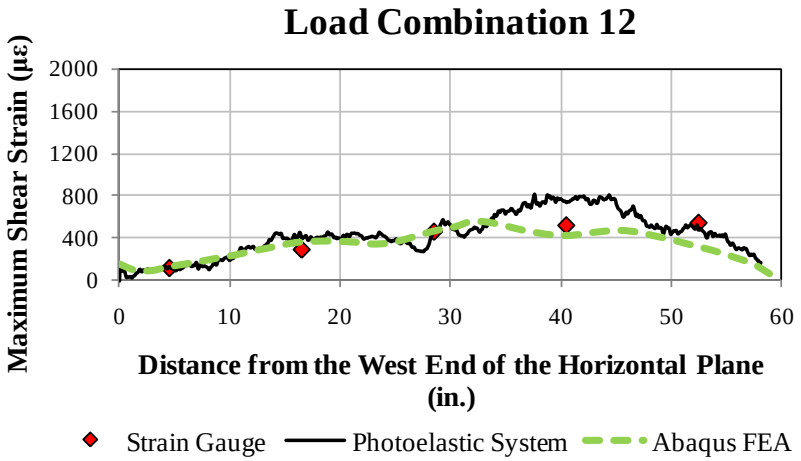

Figure 4.7.116: Comparison between the finite element analysis and experimental data (GP307-SS3 specimen-Load Combination 12)

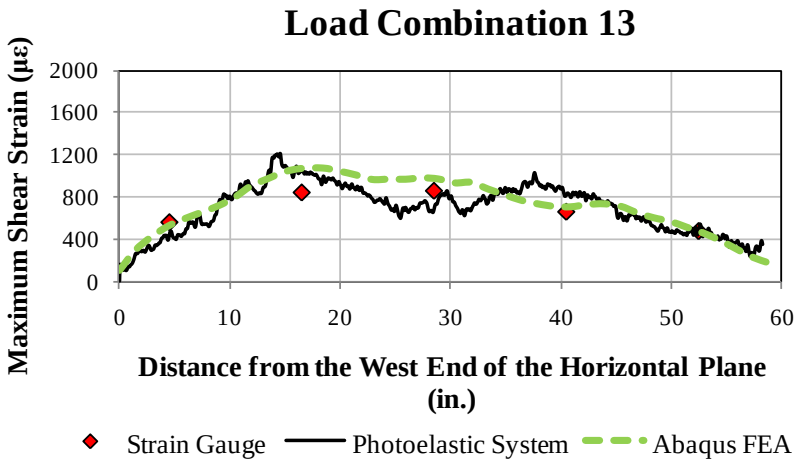

Figure 4.7.117: Comparison between the finite element analysis and experimental data (GP307-SS3 specimen-Load Combination 13)

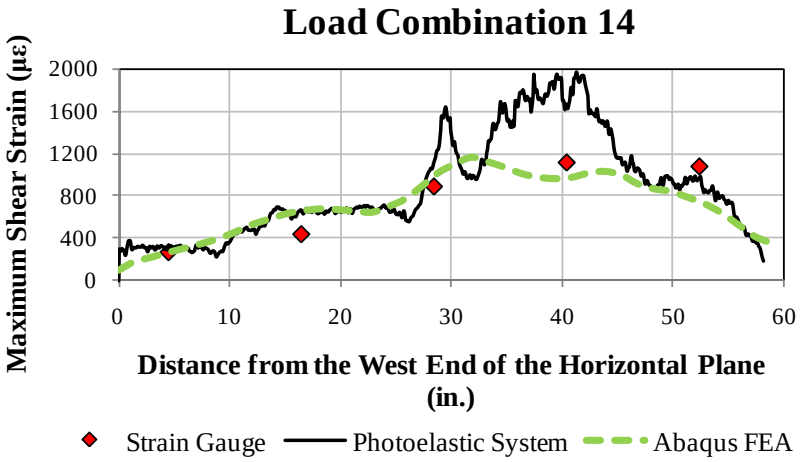

Figure 4.7.118: Comparison between the finite element analysis and experimental data (GP307-SS3 specimen-Load Combination 14)

4.7.2.2. GP307-LS3 Specimen

Table 4.7.7 summarizes the loads obtained from the tests and utilized in the finite element model of the GP307-LS3 specimen with splice plates installed.

Table 4.7.7: Member loads from the elastic load histories of the GP307-LS3 specimen with splice plates

Load Combination	F2 (kip)	F3 (kip)	F4 (kip)	F5 (kip)
1	99	38	-167	-133
2	237	0	-235	-30
3	106	1	-119	-156
4	17	0	-20	-225
5	262	-53	-199	-79
6	179	44	-219	-76
7	293	-105	-144	-109
8	108	82	-236	-79

Maximum shear strain versus the distance along the horizontal plane relationships are shown in Figure 4.7.119 through Figure 4.7.126. Except for a very local region towards the middle of the horizontal plane where the data from one strain gauge deviates from the other two data sets, all load combinations show that analytical models capture the actual test behavior.

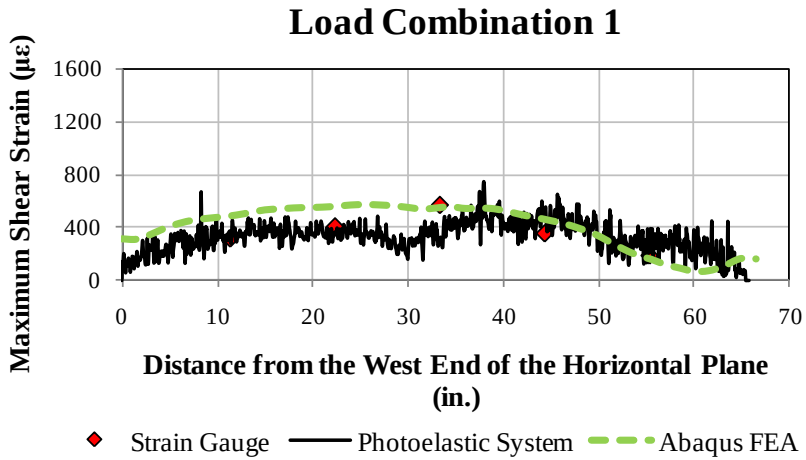

Figure 4.7.119: Comparison between the finite element analysis and experimental data (GP307-LS3 specimen - Load Combination 1)

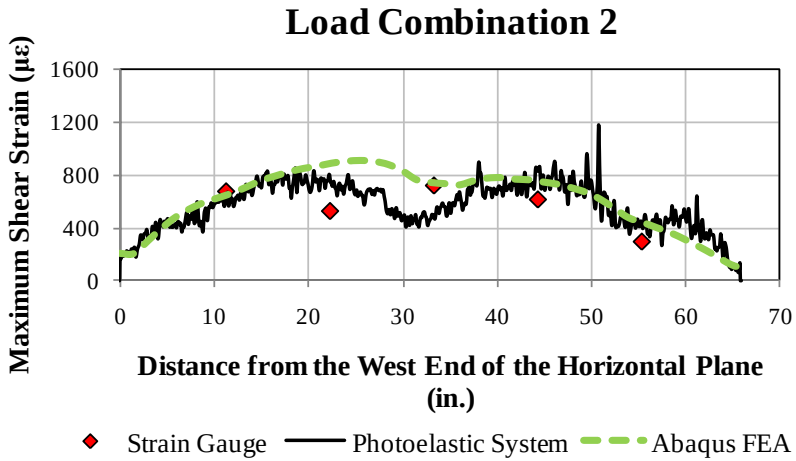

Figure 4.7.120: Comparison between the finite element analysis and experimental data (GP307-LS3 specimen - Load Combination 2)

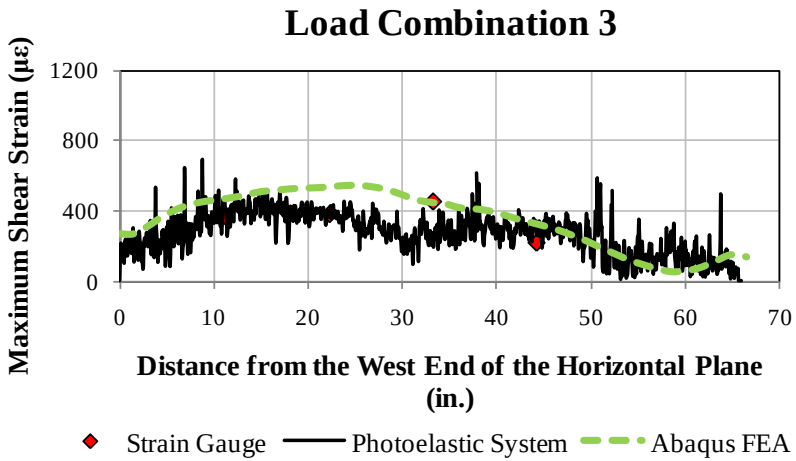

Figure 4.7.121: Comparison between the finite element analysis and experimental data (GP307-LS3 specimen - Load Combination 3)

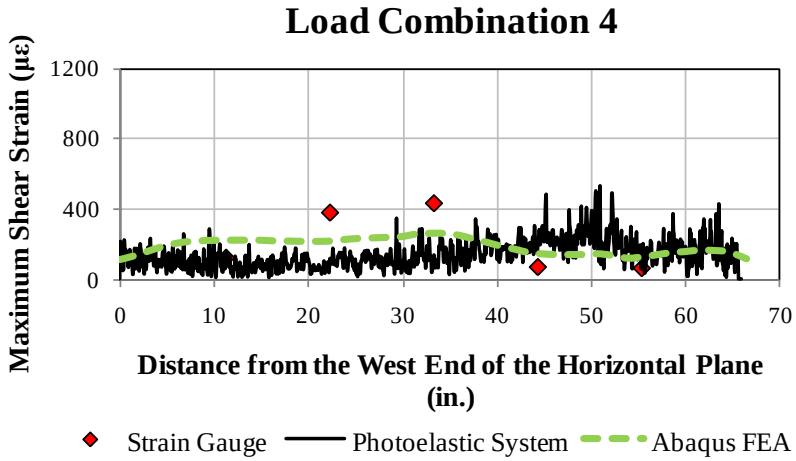

Figure 4.7.122: Comparison between the finite element analysis and experimental data (GP307-LS3 specimen - Load Combination 4)

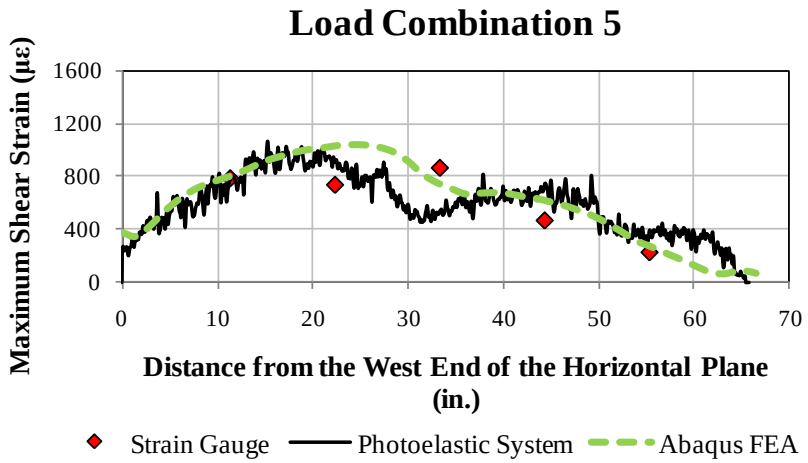

Figure 4.7.123: Comparison between the finite element analysis and experimental data (GP307-LS3 specimen - Load Combination 5)

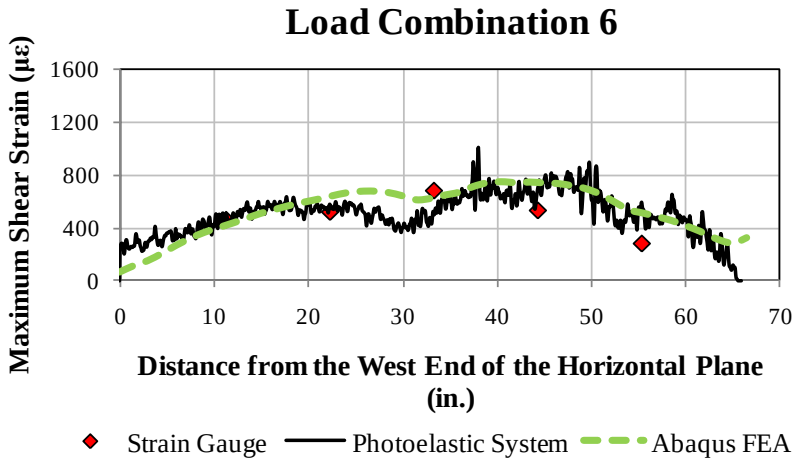

Figure 4.7.124: Comparison between the finite element analysis and experimental data (GP307-LS3 specimen - Load Combination 6)

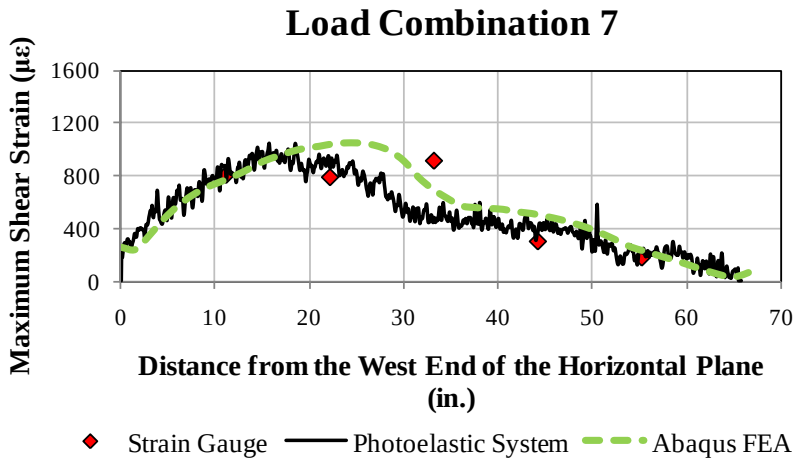

Figure 4.7.125: Comparison between the finite element analysis and experimental data (GP307-LS3 specimen - Load Combination 7)

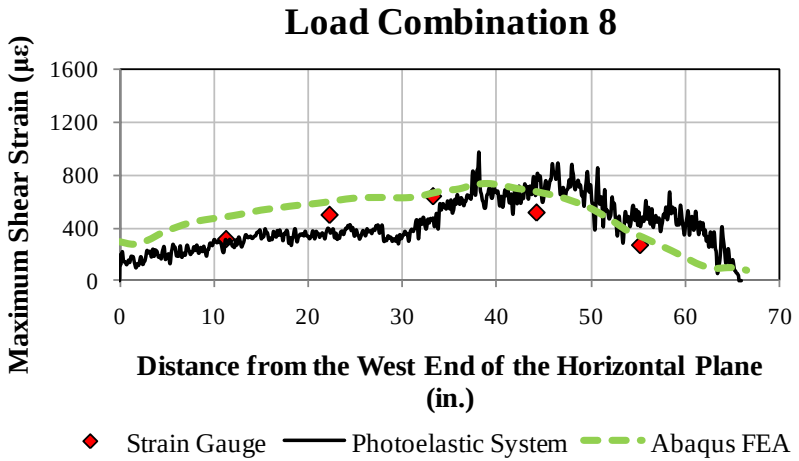

Figure 4.7.126: Comparison between the finite element analysis and experimental data (GP307-LS3 specimen - Load Combination 8)

4.7.2.3. GP307-SL3 Specimen

Load combinations and applied member loads for the GP307-SL3 specimen are shown in Table 4.7.8.

Table 4.7.8: Member loads from the elastic load histories of the GP307-SL3 specimen with splice plates

Load Combination	F2 (kip)	F3 (kip)	F4 (kip)	F5 (kip)
1	264	0	-271	10
2	292	0	-291	407
3	343	5	-362	271
4	355	-77	-273	262
5	280	84	-388	293
6	346	-76	-253	177
7	300	82	-418	208
8	190	62	-294	-4
9	272	79	-396	353
10	364	-71	-253	89
11	371	-81	-232	388
12	101	42	-171	357
13	360	-32	-301	275
14	181	147	-387	241

Figure 4.7.127 through Figure 4.7.154 show both response contour comparisons and quantitative horizontal plane results obtained from finite element analysis and two data acquisition systems. Elastic analyses provide very close results to the actual experiments.

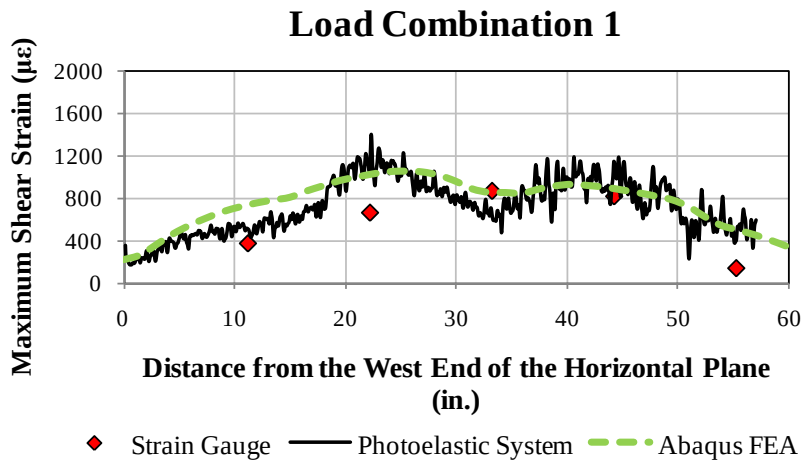

Figure 4.7.127: Comparison between the finite element analysis and experimental data (GP307-SL3 specimen - Load Combination 1)

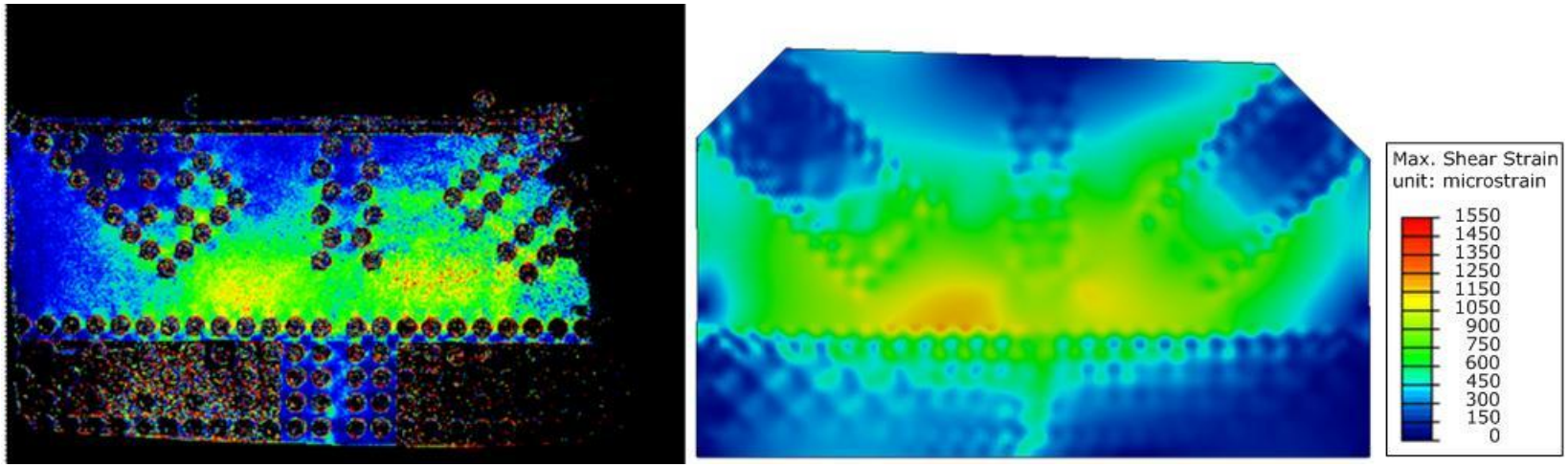

Figure 4.7.128: Comparison between the photo-elastic measurement system (left) and FEA (right) for Load Combination 1

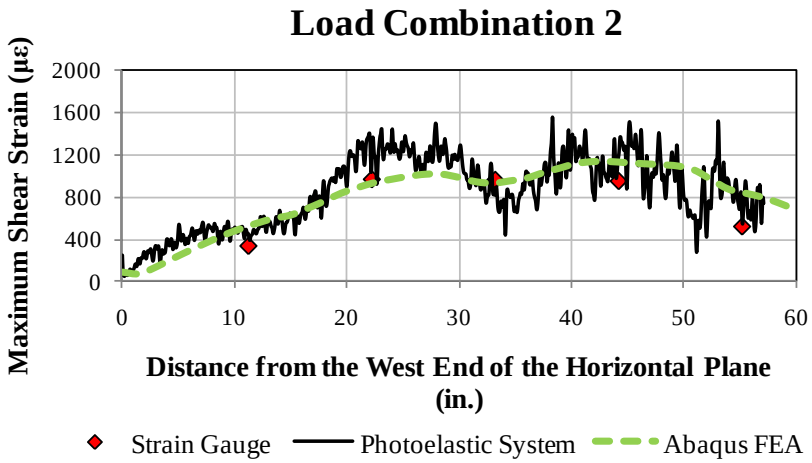

Figure 4.7.129: Comparison between the finite element analysis and experimental data (GP307-SL3 specimen - Load Combination 2)

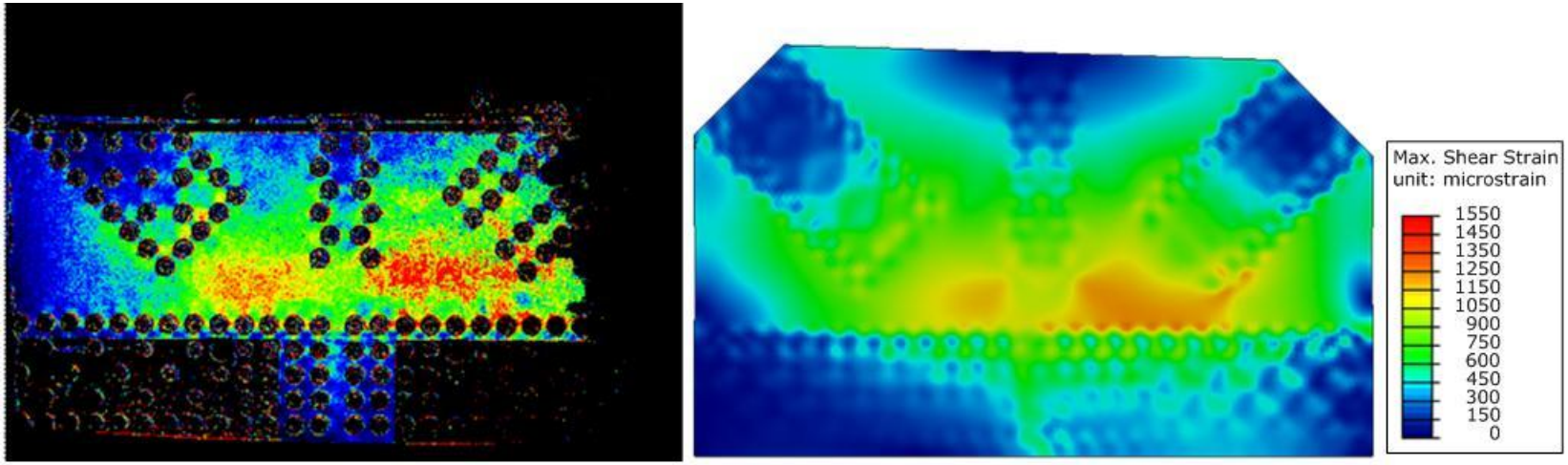

Figure 4.7.130: Comparison between the photo-elastic measurement system (left) and FEA (right) for Load Combination 2

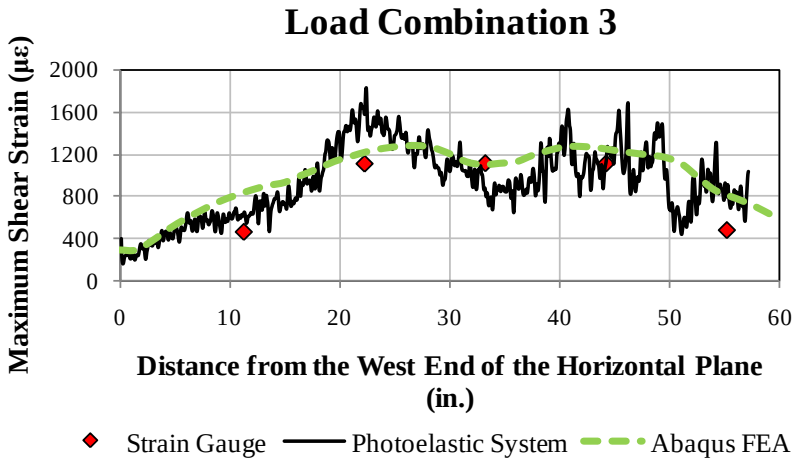

Figure 4.7.131: Comparison between the finite element analysis and experimental data (GP307-SL3 specimen - Load Combination 3)

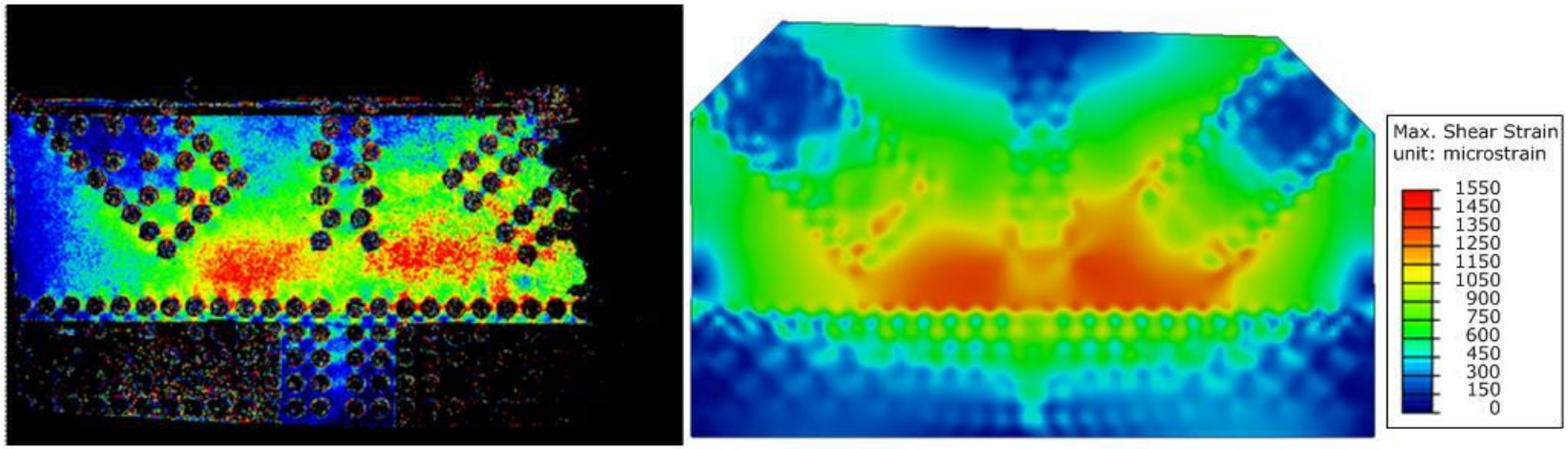

Figure 4.7.132: Comparison between the photo-elastic measurement system (left) and FEA (right) for Load Combination 3

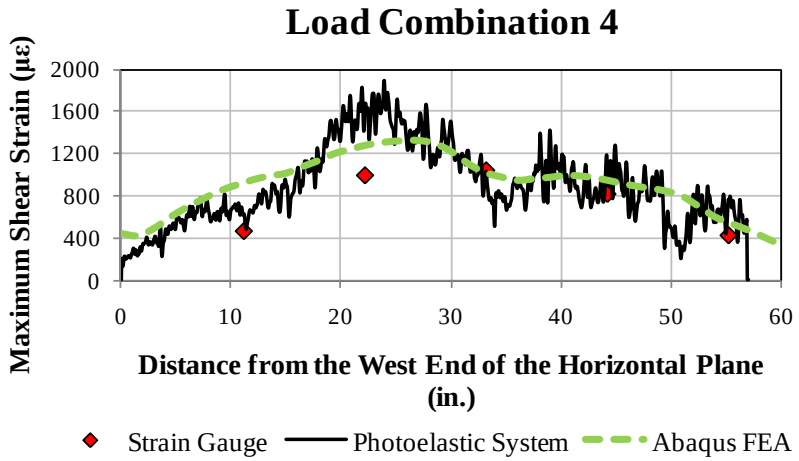

Figure 4.7.133: Comparison between the finite element analysis and experimental data (GP307-SL3 specimen - Load Combination 4)

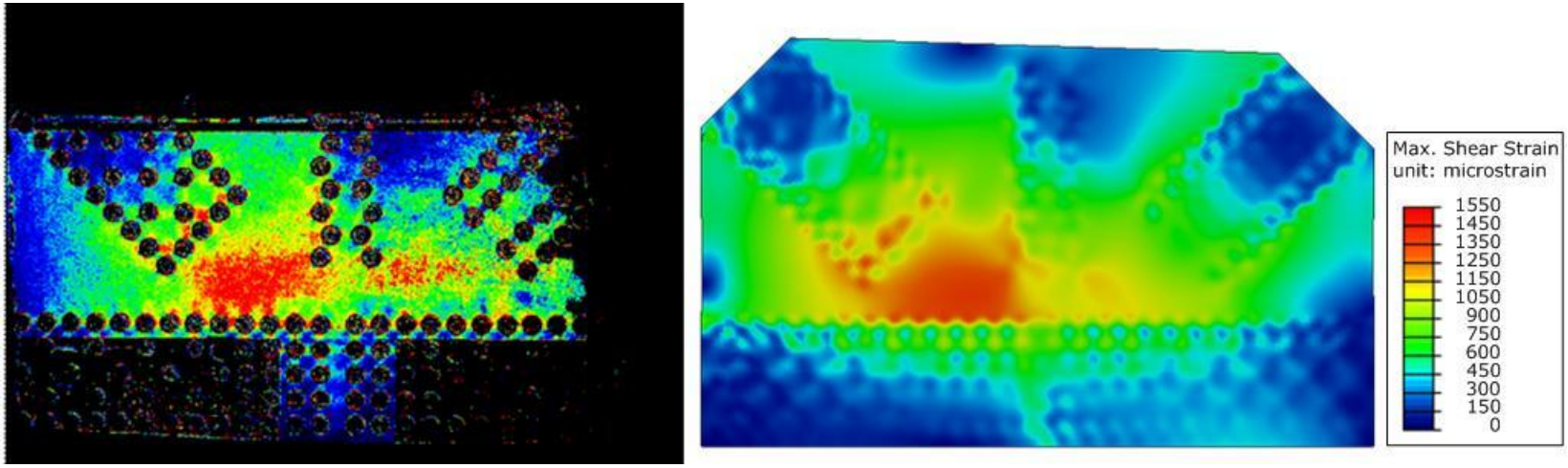

Figure 4.7.134: Comparison between the photo-elastic measurement system (left) and FEA (right) for Load Combination 4

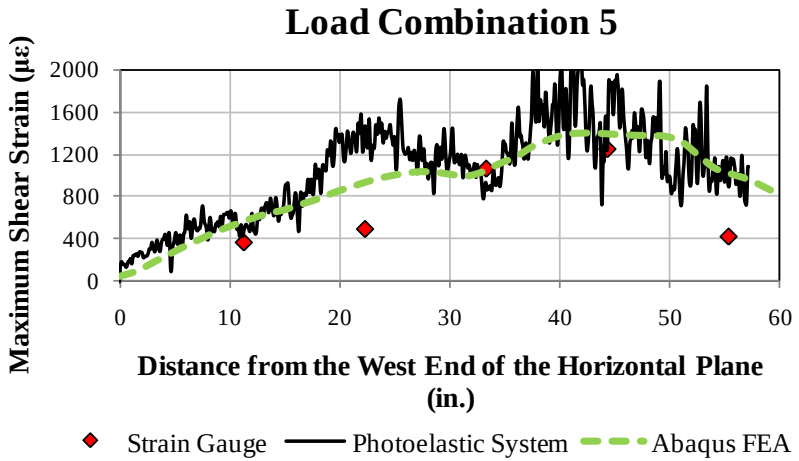

Figure 4.7.135: Comparison between the finite element analysis and experimental data (GP307-SL3 specimen - Load Combination 5)

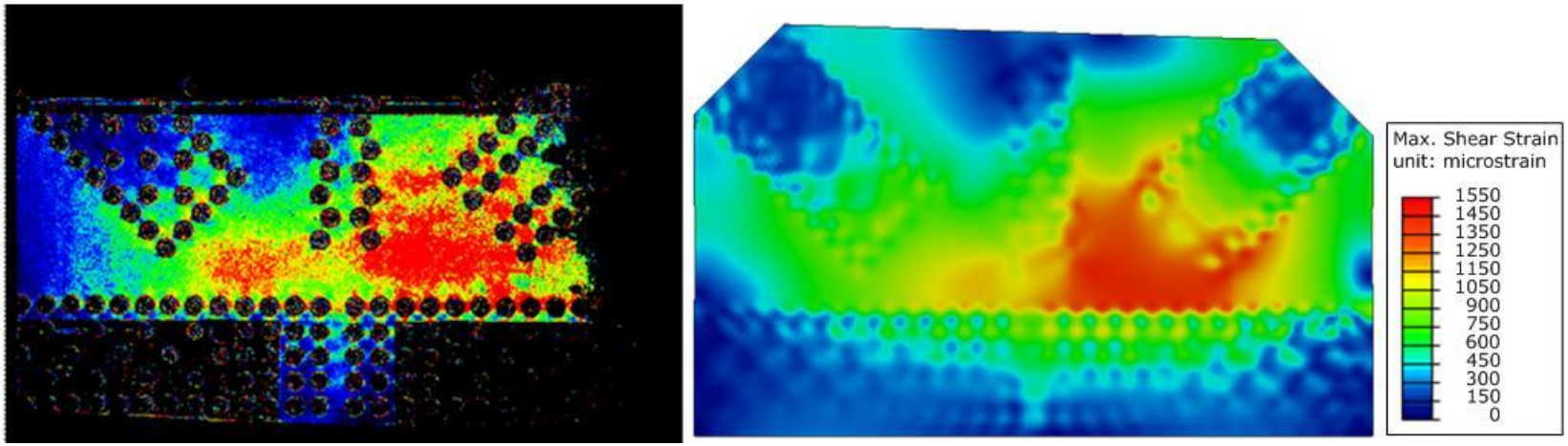

Figure 4.7.136: Comparison between the photo-elastic measurement system (left) and FEA (right) for Load Combination 5

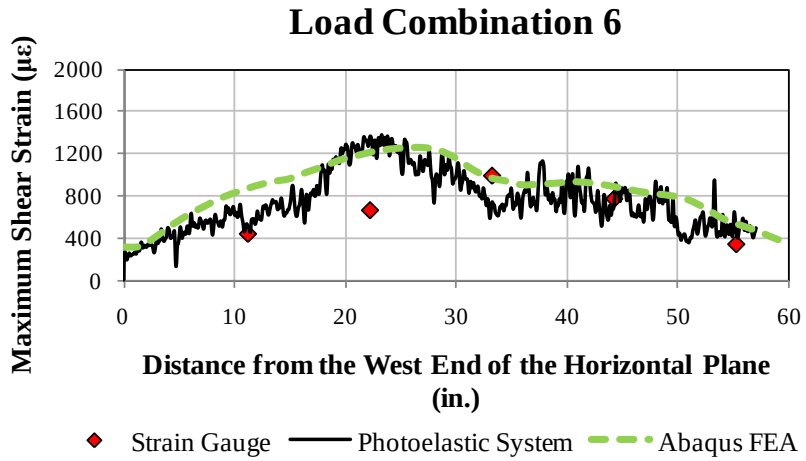

Figure 4.7.137: Comparison between the finite element analysis and experimental data (GP307-SL3 specimen - Load Combination 6)

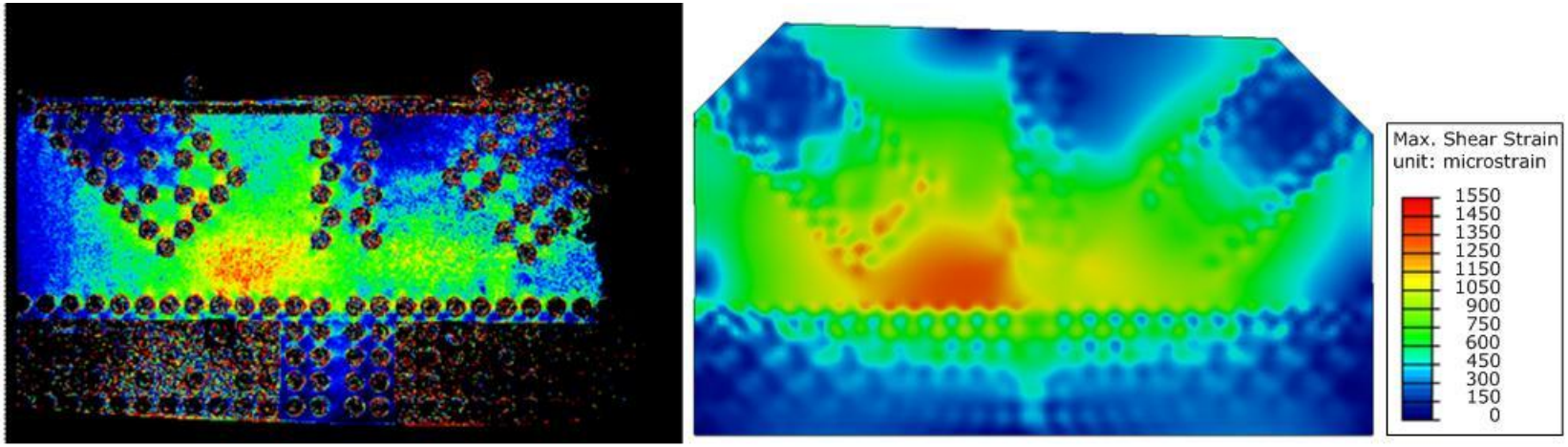

Figure 4.7.138: Comparison between the photo-elastic measurement system (left) and FEA (right) for Load Combination 6

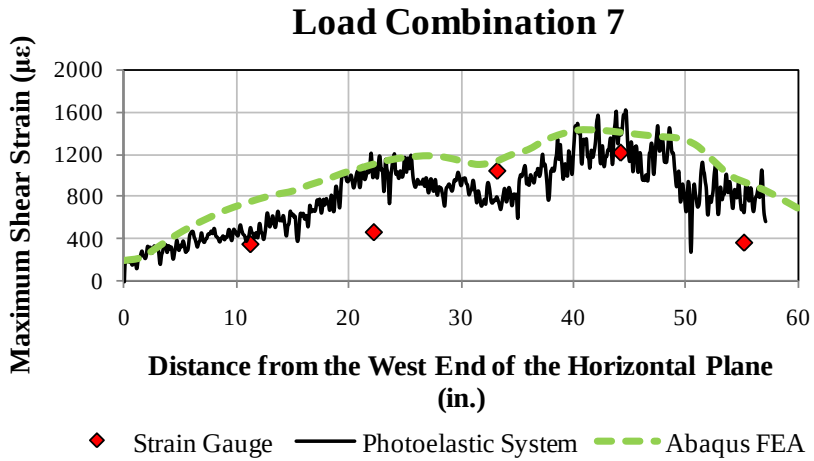

Figure 4.7.139: Comparison between the finite element analysis and experimental data (GP307-SL3 specimen - Load Combination 7)

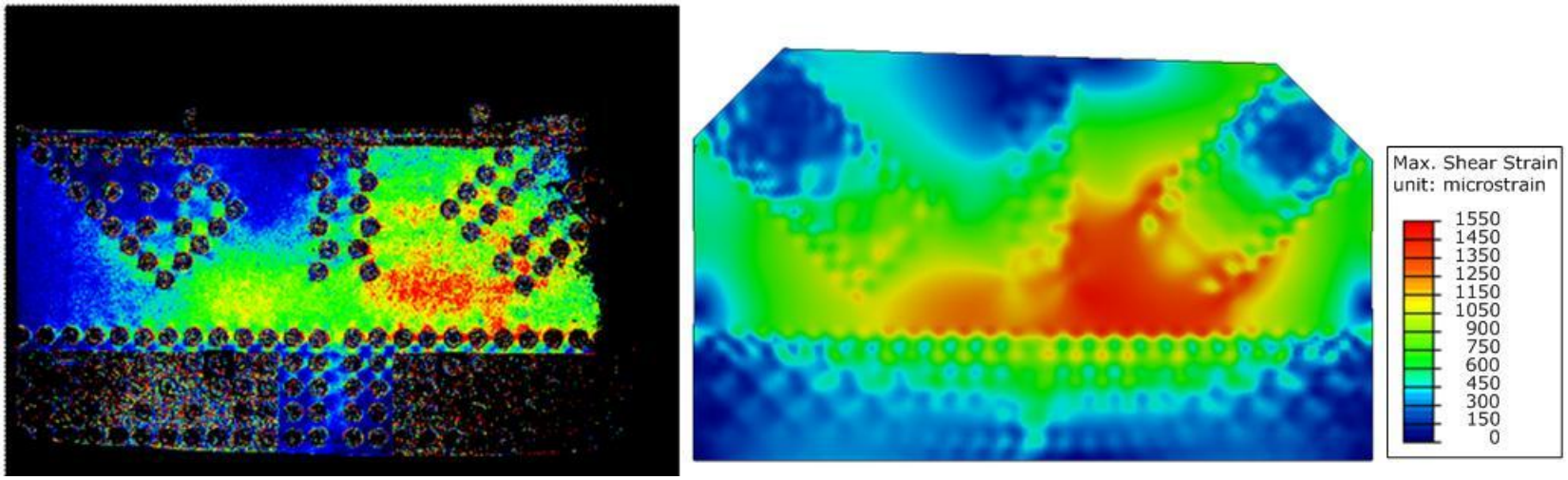

Figure 4.7.140: Comparison between the photo-elastic measurement system (left) and FEA (right) for Load Combination 7

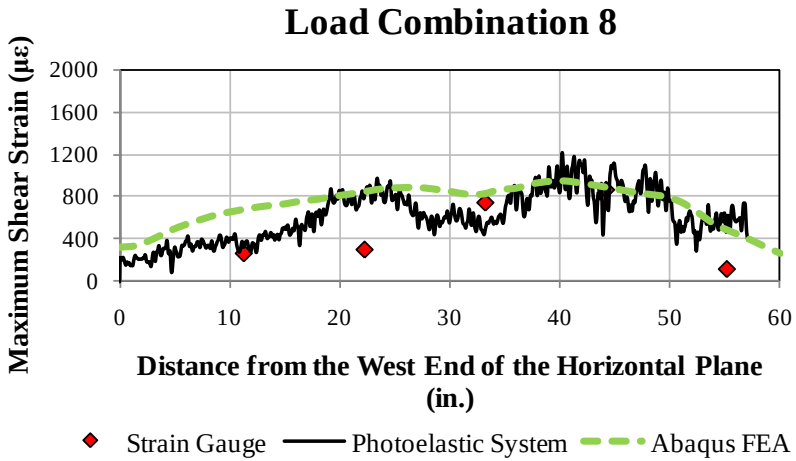

Figure 4.7.141: Comparison between the finite element analysis and experimental data (GP307-SL3 specimen - Load Combination 8)

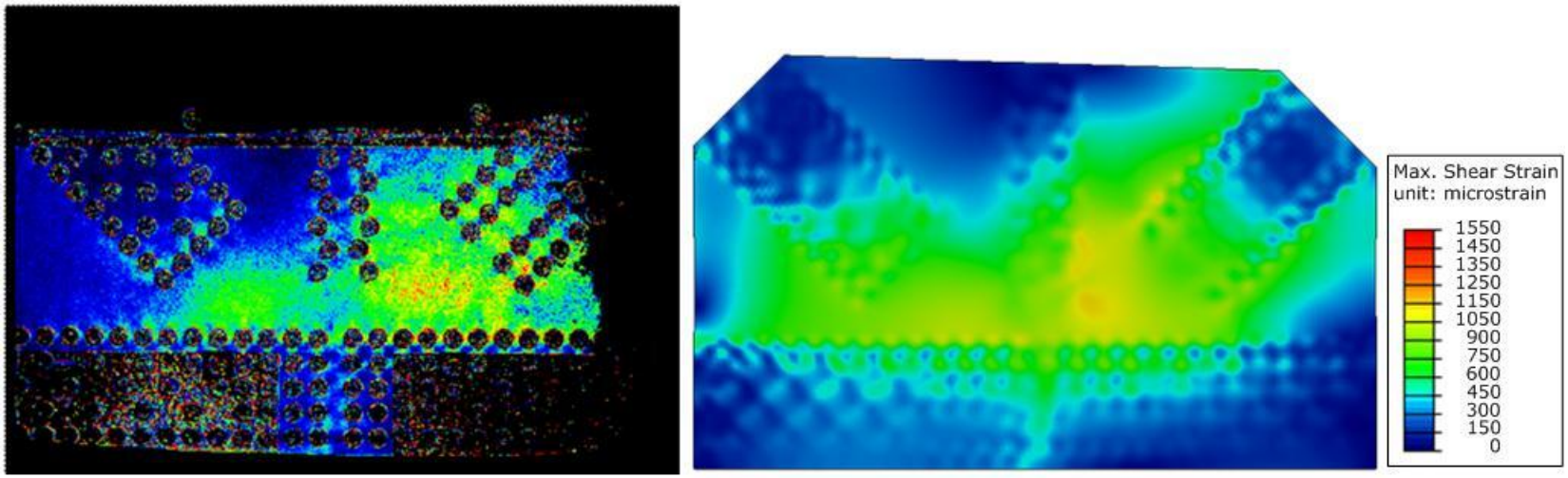

Figure 4.7.142: Comparison between the photo-elastic measurement system (left) and FEA (right) for Load Combination 8

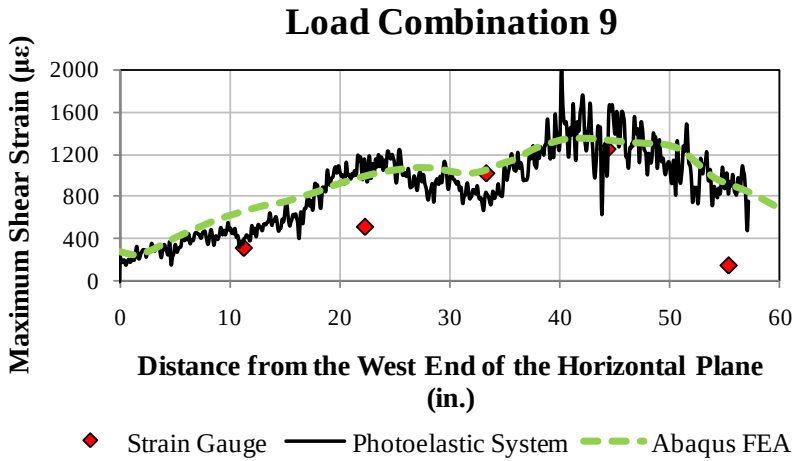

Figure 4.7.143: Comparison between the finite element analysis and experimental data (GP307-SL3 specimen - Load Combination 9)

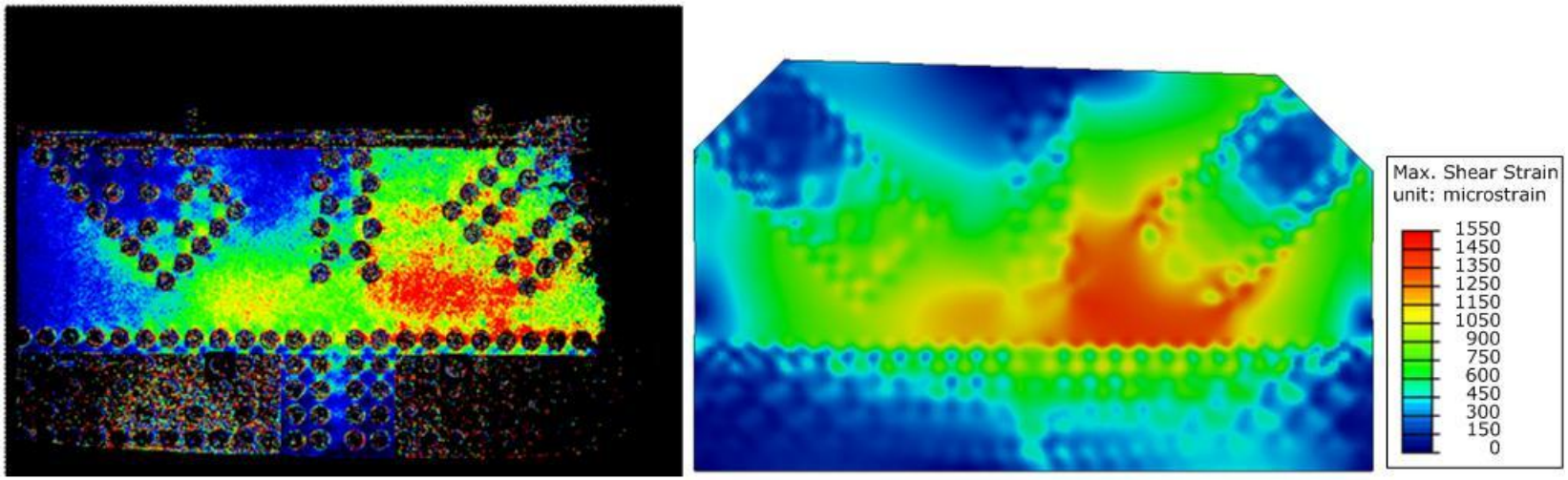

Figure 4.7.144: Comparison between the photo-elastic measurement system (left) and FEA (right) for Load Combination 9

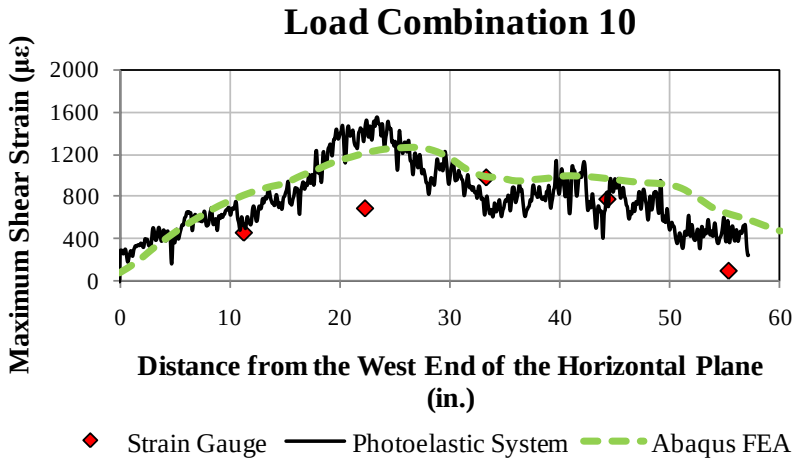

Figure 4.7.145: Comparison between the finite element analysis and experimental data (GP307-SL3 specimen-Load Combination 10)

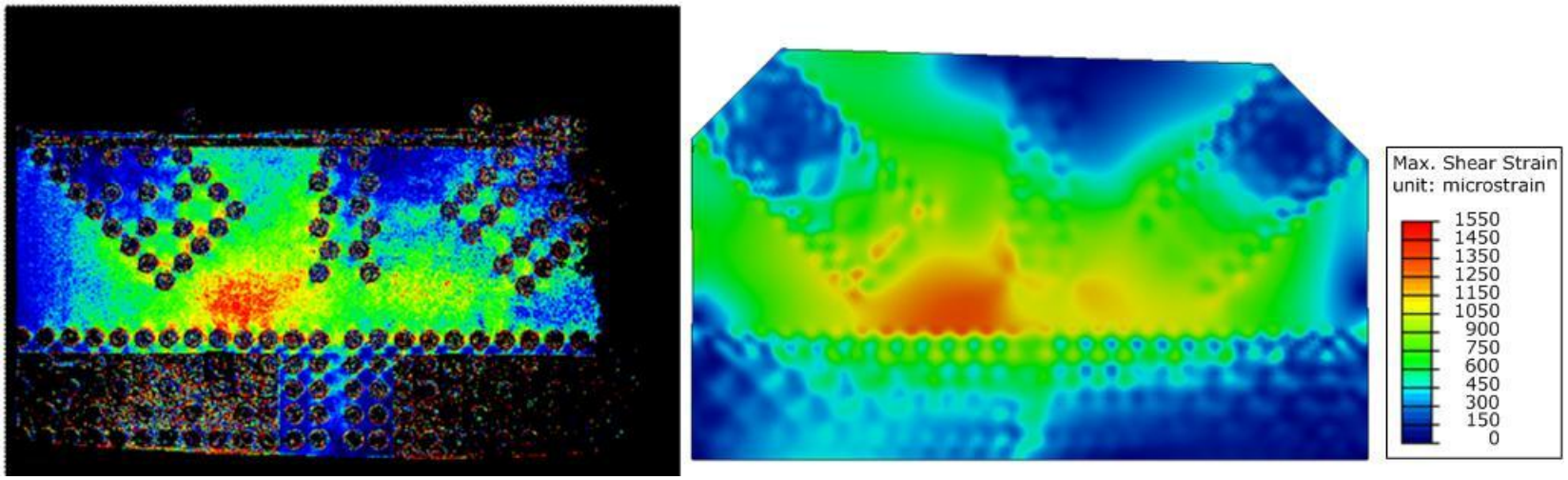

Figure 4.7.146: Comparison between the photo-elastic measurement system (left) and FEA (right) for Load Combination 10

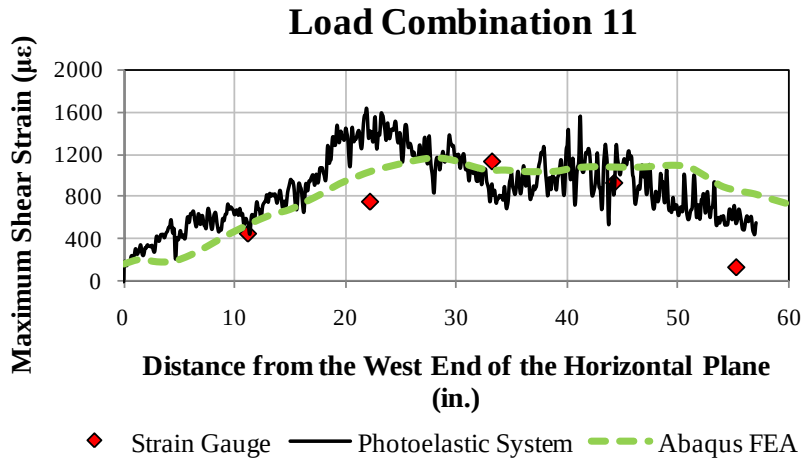

Figure 4.7.147: Comparison between the finite element analysis and experimental data (GP307-SL3 specimen-Load Combination 11)

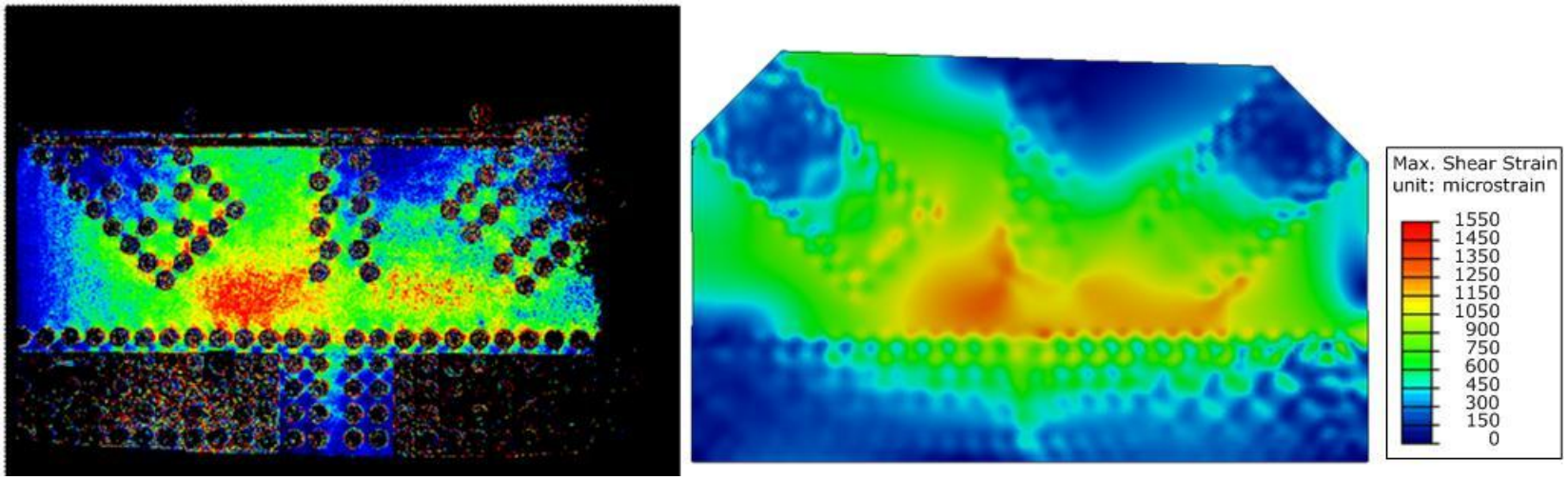

Figure 4.7.148: Comparison between the photo-elastic measurement system (left) and FEA (right) for Load Combination 11

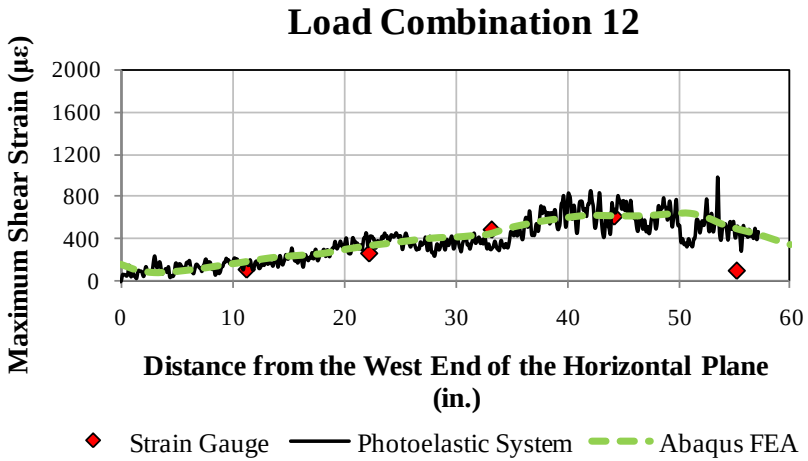

Figure 4.7.149: Comparison between the finite element analysis and experimental data (GP307-SL3 specimen-Load Combination 12)

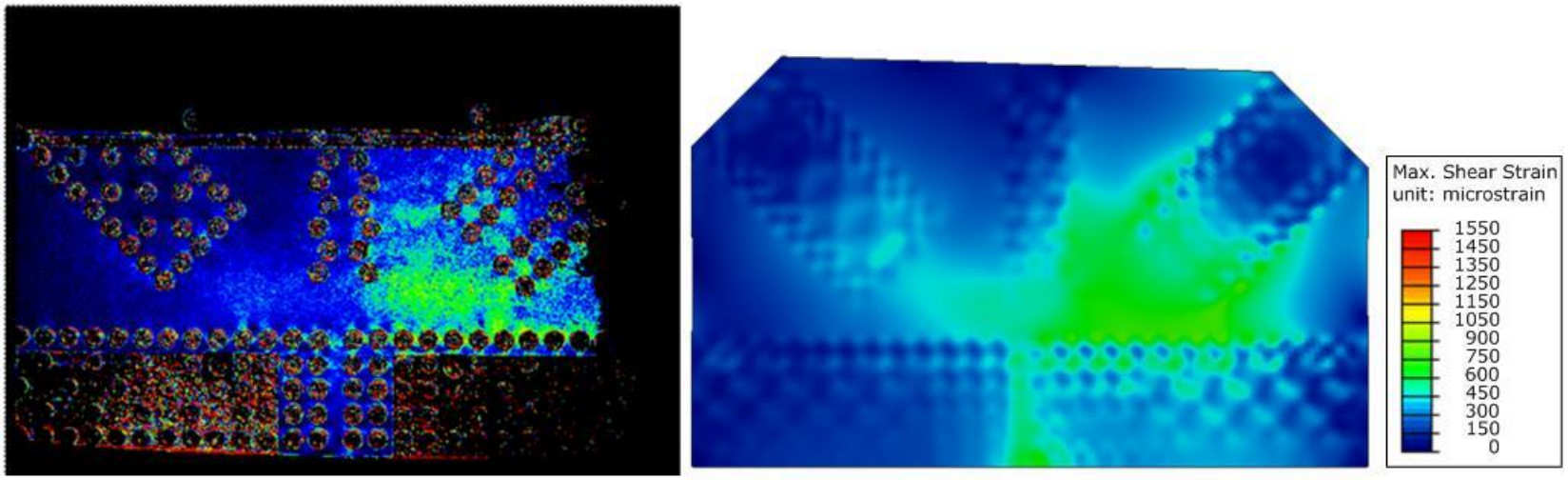

Figure 4.7.150: Comparison between the photo-elastic measurement system (left) and FEA (right) for Load Combination 12

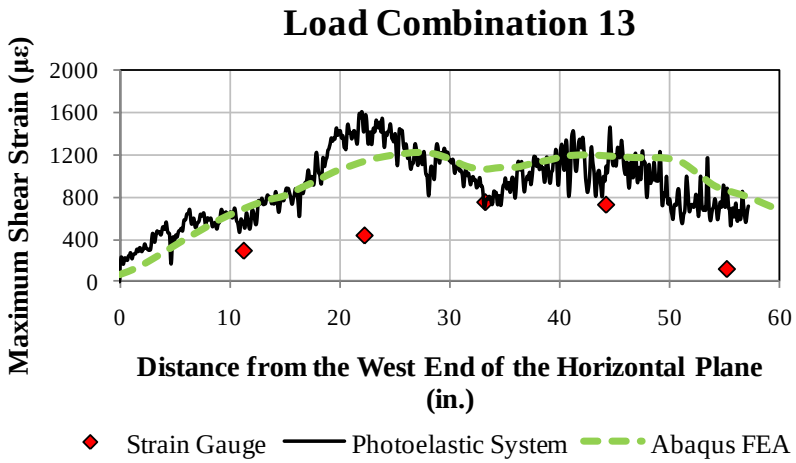

Figure 4.7.151: Comparison between the finite element analysis and experimental data (GP307-SL3 specimen-Load Combination 13)

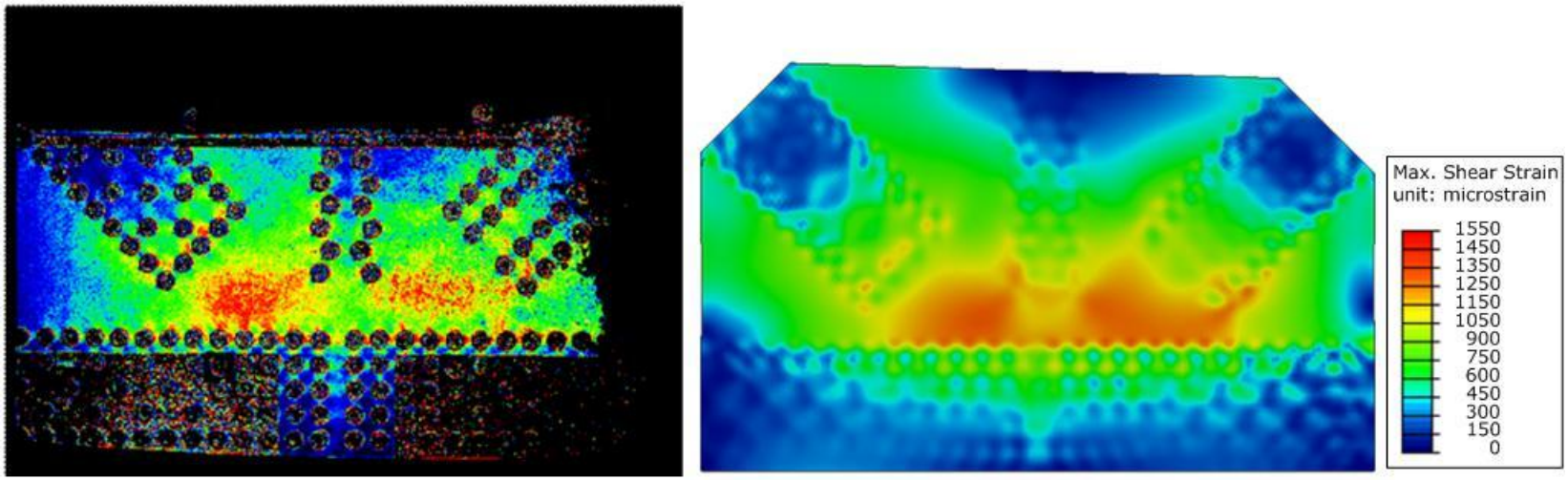

Figure 4.7.152: Comparison between the photo-elastic measurement system (left) and FEA (right) for Load Combination 13

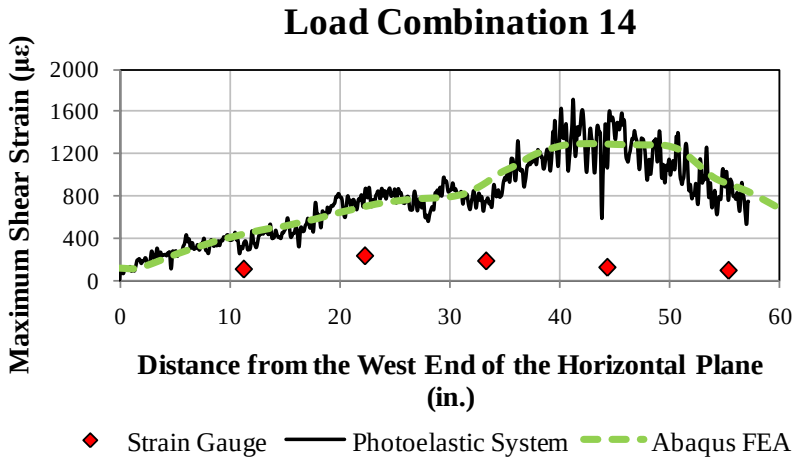

Figure 4.7.153: Comparison between the finite element analysis and experimental data (GP307-SL3 specimen-Load Combination 14)

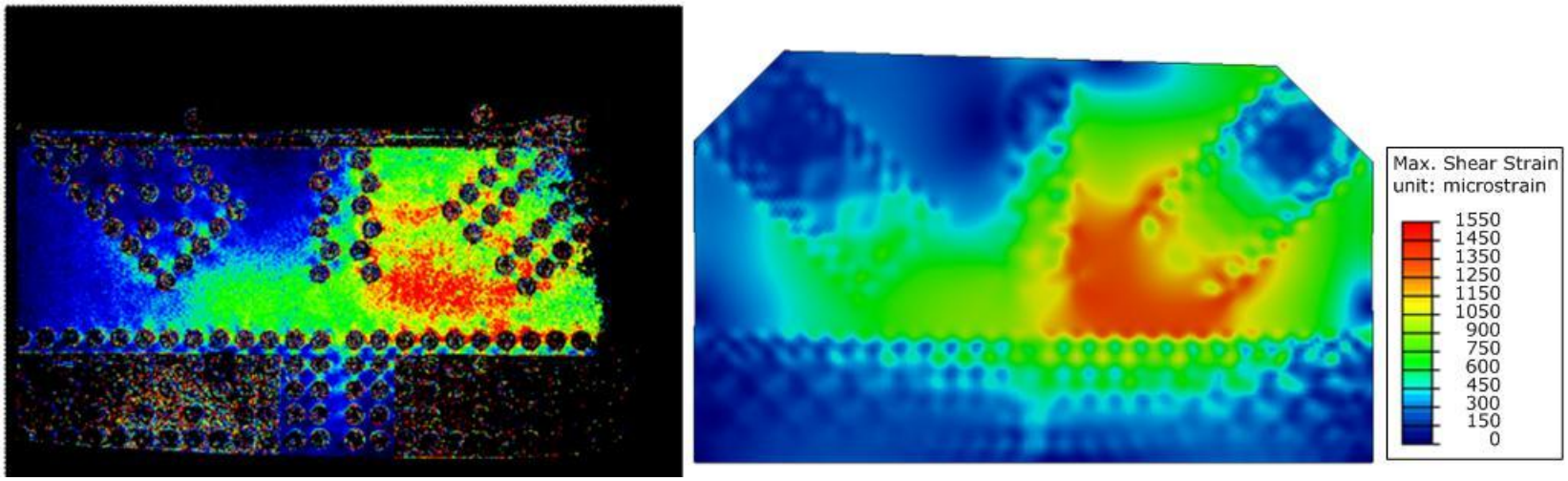

Figure 4.7.154: Comparison between the photo-elastic measurement system (left) and FEA (right) for Load Combination 14

4.7.2.4. GP490-SS3 Specimen

Table 4.7.9 summarizes the member loads for each load combination in the GP490-SS3 with splice plate model.

Table 4.7.9: Member loads from the elastic load histories of the GP490-SS3 specimen with splice plates

Load Combination	F2 (kip)	F3 (kip)	F4 (kip)	F5 (kip)
1	223	0	-263	29
2	326	-1	-322	386
3	245	0	-228	178
4	255	-56	-174	188
5	230	70	-329	260
6	249	-52	-196	141
7	233	70	-335	165
8	215	58	-300	40
9	249	64	-357	297
10	246	-49	-202	72
11	279	-56	-202	247
12	124	38	-175	313
13	254	-23	-234	225

All the response contour comparisons and the plots showing three separate results are shown in Figure 4.7.155 through Figure 4.7.180. The finite element analysis results are very close to the strain gauge data but the photoelastic data provides different values in this case. The same specimen without splice plates installed show that all three data match well with each other.

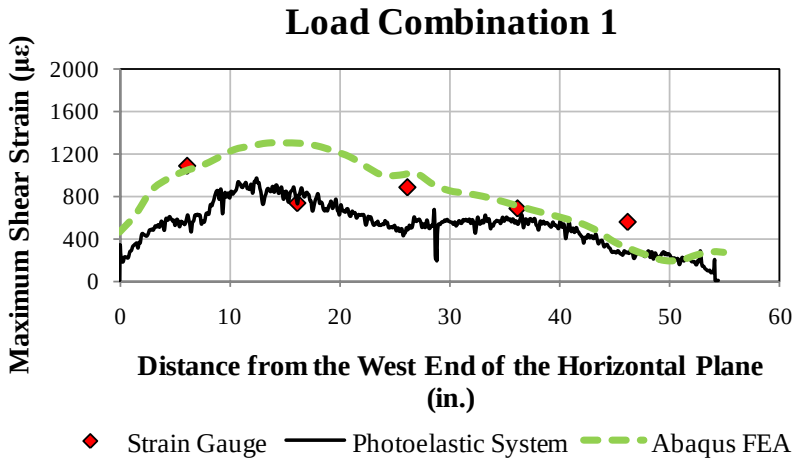

Figure 4.7.155: Comparison between the finite element analysis and experimental data (GP490-SS3 specimen - Load Combination 1)

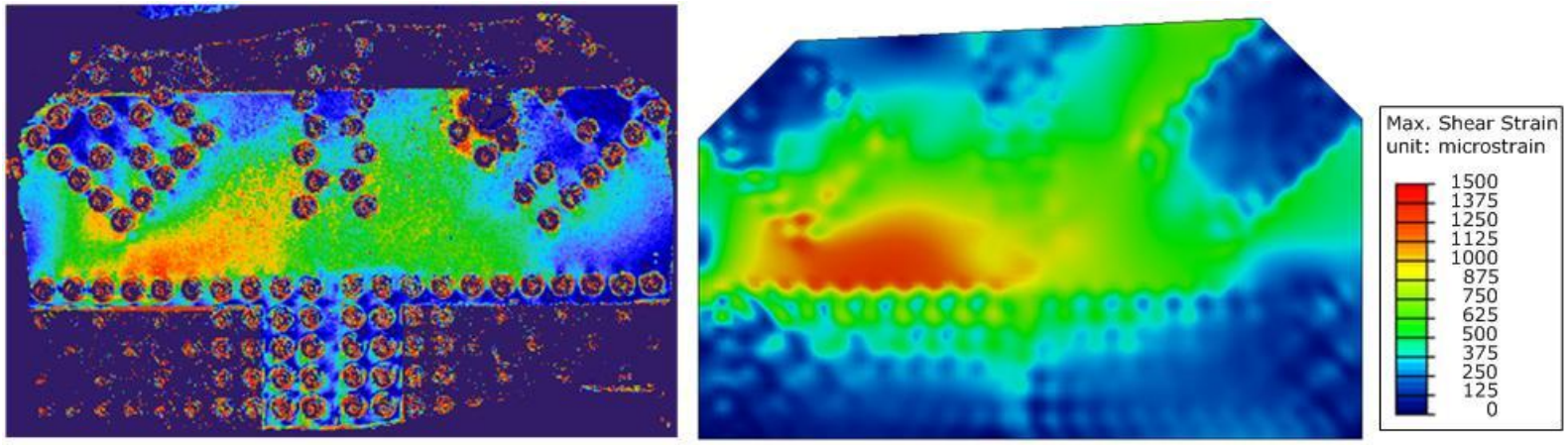

Figure 4.7.156: Comparison between the photo-elastic measurement system (left) and FEA (right) for Load Combination 1

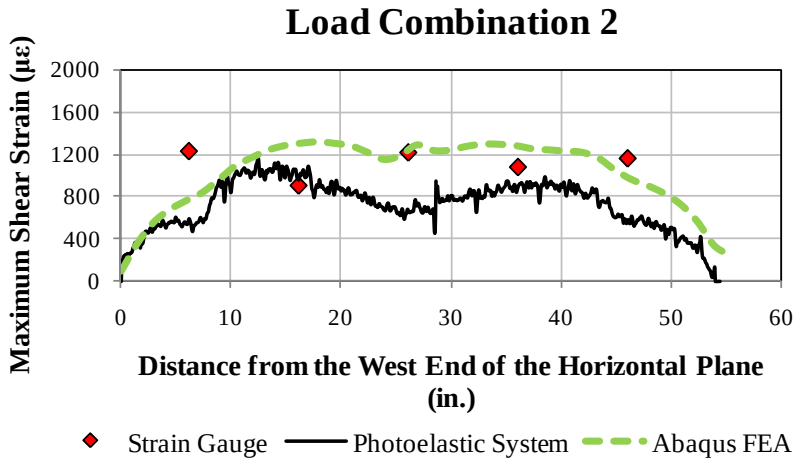

Figure 4.7.157: Comparison between the finite element analysis and experimental data (GP490-SS3 specimen - Load Combination 2)

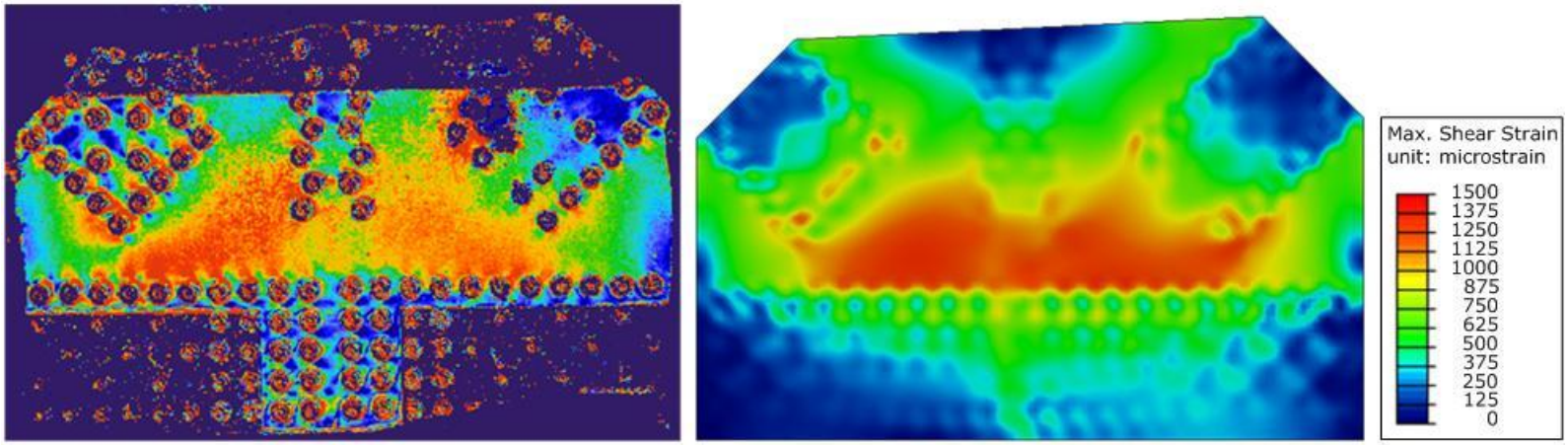

Figure 4.7.158: Comparison between the photo-elastic measurement system (left) and FEA (right) for Load Combination 2

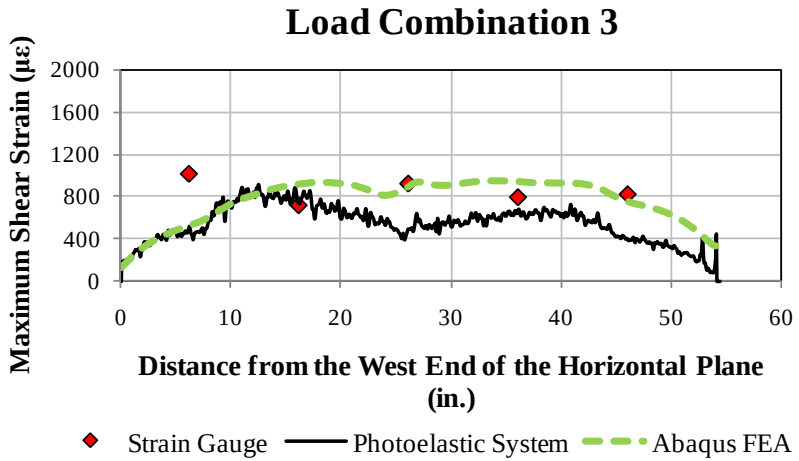

Figure 4.7.159: Comparison between the finite element analysis and experimental data (GP490-SS3 specimen - Load Combination 3)

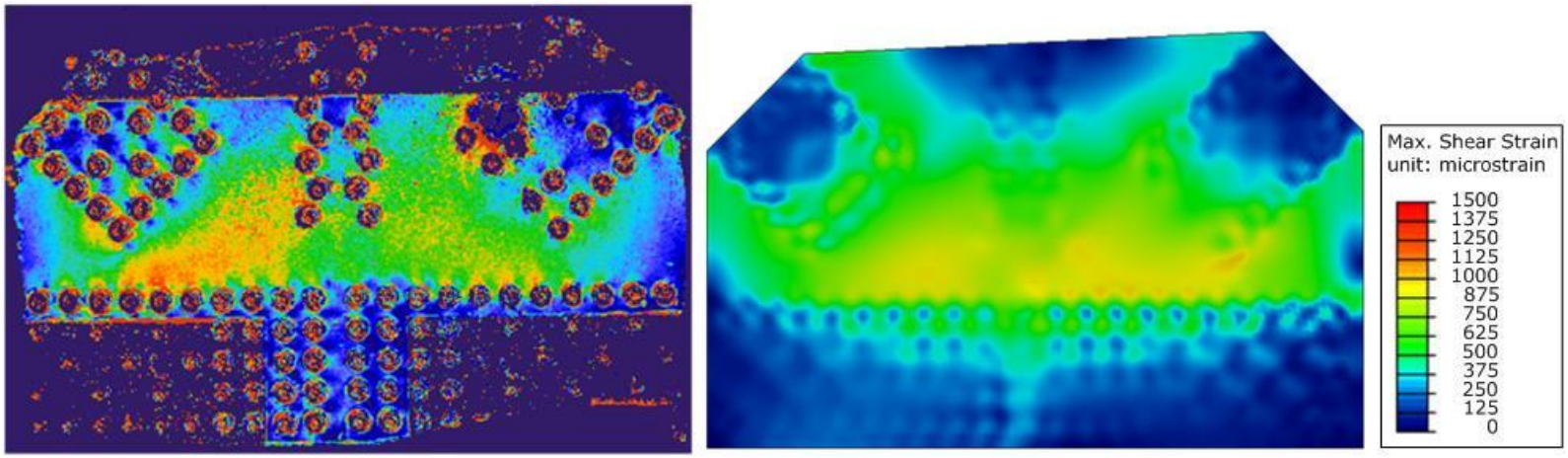

Figure 4.7.160: Comparison between the photo-elastic measurement system (left) and FEA (right) for Load Combination 3

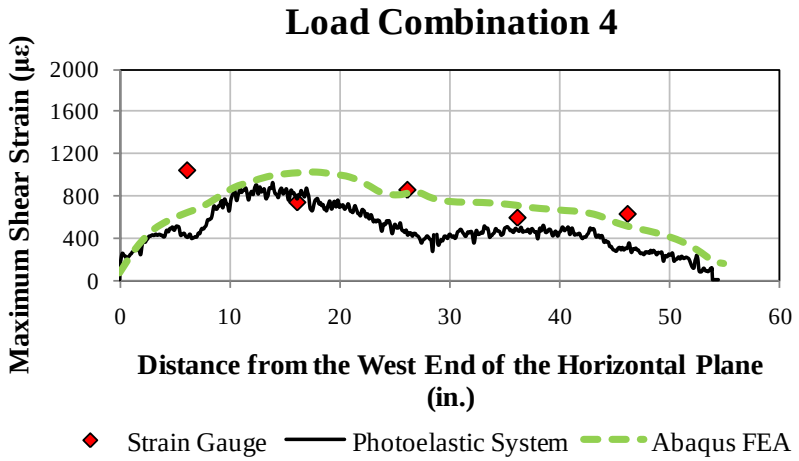

Figure 4.7.161: Comparison between the finite element analysis and experimental data (GP490-SS3 specimen - Load Combination 4)

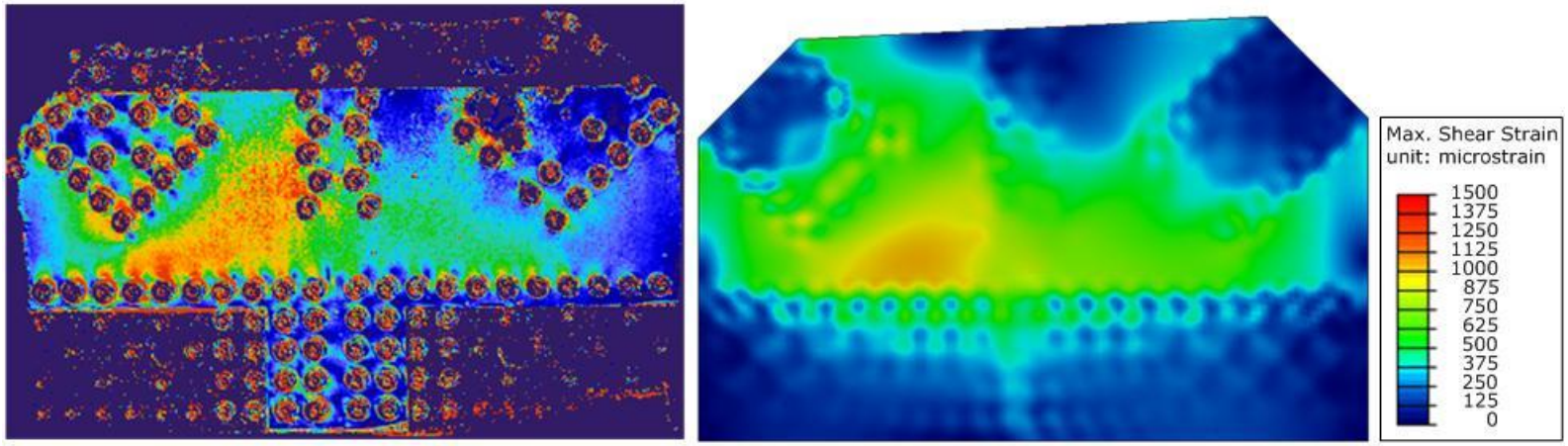

Figure 4.7.162: Comparison between the photo-elastic measurement system (left) and FEA (right) for Load Combination 4

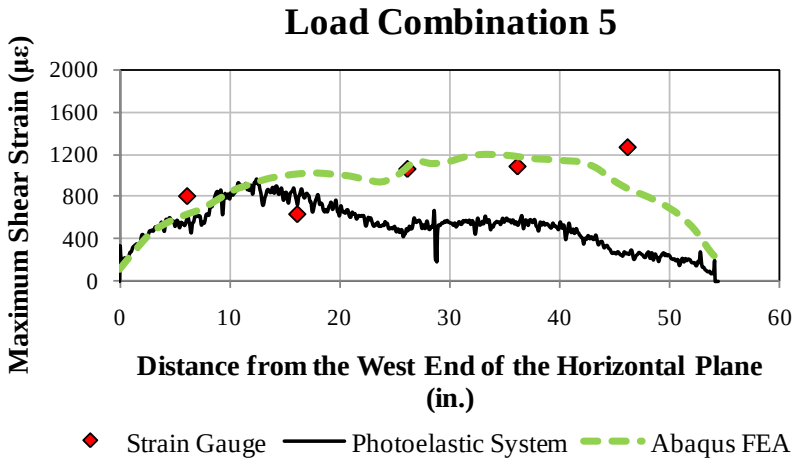

Figure 4.7.163: Comparison between the finite element analysis and experimental data (GP490-SS3 specimen - Load Combination 5)

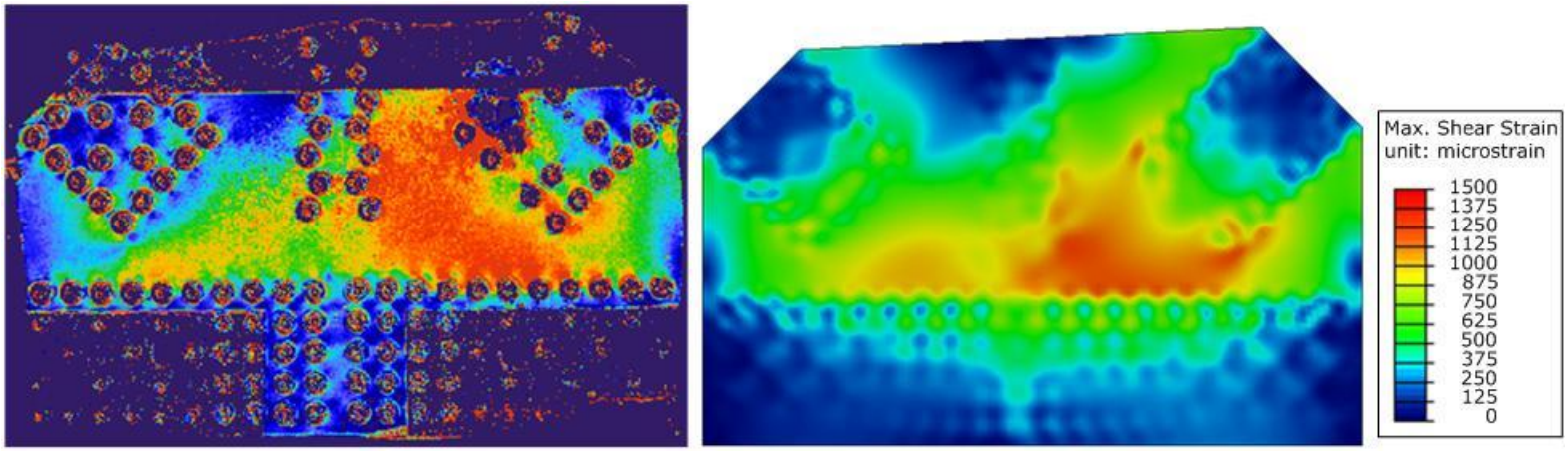

Figure 4.7.164: Comparison between the photo-elastic measurement system (left) and FEA (right) for Load Combination 5

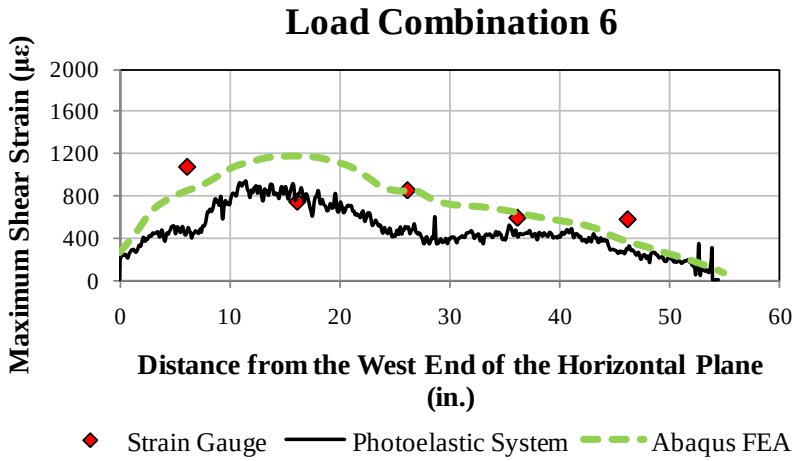

Figure 4.7.165: Comparison between the finite element analysis and experimental data (GP490-SS3 specimen - Load Combination 6)

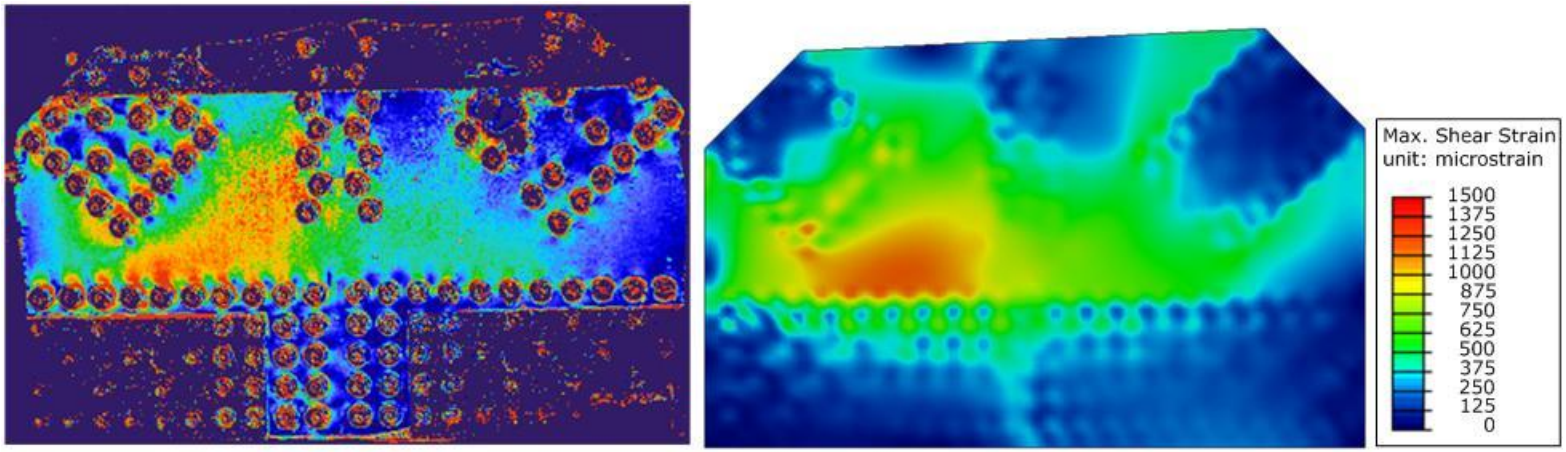

Figure 4.7.166: Comparison between the photo-elastic measurement system (left) and FEA (right) for Load Combination 6

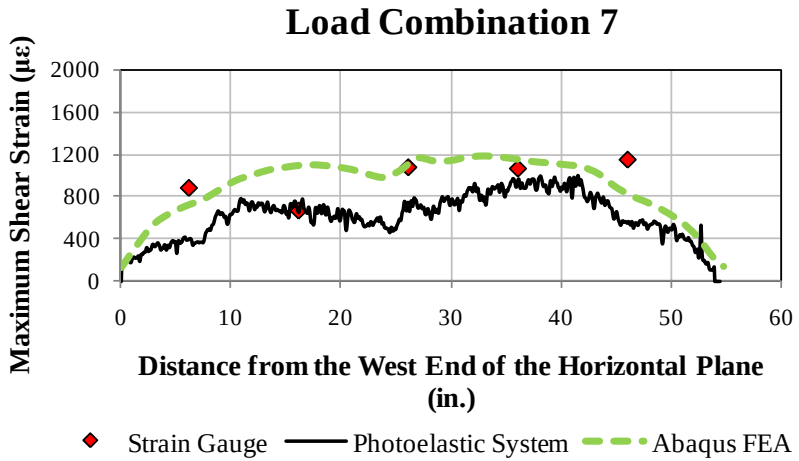

Figure 4.7.167: Comparison between the finite element analysis and experimental data (GP490-SS3 specimen - Load Combination 7)

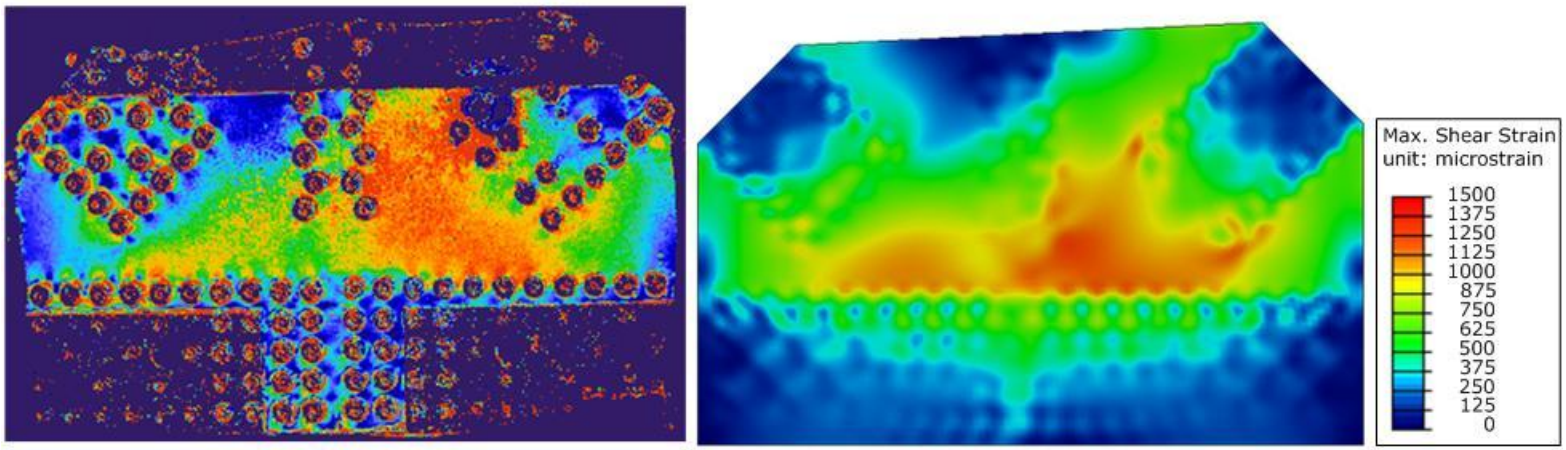

Figure 4.7.168: Comparison between the photo-elastic measurement system (left) and FEA (right) for Load Combination 7

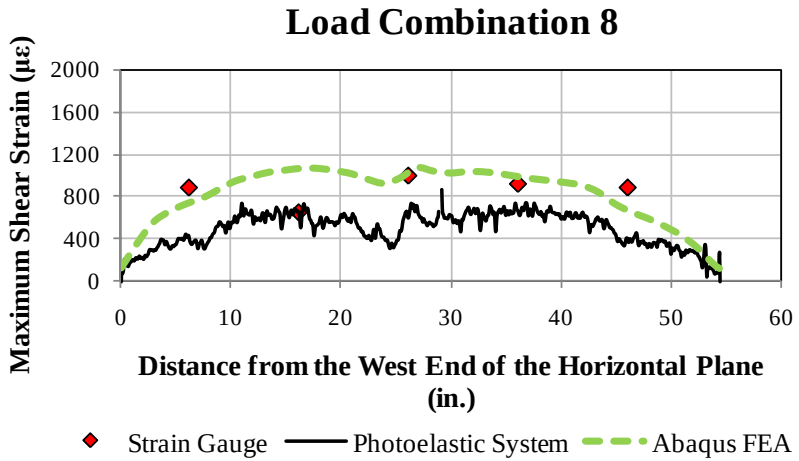

Figure 4.7.169: Comparison between the finite element analysis and experimental data (GP490-SS3 specimen - Load Combination 8)

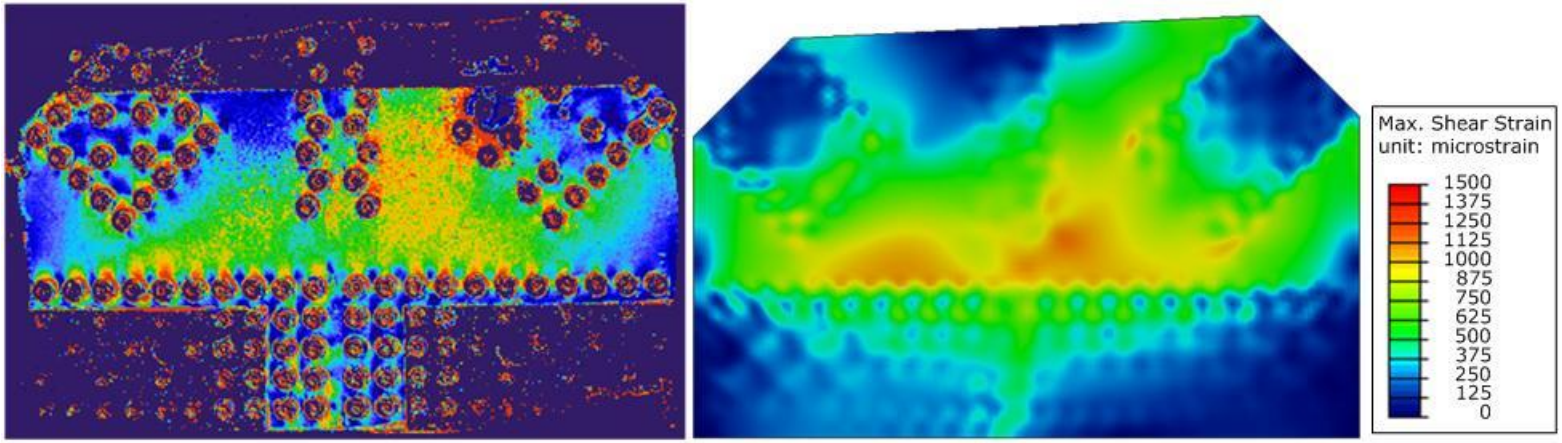

Figure 4.7.170: Comparison between the photo-elastic measurement system (left) and FEA (right) for Load Combination 8

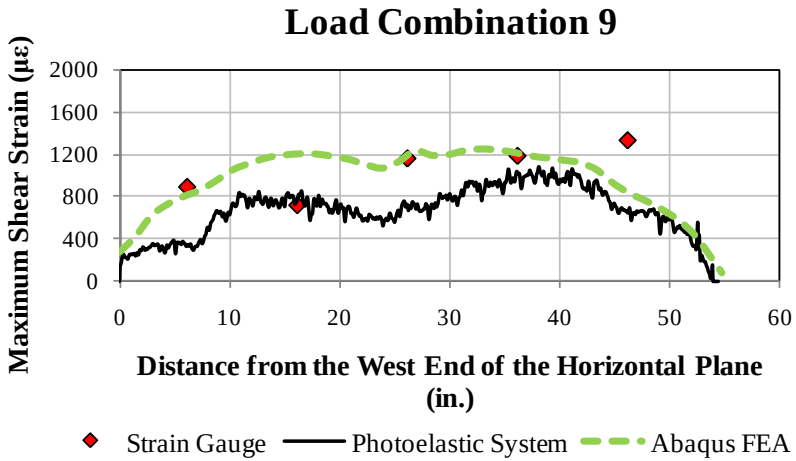

Figure 4.7.171: Comparison between the finite element analysis and experimental data (GP490-SS3 specimen - Load Combination 9)

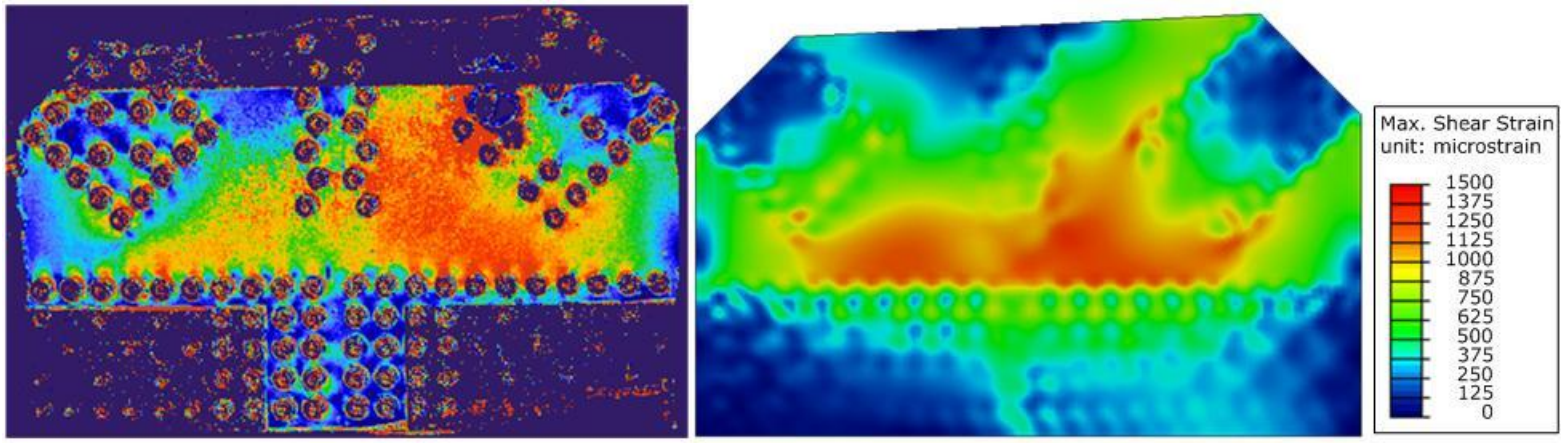

Figure 4.7.172: Comparison between the photo-elastic measurement system (left) and FEA (right) for Load Combination 9

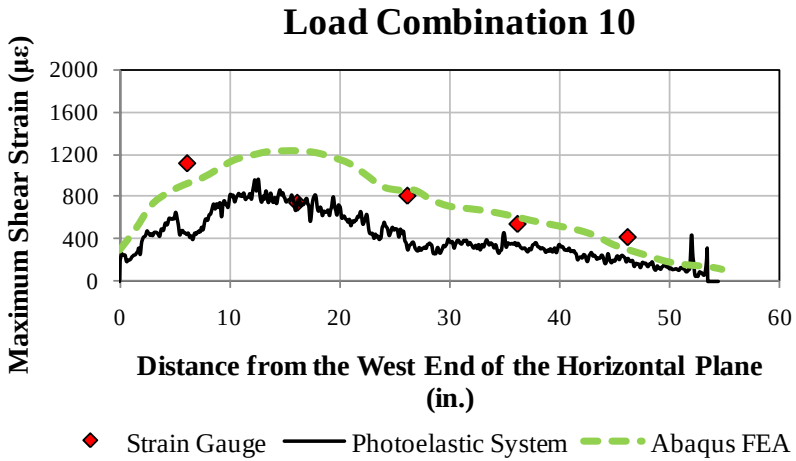

Figure 4.7.173: Comparison between the finite element analysis and experimental data (GP490-SS3 specimen-Load Combination 10)

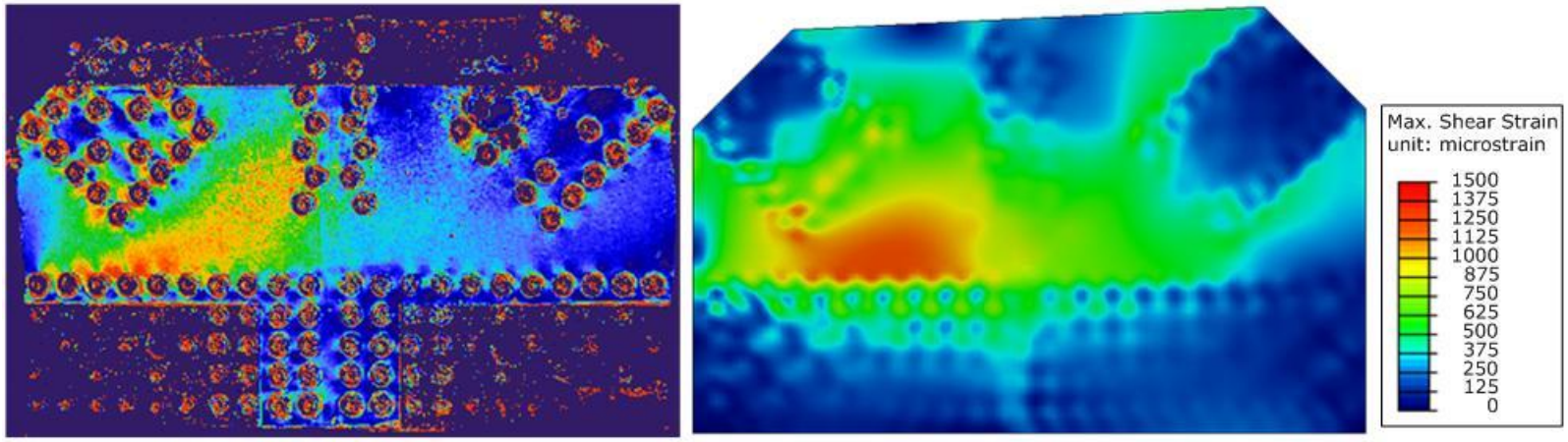

Figure 4.7.174: Comparison between the photo-elastic measurement system (left) and FEA (right) for Load Combination 10

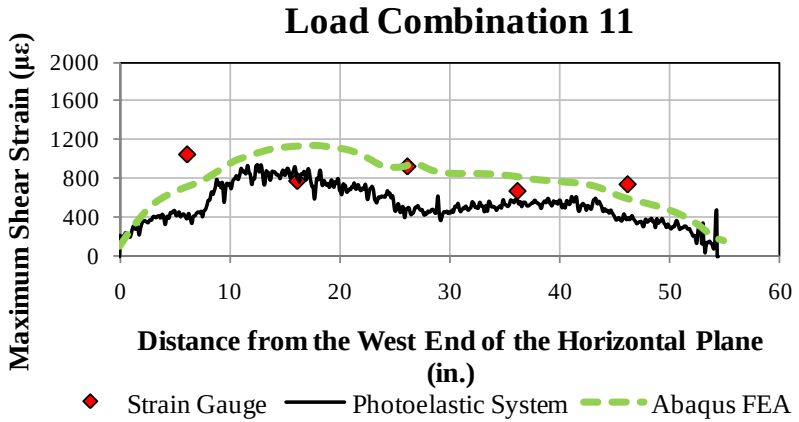

Figure 4.7.175: Comparison between the finite element analysis and experimental data (GP490-SS3 specimen-Load Combination 11)

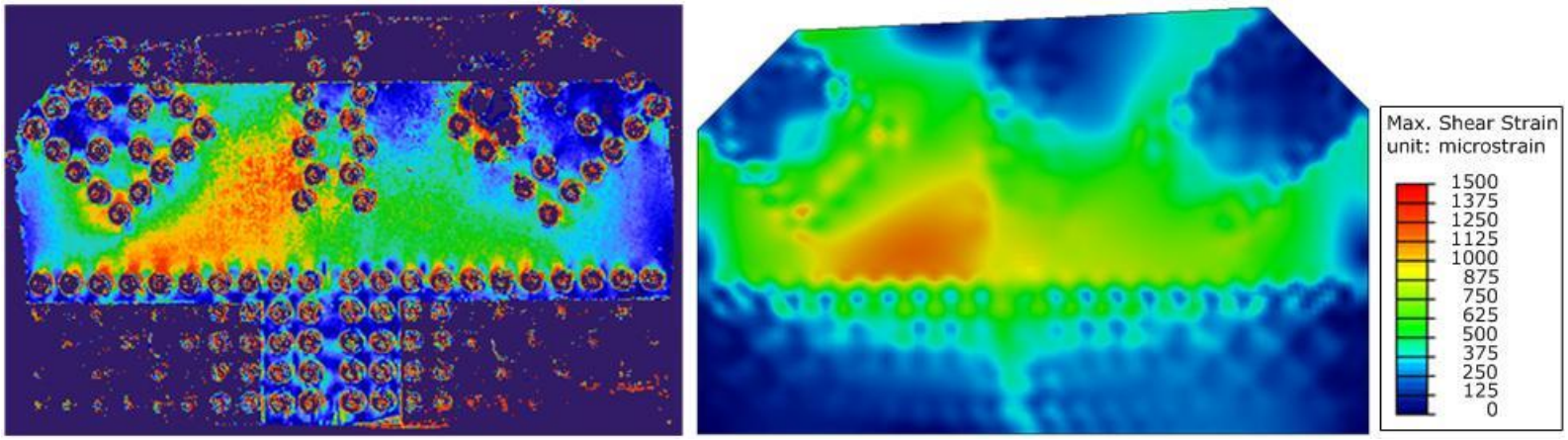

Figure 4.7.176: Comparison between the photo-elastic measurement system (left) and FEA (right) for Load Combination 11

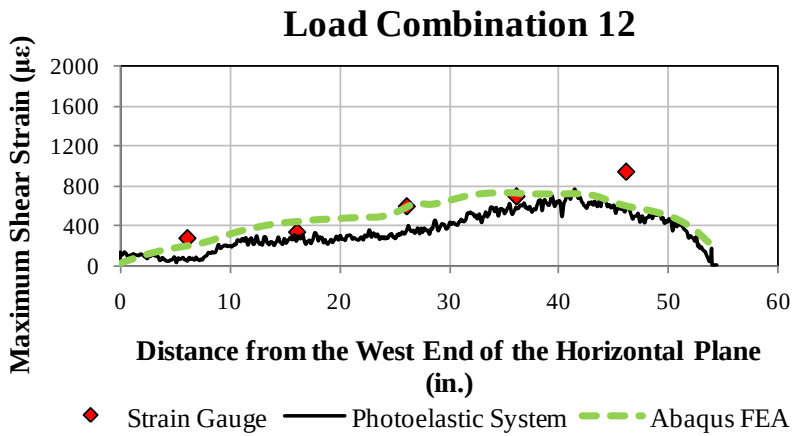

Figure 4.7.177: Comparison between the finite element analysis and experimental data (GP490-SS3 specimen-Load Combination 12)

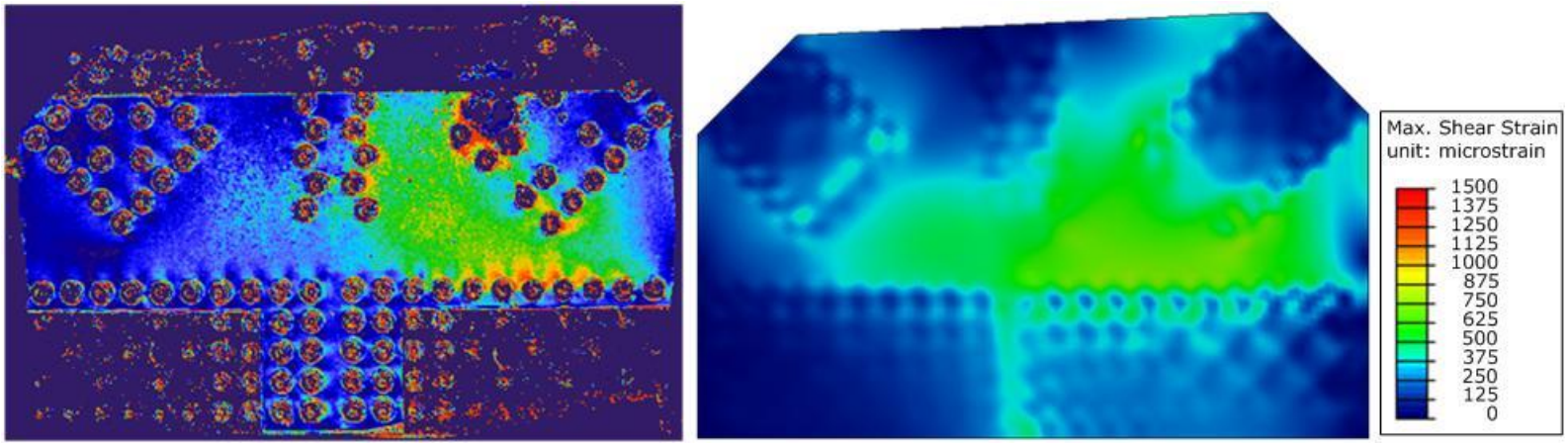

Figure 4.7.178: Comparison between the photo-elastic measurement system (left) and FEA (right) for Load Combination 12

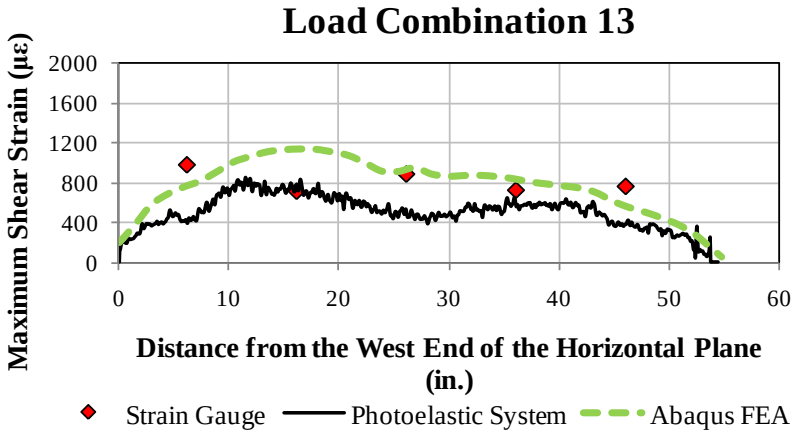

Figure 4.7.179: Comparison between the finite element analysis and experimental data (GP490-SS3 specimen-Load Combination 13)

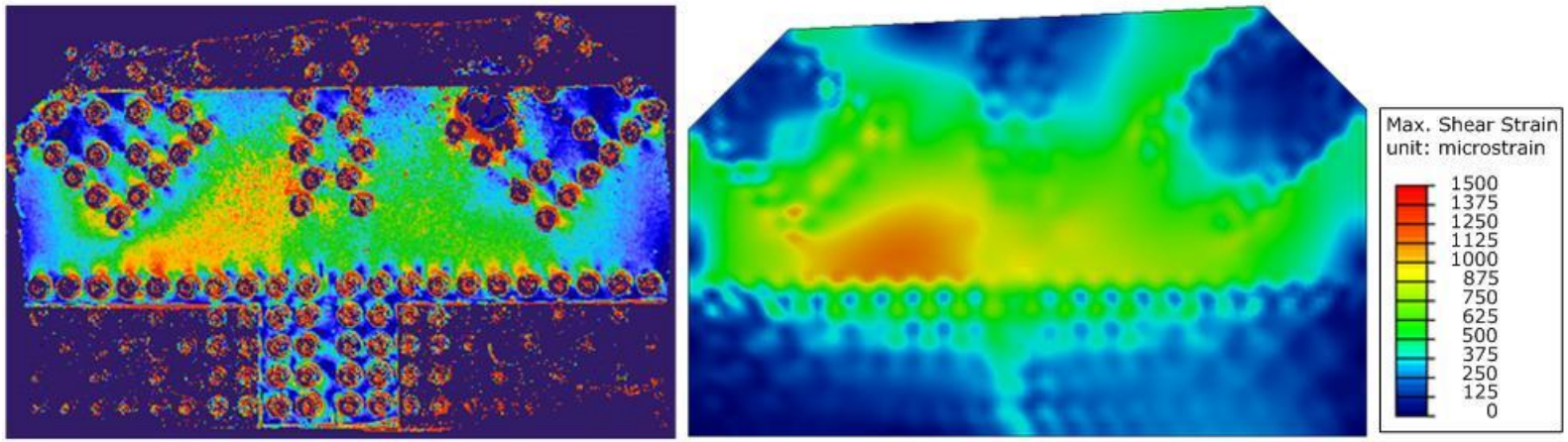

Figure 4.7.180: Comparison between the photo-elastic measurement system (left) and FEA (right) for Load Combination 13

4.7.2.5. GP490-LS3 Specimen

Load combinations with the actual member loads obtained from the tests are shown in Table 4.7.10 for the GP490-LS3 specimen.

Table 4.7.10: Member loads from the elastic load histories of the GP490-LS3 specimen with splice plates

Load Combination	F2 (kip)	F3 (kip)	F4 (kip)	F5 (kip)
1	204	0	-202	1
2	211	0	-203	265
3	251	0	-260	191
4	274	-52	-185	175
5	241	68	-320	226
6	272	-53	-204	139
7	227	68	-299	156
8	170	50	-221	3
9	221	59	-298	281
10	248	-54	-177	64
11	297	-56	-212	266
12	100	34	-149	284
13	270	-24	-256	171
14	195	91	-321	191

Quantitative data from the photoelastic system was not available so the plots only compare the finite element analysis results to the discrete strain gauge measurements for the initial GP490-LS3 specimen with splice plates. Figure 4.7.181 through Figure 4.7.208 shows the response contours and comparison plots. The finite element model predicts the behavior very well and provides very similar results when compared with the discrete strain gauge data.

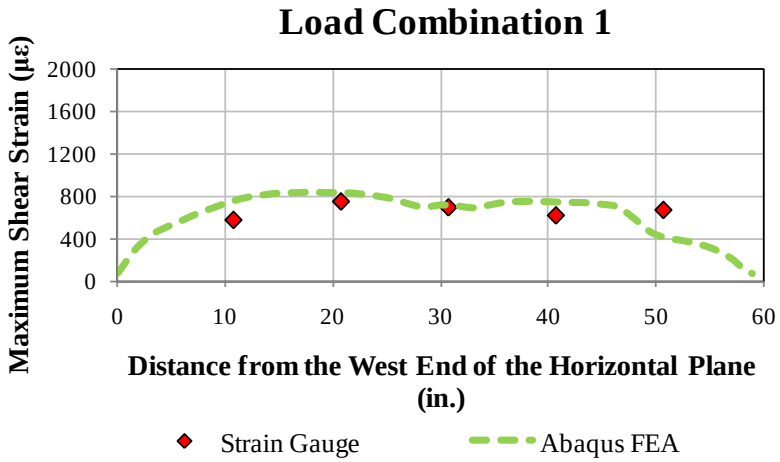

Figure 4.7.181: Comparison between the finite element analysis and experimental data (GP490-LS3 specimen - Load Combination 1)

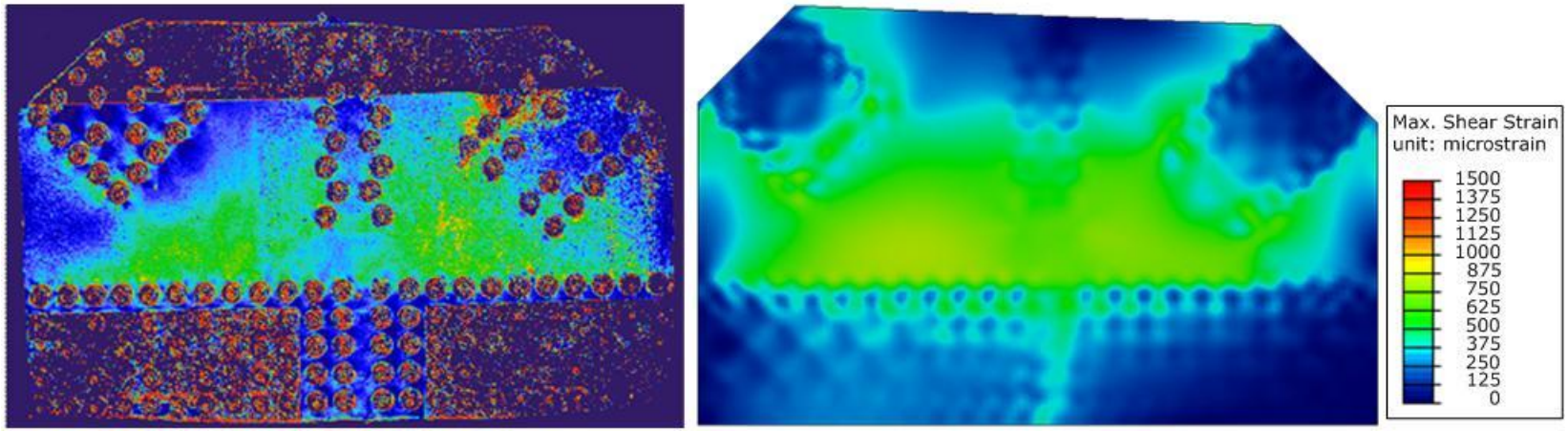

Figure 4.7.182: Comparison between the photo-elastic measurement system (left) and FEA (right) for Load Combination 1

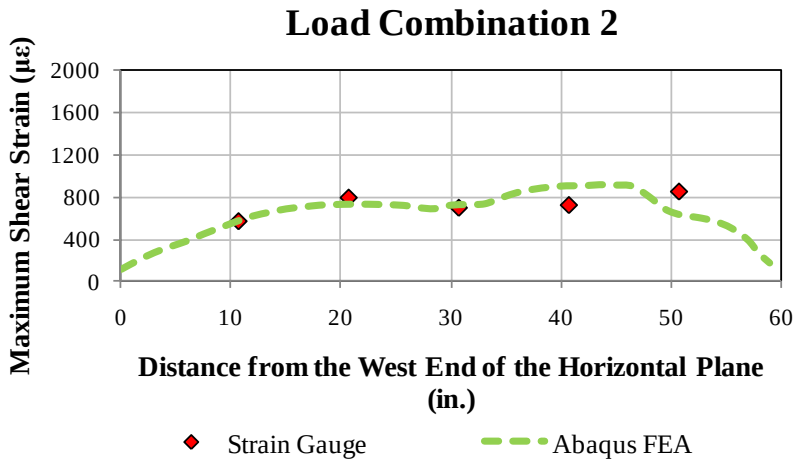

Figure 4.7.183: Comparison between the finite element analysis and experimental data (GP490-LS3 specimen - Load Combination 2)

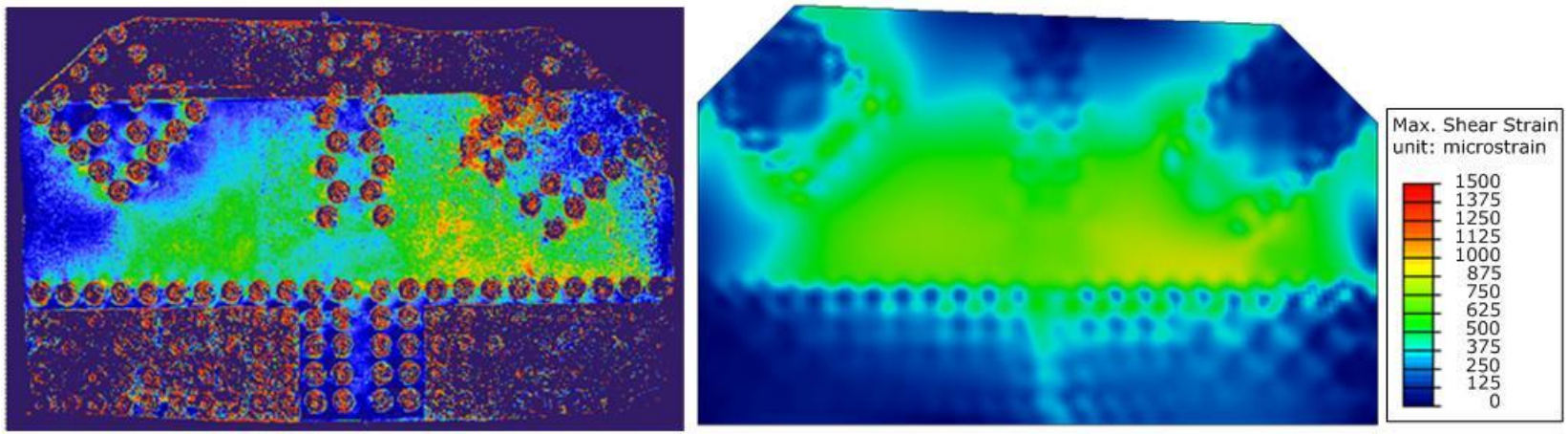

Figure 4.7.184: Comparison between the photo-elastic measurement system (left) and FEA (right) for Load Combination 2

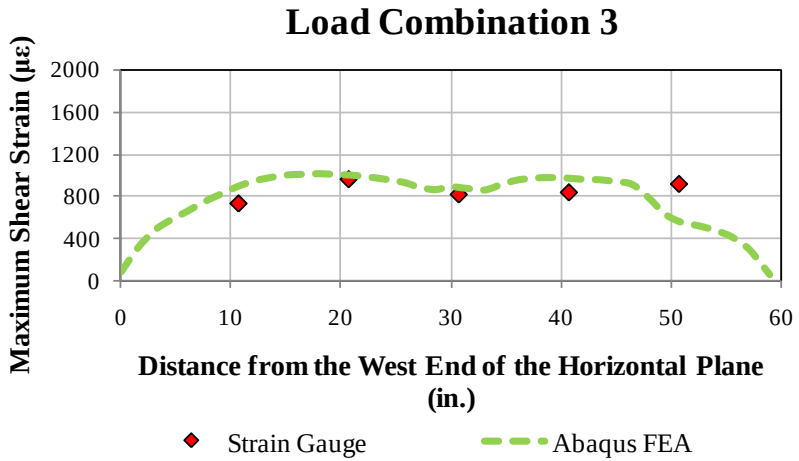

Figure 4.7.185: Comparison between the finite element analysis and experimental data (GP490-LS3 specimen - Load Combination 3)

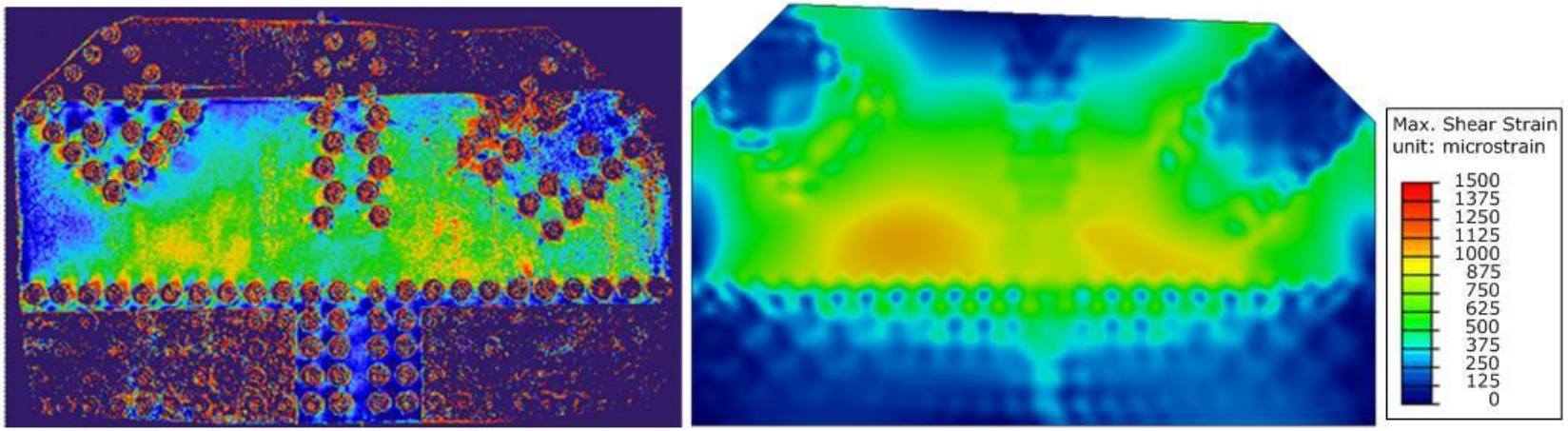

Figure 4.7.186: Comparison between the photo-elastic measurement system (left) and FEA (right) for Load Combination 3

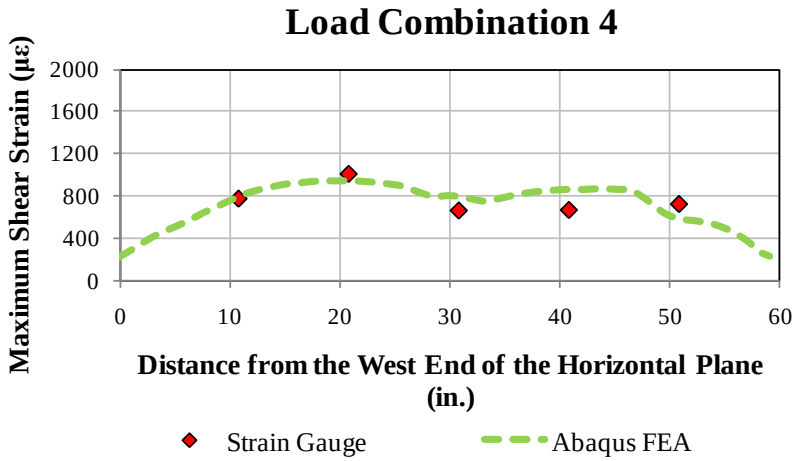

Figure 4.7.187: Comparison between the finite element analysis and experimental data (GP490-LS3 specimen - Load Combination 4)

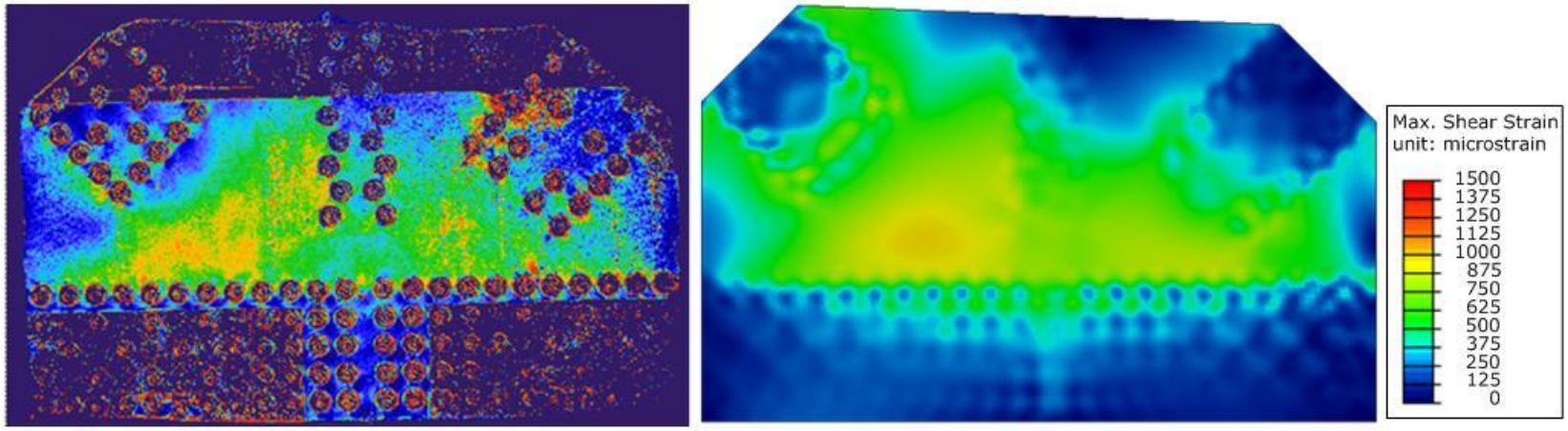

Figure 4.7.188: Comparison between the photo-elastic measurement system (left) and FEA (right) for Load Combination 4

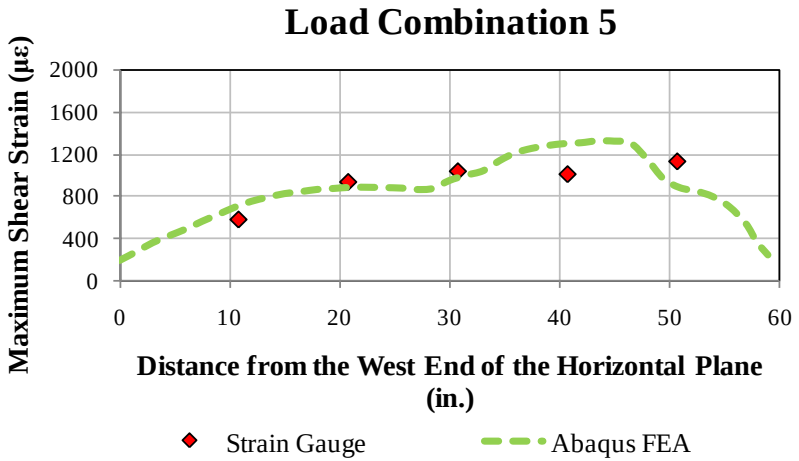

Figure 4.7.189: Comparison between the finite element analysis and experimental data (GP490-LS3 specimen - Load Combination 5)

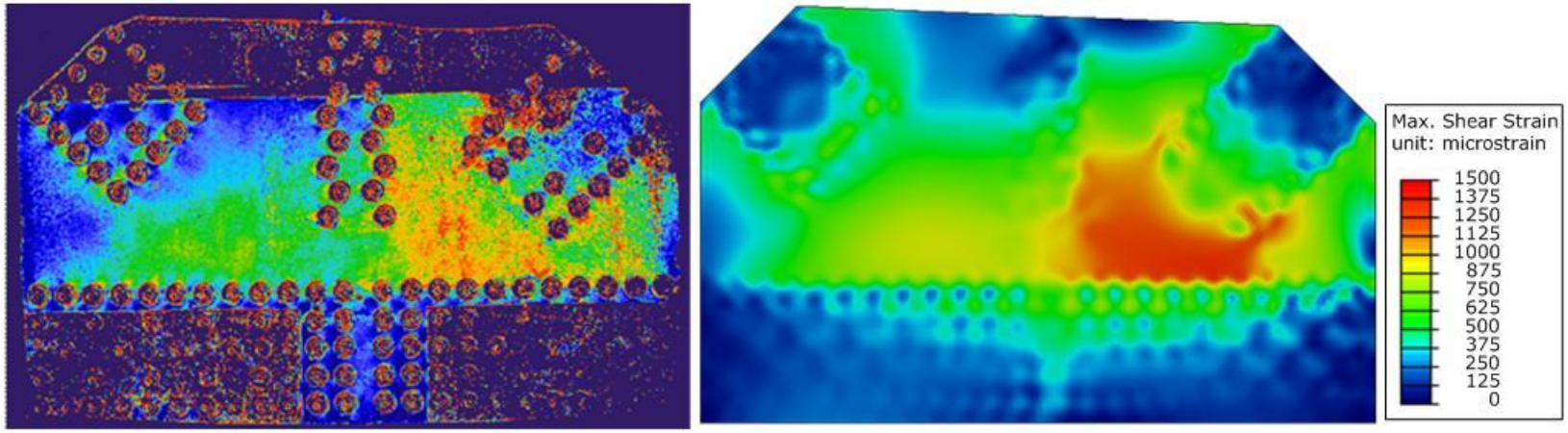

Figure 4.7.190: Comparison between the photo-elastic measurement system (left) and FEA (right) for Load Combination 5

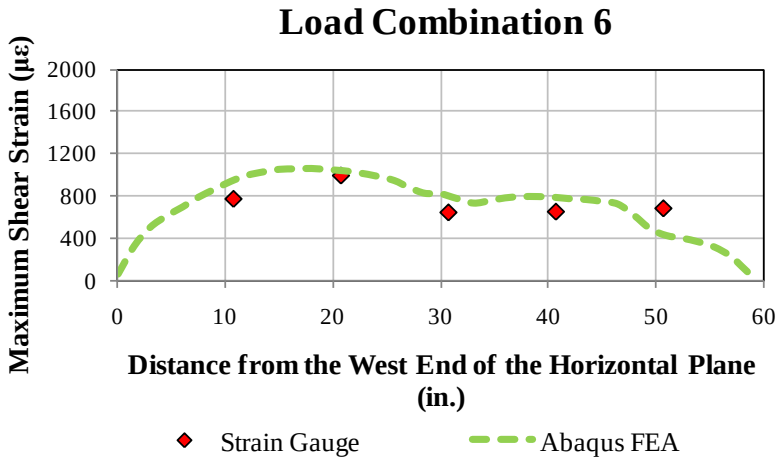

Figure 4.7.191: Comparison between the finite element analysis and experimental data (GP490-LS3 specimen - Load Combination 6)

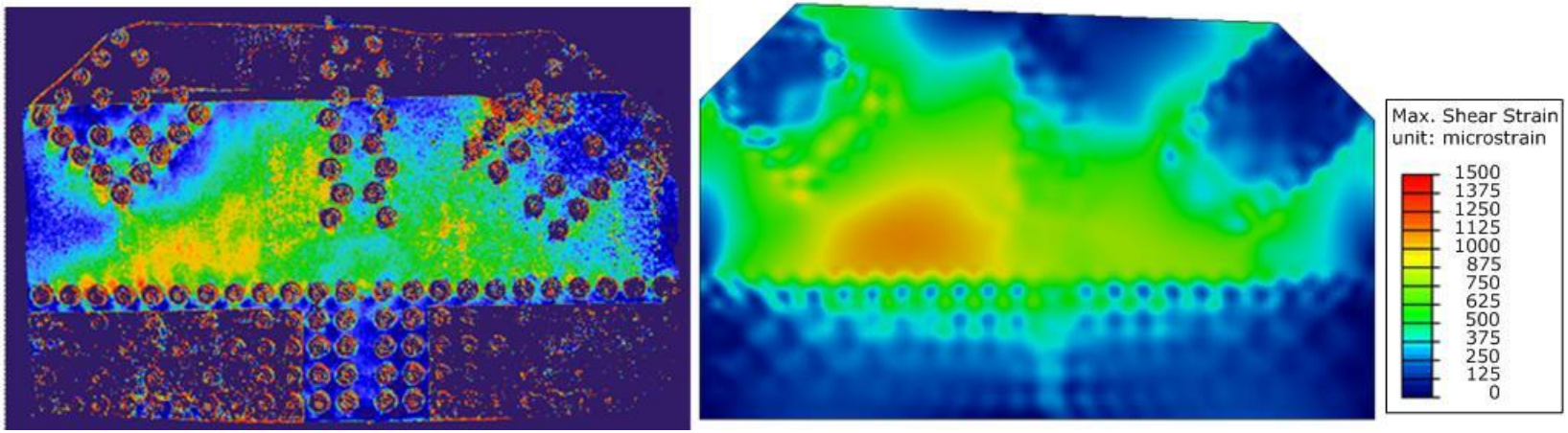

Figure 4.7.192: Comparison between the photo-elastic measurement system (left) and FEA (right) for Load Combination 6

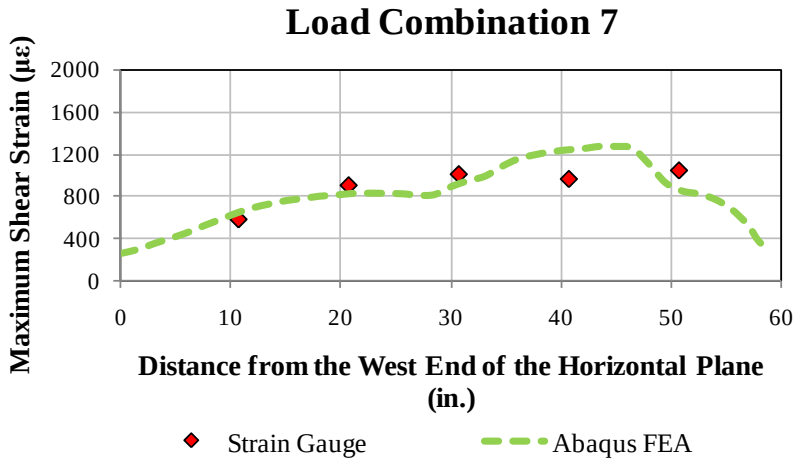

Figure 4.7.193: Comparison between the finite element analysis and experimental data (GP490-LS3 specimen - Load Combination 7)

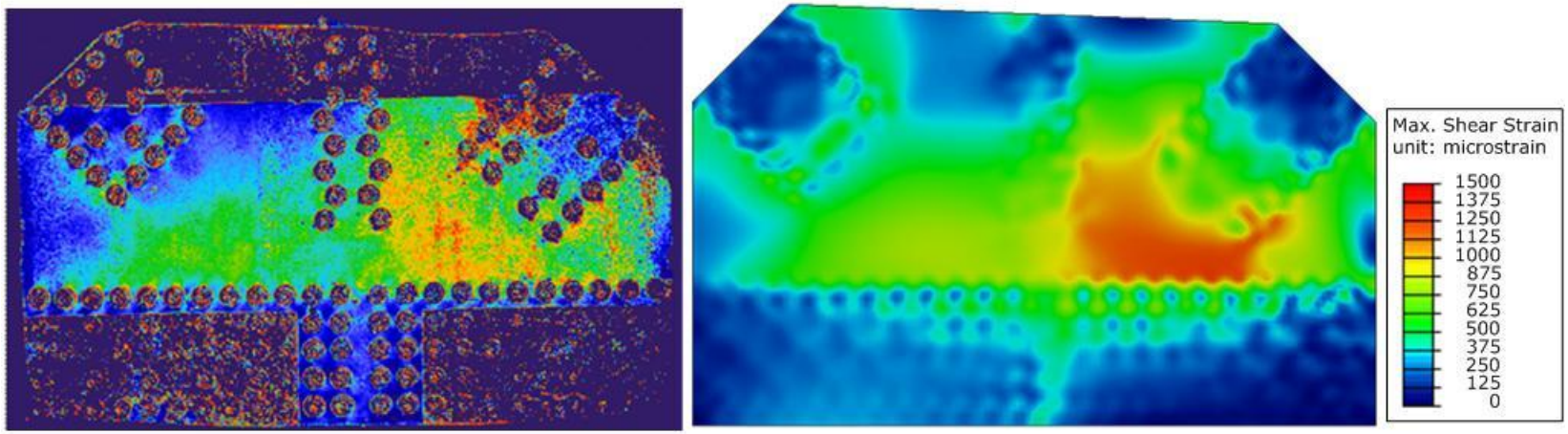

Figure 4.7.194: Comparison between the photo-elastic measurement system (left) and FEA (right) for Load Combination 7

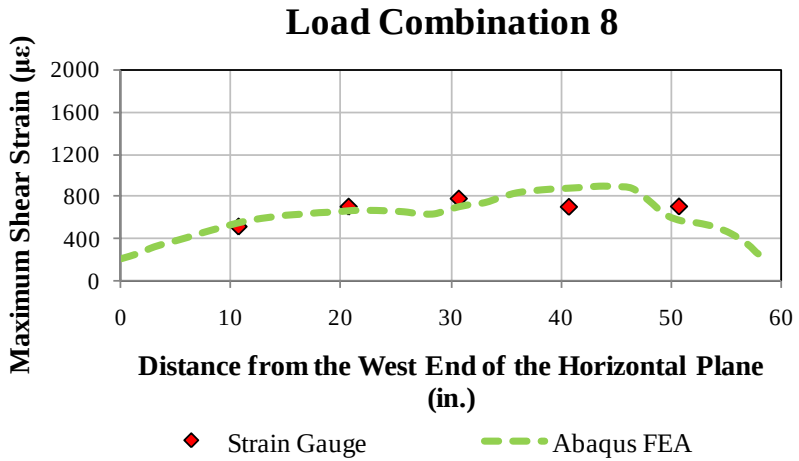

Figure 4.7.195: Comparison between the finite element analysis and experimental data (GP490-LS3 specimen - Load Combination 8)

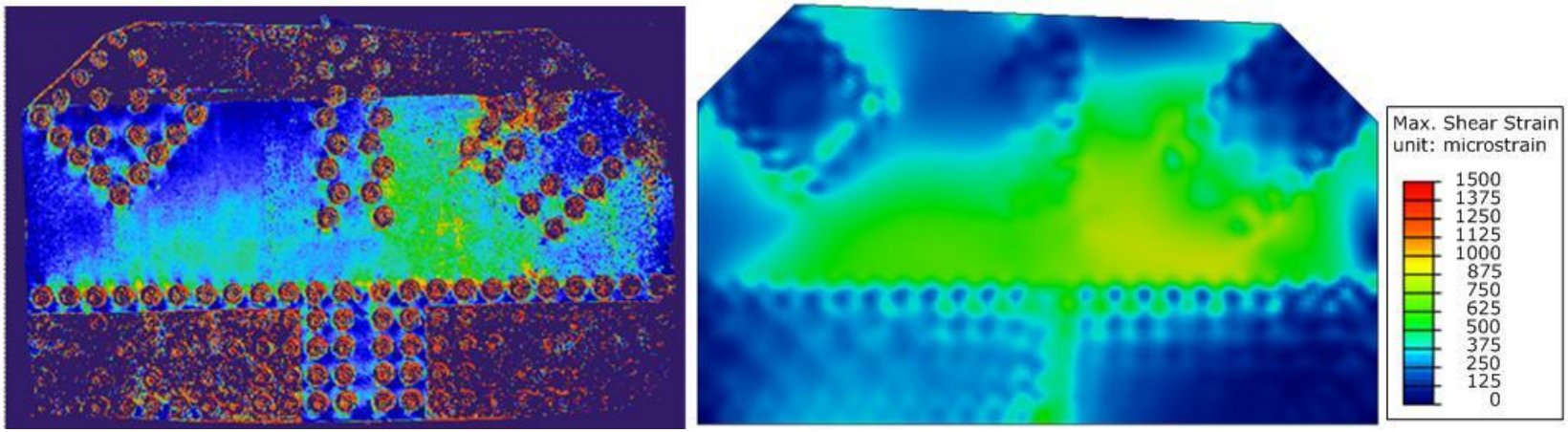

Figure 4.7.196: Comparison between the photo-elastic measurement system (left) and FEA (right) for Load Combination 8

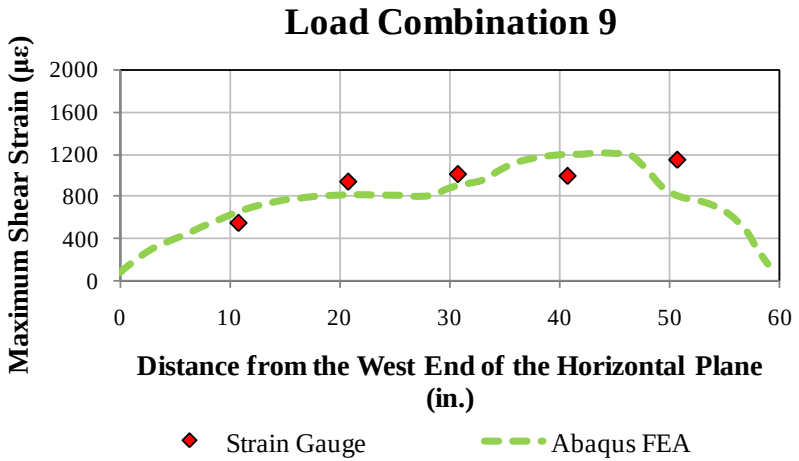

Figure 4.7.197: Comparison between the finite element analysis and experimental data (GP490-LS3 specimen - Load Combination 9)

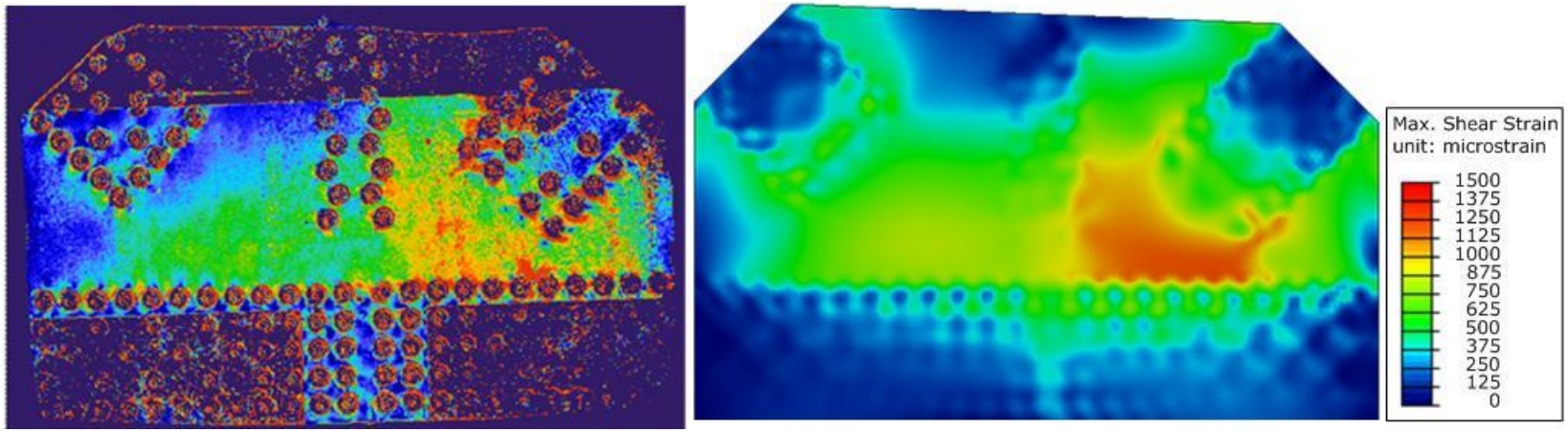

Figure 4.7.198: Comparison between the photo-elastic measurement system (left) and FEA (right) for Load Combination 9

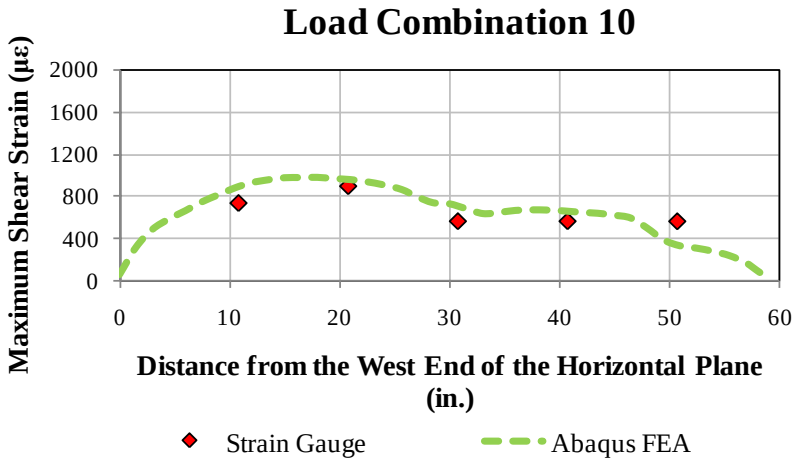

Figure 4.7.199: Comparison between the finite element analysis and experimental data (GP490-LS3 specimen-Load Combination 10)

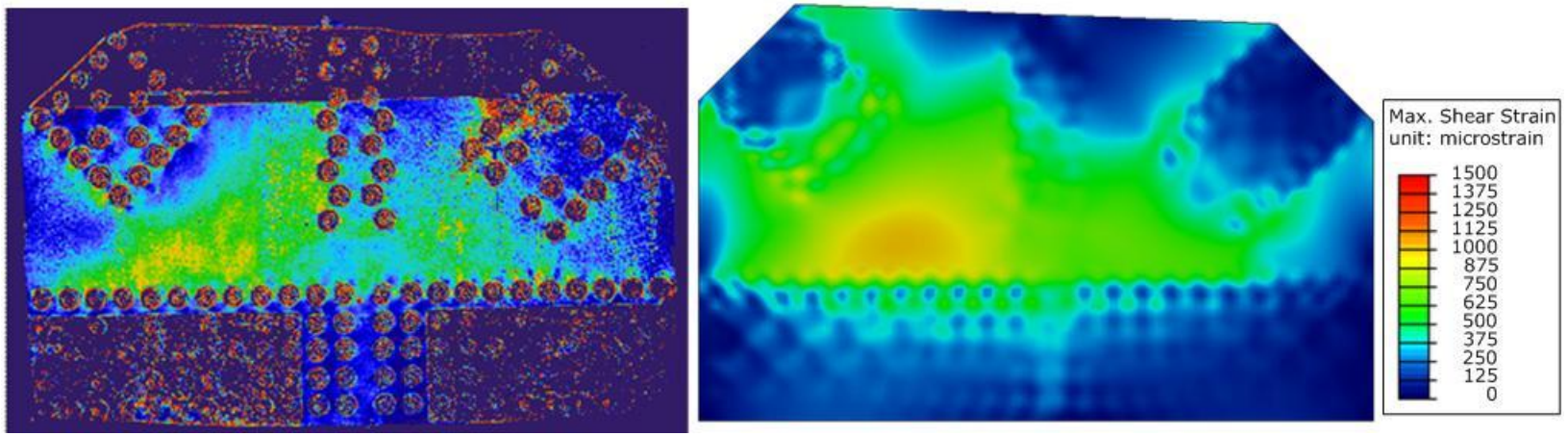

Figure 4.7.200: Comparison between the photo-elastic measurement system (left) and FEA (right) for Load Combination 10

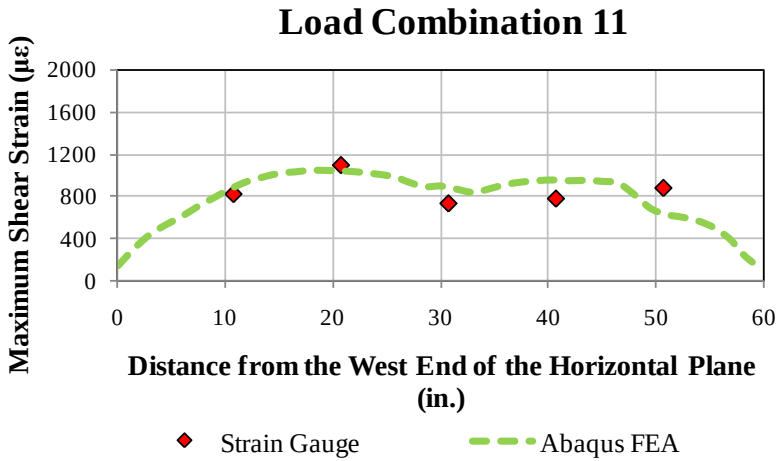

Figure 4.7.201: Comparison between the finite element analysis and experimental data (GP490-LS3 specimen-Load Combination 11)

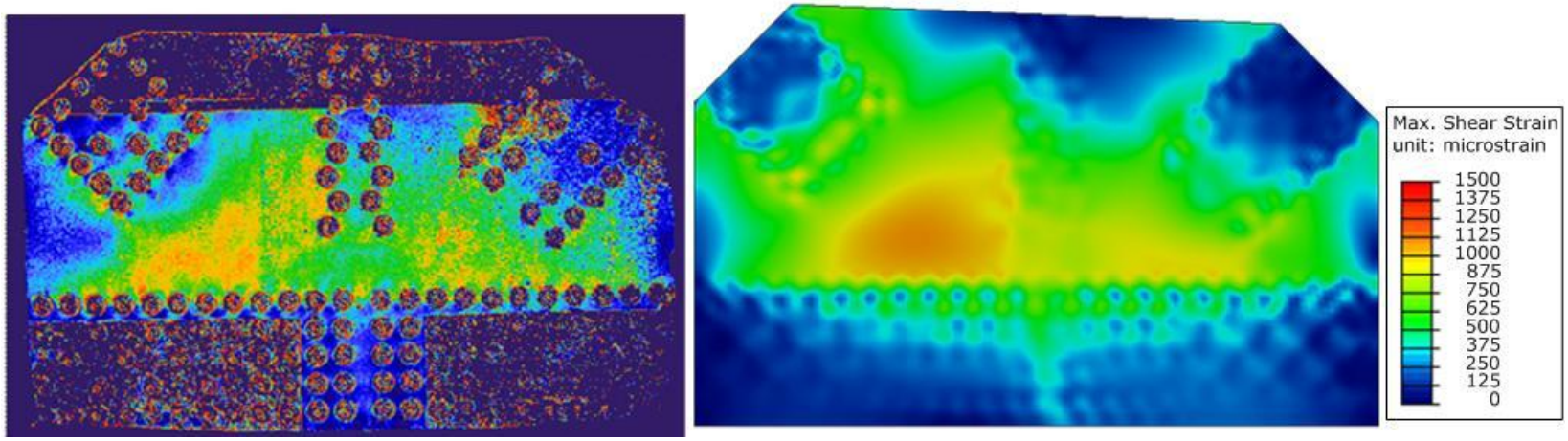

Figure 4.7.202: Comparison between the photo-elastic measurement system (left) and FEA (right) for Load Combination 11

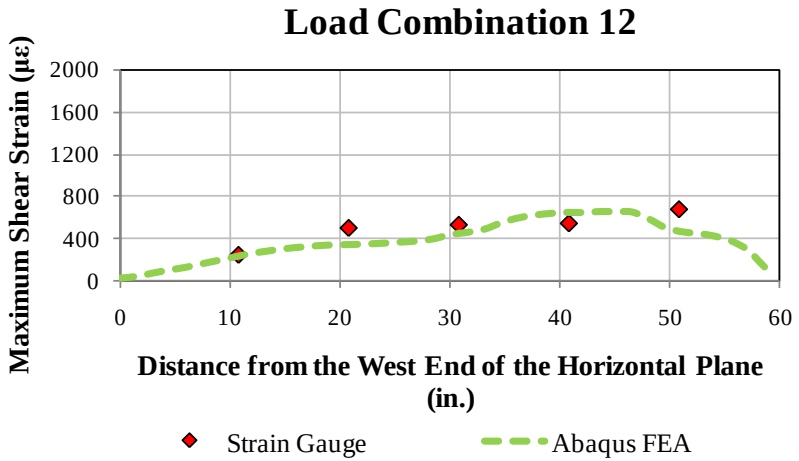

Figure 4.7.203: Comparison between the finite element analysis and experimental data (GP490-LS3 specimen-Load Combination 12)

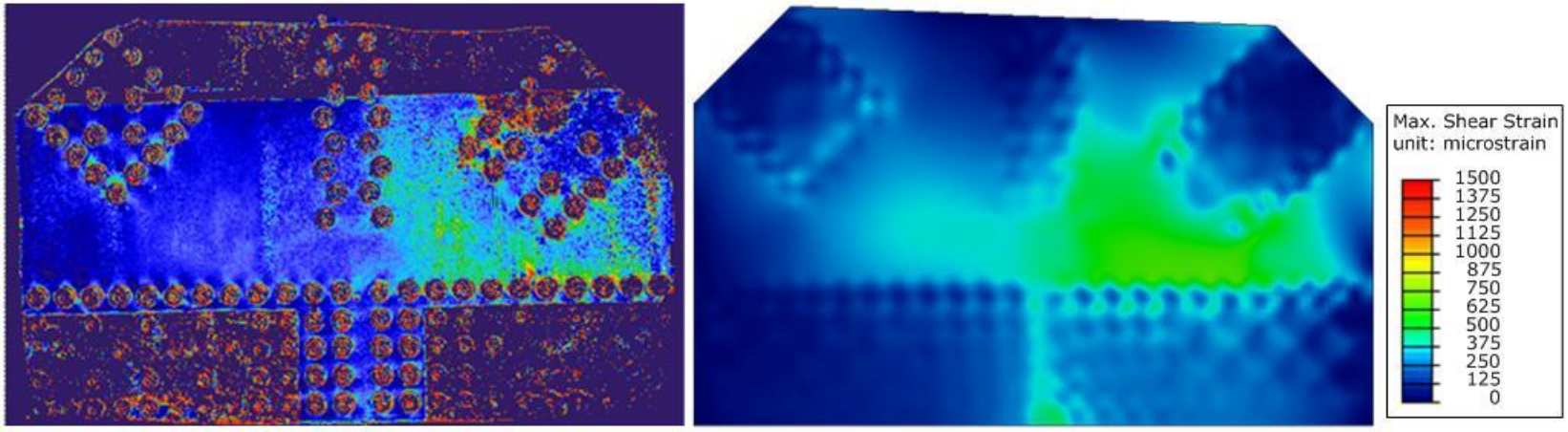

Figure 4.7.204: Comparison between the photo-elastic measurement system (left) and FEA (right) for Load Combination 12

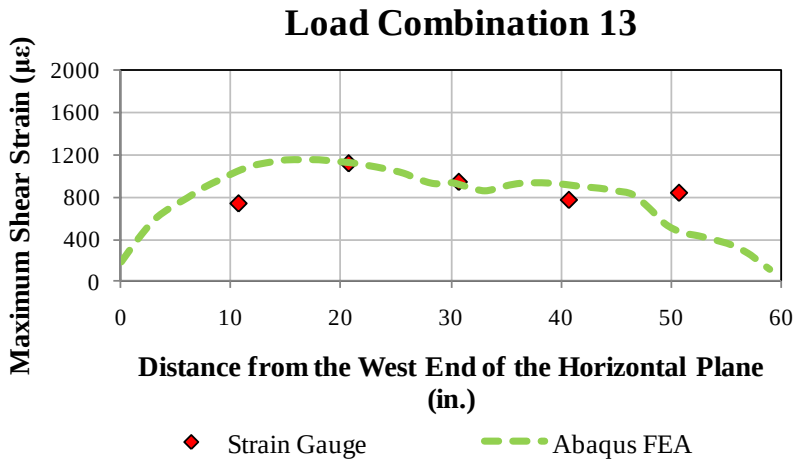

Figure 4.7.205: Comparison between the finite element analysis and experimental data (GP490-LS3 specimen-Load Combination 13)

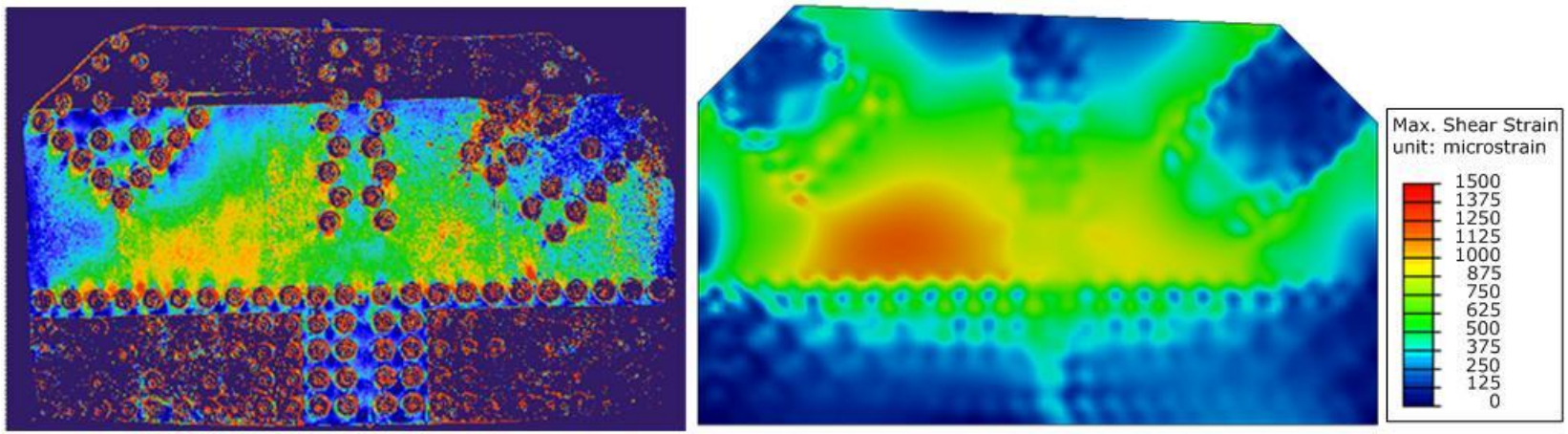

Figure 4.7.206: Comparison between the photo-elastic measurement system (left) and FEA (right) for Load Combination 13

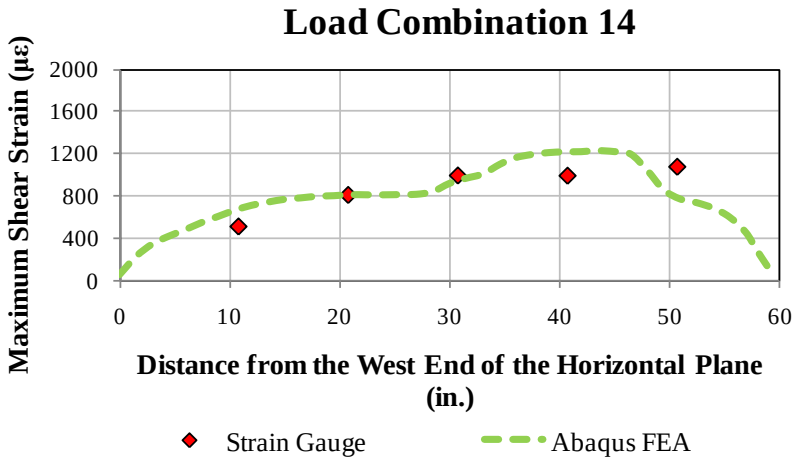

Figure 4.7.207: Comparison between the finite element analysis and experimental data (GP490-LS3 specimen-Load Combination 14)

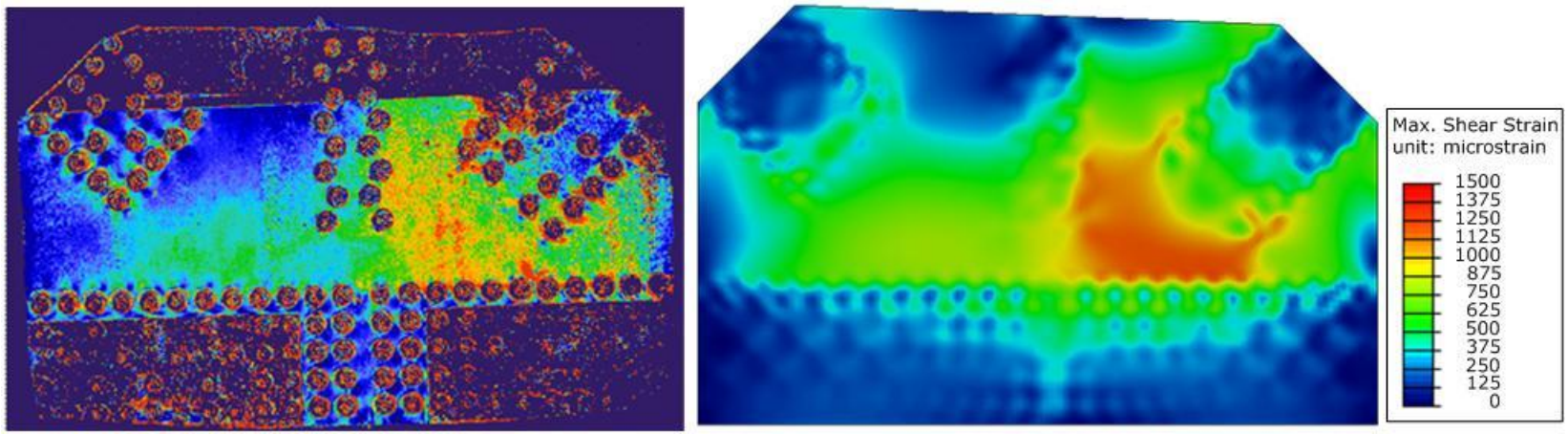

Figure 4.7.208: Comparison between the photo-elastic measurement system (left) and FEA (right) for Load Combination 14

4.7.3. Tests to Failure

After the elastic stages are completed on each specimen, one reference load combination is selected to run the specimen up to its failure. For the final failure tests, DIC contours provide qualitative measurement of the finite element model validation. With the actual test loads applied in the finite element models, corresponding applied load fraction of the test loadsare determined from the finite element analyses.

4.7.3.1. GP307-SS3 Specimen

Load combination 4 from Table 4.6.1 was selected as the reference load combination to apply on four members. The connection was proportionally loaded up to failure based on the following reference loads using the sign convention discussed previously:

Compression Diagonal (F2): 1000 kip
Vertical Member (F3): -207 kip
Tension Diagonal (F4): -707 kip
East Chord (F5): 707 kip

The failure occurred with side-sway buckling of the gusset plate on the compression diagonal side as shown in Figure 4.7.209.

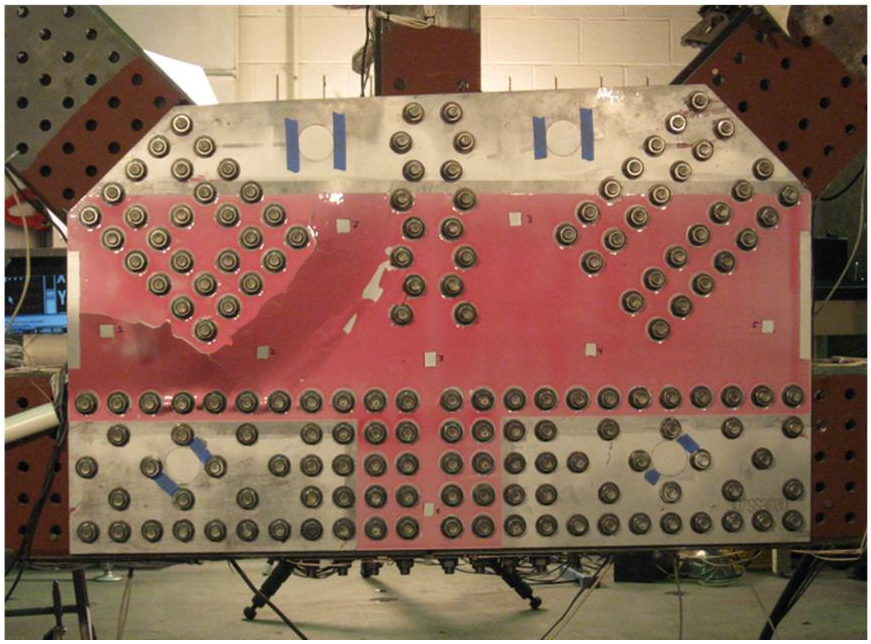

Figure 4.7.209: Post-test photo of the GP307-SS3 specimen showing the buckled gusset plate (compression diagonal is on the left)

Maximum member loads at the instant of the failure of the connection were:

Compression Diagonal (F2): 716 kip

Vertical Member (F3): -141 kip

Tension Diagonal (F4): -507 kip

East Chord (F5): 520 kip

These actual member loads, nonlinear material properties and initial gusset plate imperfections are included in the finite element analysis. The prediction from the test simulation shows that buckling occurs at 94% of the applied test loads. For this specimen, initial imperfection data is only available for one of the gusset plates and the same imperfection is used for both plates in the connection. This prediction which is only 6% lower than the experiment result can be considered good taking the testing conditions and uncertainties into account. Applied load fraction vs.displacement relationship is shown in Figure 4.7.210. The significant increase in the out-of-plane displacement compared to the in-plane (horizontal) displacement supports the evidence of buckling failure of the specimen.

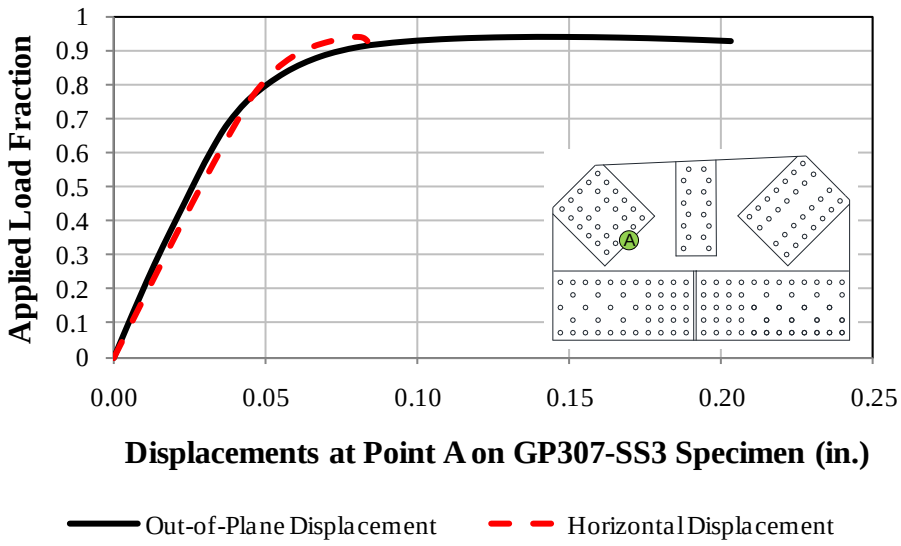

Figure 4.7.210: In-plane vs. out-of-plane displacement comparison for GP307-SS3 specimen

von Mises stresses at the maximum ALF=0.94 which is the peak of the finite element analysis, are shown in Figure 4.7.211 with a deformation scale factor of 5. The out-of-plane movement of the compression diagonal can be identified from the analysis results. The gusset plate of the GP307-SS3 specimen has static yield strength of 36.4 ksi. All the grey contours show the yielded regions in the gusset plate when buckling happened.

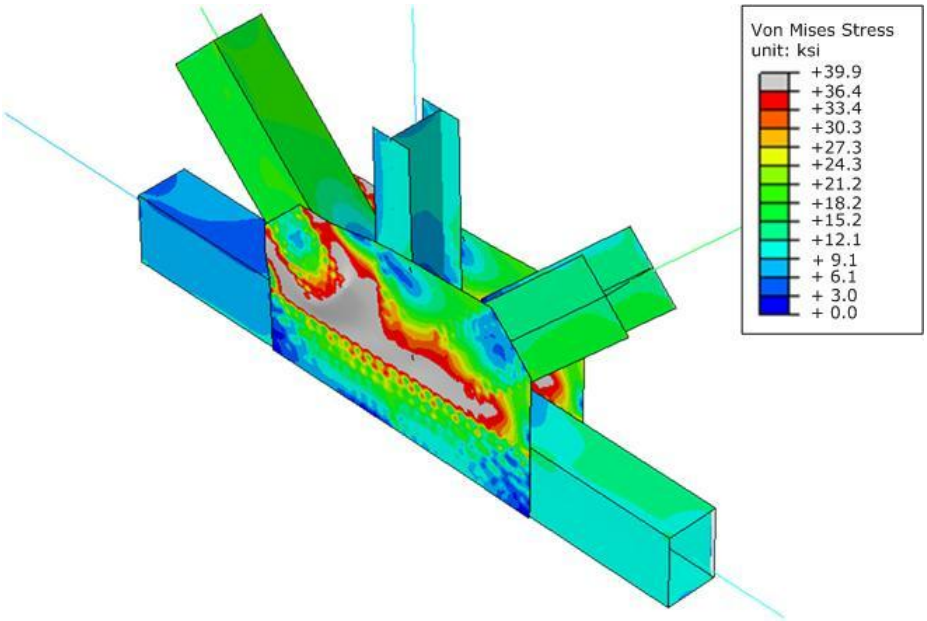

Figure 4.7.211: von Mises stress response contours at the failure (ALF=0.94)

Corresponding equivalent plastic strain contours provide information about the yielded regions as shown in Figure 4.7.212. All the contours other than dark blue show the extent of yielded areas in the gusset plate.

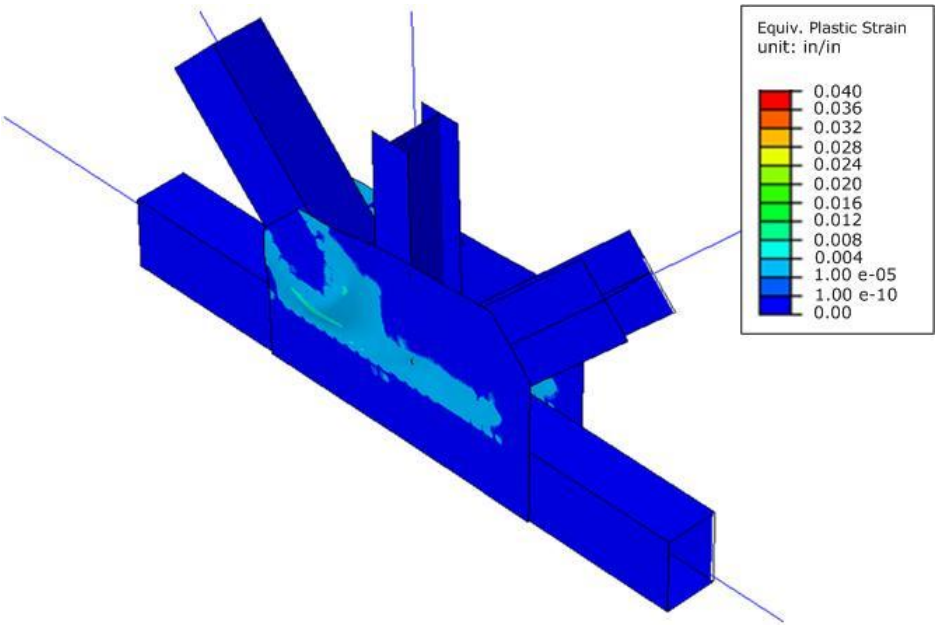

Figure 4.7.212: Equivalent plastic strain response contours at the failure (ALF=0.94)

To compare the test results with the nonlinear finite element analysis results, the digital image correlation (DIC) system which monitors the North gusset plate provides data at different load levels. The main output from the DIC is the Tresca strain, which corresponds to the radius of the Mohr's circle of strains. Two load levels are used to make comparisons between the experiment and analytical models. In the contours for DIC and corresponding finite element analysis, the compression diagonal is on the right and the tension diagonal is on the left.

The first load level for comparison is after certain plate yielding is reached but the specimen is not near incipient failure. The response contour legend is limited to maximum of 1500 με. Figure 4.7.213 shows the DIC data along with the finite element analysis result at ALF=0.61. Analysis result provides good agreement with the experimental results. Since each test simulation for the specimens reaches different applied load fractions, this initial load step comparisons provides confidence on the effectiveness of the finite element models.

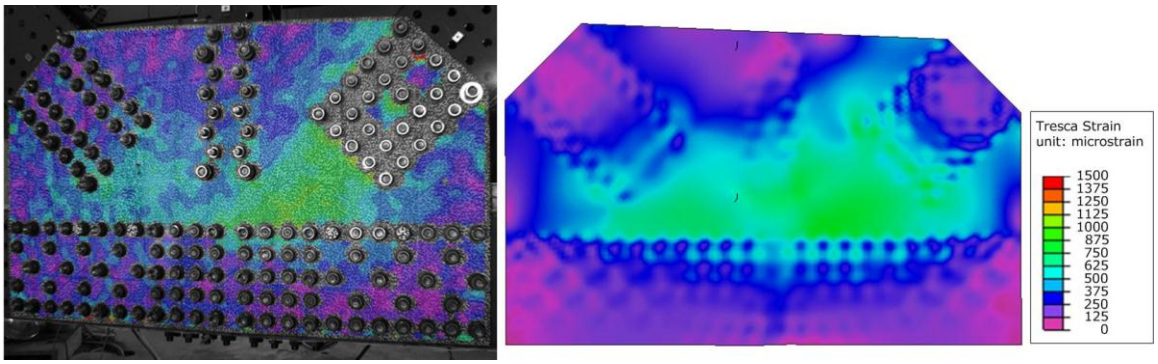

Figure 4.7.213: Comparison between the digital image correlation (left) and FEA (right) at ALF=0.61

The second load level is just before the failure takes place (incipient failure). In this case, the strain values are much higher and the contour legend is limited to 15000 με. Again the DIC result on the left in Figure 4.7.214 matches the finite element analysis result on the right. The analytical model even captures the response just above the chord member and around the compression diagonal.

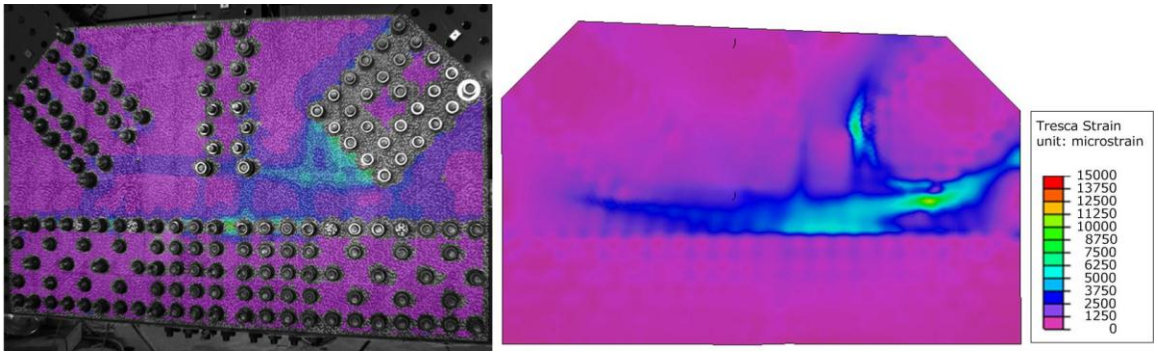

Figure 4.7.214: Comparison between the digital image correlation (left) and FEA (right) just before the failure

4.7.3.2. GP307-LS3 Specimen

Load combination 7 from Table 4.6.2 was selected as the reference load combination to apply to four members of the GP307-LS3 specimen. The connection was proportionally loaded up to failure based on the following reference loads:

Compression Diagonal (F2): 697 kip

Vertical Member (F3): -246 kip

Tension Diagonal (F4): -348 kip

East Chord (F5): -261 kip

The failure occurred by side-sway buckling of the gusset plate on the compression diagonal side. This was an expected result since the gap between the compression diagonal and the chord member is larger than for the GP307-SS3 specimen. The compression diagonal at the instant of gusset plate buckling is shown in Figure 4.7.215.

Figure 4.7.215: Post-test photo of the GP307-LS3 specimen. Buckled shape of the gusset plate is shown (compression diagonal is on the left)

Maximum member loads at the instant of the failure of the connection were:

Compression Diagonal (F2): 796 kip

Vertical Member (F3): -280 kip

Tension Diagonal (F4): -405 kip

East Chord (F5): -290 kip

The prediction from the test simulation showed that buckling occurs at 110% of the applied test loads. The East chord is in tension for this specimen and based on the information provided by FHWA, the East chord is basically free to move as a result of the jack repositioning. Hence, no displacement/rotation restraint is applied at the end of the east chord member in the finite element model. Still the finite element result is only 10% higher than the actual test results. Applied load fraction vs.displacement relationship is shown in Figure 4.7.216. Out-of-plane displacements at the base of the compression diagonal become much higher than the in-plane displacements.

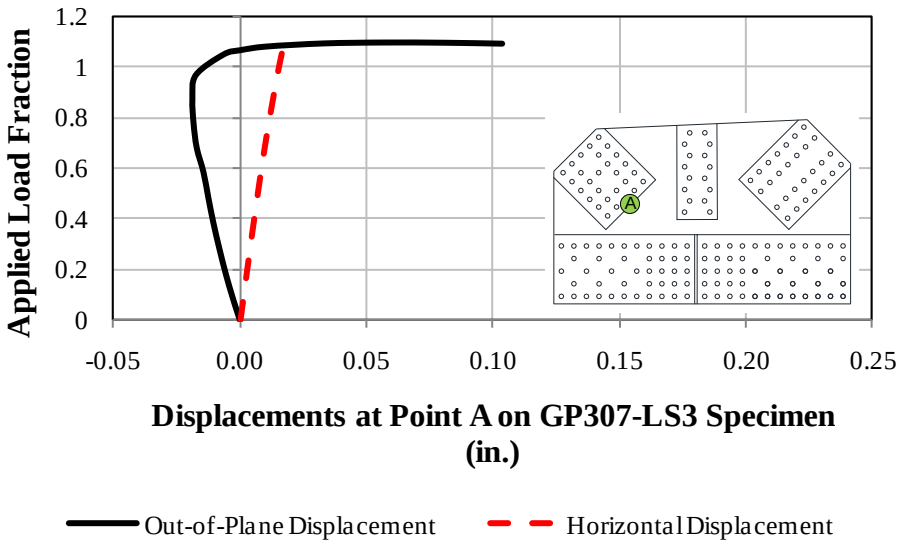

Figure 4.7.216: In-plane vs. out-of-plane displacement comparison for GP307-LS3 specimen

The von Mises stress response contours at the maximum ALF=1.10 which is the peak of the finite element analysis is shown in Figure 4.7.217 with a deformation scale factor of 20. The out-of-plane movement of the compression diagonal can be identified from the analysis results. Static yield strength of the gusset plate is 48.2 ksi.

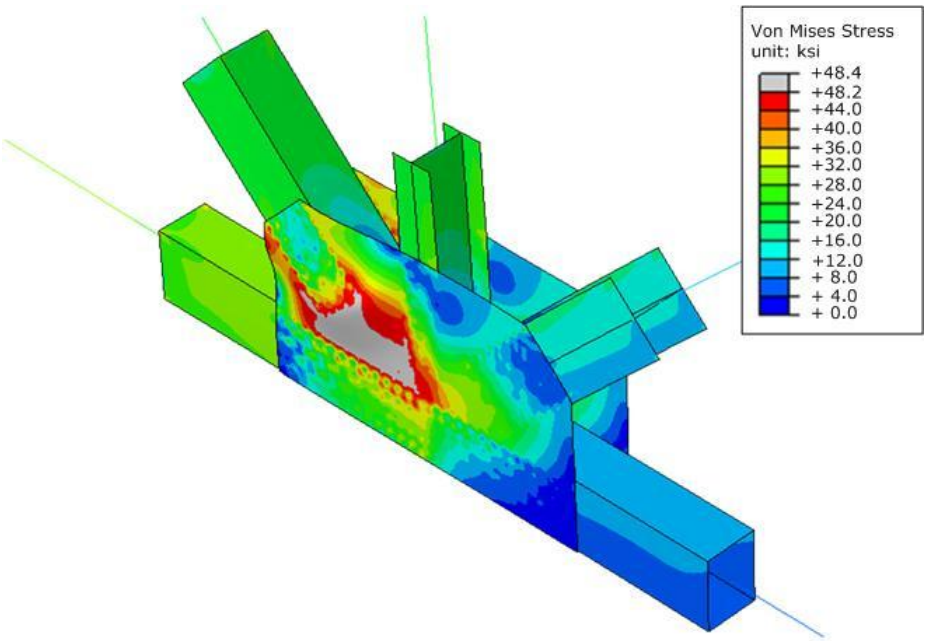

Figure 4.7.217: von Mises stress response contours at the failure (ALF=1.10)

Yielding is limited to the compression diagonal side and between the diagonal and the chord member. This can be seen in the equivalent plastic strain contours shown in Figure 4.7.218. Without yielding a lot of material, the connection reaches its maximum capacity and buckled out-of-plane. The movement of the compression diagonal is captured by the finite element model very similar to the actual test result.

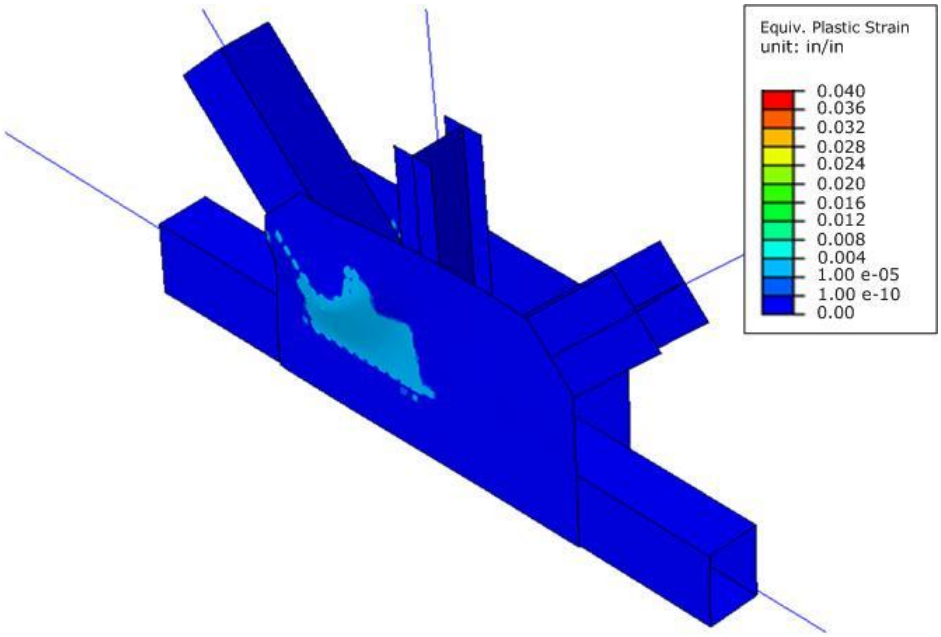

Figure 4.7.218: Equivalent plastic strain response contours at the failure (ALF=1.10)

Figure 4.7.219 shows the DIC and finite element analysis results at ALF=0.68. Strain values from the finite element analysis are slightly higher than the actual test values within the free region between the compression diagonal and chord members.

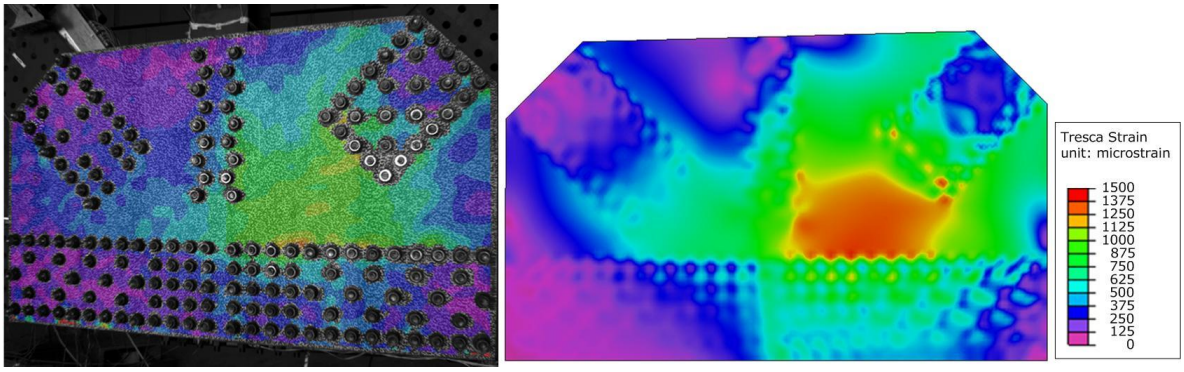

Figure 4.7.219: Comparison between the digital image correlation (left) and FEA (right) at ALF=0.68

The second comparison is near failure of the specimen as shown in Figure 4.7.220. Both DIC and finite element results provide very close results. The differences might arise from the fact that finite element model failed at 110% percent of the actual test loads (ALF=1.10) and the contours are extracted near failure.

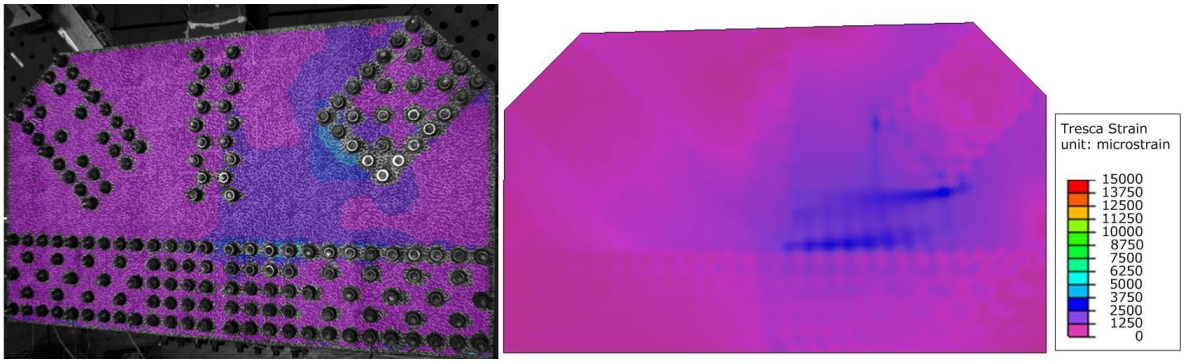

Figure 4.7.220: Comparison between the digital image correlation (left) and FEA (right) just before the failure

4.7.3.3. GP307-SL3 Specimen

GP307-SL3 specimen was the specimen with the longest free edge lengths. It was tested using the load combination 3 from Table 4.6.1. The goal was applying the load combination which provides the maximum shear force along the horizontal plane just above the chord members.

The connection was proportionally loaded up to failure based on the following reference loads:

Compression Diagonal (F2): 1000 kip

Vertical Member (F3): 0 kip

Tension Diagonal (F4): -1000 kip

East Chord (F5): 707 kip

The failure mode for GP307-SL3 specimen was different compared to other specimens. The failure was a shear failure along the horizontal plane, followed by the out-of-plane movement of the compression diagonal. Mobilization of the compression diagonal side of the gusset plate occurred after a lot of yielding took place along the horizontal plane as shown in Figure 4.7.221.

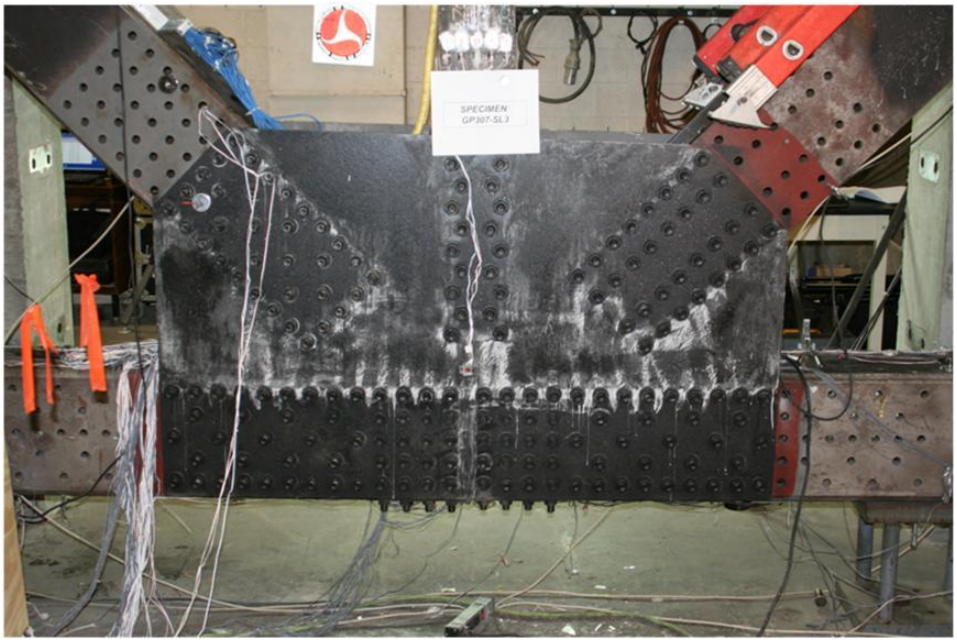

Figure 4.7.221: Post-test photo of the GP307-SL3 specimen. Yielding along the horizontal plane above the chord members is shown (compression diagonal is on the left)

Maximum member loads at the instant of the failure of the connection were:

Compression Diagonal (F2): 946 kip

Vertical Member (F3): 0 kip

Tension Diagonal (F4): -929 kip

East Chord (F5): 706 kip

Using the FARO targets placed on the gusset plate, vector plots showing the in-plane gusset plate behavior from the actual test were determined. Initial location and final location were recorded during the test. Vectors amplified 25 times in Figure 4.7.222 show both that targets above the chord have much more deformation than the others on the chord members and that the plate is mobilized horizontally. This result also confirms that the mode of failure for the GP307-SL3 specimen is a shear failure along the horizontal plane above the chord members.

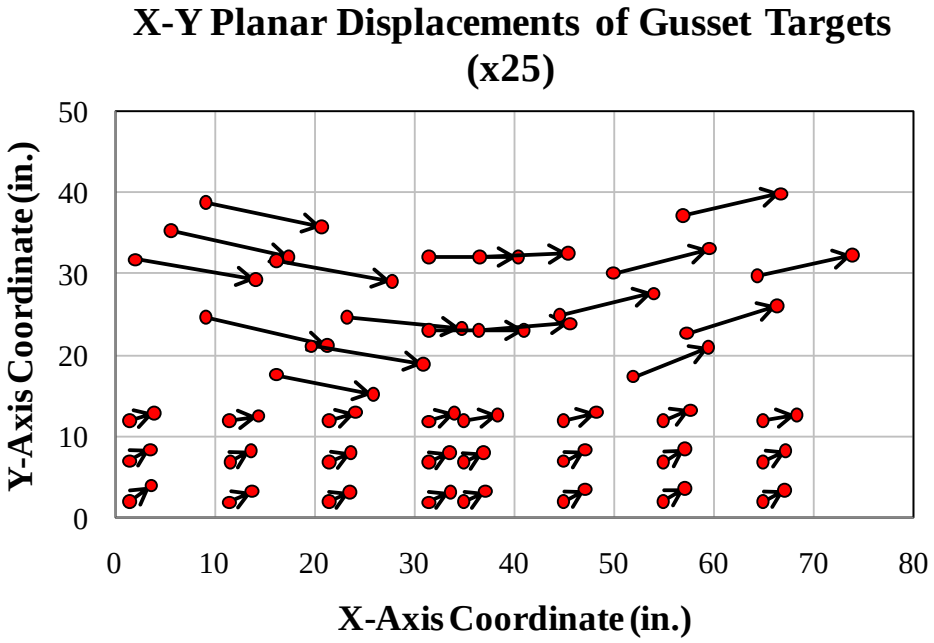

Figure 4.7.222: Displacement of the targets on the gusset plate showing the excessive horizontal movement above the chord members (multiplied 25 times)

Finite element analysis with the actual member loads shows that analysis reaches 106% of the test results. Static yield strength of the gusset plate is 46.6 ksi. Applied load fraction vs.displacement relationship in Figure 4.7.223 also supports the FARO data. Horizontal displacements continuously increase and become much larger compared to the out-of-plane displacements on the gusset plate.

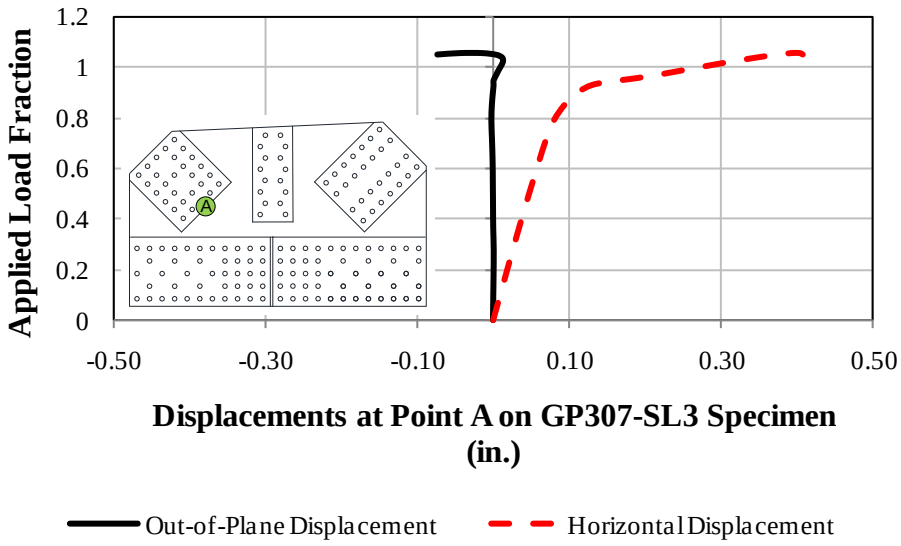

Figure 4.7.223: In-plane vs. out-of-plane displacement comparison for GP307-SL3 specimen

von Mises stress response contours and corresponding equivalent plastic strain contours at ALF=1.06 are shown in Figure 4.7.224 and Figure 4.7.225 respectively. Similar to the experiments, the horizontal plane is fully yielded and the compression diagonal moves out-of-plane at the end.

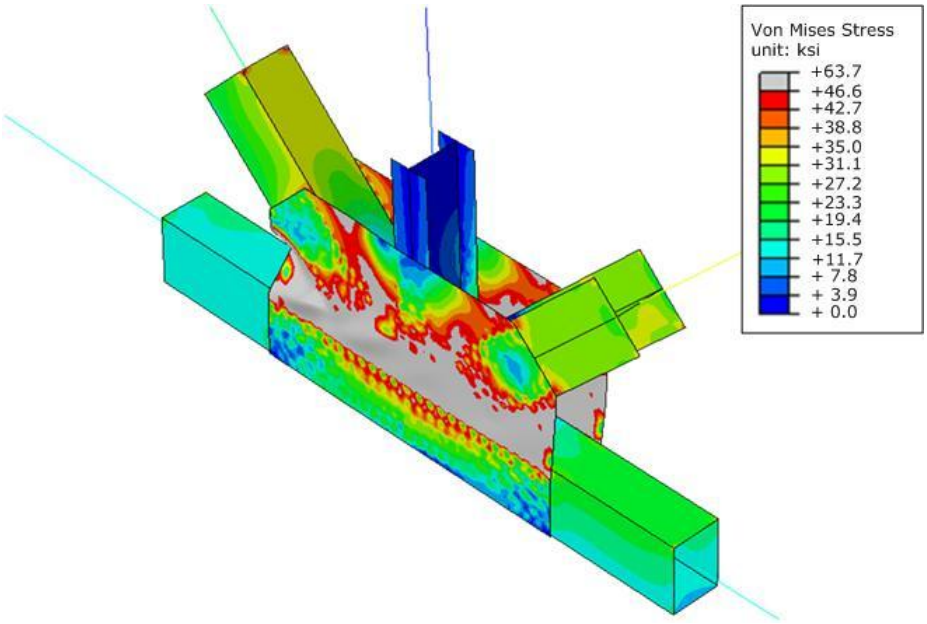

Figure 4.7.224: von Mises stress response contours at the failure (ALF=1.06)

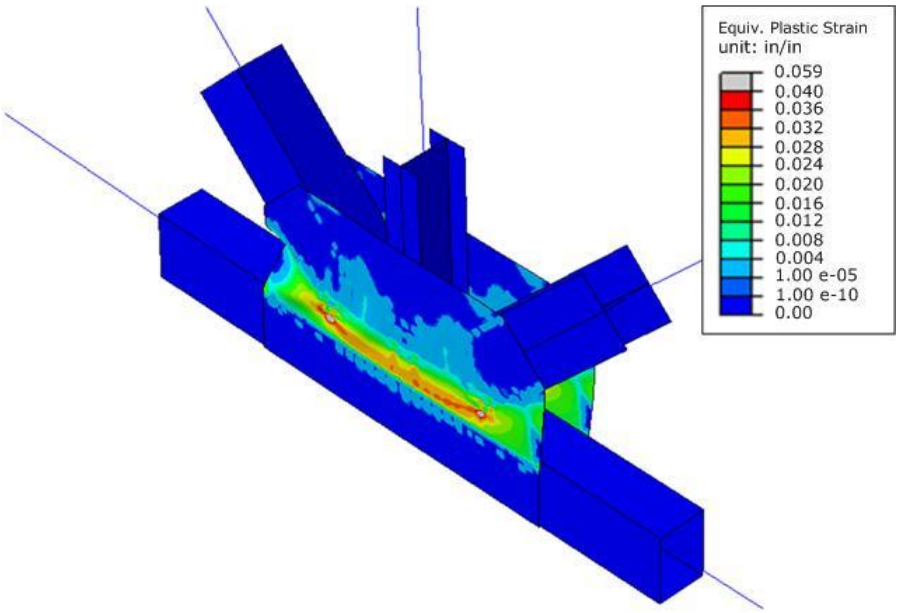

Figure 4.7.225: Equivalent plastic strain response contours at the failure (ALF=1.06)

Major benefit of this test is validating the 4% equivalent plastic strain (PEEQ) limit. For cases where failure mode is predicted as compression buckling of the gusset plate, the limit load is the peak of the applied loads from the finite element analysis. For cases, where buckling does not take place or shear failure happens with a lot of plastification along certain planes, finite element analysis applied load fraction is limited to the step where 4% PEEQ is reached in the gusset plate. This is defined as the maximum limit of useful resistance in the preliminary analyses of the four representative bridge joints. GP307-SL3 specimen result also shows that 4% PEEQ in the gusset plate mid-thickness is reached at about 102% of the actual test loads (ALF=1.02) as shown in Figure 4.7.226.

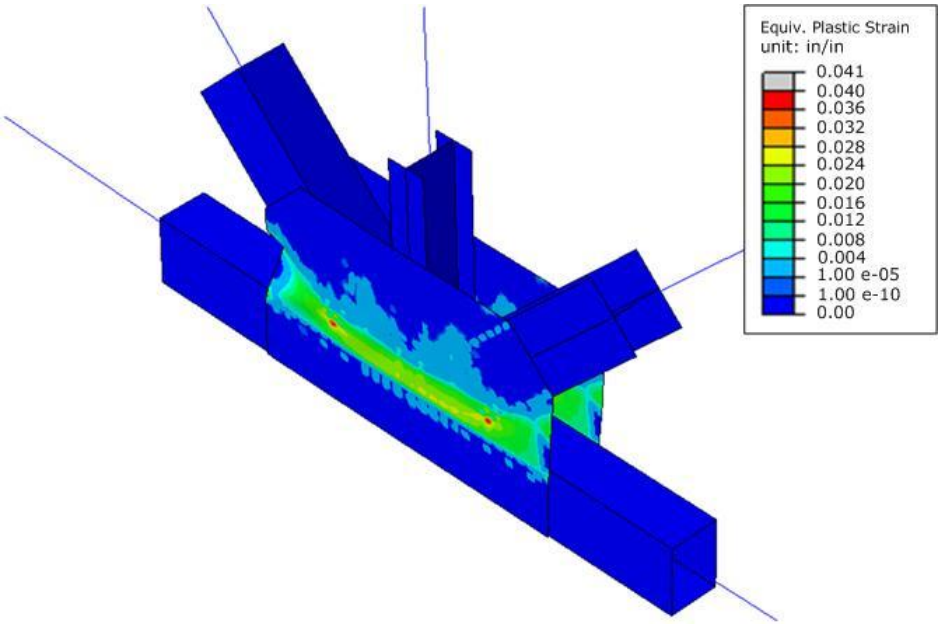

Figure 4.7.226: Equivalent plastic strain response contours at the 4% PEEQ Limit (ALF=1.02)

Shear stress response contours in Figure 4.7.227 also supports the conclusion on the shear failure of the specimen. This response is also obtained at ALF=1.02. For a static yield of 46.6 ksi, the shear yield limit is ~27 ksi. Finite element analysis result shows that almost whole horizontal plane reaches its shear yield limit. The orange and red contours show regions at or near shear yield limit.

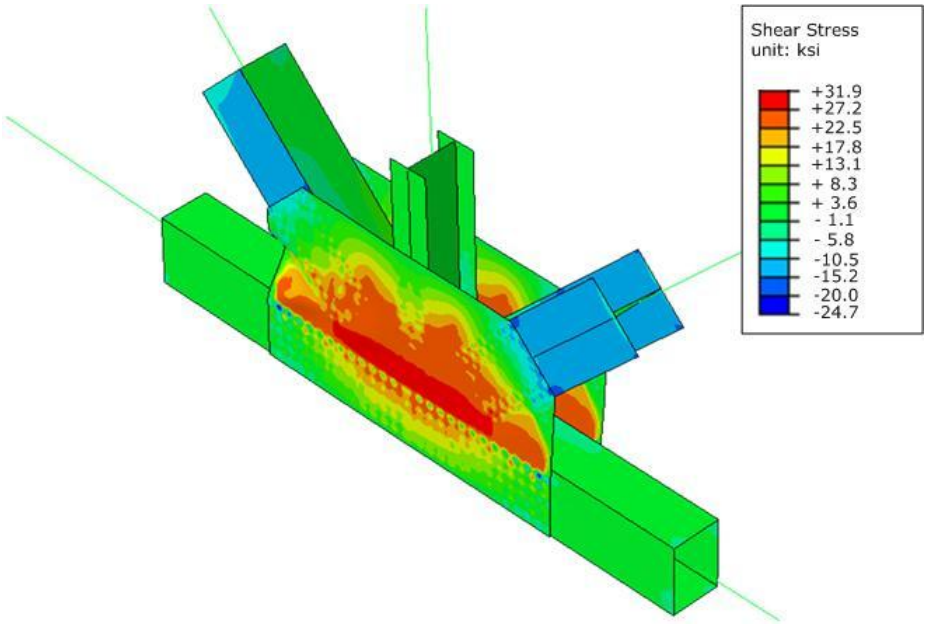

Figure 4.7.227: Shear stress response contours at the 4% PEEQ Limit (ALF=1.02)

Tresca strains from DIC and finite element model is first compared at ALF=0.72 as shown in Figure 4.7.228. Strain values from the analytical model are slightly smaller in the regions where DIC data provides the highest values.

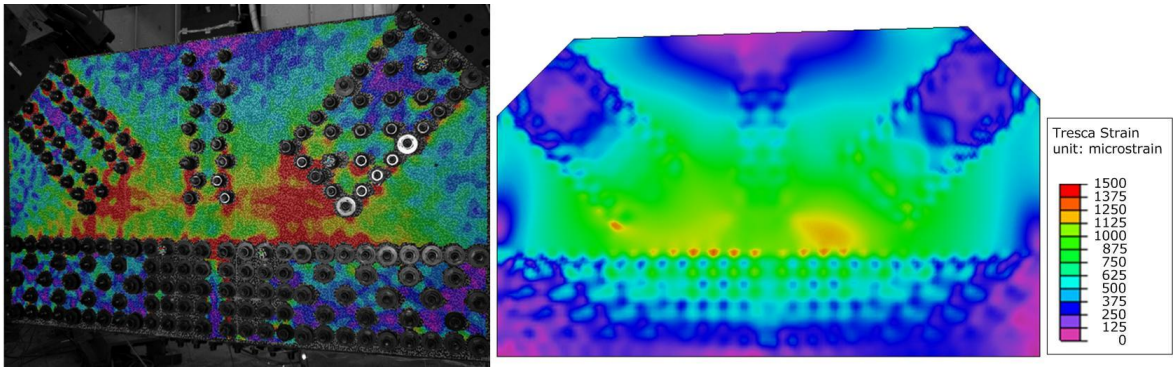

Figure 4.7.228: Comparison between the digital image correlation (left) and FEA (right) at ALF=0.72

Tresca strains are also compared near failure in Figure 4.7.229. In this case, the analytical model response is created at ALF=1.02 which is the limit of 4% equivalent plastic strains. With only slight differences, the overall behavior is well captured including the local region along the free edge on the tension diagonal side.

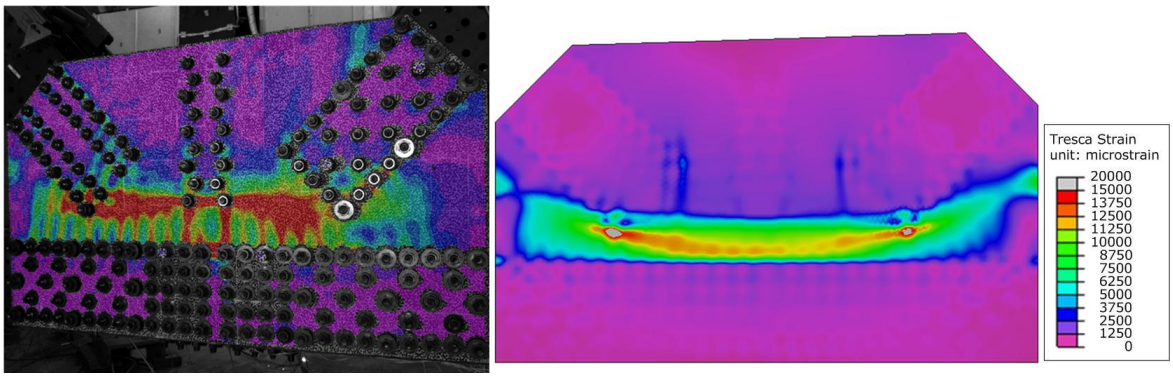

Figure 4.7.229: Comparison between the digital image correlation (left) and FEA (right) just before the failure

4.7.3.4. GP490-SS3 Specimen

Load combination 7 from Table 4.6.3 was used as the reference load combination for the GP490-SS3 specimen. The connection was proportionally loaded up to failure based on the following reference loads:

Compression Diagonal (F2): 1000 kip

Vertical Member (F3): 0 kip

Tension Diagonal (F4): -1000 kip

East Chord (F5): 707 kip

Unlike the GP307-SL3 specimen, failure occurred with side-sway buckling of the gusset plate on the compression diagonal side as shown in Figure 4.7.230. The gusset plate in this connection has static yield strength of 46.4 ksi.

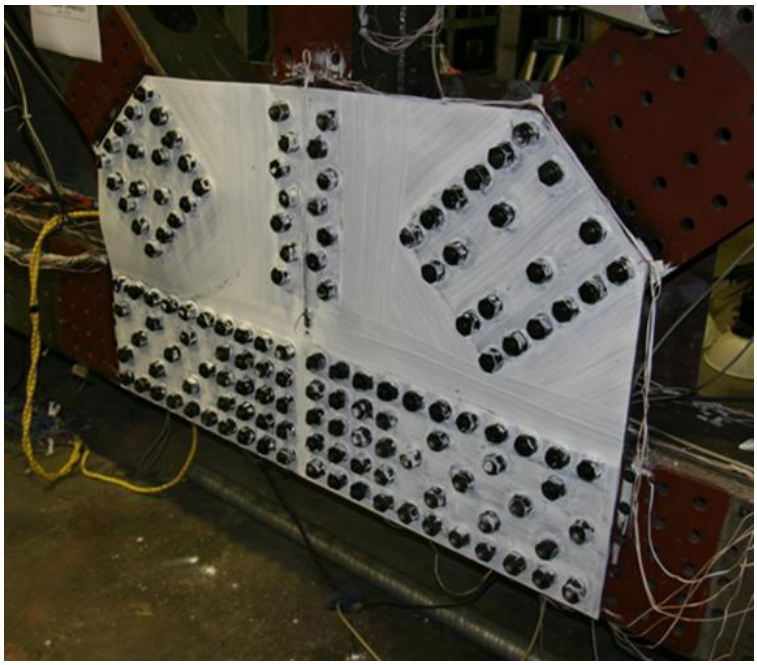

Figure 4.7.230: Post-test photo of the GP490-SS3 specimen. Buckled shape of the gusset plate is shown (compression diagonal is on the left)

Maximum loads at failure of the connection were:

Compression Diagonal (F2): 728 kip

Vertical Member (F3): 0 kip

Tension Diagonal (F4): -728 kip

East Chord (F5): 538 kip

The prediction from the test simulation shows that buckling occurs at 104% of the applied test loads. It is again a very acceptable prediction which is within +/-10 percent of the actual test loads. Figure 4.7.231 shows the gradual increase in both out-of-plane and

horizontal displacement at the base of the compression diagonal. At the peak, out-of-plane displacements start being dominant while the horizontal displacement stops increasing.

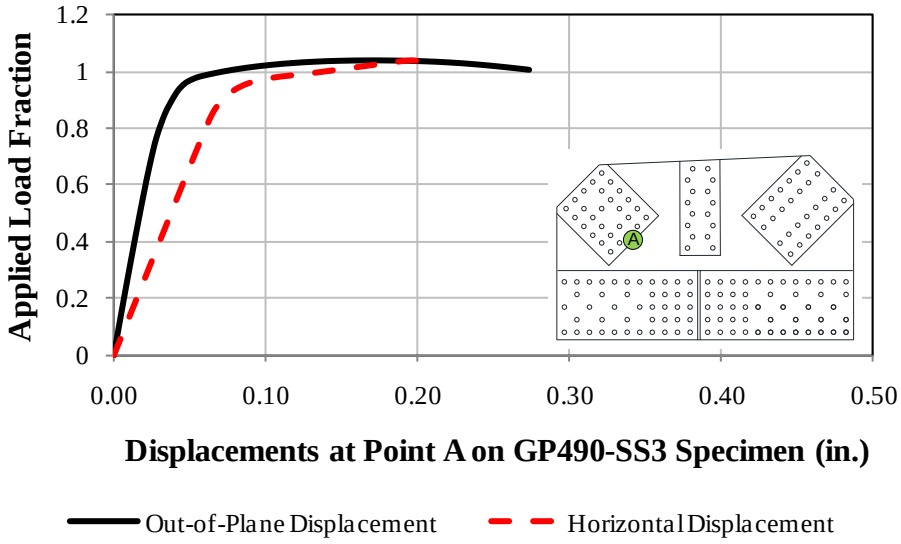

Figure 4.7.231: In-plane vs. out-of-plane displacement comparison for GP490-SS3 specimen

Out-of-plane movement of the compression diagonal is evident in the von Mises stress contours shown in Figure 4.7.232.

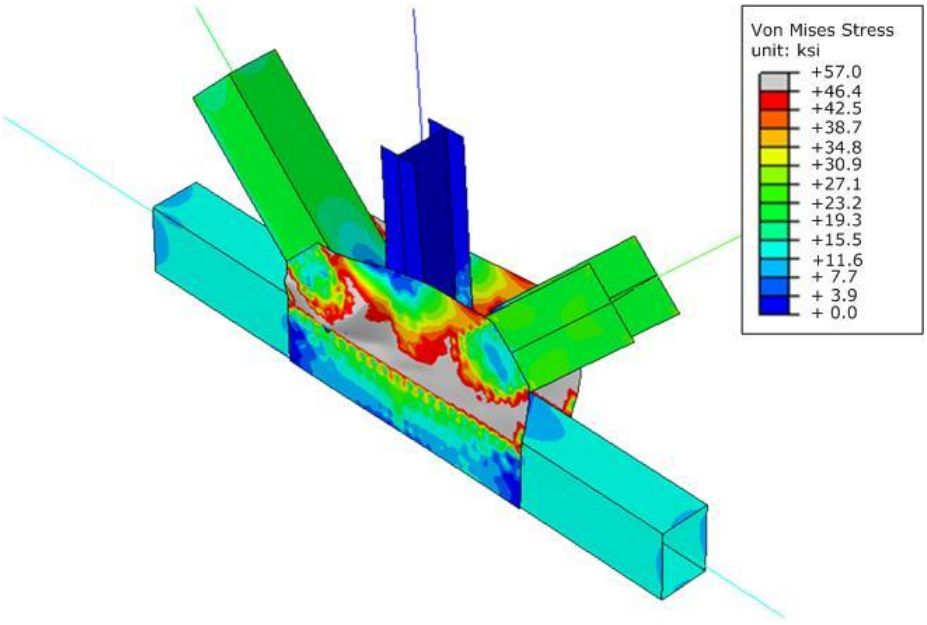

Figure 4.7.232: von Mises stress response contours at the failure (ALF=1.04)

Equivalent plastic strains in Figure 4.7.233 show that the horizontal plane above the chord members reaches yielding at the peak load. Unlike the GP307-SL3 specimen where plasticity exceeds the 4% level at the peak load, buckling of the specimen prevents horizontal plane reaching the 4% plastic strain level.

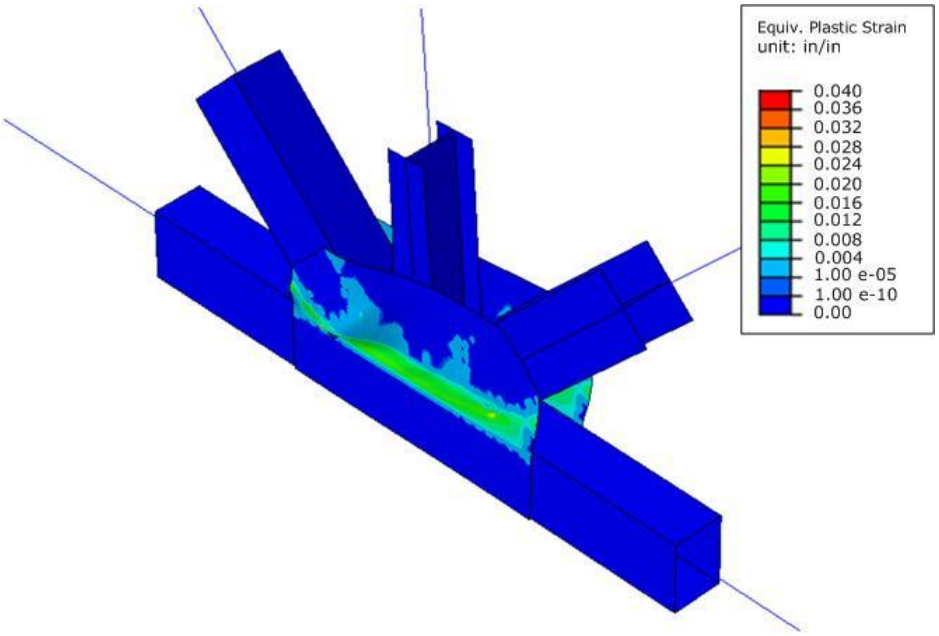

Figure 4.7.233: Equivalent plastic strain response contours at the failure (ALF=1.04)

Tresca strains from DIC and finite element analysis are shown in Figure 4.7.234 at ALF=0.85. Finite element analysis shows slight differences localized at the corner of compression diagonal and along the horizontal plane. Those two areas reach the Tresca strains of more than 1500 με based on the analytical model predictions.

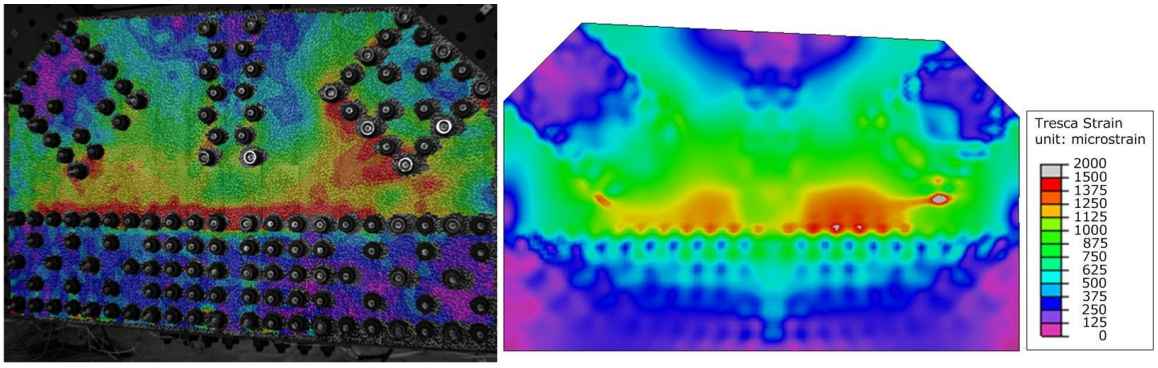

Figure 4.7.234: Comparison between the digital image correlation (left) and FEA (right) at ALF=0.85

Response contours near failure are compared in Figure 4.7.235. Tresca strains from the analysis are at approximately 100% of the test loads applied in the model. Maximum values from both test and analyses are close to each other. DIC data shows high strains at the base of the compression diagonal at the instant of gusset plate buckling. In the GP307-SL3 specimen where shear failure is observed, the Tresca strains reach up to 15000 με along the horizontal plane. However, the GP490-SS3 specimen reach its buckling capacity without being able to use its reserved shear capacity as presented in DIC test data.

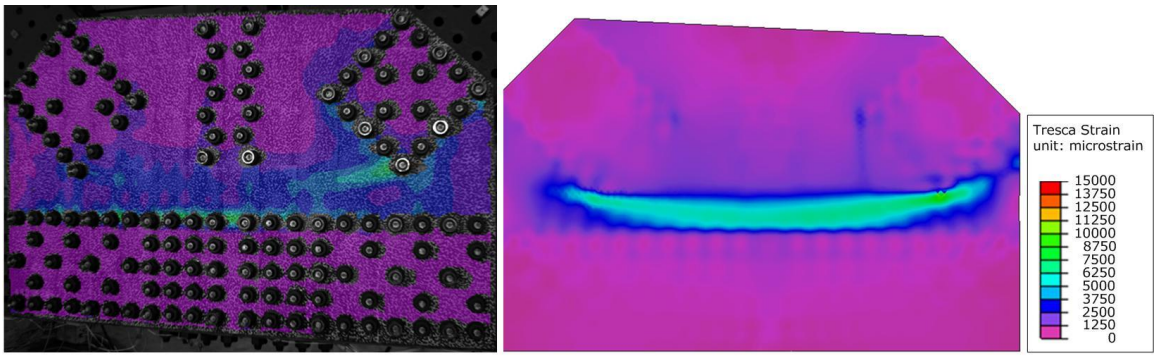

Figure 4.7.235: Comparison between the digital image correlation (left) and FEA (right) just before the failure

4.7.3.5. GP490-LS3-1 Specimen

The GP490-LS3-1 specimen was the replicate of the original GP490-LS3 specimen. This specimen was used to run the test up to its failure using the corresponding initial imperfections and nonlinear material properties. Load combination 14 from Table 4.6.4 was the load combination for this specimen with the following reference loads:

Compression Diagonal (F2): 600 kip
Vertical Member (F3): 282 kip
Tension Diagonal (F4): -1000 kip
East Chord (F5): 600 kip

The intent of selecting this load combination was keeping the tension diagonal load much higher than the compression diagonal to see if the failure mode moves to the tension diagonal side of the connection. However, failure occurred with side-sway buckling of the gusset plate on the compression diagonal as shown in Figure 4.7.236 with the following applied loads on the members:

Compression Diagonal (F2): 527 kip
Vertical Member (F3): 248 kip
Tension Diagonal (F4): -881 kip
East Chord (F5): 529 kip

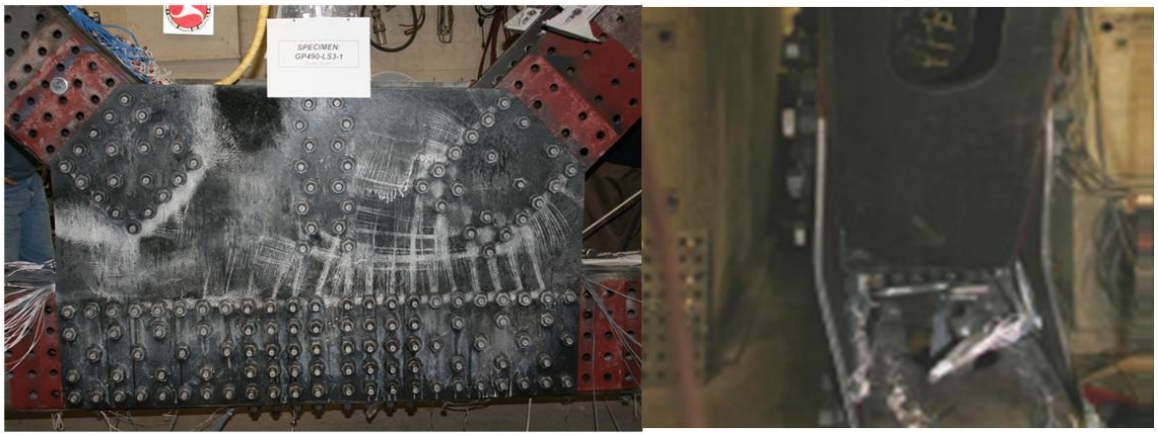

Figure 4.7.236: Post-test photo of the GP490-LS3 specimen. Buckled shape of the gusset plate and yielding pattern is shown (compression diagonal is on the left)

The prediction from the finite element analysis shows that finite element reaches up to 97% of the applied test loads. Displacements on the gusset plate are shown in Figure 4.7.237. In-plane displacements are comparatively smaller than the out-of-plane displacements for this specimen which also becomes the sign of buckling failure of the specimen.

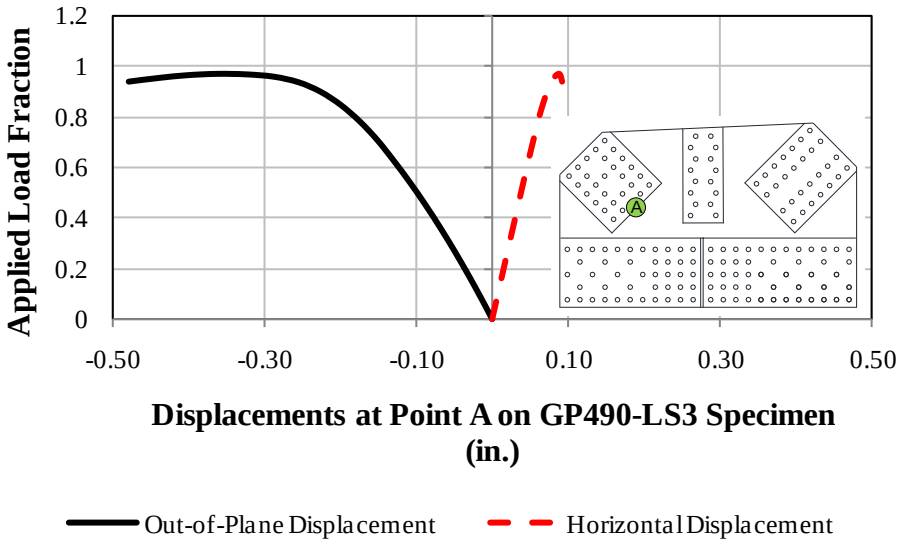

Figure 4.7.237: In-plane vs. out-of-plane displacement comparison for GP490-LS3 specimen

This analytical result is only 3% lower than the experiment which can be a very reasonable estimate. The gusset plate in this connection has static yield strength of 45.9 ksi. The yielding pattern from the sugar coating on the gusset plate is captured very well in the finite element analysis. von Mises response contours in Figure 4.7.238 and equivalent plastic strain contours in Figure 4.7.239 match the yielding pattern and out-of-plane movement of the compression diagonal at the peak load.

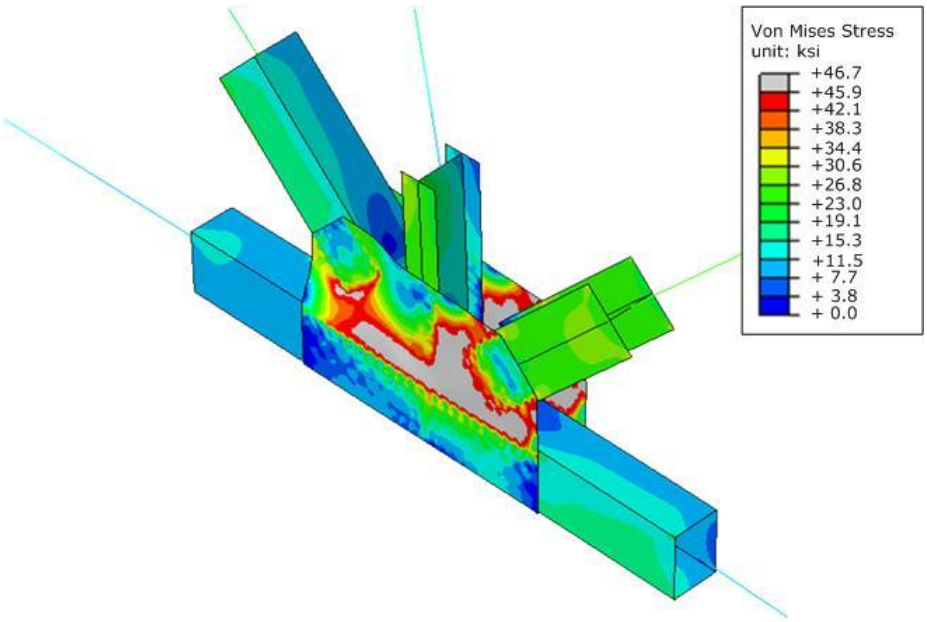

Figure 4.7.238: von Mises stress response contours at the failure (ALF=0.97)

Since the tension diagonal has much higher load, 67% higher than compression diagonal, a yielding pattern is obviously obtained around the tension diagonal. For this specimen, the gap between the corner of the compression diagonal and chord member is larger than for the GP490-SS3 specimen. Thus, the tendency to fail in buckling for the GP490-LS3-1 specimen is an expected result. However, even with the higher tension diagonal load on this specimen, gusset plate buckling still becomes the failure mode.

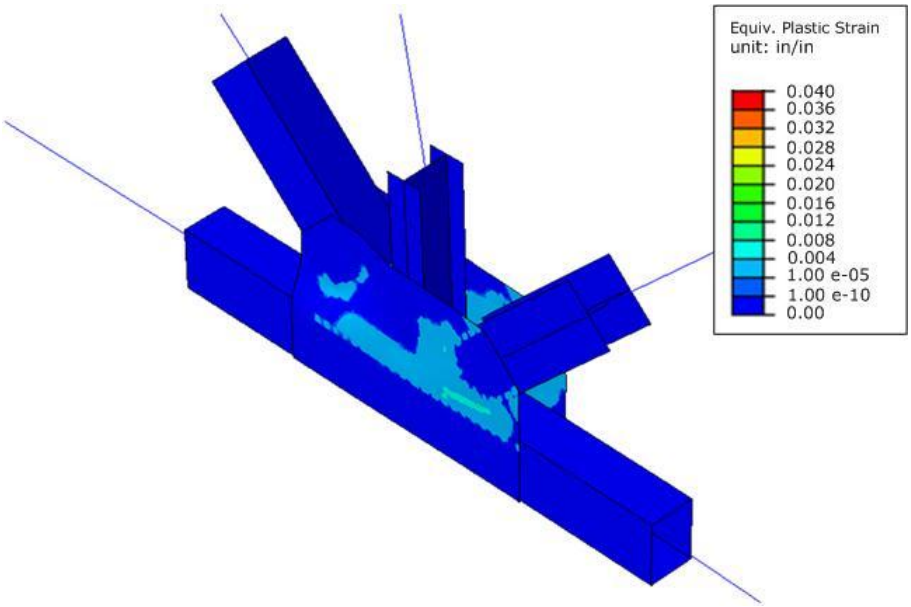

Figure 4.7.239: Equivalent plastic strain response contours at the failure (ALF=0.97)

In addition, test data is compared with the finite element analysis at two different load levels. Tresca strains at ALF=0.78 are shown in Figure 4.7.240. Although the corners of the compression diagonal and the local area above the chord member show values larger than the DIC data, the overall trend in response is captured by the analytical model.

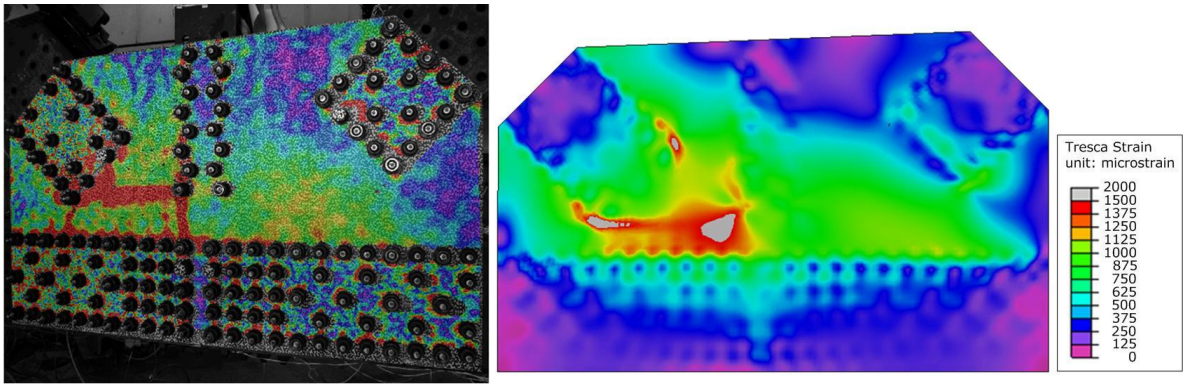

Figure 4.7.240: Comparison between the digital image correlation (left) and FEA (right) at ALF=0.78

The response near failure of the specimen is compared in Figure 4.7.241. The yield lines observed from the sugar coating on the gusset plate at the failure the specimen can also be seen in both DIC and analytical model predictions. Finite element analysis is a more continuous and smooth prediction compared to the DIC data.

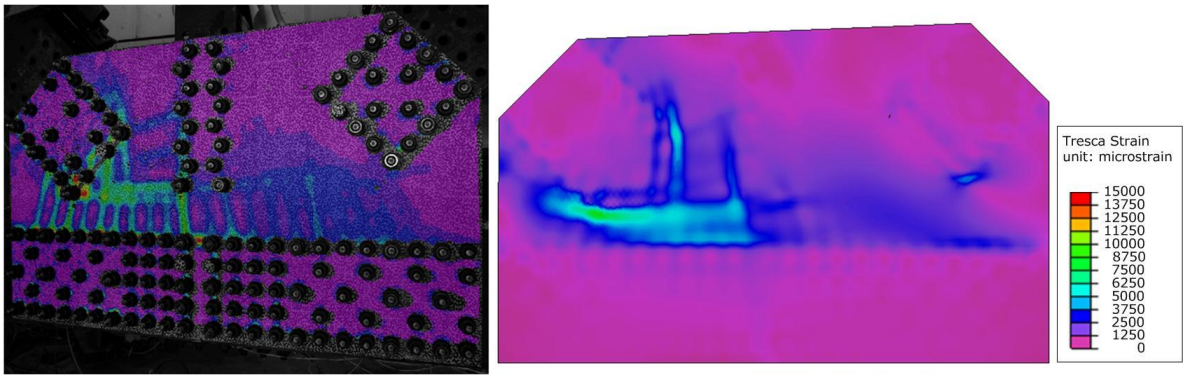

Figure 4.7.241: Comparison between the digital image correlation (left) and FEA (right) just before the failure

4.7.3.6. Summary of the Test Simulation Results

To summarize the finite element analysis results, static yield strengths for each connection and applied load fraction from the finite element analysis corresponding to the

failure of each test specimen are tabulated in Table 4.7.11. The values vary between 0.94 and 1.10. The average of the five analyses is 1.02 with a standard deviation of 0.066. Considering the testing conditions, initial imperfections and material properties as the significant factors, these results are very convincing in terms of validating the finite element models in both elastic and post-elastic range.

Table 4.7.11: Comparison of the finite element analysis results with the experiments

Specimen	Yield Strength (ksi)	F2 (kip)	F3 (kip)	F4 (kip)	F5 (kip)	Failure Mode	P_{FEA}/P_{test}
GP307-SS3	36.4	716	-141	-507	520	Buckling	0.94
GP307-LS3	48.2	796	-280	-405	-290	Buckling	1.10
GP307-SL3	46.6	946	0	-929	706	Shear	1.06
GP490-SS3	46.4	728	0	-728	538	Buckling	1.04
GP490-LS3-1	45.9	527	248	-881	529	Buckling	0.97
						Average	**1.02**
						Standard Deviation	**0.066**

CHAPTER V : ANALYTICAL PARAMETRIC STUDIES

5.1. Introduction

The discussion on the parametric study cases in this chapter parallels the more detailed description given in the draft project report (White et. al, 2011). As part of this research, parametric study joints are modeled and analyzed to capture the gusset plate limit states. In contrast to the test specimens, these parametric study joints utilize both unchamfered and chamfered members.

Table 5.1.1 and Figure 5.2.1 show the nomenclature and geometry of the 20 basic chamfered joints used in these studies. In addition to these 20 cases, an additional five cases are created by removing the vertical members of the unchamfered test specimens discussed in Chapter 4, and five more unchamfered cases are created by selecting five of the 20 chamfered joints and creating similar unchamfered cases. Thus a total of 10 additional unchamfered cases are modeled as shown in Table 5.1.2. Figure 5.1.1 shows example chamfered and unchamfered gusset plate connections for a given joint.

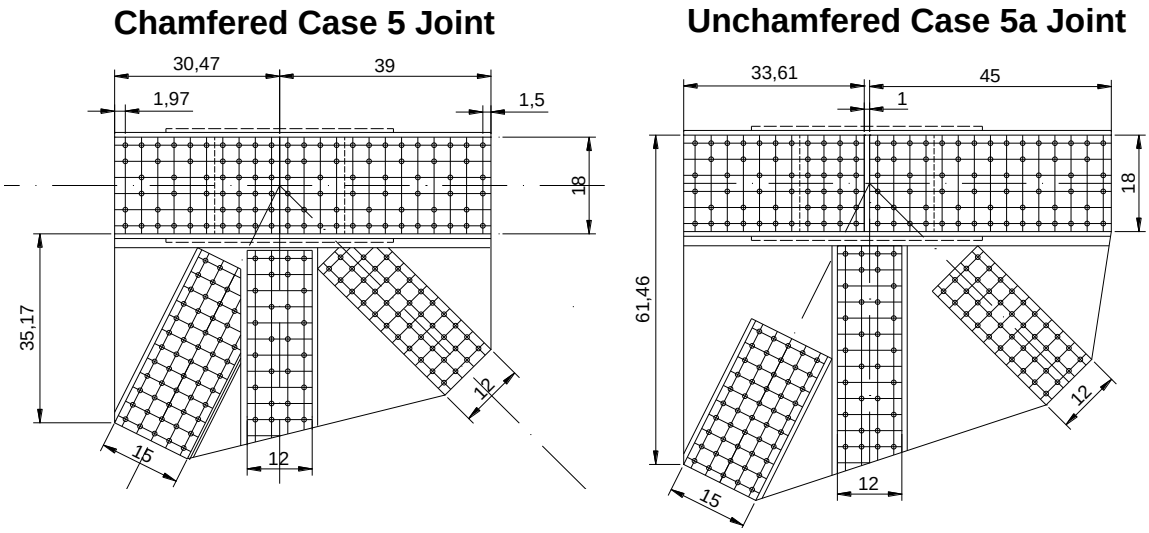

Figure 5.1.1: Chamfered vs. unchamfered connections

In addition, the above parametric studies are extended by changing the gusset plate thicknesses for the test specimens and selected joints from the parametric study cases. Considering the time and size of the analysis models, only the highlighted cases in Table 5.1.1 and Table 5.1.2 are included in these further studies. These joints are selected

based on the observed failure modes and applicability of the data points from a specific joint in the validation of the proposed design recommendations. The studies reported herein thus consist of a total of approximately 150 non-linear FE runs. The size of the models ranged from 300,000 to 800,000 degrees of freedom and included both initial imperfections and out-of-plumbness. No residual stresses are included as they are deemed to have only a small effect on the ultimate strength of the connections.

Table 5.1.1: Twenty parametric cases with chamfered members

Bridge Configuration	**Case**	**Joint Location**
Warren truss with vertical joints	1	at mid-span
	2	
	3	at pier
	4	
	5	near pier
	6	
	7	at inflection point
	8	
Pratt truss joints	9	near pier
	10	
Warren truss without vertical joints	11	at mid-span
	12	at pier
	13	near pier
	14	at inflection point
Other joints (special cases)	15	at pier
	16	
	17	at pier
	18	
	19	at pier
	20	

Table 5.1.2: Ten parametric cases with chamfered members

Bridge Configuration	Case	Joint Location
Warren truss with vertical joints	5-a	near pier
	6-a	
	8-a	at inflection point
Warren truss without vertical joints	13-a	near pier
	14-a	at inflection point
	GP307-SS3-a	test specimens
	GP307-LS3-a	
	GP307-SL3-a	
	GP490-SS3-a	
	GP490-LS3-a	

5.2. Bridge Configurations

Based on an examination of the 20 bridge plans collected for this project, it appears that longer bridges with continuous spans generally have Warren truss configurations with or without vertical members, while simple span bridges utilize Pratt truss configurations. Hence, three main truss bridge configurations are selected to conduct the finite element analyses and further parametric studies: 1) Warren trusses with vertical members, 2) Pratt trusses, and 3) Warren trusses without vertical members. In addition to typical joints for these three bridge configurations, six additional test joints are designed to incorporate different geometric configurations, such as corner joints, joints that have positive angle between chords and joints that have negative angle between chords. Figure 5.2.1 shows a summary of bridge configurations that are designed for the parametric studies. Similar to the preliminary studies performed on the four representative joints described in Chapter 3, all these test configurations, except the corner joints, are modeled as two panel truss systems (Figure 5.2.1).

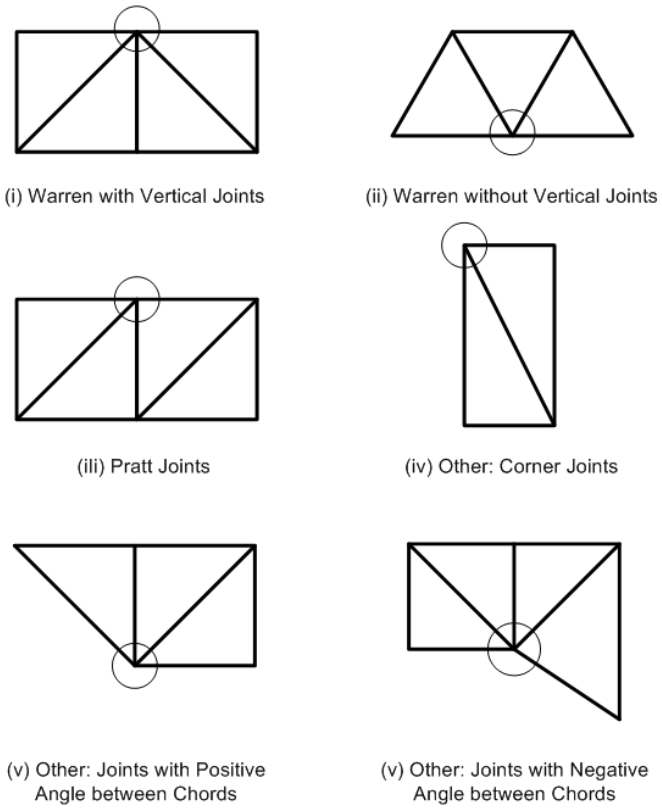

Figure 5.2.1: Summary of bridge configurations of gusset plate joints

5.3. Applied Loads

A summary of the 20 parametric load cases are shown in Figure 5.3.1 through Figure 5.3.4. The main criterion to determine the applied loads on each joint is the location of the joints in a real truss bridge. For Warren configurations with and without vertical members, four types of joint locations are selected: (1) joints at midspan, (2) joints at a pier, (3) joints near a pier, and (4) joints at inflection points. For Pratt truss configurations, only joints near a pier are studied because these joints are generally found in single span bridges. In general, Pratt joints at mid-span and at the pier locations are similar to those in Warren trusses with vertical joints.

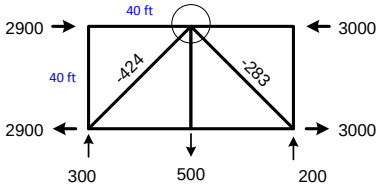

(i) Case 1, Joint at midspan

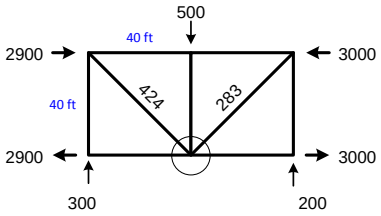

(ii) Case 2, Joint at midspan

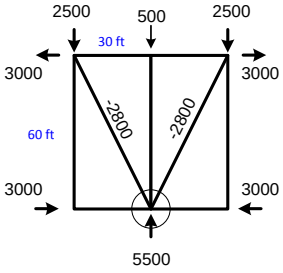

(iii) Case 3, Joint at pier

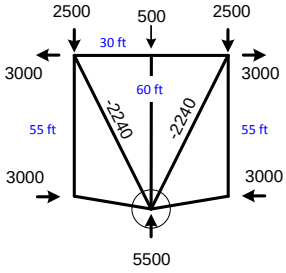

(iv) Case 4, Joint at pier

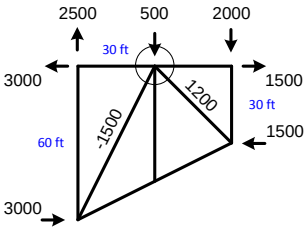

(v) Case 5, Joint near pier

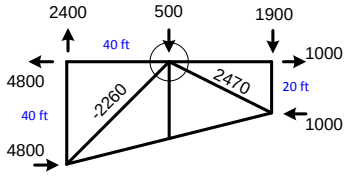

(vi) Case 6, Joint near pier

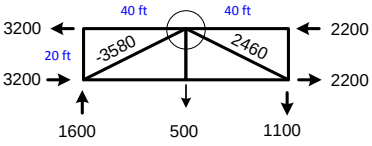

(vii) Case 7, Joint at inflection point

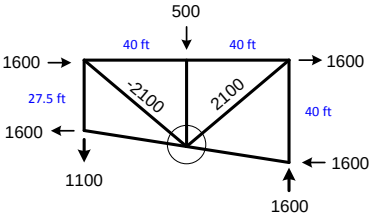

(viii) Case 8, Joint at inflection point

Figure 5.3.1: Warren truss with vertical joint configurations

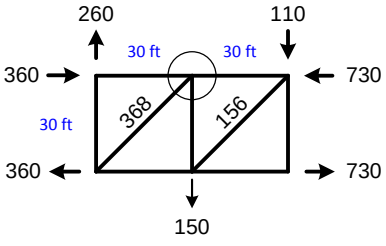

(i) Case 9, Joint near pier

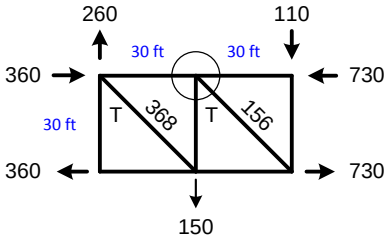

(ii) Case 10, Joint near pier

Figure 5.3.2: Pratt truss joint configurations

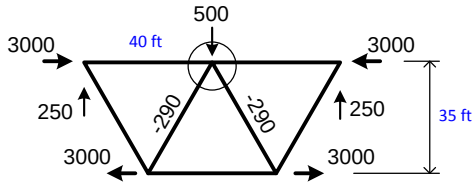

(i) Case 11, Joint at midspan

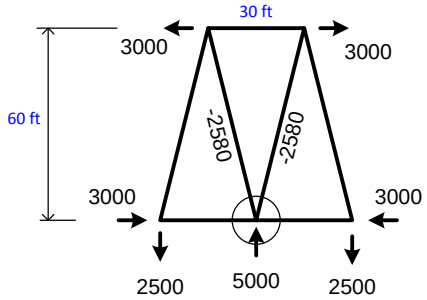

(ii) Case 12, Joint at pier

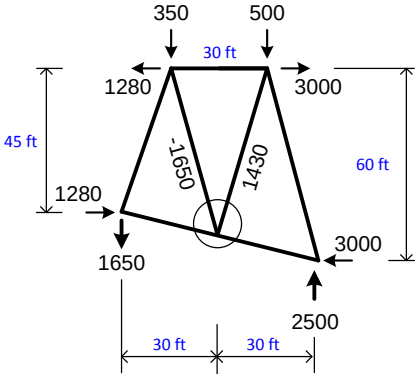

(iii) Case 13, Joint near pier

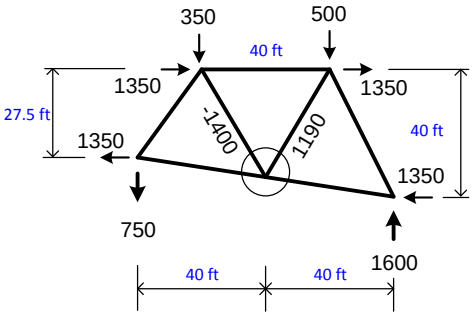

(iv) Case 14, Joint at inflection point

Figure 5.3.3: Warren truss without vertical joint configurations

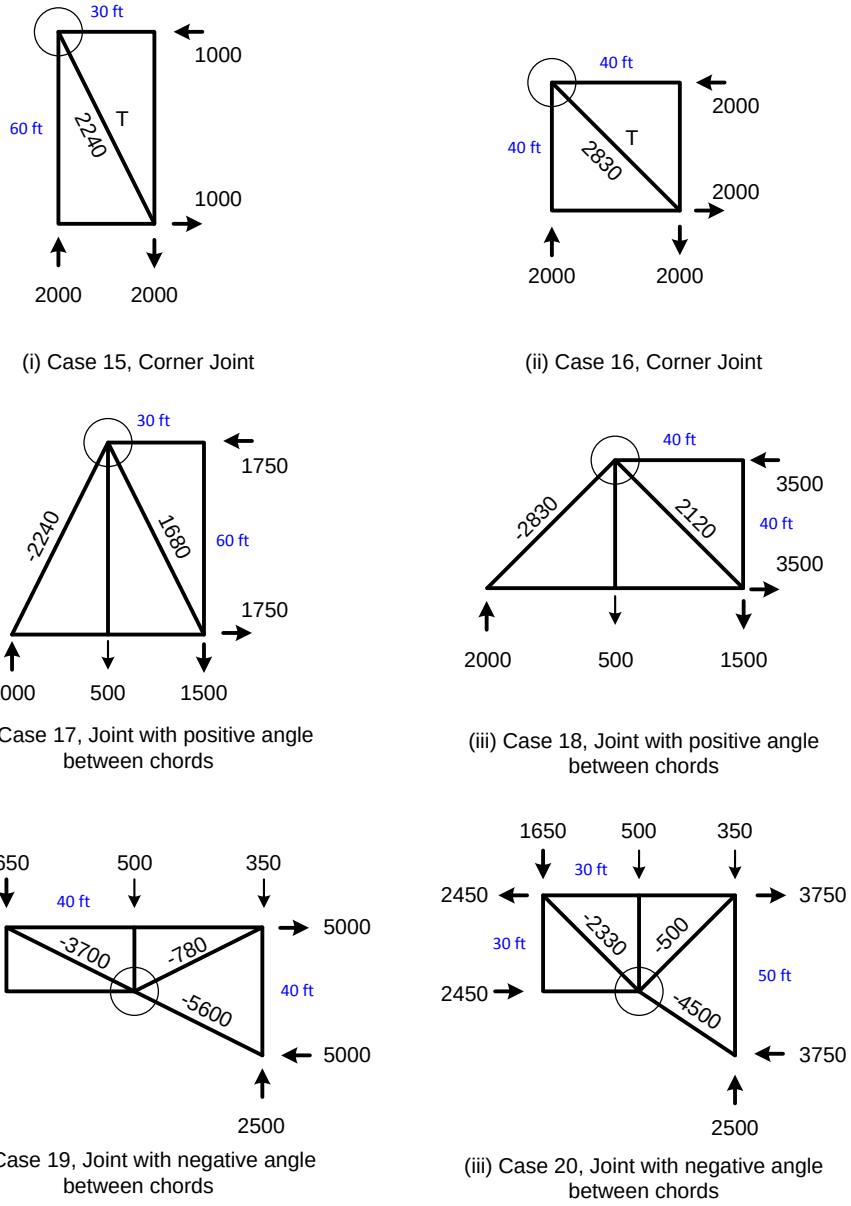

Figure 5.3.4: Other joint configurations

The methodology used to determine the applied loads at each location is discussed next. Detailed Mathcad calculations are provided in the Appendix of the parametric study report (White et. al, 2011).

5.3.1. Joints at Midspan

For joints at midspan, loadings are based on a real truss bridge with three continuous spans (main span length, L_m = 456 ft, and two adjacent span lengths L_a = 266 ft) and four traffic lanes per truss. For this case the chord to shear force ratio C/V at midspan is calculated as follows. The representative bridge has a truss depth at the midspan of d_m=36 ft and a truss panel width of b_p=38 ft. By modeling the main span using a fixed-fixed prismatic beam idealization, the maximum shear at midspan V_{max} and corresponding chord force C_{max}, are computed, For the case with dead load (q_D) applied on the full length of the bridge span, live load from lane loading (q_L) applied on half of the bridge span, and AASHTO design vehicle applied as a concentrated point load (Q_L) at the midspan, V_{max} = 317 kips and C_{max} = 2725 kips. For the case of q_D and q_L on the full span, and Q_L at the midspan, C_{max} = 2926 kips and V_{max} = 278 kips. It can be concluded that at the midspan of longer bridges with L_m/d_m = 12.7, it is reasonable to assume V_{max} = 300 kips and C_{max}/V_{max} = 10. If the bridge is shallower at midspan such that L_m/d_m = 20, the value of C_{max}/V_{max} is 16. In this study, two Warren trusses with vertical joints at the midspan (Cases 1 and 2 shown in Figure 5.3.1) have V_{max} = 300 kips and the corresponding $C_{max} = V_{max} \times (C_{max}/V_{max} = 10)$ = 3000 kips. Table 5.3.1 summarizes the C_{max}/V_{max} values for all the 20 joints shown in Figure 5.3.1 through Figure 5.3.4.

The maximum load effect Q_{tot} transferred directly to a truss panel point is Q_{tot} = 500 kips. For Warren trusses without vertical joints at midspan (Case 11 in Figure 5.3.3), V_{max} = 250 kips due to the symmetry of the joint geometry and Q_{tot} = 500 kips is applied at the joint. In addition, C_{max} is determined to be 3000 kips as for Cases 1 and 2. As a result, the C_{max}/V_{max} value for Case 11 shown in Figure 5.3.3 is 12.

5.3.2. Joints at Pier

Using the representative bridge described above, the maximum shear force at the piers (V_{max}), and the C_{max}/V_{max} ratio at the piers for bridges with L_m/d_p = 7.6 are determined. The example bridge has a truss depth at the pier d_p equal to 60 ft. To calculate the C_{max}/V_{max} ratios at the pier, two sets of moment and shear force are calculated: 1) the maximum moment at the pier and corresponding shear force caused by q_D and q_L applied on the full main span and Q_L applied at the midspan and 2) the

maximum shear force at the pier and corresponding moment caused by q_D and q_L applied on the full main span and Q_L applied adjacent to the pier. Based on these two cases, a value of V_{max} = 2500 kips and a value of C_{max}/V_{max} = 1.2 are determined for bridges with L_m/d_p = 7.6. Two Warren trusses with vertical joints (Case 3 and Case 4) and one Warren without vertical joint (Case 12) at the pier location have C_{max}/V_{max} = 1.2 as shown in Table 5.3.1.

5.3.3. Joints near Pier

The Warren truss with vertical joint at the pier has 2500 kips as a shear and 3000 kips as a chord force (Case 3 in Figure 5.3.1). A Warren truss with a vertical joint near the pier (Case 5) is assumed to be right next to Case 3. As a result, there are V_{left} = 2500 kips and C_{left} = 3000 kips on the left hand side of the panel system. Since the maximum load effect Q_{tot} of 500 kips is applied at the joint, the shear force on the right hand side of the panel system V_{right} is 2000 kips and the rest of applied loadings are calculated accordingly.

The applied loadings for the two Pratt truss joints studied in this research are determined based on an example bridge with a span length L_{total} = 240 ft, one traffic lane per truss, a truss depth at the pier d_p = 30 ft, and a truss panel width b_p = 30 ft. To calculate the appropriate V_{max} and C/V values, it is assumed that Pratt truss joints near the pier are located at $L_{total}/4$ of a simple span bridge. By considering two loading scenarios of 1) the maximum moment at $L_{total}/4$ and the corresponding shear force, 2) the maximum shear force at $L_{total}/4$ and the corresponding moment, it is found that a reasonable value of V_{max} is 260 kips with C_{max}/V_{max} = 2.8 for this representative bridge with L_{total}/d_m = 8.

5.3.4. Joints at Inflection Point

Based on the fixed-fixed prismatic beam idealization of the main span of the larger bridge considered in the initial discussions above, the inflection point is located at $0.21L_m$ from the supports where L_m is the length of the main span. As indicated above, for the example bridge with three continuous spans, L_m was 456 ft and d_i was 45 ft. A maximum shear force at the inflection point (V_{max}) of 1600 kips is determined for the test

joints. The corresponding applied loadings are calculated using Q_{tot} = 500 kips and ΣM = 0 at the joint. Table 5.3.1 shows the resulting C_{max}/V_{max} values for joints at the inflection point.

5.3.5. Other Joints

Corner joints and joints with positive and negative angles between chords are assumed to be located at the end of a truss bridge and the chord and shear forces of these joints were determined accordingly. Due to the complex geometries of these joints, C_{max}/V_{max} values are varied from 0.5 to 2.0 as shown in Table 5.3.1.

Table 5.3.1: Summary of C_{max}/V_{max} and V_{max} values

Bridge Configuration	**Joint Location**	**Case**	**C_{max}/V_{max}**	**V_{max} (kips)**	**C_{max} (kips)**
Warren truss with vertical joints	at mid-span	1	10	300	3000
		2	10	300	3000
	at pier	3	1.2	2500	3000
		4	1.2	2500	3000
	near pier	5	1.2	2500	3000
		6	2	2400	4800
	at inflection point	7	2	1600	3200
		8	1	1600	1600
Pratt truss joints	near pier	9	2.8	260	730
		10	2.8	260	730
Warren truss without vertical joints	at mid-span	11	12	250	3000
	at pier	12	1.2	2500	3000
	near pier	13	1.2	2500	3000
	at inflection point	14	0.84	1600	1350
Corner joints	at pier	15	0.5	2000	1000
		16	1	2000	2000
Joints w/ positive angle between chords	at pier	17	0.875	2000	1750
		18	1.75	2000	3500
Joints w/ negative angle between chords	at pier	19	2	2500	5000
		20	1.5	2500	3750

5.4. Member Design

Members are designed based on the loads determined for each panel truss system. Similar to the test specimens, box-sections are used for all the chord members and compression members, and I-sections are used for tension members. For the larger bridges shown in Figure 5.3.1, Figure 5.3.3, and Figure 5.3.4, five box-sections and three I-sections are designed to resist the selected ranges of compression and tension forces for the given joint geometries. The sections are given in Table 5.4.1. For these 18 cases, a full out-of-plane depth for all the members is taken as 21 inches, based on the example truss bridge used to calculate the maximum chord and shear forces. For the Pratt truss joints in Figure 5.3.2, three box-sections and two I-sections are designed. The section properties for those members are shown in Table 5.4.2. The corresponding tension yielding and tension rupture strengths, and compressive strengths for the range of member lengths used in the models (from 360 inches to 805 inches) are also shown in Table 5.4.1 and Table 5.4.2.

Table 5.4.1: Summary of member sections for joints other than Pratt joints

(a) Box Sections

Box Sections	Dimensions				Tension Yielding ($\varphi_y = 0.95$)	Tension Rupture ($\varphi_u = 0.80$)	Compressive Strength ($\varphi_c = 0.9$)	
	web		cover plate					
	b_i (in)	t_i (in)	b_o (in)	t_o (in)	P_y (kips)	P_r (kips)	L (in)	P_c (kips)
B1	12.00	0.750	20.250	0.8125	2418	2374	360 - 805	964 - 1927
B2	15.00	0.875	20.125	0.875	2920	2798		1512 - 2451
B3	18.00	1.375	19.625	0.875	3983	3609		2270 - 3408
B4	21.00	1.500	19.5	1.25	5308	4856		3521 - 4683
B5	24.00	2.0	19	1.5	7267	6500		5133 - 6492

Table 5.4.1 (continued): Summary of member sections for joints other than Pratt joints

(b) I-Sections

I Sections	Dimensions				Tension Yielding ($\varphi_y = 0.95$)	Tension Rupture ($\varphi_u = 0.80$)
	flange		web			
	b_f (in)	t_f (in)	D_w (in)	t_w (in)	P_y (kips)	P_r (kips)
I1	12	0.875	19.25	0.75	1683	1524
I2	18	1.375	18.25	1.125	3326	2891
I3	21	1.75	17.5	1.5	4738	4231

Table 5.4.2: Summary of member sections for Pratt joints

(a) Box Sections

Box Sections	Dimensions				Tension Yielding ($\varphi_y = 0.95$)	Tension Rupture ($\varphi_u = 0.80$)	Compressive Strength ($\varphi_c = 0.9$)	
	web		cover plate					
	b_i (in)	t_i (in)	b_o (in)	t_o (in)	P_y (kips)	P_r (kips)	L (in)	P_c (kips)
B1s	8.00	0.375	11.625	0.5	837	826	360 - 805	114 - 538
B2s	12.00	0.625	11.375	0.625	1388	1292		464 - 1067
B3s	15.00	0.75	11.250	0.625	1737	1560		769 - 1413

(b) I-Sections

I Sections	Dimensions				Tension Yielding ($\varphi_y = 0.95$)	Tension Rupture ($\varphi_u = 0.80$)
	flange		web			
	b_f (in)	t_f (in)	D_w (in)	t_w (in)	P_y (kips)	P_r (kips)
I1s	8	0.5625	10.875	0.5	686	648
I2s	10	0.625	10.75	0.625	913	829

5.5. Gusset Plate Design for the Parametric Cases

For the 20 joints created for the parametric studies, all the diagonals are chamfered as much as possible. This follows the conventional connection design philosophy intended to result in the smallest practicable, or "compact", connection. As shown in Figure 5.5.1 and also following the conventional design approach, the center lines of all the members intersect at a single point called "work point" in order to eliminate any significant eccentricities. All chord members have the same cross-sections and both diagonals are chamfered up to the point where they have only two fasteners at the end.

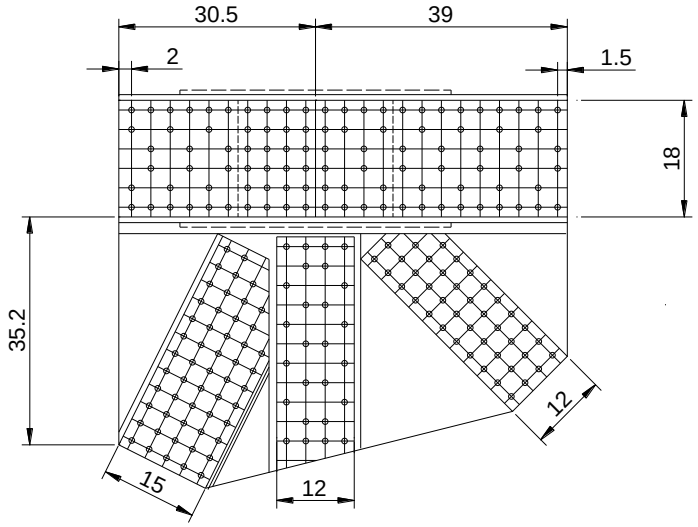

Figure 5.5.1: Typical gusset plate design (Case 5)

The main design rules and assumptions used to create the gusset plates for the parametric study cases can be listed as:

1) center lines of the members always intersect at a work point,
2) the minimum clearance between members is 1 inch,
3) the width of the gusset plates is always larger where the chord members are connected,
4) any connection should have a minimum of six rows of fasteners,
5) chord members always have the same cross-sections,
6) splice plates are always symmetric about the work point of the given joint,

7) chamfered members have a minimum of two fasteners at the end of members,

8) only 7/8" fasteners are used.

The gusset plate for Case 5 designed based on these rules is shown in Figure 5.5.1. This joint will be used as a typical connection to explain the design procedure in detail:

1) Step 1: Determine the number of fasteners connecting each member to the gusset plate based on the loads shown in Figure 5.3.1 through Figure 5.3.4. It the earlier stages of the parametric study, an A307 bolt strength of R_n=16 kips was used as a lower bound rivet strength to determine the number of fasteners. As already mentioned, A307 bolts were used in the test specimens to represent the older riveted connections. In the later stages of the parametric studies, a new rivet strength curve is obtained by calibrating tension test results of hot driven rivets taken form a number of existing bridges during repair and retrofit operations. For all the cases, the fastener spacing is taken as 3 inches and the minimum edge distance as 1.5 inches. In addition, it is decided to keep the maximum edge distance of fasteners to be around 2.5 inches.

2) Step 2: Calculation of the force transferred to the web and top/bottom splice plates in the joint. It is assumed that the member forces are distributed based on the areas of web and cover plates of the chord members. For example, the design loads of the left and right chord members of Case 5 joint are 3000 kips and 1500 kips respectively (Figure 5.3.1). Since the left chord member force will govern the splice plate designs, only the calculations based on the left chord member are discussed subsequently. Based on the web and flange plate areas of the chord members, the forces transferred through web and flange plates are 1772 kips and 1228 kips.

3) Step 3: Determine the number of fasteners required in double shear to carry the given chord member forces. For Case 5, it is decided to have 24 fasteners (four rows of six fasteners) in double shear between the web splice plates, chord web plates and gusset plates on the left hand side. Using the assumption of the maximum strength of rivets R = 16 kips and the assumption of equal force distributions between fasteners, one web splice plate transfers 24 fasteners × 16 kips = 384 kips on the left hand side. However, for the top and bottom splice plates, none of the fasteners are designed to be in double shear

since they are only connected to the chord flanges. Therefore, a total of 84 fasteners (7 rows of 6 fasteners for each of the top and bottom plate) are needed on top and bottom splice plates on the left hand side to transfer 1228 kips (84 fasteners × 16 kips = 1344 kips).

4) Step 4: Assume member dimensions. For all the cases, the widths of web splice plates are assumed to be 0.5 inches smaller than the depth of chord members. In addition, the widths of both the top and bottom splice plates are assumed to be same as the widths of the cover plates of the chord members. The required area and thickness for the splice plates in each joint are determined based on this procedure (White et. al, 2011).

5.6. Test Simulation Procedures

5.6.1. Simulation Modeling

Figure 5.6.1 shows a typical test simulation model used for the parametric studies. Critical locations in the two-panel systems are referred to as U_1 through U_3 for points on the upper chords and as L_1 through L_3 for points on the lower chords. For all cases, the gusset plate joints under consideration are located either at the U_2 or at L_2 locations. For example, for Case 5 (Figure 5.5.1), the gusset plate joint is located at U_2.

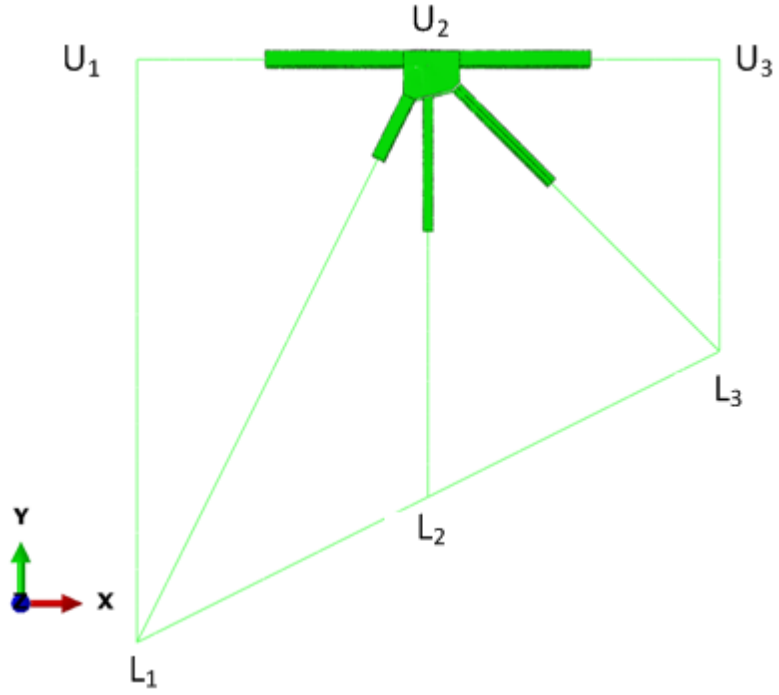

Figure 5.6.1: Typical test simulation model (Case 5)

Test simulations conducted in the current research are performed using the commercial software package ABAQUS (Simulia 2010). For all the cases, gusset plates, splice plates, and certain portions of the members in a given gusset plate joint are modeled using four-node shell elements (S4R). In modeling the truss members, the target is to use shell elements within a length of at least two times the connection length for a given truss member as shown in Figure 5.6.2. However, to increase efficiency of the finite element modeling procedures, member lengths that are modeled using shell elements are set to 200 inches unless otherwise noted. The rest of the truss members outside of the 200 inch-limit and truss members that are not connected to the gusset plate joins are modeled using beam elements (B31). These parts are shown by thin lines in Figure 5.6.2. Multi-point constraints (MPCs) are used to connect a cross-section modeled with shell elements to an end node of beam element. This modeling strategy is very similar to what had been used for the preliminary studies on the four representative joints with two panel systems in Chapter 3.

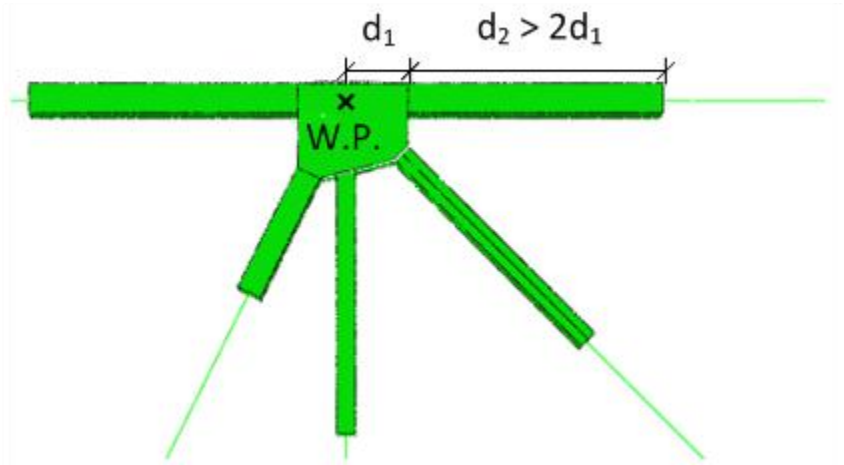

Figure 5.6.2: Shell portion of the right chord member for Case 5

5.6.2. Boundary Conditions

Typical loading and boundary conditions are shown in Figure 5.6.3. All the end nodes of truss members that are on the outside perimeter of two-panel system (L_1 to L_3, U_1, and U_3 for Case 5) are restrained in the out-of-plane direction. For in-plane movements, a simply supported condition is modeled. For Case 5 shown in Figure 5.6.3, horizontal and vertical displacements are restrained at U_1 and a vertical displacement is

restrained at U_3. In addition, an out-of-plane restraint is applied at one node at the center of the top or bottom splice plates, whichever is on the outside of the joint, to prevent the overall out-of-plane movement of the entire joint. In real bridges, this overall out-of-plane movement is larger in joints at midspan.

As shown in Figure 5.6.3, all the loads are applied at the nodes of truss members that are on the outside perimeter of the two-panel system (L_1 to L_3, U_1, and U_3 for Case 5) except for the 500-kip load applied at the vertical member. Whenever there is a load applied at a joint, it was decided to apply this load at the point of the beam element where the shell-element cross-section is attached by a multi-point constraint. By applying this load at the end node of a beam element, computational issues associated with the stress concentrations at the location where the load is applied to the shell element can be avoided in the finite element models.

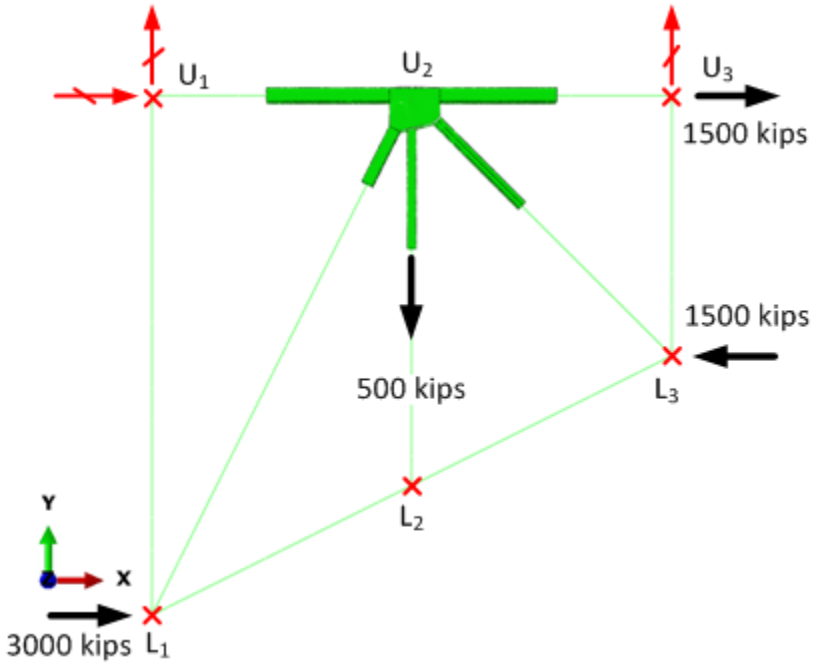

Figure 5.6.3: Typical loading and boundary conditions (Case 5)

5.6.3. Material Properties

Figure 5.6.4 shows the true stress-strain curve for Grade 50 steel that was used in the test simulations. The yield strength used in the test simulations was determined based on 10 % over-strength for a base metal strength and a reduction of 2 ksi from the 0.2 % offset yield strength for a static yield strength. It was observed in the coupon tests

performed for the test specimens that the static yield strength is generally about 2 ksi less than the 0.2 % offset yield strength. Therefore, for Grade 50 steel, the static yield strength F_y is 50 ksi × 1.10 – 2 ksi = 53 ksi.

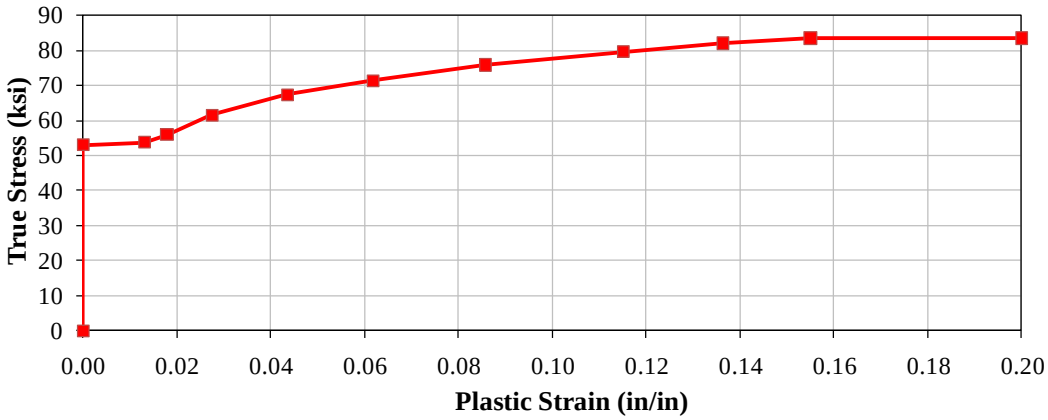

Figure 5.6.4: Grade 50 steel material properties used in the simulation models for parametric study joints

The true stress-strain curve shown in Figure 5.6.4 is was a fit to data from a coupon test performed for the one of experimental test specimen, GP307-LS3. GP307-LS3 specimen has a yield strength of 48.2 ksi. The truss stress-strain curve is obtained by scaling the data so that the true yield stress is 53.1 ksi. This 53.1 ksi true stress corresponds to the target engineering stress of 53 ksi.

For all the test simulations, the fasteners are modeled explicitly with nonlinear strength properties. As mentioned before, a new rivet strength curve was obtained by calibrating tension test results of hot driven rivets**.** Figure 5.6.5 shows the nonlinear strength curve for hot driven rivets used in the finite element models of the parametric study cases.

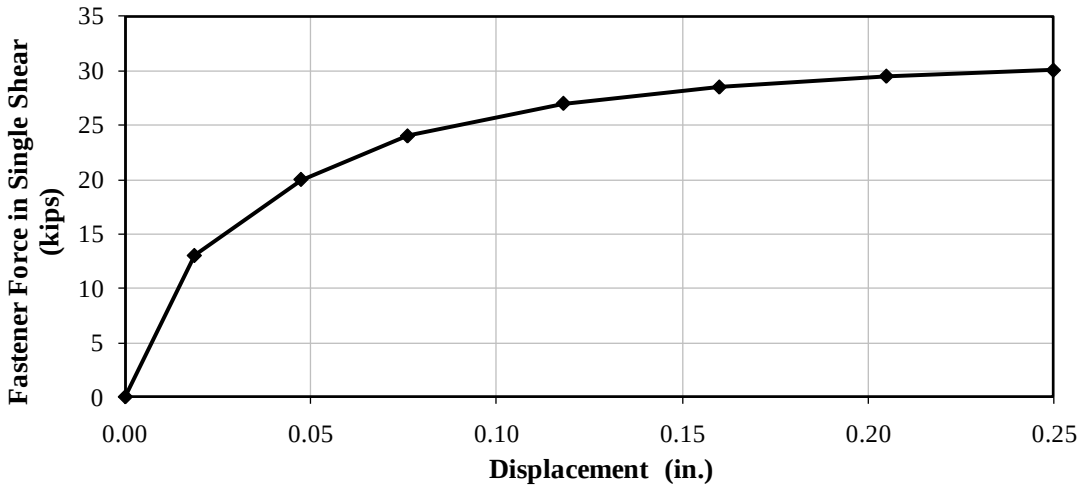

Figure 5.6.5: Fastener force vs. displacement relationship in single shear for the hot driven rivets (7/8" diameter)

5.6.4. Initial Imperfections

The initial imperfections are created using a similar methodology to that discussed in Section 3.1.3. For the initial imperfection analysis of the parametric cases, pressure loads are applied on the gusset plates so that an out-of-straightness of gusset plates on the compression diagonal side is generated and out-of-plane displacements are applied at the end of the compression diagonal so that an initial out-of-plane plumbness of the member is also generated. Figure 5.6.6 shows a deformed shape from the linear elastic analysis performed to generate the initial geometric imperfections for Case 5.

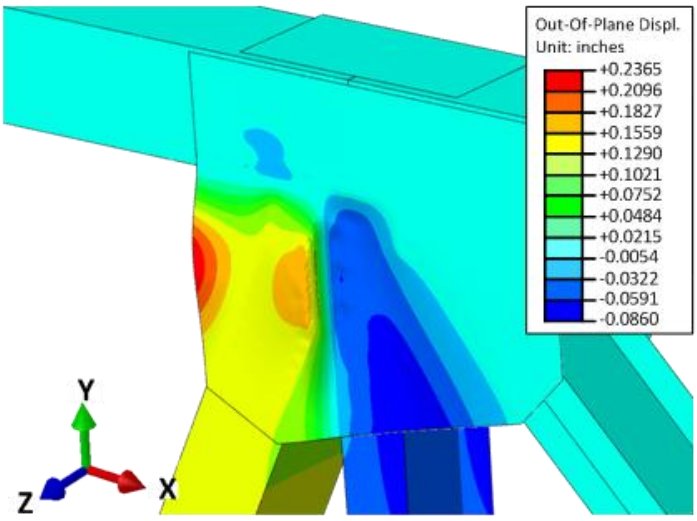

Figure 5.6.6: Typical initial imperfection shape of the gusset plates in the parametric study simulations

After the deformed shape is obtained from this analysis, the deformations are scaled such that the maximum magnitudes of the out-of-straightness of gusset plates and the out-of-plumbness of a diagonal member match a selected maximum imperfection limit. The selected limits are: 1) $L_{max}/150$ for the maximum out-of-straightness of gusset plates, where L_{max} is the maximum length of free edges adjacent to the compression diagonal and 2) $0.1L_{gap}$ for the maximum out-of-plumbness of the compression diagonal, where L_{gap} is the smallest length of the gap between the compression diagonal and the adjacent members. For Case 5 shown in Figure 5.6.6, the vertical free edge between the left chord and the compression diagonal gives L_{max} of 35.17 inches. Therefore, the maximum out-of-straightness of the gusset plate is scaled to be 0.235 inches. In addition, L_{gap} is 1 inch between the compression diagonal and the vertical member. Therefore, a maximum out-of-plumbness of the compression diagonal of 0.1 inch is used. The deformations shown are then scaled to meet the calculated limits and used as the initial imperfection shape in the final analysis of Case 5.

5.7. Test Simulation Results of the Chamfered Parametric Cases

This section briefly discusses the results of the nonlinear finite element analysis performed on the first fourteen parametric that are used in the design recommendation studies described in Chapter 6 of this dissertation. The special cases are discussed in the parametric study report of this research (White et al., 2011). For the cases under consideration, the required gusset plate thicknesses are determined based on the current FHWA guidance checks as discussed in the parametric study report (White et. al, 2011). The thickness chosen is based on the desire to achieve different failure modes. For each case, maximum applied load fraction or the defined failure load is determined based on the same criteria used for the four representative bridge joint analyses as described in Section 3.2. Hence, the maximum load capacity of a given test configuration is defined as the load level at which a test first reaches: (a) 4% maximum equivalent plastic strain at mid-thickness of the plates, or (b) the peak load.

5.7.1. Warren Trusses with Vertical Members

5.7.1.1. Case 1 (WV-M-01)

This is an upper chord joint at the midspan location of a truss bridge. The gusset plate geometry and the applied member loads are shown in Figure 5.7.1. For this joint the gusset plate is 0.400 inch thick. Chords are in compression and have considerably higher compressive forces than the diagonal members.

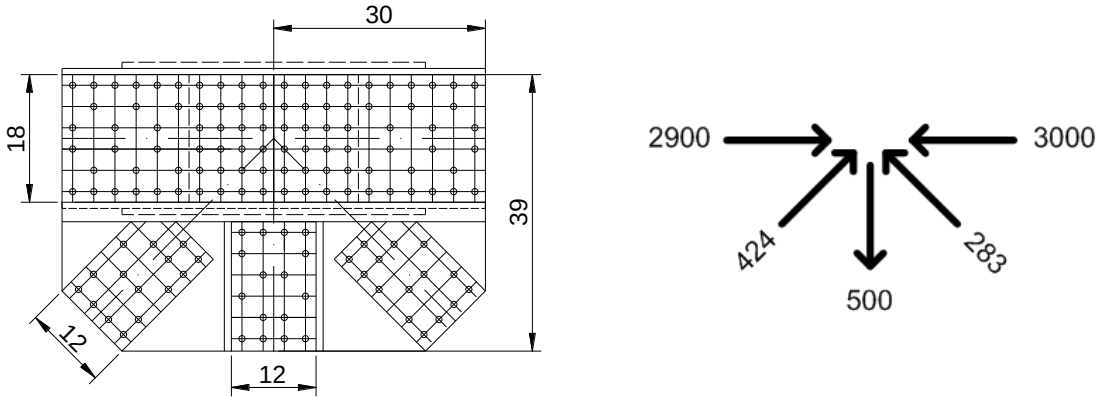

Figure 5.7.1: Case 1 gusset plate details and applied reference loads

The maximum joint capacity is governed by the 4% equivalent plastic strain criterion (PEEQ) as shown in Table 5.7.1. The joint reaches its limit at ALF=1.37 (137% of the applied reference loads shown in Figure 5.7.1).

Table 5.7.1: Maximum applied load fraction (ALF) values for Case 1

	4% PEEQ ALF	Peak ALF
Case 1 (WV-M-01)	**1.37**	1.71

Figure 5.7.2 shows the von Mises stress response contours with a deformation scale factor of 5 at ALF=1.37. The red contours indicate the areas that are close to the yield strength, while the grey contours show the areas that exceeded the yield strength of the gusset plate (F_y =53 ksi).

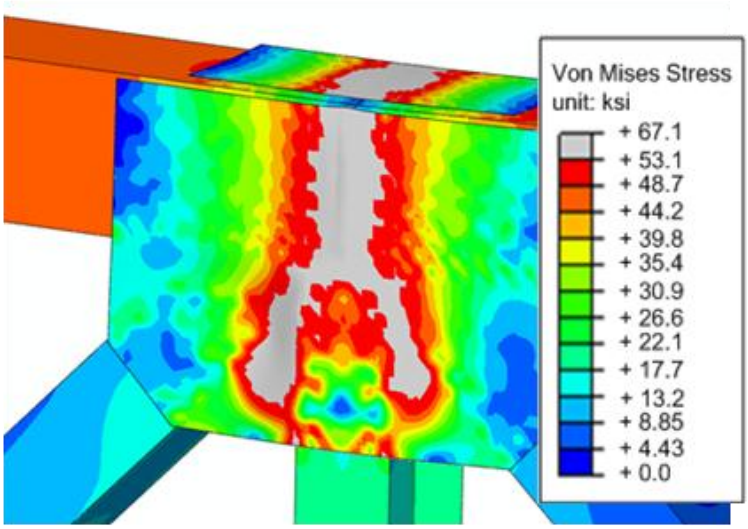

Figure 5.7.2: von Mises stress response contours for Case 1 at ALF=1.37 (Deformation scale factor=5)

The corresponding equivalent plastic strain contours are shown in Figure 5.7.3. Any contour other than dark blue shows the yielded areas in the gusset plate. Due to the high compression forces in the chord members, plastification takes place within the chord splice region including the splice plates.

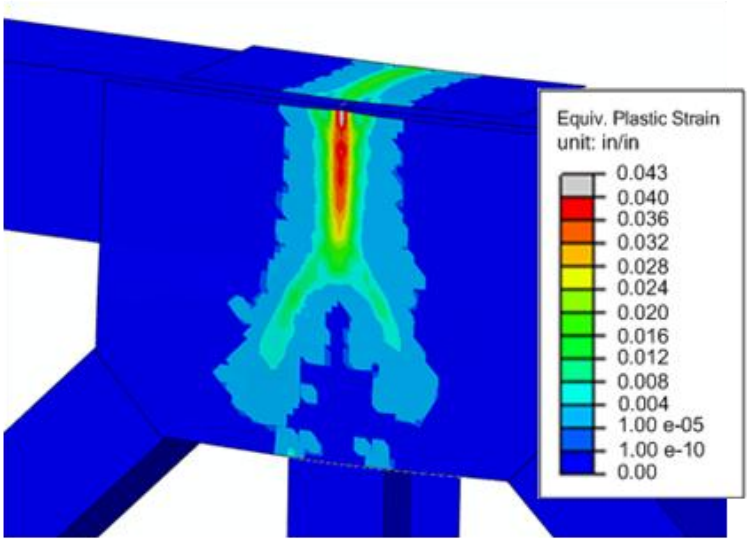

Figure 5.7.3: Equivalent plastic strain contours for Case 1 at ALF=1.37 (Deformation scale factor=5)

5.7.1.2. Case 2 (WV-M-02)

This is a lower chord joint at the midspan location of a truss bridge. The gusset plate geometry and the applied member loads are shown in Figure 5.7.4. Unlike the Case 1 joint, the chords are in tension and have considerably higher tensile forces than the diagonal members. This joint also provides valuable information about the chord splice resistance calculations that will be investigated in this research. The gusset plate thickness used in the finite element model is 0.400 inch.

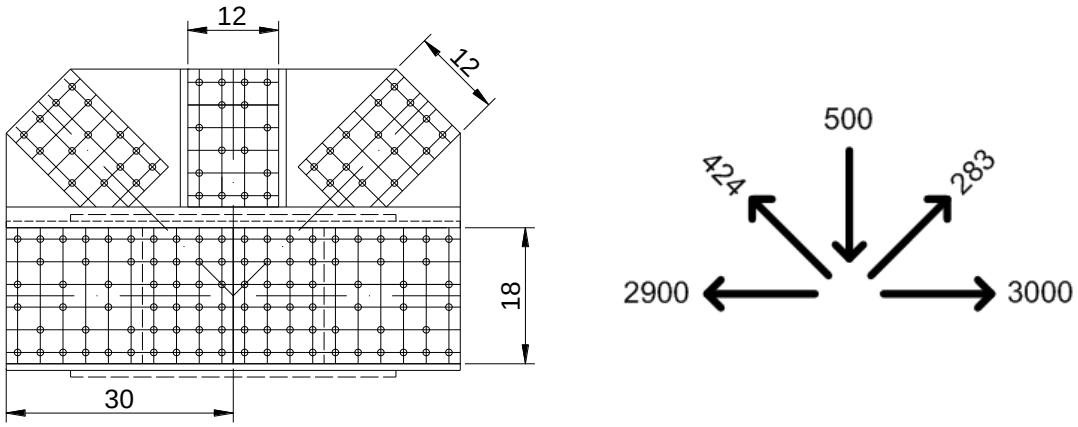

Figure 5.7.4: Case 2 gusset plate details and applied reference loads

The maximum joint capacity is again governed by the 4% equivalent plastic strain criterion (PEEQ) as shown in Table 5.7.2. The joint reaches its limit at ALF=1.33 (133% of the applied reference loads shown in Figure 5.7.4).

Table 5.7.2: Maximum applied load fraction (ALF) values for Case 2

Case 2 (WV-M-02)	4% PEEQ ALF	Peak ALF
	1.33	1.67

Figure 5.7.5 shows the von Mises stress response contours with a deformation scale factor (DSF) of 5 at ALF=1.33. Similar to Case 1 joint, splice region of the gusset plate reaches the yield strength due to high tensile loads in the chord members.

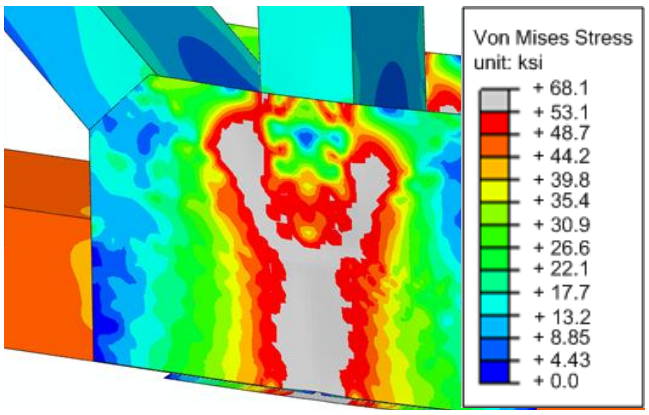

Figure 5.7.5: von Mises stress response contours for Case 2 at ALF=1.33 (Deformation scale factor=5)

Equivalent plastic strain contours for this joint are shown in Figure 5.7.6. Plastification within the splice region shows the extent of yielding through the gusset plate.

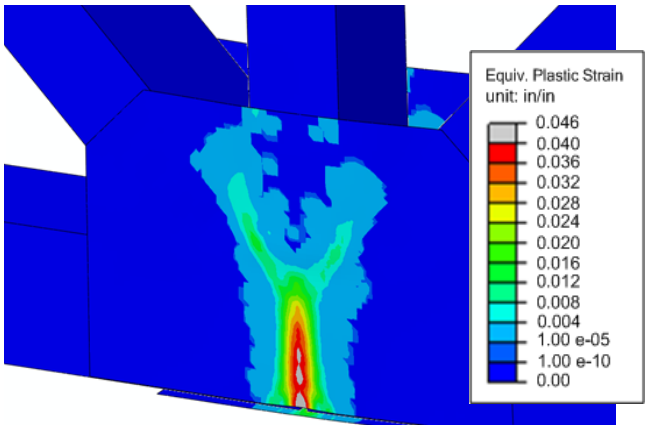

Figure 5.7.6: Equivalent plastic strain contours for Case 2 at ALF=1.33 (Deformation scale factor=5)

5.7.1.3. Case 3 (WV-P-01)

This joint represents an upper chord joint at the pier location of a truss bridge. Figure 5.7.7 shows the gusset plate configuration and applied reference loads in the members. In this joint, the diagonal members are extremely steep (63° between the chord members and diagonals). Due to this steep diagonal angle, members are chamfered significantly as shown in Figure 5.7.7. The load transferred from the pier to the gusset plate is extremely high compared to the other member loads in the joint (5000 kips). The gusset plate thickness used in the finite element analysis is 0.500 inch.

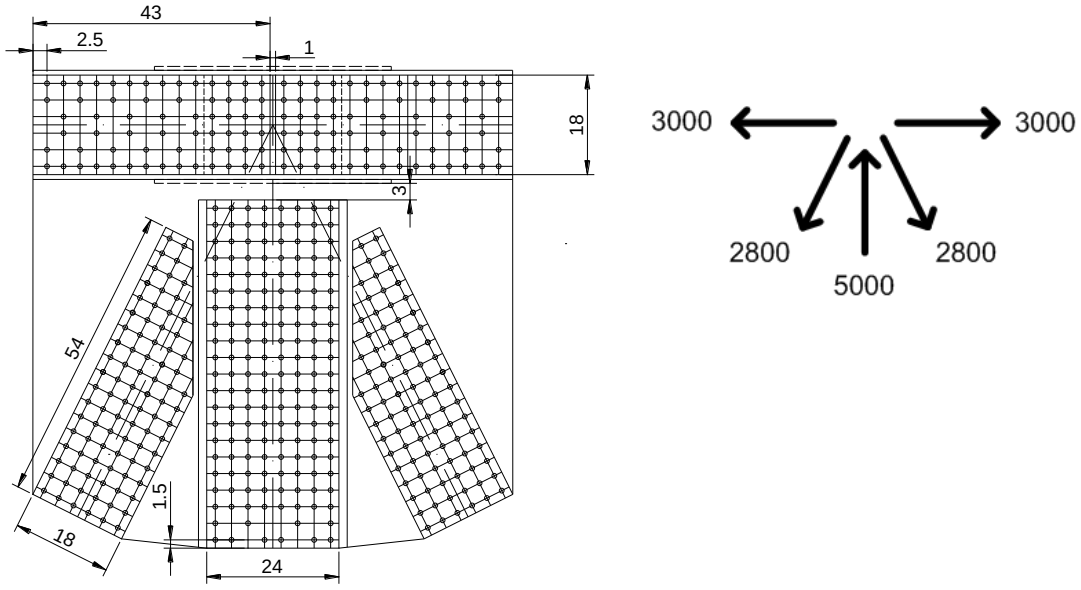

Figure 5.7.7: Case 3 gusset plate details and applied reference loads

The maximum capacity of the joint is determined by the 4% equivalent plastic strain limit at ALF = 0.96 as shown in Table 5.7.3.

Table 5.7.3: Maximum applied load fraction (ALF) values for Case 3

	4% PEEQ ALF	Peak ALF
Case 3 (WV-P-01)	**0.96**	1.29

Figure 5.7.8 shows the von Mises stress response contours at the limit ALF of 0.96. The yielding along the planes next to the vertical member progresses from bottom to top of the gusset plate. This indicates a shear transfer mechanism from the vertical components

of the diagonal member loads to the gusset plate through the critical shear planes of the gusset plate (two vertical planes on each side of the vertical member).

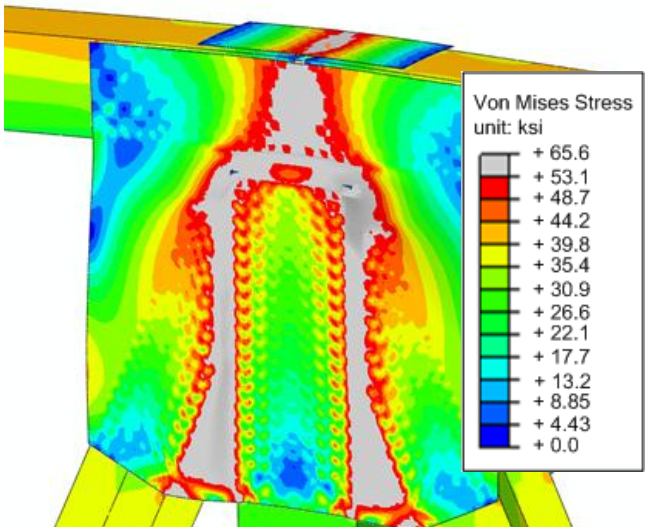

Figure 5.7.8: von Mises stress response contours for Case 3 at ALF=0.96 (Deformation scale factor=10)

The equivalent plastic strain contours in Figure 5.7.9 also shows excessive yielding around the vertical member. Due to the high compression load, the base of the vertical member buckles and moves out-of-plane. The load transfer from the vertical member to the gusset plate appears to be a combination of shear and compression.

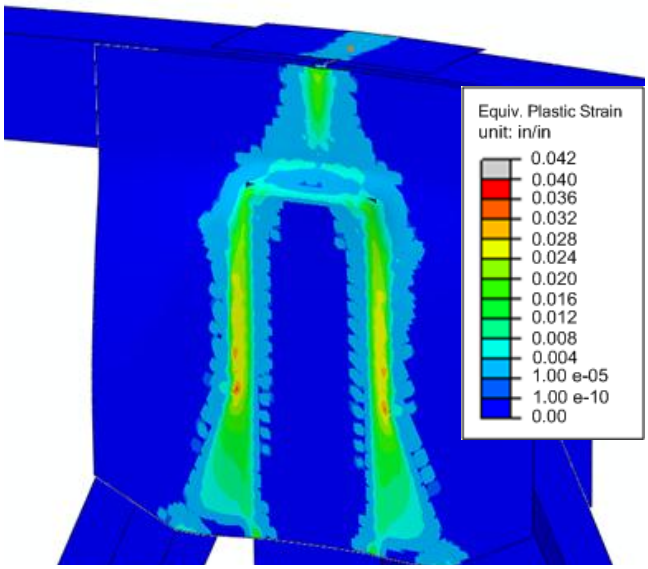

Figure 5.7.9: Equivalent plastic strain contours for Case 3 at ALF=0.96 (Deformation scale factor=10)

5.7.1.4. Case 4 (WV-P-02)

This is the second joint at the pier location of a truss bridge. Gusset plate configuration and the applied loads are shown in Figure 5.7.10**.** Similar to Case 3, very steep angles and chamfered edges are used for the diagonal members. High compression force (5500 kips) is transferred from the pier location to the gusset plate joint. The thickness of the gusset plate used in the finite element model is 0.800 inch.

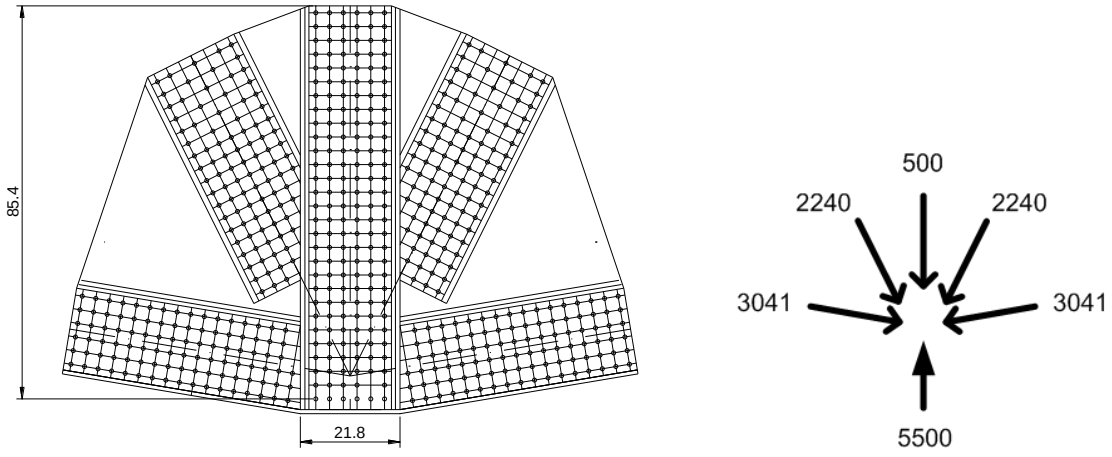

Figure 5.7.10: Case 4 gusset plate details and applied reference loads

Table 5.7.4 shows that the maximum capacity of the joint is reached at ALF = 0.97. Both 4% PEEQ limit and the peak load are the same for this connection.

Table 5.7.4: Maximum applied load fraction (ALF) values for Case 4

Case 4 (WV-P-02)	4% PEEQ ALF	Peak ALF
	0.97	**0.97**

The von Mises stress contours in Figure 5.7.11 show that yielding progresses through the vertical planes next to the vertical member.

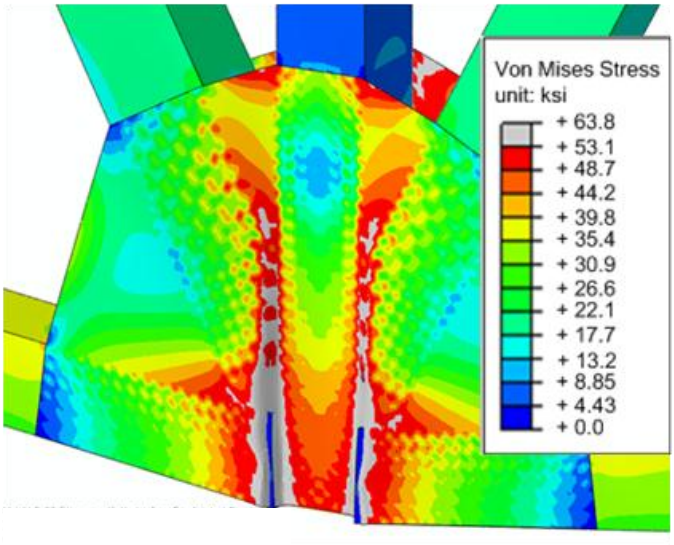

Figure 5.7.11: von Mises stress response contours for Case 4 at ALF=0.97 (Deformation scale factor=10)

Corresponding equivalent plastic strain contours in Figure 5.7.12 also show the plastification at the end of the chord members due to high compression forces. As a result, the gusset plate buckling is observed at the end of the chord members. The shear transfer through the vertical planes parallel to the chamfered edges of the diagonal members can also be seen in Figure 5.7.12**.**

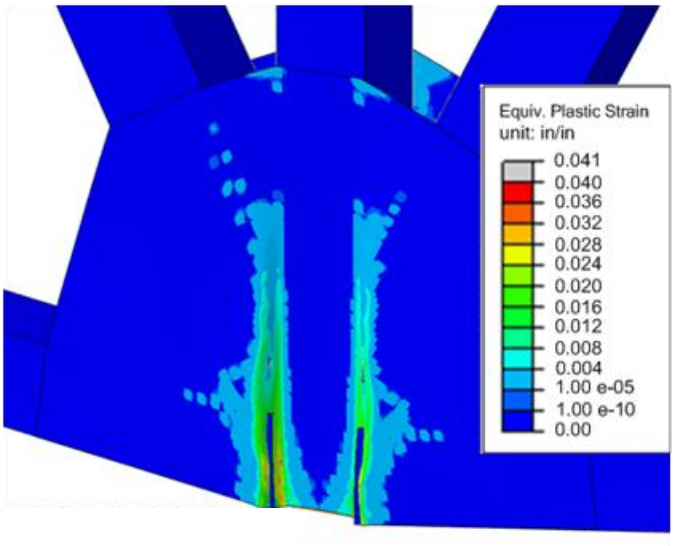

Figure 5.7.12: Equivalent plastic strain contours for Case 4 at ALF=0.97 (Deformation scale factor=10)

5.7.1.5. Case 5 (WV-NP-01)

This joint represents an upper chord joint at near pier location of a truss bridge. Reference loads and the gusset plate configuration are shown in Figure 5.7.13. Gusset plate thickness used in the finite element model is 0.400 inch for this joint.

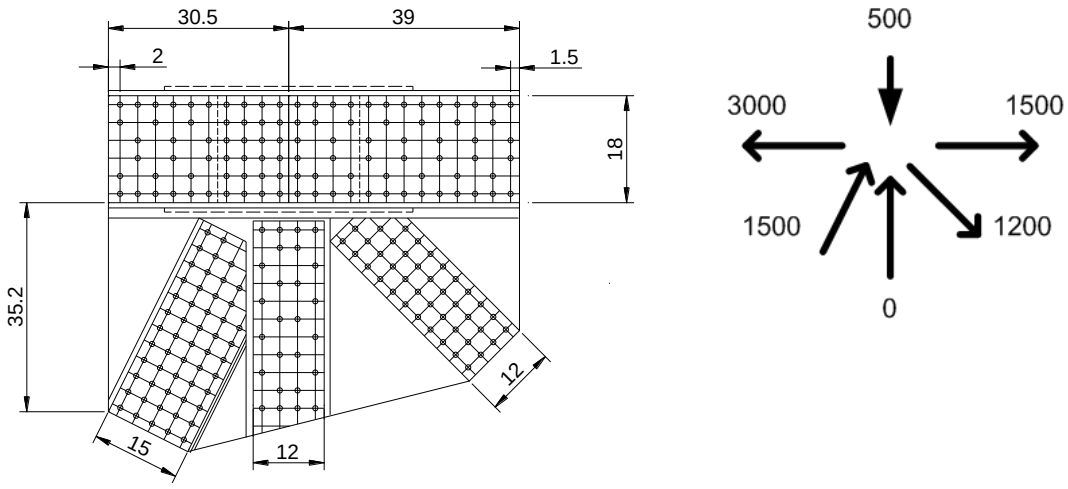

Figure 5.7.13: Case 5 gusset plate details and applied reference loads

The maximum joint capacity is reached at ALF of 0.94. Unlike the previous four cases, Table 5.7.5 shows that the 4% PEEQ limit is not applicable since the peak of the analysis is reached before the plates undergo 4% plastic strain.

Table 5.7.5: Maximum applied load fraction (ALF) values for Case 5

	4% PEEQ ALF	Peak ALF
Case 5 (WV-NP-01)	**N/A**	**0.94**

The von Mises stress response contours are shown in Figure 5.7.14. Almost full horizontal plane just below the chord members reaches the yield strength. In addition, the vertical plane on the left side of the vertical member is also yielded.

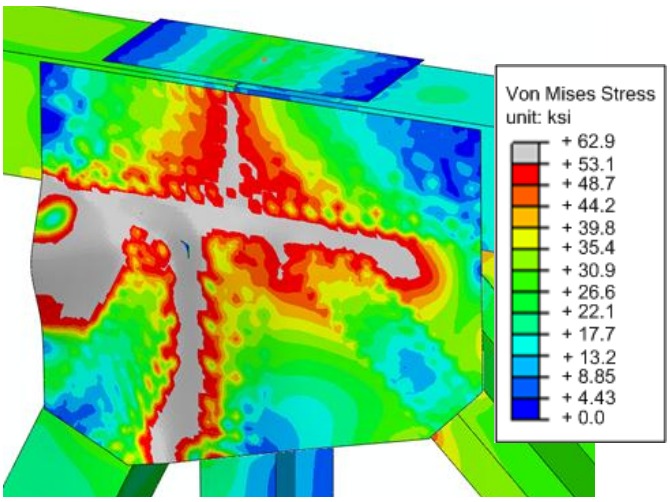

Figure 5.7.14: von Mises stress response contours for Case 5 at ALF=0.94 (Deformation scale factor=5)

The equivalent plastic strains in Figure 5.7.15 better show the extent of the yielding through the gusset plate. Both diagonals have chamfered edges in this joint. Based on the results in the previous joints, chamfered edges parallel to a critical shear plane seem to result in the major load transfer mechanism occurring in the joint. Similarly, in Case 5, the chamfering along both diagonals leads the joint failure mainly driven by shear yielding along both horizontal and vertical planes. The edge moves out-of-plane after the excessive plastification along the two planes and softening of the gusset plate at the limit load.

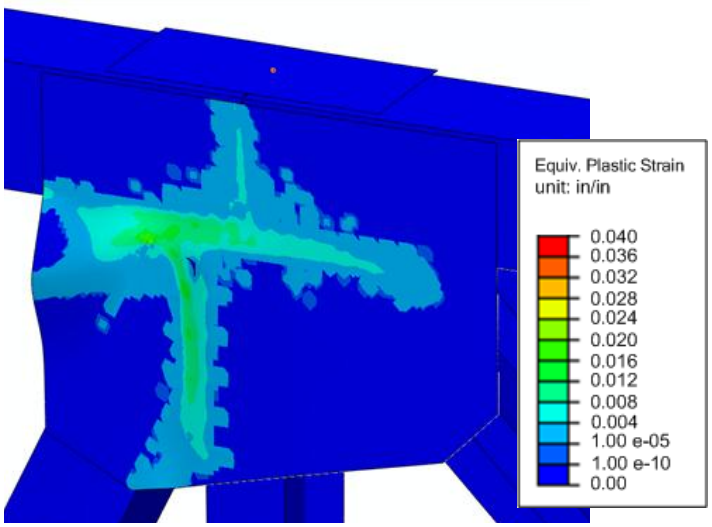

Figure 5.7.15: Equivalent plastic strain contours for Case 5 at ALF=0.94 (Deformation scale factor=5)

5.7.1.6. Case 6 (WV-NP-02)

This is another upper chord joint at near pier location of a truss bridge. Member reference loads and gusset plate configuration are shown in Figure 5.7.16. Diagonals are considerably chamfered along the horizontal edges parallel to the plane just below the chord members. The gusset plate in the finite element model of the joint is 0.500 inch.

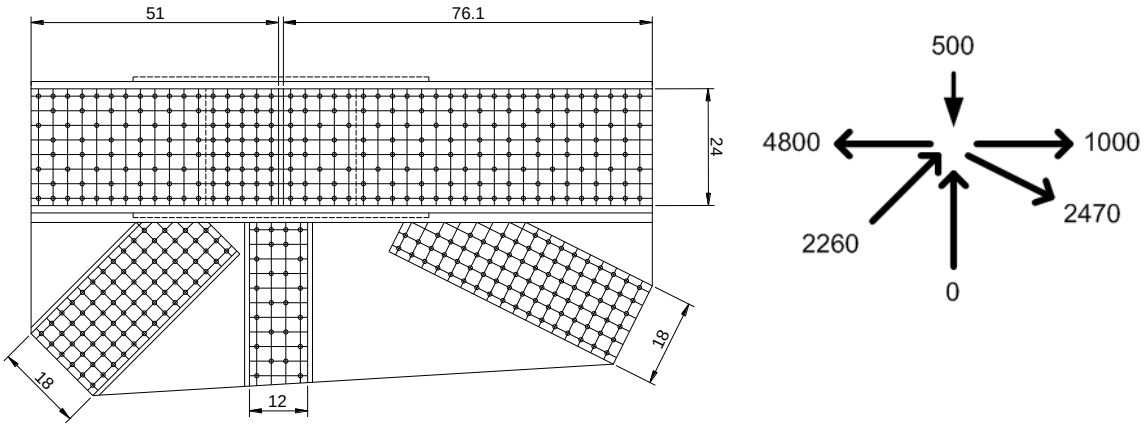

Figure 5.7.16: Case 6 gusset plate details and applied reference loads

4% PEEQ limit is reached just after the peak of the analysis and at the same applied load fraction of 0.98 as shown in Table 5.7.6.

Table 5.7.6: Maximum applied load fraction (ALF) values for Case 6

Case 6 (WV-NP-02)	4% PEEQ ALF	Peak ALF
	0.98	**0.98**

Figure 5.7.17 shows the von Mises stress contours at the limit ALF of 0.98. The equivalent plastic strain contours shown in Figure 5.7.18 also indicates that horizontal plane shear failure is observed. The fully yielded horizontal plane at the end results in the softened gusset plate and out-of-plane movement of the compression diagonal on the left.

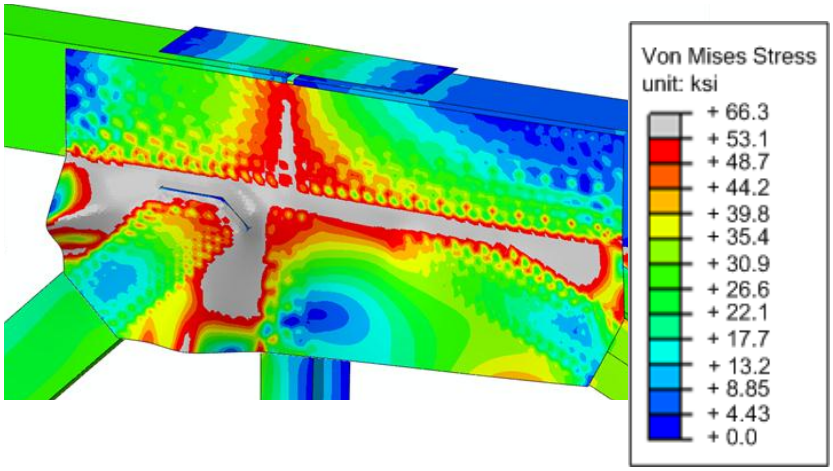

Figure 5.7.17: von Mises stress response contours for Case 6 at ALF=0.98 (Deformation scale factor=10)

Again, the conclusion for the chamfered connections being dominated by the shear yielding along the critical shear planes parallel to the chamfered member edges becomes evident in this case.

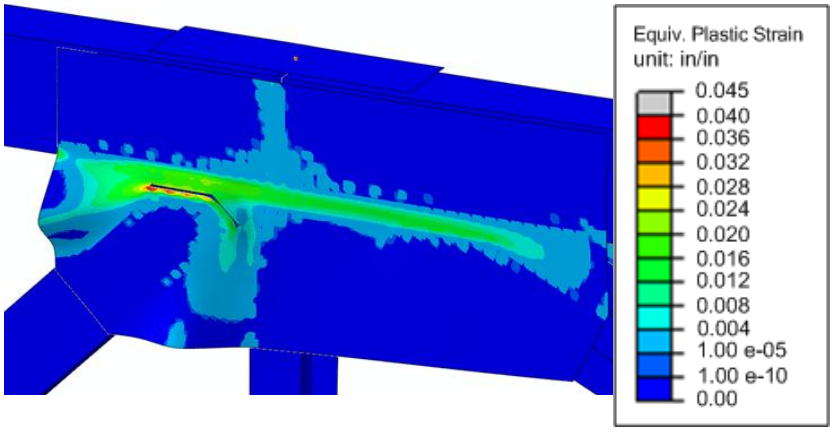

Figure 5.7.18: Equivalent plastic strain contours for Case 6 at ALF=0.98 (Deformation scale factor=10)

5.7.1.7. Case 7 (WV-INF-01)

The first joint modeled as a Warren truss configuration with vertical member at the inflection point of a bridge is Case 7. As shown in Figure 5.7.19, angle of the diagonal members are shallow and members have considerable chamfering along their edges. High forces in the compression and diagonal members lead to very high force components along the horizontal plane just below the chord members. The gusset plate thickness in the finite element analysis is 0.700 inch.

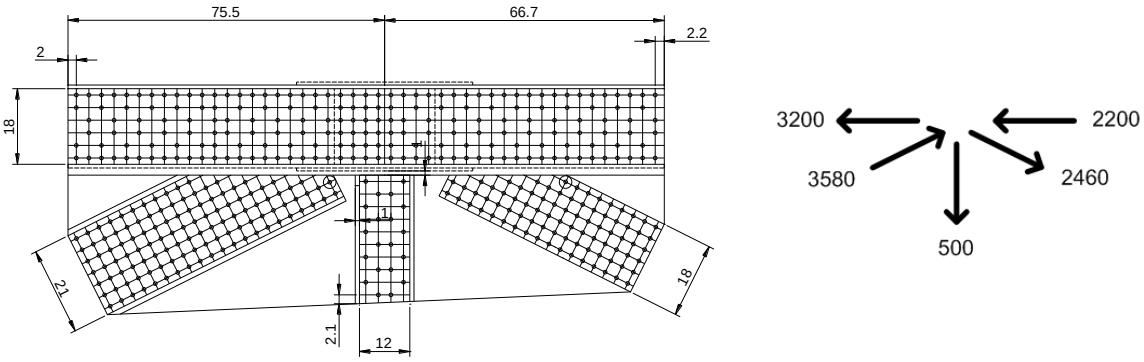

Figure 5.7.19: Case 7 gusset plate details and applied reference loads

4% equivalent plastic strain limit determines the maximum capacity of the joint. Table 5.7.7 shows that limit load is reached at ALF of 1.24

Table 5.7.7: Maximum applied load fraction (ALF) values for Case 7

Case 7 (WV-INF-01)	4% PEEQ ALF	Peak ALF
	1.24	**1.49**

The von Mises stress contour response at the limit load is shown in Figure 5.7.20. Similar to Case 6, horizontal plane below the chord members is fully yielded. As mentioned above, high shear forces act along that plane due to chamfered member edges and shallow diagonal angles.

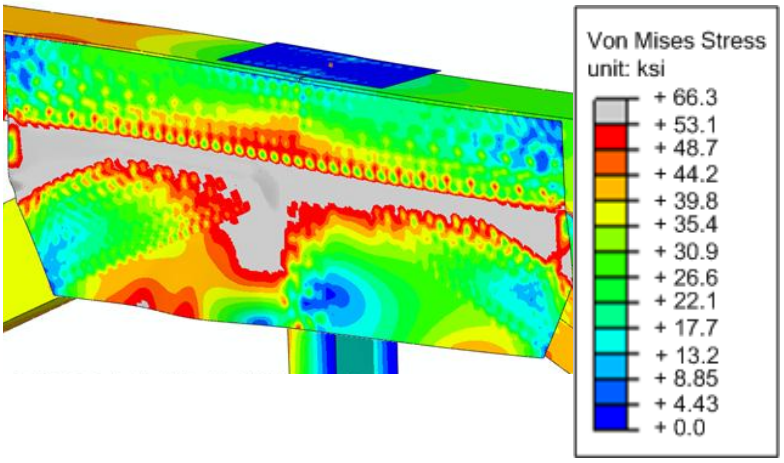

Figure 5.7.20: von Mises stress response contours for Case 7 at ALF=1.24 (Deformation scale factor=10)

Equivalent plastic strain contours are shown in Figure 5.7.21**.** It shows the extreme plastification along the horizontal plane at ALF=1.24. Similar conclusion of chamfered connections undergo mainly shear dominant failure also becomes applicable to this case.

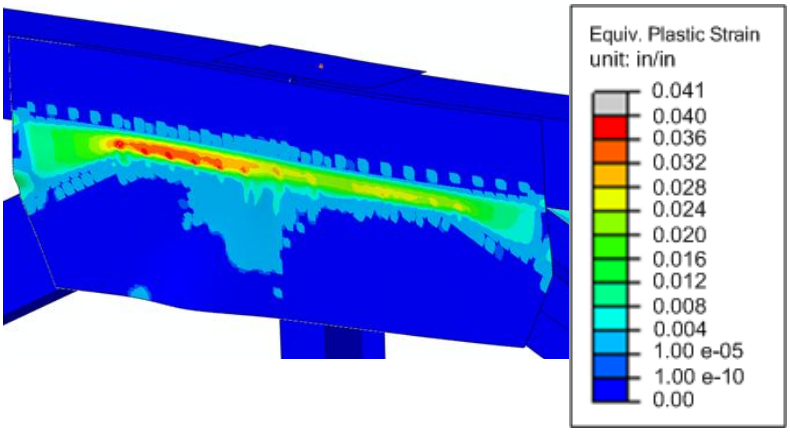

Figure 5.7.21: Equivalent plastic strain contours for Case 7 at ALF=1.24 (Deformation scale factor=10)

5.7.1.8. Case 8 (WV-INF-02)

This is another joint at the inflection point. However, the chord members are inclined for this specific case. Both compression and tension diagonals are chamfered as shown in Figure 5.7.22. Finite element analysis is performed using the 0.500 inch thick gusset plate.

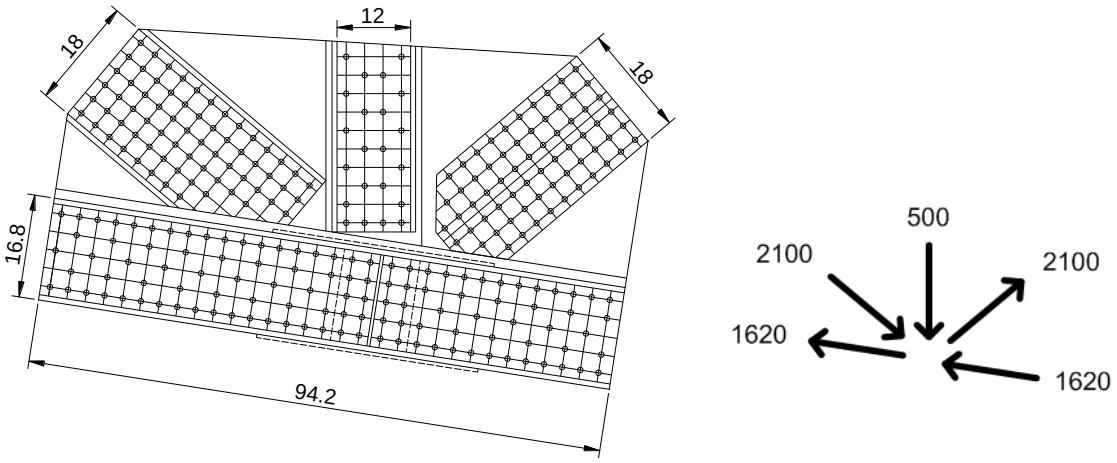

Figure 5.7.22: Case 8 gusset plate details and applied reference loads

The joint reaches its maximum capacity at ALF of 0.97 as shown in Table 5.7.8. This limit is determined based on the 4% equivalent plastic strain limit similar to Case 7 joint.

Table 5.7.8: Maximum applied load fraction (ALF) values for Case 8

Case 8 (WV-INF-02)	4% PEEQ ALF	Peak ALF
	0.97	**1.19**

The von Mises stress contours in Figure 5.7.23 show that yielding pattern extends along the inclined plane above the chord members. This plane becomes the horizontal plane based on the local axis determined using the centerline passing through the chord members.

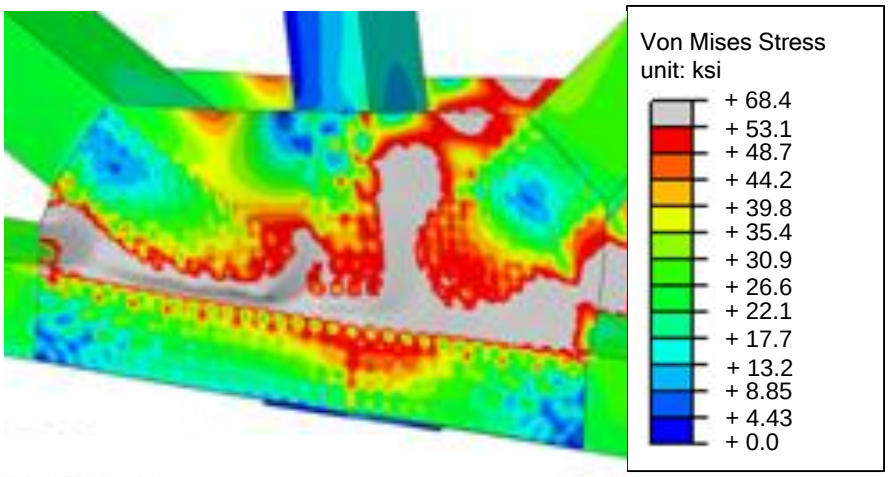

Figure 5.7.23: von Mises stress response contours for Case 8 at ALF=0.97 (Deformation scale factor=10)

Especially the high level of chamfering of the compression diagonal leads to the fully yielded inclined plane as shown in Figure 5.7.24. The shallow angle of the compression diagonal results in high shear component acting along the plane just above the chord members.

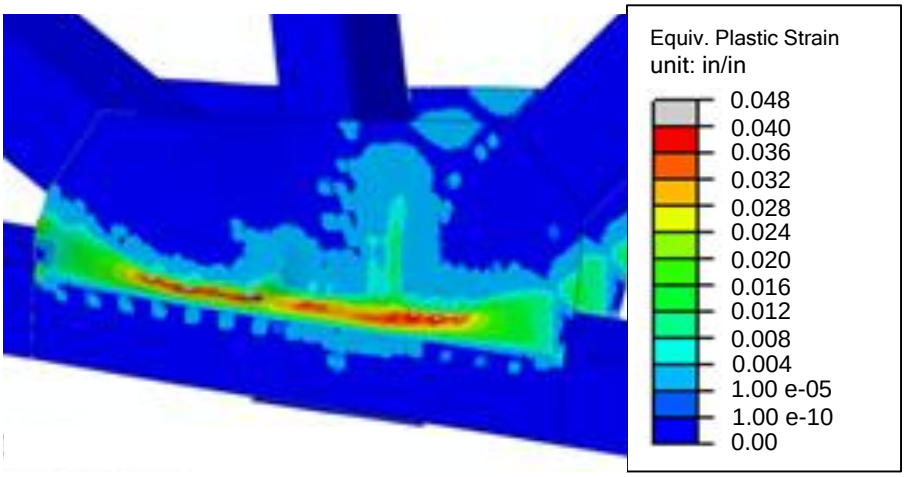

Figure 5.7.24: Equivalent plastic strain contours for Case 8 at ALF=0.97 (Deformation scale factor=10)

5.7.2. Pratt Trusses

5.7.2.1. Case 9 (P-NP-01)

Pratt trusses are smaller than the Warren type trusses with vertical members discussed in previous section. First Pratt truss configuration shown in Figure 5.7.25 has a compression diagonal with very little chamfering. Since the reference loads and joint size are smaller and a gusset plate thickness of 0.200 inch is used in the finite element analysis.

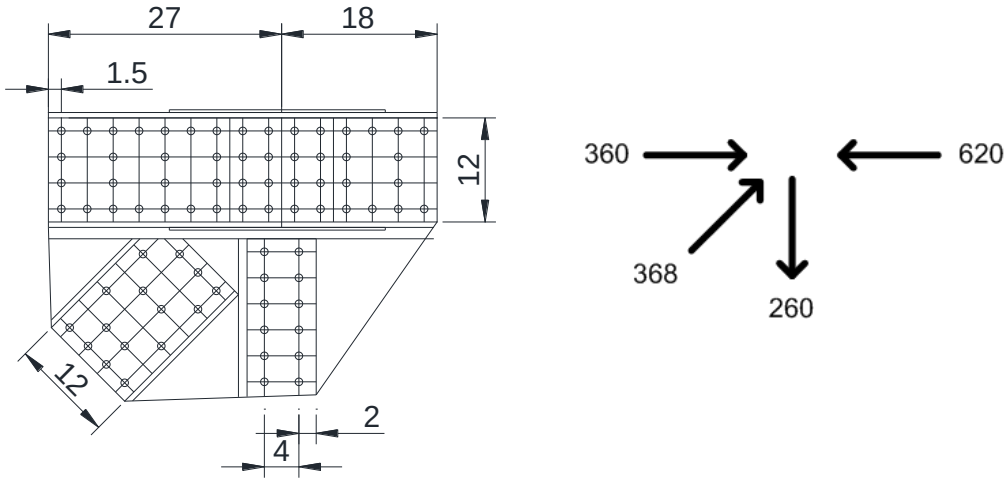

Figure 5.7.25: Case 9 gusset plate details and applied reference loads

The finite element analysis shows that the analysis reaches its limit at the peak load without reaching 4% equivalent plastic strain within the plates. Hence, 4% PEEQ limit is not applicable and failure occurs at ALF =0.96 as shown in Table 5.7.9.

Table 5.7.9: Maximum applied load fraction (ALF) values for Case 9

	4% PEEQ ALF	Peak ALF
Case 9 (P-NP-01)	**N/A**	**0.96**

The von Mises stress contours show that yielding is concentrated around the compression diagonal and gusset plate buckles at the limit load (Figure 5.7.26). This specimen has a relatively thin gusset plate (<3/8 inch) and buckling is expected since the level of chamfering is fairly small compared to the other chamfered member connections.

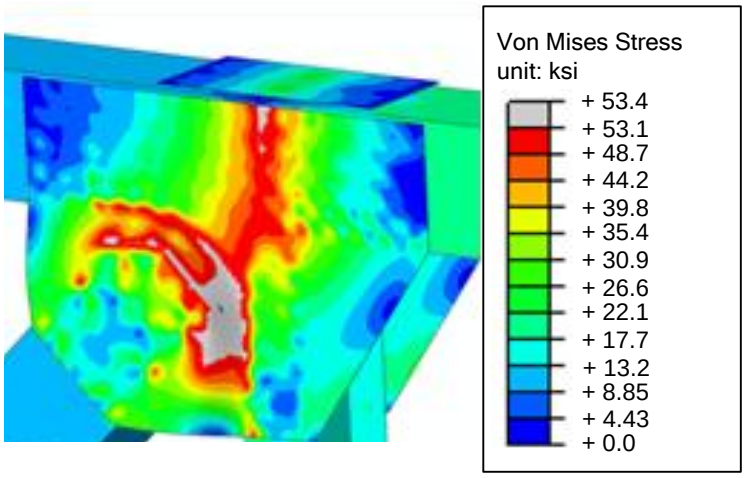

Figure 5.7.26: von Mises stress response contours for Case 9 at ALF=0.96 (Deformation scale factor=5)

Corresponding equivalent plastic strain contours are shown in Figure 5.7.27. This figure also shows the yielding around the compression diagonal edges at the base.

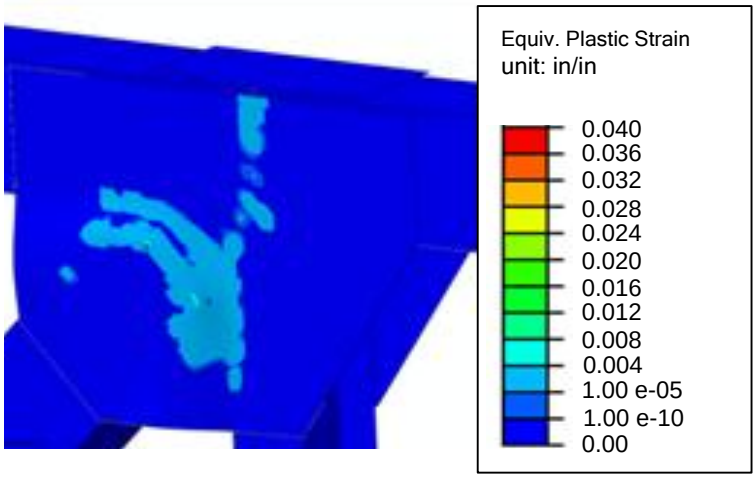

Figure 5.7.27: Equivalent plastic strain contours for Case 9 at ALF=0.96 (Deformation scale factor=5)

5.7.2.2. Case 10 (P-NP-02)

Second Pratt truss configuration is shown in Figure 5.7.28. This joint has relatively high chord forces in compression. This is also a small joint and the gusset plate thickness used in the analysis is 0.200 inch.

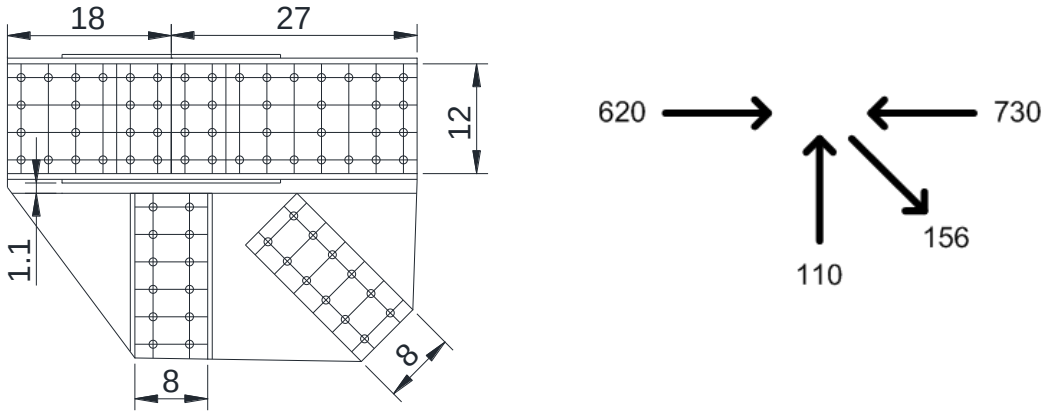

Figure 5.7.28: Case 10 gusset plate details and applied reference loads

The joint reaches its maximum capacity at ALF of 1.73 which is determined based on the 4% equivalent plastic strain limit as shown in Table 5.7.10.

Table 5.7.10: Maximum applied load fraction (ALF) values for Case 10

	4% PEEQ ALF	Peak ALF
Case 10 (P-NP-02)	**1.73**	**1.84**

The von Mises stress response contours are shown in Figure 5.7.29. As expected, yielding mainly concentrated within the splice region and both splice plates and gusset plates reach the yield strength in the chord splice area.

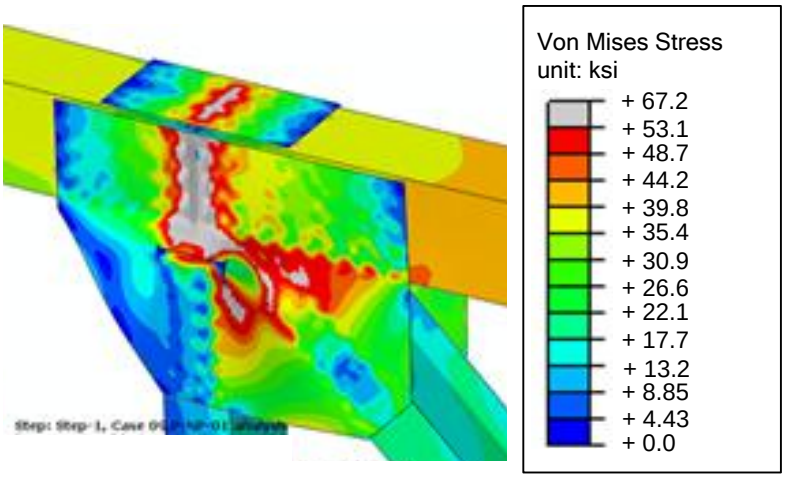

Figure 5.7.29: von Mises stress response contours for Case 10 at ALF=1.73 (Deformation scale factor=5)

The equivalent plastic strain contours in Figure 5.7.30 better show the degree of yielding taking place within the gusset plate and top splice plate of the joint.

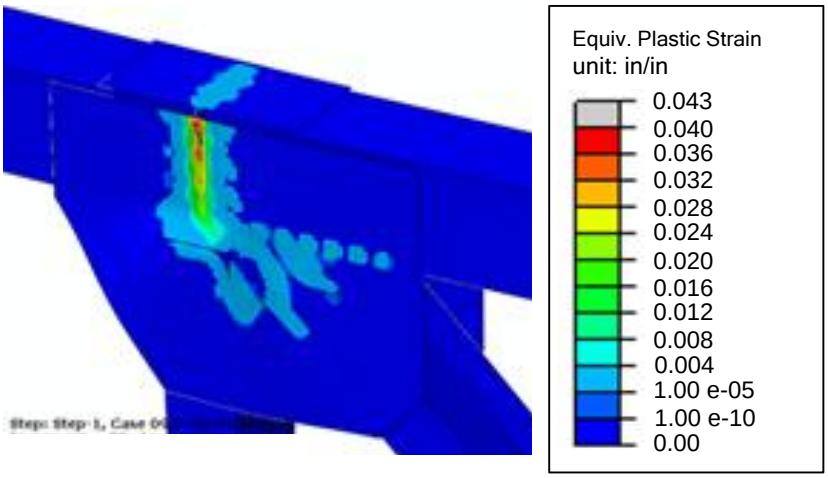

Figure 5.7.30: Equivalent plastic strain contours for Case 10 at ALF=1.73 (Deformation scale factor=5)

5.7.3. Warren Trusses without Vertical Members

5.7.3.1. Case 11 (W-M-01)

This is a Warren type truss without a vertical member at the midspan location of a truss bridge. Although the size of the gusset plate joint is small, chord forces have fairly high compression forces applied. Overall configuration with the applied reference loads are shown in Figure 5.7.31. A 0.450 inch thick gusset plate is used to perform the finite element analysis of the joint.

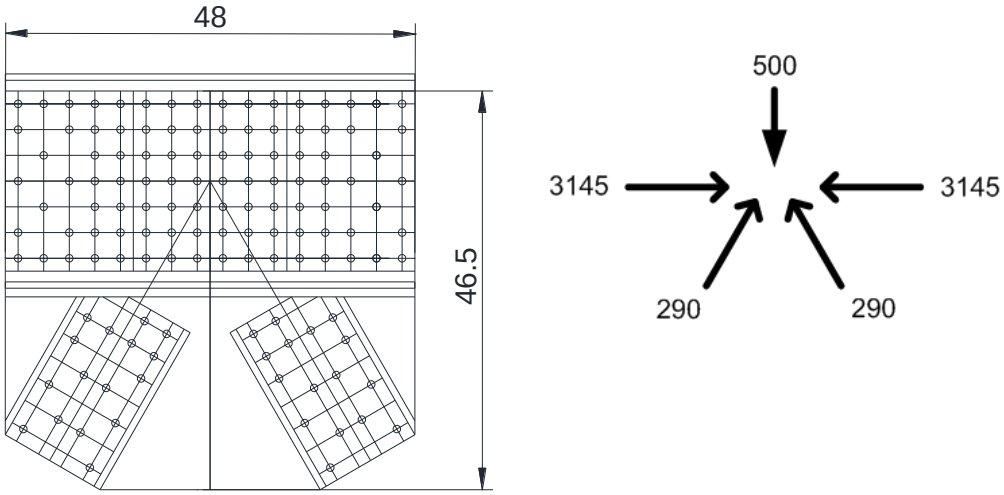

Figure 5.7.31: Case 11 gusset plate details and applied reference loads

Table 5.7.11 shows that the failure load is limited with the 4% equivalent plastic strain criterion. Joint maximum capacity is reached at ALF of 1.41.

Table 5.7.11: Maximum applied load fraction (ALF) values for Case 11

	4% PEEQ ALF	Peak ALF
Case 11 (W-M-01)	**1.41**	**1.76**

Figure 5.7.32 and Figure 5.7.33 shows the von Mises stress and equivalent plastic strain contours respectively. Whole splice region within the splice plates and gusset plate are yielded and excessively plastified. The contours look very similar to Case 1joint which is a Warren truss with vertical member.

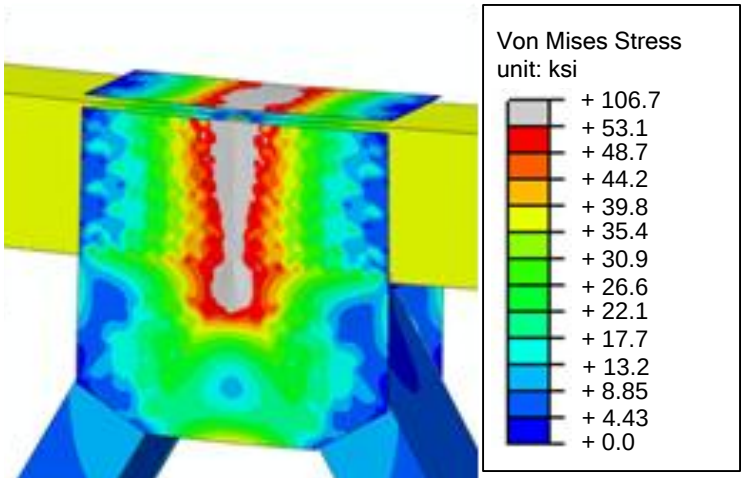

Figure 5.7.32: von Mises stress response contours for Case 11 at ALF=1.41 (Deformation scale factor=5)

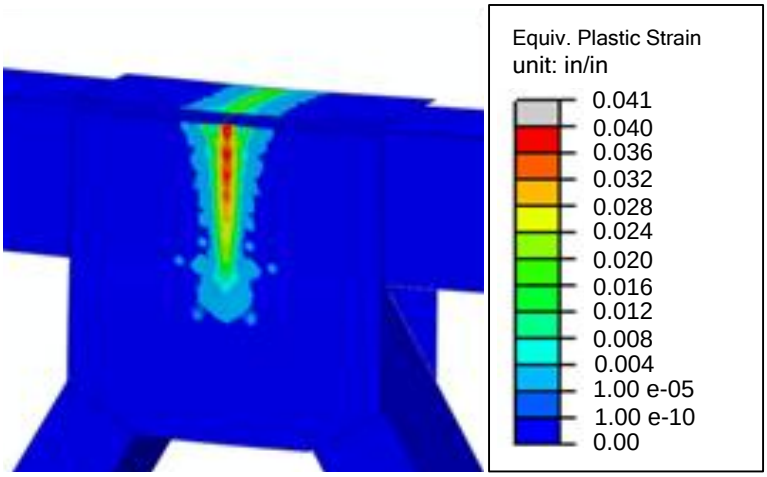

Figure 5.7.33: Equivalent plastic strain contours for Case 11 at ALF=1.41 (Deformation scale factor=5)

5.7.3.2. Case 12 (W-P-01)

This is a lower chord joint at the pier location. Joint configuration and loads are shown in Figure 5.7.34. High compression force (5000 kips) is transferred from the bearing to the gusset plate. Very steep diagonals require high level of chamfering along the edges. The analysis is performed using a 1.0 inch thick gusset plate.

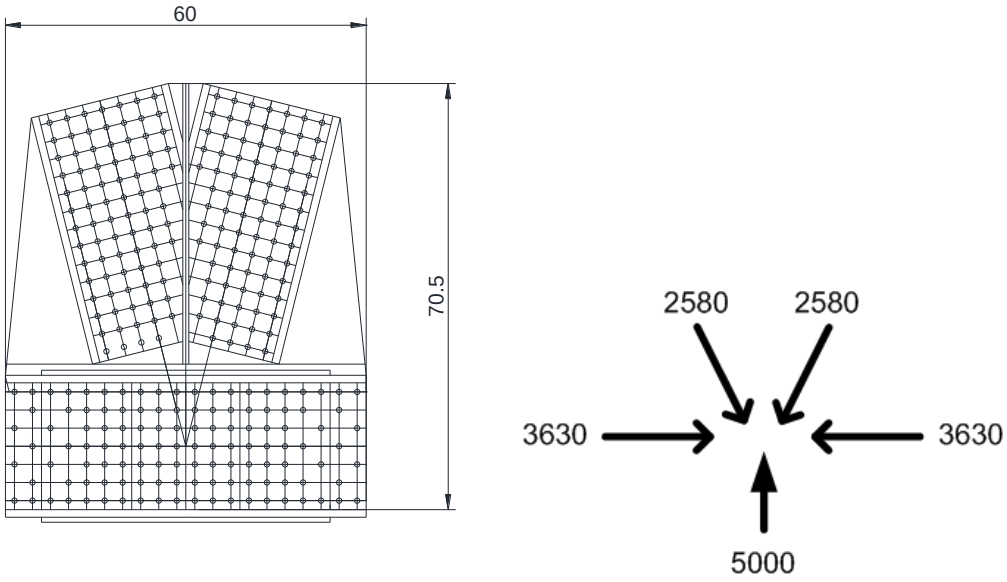

Figure 5.7.34: Case 12 gusset plate details and applied reference loads

The failure occurs at the peak load without reaching 4% plastic strain in any of the plates. Maximum ALF becomes 1.05 as shown in Table 5.7.12.

Table 5.7.12: Maximum applied load fraction (ALF) values for Case 12

Case 12 (W-P-01)	4% PEEQ ALF	Peak ALF
	N/A	**1.05**

The joint basically tries to transfer the high compressive force at the pier. The von Mises stress response contours in Figure 5.7.35 show that the gusset plate yields around the base of the diagonal members and buckles out-of-plane.

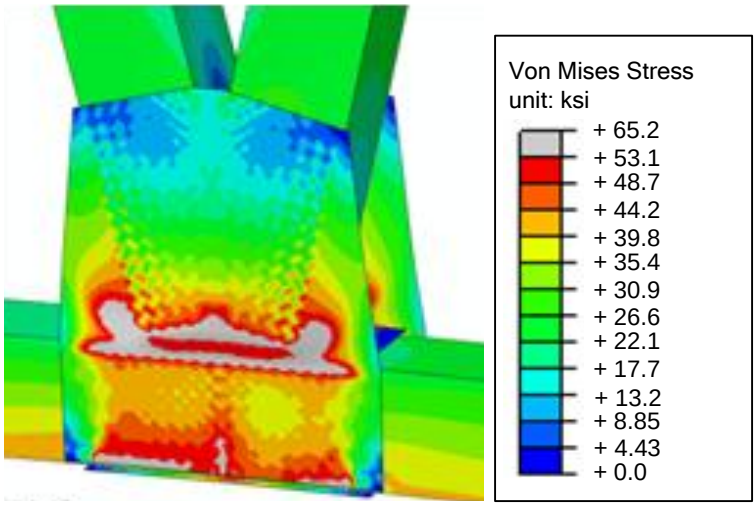

Figure 5.7.35: von Mises stress response contours for Case 12 at ALF=1.05 (Deformation scale factor=5)

This joint differs from the other chamfered connections since it cannot undergo as much plastification as Cases 5, 6, 7, and 8. The plastification pattern is shown in Figure 5.7.36. Since the diagonal members have very long chamfered edges, there is not a shear transfer mechanism. The vertical components balance the compressive force coming from the pier.

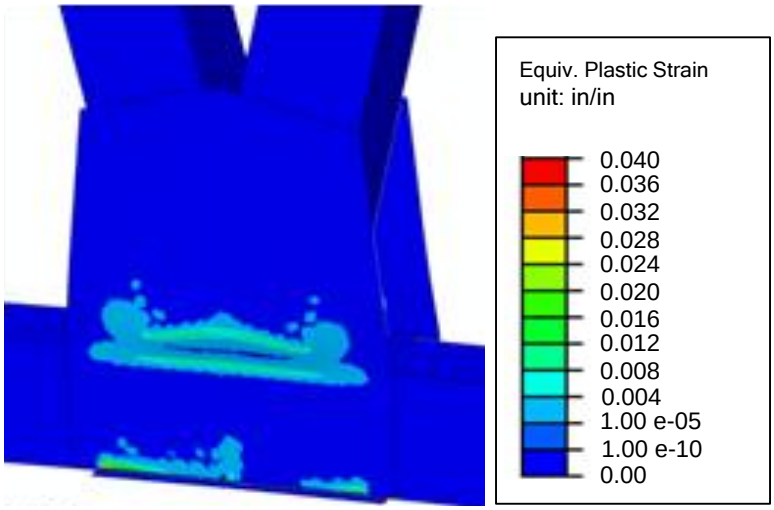

Figure 5.7.36: Equivalent plastic strain contours for Case 12 at ALF=1.05 (Deformation scale factor=5)

5.7.3.3. Case 13 (W-NP-01)

Case 13 also has inclined chord members as shown in Figure 5.7.37. This joint represents a Warren truss without vertical member at nier pear location. Compression diagonal is the only chamfered member in the connection. The gusset plate thickness used in the analysis is 0.400 inch.

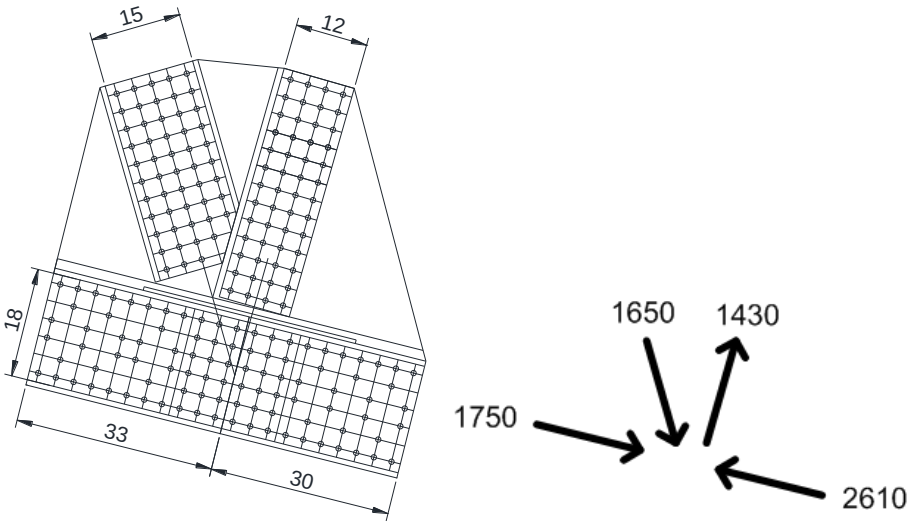

Figure 5.7.37: Case 13 gusset plate details and applied reference loads

4% equivalent plastic strain limit is reached just one increment before the peak load. Both ALF values are essentially the same as shown in Table 5.7.13.

Table 5.7.13: Maximum applied load fraction (ALF) values for Case 13

	4% PEEQ ALF	Peak ALF
Case 13 (W-NP-01)	**0.99**	**0.99**

Taking the previous analysis results into consideration, expectation is having a yielding pattern along the plane next to the chamfered edge of the compression diagonal. The von Mises stress contours in Figure 5.7.38 show that the local vertical plane (with respect to the chord orientation) is fully yielded.

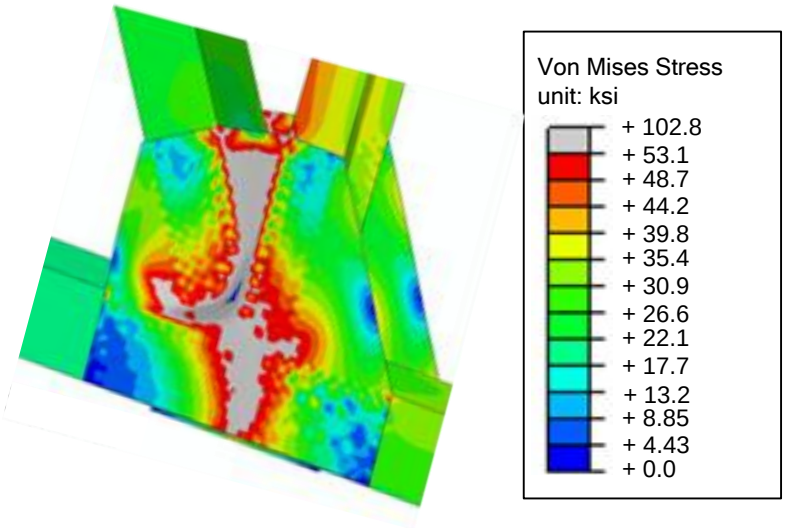

Figure 5.7.38: von Mises stress response contours for Case 13 at ALF=0.99 (Deformation scale factor=5)

Equivalent plastic strain contours in Figure 5.7.39 show the concentrated plasticity along the chamfered edge. As expected, with the chamfering on the members, shear plane becomes the critical component of the load path. Force component of the compression diagonal parallel to the shear plane next to the vertical member drive the failure of the whole joint.

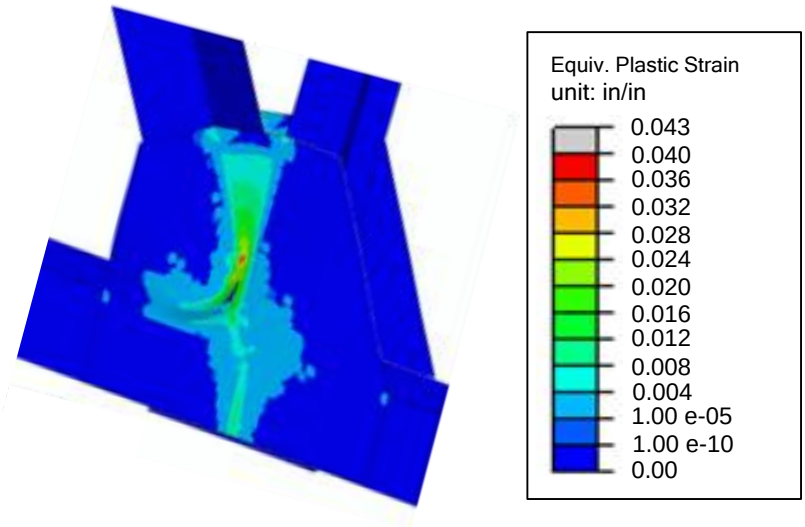

Figure 5.7.39: Equivalent plastic strain contours for Case 13 at ALF=0.99 (Deformation scale factor=5)

5.7.3.4. Case 14 (W-INF-01)

This is the last Warren truss without a vertical member. This joint is at the inflection point location of a truss bridge. Both diagonals are chamfered but not as significant as the previous chamfered connections. Chord members are inclined and compression diagonal has slightly higher load than the tension diagonal. Reference loads, and gusset plate joint configuration is shown in Figure 5.7.40. Selected gusset plate thickness for the analysis is 0.500 inch.

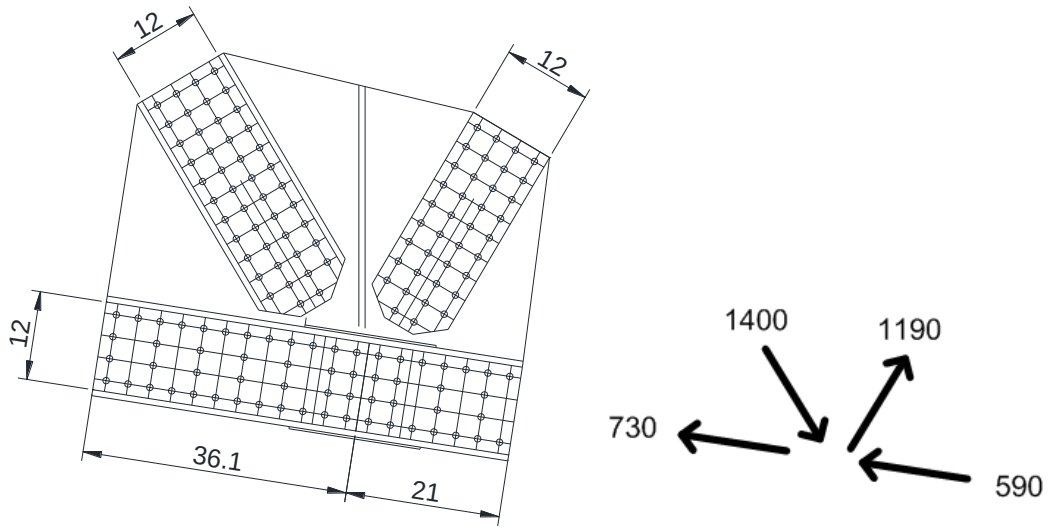

Figure 5.7.40: Case 14 gusset plate details and applied reference loads

Again, the peak of the analysis is one increment after the 4% equivalent plastic strain limit and at the same ALF of 1.22 as shown in Table 5.7.14.

Table 5.7.14: Maximum applied load fraction (ALF) values for Case 14

Case 14 (W-INF-01)	4% PEEQ ALF	Peak ALF
	1.22	**1.22**

The inclined plane above the chord members reaches the yield strength limit of the plate at ALF=1.22 (Figure 5.7.41). In addition, the gusset plate buckles and the free edges moves out-of-plane at the instant of failure.

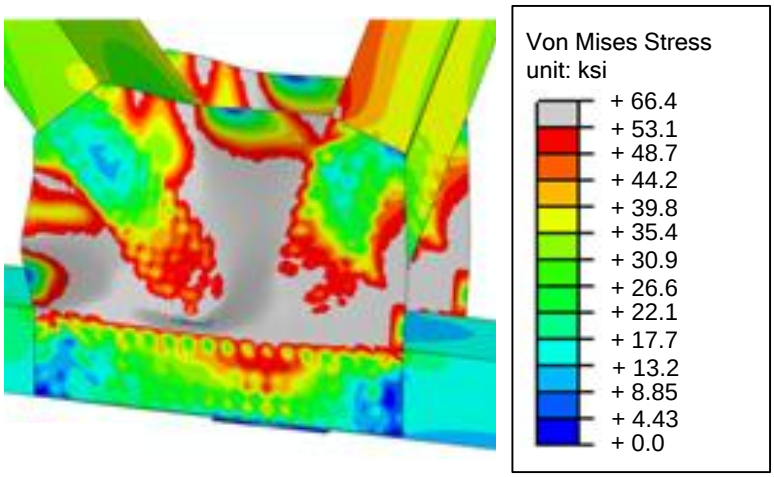

Figure 5.7.41: von Mises stress response contours for Case 14 at ALF=1.22 (Deformation scale factor=5)

The equivalent plastic strain contours in Figure 5.7.42 better explains the behavior of the joint by showing the degree of plastification along the horizontal plane parallel to the chord member centerline. Plastic strains along the shear plane are much higher and reach the 4% limit at the instant of failure. There is no more capability of that plane to carry more load and it is softened which finally resulted in the out-of-plane movement of the compression diagonal by forming a plastic hinge at the base of the diagonal member.

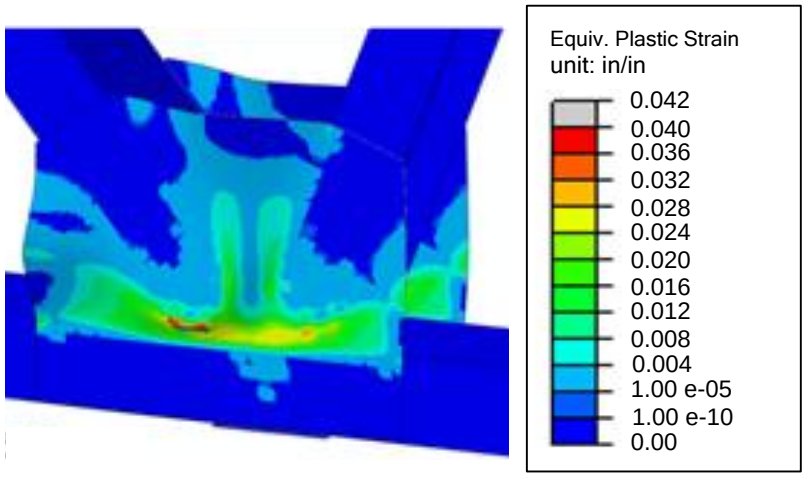

Figure 5.7.42: Equivalent plastic strain contours for Case 14 at ALF=1.22 (Deformation scale factor=5)

5.7.4. Other Joints

Detailed analysis results of the special cases are discussed in the project parametric study report (White et. al, 2011).

5.8. Test Simulation Results of the Unchamfered Parametric Cases

After the initial set of parametric studies with chamfered member connections, 5 of the joints are selected to be modeled as unchamfered connections similar to the test specimens. Three of these unchamfered joints are Warren type trusses with vertical members and the two are Warren trusses without vertical members. This section discusses the results of the nonlinear finite element analysis conducted on these five additional parametric cases.

5.8.1. Warren Trusses with Vertical Members

5.8.1.1. Case 5-a (WV-NP-01)

This case is created by changing the two diagonal members to unchamfered members as shown in Figure 5.8.1. The compression diagonal needs to move away from the chord members to accommodate the updated member shapes. Reference loads and the gusset plate thickness (0.400 inch) are the same as original Case 5 joint.

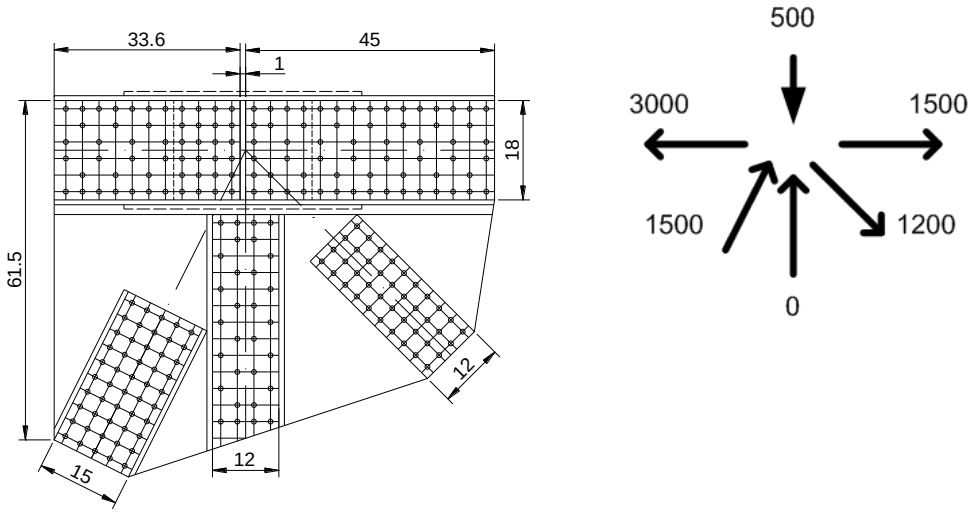

Figure 5.8.1: Case 5-a gusset plate details and applied reference loads

For this joint, maximum capacity is reached at the peak load without significant plastification within the gusset plate. Hence, 4% equivalent plastic strain does not apply. Peak ALF that joint can attain is 0.78 as shown in Table 5.8.1.

Table 5.8.1: Maximum applied load fraction (ALF) values for Case 5-a

Case 5-a (WV-NP-01)	4% PEEQ ALF	Peak ALF
	N/A	**0.78**

The von Mises stress contours in Figure 5.8.2 show that only the areas at the base of the compression diagonal are yielded. At the limit load the compression diagonal starts moving out-of-plane due to gusset plate buckling which can be seen from the bowed free edge on the left.

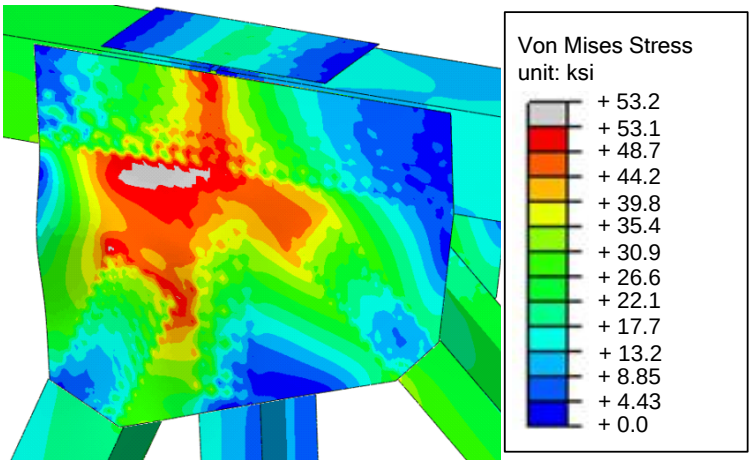

Figure 5.8.2: von Mises stress response contours for Case 5-a at ALF=0.78 (Deformation scale factor=5)

The equivalent plastic strain contours are very different than the original Case 5 joint. As shown in Figure 5.8.3, the gusset plate plastifies very locally on the compression diagonal side of the joint. The joint cannot undergo further plastification since it already reaches its buckling capacity at ALF=0.78.

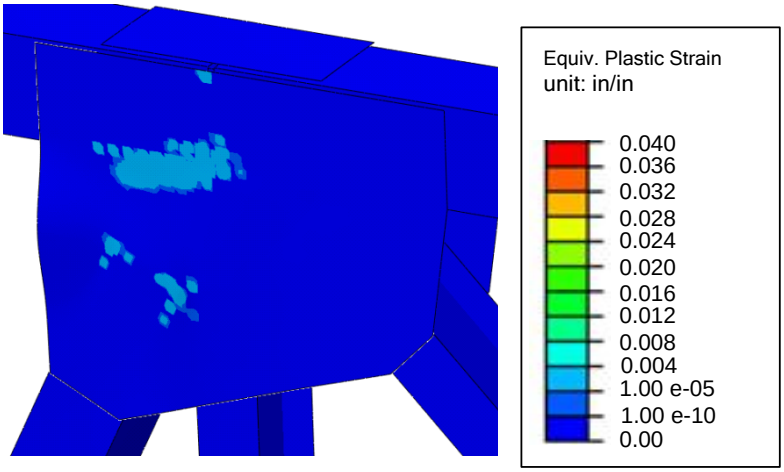

Figure 5.8.3: Equivalent plastic strain contours for Case 5-a at ALF=0.78 (Deformation scale factor=5)

Buckling failure is easily observed in the post-peak deflected shape of the gusset plate joint. Both von Mises stresses in Figure 5.8.4 and equivalent plastic strains in Figure 5.8.5 clearly indicate the buckled gusset plate after the joint reach its failure load.

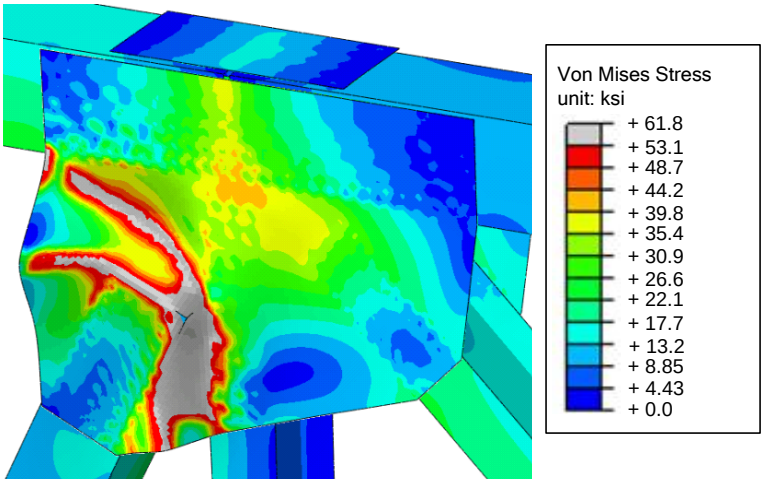

Figure 5.8.4: von Mises stress response contours for Case 5-a at post-peak (Deformation scale factor=5)

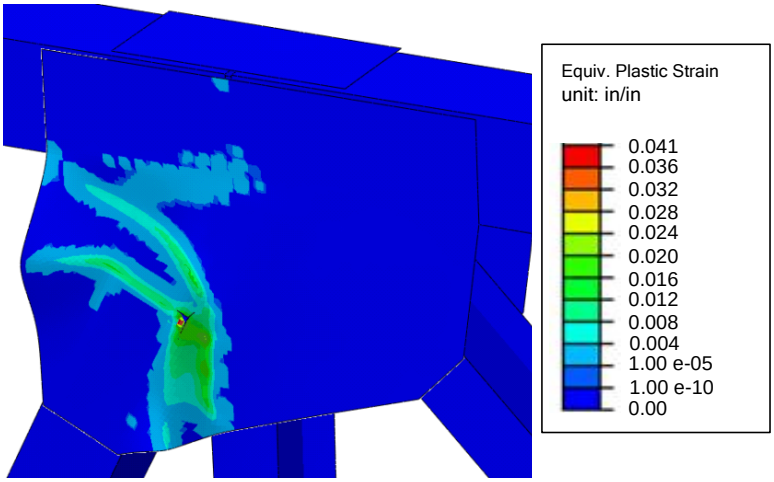

Figure 5.8.5: Equivalent plastic strain contours for Case 5-a at post-peak (Deformation scale factor=5)

5.8.1.2. Case 6-a (WV-NP-02)

Second unchamfered connection of the parametric study joints is obtained by removing the member chamfering in Case 6. Joint configuration and the applied loads are shown in Figure 5.8.6. To be able to see the difference in failure mode and gusset plate behavior, same thickness of 0.500 inch is used in the finite element analysis.

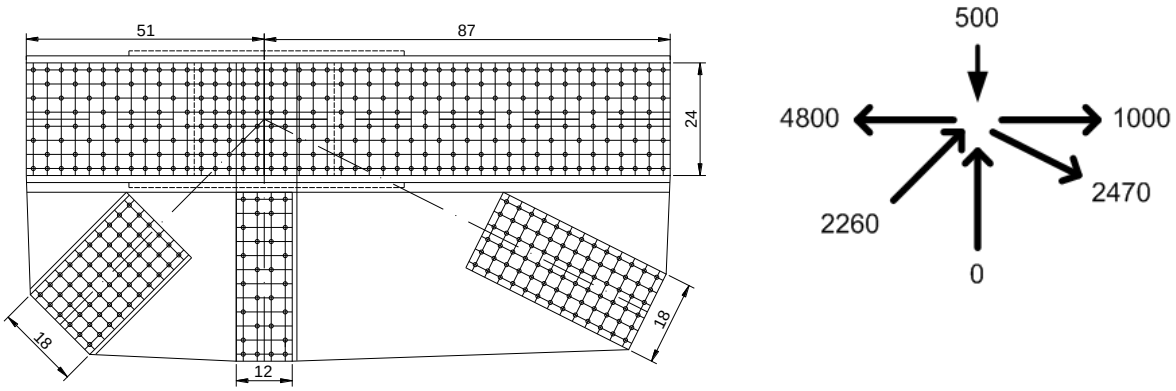

Figure 5.8.6: Case 6-a gusset plate details and applied reference loads

The failure occurs at the peak load similar to Case 5-a. 4% equivalent plastic strain is not reached within the plates. Table 5.8.2 shows that maximum joint capacity is reached at ALF=0.80.

Table 5.8.2: Maximum applied load fraction (ALF) values for Case 6-a

	4% PEEQ ALF	Peak ALF
Case 6-a (WV-NP-02)	**N/A**	**0.80**

The gusset plate reaches the yield strength at the areas shown with grey in the von Mises stress response contours (Figure 5.8.7). Triangular region at the base of the compression diagonal indicates the buckling failure since the compression diagonal starts moving out-of-plane at the failure load.

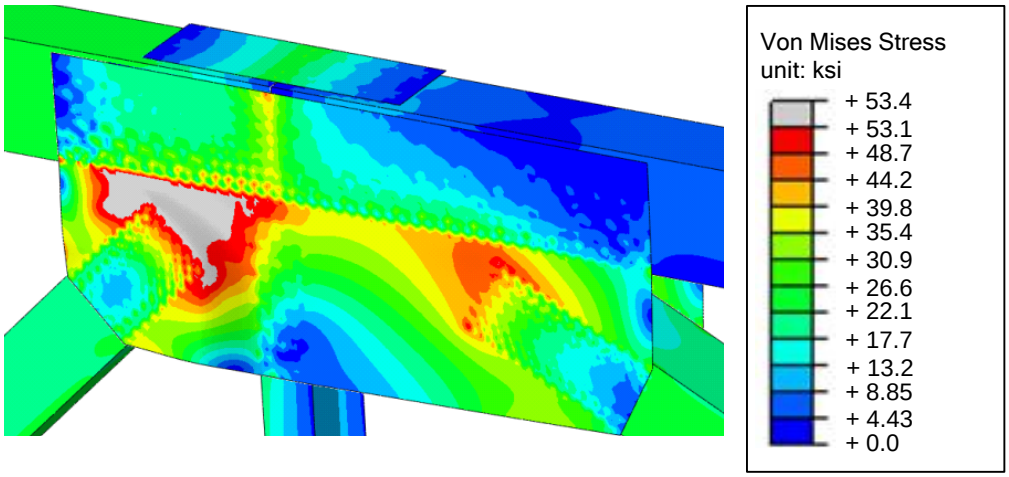

Figure 5.8.7: von Mises stress response contours for Case 6-a at ALF=0.80 (Deformation scale factor=5)

Corresponding equivalent plastic strains (Figure 5.8.8) also show that gusset plate buckles and reaches its limit capacity.

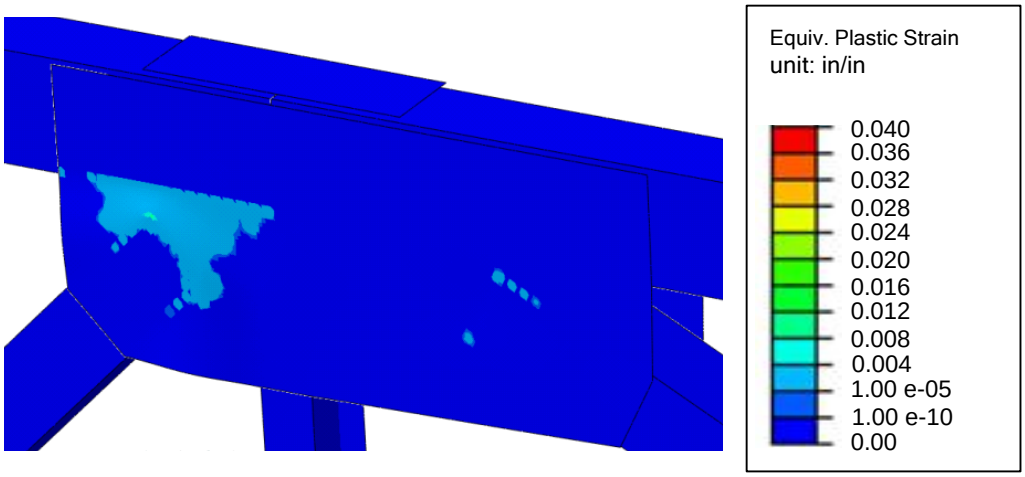

Figure 5.8.8: Equivalent plastic strain contours for Case 6-a at ALF=0.80 (Deformation scale factor=5)

To better visualize the buckling failure mode, von Mises stress and equivalent plastic strain response contours in the post-peak of the analysis are extracted. Figure 5.8.9 and Figure 5.8.10 shows how the gusset plate buckling takes place around the compression diagonal after the joint reaches its maximum capacity.

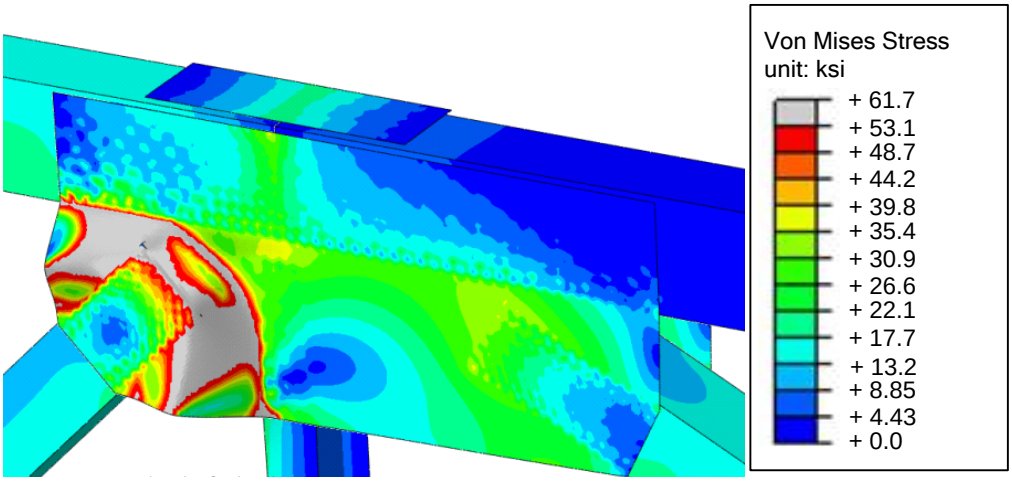

Figure 5.8.9: von Mises stress response contours for Case 6-a at post-peak (Deformation scale factor=5)

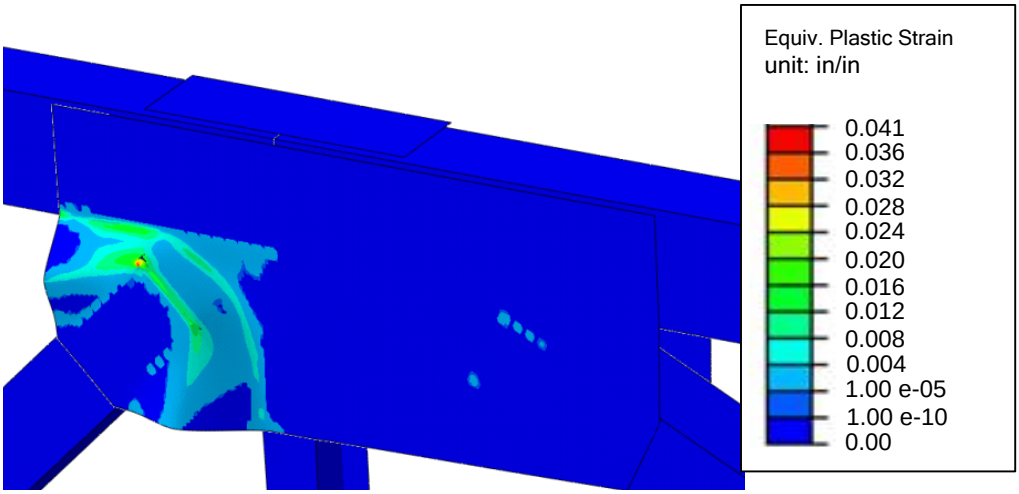

Figure 5.8.10: Equivalent plastic strain contours for Case 6-a at post-peak (Deformation scale factor=5)

5.8.1.3. Case 8-a (WV-INF-02)

This case has inclined chord members and represents an unchamfered Warren truss with vertical member at the inflection point of a truss bridge. By removing the chamfering on the compression diagonal of the original Case 8, the gap between the diagonal and the chord member increases. This feature possibly drives the failure towards buckling mode. Finite element analysis was performed using the 0.500 inch thick gusset plate. Gusset plate configuration and the reference loads are shown in Figure 5.8.11.

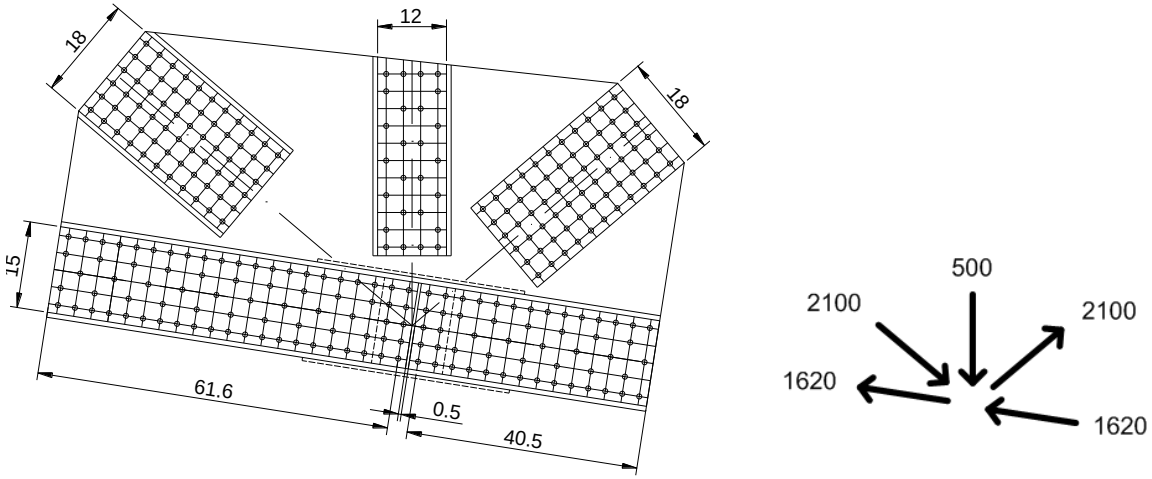

Figure 5.8.11: Case 8-a gusset plate details and applied reference loads

Failure occurs at ALF of 0.94 and the failure load is determined based on the peak load that the analysis can reach. 4% equivalent plastic strain limit is not reached before the peak load of the finite element analysis. As in Case 5-a and Case 6-a, 4% PEEQ limit does not apply and this is shown in Table 5.8.3.

Table 5.8.3: Maximum applied load fraction (ALF) values for Case 8-a

	4% PEEQ ALF	Peak ALF
Case 8-a (WV-INF-02)	**N/A**	**0.94**

The von Mises stress response contour at the failure load is shown in Figure 5.8.12. Yielding pattern is around both diagonals and the inclined plane above the chord members.

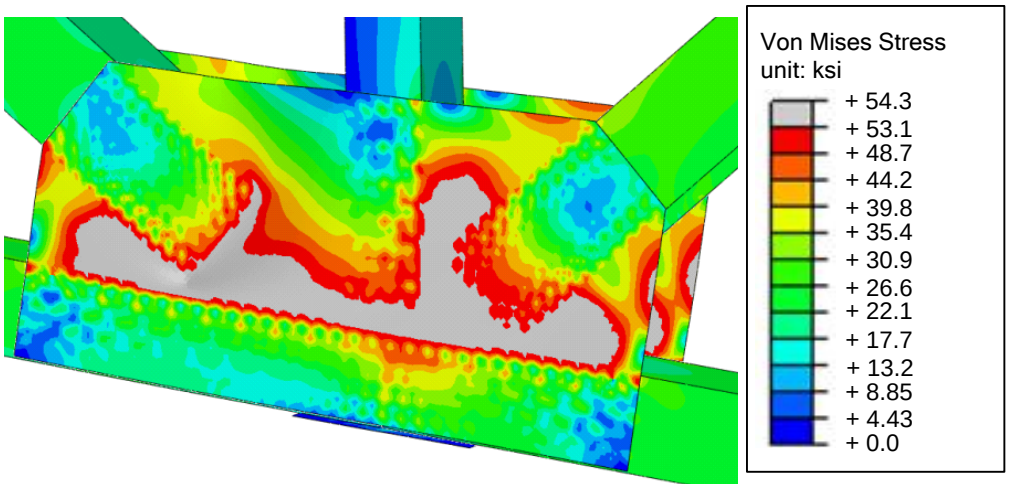

Figure 5.8.12: von Mises stress response contours for Case 8-a at ALF=0.94 (Deformation scale factor=5)

The equivalent plastic strain contours indicate the degree of plasticity along the inclined plane and the compression diagonal (Figure 5.8.13).

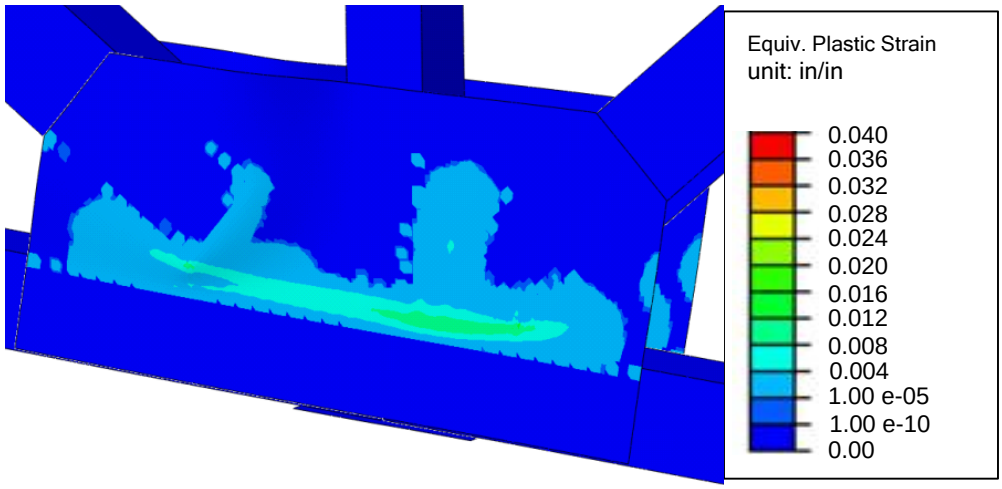

Figure 5.8.13: Equivalent plastic strain contours for Case 8-a at ALF=0.94 (Deformation scale factor=5)

At the failure load, gusset plate buckles and the compression diagonal starts moving out-of-plane. von Mises stress and equivalent plastic strain contours after the peak load are shown in Figure 5.8.14 and Figure 5.8.15 respectively. From these figures, deformed shape shows the buckled gusset plate and significant plasticity through the inclined shear plane of the joint. The shear plane still does not reach the 4% plastic strain limit at this

point. However, this joint provides data points to be used in both buckling and shear resistance calculations.

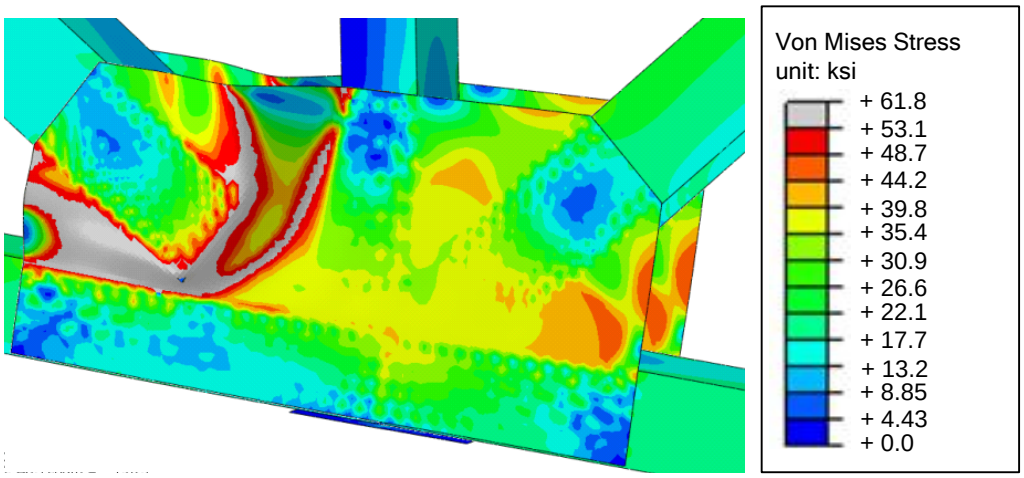

Figure 5.8.14: von Mises stress response contours for Case 8-a at post-peak (Deformation scale factor=5)

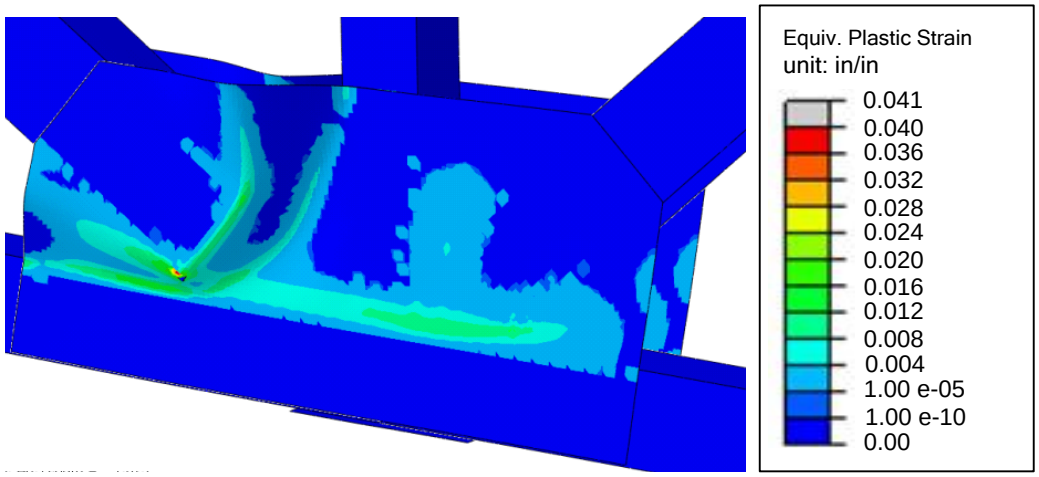

Figure 5.8.15: Equivalent plastic strain contours for Case 8-a at post-peak (Deformation scale factor=5)

5.8.2. Warren Trusses with Vertical Members

5.8.2.1. Case 13-a (W-NP-01)

This joint is a Warren truss without vertical member near pier location. The compression diagonal in Case 13 is changed and chamfering is removed. Same loads and gusset plate thickness of 0.400 inch is used in the finite element model. Final configuration with unchamfered members is shown in Figure 5.8.16.

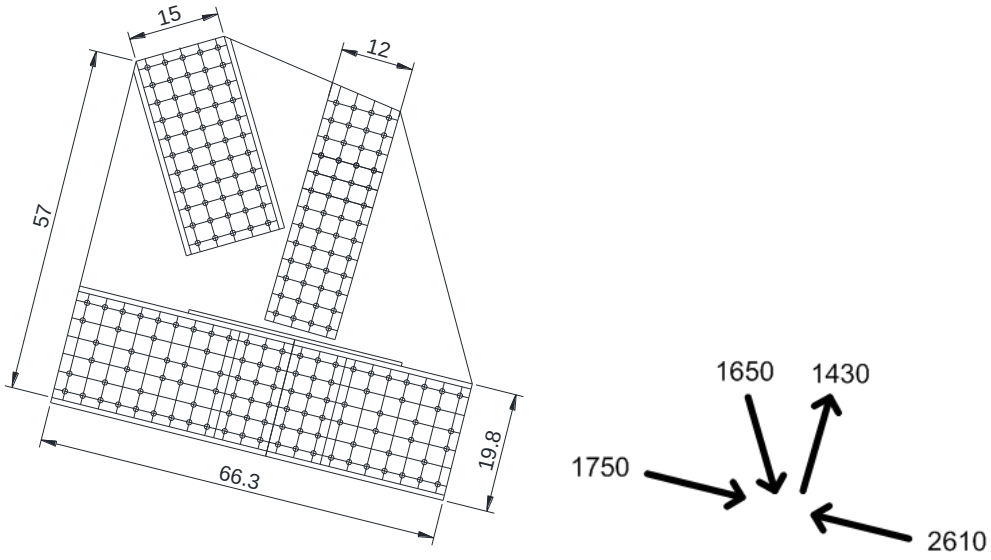

Figure 5.8.16: Case 13-a gusset plate details and applied reference loads

Similar to previous three unchamfered parametric cases, peak load determines the maximum capacity of the joint. Limit load is reached at ALF of 0.85 as shown in Table 5.8.4.

Table 5.8.4: Maximum applied load fraction (ALF) values for Case 13-a

	4% PEEQ ALF	Peak ALF
Case 13-a (W-NP-01)	**N/A**	**0.85**

By making the compression diagonal unchamfered, the gap between the diagonal centerline and the chord member increases a lot compared to the original Case 13 joint. In this case, the von Mises stress contours in Figure 5.8.17 shows that the base of the

compression diagonal moves out-of-plane due to gusset plate buckling. Yielding is concentrated around the compression diagonal.

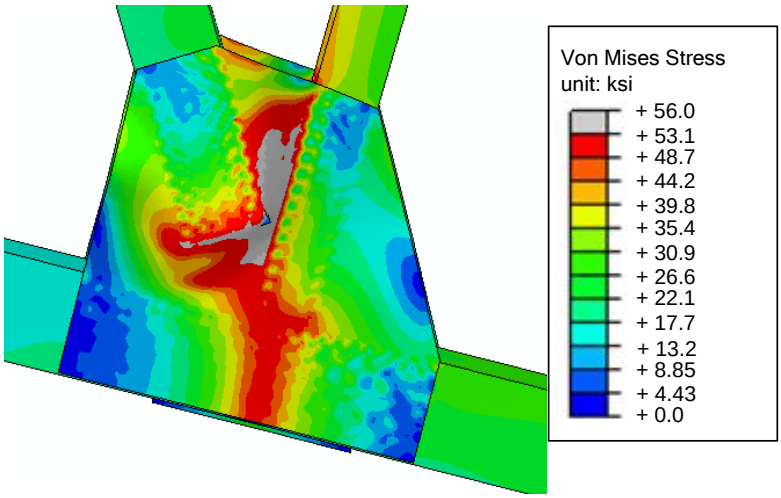

Figure 5.8.17: von Mises stress response contours for Case 13-a at ALF=0.85 (Deformation scale factor=10)

At the failure load, corresponding equivalent plastic strain contours (Figure 5.8.18) also support the conclusion that buckling failure occurs before the gusset plate can reach high level of plasticity (i.e. 4% PEEQ limit). At the same time, the whole inclined plane on the left side of the vertical member fully yields due to high forces transferred from the compression diagonal. This joint also provides data points to be used in both buckling and shear resistance calculations which will be discussed in Chapter 6.

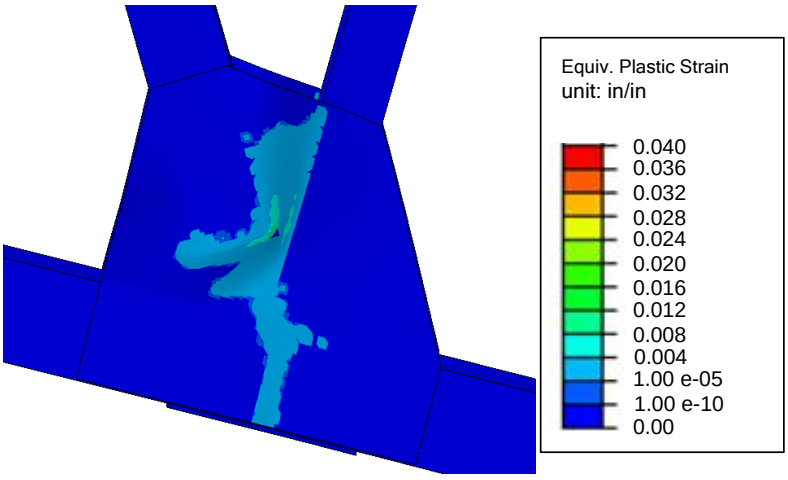

Figure 5.8.18: Equivalent plastic strain contours for Case 13-a at ALF=0.85 (Deformation scale factor=10)

5.8.2.2. Case 14-a (W-INF-01)

Last parametric joint with unchamfered members is Case 14-a at the inflection point location. There is no significant difference in the gusset plate size with respect to the Case 14 joint with chamfered members. The main reason is the level of chamfering was very small in the original joint. Same gusset plate thickness of 0.500 inch is used in this model. Gusset plate and the reference loads are shown in Figure 5.8.19.

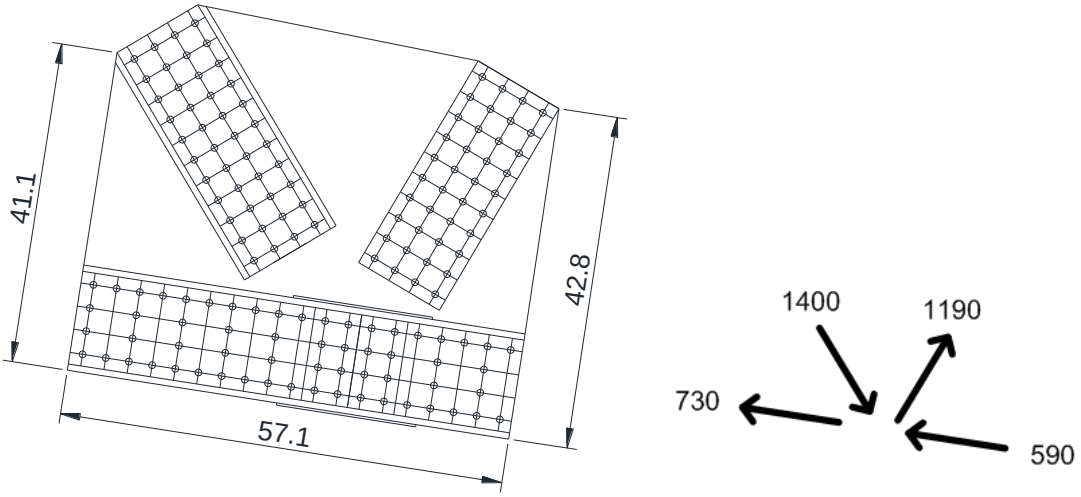

Figure 5.8.19: Case 14-a gusset plate details and applied reference loads

Both 4% equivalent plastic strain limit and the peak load are reached at the same applied load fraction. Table 5.8.5 shows that the joint fails at ALF of 1.17.

Table 5.8.5: Maximum applied load fraction (ALF) values for Case 14-a

	4% PEEQ ALF	Peak ALF
Case 14-a (W-INF-01)	**1.17**	**1.17**

At the limit load, gusset plate buckles and free edges move out-of-plane. In addition, the inclined plane above the chord members reaches the yield strength limit at ALF=1.17 (Figure 5.8.20).

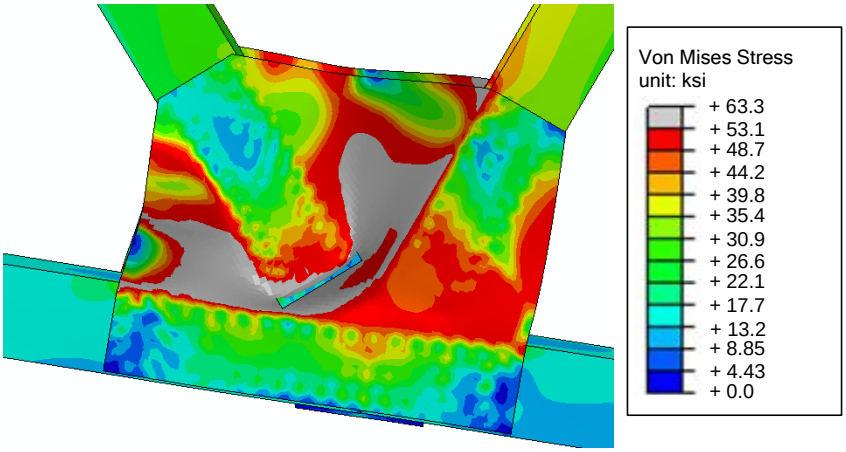

Figure 5.8.20: von Mises stress response contours for Case 14-a at ALF=1.17 (Deformation scale factor=10)

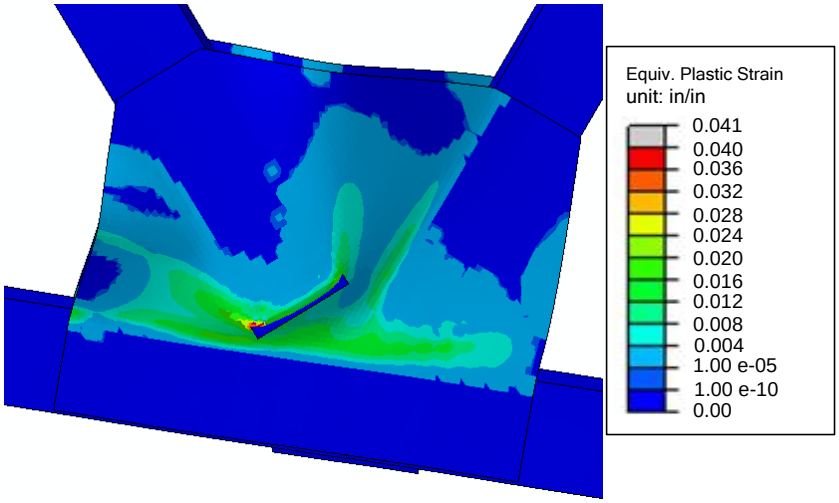

Figure 5.8.21: Equivalent plastic strain contours for Case 14-a at ALF=1.17 (Deformation scale factor=10)

The equivalent plastic strain contours in Figure 5.8.21 show the plastification along the horizontal plane parallel to the chord member centerline. Whole inclined plane above the use its capacity to carry more load. Force components from the two diagonals result in the yielding of the inclined plane. For this joint, excessive plastification along the critical shear plane finally results in the softening and buckling of the gusset plate (similar to the GP307-SL3 specimen discussed in Chapter 4).

5.9. Further Parametric Studies with Different Gusset Plate Thickness

All the analytical models created for the five test specimens, 14 chamfered parametric cases, and 5 unchamfered parametric cases are analyzed using a single gusset plate thickness and results are discussed in Chapter 4 and the first 7 sections of Chapter 5. The gusset plate thicknesses used in those analyses are summarized in Table 5.9.1.

Table 5.9.1: Gusset plate thickness values used in the initial finite element analysis of the test specimens and parametric cases

Specimen	Gusset Plate Thickness (inch)
GP307-SS3	0.375
GP307-LS3	0.375
GP307-SL3	0.375
GP490-SS3	0.375
GP490-LS3	0.375
Case 1	0.400
Case 2	0.400
Case 3	0.500
Case 4	0.800
Case 5	0.400
Case 6	0.500
Case 7	0.700
Case 8	0.500
Case 9	0.200
Case 10	0.200
Case 11	0.450
Case 12	1.000
Case 13	0.400
Case 14	0.500
Case 5-a	0.400
Case 6-a	0.500
Case 8-a	0.500
Case 13-a	0.400
Case 14-a	0.500

As shown in Table 5.9.1, thicknesses of 0.375, 0.400, and 0.500 inch are used in most of the analyses with few exceptions such as the 0.200 inch for the Pratt truss configurations

(Case 9 and Case 10), the 1.000 inch for Case 12, etc. However, a single analysis for each case is not enough to gather enough data points to be used in developing and calibrating the proposed gusset plate resistance calculations to be summarized in Chapter 6. One of the major goals of this research is to be able to better quantify the strength of the gusset plate connections in steel truss bridges. Hence, depending on the gusset plate thickness of the joints, a transition from a "pure" buckling failure for a very thin gusset plate to a "pure" shear failure for a thick gusset plate is investigated for most of the joint configurations under study.

Based on the detailed studies on the 20 bridge plans, the thinnest gusset plate used in those bridges is a 0.375 inch plate. However, for a complete parametric study, gusset plate thicknesses are varied between 0.250 inch and 0.625 inch unless otherwise noted. Similar to the test specimens, the 5 additional cases created by removing the vertical members are also included in these studies. Considering the time and size of the analysis models, some of the chamfered (Cases 4, 9, 10, 11, 12) and unchamfered (Case 8-a) parametric cases are not included.

5.9.1. Example Results for Case 5 Joint

The Case 5 joint will be used to show typical results for the variable gusset plate thickness studies. From the initial studies with 0.400 inch thick gusset plate, von Mises stress contours in Figure 5.7.14 shows that the gusset plate yields both along the vertical plane next to the vertical member and the horizontal plane below the chord members. The conclusions from the initial studies showed that chamfered connections undergo shear dominated failures due to chamfering of the members and load transfer mechanism through the planes parallel to those chamfered edges. In these parametric studies, the two planes shown in Figure 5.9.1 are further investigated to determine how much shear dominates the yielding criteria. This information will enable gusset plate design checks to be limited to just a simple shear check, avoiding having to couple this check with membrane stresses along the critical planes when the gusset plate reaches its limit load. For the unchamfered connections, the buckling failure mode can be easily identified from the plasticity pattern of the joint along with the out-of-plane movement of the compression diagonal due to gusset plate buckling. When the gusset plate undergoes

significant plasticity, the limit load is determined based on the 4% equivalent plastic strain limit and the studies explained in this section for the critical shear planes help which cases can be picked to be included in the shear resistance calculation checks for unchamfered connections.

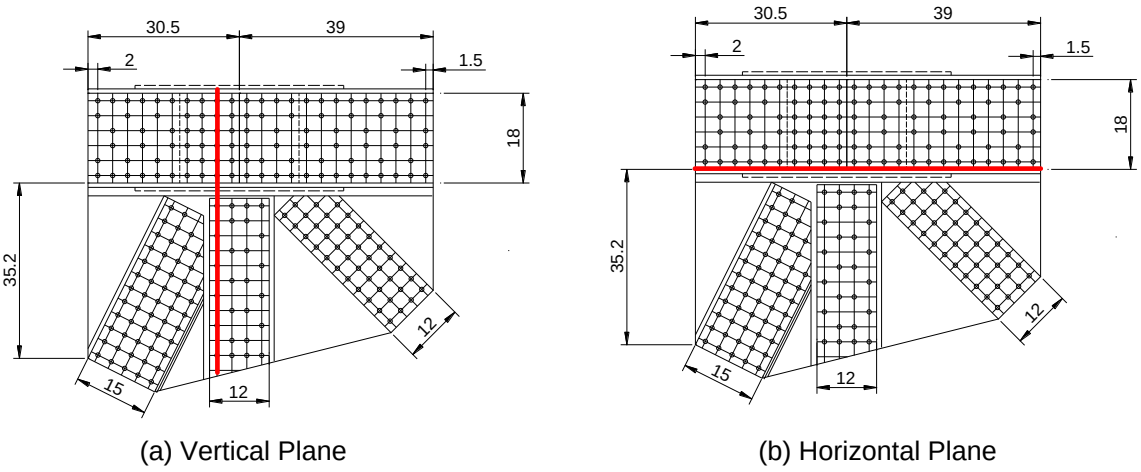

Figure 5.9.1: Vertical and horizontal planes to extract stress output for Case 5

5.9.1.1. Results for t_{GP} = 0.250 inch

Figure 5.9.2 shows the von Mises stress contours for the thinnest plate (t_{GP} =0.250 inch) used in the studies. Yielding is concentrated along the horizontal and vertical planes. The base of the compression diagonal on the left along with the chamfered edge is fully yielded. For this relatively thin plate, the yielding around the compression diagonal results in the buckling of the gusset plate at the limit load. It is worth looking at the stresses along the horizontal and vertical planes to see the significance of the shear yielding.

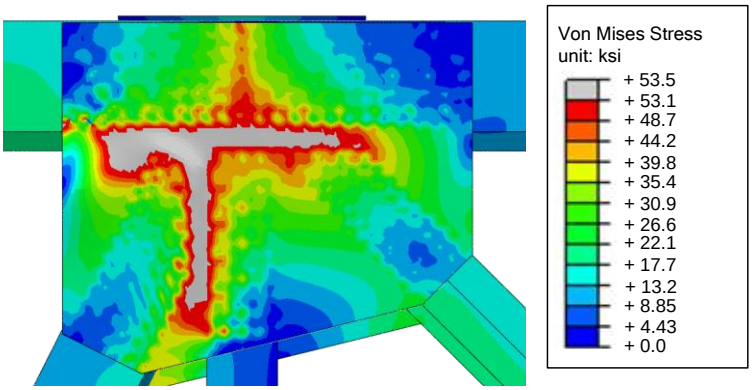

Figure 5.9.2: von Mises stress response contours for Case 5 for t_{GP} =0.250 inch

Figure 5.9.3 shows the three different stresses along the horizontal plane at the limit load of the joint. The von Mises stresses (shown with black diamond sign) support the contours shown above. The black dashed line is the yield strength limit of the gusset plate, and thus a very significant portion of the horizontal plane is at its yield limit. The shear stresses (shown with the red triangles) indicate that the yielded regions already reached or exceeded the shear yield strength limit which is shown with the dashed red line. The green curve shows the axial stress values along the horizontal plane. These results indicate that both axial and shear stresses contribute to the von Mises yield criterion. However, checking the plane for the shear yield resistance at the failure load becomes a reasonable resistance check for the gusset plate based on the results from the red curve in Figure 5.9.3.

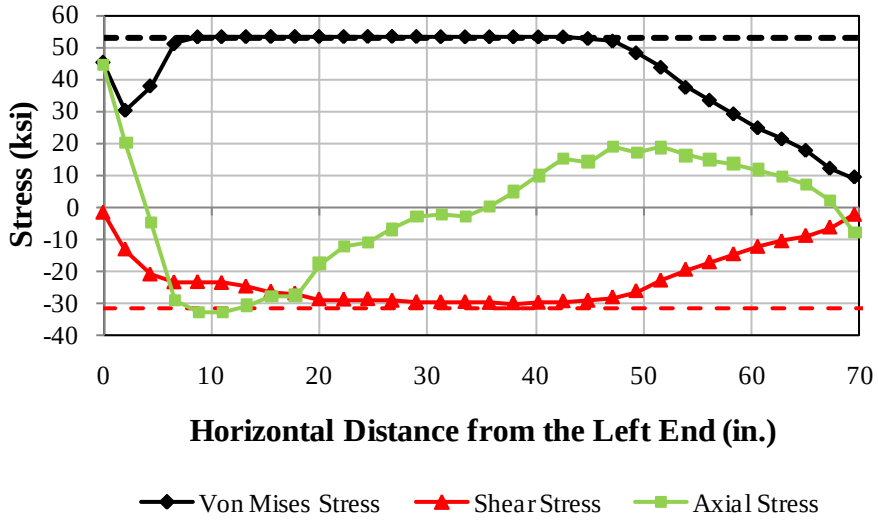

Figure 5.9.3: Comparison of the stresses along the horizontal plane of the Case 5 joint (t_{GP} =0.250 inch)

Similar results along the vertical plane are shown in Figure 5.9.4. The yielded regions basically reach their shear yield limit at the same time which shows the dominant role of shear stress along the two paths of load transfer within the gusset plate. It also shows how shear yielding progressed along the two planes even with 0.250 inch thick gusset plate. This is mainly due to the chamfering of the members as concluded from the previous analyses performed on the chamfered parametric cases. Although the shear stresses start dissipating within the chord member regions, shear resistance calculations are based on the full vertical plane length basically because it results in a simple free body diagram of the gusset plate along that path. This issue will be discussed in more detail in Chapter 6.

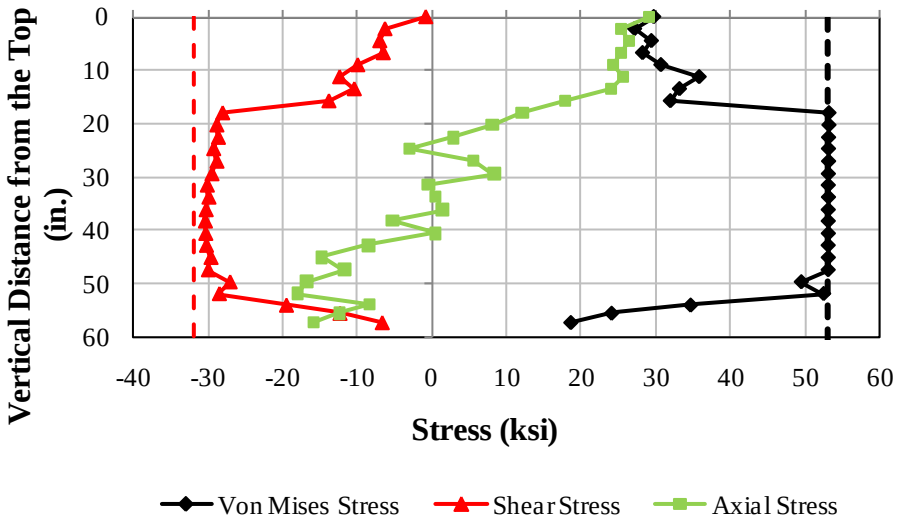

Figure 5.9.4: Comparison of the stresses along the vertical plane of the Case 5 joint (t_{GP} =0.250 inch)

5.9.1.2. Results for t_{GP} = 0.375 inch

The next analysis is performed using a gusset plate thickness of 0.375 inch. The trend of the yielding is similar to the previous case except that the yielding is more significant along the two planes (Figure 5.9.5).

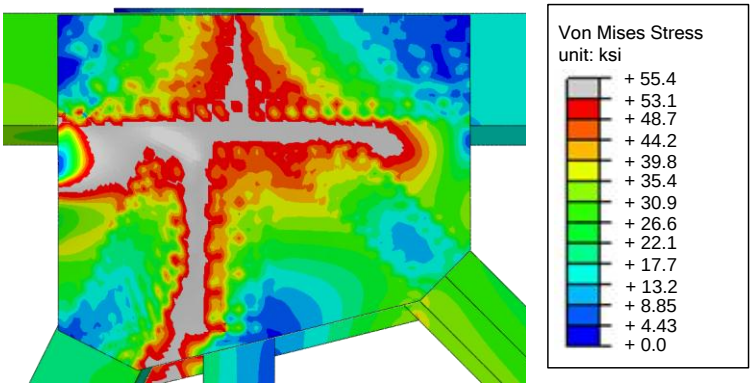

Figure 5.9.5: von Mises stress response contours for Case 5 for t_{GP} =0.375 inch

The stress plots along the horizontal plane (Figure 5.9.6) show that von Mises yield limit is reached along almost the full horizontal plane below the chord members. Shear stresses are also at the shear yield limit at the instant of the failure. This shows that the failure is mainly due to shear along that path.

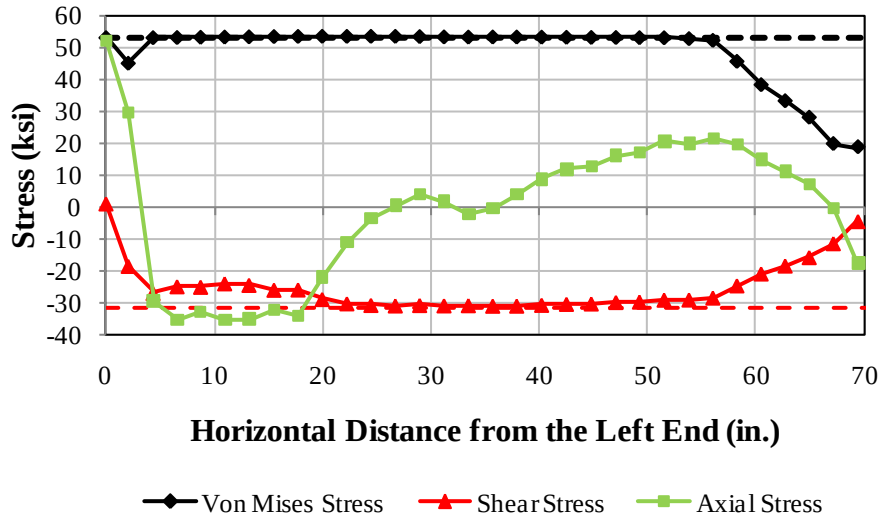

Figure 5.9.6: Comparison of the stresses along the horizontal plane of the Case 5 joint (t_{GP} =0.375 inch)

Similarly, the vertical plane stress plots in Figure 5.9.7 again shows how the von Mises stresses and shear stresses are at their limits.

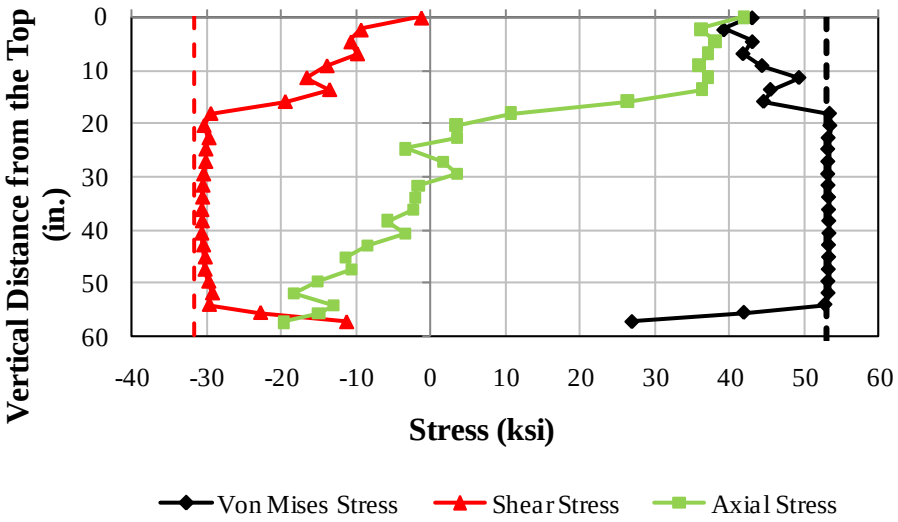

Figure 5.9.7: Comparison of the stresses along the vertical plane of the Case 5 joint (t_{GP} =0.375 inch)

5.9.1.3. Results for t_{GP} = 0.500 inch

The third analysis is performed a thicker plate (0.500 inch). As expected, shear planes are fully yielded as shown in Figure 5.9.8.

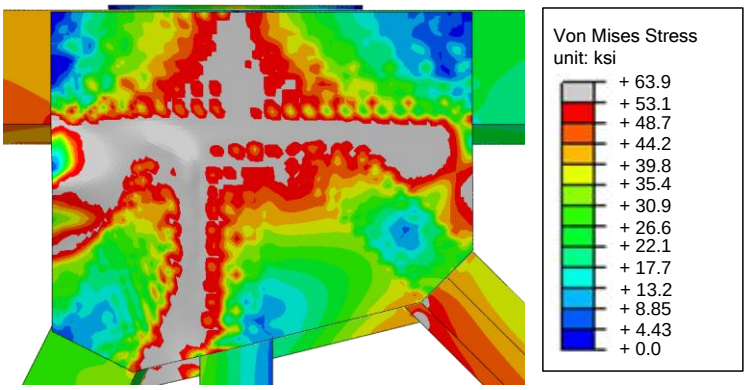

Figure 5.9.8: von Mises stress response contours for Case 5 for t_{GP} =0.500 inch

The full horizontal plane yielding shown by the von Mises and shear stress plots in Figure 5.9.9 indicate that the horizontal plane reaches its maximum shear yield capacity at the limit load of the joint.

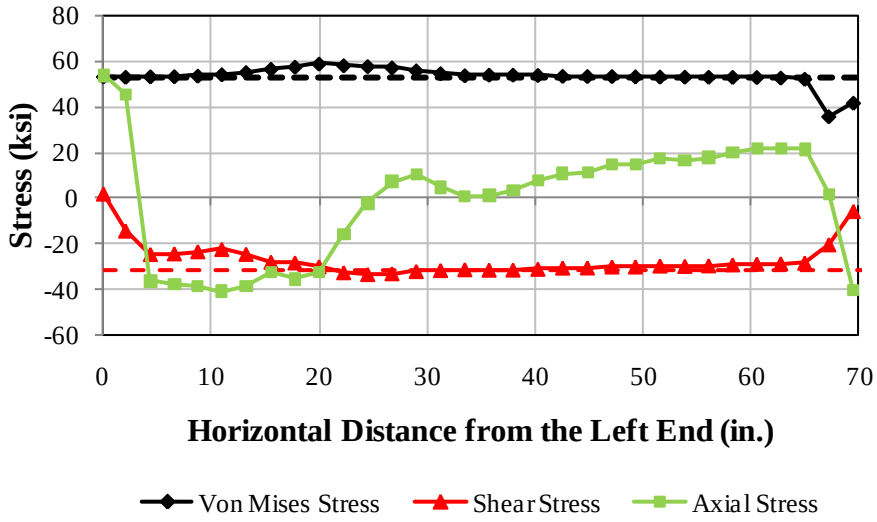

Figure 5.9.9: Comparison of the stresses along the horizontal plane of the Case 5 joint (t_{GP} =0.500 inch)

Vertical plane stresses are similar to the previous case. The yielding is mainly dominated by shear as shown in Figure 5.9.10.

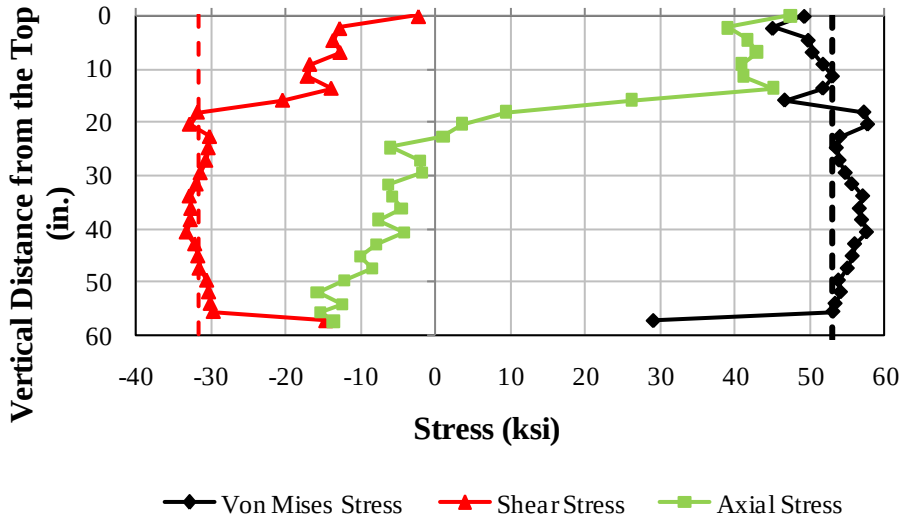

Figure 5.9.10: Comparison of the stresses along the vertical plane of the Case 5 joint (t_{GP} =0.500 inch)

5.9.1.4. Results for t_{GP} = 0.625 inch

The analysis using the 0.625 inch thick gusset plate provides the same conclusions as the previous cases, and is very similar to the 0.500 inch gusset plate case. The von Mises stress contours in Figure 5.9.11 shows the yielding along the horizontal and vertical planes.

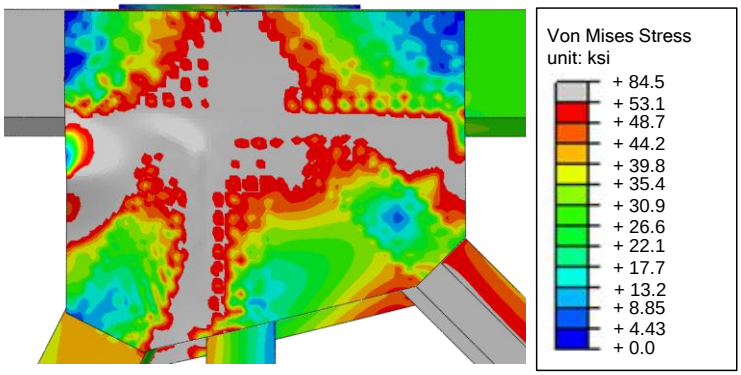

Figure 5.9.11: von Mises stress response contours for Case 5 for t_{GP} =0.625 inch

Stress plots along the horizontal plane show that the shear stresses reach the yield limit at the failure load (Figure 5.9.12).

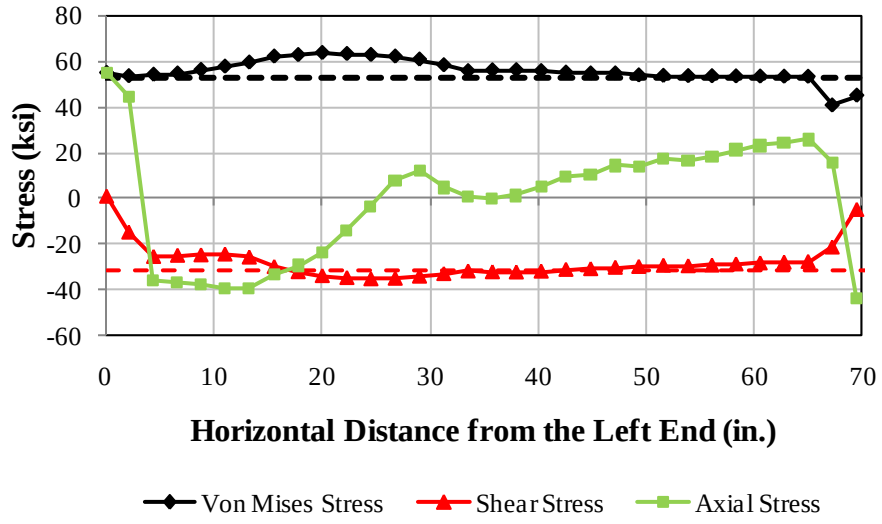

Figure 5.9.12: Comparison of the stresses along the horizontal plane of the Case 5 joint (t_{GP} =0.625 inch)

The stresses along the vertical shear plane are shown in Figure 5.9.13. These are no different than the previous cases and the same conclusion on the critical plane resistance checks can be reached using this analysis. Gusset plate resistance along the horizontal or vertical planes can be checked using the shear yield strength of the gusset plate.

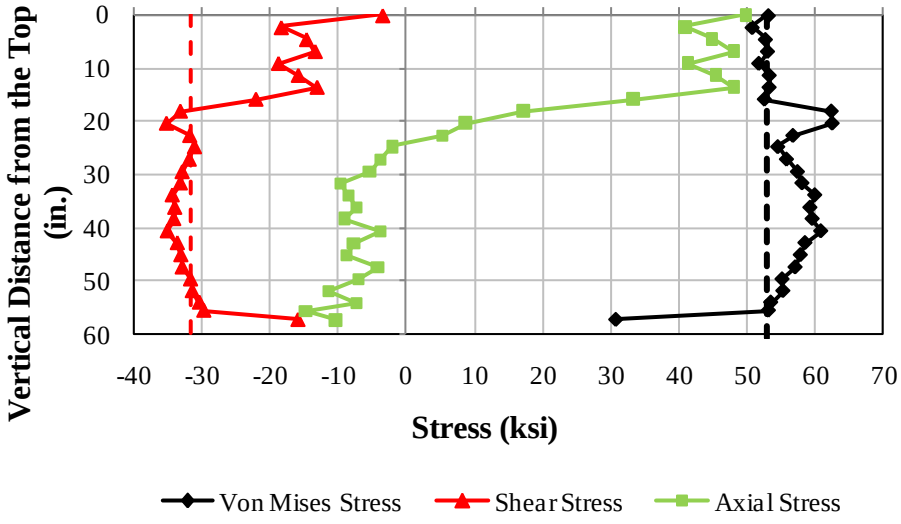

Figure 5.9.13: Comparison of the stresses along the vertical plane of the Case 5 joint (t_{GP} =0.625 inch)

CHAPTER VI : PROPOSED DESIGN RECOMMENDATIONS

6.1. Compression Resistance Checks

The compression resistance of gusset plates in truss bridge connections has been vigorously discussed by design engineers and researchers in the aftermath of the I-35W bridge collapse. FHWA provided a preliminary Guidance in this area in terms of both an edge slenderness limit and a calculation of the buckling capacity (FHWA, 2009). The buckling capacity is based on the Whitmore width with 30° stress dispersion and using an equivalent column calculated by taking the average of three lengths extended from the column width until they intersect the closest bolt lines (Figure 6.1.1). However, the correct effective length factor, K and column length to be used in resistance calculations are still open to engineering judgment. The suggested use of a K=1.2 and an average effective column length approach as defined in the FHWA Guidance provide significant amount of conservatism into design calculations.

For the purposes of this study, the compression resistance recommendations are divided into four parts. The first part deals with the resistance of the unchamfered connections, which can be treated by using the column buckling analogy with the appropriate K factor. The second part deals with the extension of this approach to the chamfered connections. The third part deals with the compression block shear check which best defines the resistance for certain common cases. Finally, the fourth part deals with assessing the validity of the current edge slenderness limit as defined in the FHWA Guidance. The following subsections address each of these issues.

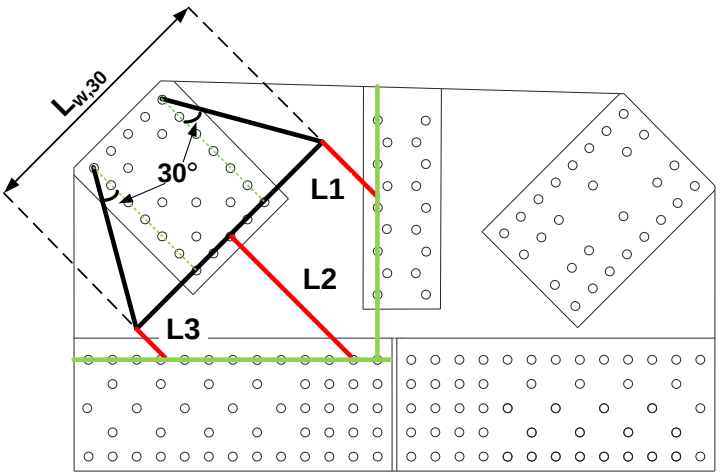

Figure 6.1.1: Equivalent column lengths used in the current FHWA guidance buckling resistance calculations

6.1.1. Buckling of Unchamfered Member Connections

All members utilized in the experimental studies are unchamfered, and this data is complemented by a large number of the test specimens investigated in the parametric analytical studies. This data set provides valuable data to assess the buckling resistance of the gusset plates for unchamfered member connections. For the five experimental test specimens, parametric analytical studies are performed by changing the thickness between 1/8" and 5/8" in increments of 1/16". The objective is to capture a change from one failure mode to another (i.e., from pure buckling to buckling/shear and/or buckling/shear to pure shear). The parametric cases are limited to a 5/8" gusset plate thickness as a practical upper limit for which a buckling failure can be achieved. Although the smallest gusset plate thickness found in the 20 bridge plans used was 3/8", all the final recommendation calculations are applicable to a range of 1/4" to 5/8" thick plates. Plate material properties and applied member loads used in the parametric studies of five test specimens are shown in Table 6.1.1**.** F2 represents the compression diagonal load using the sign convention defined previously in Figure 4.6.20. For these studies, the member loads are taken from the tests to failure of each specimen, except for the GP490-LS3 specimen. The load combination originally used for this specimen has a much higher tension diagonal load as compared to the compression diagonal. For the parametric studies, a different load combination is applied to be able to capture a buckling failure for different thicknesses.

Table 6.1.1: Plate material properties and member loads applied in the parametric studies for the five specimens

Specimen	F_y (ksi)	F_u (ksi)	E (ksi)	F2 (kip)	F3 (kip)	F4 (kip)	F5 (kip)
GP307-SS3	36.4	62.6	29000	716	-141	-507	520
GP307-LS3	48.2	67.4		796	-280	-405	-290
GP307-SL3	46.6	64.9		946	0	-929	706
GP490-SS3	46.4	65.2		728	0	-728	538
GP490-LS3	45.6	63.7		478	0	-478	491

For each specimen, the gusset plate thicknesses at which a buckling failure occurred are determined. The compression load transferred from the diagonal and applied to single gusset plate at the instant of failure of each specimen is shown in Table 6.1.2**.** The P_{FEA} shown in this table is the finite element analysis load, which becomes the critical buckling load, P_{cr} for the gusset plate for the cases where buckling takes place. Since the connection has two gusset plates connected to the compression diagonal, the diagonal load is multiplied by the corresponding ALF and divided by two. Thus the resistance calculations are performed for a single gusset plate by assuming each plate equally shares the total member load at the instant of failure.

Table 6.1.2: Compression loads transferred from the compression diagonal to the single gusset plate for different thickness analysis runs (buckling failures are highlighted)

Specimen	t_{GP} (in)	ALF	P_{FEA} (kip)	Buckling Failure
GP307-SS3	0.1250	0.17	61	Yes
	0.1875	0.34	122	Yes
	0.2500	0.53	190	Yes
	0.3125	0.74	265	Yes
	0.3750	0.94	337	Yes
	0.4375	1.14	408	No
	0.5000	1.36	487	No
	0.6250	1.89	677	No

Table 6.1.2 (continued): Compression loads transferred from the compression diagonal to the single gusset plate for different thickness analysis runs (buckling failures are highlighted)

Specimen	t_{GP} (in)	ALF	P_{FEA} (kip)	Buckling Failure
GP307-LS3	0.1250	0.10	40	Yes
	0.1875	0.25	100	Yes
	0.2500	0.50	199	Yes
	0.3125	0.82	326	Yes
	0.3750	1.10	438	Yes
	0.4375	1.37	545	Yes
	0.5000	1.64	653	Yes
	0.6250	2.14	852	No
GP307-SL3	0.1250	0.15	71	Yes
	0.1875	0.37	175	Yes
	0.2500	0.60	284	Yes
	0.3125	0.78	369	No
	0.3750	1.02	482	No
	0.4375	1.21	572	No
	0.5000	1.37	648	No
	0.6250	1.73	818	No
GP490-SS3	0.1250	0.16	58	Yes
	0.1875	0.38	138	Yes
	0.2500	0.61	222	Yes
	0.3125	0.82	298	Yes
	0.3750	1.04	379	Yes
	0.4375	1.25	455	No
	0.5000	1.46	531	No
	0.6250	1.82	662	No
GP490-LS3	0.1250	0.13	31	Yes
	0.1875	0.34	81	Yes
	0.2500	0.62	148	Yes
	0.3125	0.96	229	Yes
	0.3750	1.31	313	Yes
	0.4375	1.68	402	Yes
	0.5000	2.04	488	No
	0.6250	2.67	638	No

The equivalent column width for cross-section calculations is determined based on the 30° dispersion angle, as proposed by Whitmore (1952). The radius of gyration, r_s calculation requires the calculation of the area, A_{GP} and moment of inertia, $I_{g,GP}$ of the equivalent column section of the gusset plate.

$$A_{GP} = L_{w,30}(t_{GP}) \qquad \text{(Eq. 6.1-1)}$$

$$I_{g,GP} = \frac{1}{12} L_{w,30}(t_{GP})^3 \qquad \text{(Eq. 6.1-2)}$$

$$r_s = \sqrt{\frac{I_{g,GP}}{A_{GP}}} = \sqrt{\frac{[\frac{1}{12} L_{w,30}(t_{GP})^3]}{L_{w,30}(t_{GP})}} = \frac{t_{GP}}{\sqrt{12}} \qquad \text{(Eq. 6.1-3)}$$

Although the column widths change from one connection to another, the r_s value becomes primarily a function of the gusset plate thickness. However, different A_{GP} values mean different yield strength for the equivalent columns from each connection. A summary of the cross-sectional property calculations for equivalent columns representing the gusset plate buckling in each connection are shown in Table 6.1.3**.**

Table 6.1.3: Cross-sectional properties for the equivalent columns used in the buckling calculations of the five test specimens

Specimen	t_{GP} (in)	$L_{w,30}$ (in)	A_{GP} (in^2)	$I_{g,GP}$ (in^4)	r_s (in)
GP307-SS3	0.1250	24.4	3.1	0.004	0.036
	0.1875	24.4	4.6	0.013	0.054
	0.2500	24.4	6.1	0.032	0.072
	0.3125	24.4	7.6	0.062	0.090
	0.3750	24.4	9.2	0.107	0.108
	0.4375	24.4	10.7	0.170	0.126
	0.5000	24.4	12.2	0.254	0.144
	0.6250	24.4	15.3	0.496	0.180

Table 6.1.3 (continued): Cross-sectional properties for the equivalent columns used in the buckling calculations of the five test specimens

Specimen	t_{GP} (in)	$L_{w,30}$ (in)	A_{GP} (in^2)	$I_{g,GP}$ (in^4)	r_s (in)
GP307-LS3	0.1250	27.5	3.4	0.004	0.036
	0.1875	27.5	5.2	0.015	0.054
	0.2500	27.5	6.9	0.036	0.072
	0.3125	27.5	8.6	0.070	0.090
	0.3750	27.5	10.3	0.121	0.108
	0.4375	27.5	12.0	0.192	0.126
	0.5000	27.5	13.8	0.286	0.144
	0.6250	27.5	17.2	0.559	0.180
GP307-SL3	0.1250	33.1	4.1	0.005	0.036
	0.1875	33.1	6.2	0.018	0.054
	0.2500	33.1	8.3	0.043	0.072
	0.3125	33.1	10.3	0.084	0.090
	0.3750	33.1	12.4	0.145	0.108
	0.4375	33.1	14.5	0.231	0.126
	0.5000	33.1	16.6	0.345	0.144
	0.6250	33.1	20.7	0.673	0.180
GP490-SS3	0.1250	21.5	2.7	0.003	0.036
	0.1875	21.5	4.0	0.012	0.054
	0.2500	21.5	5.4	0.028	0.072
	0.3125	21.5	6.7	0.055	0.090
	0.3750	21.5	8.1	0.094	0.108
	0.4375	21.5	9.4	0.150	0.126
	0.5000	21.5	10.8	0.224	0.144
	0.6250	21.5	13.4	0.437	0.180
GP490-LS3	0.1250	21.5	2.7	0.003	0.036
	0.1875	21.5	4.0	0.012	0.054
	0.2500	21.5	5.4	0.028	0.072
	0.3125	21.5	6.7	0.055	0.090
	0.3750	21.5	8.1	0.094	0.108
	0.4375	21.5	9.4	0.150	0.126
	0.5000	21.5	10.8	0.224	0.144
	0.6250	21.5	13.4	0.437	0.180

The nominal buckling resistance calculations based on the AISC column formulas are:

$$P_{cr} = 0.658^{\lambda}(F_y)(A_{GP}) \quad \text{if} \quad \lambda \le 2.25 \qquad \text{(Eq. 6.1-4)}$$

$$P_{cr} = \frac{0.877(F_y)(A_{GP})}{\lambda} \quad \text{if} \quad \lambda > 2.25 \qquad \text{(Eq. 6.1-5)}$$

where λ was defined with the formula:

$$\lambda = \left(\frac{KL}{r_s \pi}\right)^2 \left(\frac{F_y}{E}\right) \qquad \text{(Eq. 6.1-6)}$$

From the finite element analyses, a critical buckling load is determined for the buckling failure cases. For all the specimens, the yield strength (F_y) and area of the equivalent column (A_{GP}) are known. The λ is an unknown parameter in this formulation. The two unknown parameters used in calculating λ are effective length factor, K and equivalent column length, L. For each of the specimen, actual KL values are back-calculated using the critical buckling loads obtained from the finite element analysis. The first step is back-calculating the λ using the formulas:

$$\lambda_{calc} = \frac{\ln\left(\frac{P_{cr}}{F_y A_{GP}}\right)}{\ln(0.658)} \qquad \text{if} \qquad \lambda_{calc} \le 2.25 \qquad \text{(Eq. 6.1-7)}$$

$$\lambda_{calc} = \frac{0.877(F_y)(A_{GP})}{P_{cr}} \qquad \text{if} \qquad \lambda_{calc} > 2.25 \qquad \text{(Eq. 6.1-8)}$$

The second step is back-calculating the actual KL from the different gusset plate thickness analyses using the formula:

$$KL_{calc} = \sqrt{\frac{\lambda_{calc} E}{F_y}} (r_s \pi) \quad \text{if} \quad \lambda_{calc} > 0 \qquad \text{(Eq. 6.1-9)}$$

$$KL_{calc} = 0 \quad \text{if} \quad \lambda_{calc} \leq 0 \qquad \text{(Eq. 6.1-10)}$$

When λ_{calc} is a negative value, the corresponding KL_{calc} value becomes zero; this represents the full yield capacity of the column cross-section. As the third step, the maximum of the KL_{calc} values is picked for each specimen. Although the maximum value does not correspond to the thinnest plate for some of the specimens, the difference is not significant. This maximum value is assumed to represent the effective column length of each specimen. The yield strength, P_y of the column-cross section is then calculated using the formula:

$$P_y = F_y A_{GP} \qquad \text{(Eq. 6.1-11)}$$

This equation is used in the λ_{calc} formulation described previously. Table 6.1.4 shows the summary of KL_{calc} and λ_{calc} calculations for the five specimens. The maximum of the calculated effective column lengths are also shown in this table.

Table 6.1.4: Back-calculated λ, KL, and $(KL)_{max}$ values derived from the buckling failure cases of the five specimens

Specimen	t_{GP} (in)	P_{cr} (kip)	P_y (kip)	P_{cr}/P_y	λ_{calc}	KL_{calc} (in)	$(KL)_{max}$ (in)
GP307-SS3	0.1250	61	111	0.55	1.45	3.8	4.2
	0.1875	122	167	0.73	0.75	4.2	
	0.2500	190	222	0.85	0.38	3.9	
	0.3125	265	278	0.95	0.11	2.7	
	0.3750	337	333	1.01	-0.02	0.0	
GP307-LS3	0.1250	40	166	0.24	3.66	5.3	6.2
	0.1875	100	249	0.40	2.20	6.2	
	0.2500	199	331	0.60	1.23	6.2	
	0.3125	326	414	0.79	0.57	5.3	
	0.3750	438	497	0.88	0.31	4.6	
	0.4375	545	580	0.94	0.15	3.7	
	0.5000	653	663	0.98	0.04	2.1	

Table 6.1.4 (continued): Back-calculated λ, KL, and $(KL)_{max}$ values derived from the buckling failure cases of the five specimens

Specimen	t_{GP} (in)	P_{cr} (kip)	P_y (kip)	P_{cr}/P_y	λ_{calc}	KL_{calc} (in)	$(KL)_{max}$ (in)
GP307-SL3	0.1250	71	193	0.37	2.39	4.4	4.9
	0.1875	175	289	0.61	1.21	4.7	
	0.2500	284	386	0.74	0.74	4.9	
GP490-SS3	0.1250	58	125	0.47	1.83	3.8	3.8
	0.1875	138	187	0.74	0.73	3.6	
	0.2500	222	249	0.89	0.28	3.0	
	0.3125	298	312	0.96	0.10	2.3	
	0.3750	379	374	1.01	-0.03	0.0	
GP490-LS3	0.1250	31	123	0.25	3.47	5.3	6.3
	0.1875	81	184	0.44	1.96	6.0	
	0.2500	148	245	0.60	1.21	6.3	
	0.3125	229	306	0.75	0.70	6.0	
	0.3750	313	368	0.85	0.39	5.3	
	0.4375	402	429	0.94	0.16	4.0	

In the proposed methodology, the use of a single length rather than an average of three different lengths is preferred, as there is no agreement on how to define the three lengths for cases in which the equivalent column width interferes with other members. In those cases, there is no consensus on whether to use a "zero" length or a "negative" length in the average length calculations. The use of a single column length will provide designers with an easy interpretation of the equivalent column length approach. This length is called L_{mid} and is defined as the length from the centerline of the first bolt line in the compression member to the intersection of the first bolt line of the closest member (Figure 6.1.2). This is a much easier representation of the buckling length of the gusset plate. L_2 in the current FHWA guidance check is basically the same as L_{mid} in the current approach. However, this name convention is used since the plate is represented by a single length, in this case, L_{mid}.

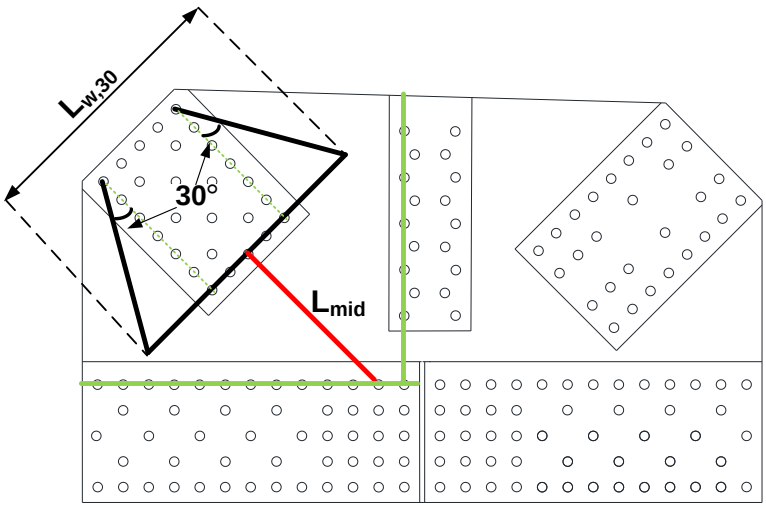

Figure 6.1.2: Proposed equivalent column length for buckling resistance calculations

The final step in this approach is determining the actual effective length factor for the gusset plate connections. This is obtained by dividing the $(KL)_{max}$ values with the corresponding L_{mid} values. For each connection, using the results from analyses of connections with different thickness, an actual effective column length is determined. Finally, using the column length of L_{mid}, a "real" effective length factor is calculated. The corresponding K values for each specimen are summarized in Table 6.1.5**.**

Table 6.1.5: Back calculated K values

Specimen	L_{mid} (in)	$(KL)_{max}$ (in)	$(KL)_{max}/L_{mid}$
GP307-SS3	13.1	4.2	0.32
GP307-LS3	18.1	6.2	0.34
GP307-SL3	13.1	4.9	0.37
GP490-SS3	13.1	3.8	0.29
GP490-LS3	18.1	6.3	0.35
		Average	**0.33**

For design and evaluation, a proposed K value for the buckling resistance calculation is 0.35. The K values are clustered around 0.33 with a standard deviation of 0.03. An analysis using L_{mid} and K = 0.35 provides a good approximation to the gusset plate buckling capacity when treating it as a one-dimensional problem.

The recommended K value is further investigated to measure its effectiveness and applicability. For each of the five specimens, one additional case is created by removing

the vertical member. These cases provide another data set to use throughout the parametric studies. For these analyses, the diagonals have equal loads applied in the finite element model since the angle between the diagonals and chord members is 45° which leeads to zero vertical member loads. Equilibrium load combinations for the five additional cases are summarized in Table 6.1.6

Table 6.1.6: Plate material properties and member loads applied in the five additional parametric cases (test specimens without vertical member)

Specimen	F_y (ksi)	F_u (ksi)	E (ksi)	F2 (kip)	F3 (kip)	F4 (kip)	F5 (kip)
GP307-SS3-a	36.4	62.6	29000	716	0	-716	520
GP307-LS3-a	48.2	67.4		796	0	-796	-290
GP307-SL3-a	46.6	64.9		946	0	-929	706
GP490-SS3-a	46.4	65.2		728	0	-728	538
GP490-LS3-a	45.6	63.7		478	0	-478	491

The compression loads applied to the single gusset plate at the instant of failure of each specimen are shown in Table 6.1.7**.** The thicknesses for which buckling is the failure mode are highlighted.

Table 6.1.7: Compression loads transferred from the compression diagonal to the single gusset plate for different thickness analysis runs (buckling failures are highlighted)

Specimen	t_{GP} (in)	ALF	P_{FEA} (kip)	Buckling Failure
GP307-SS3-a	0.1250	0.11	39	Yes
	0.1875	0.26	93	Yes
	0.2500	0.45	161	Yes
	0.3125	0.65	233	Yes
	0.3750	0.83	297	Yes
	0.4375	1.01	362	No
	0.5000	1.23	440	No
	0.6250	1.70	609	No

Table 6.1.7 (continued): Compression loads transferred from the compression diagonal to the single gusset plate for different thickness analysis runs (buckling failures are highlighted)

Specimen	t_{GP} (in)	ALF	P_{FEA} (kip)	Buckling Failure
GP307-LS3-a	0.1250	0.08	32	Yes
	0.1875	0.21	84	Yes
	0.2500	0.41	163	Yes
	0.3125	0.68	271	Yes
	0.3750	0.95	378	Yes
	0.4375	1.21	482	Yes
	0.5000	1.44	573	Yes
	0.6250	1.89	752	No
GP307-SL3-a	0.1250	0.11	52	Yes
	0.1875	0.29	137	Yes
	0.2500	0.53	251	Yes
	0.3125	0.77	364	Yes
	0.3750	1.00	473	No
	0.4375	1.19	563	No
	0.5000	1.38	653	No
	0.6250	1.73	818	No
GP490-SS3-a	0.1250	0.13	47	Yes
	0.1875	0.31	113	Yes
	0.2500	0.55	200	Yes
	0.3125	0.78	284	Yes
	0.3750	0.98	357	Yes
	0.4375	1.20	437	No
	0.5000	1.42	517	No
	0.6250	1.82	662	No
GP490-LS3-a	0.1250	0.11	26	Yes
	0.1875	0.28	67	Yes
	0.2500	0.53	127	Yes
	0.3125	0.86	206	Yes
	0.3750	1.22	292	Yes
	0.4375	1.59	380	Yes
	0.5000	1.96	468	Yes
	0.6250	2.61	624	No

Since the only change from the original specimens is the removal of the vertical member, the equivalent column width determined based on 30° dispersion is the same. In other words, the cross-sectional properties such as A_{GP}, $I_{g,GP}$ and r_s have the same values as for the original specimens as shown in Table 6.1.3**.** Similar procedure is applied to back-calculate the actual KL values (KL_{calc}) for these additional cases. The maximum of the KL_{calc} values is determined for each case and a summary of the results is shown in Table 6.1.8.

Table 6.1.8: Back-calculated λ, KL, and $(KL)_{max}$ values derived from the buckling failure cases of the five additional cases

Specimen	t_{GP} (in)	P_{cr} (kip)	P_y (kip)	P_{cr}/P_y	λ_{calc}	KL_{calc} (in)	$(KL)_{max}$ (in)
GP307-SS3-a	0.1250	39	111	0.35	2.48	5.0	5.7
	0.1875	93	167	0.56	1.40	5.7	
	0.2500	161	222	0.73	0.77	5.6	
	0.3125	233	278	0.84	0.42	5.2	
	0.3750	297	333	0.89	0.27	5.0	
GP307-LS3-a	0.1250	32	166	0.19	4.58	6.0	7.3
	0.1875	84	249	0.34	2.62	6.7	
	0.2500	163	331	0.49	1.70	7.3	
	0.3125	271	414	0.65	1.02	7.0	
	0.3750	378	497	0.76	0.66	6.8	
	0.4375	482	580	0.83	0.45	6.5	
	0.5000	573	663	0.86	0.35	6.6	
GP307-SL3-a	0.1250	52	193	0.27	3.26	5.1	5.8
	0.1875	137	289	0.47	1.80	5.7	
	0.2500	251	386	0.65	1.04	5.8	
	0.3125	364	482	0.76	0.67	5.8	

Table 6.1.8 (continued): Back-calculated λ, KL, and $(KL)_{max}$ values derived from the buckling failure cases of the five additional cases

Specimen	t_{GP} (in)	P_{cr} (kip)	P_y (kip)	P_{cr}/P_y	λ_{calc}	KL_{calc} (in)	$(KL)_{max}$ (in)
GP490-SS3-a	0.1250	47	125	0.38	2.32	4.3	4.7
	0.1875	113	187	0.60	1.22	4.7	
	0.2500	200	249	0.80	0.53	4.1	
	0.3125	284	312	0.91	0.23	3.4	
	0.3750	357	374	0.95	0.11	2.9	
GP490-LS3-a	0.1250	26	123	0.21	4.10	5.8	7.2
	0.1875	67	184	0.36	2.42	6.7	
	0.2500	127	245	0.52	1.59	7.2	
	0.3125	206	306	0.67	0.96	7.0	
	0.3750	292	368	0.79	0.56	6.4	
	0.4375	380	429	0.89	0.29	5.4	
	0.5000	468	490	0.96	0.11	3.8	

If designers were to apply the current available guidance (K=1.2 and an average of the lengths) for the equivalent column length calculation to these warren trusses without vertical cases, the length of the column ends up being extremely high. K values are again calculated by dividing the $(KL)_{max}$ values with the L_{mid} of each connection. Results for all 10 cases are shown in Table 6.1.9.

Even though the cases without a vertical member have slightly higher K values, with an average of the 10 cases at K= 0.37 and standard deviation of 0.04, the proposed K = 0.35 appears to be a simple and rational estimate to apply for all different cases.

The nominal resistance calculations are performed also by looking at different dispersion angle or different effective length factor. The dispersion angle of 45° and the K=0.40 have been applied in the resistance calculations for completeness. However, best correlation with the experiments and analytical studies are obtained using the 30° dispersion with K=0.35 and $L=L_{mid}$. Plate buckling is treated as a one-dimensional problem with the appropriate effective length factor and gain from the membrane action along with the plasticity at the instant of failure can be considered as the two major components of the value of 0.35 determined in this research.

Table 6.1.9: Back calculated K values for five test specimens and five additional cases

Specimen	L_{mid} (in)	$(KL)_{max}$ (in)	$(KL)_{max}/L_{mid}$
GP307-SS3	13.1	4.2	0.32
GP307-SS3-a	13.1	5.7	0.43
GP307-LS3	18.1	6.2	0.34
GP307-LS3-a	18.1	7.3	0.40
GP307-SL3	13.1	4.9	0.37
GP307-SL3-a	13.1	5.8	0.44
GP490-SS3	13.1	3.8	0.29
GP490-SS3-a	13.1	4.7	0.36
GP490-LS3	18.1	6.3	0.35
GP490-LS3-a	18.1	7.2	0.40
		Average	**0.37**

Once the width of the equivalent column ($L_{w,30}$), length to use in buckling calculations (L_{mid}), and effective length factor (K=0.35) are determined, the next step is to apply the proposed methodology to different connections including both the test specimens and parametric joints. After applying the buckling resistance calculations using K=0.35 and L=L_{mid}, the critical buckling load is divided with the nominal buckling capacity calculated based on the proposed methodology to see how well it can be estimated.

Table 6.1.10 shows the results for all 14 connections. The analysis of 20 truss bridge plans found no instances of gussets thinner than 3/8 in. For completeness the resistance calculations were performed starting from 1/4 in thick plates. The method works well with an average ratio of 0.98 and a standard deviation of 0.15. Since the recommended resistance calculations are nominal and do not include a resistance factor, the critical loads from the finite element analysis and the nominal calculated resistances can be considered as well correlated.

Table 6.1.10: Comparison between the calculated nominal buckling resistance (using K=0.35 and L=L_{mid}) with the critical buckling load from the finite element analysis

Specimen	t_{GP} (in)	$L_{w,30}$ (in)	P_{cr} (kip)	K	L_{mid} (in)	KL_{mid}/r_s	P_n (kip)	P_{cr}/P_n
GP307-SS3	0.2500	24.4	190	0.35	13.1	63.5	179	**1.06**
	0.3125	24.4	265			50.8	242	**1.09**
	0.3750	24.4	337			42.4	303	**1.11**
GP307-SS3-a	0.2500	24.4	161	0.35	13.1	63.5	179	**0.90**
	0.3125	24.4	233			50.8	242	**0.96**
	0.3750	24.4	297			42.4	303	**0.98**
GP307-LS3	0.2500	27.5	199	0.35	18.1	87.8	193	**1.03**
	0.3125	27.5	326			70.2	293	**1.11**
	0.3750	27.5	438			58.5	391	**1.12**
	0.4375	27.5	545			50.2	486	**1.12**
	0.5000	27.5	653			43.9	579	**1.13**
GP307-LS3-a	0.2500	27.5	163	0.35	18.1	87.8	193	**0.84**
	0.3125	27.5	271			70.2	293	**0.92**
	0.3750	27.5	378			58.5	391	**0.97**
	0.4375	27.5	482			50.2	486	**0.99**
	0.5000	27.5	573			43.9	579	**0.99**
GP307-SL3	0.2500	33.1	284	0.35	13.1	63.5	293	**0.97**
GP307-SL3-a	0.2500	33.1	251	0.35	13.1	63.5	293	**0.85**
	0.3125	33.1	364			50.8	405	**0.90**
GP490-SS3	0.2500	21.5	222	0.35	13.1	63.5	190	**1.17**
	0.3125	21.5	298			50.8	262	**1.14**
	0.3750	21.5	379			42.4	332	**1.14**
GP490-SS3-a	0.2500	21.5	200	0.35	13.1	63.5	190	**1.05**
	0.3125	21.5	284			50.8	262	**1.08**
	0.3750	21.5	357			42.4	332	**1.08**
GP490-LS3	0.2500	21.5	148	0.35	18.1	87.8	147	**1.01**
	0.3125	21.5	229			70.2	221	**1.04**
	0.3750	21.5	313			58.5	293	**1.07**
	0.4375	21.5	402			50.2	363	**1.11**
GP490-LS3-a	0.2500	21.5	127	0.35	18.1	87.8	147	**0.86**
	0.3125	21.5	206			70.2	221	**0.93**
	0.3750	21.5	292			58.5	293	**0.99**
	0.4375	21.5	380			50.2	363	**1.05**
	0.5000	21.5	468			43.9	432	**1.09**

Table 6.1.10 (continued): Comparison between the calculated nominal buckling resistance (using K=0.35 and L=L_{mid}) with the critical buckling load from the finite element analysis

Specimen	t_{GP} (in)	$L_{w,30}$ (in)	P_{cr} (kip)	K	L_{mid} (in)	KL_{mid}/r_s	P_n (kip)	P_{cr}/P_n
5-a	0.2500	43.2	263	0.35	25.5	123.7	178	**1.48**
	0.3125	43.2	390			98.9	337	**1.16**
	0.3750	43.2	525			82.4	509	**1.03**
	0.4000	43.2	585			77.3	578	**1.01**
	0.4375	43.2	675			70.7	682	**0.99**
	0.5000	43.2	818			61.8	853	**0.96**
6-a	0.2500	46.2	271	0.35	18.5	89.7	330	**0.82**
	0.3125	46.2	396			71.8	515	**0.77**
	0.3750	46.2	554			59.8	697	**0.79**
	0.4375	46.2	723			51.3	875	**0.83**
	0.5000	46.2	904			44.9	1049	**0.86**
13-a	0.2500	46.6	322	0.35	19.5	94.6	310	**1.04**
	0.3125	46.6	479			75.7	497	**0.96**
	0.3750	46.6	635			63.0	682	**0.93**
	0.4000	46.6	701			59.1	755	**0.93**
	0.4375	46.6	792			54.0	863	**0.92**
	0.5000	46.6	957			47.3	1040	**0.92**
14-a	0.2500	46.2	273	0.35	11.8	57.2	449	**0.61**
	0.3125	46.2	406			45.8	615	**0.66**
	0.3750	46.2	553			38.2	775	**0.71**
	0.4375	46.2	693			32.7	931	**0.74**
	0.5000	46.2	819			28.6	1085	**0.75**
							Average	**0.98**

Once these ratios are plotted, the band between 0.9 and 1.2 can be seen easily. Figure 6.1.3 shows the data points from 14 different joints. The dashed black line shows the trendline of the data set which is at approximately 1.0.

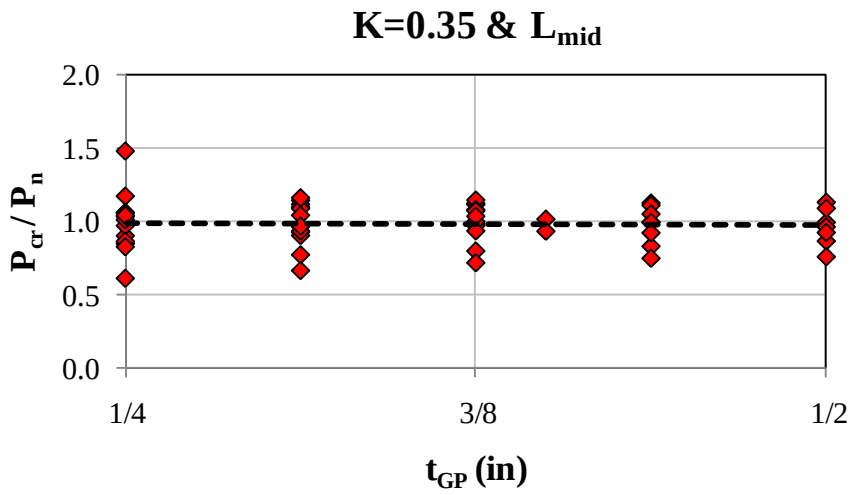

Figure 6.1.3: P_{cr}/P_n ratios using the proposed approach for various gusset plate thicknesses from the parametric studies with buckling failure mode (trendline is shown with the dashed line)

Case 14-a provides 5 data points considered to be outliers since the resistance calculations using the current FHWA guidance with K=1.2 or K=0.65 provides almost the same values for that joint. All the data set will be used by FHWA in a statistical analysis to provide the appropriate LRFD resistance factor or for possible modifications in the resistance check calculations in the future.

Figure 6.1.4 shows the comparison between the proposed method and current available method described in FHWA guidance using the average of the three lengths and K=1.2 drawn to same scale. In addition to the difficulty on describing three lengths, the FHWA guidance gives very conservative results (up to 600% in some cases) with enormous scatter in the data set. For Case 14-a, similar ratios are obtained in both approaches and they are considered to be outliers with their low ratios. However, the effectiveness of the proposed method will not come into question due to this similarity for those 5 data points.

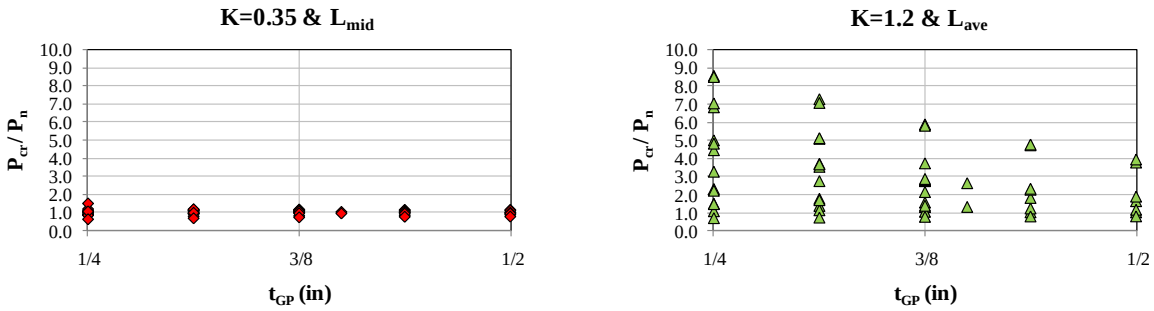

Figure 6.1.4: Comparison between the proposed approach using K=0.35 & L=L_{mid} (left) and the current FHWA guidance approach using K=1.2 & L=L_{ave} (right)

Similarly, the proposed method is compared with average length approach defined in FHWA guidance using K=0.65 which is also discussed by the engineering community as an option to the current K=1.2 factor. Figure 6.1.5 shows how the proposed method better represents the joint capacity compared to the average length approach with K=0.65. The conservatism of using K=0.65 and L_{ave} is obvious, and in some cases it reaching up to 150%. All the data points at the lower bound of the two plots are from Case 14-a and that joint provides lower values using the methods described.

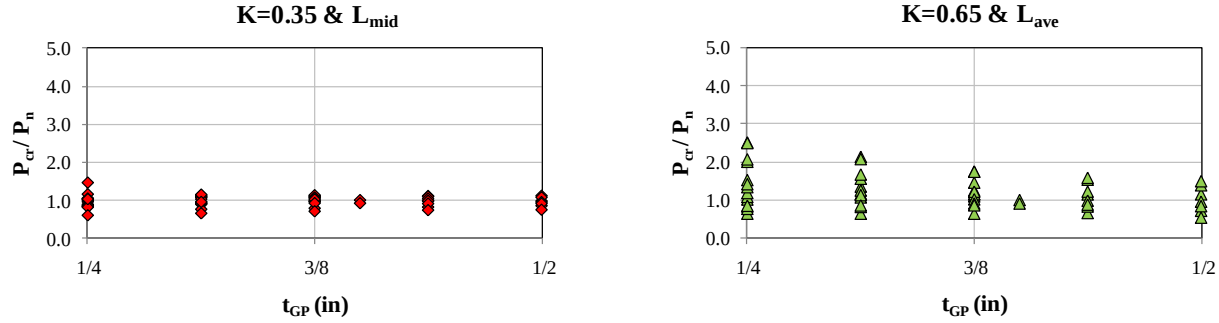

Figure 6.1.5: Comparison between the proposed approach using K=0.35 & L=L_{mid} (left) and the current FHWA guidance approach using K=0.65 & L=L_{ave} (right)

The proposed methodology is simple and shows good agreement with both experiments and advanced simulations, and appears applicable to a wide variety of cases. It eliminates the need to figure out three column lengths, avoids confusions, and substantially and consistently reduces the conservatism of the current guidance on buckling of gusset plates.

6.1.2. Buckling of Chamfered Member Connections

Analyses performed on the parametric cases show that connections with chamfered members have different compression/buckling behavior than those with unchamfered ones. For connections having chamfered members, checking the compression resistance using the full Whitmore width does not work well.

Using the four connections with gusset plate thicknesses below 3/8", column buckling equations are applied without considering the shear path in the resistance calculations just to verify the inapplicability of column buckling analogy to the chamfered cases with thin gusset plates. As shown in Table 6.1.11**,** the average of all data points is 0.74 and applying the full equivalent column width results in an unconservative estimate of the compression capacity.

Table 6.1.11: Comparison between the calculated nominal buckling resistance (using K=0.35 and L=L_{mid}) with the loads from the finite element analysis of the chamfered connections (t_{GP}<3/8 inch and buckling mode observed)

Specimen	t_{GP} (in)	$L_{w,30}$ (in)	P_{FEA} (kip)	K	L_{mid} (in)	KL_{mid}/r_s	P_n (kip)	P_{FEA}/P_n
5	0.2500	49.8	390	0.35	10.3	50.0	544	0.72
	0.3125	49.8	525			40.0	729	0.72
6	0.2500	60.0	407	0.35	7.8	37.8	712	0.57
	0.3125	60.0	576			30.3	927	0.62
7	0.2500	56.9	609	0.35	0.9	4.4	752	0.81
	0.3125	56.9	823			3.5	941	0.88
8	0.2500	49.2	441	0.35	8.5	41.2	572	0.77
	0.3125	49.2	609			33.0	750	0.81
							Average	**0.74**

Figure 6.1.6 also shows that the trendline for the calculated ratios is around 0.74.

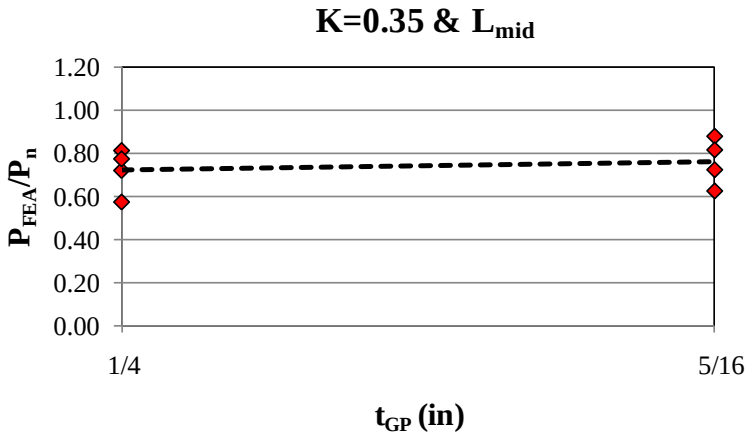

Figure 6.1.6: P_{FEA}/P_n ratios for buckling critical chamfered connections with t_{GP}<3/8 inch (trendline is shown with the dashed line)

For a chamfered connection, failure is dominated by the shear except for the relatively thin plates (below 3/8" thickness). As shown in the von Mises stress response contours (Figure 6.1.7 and Figure 6.1.8), the load transfer from the chamfered members is generally more of a shear resistance problem in the area of the plates between the chamfered member edge and adjacent edges of other members.

In those cases, an alternative approach is investigated that involved summing the compression and shear resistances along two member widths (one being the width normal to the compression direction, b_{cg} and the other being a width parallel to the chamfer, b_{vg} along which the response is usually dominated by shear).. The total resistance of the gusset plate in compression is taken as the sum of the compression plane resistance and component of the gross shear yield capacity along the shear path (Figure 6.1.7 and Figure 6.1.8).

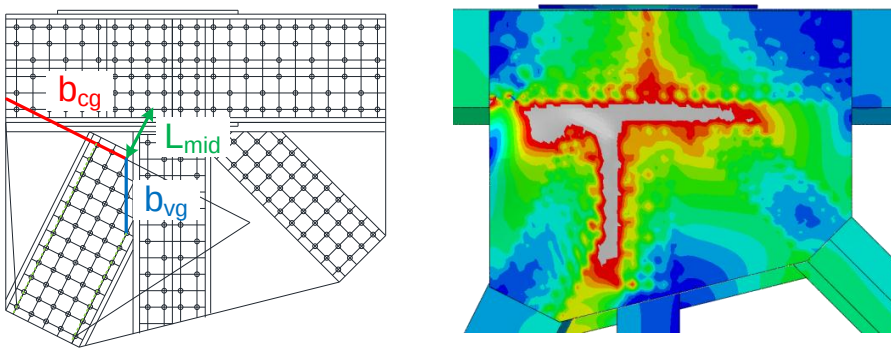

Case 5
(1/4 inch gusset plate)

Figure 6.1.7: Shear and compression paths transferring the compression diagonal load to the gusset plate of the Case 5 joint with 1/4 inch thick gusset plate

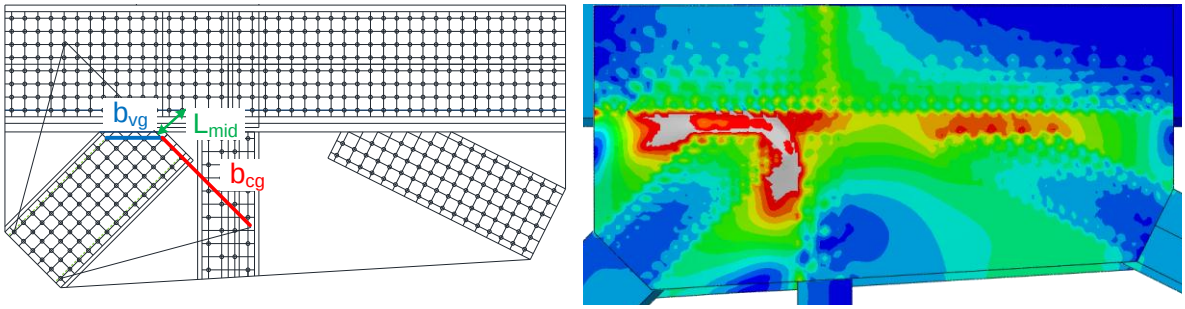

Case 6
(1/4 inch gusset plate)

Figure 6.1.8: Shear and compression paths transferring the compression diagonal load to the gusset plate of the Case 6 joint with 1/4 inch thick gusset plate

This approach is called the combined shear-buckling capacity calculation for chamfered connections with thin plates (< 3/8 inch). For the same cases discussed above where compression buckling equation induced conservatism into resistance calculations, proposed method is applied. The length and area of the compression and shear planes of resistance are summarized in Table 6.1.12.

Table 6.1.12: Length and area of the proposed compression and shear planes of the four chamfered cases

Specimen	t_{GP} (in)	b_{cg} (in)	b_{vg} (in)	$A_{cg,GP}$ (in^2)	$A_{vg,GP}$ (in^2)
5	0.2500	24.8	13.4	6.2	3.4
	0.3125	24.8	13.4	7.8	4.2
6	0.2500	28.5	12.7	7.1	3.2
	0.3125	28.5	12.7	8.9	4.0
7	0.2500	32.0	33.5	8.0	8.4
	0.3125	32.0	33.5	10.0	10.5
8	0.2500	26.8	17.5	6.7	4.4
	0.3125	26.8	17.5	8.4	5.5

The critical compression strength of the compression plane is estimated using the proposed K=0.35 and $L=L_{mid}$ since we cannot directly apply F_y for the critical stress. The summary of F_{cr} calculations are shown in Table 6.1.13.

Table 6.1.13: Critical compressive stress values calculated using the proposed buckling resistance approach (K=0.35 & $L=L_{mid}$)

Specimen	t_{GP} (in)	K	L_{mid} (in)	KL_{mid}/r_s	λ	F_{cr}/F_y	F_{cr} (ksi)
5	0.2500	0.35	10.3	50.0	0.46	0.83	43.7
	0.3125			40.0	0.30	0.88	46.9
6	0.2500	0.35	7.8	37.8	0.27	0.90	47.5
	0.3125			30.3	0.17	0.93	49.4
7	0.2500	0.35	0.9	4.4	0.00	1.00	53.0
	0.3125			3.5	0.00	1.00	53.0
8	0.2500	0.35	8.5	41.2	0.32	0.88	46.5
	0.3125			33.0	0.20	0.92	48.7

Once the critical compressive stress to be applied in the combined shear-buckling calculations is determined, the shear-buckling resistance of the single gusset plate is compared with the force transferred by the compression diagonal. Ratios of the finite element analysis result to the calculated resistance are summarized in Table 6.1.14.

Table 6.1.14: Comparison between the calculated resistance from the combined shear and buckling resistance with the loads from the finite element analysis

Specimen	t_{GP} (in)	P_{FEA} (kip)	P_n (kip)	P_{FEA}/P_n
5	0.2500	390	363	1.07
	0.3125	525	478	1.10
6	0.2500	407	407	1.00
	0.3125	576	526	1.10
7	0.2500	609	654	0.93
	0.3125	823	818	1.01
8	0.2500	441	427	1.03
	0.3125	609	552	1.10
			Average	**1.04**

This method represented the load transfer mechanism in relatively thin gusset plates much better than the application of direct column buckling utilizing the full column width in the resistance calculations. The average ratio is 1.04 with a standard deviation of 0.06. When the two approaches are plotted together, the difference in the validity of each one can be easily identified as shown in Figure 6.1.9.

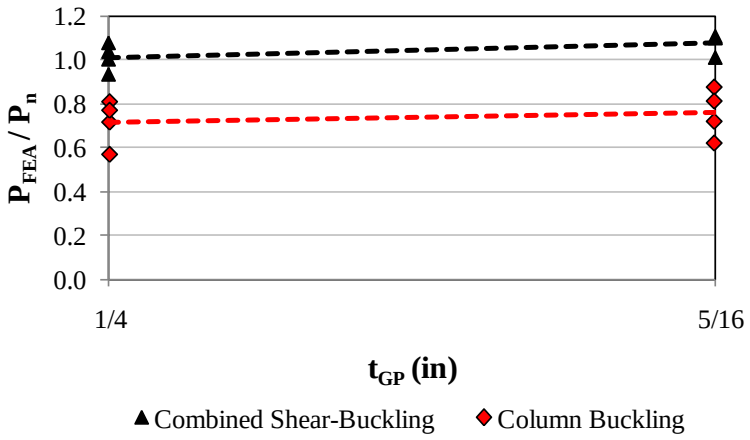

Figure 6.1.9: P_{FEA}/P_n ratios for buckling critical chamfered connections. Comparison between the combined shear-buckling approach and the column buckling approach

This method helps designers identify the correct load path resistance in thin gusset plate connections with chamfered members. Another approach to eliminate the need of calculating the compression resistance in chamfered members will be discussed in Section 6.2.2.

6.1.3. Free Edge Slenderness Limit

Current FHWA guidance sets a limit for the free edge slenderness of a gusset plate. In this study, further investigation on the applicability and validity of the free edge slenderness limit is performed. The current slenderness limit is defined as:

$$\frac{b}{t} \leq 2.06\sqrt{\frac{E}{F_y}} \qquad \text{(Eq. 6.1-12)}$$

From all the 14 cases where buckling failure is observed, free edge lengths are calculated by drawing a straight line between the corner fastener on the compression diagonal and the closest member. Figure 6.1.10 shows two examples, one from the GP307-LS3 specimen and the other from the parametric case, GP307-LS3-a created by removing the vertical member.

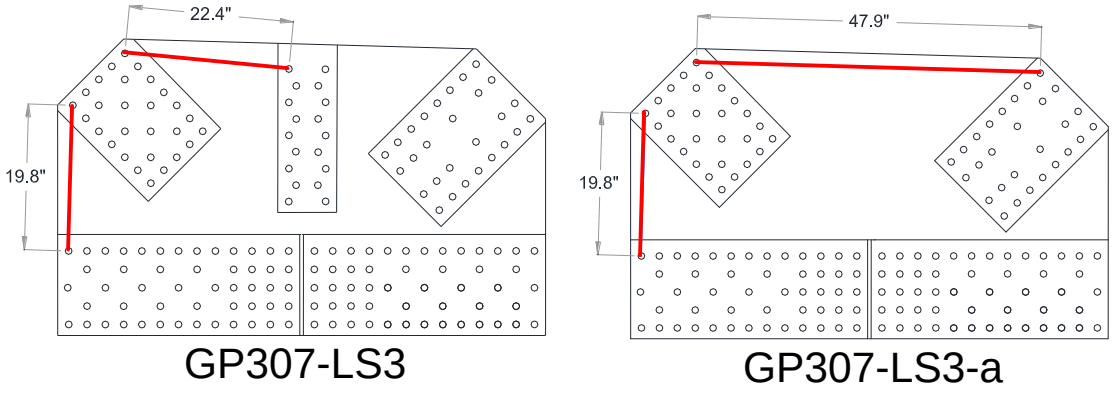

Figure 6.1.10: Free edge lengths for the GP307-LS3 and GP307-LS3-a

The nominal compression resistance is quantified using the column buckling analogy for different thicknesses of gusset plates for 14 cases. That method captures the compression capacity with F_{cr}/F_y ratios calculated based on the KL_{mid}/r_s ratios. Table 6.1.15 shows the calculated F_{cr}/F_y values, maximum free edge slenderness, and edge slenderness limit based on the current formula in the Guidance.

Table 6.1.15: Maximum free edge slenderness values ($L_{free,max}/t_{GP}$) for the parametric cases with buckling failure mode (current limits are shown with bold values)

Specimen	t_{GP} (in)	KL_{mid}/r_s	F_{cr}/F_y	$L_{free,max}$ (in)	$L_{free,max}/t_{GP}$	$2.06\sqrt{\frac{E}{F_y}}$
GP307-SS3	0.2500	63.5	0.81	18.1	72.4	**58.1**
	0.3125	50.8	0.87	18.1	57.9	
	0.3750	42.4	0.91	18.1	48.3	
GP307-SS3-a	0.2500	63.5	0.81	40.8	163.2	**58.1**
	0.3125	50.8	0.87	40.8	130.6	
	0.3750	42.4	0.91	40.8	108.8	
GP307-LS3	0.2500	87.8	0.58	22.4	89.6	**50.5**
	0.3125	70.2	0.71	22.4	71.7	
	0.3750	58.5	0.79	22.4	59.7	
	0.4375	50.2	0.84	22.4	51.2	
	0.5000	43.9	0.87	22.4	44.8	
GP307-LS3-a	0.2500	87.8	0.58	47.9	191.6	**50.5**
	0.3125	70.2	0.71	47.9	153.3	
	0.3750	58.5	0.79	47.9	127.7	
	0.4375	50.2	0.84	47.9	109.5	
	0.5000	43.9	0.87	47.9	95.8	
GP307-SL3	0.2500	63.5	0.76	22.5	90.0	**51.4**
GP307-SL3-a	0.2500	63.5	0.76	47.9	191.6	**51.4**
	0.3125	50.8	0.84	47.9	153.3	
GP490-SS3	0.2500	63.5	0.76	15.3	61.2	**51.5**
	0.3125	50.8	0.84	15.3	49.0	
	0.3750	42.4	0.89	15.3	40.8	
GP490-SS3-a	0.2500	63.5	0.76	37.3	149.2	**51.5**
	0.3125	50.8	0.84	37.3	119.4	
	0.3750	42.4	0.89	37.3	99.5	
GP490-LS3	0.2500	87.8	0.60	19.8	79.2	**51.9**
	0.3125	70.2	0.72	19.8	63.4	
	0.3750	58.5	0.80	19.8	52.8	
	0.4375	50.2	0.85	19.8	45.3	
GP490-LS3-a	0.2500	87.8	0.60	40.8	163.2	**51.9**
	0.3125	70.2	0.72	40.8	130.6	
	0.3750	58.5	0.80	40.8	108.8	
	0.4375	50.2	0.85	40.8	93.3	
	0.5000	43.9	0.88	40.8	81.6	

Table 6.1.15 (continued): Maximum free edge slenderness values ($L_{free,max}/t_{GP}$) for the parametric cases with buckling failure mode (current limits are shown with bold values)

Specimen	t_{GP} (in)	KL_{mid}/r_s	F_{cr}/F_y	$L_{free,max}$ (in)	$L_{free,max}/t_{GP}$	$2.06\sqrt{\frac{E}{F_y}}$
5-a	0.2500	123.7	0.31	44.3	177.2	**48.2**
	0.3125	98.9	0.47	44.3	141.8	
	0.3750	82.4	0.59	44.3	118.1	
	0.4000	77.3	0.63	44.3	110.8	
	0.4375	70.7	0.68	44.3	101.3	
	0.5000	61.8	0.75	44.3	88.6	
6-a	0.2500	89.7	0.54	33.0	132.0	**48.2**
	0.3125	71.8	0.67	33.0	105.6	
	0.3750	59.8	0.76	33.0	88.0	
	0.4375	51.3	0.82	33.0	75.4	
	0.5000	44.9	0.86	33.0	66.0	
13-a	0.2500	94.6	0.50	39.9	159.6	**48.2**
	0.3125	75.7	0.64	39.9	127.7	
	0.3750	63.0	0.74	39.9	106.4	
	0.4000	59.1	0.76	39.9	99.8	
	0.4375	54.0	0.80	39.9	91.2	
	0.5000	47.3	0.84	39.9	79.8	
14-a	0.2500	57.2	0.78	37.4	149.6	**48.2**
	0.3125	45.8	0.85	37.4	119.7	
	0.3750	38.2	0.89	37.4	99.7	
	0.4375	32.7	0.92	37.4	85.5	
	0.5000	28.6	0.94	37.4	74.8	

Each free edge slenderness value is plotted against the F_{cr}/F_y ratio. Figure 6.1.11 shows how the scatter in the data summarizes the weakness of the edge slenderness limit. For $L_{free,max}/t_{GP}$ ratios of 50 to 150, the same strength level can be reached regardless of the free edge length. The current limit for each of the different connection is around 50 as shown in Table 6.1.15. Based on this, designers would not be able to use even 1/2" thick gusset plates based on the calculated $L_{free,max}/t_{GP}$ ratios in Table 6.1.15.

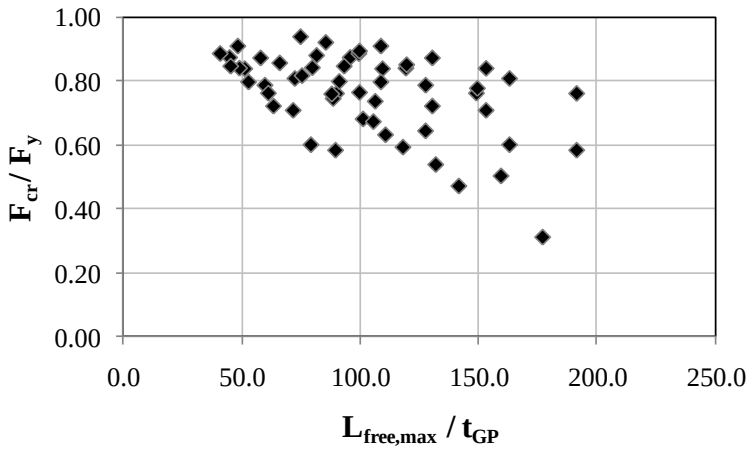

Figure 6.1.11: F_{cr}/F_y vs. free edge slenderness relationship showing the scatter in the data gathered from the parametric studies

In addition, the data points from the three test specimens with the same L_{mid} values are shown in Figure 6.1.12. These data points belong to the buckling critical cases for which the buckling resistance is well estimated using the K=0.35 and L_{mid}=13.1 in the column buckling formula. For the GP307-SL3 specimen, free edge length significantly increases compared to the GP307-SS3 and GP490-SS3 specimens. However, the corresponding F_{cr}/F_y ratios does not vary substantially. The reduction in buckling strength is due to the decrease in gusset plate thickness. For the same L_{mid} and t_{GP} values, almost the same strength levels can be reached for three specimens. The three data points at the bottom represent the 1/4" gusset plate in each case.

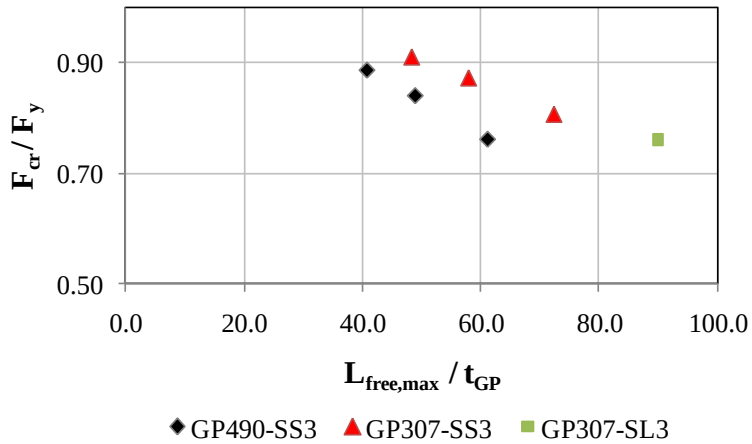

Figure 6.1.12: F_{cr}/F_y vs. free edge slenderness relationship for the three test specimens

Similarly, for the Warren without vertical member cases created based on the test specimens, the same relationship is plotted as shown in Figure 6.1.13. For the same

effective column length with longer free edge in GP307-SL3 connection, very close F_{cr}/F_y ratios are observed.

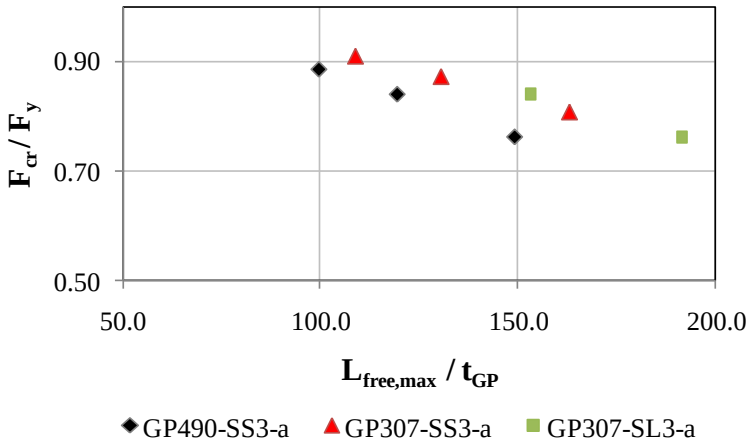

Figure 6.1.13: F_{cr}/F_y vs. free edge slenderness relationship for the three parametric cases (test specimens without vertical member)

For the buckling critical cases, the relationship between P_{FEA}/P_y and free edge slenderness is plotted and compared with the plot showing the relationship between P_{FEA}/P_y and"KLmid/r" of each joint. Since the test specimens and parametric study joints had different yield strengths, the non-dimensionless quantity of $\sqrt{\frac{F_y}{E}}$ is also included in the formulation as shown in both plots.

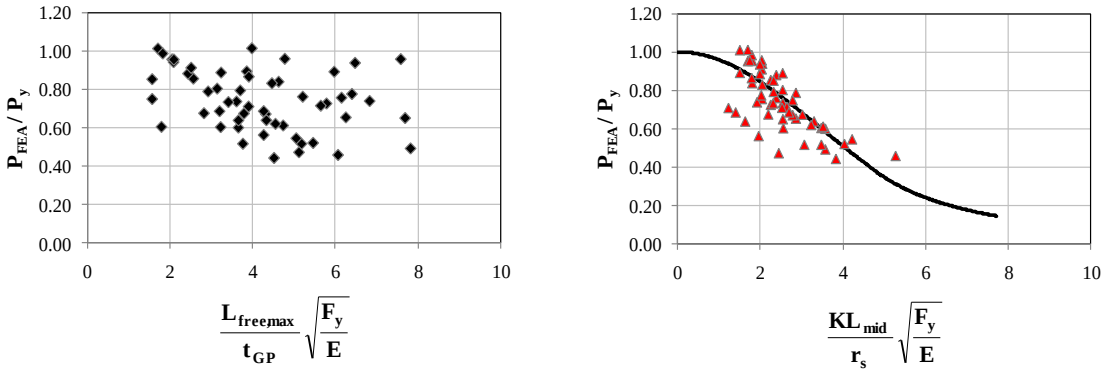

Figure 6.1.14: Correlation studies for the free edge slenderness limit

The scatter in the data shows that the strength is not strongly correlated with the free edge slenderness. The edge slenderness limit can be eliminated in the gusset plate compression resistance checks as a result of these studies. The first reason is the fact that compression capacity can be calculated with the proposed column buckling formula and

an appropriate K factor, so setting up another limit in this area would not be needed. The second reason is the overall scatter in the observations with respect to the edge slenderness ratios from different joints as shown in Figure 6.1.11. The same strength ratios have been obtained regardless of the significant changes in edge slenderness values.

6.1.4. Compression Block Shear Approach

Throughout the parametric studies, a special check called the "Compression Block Shear Check" is proposed for typical joints at pier locations. These joints transfer extremely high compression load through gusset plates. Considering the yielding pattern observed in the finite element analyses, the load transfer mechanism for the vertical member to the gusset plate is assumed to be a combination of shear and compression through the two shear planes and a compression plane at the base of the vertical member as shown in Figure 6.1.15. Gusset plate capacity is estimated by summing the gross-section shear yield capacity of the two shear planes and the compression capacity of the compression plane. Based on the slenderness of an equivalent column, a corresponding F_{cr} is determined and used in the calculations.

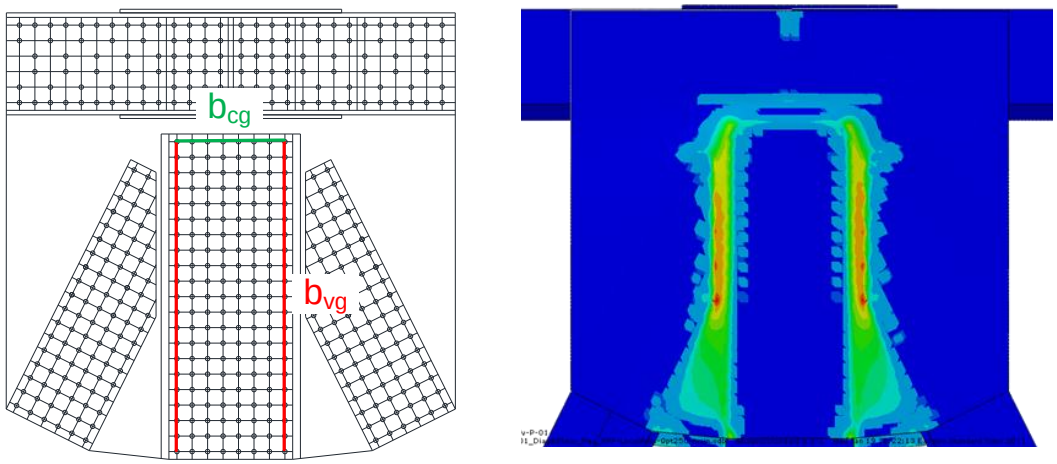

Figure 6.1.15: Compression plane and two shear planes of resistance (left) used in the compression block shear approach calculations. Equvalent plastic strains for the FEA with 0.250 inch thick gusset plate

The length and area of the shear and compression planes are shown in Table 6.1.16 for six different thickness analyses. In all the cases, the same yielding pattern is

observed and it is important to check how well the proposed approach estimates the load transfer mechanism.

Table 6.1.16: Length and area of the compression and shear planes for different thickness analysis runs

t_{GP} (in)	$b_{cg,GP}$ (in)	$b_{vg,GP}$ (in)	$A_{cg,GP}$ (in^2)	$A_{vg,GP}$ (in^2)
0.2500	20.9	61.5	5.2	15.4
0.3125			6.5	19.2
0.3750			7.8	23.1
0.4375			9.1	26.9
0.5000			10.5	30.8
0.6250			13.1	38.4

In this approach, K=0.5 is used to calculate the critical compression stress along the compression path. K=0.5 represents the uniform compression area underneath the vertical member, as it behaves more like a fixed-fixed stocky column. The equivalent column length is determined based on the distance between the bolt lines in the vertical compression member and the first bolt line passing in the chord members (L in Figure 6.1.16).

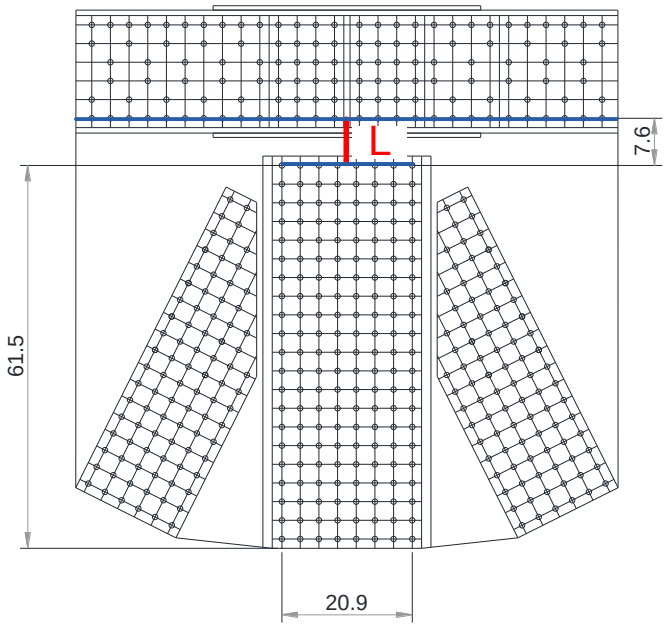

Figure 6.1.16: Equivalent column length, L between the compression plane bolt line and chord member bolt lines

The calculated critical stresses based on the K=0.5 and equivalent column length, L are shown in Table 6.1.17.

Table 6.1.17: Critical compressive stress values of the compression plane

t_{GP} (in)	K	L (in)	KL/r_s	λ	F_{cr}/F_y	$F_{cr,GP}$ (ksi)
0.2500	0.5	7.6	52.5	0.511	0.81	42.9
0.3125			42.0	0.327	0.87	46.3
0.3750			35.0	0.227	0.91	48.2
0.4375			30.0	0.167	0.93	49.5
0.5000			26.3	0.128	0.95	50.3
0.6250			21.0	0.082	0.97	53.0

The method is applied for different thickness analyses using the compression block shear check for the gusset plate based on the formula:

$$P_{CBS,GP} = 2[(0.577F_y)(t_{GP})(b_{vg,GP})] + (F_{cr,GP})(t_{GP})(b_{cg,GP}) \quad \text{(Eq. 6.1-13)}$$

Table 6.1.18 shows the ratio of the finite element analysis load to the predicted nominal resistance using the proposed formulation. The ratios also show that this approach predicted well the resistance of the gusset plate.

Table 6.1.18: Comparison between the forces from the finite element analysis with the calculated nominal compression block shear resistance values

t_{GP} (in)	P_{FEA} (kip)	$P_{CBS,GP}$ (kip)	$P_{FEA}/P_{CBS,GP}$
0.2500	1100	1169	**0.94**
0.3125	1425	1484	**0.96**
0.3750	1725	1796	**0.96**
0.4375	2075	2106	**0.99**
0.5000	2400	2416	**0.99**
0.6250	3000	3055	**0.98**

For the same joint with a shingle plate on top of the gusset plate, the proposed method is applied using the 0.4" gusset plate and 0.2" shingle plate case. The corresponding b_{cg} and b_{vg} lengths for the shingle plate are shown in Figure 6.1.17.

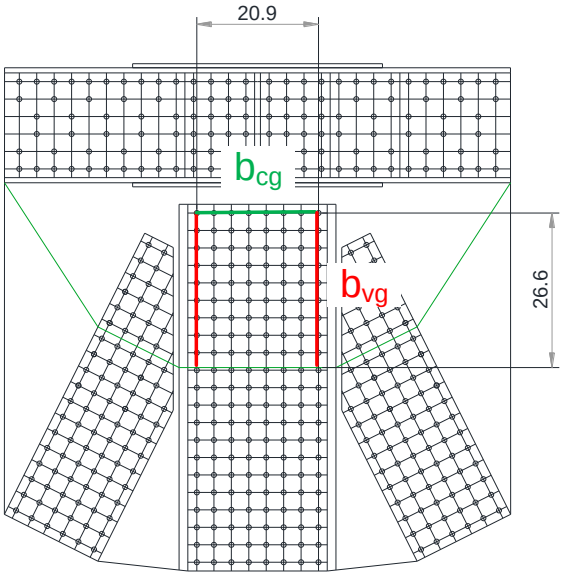

Figure 6.1.17: : Compression plane and two shear planes of resistance for the shingle plate

The length and area values of the shear and compression planes are shown in Table 6.1.19.

Table 6.1.19: Length and area of the compression and shear planes for the gusset plate and shingle plate

t_{GP} (in)	$b_{cg,GP}$ (in)	$b_{vg,GP}$ (in)	$A_{cg,GP}$ (in^2)	$A_{vg,GP}$ (in^2)
0.4000	20.9	61.5	8.4	24.6
t_{SHP} (in)	$b_{cg,SHP}$ (in)	$b_{vg,SHP}$ (in)	$A_{cg,SHP}$ (in^2)	$A_{vg,SHP}$ (in^2)
0.2000	20.9	26.6	4.2	5.3

The critical compressive stress is calculated using the column formula with K=0.5 and L determined based on Figure 6.1.16. In this case, L is the same for both gusset plate and shingle plate. The critical compressive stress for each plate is shown in Table 6.1.20.

Table 6.1.20: Critical compressive stress values of the compression plane for the gusset plate and shingle plate

t_{GP} (in)	K	L (in)	KL/r_s	λ	F_{cr}/F_y	$F_{cr,GP}$ (ksi)
0.4000	0.5	7.6	32.8	0.199	0.92	48.8
t_{SHP} (in)	K	L (in)	KL/r_s	λ	F_{cr}/F_y	$F_{cr,SHP}$ (ksi)
0.2000	0.5	7.6	65.6	0.798	0.72	38.0

The compression block shear resistance for the shingle plate is calculated using the formula:

$$P_{CBS,SHP} = 2[(0.577F_y)(t_{SHP})(b_{vg,SHP})] + (F_{cr,SHP})(t_{SHP})(b_{cg,SHP}) \quad \text{(Eq. 6.1-14)}$$

Total resistance is calculated by summing the two resistances from individual plates using:

$$P_{CBS,total} = P_{CBS,GP} + P_{CBS,SHP} \quad \text{(Eq. 6.1-15)}$$

The finite element result is compared with the calculated resistance based on the compression block shear approach, resulting in a ratio of 0.92 as shown in Table 6.1.21.

Table 6.1.21: Comparison between the finite element analysis and the calculated nominal resistance (gusset plate+shingle plate)

P_{FEA} (kip)	$P_{CBS,total}$ (kip)	$P_{FEA}/P_{CBS,total}$
2225	2406	**0.92**

This check is proposed for a specific case commonly found at pier locations of steel truss bridges. For the same case, the applicability of the uniform gross-section shear yield check along the full vertical plane is assessed. The formulation captures the resistance very well as will be shown in more detail in Section 6.2.2.

6.2. Shear Resistance Checks

Nominal gross-section yield resistance of the critical shear planes in gusset plates can be calculated using the formula defined in the AASHTO Bridge Design Specifications and the FHWA Guidance. This nominal shear resistance calculation includes an omega (Ω) reduction factor built in as shown in the formula:

$$P_{ng,GP} = (0.577F_y)(t_{GP})(L_{vg,GP})(\Omega) \qquad \text{(Eq. 6.2-1)}$$

L_{vg} in this calculation represents the length of the critical shear plane (horizontal, vertical). The Ω-factor was used to account for the shape of the shear stress distribution and whether or not it is believed the plate can fully plastify prior to shear buckling. A large part of the work in this project is an effort to understand the role of the omega Ω-factor and determine its value. Using the variable thickness parametric studies, important conclusions on this resistance check are reached. These conclusions are summarized in the next two subsections, which discuss the unchamfered and chamfered member connection shear resistance separately.

6.2.1. Shear Resistance of Unchamfered Member Connections

All the five test specimens along with the additional five cases without vertical members and those dealing with gusset plate geometry provide a large and varied database to determine the Ω value that best represents the shear behavior of each connection. The resistance checks are developed from the results of 14 unique connections that are identified to have failed in shear in a horizontal, vertical, or inclined plane. These included a total of 15 planes (10 of these from the test specimens with and without vertical members, 2 of those being vertical and horizontal planes of Case 5-a, and last three are from Case 6-a, Case 13-a, and Case 14-a). For the unchamfered connections, only the cases with shear failure are taken into the data pool. From the finite element analyses, a transition from buckling failure to the shear failure is observed as the gusset plate thickness changes. The variable thickness analyses help to provide enough data for the shear resistance checks and to determine the relevant Ω value.

The critical horizontal (Figure 6.2.1) and vertical (Figure 6.2.2) shear planes are determined using the free-body diagram of the gusset plate and by looking at the load transfer mechanism of the horizontal or vertical components of the diagonal members.

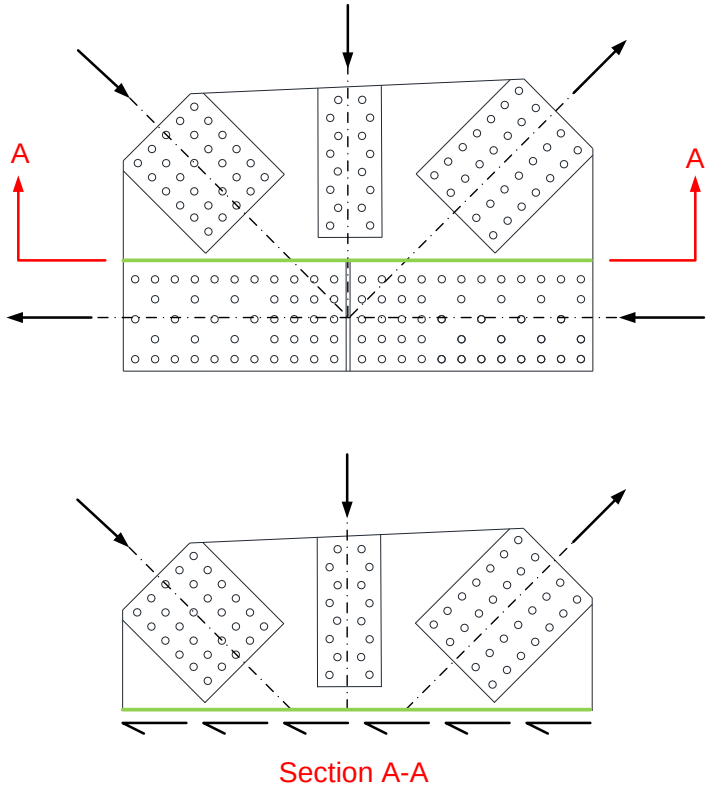

Figure 6.2.1: Horizontal shear plane of the GP307-SS3 specimen

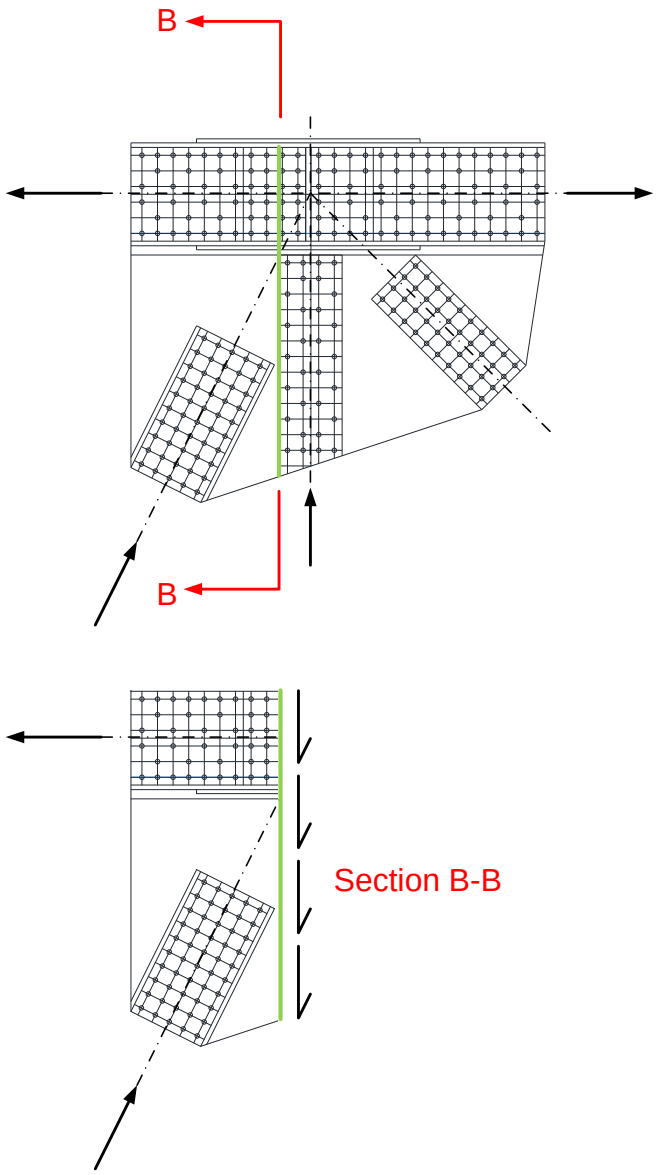

Figure 6.2.2: Vertical shear plane of the parametric Case 5-a joint

For the inclined chord member cases, the shear plane still becomes the local vertical or horizontal plane with respect to the chord member orientation (Figure 6.2.3).

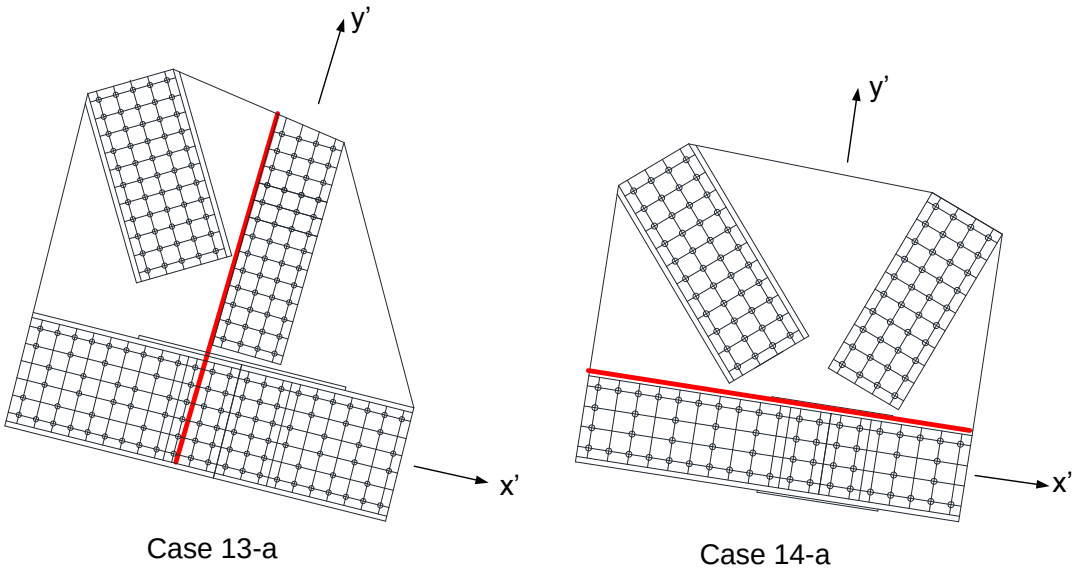

Figure 6.2.3: Inclined shear planes from two parametric joints (local vertical and horizontal shear planes are shown)

Although the resistance checks are based on the gross-section yield resistance, the planes are determined by drawing the plane passing through the bolt lines of the vertical members or chord members. The main reason for this choice is that the current FHWA guidance requires a net section rupture resistance for shear calculations. Hence, the actual plane can be assumed to pass through the bolt lines of the connected members; in most cases, both lines will be equal to each other. Whitmore (1952) also concludes that the critical plane of the gusset plates becomes the horizontal plane just above the chord members. This was an important result of his early studies. However, this research also takes the vertical and inclined shear planes into account. From the 14 cases, all the analyses are considered to pick the appropriate data points which are representing the shear failure cases. The length of the shear plane, $L_{vg,GP}$ for each connection is measured and areas are calculated using the formula:

$$A_{vg,GP} = (t_{GP})(L_{vg,GP}) \qquad \text{(Eq. 6.2-2)}$$

The nominal gross shear yield formula was modified using the calculated area:

$$P_{ng,GP} = (0.577F_y)(A_{vg,GP})(\Omega) \qquad \text{(Eq. 6.2-3)}$$

Since the aim is trying to determine the appropriate Ω value using the finite element analysis, the shear force acting on the defined shear plane of a single gusset at failure is calculated using the member loads. The ultimate shear force from the finite element analysis divided by the nominal shear resistance of the failure plane is essentially the back-calculated Ω for each analysis run as shown by the formula:

$$\Omega_{calc} = \frac{P_{v,FEA}}{P_{ng,GP}} = \frac{P_{v,FEA}}{(0.577F_y)(A_{vg,GP})} \qquad \text{(Eq. 6.2-4)}$$

The length of the shear plane, calculated areas, and $P_{v,FEA} / P_{ng,GP}$ ratios are highlighted in Table 6.2.1 for all the analysis runs where shear failure is observed. The rest of the data is utilized in the buckling resistance checks for the unchamfered connections since the failure is driven by buckling and their resistance is captured using the column buckling formulation.

Table 6.2.1: Length of the critical shear planes and back calculated Ω values (parametric cases with shear failure are highlighted) for unchamfered connections

Case	t_{GP} (in)	F_y (ksi)	$L_{vg,GP}$ (in)	$A_{vg,GP}$ (in^2)	$P_{v,FEA}$ (kip)	$P_{ng,GP}$ (kip)	$P_{v,FEA}/P_{ng,gP}$
GP307-SS3	0.2500	36.4	59.0	14.8	229	311	0.74
	0.3125		59.0	18.4	320	389	0.82
	0.3750		59.0	22.1	406	467	0.87
	0.4375		59.0	25.8	493	545	**0.90**
	0.5000		59.0	29.5	588	623	**0.94**
	0.6250		59.0	36.9	817	779	**1.05**
GP307-SS3-a	0.2500	36.4	59.0	14.8	228	311	0.73
	0.3125		59.0	18.4	329	389	0.85
	0.3750		59.0	22.1	420	467	0.90
	0.4375		59.0	25.8	511	545	**0.94**
	0.5000		59.0	29.5	623	623	**1.00**
	0.6250		59.0	36.9	861	779	**1.11**

Table 6.2.1 (continued): Length of the critical shear planes and back calculated Ω values (parametric cases with shear failure are highlighted) for unchamfered connections

Case	t_{GP} (in)	F_y (ksi)	$L_{vg,GP}$ (in)	$A_{vg,GP}$ (in^2)	$P_{v,FEA}$ (kip)	$P_{ng,GP}$ (kip)	$P_{v,FEA}/P_{ng,gP}$
GP307-LS3	0.2500	48.2	66.5	16.6	212	465	0.46
	0.3125		66.5	20.8	348	581	0.60
	0.3750		66.5	24.9	467	697	0.67
	0.4375		66.5	29.1	582	813	0.72
	0.5000		66.5	33.3	696	930	0.75
	0.6250		66.5	41.6	909	1162	0.78
GP307-LS3-a	0.2500	48.2	66.5	16.6	231	465	0.50
	0.3125		66.5	20.8	383	581	0.66
	0.3750		66.5	24.9	535	697	0.77
	0.4375		66.5	29.1	681	813	0.84
	0.5000		66.5	33.3	811	930	0.87
	0.6250		66.5	41.6	1064	1162	**0.92**
GP307-SL3	0.2500	46.6	66.5	16.6	398	449	0.89
	0.3125		66.5	20.8	517	562	**0.92**
	0.3750		66.5	24.9	676	674	**1.00**
	0.4375		66.5	29.1	802	786	**1.02**
	0.5000		66.5	33.3	908	899	**1.01**
	0.6250		66.5	41.6	1147	1123	**1.02**
GP307-SL3-a	0.2500	46.6	66.5	16.6	351	449	0.78
	0.3125		66.5	20.8	510	562	0.91
	0.3750		66.5	24.9	663	674	**0.98**
	0.4375		66.5	29.1	789	786	**1.00**
	0.5000		66.5	33.3	915	899	**1.02**
	0.6250		66.5	41.6	1147	1123	**1.02**
GP490-SS3	0.2500	46.4	54.8	13.7	314	369	0.85
	0.3125		54.8	17.1	422	461	0.92
	0.3750		54.8	20.6	535	553	0.97
	0.4375		54.8	24.0	643	645	**1.00**
	0.5000		54.8	27.4	752	737	**1.02**
	0.6250		54.8	34.3	937	922	**1.02**

Table 6.2.1 (continued): Length of the critical shear planes and back calculated Ω values (parametric cases with shear failure are highlighted) for unchamfered connections

Case	t_{GP} (in)	F_y (ksi)	$L_{vg,GP}$ (in)	$A_{vg,GP}$ (in^2)	$P_{v,FEA}$ (kip)	$P_{ng,GP}$ (kip)	$P_{v,FEA}/P_{ng,gP}$
GP490-SS3-a	0.2500	46.4	54.8	13.7	283	369	0.77
	0.3125		54.8	17.1	402	461	0.87
	0.3750		54.8	20.6	504	553	0.91
	0.4375		54.8	24.0	618	645	**0.96**
	0.5000		54.8	27.4	731	737	**0.99**
	0.6250		54.8	34.3	937	922	**1.02**
GP490-LS3	0.2500	45.6	59.0	14.8	210	390	0.54
	0.3125		59.0	18.4	324	488	0.67
	0.3750		59.0	22.1	443	585	0.76
	0.4375		59.0	25.8	568	683	0.83
	0.5000		59.0	29.5	690	780	**0.88**
	0.6250		59.0	36.9	902	975	**0.93**
GP490-LS3-a	0.2500	45.6	59.0	14.8	179	390	0.46
	0.3125		59.0	18.4	291	488	0.60
	0.3750		59.0	22.1	412	585	0.70
	0.4375		59.0	25.8	537	683	0.79
	0.5000		59.0	29.5	662	780	0.85
	0.6250		59.0	36.9	882	975	**0.90**
5-a-V	0.2500	53.0	62.7	15.7	235	482	0.49
	0.3125		62.7	19.6	349	602	0.58
	0.3750		62.7	23.5	470	723	0.65
	0.4000		62.7	25.1	523	771	0.68
	0.4375		62.7	27.4	604	843	0.72
	0.5000		62.7	31.4	731	964	0.76
	0.6250		62.7	39.2	959	1205	0.80
5-a-H	0.2500	53.0	79.6	19.9	266	612	0.43
	0.3125		79.6	24.9	395	765	0.52
	0.3750		79.6	29.9	532	918	0.58
	0.4000		79.6	31.8	593	979	0.61
	0.4375		79.6	34.8	684	1071	0.64
	0.5000		79.6	39.8	828	1223	0.68
	0.6250		79.6	49.8	1086	1529	0.71

Table 6.2.1 (continued): Length of the critical shear planes and back calculated Ω values (parametric cases with shear failure are highlighted) for unchamfered connections

Case	t_{GP} (in)	F_y (ksi)	$L_{vg,GP}$ (in)	$A_{vg,GP}$ (in^2)	$P_{v,FEA}$ (kip)	$P_{ng,GP}$ (kip)	$P_{v,FEA}/P_{ng,gP}$
6-a-H	0.2500	53.0	138.0	34.5	457	1061	0.43
	0.3125		138.0	43.1	666	1326	0.50
	0.3750		138.0	51.8	933	1591	0.59
	0.4375		138.0	60.4	1218	1856	0.66
	0.5000		138.0	69.0	1523	2121	0.72
	0.6250		138.0	86.3	2132	2651	0.80
13-a-V	0.2500	53.0	61.2	15.3	279	470	0.59
	0.3125		61.2	19.1	414	588	0.70
	0.3750		61.2	23.0	550	705	0.78
	0.4000		61.2	24.5	607	753	0.81
	0.4375		61.2	26.8	686	823	0.83
	0.5000		61.2	30.6	829	941	**0.88**
	0.6250		61.2	38.3	1093	1176	**0.93**
14-a-H	0.2500	53.0	57.1	14.3	260	439	0.59
	0.3125		57.1	17.8	386	549	0.70
	0.3750		57.1	21.4	526	658	0.80
	0.4375		57.1	25.0	660	768	**0.86**
	0.5000		57.1	28.6	779	878	**0.89**
	0.6250		57.1	35.7	1026	1097	**0.94**

Figure 6.2.4 shows the plot of the calculated $P_{v,FEA} / P_{ng,GP}$ ratios versus the gusset plate thickness. The mean of the data is shown as a dashed line varying from 0.95-0.99 over plate thicknesses of 1/4 to 5/8 inch.

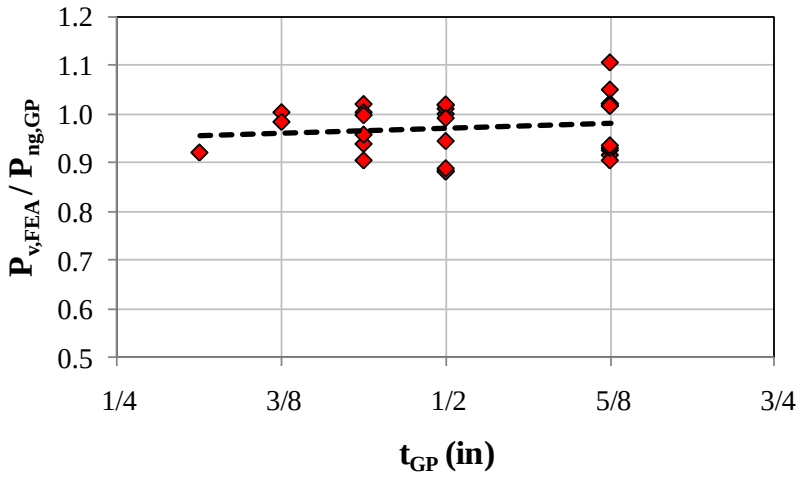

Figure 6.2.4: Relationship between the back-calculated $\Omega = P_{v,FEA} / P_{ng,GP}$ values and the gusset plate thickness for unchamfered connections (shear failure cases only)

Since the slope of the mean line through the data is so shallow, there is no need to define a relation between Ω and the plate thickness. The best approach would be using Ω=1.0 in gross section yield resistance checks for all unchamfered member cases and let the phi-factor handle the scatter in the data. Similar to the buckling resistance calculations, one of the future studies to be performed by FHWA will be defining the appropriate resistance factor using the data set created for this check.

6.2.2. Shear Resistance of Chamfered Member Connections

The critical shear planes of the chamfered connections are determined using the same method as the unchamfered connections. The evaluations of the shear resistance of the chamfered connections become tedious because for thin plates (<3/8 inch thick), the plate would tend to buckle prior to shearing, and as described in section 6.1.2, the Whitmore buckling check with K=0.35 and L=L_{mid} in column buckling calculations was not a good predictor of buckling for chamfered connections. In section 6.1.2, an approach which combines the shear and buckling plane resistances is discussed for calculating the resistance of relatively thin plate cases in chamfered connections.

As an alternative for chamfered connections with thin plates (<3/8 inch), the buckling resistance check can be built into the shear limit state check via the Ω-factor. Therefore, there would essentially be two Ω-factors, one for thin (<3/8 inch thick) and one for thick plates (>3/8 inch thick). The studies on the parametric chamfered

connections include variable thickness analyses of 7 different joints with a total of 8 shear planes. In this study, the joint on which compression block shear approach has been performed (Case 3) is also included since it has extreme chamfering parallel to the vertical plane and the vertical plane exhibits a shear failure. The length and area information for each case are shown in Table 6.2.2. As in the previous section, the Ω-factor is expressed as the load ratio between the resistance from the finite element analysis and unreduced nominal strength calculation (this ratio is equal to the back-calculated Ω). This ratio is also shown in Table 6.2.2.

Table 6.2.2: Length of the critical shear planes and back calculated Ω values for chamfered connections

Case	t_{GP} (in)	F_y (ksi)	$L_{vg,GP}$ (in)	$A_{vg,GP}$ (in^2)	$P_{v,FEA}$ (kip)	$P_{ng,GP}$ (kip)	$P_{v,FEA}/P_{ng,GP}$
3-V	0.2500	53.0	85.6	21.4	551	658	0.84
	0.3125		85.6	26.8	714	822	0.87
	0.3750		85.6	32.1	864	987	0.88
	0.4375		85.6	37.5	1039	1151	0.90
	0.5000		85.6	42.8	1202	1316	0.91
	0.6250		85.6	53.5	1503	1645	0.91
5-V	0.2500	53.0	56.7	14.2	349	436	0.80
	0.3125		56.7	17.7	470	545	0.86
	0.3750		56.7	21.3	584	654	0.89
	0.4000		56.7	22.7	631	697	0.90
	0.4375		56.7	24.8	711	763	0.93
	0.5000		56.7	28.4	839	871	0.96
	0.6250		56.7	35.4	1107	1089	1.02
5-H	0.2500	53.0	69.5	17.4	395	534	0.74
	0.3125		69.5	21.7	532	668	0.80
	0.3750		69.5	26.1	661	801	0.82
	0.4000		69.5	27.8	714	855	0.84
	0.4375		69.5	30.4	805	935	0.86
	0.5000		69.5	34.8	950	1068	0.89
	0.6250		69.5	43.4	1253	1335	0.94

Table 6.2.2 (continued): Length of the critical shear planes and back calculated Ω values for chamfered connections

Case	t_{GP} (in)	F_y (ksi)	$L_{vg,GP}$ (in)	$A_{vg,GP}$ (in^2)	$P_{v,FEA}$ (kip)	$P_{ng,GP}$ (kip)	$P_{v,FEA}/P_{ng,GP}$
6-H	0.2500	53.0	128.1	32.0	685	984	0.70
	0.3125		128.1	40.0	971	1231	0.79
	0.3750		128.1	48.0	1275	1477	0.86
	0.4375		128.1	56.0	1561	1723	0.91
	0.5000		128.1	64.1	1866	1969	0.95
	0.6250		128.1	80.1	2456	2461	1.00
7-H	0.2500	53.0	142.1	35.5	918	1092	0.84
	0.3125		142.1	44.4	1243	1365	0.91
	0.3750		142.1	53.3	1594	1638	0.97
	0.4375		142.1	62.2	1972	1911	1.03
	0.5000		142.1	71.1	2323	2184	1.06
	0.6250		142.1	88.8	3025	2730	1.11
8-H	0.2500	53.0	94.1	23.5	665	723	0.92
	0.3125		94.1	29.4	918	904	1.02
	0.3750		94.1	35.3	1140	1085	1.05
	0.4375		94.1	41.2	1330	1266	1.05
	0.5000		94.1	47.1	1536	1446	1.06
	0.6250		94.1	58.8	1900	1808	1.05
13-V	0.2500	53.0	58.3	14.6	372	448	0.83
	0.3125		58.3	18.2	507	560	0.91
	0.3750		58.3	21.9	650	672	0.97
	0.4000		58.3	23.3	707	717	0.99
	0.4375		58.3	25.5	779	784	0.99
	0.5000		58.3	29.2	886	896	0.99
	0.6250		58.3	36.4	1108	1120	0.99
14-H	0.2500	53.0	57.1	14.3	306	439	0.70
	0.3125		57.1	17.8	433	549	0.79
	0.3750		57.1	21.4	566	658	0.86
	0.4375		57.1	25.0	686	768	0.89
	0.5000		57.1	28.6	813	878	0.93
	0.6250		57.1	35.7	1066	1097	0.97

The plot for the Ω-factor versus plate thickness is shown in Figure 6.2.5. This plot shows a linear trend of decreasing Ω values as plates become thinner.

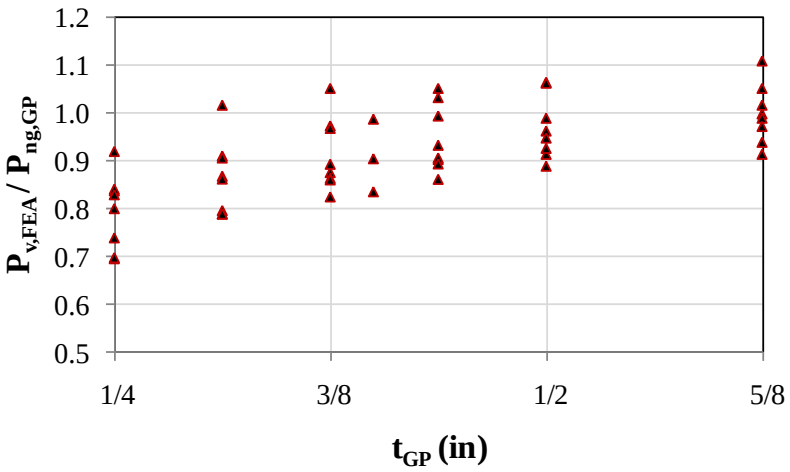

Figure 6.2.5: Relationship between the back-calculated $\Omega = P_{v,FEA} / P_{ng,GP}$ values and the gusset plate thickness

The thin plate cases are plotted separately to have a close look at the Ω values. Figure 6.2.6 shows the data points with the dashed red line representing the trend of the data set. For those plates thinner than 3/8 inch, Ω=0.80 seems the most appropriate lower bound value.

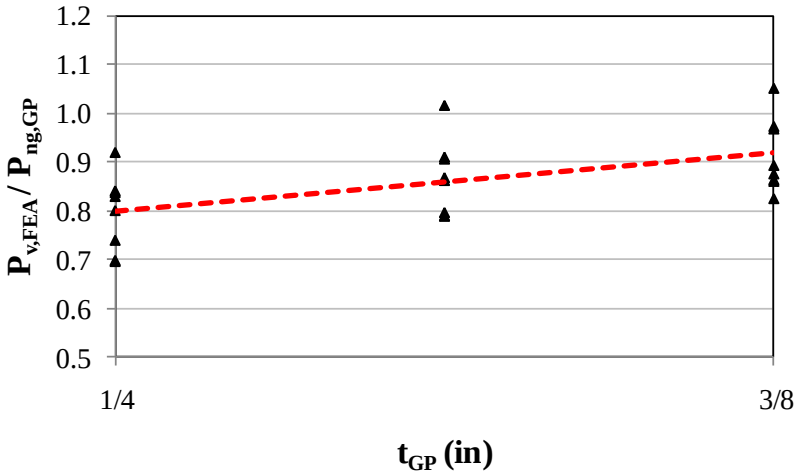

Figure 6.2.6: Back-calculated Ω values for chamfered connections with $t_{GP} \leq 3/8$ inch

Ω values for cases with gusset plate thickness between 3/8 inch and 5/8 inch are plotted in Figure 6.2.7. Similar to the situation for unchamfered members, Ω ranges from 0.9 to 1.0 for increasing plate thicknesses over 3/8 inch thick.

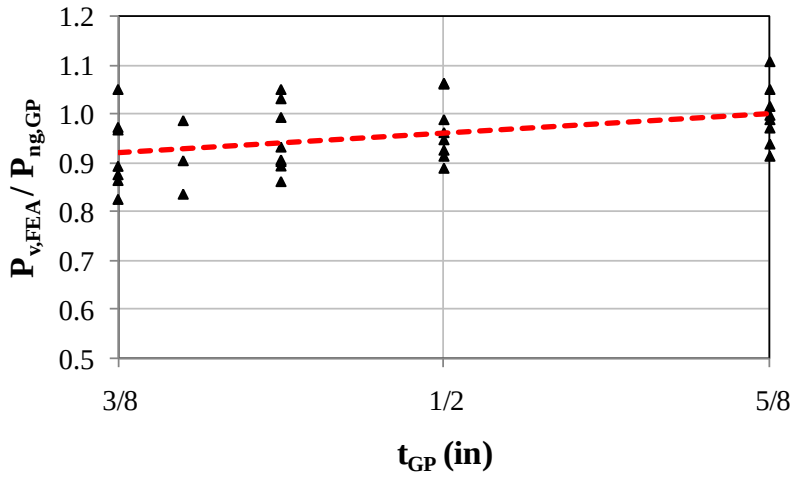

Figure 6.2.7: Back-calculated Ω values for chamfered connections with $t_{GP} \geq 3/8$ inch

To support the similarity in the trend for both unchamfered and chamfered connections having gusset plates of at least 3/8 inch, calculated Ω values are plotted separately. Figure 6.2.8 shows the relation between the back-calculated Ω-value and plate thickness for both chamfered and unchamfered members. The trend and scatter of the back-calculated Ω-values for chamfered and unchamfered members is very close to each other. The mean of the data varies from 0.9 to 1.0 as the plate thickness increases. Since there will be a resistance factor calibration performed by FHWA, the resistance factor can account for the difference and the scatter in the plot between the assumed nominal value and the data. The Ω-value can be assumed to be either 0.9 or 1.0, but the resistance factor associated with each of these would likely be different. For simplicity, it will be the best to assume Ω=1.0, but the trade-off will be a higher coefficient of variation leading to a more conservative resistance factor.

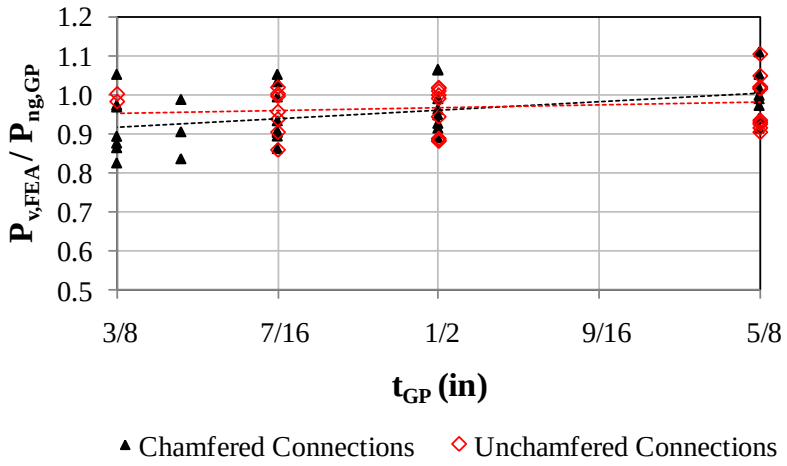

Figure 6.2.8: Relationship between the Ω and the gusset plate thickness for both chamfered and unchamfered connections

As the chamfering of the member increases, tendency towards having a shear failure also increases. The degree of chamfering on the trend of the Ω-value is also investigated. Figure 6.2.9 shows one of the chamfered connections from the parametric study. In this case, total chamfered width ($L_{cham,GP}$) along the horizontal plane is 14.9+25.3=40.2 inch and total horizontal plane width ($L_{vg,GP}$) is 128.2 inch, therefore a chamfer ratio can be calculated as 40.2/128.2 = 0.31.

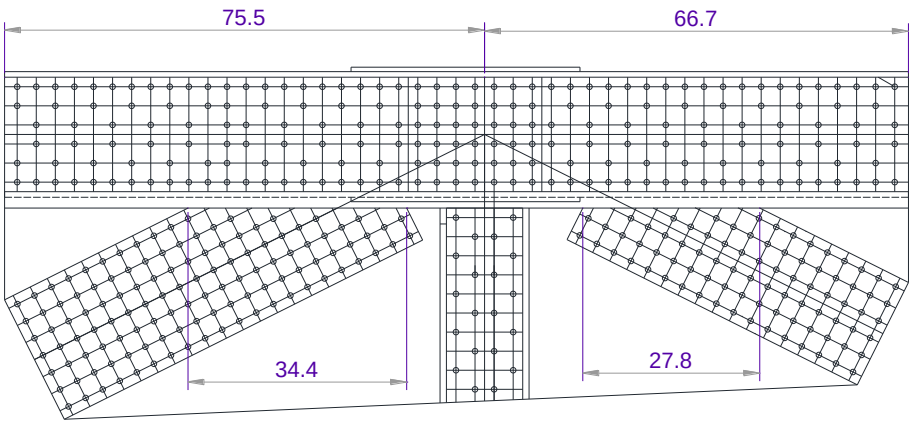

Figure 6.2.9: One chamfered connection showing the dimensions for chamfering and the corresponding horizontal plane

The length of the total chamfer length and total shear plane length are shown in Table 6.2.3.

Table 6.2.3: Chamfering ratios for critical shear plane from different parametric cases

Case	$L_{vg,GP}$ (in)	$L_{cham,gP}$ (in)	$L_{cham,GP}$ / $L_{vg,gP}$
3-V	85.6	28.0	0.33
	85.6	28.0	0.33
	85.6	28.0	0.33
	85.6	28.0	0.33
	85.6	28.0	0.33
	85.6	28.0	0.33
5-V	56.7	17.6	0.31
	56.7	17.6	0.31
	56.7	17.6	0.31
	56.7	17.6	0.31
	56.7	17.6	0.31
	56.7	17.6	0.31
	56.7	17.6	0.31
5-H	69.5	9.1	0.13
	69.5	9.1	0.13
	69.5	9.1	0.13
	69.5	9.1	0.13
	69.5	9.1	0.13
	69.5	9.1	0.13
	69.5	9.1	0.13
6-H	128.1	40.2	0.31
	128.1	40.2	0.31
	128.1	40.2	0.31
	128.1	40.2	0.31
	128.1	40.2	0.31
	128.1	40.2	0.31
7-H	142.1	62.2	0.44
	142.1	62.2	0.44
	142.1	62.2	0.44
	142.1	62.2	0.44
	142.1	62.2	0.44
	142.1	62.2	0.44

Table 6.2.3 (continued): Chamfering ratios for critical shear plane from different parametric cases

Case	$L_{vg,GP}$ (in)	$L_{cham,gP}$ (in)	$L_{cham,GP}$ / $L_{vg,gP}$
8-H	94.1	28.9	0.31
	94.1	28.9	0.31
	94.1	28.9	0.31
	94.1	28.9	0.31
	94.1	28.9	0.31
	94.1	28.9	0.31
13-V	58.3	9.9	0.17
	58.3	9.9	0.17
	58.3	9.9	0.17
	58.3	9.9	0.17
	58.3	9.9	0.17
	58.3	9.9	0.17
	58.3	9.9	0.17
14-H	57.1	5.7	0.10
	57.1	5.7	0.10
	57.1	5.7	0.10
	57.1	5.7	0.10
	57.1	5.7	0.10
	57.1	5.7	0.10

Figure 6.2.10 shows the back-calculated Ω-values versus plate thickness for four different chamfer ratios ranging from 0.0 (the unchamfered case) to 0.17. The data in the plot suggest as the chamfer ratio increases, the back-calculated Ω-values generally move towards 1.0.

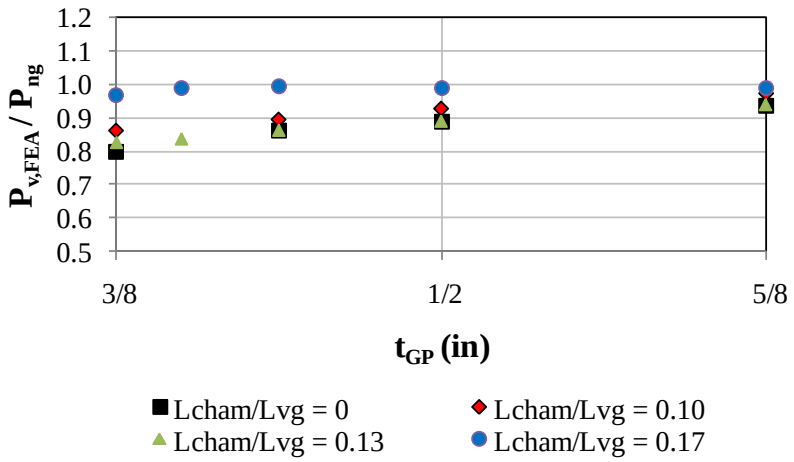

Figure 6.2.10: Ω vs. gusset plate thickness relationship for different chamfering ratios

This plot also shows that the unchamfered connections do not represent the lower bound of the data. Setting up the same Ω=1.0 value with different resistance factors calibration would take care of the generalization of the shear resistance calculations for gusset plates in steel truss bridges.

Although a very significant effort was spent on quantifying the resistance of thin plate cases (<3/8 inch thick) for completeness of the study, designers ought not to use plates smaller than 3/8 inch. This would be an easy approach for the designers so that they could check the shear resistance for chamfered connections and not worry about the buckling checks. If they would still prefer to use thinner plates, the proposed lower reduction factor of Ω=0.80 should be applied into the shear resistance calculations.

6.3. Chord Splice Resistance Checks

When the chord members are not milled to bear, i.e. acting as two individual members connected to the gusset plate, steel truss bridge designers prefer to use splice (continuity) plates at the chord splice location. Currently, there is no mechanistic approach which would quantify the chord splice resistance in both compression and tension. The current FHWA guidance had an estimation of the load sharing between the gusset plate and splice plates based on the ratio of the corresponding cross-sectional areas. However, questions on how to determine the effective gusset plate width have arisen within the engineering profession. From the parametric studies, cases where chord splice failure took place were picked to come up with a mechanistic resistance calculation approach which best represents this failure mode.

6.3.1. Compression Chord Splice

The FHWA guidance determines the effective width based on 30° Whitmore width and applies a K=1.2 for column buckling calculations for compression chord splices. However, K=1.2 in gusset plate buckling calculations induces excessive conservatism into the resistance estimation. The chord splice compression behavior is more like a fixed-fixed column. Hence, it would be more applicable to use a K=0.5 in the calculations. Studies on the parametric cases show that Case #1, as shown in Figure 6.3.1**,** has a compression chord splice failure.

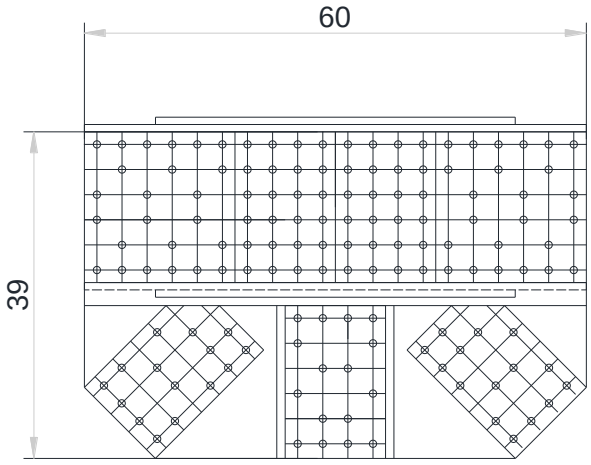

Figure 6.3.1: Gusset plate of the Case 1 joint at mid-span location (chords are in compression)

Figure 6.3.2 shows the general chord splice connection geometry. The chord member webs are connected to both gusset plate and web splice plate. The flange of the chord is connected to the top and bottom splice plates. The work point passes through the centroid of the chord member. The naming convention used for the gusset plate, splice plates, and chord web/flange plates is also shown in this figure.

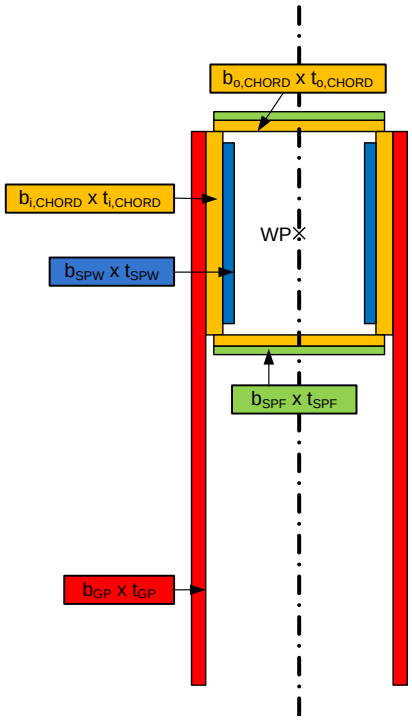

Figure 6.3.2: Chord splice connection geometry with the splice plate and chord member cross-sections

The chord compression resistance is calculated by using a pseudo-plastic section analysis. The pseudo-plastic section analysis utilizes an equivalent column resistance for the compressive stress, the yield resistance for the tension stress, and determines resistance of the splice using a beam-column plastic section analysis accounting for any eccentricity of the chord relative to the gusset plate and splice plate centroids. The use of the yield strength for the gusset and splice plates is reasonable for this check as long as the KL/r values of the equivalent columns are less than 25, which is practically always the case for gusset plates of this type (AISC, 2005). Figure 6.3.3 shows the stress state through the gusset plate and splice plates. The chord force is carried by the gusset plates and splice plates. All the splice plates and the effective gusset plate width are under compression. Their critical compressive stress needs to be determined. The bottom

portion of the gusset plate is assumed to reach its tension yield capacity in this plastic section approach. The two unknowns in this geometry are the y_{GP}, which represents the tension area in the gusset plate, and d* which is the distance between the bottom of the flange splice plate and the point where tension zone of the gusset plate begins.

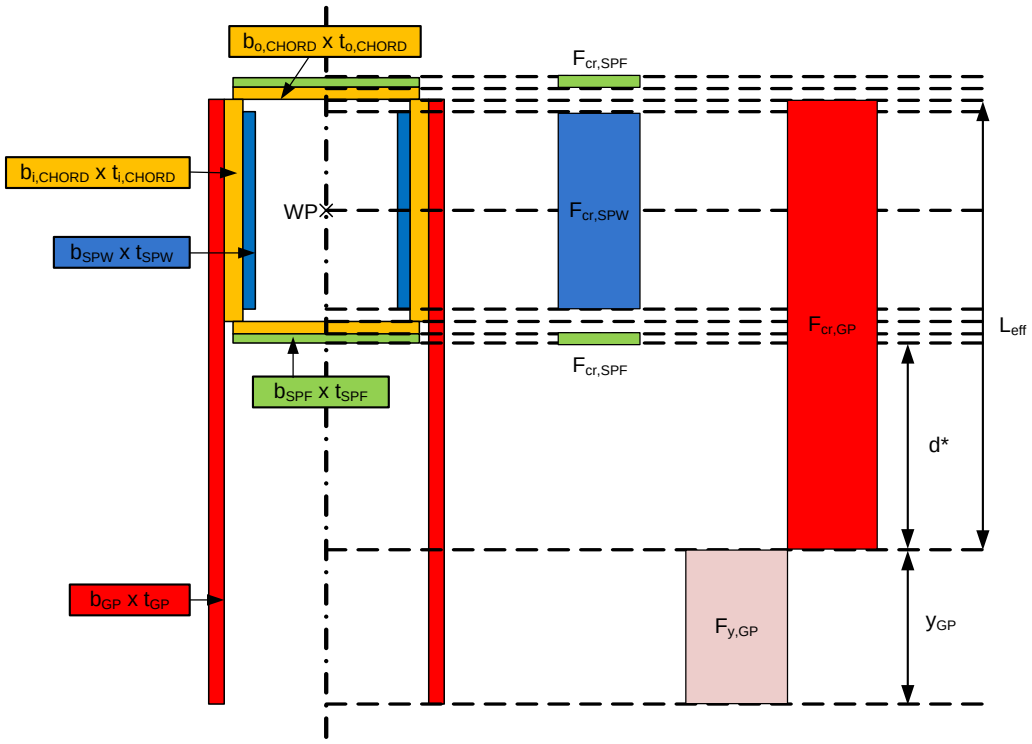

Figure 6.3.3: Pseudo-plastic section stress state for the compression chord splice

To be able to calculate the critical stress in each of the plates, the AISC column formula is used. The radius of gyration, r_s calculation requires the calculation of the area (A_{GP}) and moment of inertia ($I_{g,GP}$) of the equivalent column section for the gusset plate. In this calculation, the entire gusset plate height can be used to calculate the r_s. In the end, whatever initial effective width is picked, it would not change the r_s value since;

$$A_{GP} = b_{GP}t_{GP} \qquad \text{(Eq. 6.3-1)}$$

$$I_{g,GP} = \frac{1}{12} b_{GP}(t_{GP})^3 \qquad \text{(Eq. 6.3-2)}$$

$$r_s = \sqrt{\frac{I_{g,GP}}{A_{GP}}} = \sqrt{\frac{[\frac{1}{12} b_{GP}(t_{GP})^3]}{b_{GP}t_{GP}}} = \frac{t_{GP}}{\sqrt{12}} \qquad \text{(Eq. 6.3-3)}$$

For the splice plates, the full width of each plate is used to calculate the corresponding r_s values. Calculations for each plate are summarized in Table 6.3.1**.** The next step is to calculate the critical compressive stress within each plate using the column buckling calculations. Three main aspects of these calculations were:

1) An effective column length factor of K= 0.5 better represents the buckling mode within the splice region since it resembles a fixed-fixed column buckling case.
2) The column length (L) is taken as the distance between the first bolt lines along the two chord members. Buckling or crushing of the plate takes place within this region and it is a reasonable estimate of the column length to be used in critical stress calculations.
3) The yield strength of the plate can be used as long as the KL/r_s value of the equivalent column is less than 25.

Table 6.3.2 shows the critical compressive stress calculations for the plates in this connection. The F_{cr}/F_y ratios are almost 1.0 since the equivalent column length is fairly short. Since all the KL/r_s values were smaller than 25, $F_{cr} = F_y$ is used in further calculations. The gusset plate thickness varies between 0.250” and 0.625” and chord splice failure is observed in all cases. Hence, resistance calculation will be compared with the finite element results for all the different thickness cases.

Table 6.3.1: Cross-sectional properties for the gusset plate and splice plates

Gusset Plate					Web Splice Plate					Top/Bottom Flange Splice Plate				
b_{GP} (in)	t_{GP} (in)	A_{GP} (in^2)	$I_{g,GP}$ (in^4)	r_s (in)	b_{SPW} (in)	t_{SPW} (in)	A_{SPW} (in^2)	$I_{g,SPW}$ (in^4)	r_s (in)	b_{SPF} (in)	t_{SPF} (in)	A_{SPF} (in^2)	$I_{g,SPF}$ (in^4)	r_s (in)
39.0	0.2500	9.8	0.051	0.072										
39.0	0.3125	12.2	0.099	0.090										
39.0	0.3750	14.6	0.171	0.108										
39.0	0.4000	15.6	0.208	0.115	17.5	0.5090	8.9	0.192	0.147	19.6	0.7750	15.2	0.761	0.224
39.0	0.4375	17.1	0.272	0.126										
39.0	0.5000	19.5	0.406	0.144										
39.0	0.6250	24.4	0.793	0.180										

Table 6.3.2: Critical compressive stresses for gusset plate and splice plates

Gusset Plate							Web Splice Plate						Top/Bottom Flange Splice Plate					
t_{GP} (in)	K	L (in)	KL/r_s	λ	F_{cr}/F_y	F_{cr} (ksi)	K	L (in)	KL/r_s	λ	F_{cr}/F_y	F_{cr} (ksi)	K	L (in)	KL/r_s	λ	F_{cr}/F_y	F_{cr} (ksi)
0.2500			20.8	0.080	0.97	53.0												
0.3125			16.6	0.051	0.98	53.0												
0.3750			13.9	0.036	0.99	53.0												
0.4000	0.5	3.0	13.0	0.031	0.99	53.0	0.5	3.0	10.2	0.019	0.99	53.0	0.5	3.0	6.7	0.008	1.00	53.0
0.4375			11.9	0.026	0.99	53.0												
0.5000			10.4	0.020	0.99	53.0												
0.6250			8.3	0.013	0.99	53.0												

After the critical stress is calculated, both y_{GP} and d* are determined by taking moments about the work point of the connection using the calculated stresses. These calculations consider the eccentricity of the plates with respect to the work point. The moment of the forces acting through the top and bottom splice plates cancels each other since they are symmetric. Similarly, the web splice plates provide a net zero moment along the work point since their centroid coincides with the work point. The sum of all the moments should be equal to zero. Thus the only eccentric force comes from the gusset plate and the net moment about the work point can be calculated as:

$$\begin{aligned} M_{WP,c} = {} & [(F_{cr,GP})(t_{GP})(t_{o,CHORD})(b_{i,CHORD}/2 + t_{o,CHORD}/2)] + \\ & [(F_{cr,GP})(t_{GP})(t_{SPF})(b_{i,CHORD}/2 + t_{o,CHORD} + t_{SPF}/2)] + \\ & [(F_{cr,GP})(t_{GP})(d^*)(b_{i,CHORD}/2 + t_{o,CHORD} + t_{SPF} + d^*/2)] - \\ & [(F_{y,GP})(t_{GP})(y_{GP})(b_{GP} - b_{i,CHORD}/2 - y_{GP}/2)] = 0 \end{aligned} \qquad \text{(Eq. 6.3-4)}$$

y_{GP} can be written in terms of d* as:

$$y_{GP} = b_{GP} - b_{i,CHORD} - t_{o,CHORD} - t_{SPF} - d^* \qquad \text{(Eq. 6.3-5)}$$

By changing the d* value, the y_{GP} value which makes the M_{WP} formula equal to zero can be calculated. All the calculations were done in an Excel spreadsheet and the "goal seek" function was utilized to calculate the y_{GP} values for each case. Table 6.3.3 shows the L_{eff} calculation summary for the different gusset plate thicknesses. Since $F_{cr,GP} = F_y$ in all the cases, corresponding y_{GP} and L_{eff} values are also the same for the different plate thicknesses.

Table 6.3.3: L_{eff} values for different gusset plate thickness analyses

t_{GP} (in)	$t_{o,CHORD}$ (in)	$b_{i,CHORD}$ (in)	$F_{cr,GP}$ (ksi)	$F_{cr,SPW}$ (ksi)	$F_{cr,SPF}$ (ksi)	d* (in)	y_{GP} (in)	$M_{WP,c}$ (kip-in)	L_{eff} (in)
0.2500	0.8750	18.0	53.0	53.0	53.0	11.5	7.9	0.0	31.1
0.3125	0.8750	18.0	53.0			11.5	7.9	0.0	31.1
0.3750	0.8750	18.0	53.0			11.5	7.9	0.0	31.1
0.4000	0.8750	18.0	53.0			11.5	7.9	0.0	31.1
0.4375	0.8750	18.0	53.0			11.5	7.9	0.0	31.1
0.5000	0.8750	18.0	53.0			11.5	7.9	0.0	31.1
0.6250	0.8750	18.0	53.0			11.5	7.9	0.0	31.1

After determining the two unknown parameters y_{GP} and d* for the gusset plate cross section, the total nominal compression chord splice resistance is calculated. The chord force is carried by two gusset plates, two web splice plates, and top/bottom splice plates. Half of the total chord splice resistance is compared with half of the total chord force at failure. The resistance of one gusset plate, one web splice plate and one top/bottom splice plate is calculated using the formula:

$$P_n = [(F_{cr,SPF})(A_{SPF})] + [(F_{cr,SPW})(A_{SPW})] + [(F_{cr,GP})(t_{GP})(b_{GP} - y_{GP})] - [(F_{y,GP})(t_{GP})(y_{GP})] \quad \text{(Eq. 6.3-6)}$$

The calculated resistance is compared with half of the chord forces from the finite element analysis. A summary of the results is shown in Table 6.3.4**.**

Table 6.3.4: Comparison between the finite element analysis and the calculated compression splice resistance using the pseudo-plastic section analysis

t_{GP} (in)	$F_{y,GP}$ (ksi)	$F_{cr,GP}$ (ksi)	$F_{cr,SPW}$ (ksi)	$F_{cr,SPF}$ (ksi)	P_{FEA} (kip)	P_{calc} (kip)	P_{FEA} /Pcalc
0.2500	53.0	53.0	53.0	53.0	1455	1587	0.92
0.3125	53.0	53.0			1890	1664	1.14
0.3750	53.0	53.0			1950	1741	1.12
0.4000	53.0	53.0			2055	1772	1.16
0.4375	53.0	53.0			2130	1818	1.17
0.5000	53.0	53.0			2205	1895	1.16
0.6250	53.0	53.0			2475	2050	1.21

This approach works reasonably well to estimate the compression chord splice resistance by applying a beam-column plastic section analysis to the plates transferring the chord forces. The conservatism induced by the methodology can be considered to be acceptable since this was an effort to define the splice resistance using a more mechanistic (i.e. rational) approach than has been done previously.

6.3.2. Tension Chord Splice

Case #2 as shown in Figure 6.3.4 had a tension chord splice failure. The tension chord splice resistance is also calculated by using the pseudo-plastic section analysis described in the previous section. All the splice plates, and the effective gusset plate width are under tension in this case. The bottom portion of the gusset plate is under compressive stress. Hence, a critical stress calculation is performed only for the gusset plate. Since the tension chord splice is rupture critical along the splice region, both gross section yield and net section rupture within the tension regions needs to be checked, and lower of the two should be used.

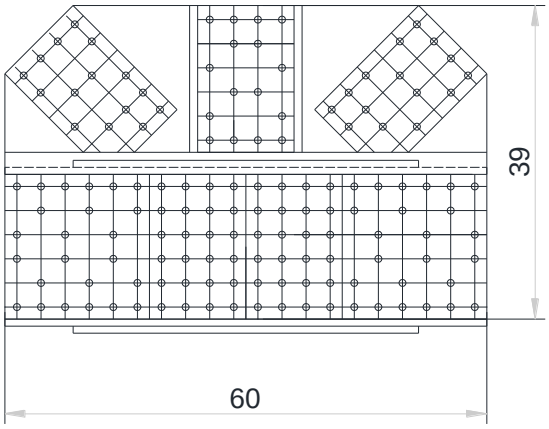

Figure 6.3.4: Gusset plate of the Case 2 joint at mid-span location (chords are in tension)

6.3.2.1. Tension Chord Splice Gross Section Yield Capacity

Figure 6.3.5 shows the stress state through the gusset plate and splice plates. To be able to calculate the critical stress for the lower portion of the gusset plate, the AISC column formula is used. Similar to the compression splice calculations, a radius of gyration, r_s is determined using the whole gusset height. As mentioned before, whatever width is picked

to use in this calculation, r_s becomes a function of the gusset plate thickness only. In most cases, depending on the KL/ r_s value, F_{cr} is equal to the yield strength, F_y of the gusset plate. The same K value of 0.5 was used along with the equivalent column length (L) being the distance between the first bolt lines of the chord members. The stress state for the tension splice yield capacity is shown in Figure 6.3.5.

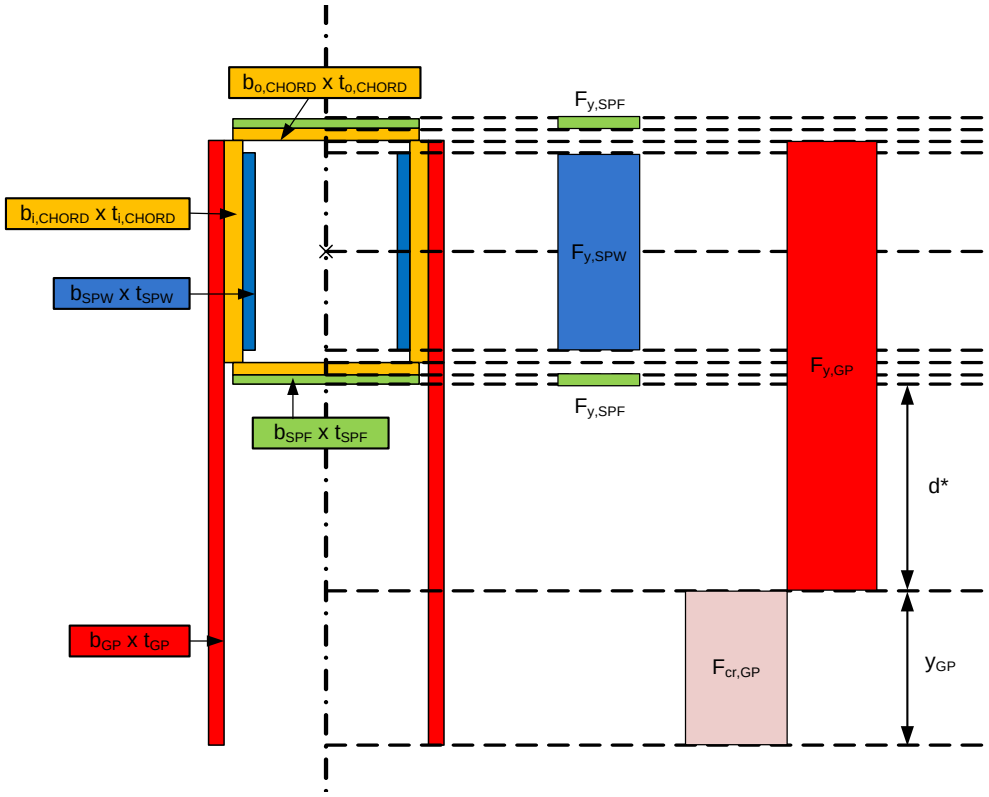

Figure 6.3.5: Pseudo-plastic section stress state for the tension chord splice (gross-section yield resistance)

The calculated r_s and F_{cr} values for different thickness cases are shown in Table 6.3.5 and Table 6.3.6 respectively**.** Since the effective column length is very short, $F_{cr} = F_y$ in all cases.

Table 6.3.5: Cross-sectional properties for the gusset plate based on the full gusset plate height

Gusset Plate				
b_{GP} (in)	t_{GP} (in)	A_{GP} (in^2)	$I_{g,GP}$ (in^2)	r_s (in)
39.0	0.2500	9.8	0.051	0.072
39.0	0.3125	12.2	0.099	0.090
39.0	0.3750	14.6	0.171	0.108
39.0	0.4000	15.6	0.208	0.115
39.0	0.4375	17.1	0.272	0.126
39.0	0.5000	19.5	0.406	0.144
39.0	0.6250	24.4	0.793	0.180

Table 6.3.6: Critical compressive stress values for the gusset plate

Gusset Plate						
t_{GP} (in)	K	L (in)	KL/r_s	λ	F_{cr}/F_y	F_{cr} (ksi)
0.2500	0.5	3.0	20.8	0.080	0.97	53.0
0.3125			16.6	0.051	0.98	53.0
0.3750			13.9	0.036	0.99	53.0
0.4000			13.0	0.031	0.99	53.0
0.4375			11.9	0.026	0.99	53.0
0.5000			10.4	0.020	0.99	53.0
0.6250			8.3	0.013	0.99	53.0

Both y_{GP} and d* are determined by using a similar moment formula along the work point as had been done for the compression case. It has slight differences in terms of the stresses used as shown in the formula:

$$\begin{aligned} M_{WP,t} = {} & [(F_{cr,GP})(t_{GP})(t_{o,CHORD})(b_{i,CHORD}/2 + t_{o,CHORD}/2)] + \\ & [(F_{cr,GP})(t_{GP})(t_{SPF})(b_{i,CHORD}/2 + t_{o,CHORD} + t_{SPF}/2)] + \\ & [(F_{cr,GP})(t_{GP})(d^*)(b_{i,CHORD}/2 + t_{o,CHORD} + t_{SPF} + d^*/2)] - \\ & [(F_{y,GP})(t_{GP})(y_{GP})(b_{GP} - b_{i,CHORD}/2 - y_{GP}/2)] = 0 \end{aligned} \qquad \text{(Eq. 6.3-7)}$$

Mainly the difference is that wherevere $F_{cr,GP}$ was found in the compression splice formula, it is replaced by $F_{y,GP}$. Similarly, $F_{y,GP}$ is replaced by $F_{cr,GP}$ in the tension splice moment formula since lower portion is in compression for this case. The same y_{GP} formula is used for the tension chord splice resistance calculations. A summary of the y_{GP} and L_{eff} calculations is shown in Table 6.3.7.

Table 6.3.7: L_{eff} values for different gusset plate thickness analyses

t_{GP} (in)	$t_{o,CHORD}$ (in)	$b_{i,CHORD}$ (in)	$F_{cr,GP}$ (ksi)	d* (in)	y_{GP} (in)	$M_{WP,t}$ (kip-in)	L_{eff} (in)
0.2500	0.8750	18.0	53.0	11.5	7.9	0.0	31.1
0.3125	0.8750	18.0	53.0	11.5	7.9	0.0	31.1
0.3750	0.8750	18.0	53.0	11.5	7.9	0.0	31.1
0.4000	0.8750	18.0	53.0	11.5	7.9	0.0	31.1
0.4375	0.8750	18.0	53.0	11.5	7.9	0.0	31.1
0.5000	0.8750	18.0	53.0	11.5	7.9	0.0	31.1
0.6250	0.8750	18.0	53.0	11.5	7.9	0.0	31.1

The resistance of one gusset plate, one web splice plate and one top/bottom splice plate is calculated using the formula:

$$P_{n,gross} = [(F_{y,SPF})(A_{SPF})] + [(F_{y,SPW})(A_{SPW})] + [(F_{y,GP})(t_{GP})(b_{GP} - y_{GP})] - [(F_{cr,GP})(t_{GP})(y_{GP})] \quad \text{(Eq. 6.3-8)}$$

The calculated resistance is compared with half of the chord forces from the finite element analysis. A summary of the results is shown in Table 6.3.8.

Table 6.3.8: Comparison between the finite element analysis and the calculated tension splice gross section yield resistance using the pseudo-plastic section analysis

t_{GP} (in)	$F_{y,GP}$ (ksi)	$F_{cr,GP}$ (ksi)	$F_{y,SPW}$ (ksi)	$F_{y,SPF}$ (ksi)	P_{FEA} (kip)	$P_{n,gross}$ (kip)	$P_{FEA}/P_{n,gross}$
0.2500	53	53.0	53.0	53.0	1575	1587	0.99
0.3125	53	53.0			1740	1664	1.05
0.3750	53	53.0			1860	1741	1.07
0.4000	53	53.0			1935	1772	1.09
0.4375	53	53.0			2010	1818	1.11
0.5000	53	53.0			2145	1895	1.13
0.6250	53	53.0			2415	2050	1.18

The pseudo-plastic section approach estimates well the tension chord splice nominal yield resistance for different thicknesses of gusset plates.

6.3.2.2. Tension Chord Splice Net Section Rupture Capacity

The tension splice should also be checked for net section rupture using the net areas within the tension stress areas. The stress state for this check is shown in Figure 6.3.6**.** The ultimate plate strength is used in the net section rupture resistance calculations.

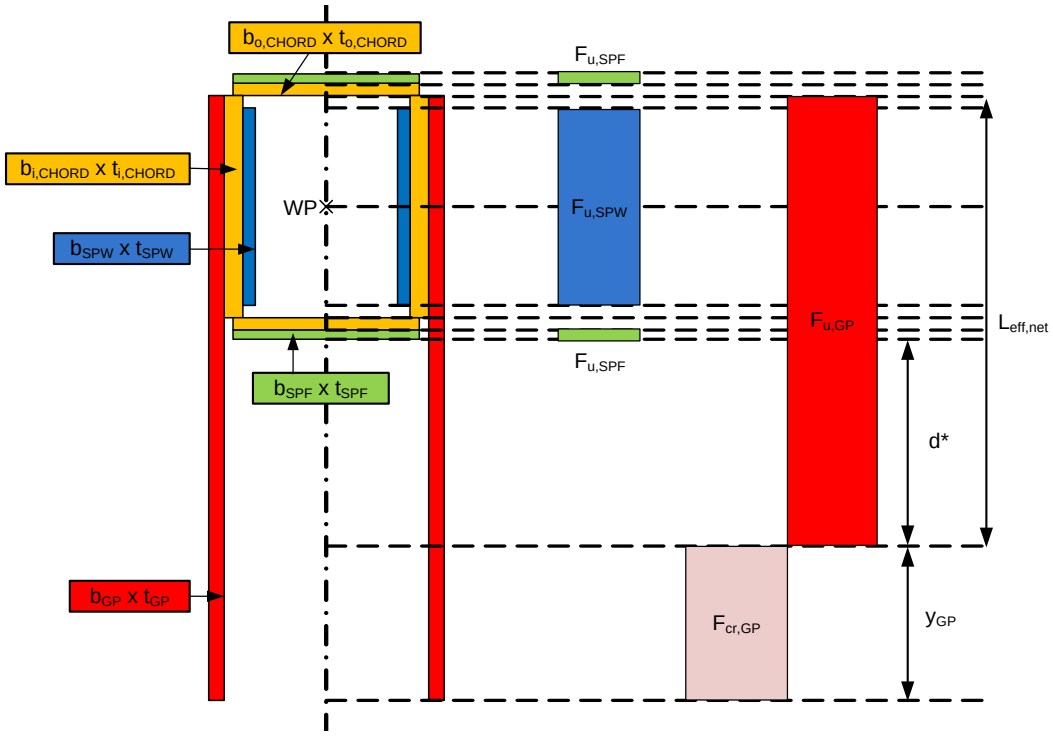

Figure 6.3.6: Pseudo-plastic section stress state for the tension chord splice (net section rupture resistance)

Using the same L_{eff} values and critical stress (F_{cr}) for the gusset plate, the net section rupture resistance was calculated as:

$$P_{n,net} = [(F_{u,SPF})(A_{SPF,net})] + [(F_{u,SPW})(A_{SPW,net})] + [(F_{u,GP})(t_{GP})(b_{GP} - y_{GP})_{net}] - [(F_{cr,GP})(t_{GP})(y_{GP})] \quad \text{(Eq. 6.3-9)}$$

The net area for the splice plates was calculated by subtracting the fastener holes.

$$A_{SPF,net} = t_{SPF}[b_{SPF} - (\#\text{of fasteners})(d_f + 1/8)] \quad \text{(Eq. 6.3-10)}$$

$$A_{SPW,net} = t_{SPW}[b_{SPW} - (\#\text{of fasteners})(d_f + 1/8)] \quad \text{(Eq. 6.3-11)}$$

$$L_{eff,net} = (b_{GP} - y_{GP})_{net} = (b_{GP} - y_{GP}) - (\#\text{of fasteners})(d_f + 1/8)] \quad \text{(Eq. 6.3-12)}$$

The calculated resistance is compared with the finite element analysis results as shown in Table 6.3.9**.**

Table 6.3.9: Comparison between the finite element analysis and the calculated tension splice gross section yield resistance using the pseudo-plastic section analysis

t_{GP} (in)	$F_{u,GP}$ (ksi)	$F_{cr,GP}$ (ksi)	$F_{u,SPW}$ (ksi)	$F_{u,SPF}$ (ksi)	P_{FEA} (kip)	$P_{n,net}$ (kip)	$P_{FEA}/P_{n,net}$
0.2500	71.4	53.0	71.4	71.4	1575	1481	1.06
0.3125	71.4	53.0			1740	1558	1.12
0.3750	71.4	53.0			1860	1636	1.14
0.4000	71.4	53.0			1935	1666	1.16
0.4375	71.4	53.0			2010	1713	1.17
0.5000	71.4	53.0			2145	1790	1.20
0.6250	71.4	53.0			2415	1945	1.24

For this joint, the net section rupture resistance is slightly lower than the gross section yield resistance. However, this is only an illustrative example of the process as the finite element models cannot capture the rupture failure mode since the bolt holes are not explicitly modeled. The experimental specimens also do not reach any rupture limit states. Cracking or other evidence of rupture limit states are not observed in the experiments.

6.4. Effect of Corrosion on the Gusset Plate Capacity

As part of the experimental program, three different simulated corrosion specimens have been tested. One specimen aimed to investigate the reduction on buckling resistance and the remaining two were intended to investigate the effect on shear failure of simulated corrosion. One of these shear corrosion specimens had an unsymmetric section loss pattern. For that specimen, one plate was kept at its nominal thickness and second plate had concentrated corrosion just above the chord members. The results of these three experiments will be discussed thoroughly in the two following sections.

6.4.1. Effect on the Buckling Resistance

GP307-SS3-1 specimen is the first corrosion specimen with a section loss pattern as shown in Figure 6.4.1. The geometry of the specimen is the same as that of the GP307-SS3 specimen discussed previously, except that portions of the gusset plate thickness is milled and reduced based on the proposed pattern. Since the nominal thickness is 0.375 inch, the region for 50% section loss is milled to 0.188 inch, and the region with 30% section loss is milled to 0.255 inch. Since more section loss is induced on the compression diagonal side of the plate, the load combination selected to fail the specimen has more load on the compression diagonal to promote a buckling failure.

The reference load combination had the following loads:

Compression Diagonal (F2): 1000 kip

Vertical Member (F3): -207 kip

Tension Diagonal (F4): -707 kip

East Chord (F5): 707 kip

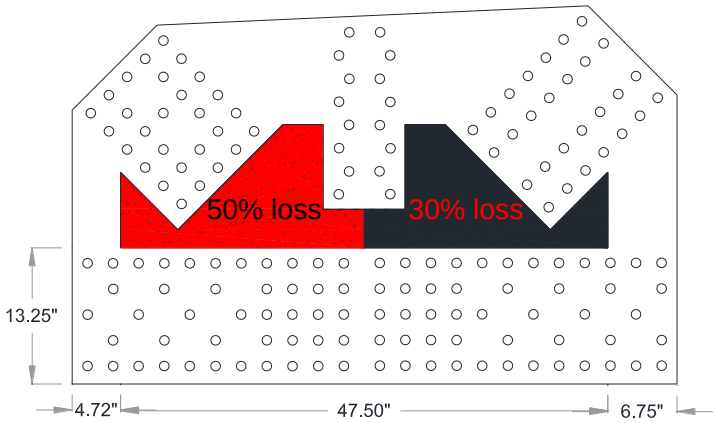

Figure 6.4.1: Simulated corrosion pattern for the GP307-SS3-1 specimen (50% loss on the compression diagonal side)

The failure occurs with side-sway buckling of the gusset plate on the compression diagonal side as shown in Figure 6.4.2. This figure shows the DIC contours just after the failure of the specimen. The deformation is concentrated around the compression diagonal (on the right). Similar to the GP307-SS3 specimen without any corrosion, the failure mode is buckling.

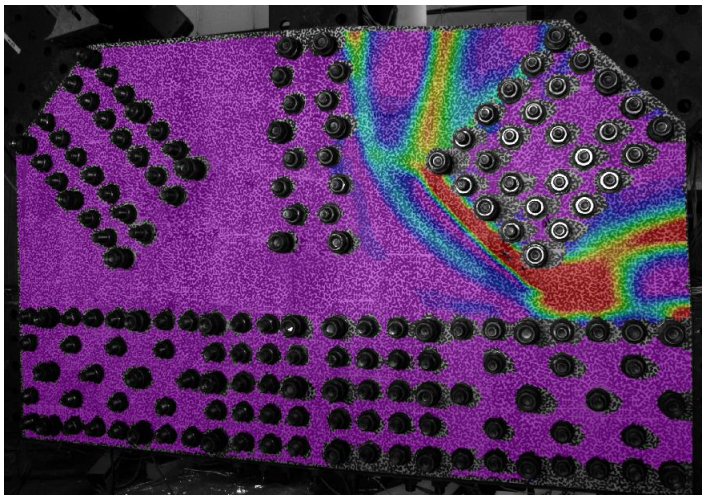

Figure 6.4.2: Tresca strain response from the DIC system at the failure load of the GP307-SS3-1 specimen (compression diagonal on the right)

The maximum member loads at the instant of the failure of the connection are:

Compression Diagonal (F2): 446 kip

Vertical Member (F3): -90 kip

Tension Diagonal (F4): -285 kip

East Chord (F5): 321 kip

6.4.1.1. Buckling Resistance Check with Equivalent Thickness Approach

This corrosion pattern represents a critical pattern that would be possible to see in steel truss bridge gusset plate connections. To quantify the gusset plate buckling resistance, preliminary calculations are performed using the reduced thickness of 0.188" for the whole equivalent column. The proposed method with K=0.35 and L=L_{mid} is compared with the current FHWA guidance formula using K=1.2 and L=L_{ave}. The buckling occurs at 446 kip compression diagonal load. Assuming half of this load is carried by single gusset plate (both plates had the same corrosion pattern), calculated resistance of one gusset is compared with 223 kip buckling load in Table 6.4.1. The proposed method works much better than the current guidance although both of them provide conservative results for the buckling calculations. Since corrosion is a critical condition for gusset plate connections, this simple calculation would be easy to apply to the current bridges with corroded gusset plates. The assumption of applying the reduced thickness to whole cross-section of the equivalent column has an effect in this conservatism.

Table 6.4.1: Comparison between the buckling load from the test and two different resistance calculation methods using the reduced thickness

Method	t_{GP} (in)	F_y (ksi)	P_{cr} (kip)	P_n (kip)	P_{cr}/P_n
K=0.35 and L=L_{mid}	0.188	47.2	223	133	**1.68**
K=1.20 and L=L_{ave}	0.188	47.2	223	64	3.51

To be able to quantify the buckling resistance with the induced corrosion in the gusset plate, an equivalent thickness approach is proposed. Since the column length used is L_{mid} for the proposed buckling resistance calculations, it would be ideal to look at the thickness distribution of L_{mid} throughout the corrosion pattern. As shown in Figure 6.4.3, three different portions of L_{mid} are measured as 1.5", 9.5" and 2.1" which makes the total length of L_{mid} = 13.1".

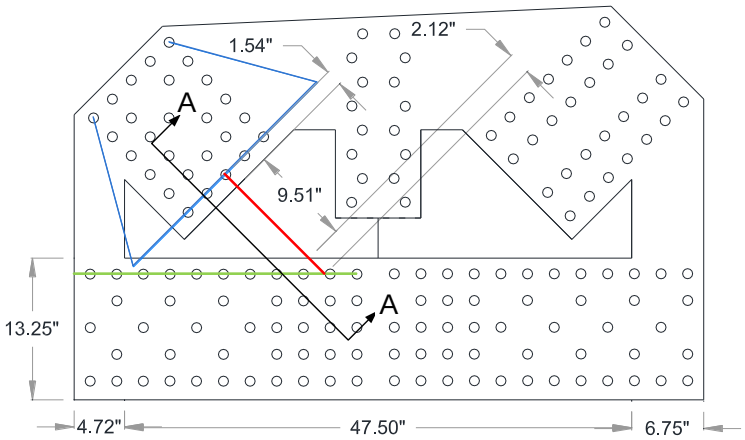

Figure 6.4.3: Dimensions for the three portions with different plate thicknesses through L_{mid}

If we look at the cross-section of the L_{mid}, we can see three portions with their corresponding thicknesses as shown in Figure 6.4.4.

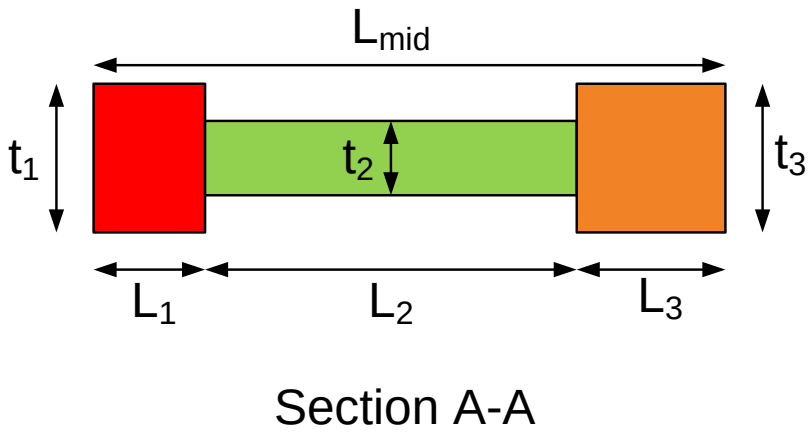

Figure 6.4.4: Cross-section of the equivalent column length, L_{mid} represented by three different lengths and corresponding plate thicknesses

Using the variable thicknesses and length of each portion, an equivalent thickness is calculated based on the formula:

$$t_{eq} = \frac{t_1 L_1 + t_2 L_2 + t_3 L_3 + ... + t_n L_n}{L_{mid}} \qquad \text{(Eq. 6.4-1)}$$

For this specific case, n=3 and the calculated t_{eq} becomes:

$$t_{eq} = \frac{(0.375)(1.5) + (0.188)(9.5) + (0.375)(2.1)}{13.1} = 0.239\,\text{inch}$$

Now the equivalent column has its equivalent thickness to be used in the buckling resistance calculations as shown in Figure 6.4.5.

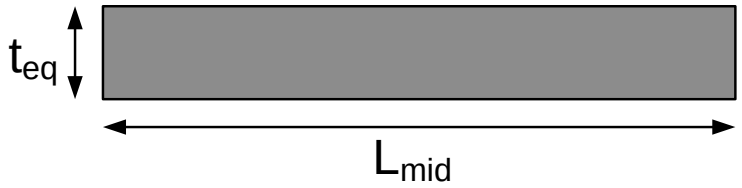

Figure 6.4.5: Equivalent gusset plate thickness used for L_{mid}

Table 6.4.2 summarizes the results using the current FHWA method and the proposed method.

Table 6.4.2: Comparison between the buckling load from the test and two different resistance calculation methods using the equivalent thickness

Method	t_{eq} (in)	F_y (ksi)	P_{cr} (kip)	P_n (kip)	P_{cr}/P_n
K=0.35 and L=L_{mid}	0.239	47.2	223	203	**1.10**
K=1.20 and L=L_{ave}	0.239	47.2	223	127	1.75

The equivalent thickness approach works reasonably well using the proposed method. Conservatism observed in the previous method from FHWA guidance is obvious even though the equivalent thickness is used in the calculations.

6.4.2. Effect on the Shear Resistance

The second specimen with simulated corrosion is the GP307-SS3-2 specimen. It has a similar corrosion pattern as GP307-SS3-1. However, in this case, the 50% section loss is applied on the tension diagonal side. The compression diagonal side has a 30% section loss. The corrosion pattern is shown in Figure 6.4.6.

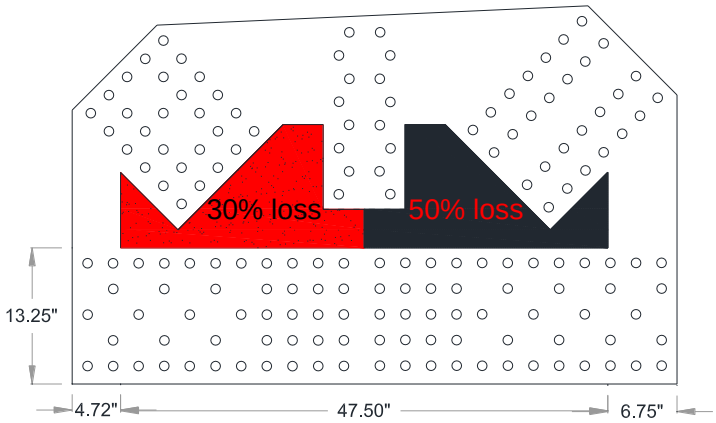

Figure 6.4.6: Simulated corrosion pattern for the GP307-SS3-2 specimen (50% loss on the tension diagonal side)

Since more section loss is induced on the tension diagonal side, the load combination selected to fail the specimen has more load applied on the tension diagonal.

The reference load combination has the following loads:

Compression Diagonal (F2): 707 kip

Vertical Member (F3): 207 kip

Tension Diagonal (F4): -1000 kip

East Chord (F5): 707 kip

Failure occurs with mobilization of the horizontal plane above the chord members due to a significantly reduced shear plane area. As shown in Figure 6.4.7, the displacement is concentrated along the horizontal plane and DIC contours support this conclusion with significant yielding through this shear plane.

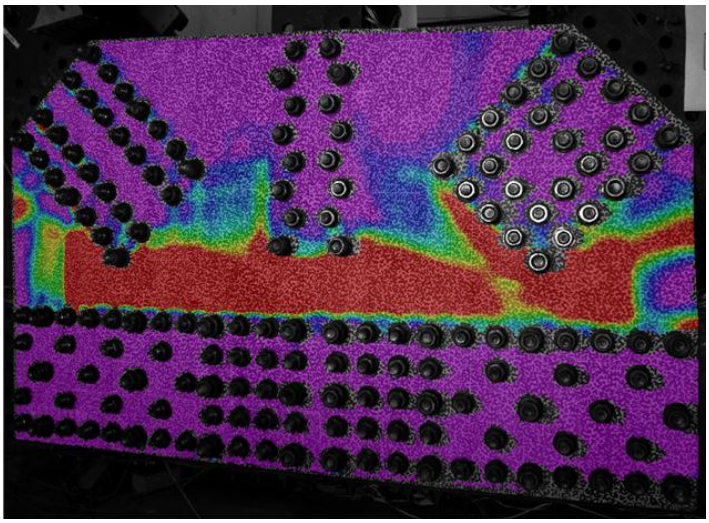

Figure 6.4.7: Tresca strain response from the DIC system at the failure load of the GP307-SS3-2 specimen (compression diagonal on the right)

The maximum member loads at the failure of the specimen are:

Compression Diagonal (F2): 482 kip

Vertical Member (F3): 148 kip

Tension Diagonal (F4): -696 kip

East Chord (F5): 512 kip

The third corrosion specimen is the GP307-SS3-3 specimen which focuses on the effect of unymmetric stiffness due to different corrosion patterns in the two gusset plates as shown in Figure 6.4.8. The simulated corrosion has a concentrated narrow band for one of the gusset plates in the connection. This area is just above the chord members which is the critical shear plane for the connection. One plate is kept at its nominal thickness of 0.375 inch. However, the other plate with the simulated corrosion has 50% thickness reduction (0.188” thickness) along the narrow band above the chord members.

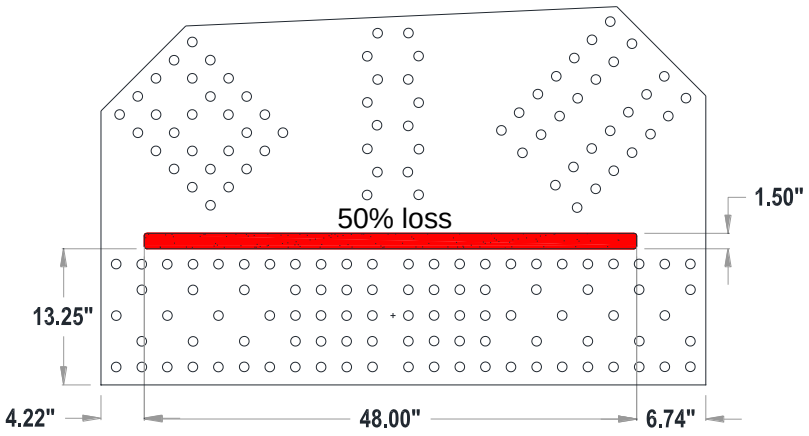

Figure 6.4.8: Simulated corrosion pattern for the GP307-SS3-3 specimen (50% loss concentrated along the horizontal plane)

The connection is loaded with the following reference load combination in order to have a shear failure along the horizontal plane and investigate the resistance with unbalanced corrosion and stiffness in the gusset plates:

Compression Diagonal (F2): 707 kip

Vertical Member (F3): 207 kip

Tension Diagonal (F4): -1000 kip

East Chord (F5): 707 kip

Failure of the connection occurs as a shear failure across the horizontal plane above the chords at the following applied loads:

Compression Diagonal (F2): 519 kip

Vertical Member (F3): 154 kip

Tension Diagonal (F4): -735 kip

East Chord (F5): 533 kip

The DIC response contours at the instant of failure are shown in Figure 6.4.9. This figure indicates the excessive yielding along the horizontal plane of the corrosion simulated plate (north plate) which is mobilized in shear due to high section loss.

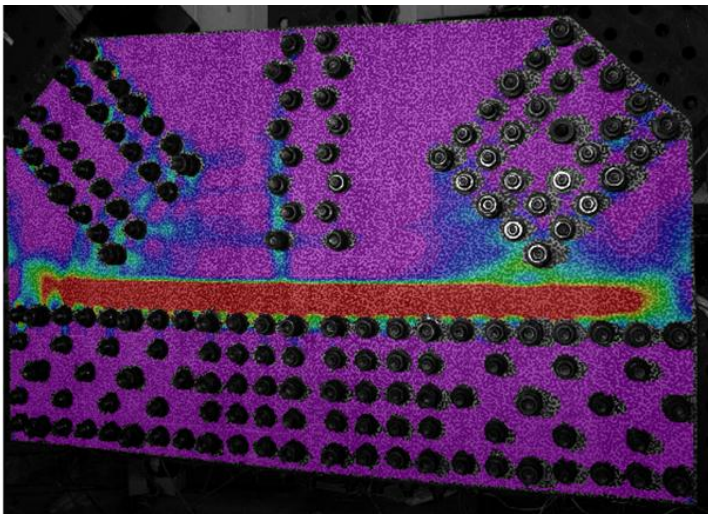

Figure 6.4.9: Tresca strain response from the DIC system at the failure load of the GP307-SS3-3 specimen (compression diagonal on the right)

6.4.2.1. Shear Resistance Check with Equivalent Thickness Approach

An equivalent thickness approach is applied in the shear resistance calculations to compare the calculated resistance with the actual shear forces from the tests of simulated corrosion specimens. For the GP307-SS3-2 specimen, both plates have the same corrosion pattern. By looking at the cross-section along the horizontal plane above the chord members, four different portions can be identified, two of which are on the sides without corrosion and the remaining two in the middle portion with their corresponding reduced thicknesses (Figure 6.4.10**)**.

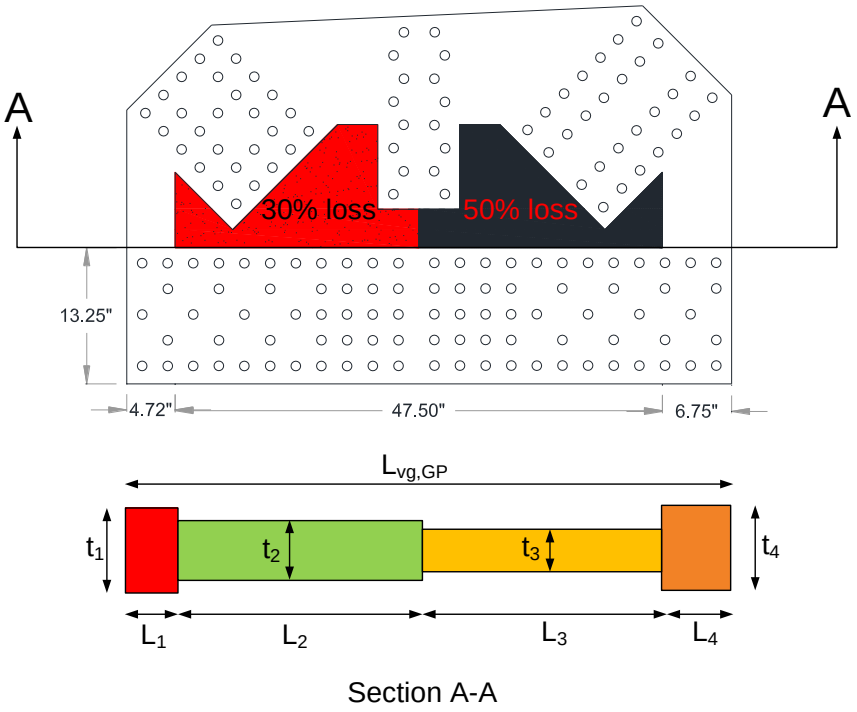

Figure 6.4.10: Cross-section of the horizontal shear plane length, $L_{vg,GP}$ represented by four different lengths and corresponding plate thicknesses (GP307-SS3-2 specimen)

The equivalent thickness for each gusset plate can be calculated using the previous formula:

$$t_{eq} = \frac{(0.375)(4.7) + (0.255)(47.5/2) + (0.188)(47.5/2) + (0.375)(6.8)}{59.0} = 0.251\,\text{inch}$$

The total shear force which mobilizes the horizontal plane of two gusset plates and fails the specimen can be calculated using the 45° alignment of diagonal members as:

$$P_{v,test} = (482 + 696)(\cos 45°) = 833\,\text{kip}$$

Since both plates have the same corrosion pattern through the horizontal plane, the total nominal shear capacity of two plates is calculated using the formula:

$$P_{ng,GP} = 2[(0.577F_y)(t_{eq})(L_{vg,GP})] \quad \text{(Eq. 6.4-2)}$$

A comparison of the test load with the nominal shear resistance using the equivalent thickness approach is shown in Table 6.4.3.

Table 6.4.3: Comparison between the total shear force from the test and the shear resistance using the equivalent thickness

t_{GP} (in)	F_y (ksi)	$L_{vg,GP}$ (in)	$P_{v,test}$ (kip)	$P_{ng,GP}$ (kip)	$P_{v,test}/P_{ng,gP}$
0.251	47.8	59.0	833	817	**1.02**

This result also shows that converting the non-uniform plate thickness into a uniform equivalent thickness matches well the shear resistance calculation. The back-calculated Ω based on this ratio is 1.02. Thus, an Ω =1.0 should be valid for corroded gusset plate shear resistance calculations. The same conclusion was also reached from the shear resistance calculations previously performed.

For GP307-SS3-3 specimen, only one of the plates has simulated corrosion. By looking at the cross-section along the horizontal plane above the chord members, three different portions can be identified, two of which are on the sides without corrosion and remaining is in the middle portion with reduced thickness as shown in Figure 6.4.11.

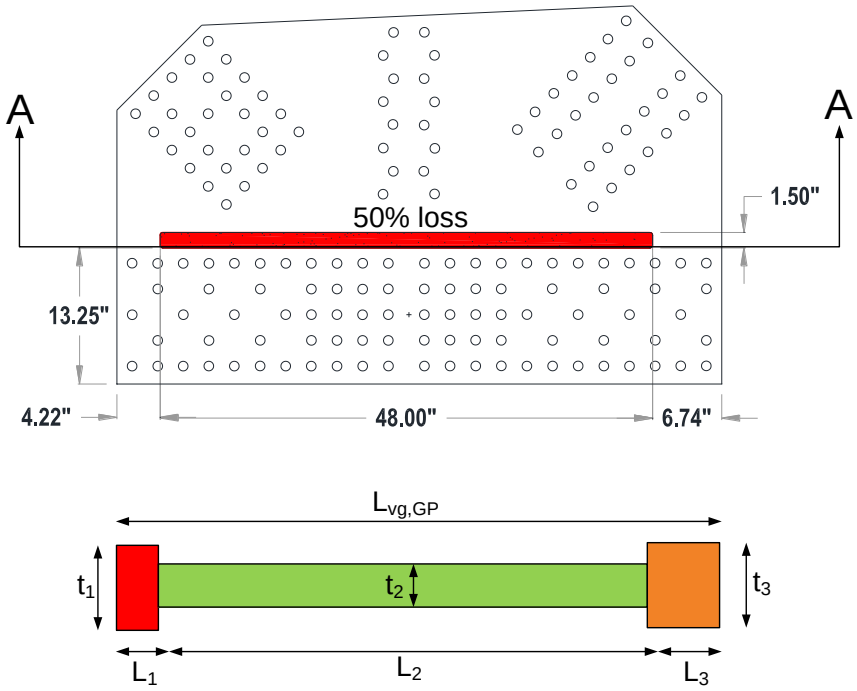

Figure 6.4.11: Cross-section of the horizontal shear plane length, $L_{vg,GP}$ represented by three different lengths and corresponding plate thicknesses (GP307-SS3-2 specimen)

The equivalent thickness for the corroded gusset plate can be calculated using the defined equation as:

$$t_{eq} = \frac{(0.375)(4.2) + (0.188)(48.0) + (0.375)(6.8)}{59.0} = 0.223\,\text{inch}$$

The total shear force which mobilizes the horizontal plane of the two gusset plates and failed the specimen is:

$$P_{v,test} = (519 + 735)(\cos 45°) = 887\,\text{kip}$$

The total resistance calculation hasto be performed differently since two plates have different thicknesses:

$$P_{ng,GP} = 0.577F_y(L_{vg,GP})[(t_{eq}) + (t_{GP})] \quad \text{(Eq. 6.4-3)}$$

A comparison of the actual test load with the nominal shear resistance using the equivalent thickness approach is shown in Table 6.4.4.

Table 6.4.4: Comparison between the total shear force from the test and the shear resistance using the equivalent thickness

t_{GP} (in)	t_{eq} (in)	F_y (ksi)	$L_{vg,GP}$ (in)	$P_{v,test}$ (kip)	$P_{ng,GP}$ (kip)	$P_{v,test}/P_{ng,gP}$
0.375	0.223	39.9	59.0	887	812	**1.09**

Summing the nominal shear resistances of two plates provides very close results with respect to the actual test load. Converting the variable thickness due to corrosion into an equivalent thickness also works for this specimen. The result also shows that Ω =1.0 should be valid for shear resistance calculations.

6.5. Recommendations for Retrofit Strategies

6.5.1. Edge Stiffeners for Buckling Critical Connections

6.5.1.1. Preliminary Studies on the Current Practice

In addition to quantifying the resistance of gusset plates, retrofit and rehabilitation of the existing truss bridges is one of the major issues in the bridge community. In this research, a better method to improve the buckling resistance of gusset plate connections was investigated. One of the current methods frequently used by engineers/designers is applying angle sections as internal stiffeners along the free edges on the compression diagonal side of the connection as shown in Figure 6.5.1. Finite element analysis was performed on two of the test specimens to investigate the effectiveness of this method on increasing the buckling resistance.

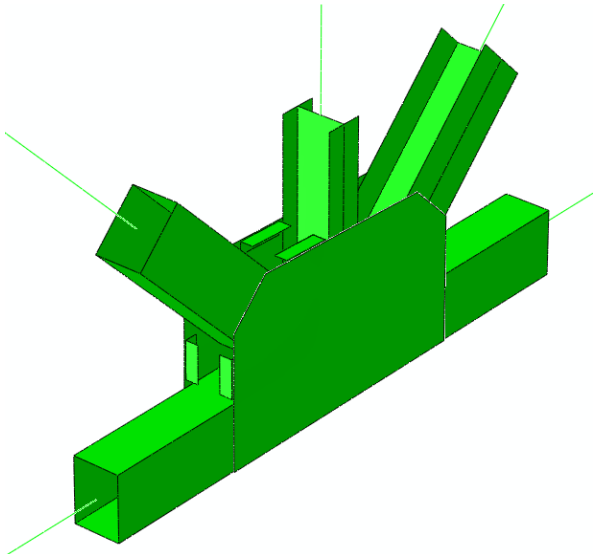

Figure 6.5.1: Short stiffening angle sections internally applied through the free edges of the gusset plates

For the analyses, L3x3x1/2 angle sections are attached on the free edges of both the GP490-SS3 and the GP490-LS3 specimens. These specimens failed by buckling as discussed previously. The load combination applied to both specimens for this study is shown in Figure 6.5.2. Finite element analysis is performed with and without the angle stiffeners for each specimen.

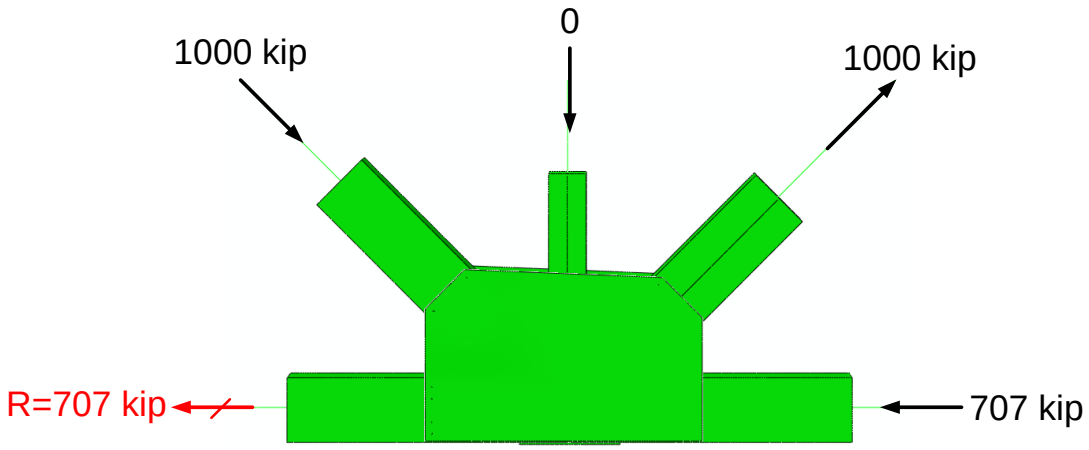

Figure 6.5.2: Reference load combinations used in the preliminary studies of the edge stiffening retrofit strategies

Table 6.5.1 shows the summary of maximum applied load fraction reached in each analysis. The percent increase with respect to no stiffener cases are shown in this table.

Table 6.5.1: Increase in the buckling load capacity using the internally applied short stiffening angle sections

Specimen	Case	ALF	% Increase
GP490-SS3	w/o Stiffener	0.712	**0.4**
	w/ Stiffener	0.715	
GP490-LS3	w/o Stiffener	0.579	**3.3**
	w/ Stiffener	0.598	

These preliminary studies show that there is almost no benefit of using these short angles internally attached to the free edges on the compression diagonal side. This is especially true if one considers the effort of installation with respect to percent increase in the capacity. Thus, a more effective approach has to be pursued.

6.5.1.2. Proposed Stiffening Methodology

Instead of stiffening the free edges with short angle sections, a new approach is proposed in which the stiffening angles are attached externally on the gusset plates, engaging the connected members in the overall sidesway movement capacity of the gusset plates. These long angle sections are attached through the full horizontal or vertical edges as shown in Figure 6.5.3.

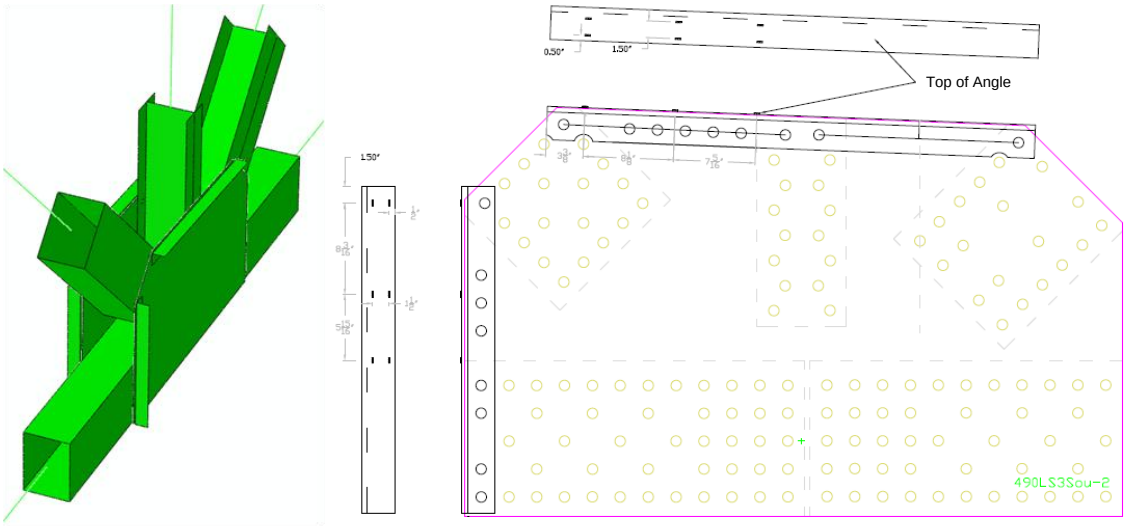

Figure 6.5.3: Long stiffening angles applied externally on the horizontal and vertical edges of the GP490-LS3 specimen

Table 6.5.2 shows how this approach improves the out-of-plane sidesway movement behavior of the connection. A comparison between the stiffened case and the original specimen without stiffeners is shown in terms of the percent increase in the maximum applied load fraction (ALF) at failure.

Table 6.5.2: Increase in the buckling load capacity using the externally applied long stiffening angle sections

Specimen	Case	ALF	% Increase
GP490-SS3	w/o Stiffener	0.712	**17.3**
	w/ Stiffener	0.835	
GP490-LS3	w/o Stiffener	0.579	**44.9**
	w/ Stiffener	0.839	

The maximum load the connection could attain is constrained by reaching the shear resistance limit along the horizontal plane above the chord members in both cases. Since GP490-SS3 specimen was a more compact specimen and the buckling load was higher than the GP490-LS3 specimen, its percent increase in the applied load fraction was less although both specimens reached failure almost at the same fraction of the load. The Case 5-a joint from the parametric study has been selected to study the effect of edge stiffeners on the buckling capacities of gusset plate connections. This connection has

comparatively long vertical free edge. Since the free edge between the compression diagonal and the vertical members is fairly short, edge stiffeners are placed only on the vertical free edges of both gusset plates in the connection. Figure 6.5.4 shows the modified geometry with the externally applied angle stiffeners (this is referred to as Case 5-b). The stiffeners are connected from the top of the left chord member through the first fastener of the compression diagonal on the left.

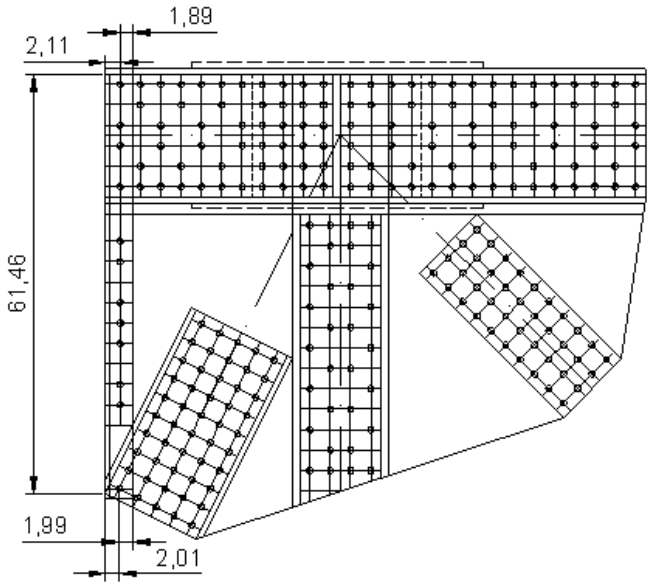

Figure 6.5.4: Stiffening angles applied on the gusset plate of Case 5-b

To determine a required stiffness of the added elements, the size of angles is varied between L1x1x1/8 and L4x4x5/8. Based on the cross-section configurations shown in Figure 6.5.5, two stiffness parameters corresponding to gusset plate and the stiffener are defined as I_{GP} and $I_{stiffener}$.

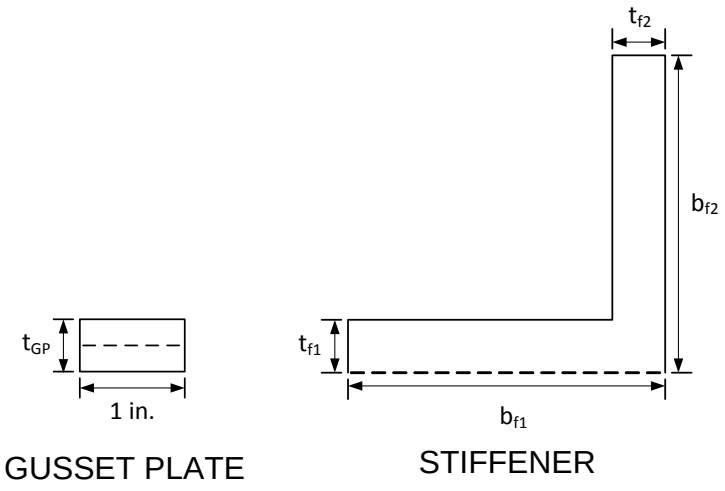

Figure 6.5.5: Cross-sectional properties for the gusset plate and the stiffening angle

The moment of inertia of the stiffener angles ($I_{stiffener}$) is taken about the connected plane shown with the dashed line in Figure 6.5.5**.** The moment of inertia of gusset plate (I_{GP}) is calculated about the plane passing through the mid-thickness (shown with dashed line) and using a unit gusset plate width. These two stiffness parameters are calculated using the formulas:

$$I_{GP} = \frac{1}{12}(1\text{in.})(t_{GP})^3 \qquad \text{(Eq. 6.5-1)}$$

$$I_{stiffener} = \frac{1}{3}(b_{f1})(t_{f1})^3 + \frac{1}{12}(t_{f2})(b_{f2} - t_{f1})^3 + (b_{f2} - t_{f1})(t_{f2})[\frac{(b_{f2} - t_{f1})}{2} + t_{f1}]^2 \qquad \text{(Eq. 6.5-2)}$$

To create a non-dimensional stiffness parameter, the inertia of the stiffener ($I_{stiffener}$) is divided by the stiffness of the gusset plate (I_{GP}). This is mainly to see the trend of increase in the maximum buckling load by varying the gusset plate thickness and stiffening angle cross-sections. The relationship between the non-dimensional stiffness parameter and percent gain in the peak load is shown in Figure 6.5.6.

For $I_{stiffener} / I_{GP}$ ratios of approximately 300, a significant benefit is observed in the buckling capacity increase of the Case 5-b joint. Ratios above 300 provide little additional benefit on the compression buckling capacity.

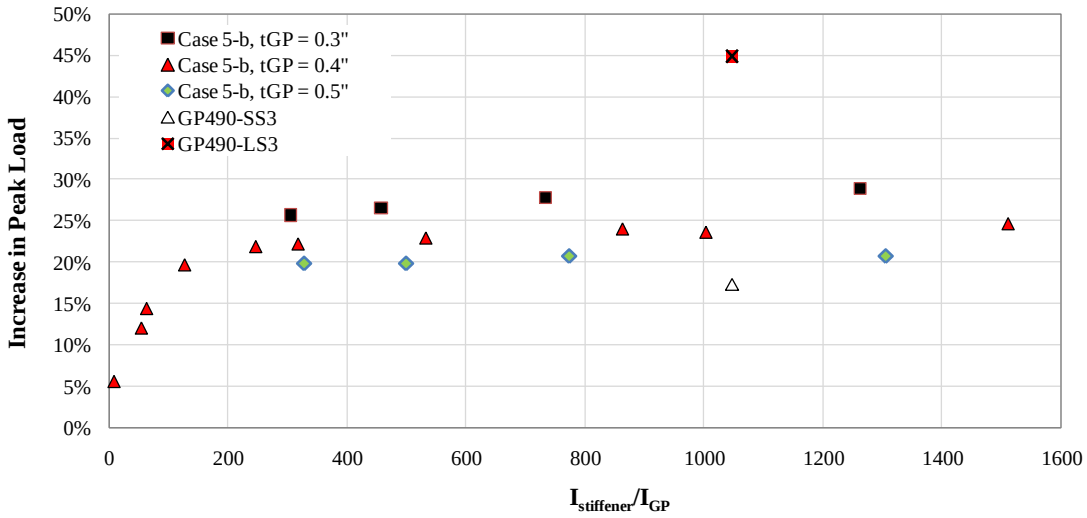

Figure 6.5.6: Relationship between the increase in buckling capacity and the relative stiffness of the stiffening angle ($I_{stiffener}/I_{GP}$)

Therefore to be on the conservative side, providing an $I_{stiffener}/I_{GP}$ ratio of 500 will be recommended for Case 5-b joint to achieve about a 20% increase in the compression buckling capacity. This figure also shows the results for different gusset plate thicknesses. As the gusset plate thickness decreases, the benefit from the external stiffening angles increases. This conclusion is also reached using the analyses performed on the two specimens.

Without edge stiffeners, GP490-LS3 had a significantly lower load capacity relative to the GP490-SS3 specimen. With stiffeners which have an $I_{stiffener}/I_{GP}$ ratio of 1048, the peak load of GP490-LS3 is increased by 45%. On the other hand, the increase for the GP490-SS3 specimen with the same $I_{stiffener}/I_{GP}$ ratio is about 17% (at that level, shear capacity along the horizontal plane is reached). There appears to be a trend of increased compression capacities due to edge stiffeners for joints that originally has low compression capacities without stiffeners. Based on the studies, angles with non-compact legs fails prematurely and as a result, the increase in buckling capacities is reduced. Hence, angles with compact legs should be used to achieve maximum benefit.

CHAPTER VII : CONCLUSIONS

7.1. Summary and Originality of the Research

This thesis focuses on comprehensive analytical studies on steel truss bridge gusset plate behavior. The studies include comparisons of advanced analytical models with the responses from large-scale experimental tests using discrete and innovative full-field measurements. The experimental data allow for careful calibration of the analytical models. These robust finite element analysis models are then utilized to study a variety of gusset plate configurations. This approach is aimed at developing rational and practical design recommendations to replace or buttress those available in the current FHWA Guidance. Improved mechanistic idealizations that better capture the observed behavior are proposed as the result of this work. The design checks recommended in this thesis present a comprehensive methodology for determining the ultimate gusset plate resistance. This effort has produced significant original contributions in at least four areas: (a) the generation of a large database of original results that will be useful for future similar studies; (b) the development of robust modeling procedures that permit the study of connections and their immediate framing members using truss sub-assemblages; (c) the determination of clear load paths in these complex connections; and (d) the proposal of simple, accurate and comprehensive methodologies to assess the nominal ultimate strength of steel truss gusset plate connections

7.2. Conclusions

The following recommendations are driven by the experimental and parametric studies, which indicated a tendency towards buckling failures for thin plates (<3/8 inch, a case not often seen in practice) and shear failures for thicker plates (>5/8 inch), a more typical situation in practice) regardless of the geometry and loading conditions.

7.2.1. Compression Resistance with Unchamfered Members

The buckling resistance of gusset plate connections with unchamfered members is quantified using the Whitmore section buckling approach. Two significant improvements to the current FHWA Guidance are proposed. First, the effective length

factor should be taken as K=0.35 instead of K=1.2. Second, the effective length should be based on the projected length between the middle of the member cross-section and closest member bolt line (L_{mid}) and not as the average of three lengths. No change was recommended to the 30° dispersion angle which determines the equivalent column width to be used in the buckling resistance calculations. These improvements result in a more accurate assessment of gusset plate resistance to buckling and considerably reduce the number of existing steel truss bridge connections that will be considered buckling critical.

7.2.2. Compression Resistance with Chamfered Members

These studies indicate that load transfer in connections with heavily chamfered members occurs primarily via shear forces except for very thin plates. For ordinary plates (>3/8 inch thick), the shear check provides a good estimate of the connection strength and a buckling check is not necessary. For relatively thin gusset plates (<3/8 inch thick) a method is proposed which sums the compression and shear resistances along the two planes through which the member load is transferred. The critical buckling stress on the compression plane can be calculated using the same assumptions as for the unchamfered case, while the shear resistance can be taken as the shear yield strength limit.

7.2.3. Edge Slenderness

One of the most interesting results of this study regards edge slenderness. Intuitively one would expect that the plate capacity will drop significantly with increasing edge slenderness as currently reflected in both the FHWA Guidance and AASHTO Bridge Design Specifications. These studies indicated a similar general trend, with decreasing buckling resistance as the free edge slenderness increases. However, the data had significant scatter, and in some cases significantly different slenderness values reached the same strength level. For common connection proportions, as taken from 20 actual bridge plans examined as part of this project, it appears that edge instability is driven by the overall buckling behavior of the plate around the compression diagonal and not the other way around Once the compression resistance of the plate is accurately

established, as has been accomplished in this research, the loss of capacity due to buckling of the plate edges is limited and the edge slenderness limit can be eliminated.

7.2.4. Compression Checks for Plates in Pier Connections

Based on the parametric studies performed on a representative upper chord joint over the pier location, a compression block shear check that considers a fully yielded pattern around the vertical member is proposed. The critical buckling stress on the compression plane can be calculated using the same buckling resistance as in unchamfered connections, but using an effective length factor, K=0.5. The shear resistance along the shear planes can be taken as the shear yield strength.

7.2.5. Shear Resistance with Unchamfered Members

The principal question with regards to shear resistance in gusset plate connections is the need for a Ω reduction factor as currently used in both the FHWA guidance and AASHTO Bridge Design Specifications. The results clearly indicate that for unchamfered connections, the shear resistance along critical planes can be calculated using Ω=1.0. Based on the parametric studies, there was very weak correlation between the Ω factor and gusset plate thickness. Hence, only one Ω value (Ω=1.0) is proposed for the nominal shear resistance calculations of all unchamfered connections. As the gusset plate thickness increases, the governing failure mode shifted from plate buckling to shear failure mode along the critical shear planes. The behavior over the full range of slenderness values is captured by the proposed nominal shear resistance calculations with Ω=1.0 and the buckling checks discussed in Section 7.2.1. The small scatter in the data can be handled by an appropriately derived LRFD resistance factor.

7.2.6. Shear Resistance with Chamfered Members

As for the compression checks, for chamfered members the studies suggest different behavior when the plates are very thin (<3/8 inch thick). Considering that all resistance calculations are at the nominal level, for thin plates an Ω=0.8 is the most appropriate value. For gusset plates thicker than 3/8 inch, the trend is very similar to that of chamfered connections, but with a slightly lower Ω –value (0.9 to 1.0). An Ω = 1.0 is proposed for plates thicker than 3/8 inch, with the understanding that this will lead to a

somewhat lower resistance factor. In addition, the parametric studies indicate that as the chamfer of the member increases, the likelihood of having a shear failure also increases. The proposed Ω values cover members raging from no chamfer up to high chamfer ratios.

7.2.7. Chord Splice Resistance

The current guidance checks for the chord splice resistance do not specify how to proportion the load between the main gusset plate and any shingle or splice plates and how to determine the effective gusset plate area contributing to the splice resistance. To address these shortcomings, a new, mechanistic approach to quantify the chord splice resistance (compression or tension) is recommended. When the chord splice is "milled to bear", no further action is needed to quantify the chord splice resistance. However, when the compression chord splice is not "milled-to-bear", the resistance can be calculated using a pseudo-plastic section analysis approach. The pseudo-plastic section analysis treats all the plates as a composite unit directly accounting for any eccentricity of the chord relative to the gusset and splice plates. An equivalent column resistance is used to determine the critical compressive stresses and the yield resistance is assumed for any tensile stresses. The critical compressive stress is equal to the yield strength of the plates as long as the *KL/r* values of the equivalent columns over the chord splice are less than 25. In this case, "*L*" is the distance between the first bolt lines along the chord members in the splice buckling region, and *K* is taken as 0.5 to reflect the fixed-fixed boundary condition. For most practical cases, *KL/r* is smaller than 25, and thus both tension and compression regions were at the yield stress level at ultimate.

7.2.8. Corroded Plates

The effect of corrosion on the gusset plate resistance is investigated and corresponding resistance calculations to quantify the buckling and shear limit states were performed using experimental results for calibration. For buckling critical gusset plate connections with concentrated corrosion within the areas where buckling occurs, an equivalent gusset plate thickness should be calculated for the length (L_{mid}) and the buckling resistance calculations should be performed using the proposed K=0.35. A similar equivalent thickness approach is proposed for shear. For cases with unsymmetric

corrosion patterns on the gusset plates, issues related to an unbalanced stiffness were a concern. However, the experiment performed with one virgin plate and one corroded plate (concentrated along the horizontal shear plane) showed that the overall performance of the joint was determined by summing the resistances of the two plates based on the available cross-sections through the critical shear planes. The total resistance can be calculated by applying the equivalent thickness approach to the corroded plate and adding the resistance from the second gusset plate.

7.2.9. Retrofits

The effectiveness of current retrofit practices is also investigated. Finite element analyses performed on retrofits utilizing short internal angles attached to the free edges on the compression diagonal side of the gusset plates indicate very limited increases in either buckling resistance or load redistribution capacity. Similar studies on retrofits utilizing external angles engaging the members active in the overall sidesway buckling mechanism of the gusset plates proved much more effective, This technique requires a minimum relative stiffness of the stiffening angle ($I_{stiffener} / I_{GP}$), where $I_{stiffener}$ is calculated about the plane where the stiffener connects, and I_{GP} is calculated about the plane passing through the mid-thickness of the gusset plate. When this ratio is greater than 500, a significant increase in buckling capacity of gusset plate connections is achieved. The increase in buckling capacity varies depending on gusset plate connection geometries, but in gerenal an increase at least 20 % in buckling capacities can be achieved for buckling critical cases unless other failure mode becomes critical. Angle sections with compact legs in flexure should be used for this retrofit strategy.

7.3. Recommendations for Further Research

This research provided a comprehensive assessment of steel truss bridge gusset plate connections via full-scale experiments and analytical parametric studies. Practical design checks to quantify the gusset plate resistance were proposed using the advanced modeling techniques and nonlinear finite element analysis. The analytical studies were supported with large-scale experimental test results to reach robustness and confidence in

the proposed recommendations. This research can be used as a leading effort towards further evaluations and research on gusset plate connections in the following directions:

- **LRFD calibration for the recommended limit state checks**

This research focused on determining the nominal resistance calculations without any LRFD resistance factors built into the proposed formulations. Calibration studies need to be performed for each limit state check recommended as part of this research. This effort is expected to be performed by FHWA in the near future as a continuation of the current research using the available data produced in this dissertation.

- **Modeling the gusset plate connections with actual bolt holes**

The models used in this study do not have the explicit bolt holes and fasteners. Hence, the rupture limit state possible in gusset plate connections were not captured in these studies. Large-scale tests performed as part of the current research also did not reach any rupture limit state in parallel to the analytical model results. However, further verification of the proposed limit state checks should be performed with models utilizing the actual bolt holes in the models. The computational effort and time constraints associated with these studies must be taken into account especially for modeling fracture in the finite element models.

- **Extension of the local joint models to more detailed joint models**

The experimental test specimens and two panel truss joints in this study focused directly on the local gusset plate behavior with the appropriate boundary conditions applied in the finite element models. Changes in gusset plate behavior due to global truss bridge effects should be further investigated by including the out-of-plane members such as floor beams, and diagonals connected to the gusset plates. This would also provide the effect of out-of-plane restraints in the actual truss bridges. As for the issue of bolt holes, the computational effort for this work is not trivial.

- **Effect of member buckling on the gusset plate connection behavior**

In this research, connected members are assumed to remain in the elastic regime to mainly focus on the gusset plate itself and investigate the ultimate resistance without failing the other members in the connection. Further research can be pursued to see the effects of member buckling on the joint behavior.

- **Further experimental studies for the tension limit states**

This research aims to present rational and mechanistic design formulations for different limit states including the buckling which was the major concern in the design community after the I-35W bridge collapse. In addition, the experiments and parametric studies provided enough evidence to come up better idealizations for the buckling and shear yield limit states. Further experimental effort can be performed to mainly focus on tensile or rupture limit states.

APPENDIX A: EXAMPLE CALCULATIONS FOR THE BUCKLING RESISTANCE OF UNCHAMFERED CONNECTIONS

Example Calculations, Buckling Resistance of Unchamfered Connections

This example provides detailed MathCAD calculations pertaining to the compression resistance of unchamfered connections. These calculations correspond to the GP307-LS3 test specimen with 0.375 inch thick gusset plate. The unity check is shown by comparing the the buckling load from the experiment with the nominal buckling resistance using the proposed methodology

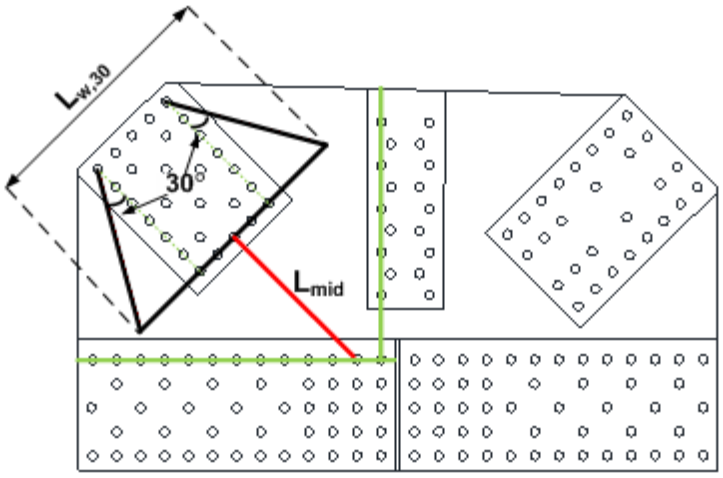

Material Properties:

$F_y := 48.2 \cdot ksi$ $E := 29000 \cdot ksi$

Cross-section Properties:

$L_{w.30} := 27.5 \cdot in$ $L_{mid} := 18.1 \cdot in$ $t_{GP} := 0.375 \cdot in$

$A_{GP} := t_{GP} \cdot L_{w.30}$ $A_{GP} = 10.3\,in^2$ *Area of the equivalent column section*

$I_{g.GP} := \frac{1}{12}\left(L_{w.30}\right)\left(t_{GP}^{3}\right)$ $I_{g.GP} = 0.121\,in^4$ *Moment of inertia of the equivalent column section*

$r_s := \sqrt{\frac{I_{g.GP}}{A_{GP}}}$ $r_s = 0.108\,in$ *Radius of gyration*

Buckling Resistance Calculations:

$K := 0.35$ Proposed effective length factor

$$\frac{K \cdot L_{mid}}{r_s} = 58.5 \qquad \lambda := \left(\frac{K \cdot L_{mid}}{r_s \cdot \pi}\right)^2 \cdot \left(\frac{F_y}{E}\right) \qquad \lambda = 0.577$$

$$P_n := \begin{cases} 0.658^{\lambda} \cdot F_y \cdot A_{GP} & \text{if } \lambda \le 2.25 \\ \frac{0.877}{\lambda} \cdot F_y \cdot A_{GP} & \text{otherwise} \end{cases} \qquad P_n = 390\,kip$$

Nominal buckling resistance of one gusset plate in the connection

Unity Check:

Compression diagonal load at the instant of buckling is carried by the two gusset plates in the connection.

$P_{CD.test} := 796 \cdot kip$ *Compression diagonal load from the experiment*

$$P_{cr.test} := \frac{P_{CD.test}}{2} \qquad P_{cr.test} = 398\,kip$$

Buckling load for one gusset plate from the experiment

$$\frac{P_{cr.test}}{P_n} = 1.02$$

Comparison between the buckling load from the experiment and nominal buckling resistance

APPENDIX B: EXAMPLE CALCULATIONS FOR THE COMBINED BUCKLING/SHEAR RESISTANCE OF CHAMFERED CONNECTIONS

Example Calculations, Combined Buckling/Shear Resistance of Chamfered Connections

This example provides detailed MathCAD calculations pertaining to the compression resistance of unchamfered connections. These calculations correspond to the parametric study joint Case 5 with 0.250 inch thick gusset plate. The unity check is shown by comparing the the load from the finite element analysis with the nominal resistance

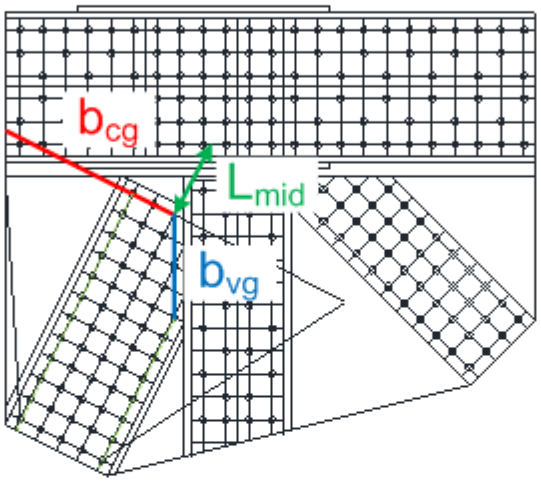

Material Properties:

$F_y := 53 \cdot ksi$ $E := 29000 \cdot ksi$

Cross-section Properties:

$b_{cg} := 24.8 \cdot in$ $b_{vg} := 13.4 \cdot in$ $L_{mid} := 10.3 \cdot in$ $t_{GP} := 0.250 \cdot in$

$A_{GP} := t_{GP} \cdot b_{cg}$ $A_{GP} = 6.2\,in^2$ *Area of the equivalent column section*

$I_{g.GP} := \frac{1}{12}\left(b_{cg}\right)\left(t_{GP}^{3}\right)$ $I_{g.GP} = 0.032\,in^4$ *Moment of inertia of the equivalent column section*

$r_s := \sqrt{\frac{I_{g.GP}}{A_{GP}}}$ $r_s = 0.072\,in$ *Radius of gyration*

Compression Resistance Component:

$K := 0.35$ Proposed effective length factor

$$\frac{K \cdot L_{mid}}{r_s} = 50 \qquad \lambda := \left(\frac{K \cdot L_{mid}}{r_s \cdot \pi}\right)^2 \cdot \left(\frac{F_y}{E}\right) \qquad \lambda = 0.462$$

$$P_{nc} := \begin{cases} 0.658^{\lambda} \cdot F_y \cdot A_{GP} & \text{if } \lambda \le 2.25 \\ \frac{0.877}{\lambda} \cdot F_y \cdot A_{GP} & \text{otherwise} \end{cases}$$

$P_{nc} = 271\,kip$ *Buckling resistance component for one gusset plate in the connection*

Shear Resistance Component:

α=63° is the angle between the compression diagonal and the chord member

$$\alpha := \frac{63}{180}\pi \qquad \alpha = 1.1 \qquad \sin(\alpha) = 0.891 \qquad \cos(\alpha) = 0.454$$

$P_{nv} := (0.577 F_y) \cdot b_{vg} \cdot (t_{GP}) \cdot \sin(\alpha)$ ***when the chamfering is parallel to the horizontal plane just above the chord member, sin(α) is replaced by cos(α)***

$P_{nv} = 91\,kip$

Total Resistance:

$P_n := P_{nc} + P_{nv}$ $P_n = 362\,kip$

Unity Check:

Compression diagonal load at the instant of buckling is carried by the two gusset plates in the connection.

$P_{CD.FEA} := 780 \cdot kip$ *Compression diagonal load from FEA*

$P_{FEA} := \frac{P_{CD.FEA}}{2}$ $P_{FEA} = 390\,kip$ *Compression load transferred by one gusset plate based on FEA*

$\frac{P_{FEA}}{P_n} = 1.08$ *Comparison between the buckling load from the experiment and nominal buckling resistance*

APPENDIX C: EXAMPLE CALCULATIONS FOR THE COMPRESSION BLOCK SHEAR RESISTANCE

Example Calculations, Compression Block Shear Approach

This example provides detailed MathCAD calculations pertaining to the compression block shear resistance for parametric study Case 3 joint with 0.375 inch thick gusset plate at pier location. The unity check is shown by comparing the the load from the finite element analysis with the nominal resistance

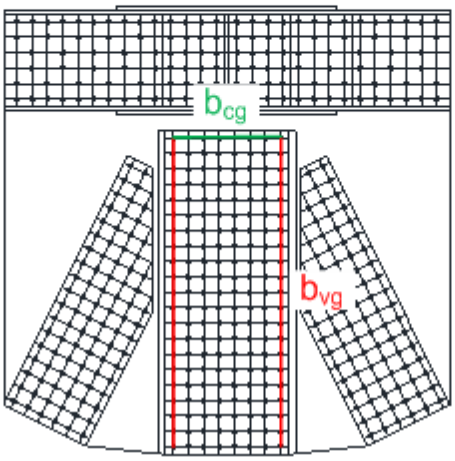

Material Properties:

$F_y := 53 \cdot ksi$ $E := 29000 \cdot ksi$

Cross-section Properties:

$b_{cg} := 20.9 \cdot in$ $b_{vg} := 61.5 \cdot in$ $L_{mid} := 7.6 \cdot in$ $t_{GP} := 0.375 \cdot in$

$A_{GP} := t_{GP} \cdot b_{cg}$ $A_{GP} = 7.8\,in^2$ *Area of the equivalent column section*

$I_{g.GP} := \frac{1}{12}\left(b_{cg}\right)\left(t_{GP}^{3}\right)$ $I_{g.GP} = 0.092\,in^4$ *Moment of inertia of the equivalent column section*

$r_s := \sqrt{\frac{I_{g.GP}}{A_{GP}}}$ $r_s = 0.108\,in$ *Radius of gyration*

Compression Resistance Component:

$K := 0.5$ *Effective length factor for compression block shear resistance calculations*

$$\frac{K \cdot L_{mid}}{r_s} = 35.1 \qquad \lambda := \left(\frac{K \cdot L_{mid}}{r_s \cdot \pi}\right)^2 \cdot \left(\frac{F_y}{E}\right) \qquad \lambda = 0.228$$

$$P_{nc} := \begin{cases} 0.658^{\lambda} \cdot F_y \cdot A_{GP} & \text{if } \lambda \le 2.25 \\ \frac{0.877}{\lambda} \cdot F_y \cdot A_{GP} & \text{otherwise} \end{cases}$$

$P_{nc} = 378\,kip$ *Buckling resistance component for one gusset plate*

Shear Resistance Component:

$$P_{nv} := \left(0.577 F_y\right) \cdot b_{vg} \cdot \left(t_{GP}\right) \cdot 2$$

Shear resistance component for the two shear planes transferring the load through one gusset plate

$P_{nv} = 1411\,kip$

Total Resistance:

$P_{CBS.GP} := P_{nc} + P_{nv}$ $P_{CBS.GP} = 1788\,kip$

Unity Check:

Compression load on the vertical member at the failure is:

$P_{vert.FEA} := 3450 \cdot kip$ *Compression load in the vertical member from FEA*

$P_{FEA} := \frac{P_{vert.FEA}}{2}$ $P_{FEA} = 1725\,kip$ *Compression load transferred by one gusset plate based on FEA*

$\frac{P_{FEA}}{P_{CBS.GP}} = 0.96$ *Comparison between the buckling load from the experiment and nominal buckling resistance*

APPENDIX D: EXAMPLE CALCULATIONS FOR THE SHEAR RESISTANCE

Example Calculations, Shear Resistance of the Horizontal Shear Plane

This example provides detailed MathCAD calculations pertaining to the shear resistance of the horizontal plane from the unchamfered GP307-SS3 specimen with 0.500 inch thick gusset plate. The unity checks are shown by comparing the the loads from the finite element analysis with the nominal resistance values

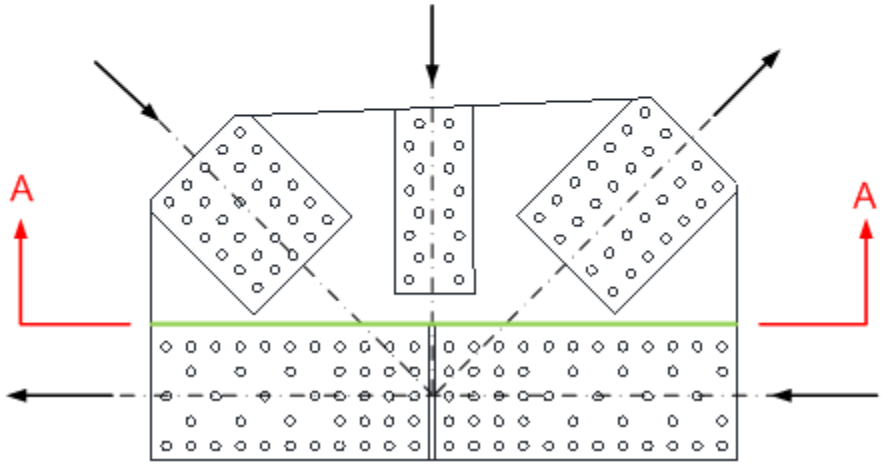

Material Properties:

$F_y := 36.4 \cdot ksi$ $E := 29000 \cdot ksi$ $\Omega := 1.0$ *Proposed Ω=1.0*

Cross-section Properties:

$L_{vg.GP} := 59 \cdot in$ *Length of the horizontal shear plane*

$t_{GP} := 0.500 \cdot in$

Nominal Gross-Section Shear Yield Resistance Calculations with Ω=1.0:

$P_{ng.GP} := \left(0.577 F_y\right) \cdot L_{vg.GP} \cdot \left(t_{GP}\right) \cdot \Omega$ *Shear resistance of one gusset plate*

$P_{ng.GP} = 620\,kip$

Applied Shear Force from FEA:

Applied member loads in the finite element analysis are:

$P_{CD} := 716 \cdot kip$ *Compression diagonal force applied in the FEA*

$P_{TD} := 507 \cdot kip$ *Tension diagonal force applied in the FEA*

$\alpha_{CD} := \frac{\pi}{4}$ $\alpha_{TD} := \frac{\pi}{4}$ *Angle between the diagonals and the chord members*

$ALF := 1.36$ *Applied load fraction at the failure for 0.500 thick gusset plate case*

$$P_{FEA} := \frac{\left[\left(P_{CD} \cdot \cos\left(\alpha_{CD}\right)\right) + \left(P_{TD} \cdot \cos\left(\alpha_{TD}\right)\right)\right] \cdot ALF}{2}$$

$P_{FEA} = 588\,kip$ *Shear force applied along the horizontal plane for one gusset plate based on FEA*

$\frac{P_{FEA}}{P_{ng.GP}} = 0.95$ *Comparison between the finite element analysis and nominal shear resistance with Ω=1.0*

Example Calculations, Shear Resistance of the Vertical Shear Plane

This example provides detailed MathCAD calculations pertaining to the shear resistance of the horizontal plane from the chamfered Case 5 joint with 0.500 inch thick gusset plate. The unity checks are shown by comparing the the loads from the finite element analysis with the nominal resistance values

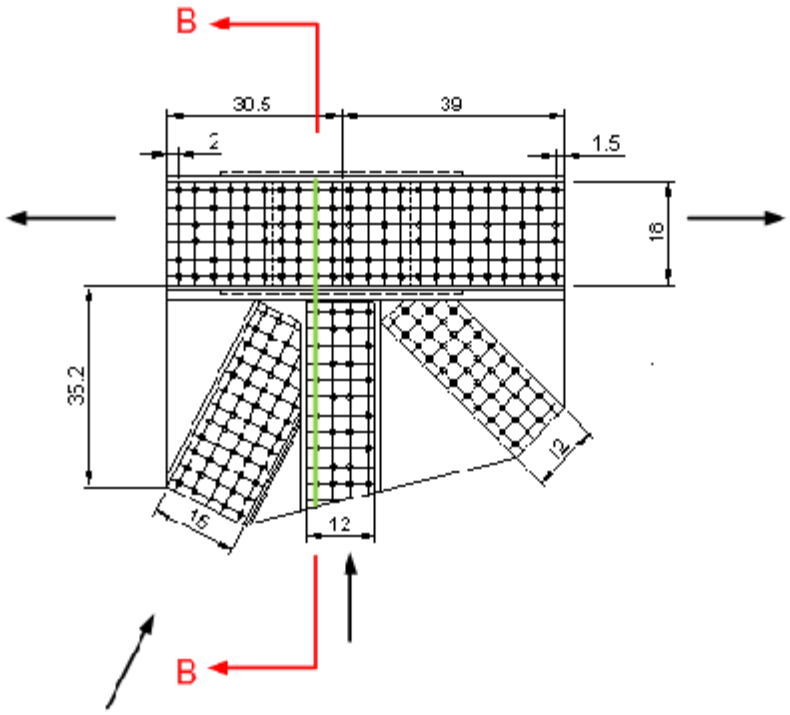

Material Properties:

$F_y := 53 \cdot ksi$ $E := 29000 \cdot ksi$ $\Omega := 1.0$ *Proposed Ω=1.0*

Cross-section Properties:

$L_{vg.GP} := 56.7 \cdot in$ *Length of the vertical shear plane*

$t_{GP} := 0.500 \cdot in$

Nominal Gross-Section Shear Yield Resistance Calculations with Ω=1.0:

$P_{ng.GP} := (0.577 F_y) \cdot L_{vg.GP} \cdot (t_{GP}) \cdot \Omega$ *Shear resistance of one gusset plate*

$P_{ng.GP} = 867\ kip$

Applied Shear Force from FEA:

Applied member loads in the finite element analysis are:

$P_{CD} := 1500 \cdot kip$ *Compression diagonal force applied in the FEA*

α=63° is the angle between the compression diagonal and the chord member

$\alpha_{CD} := \frac{63}{180}\pi$ $\alpha_{CD} = 1.1$ $\sin(\alpha_{CD}) = 0.891$ $\cos(\alpha_{CD}) = 0.454$

$ALF := 1.25$ *Applied load fraction at the failure for 0.500 thick gusset plate case*

$P_{FEA} := \frac{(P_{CD} \cdot \sin(\alpha_{CD})) \cdot ALF}{2}$ *Vertical component of the compression diagonal provides the applied shear force along the vertical plane*

$P_{FEA} = 835\,kip$ *Shear force applied along the horizontal plane for one gusset plate based on FEA*

$\frac{P_{FEA}}{P_{ng.GP}} = 0.96$ *Comparison between the finite element analysis and nominal shear resistance with Ω=1.0*

APPENDIX E: EXAMPLE CALCULATIONS FOR THE CHORD SPLICE RESISTANCE

Example Calculations, Chord Splice Resistance Calculations

This example provides detailed MathCAD calculations pertaining to the compression chord splice resistance of the gusset plate connections. These calculations correspond to the Case 1 joint with 0.375 inch thick gusset plate. The unity check is shown by comparing the force from FEA with the nominal chord splice resistance using the proposed methodology

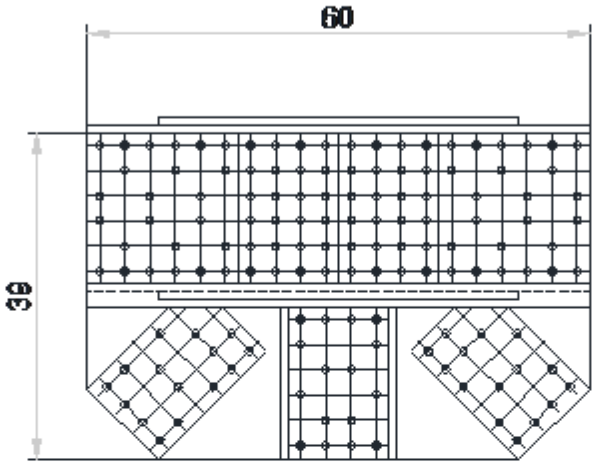

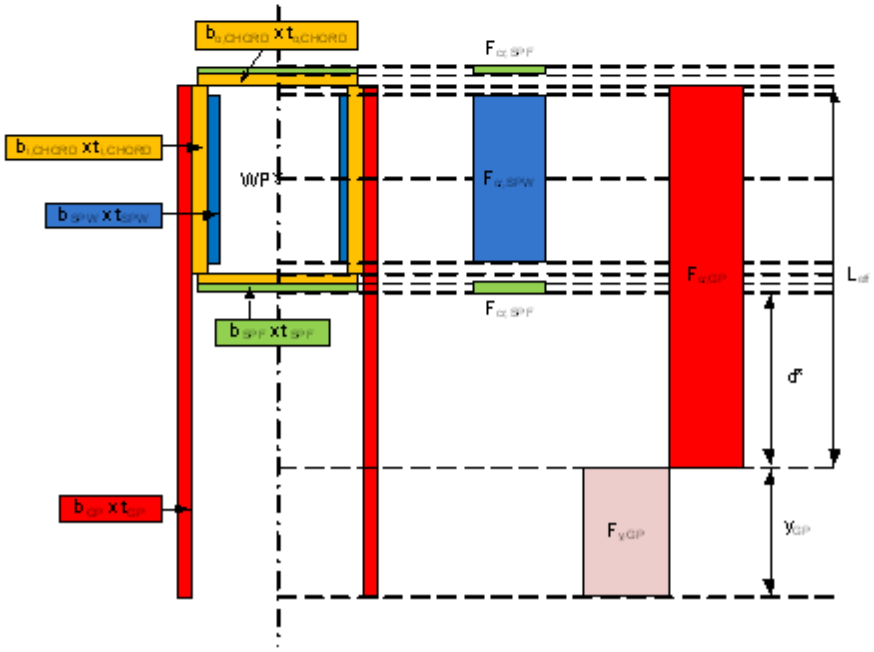

Material Properties:

$F_y := 53 \cdot ksi$ $E := 29000 \cdot ksi$

Gusset Plate Cross-section Properties:

$b_{GP} := 39 \cdot in$ $t_{GP} := 0.375 \cdot in$ $L_{GP} := 3 \cdot in$ *Length of the equivalent column measured between the two chord member bolt lines*

$A_{GP} := t_{GP} \cdot b_{GP}$ $A_{GP} = 14.6\,in^2$ *Area of the equivalent column section*

$I_{g.GP} := \frac{1}{12}\left(b_{GP}\right)\left(t_{GP}^{3}\right)$ $I_{g.GP} = 0.171\,in^4$ *Moment of inertia of the equivalent column section*

$r_{s.GP} := \sqrt{\frac{I_{g.GP}}{A_{GP}}}$ $r_{s.GP} = 0.108\,in$ *Radius of gyration*

Web Splice Plate Cross-section Properties:

$b_{SPW} := 17.5 \cdot in$ $t_{SPW} := 0.509 \cdot in$ $L_{SPW} := 3 \cdot in$ *Length of the equivalent column measured between the two chord member bolt lines*

$A_{SPW} := t_{SPW} \cdot b_{SPW}$ $A_{SPW} = 8.9\,in^2$ *Area of the equivalent column section*

$I_{g.SPW} := \frac{1}{12}\left(b_{SPW}\right)\left(t_{SPW}^{3}\right)$ $I_{g.SPW} = 0.192\,in^4$ *Moment of inertia of the equivalent column section*

$r_{s.SPW} := \sqrt{\frac{I_{g.SPW}}{A_{SPW}}}$ $r_{s.SPW} = 0.147\,in$ *Radius of gyration*

Top/Bottom Flange Splice Plate Cross-section Properties:

$b_{SPF} := 19.6 \cdot in$ $t_{SPF} := 0.775 \cdot in$ $L_{SPF} := 3 \cdot in$ *Length of the equivalent column measured between the two chord member bolt lines*

$A_{SPF} := t_{SPF} \cdot b_{SPF}$ $A_{SPF} = 15.2 in^2$ *Area of the equivalent column section*

$I_{g.SPF} := \frac{1}{12}\left(b_{SPF}\right)\left(t_{SPF}^{3}\right)$ $I_{g.SPF} = 0.76 in^4$ *Moment of inertia of the equivalent column section*

$r_{s.SPF} := \sqrt{\frac{I_{g.SPF}}{A_{SPF}}}$ $r_{s.SPF} = 0.224 in$ *Radius of gyration*

Critical Compressive Stress Calculation for the Gusset Plate:

$K := 0.5$ *Effective length factor for chord splice resistance calculations*

$\frac{K \cdot L_{GP}}{r_{s.GP}} = 13.9$ $\lambda_{GP} := \left(\frac{K \cdot L_{GP}}{r_{s.GP} \cdot \pi}\right)^2 \cdot \left(\frac{F_y}{E}\right)$ $\lambda_{GP} = 0.036$

$$F_{cr.GP} := \begin{cases} F_y \text{ if } \frac{K \cdot L_{GP}}{r_{s.GP}} \le 25 \\ \text{otherwise} \\ \quad \begin{cases} 0.658^{\lambda_{GP}} \cdot F_y \text{ if } \lambda_{GP} \le 2.25 \\ \frac{0.877}{\lambda_{GP}} \cdot F_y \text{ otherwise} \end{cases} \end{cases}$$

$F_{cr.GP} = 53 ksi$

Critical Compressive Stress Calculation for the Web Splice Plate:

$K := 0.5$ *Effective length factor for chord splice resistance calculations*

$$\frac{K \cdot L_{SPW}}{r_{s.SPW}} = 10.2 \qquad \lambda_{SPW} := \left(\frac{K \cdot L_{SPW}}{r_{s.SPW} \cdot \pi}\right)^2 \cdot \left(\frac{F_y}{E}\right) \qquad \lambda_{SPW} = 0.019$$

$$F_{cr.SPW} := \begin{cases} F_y \text{ if } \dfrac{K \cdot L_{SPW}}{r_{s.SPW}} \le 25 \\ \text{otherwise} \\ \quad \begin{cases} 0.658^{\lambda_{SPW}} \cdot F_y \text{ if } \lambda_{SPW} \le 2.25 \\ \dfrac{0.877}{\lambda_{SPW}} \cdot F_y \text{ otherwise} \end{cases} \end{cases} \qquad F_{cr.SPW} = 53\text{ksi}$$

Critical Compressive Stress Calculation for the Top/Bottom Flange Splice Plate:

$K := 0.5$ *Effective length factor for chord splice resistance calculations*

$$\frac{K \cdot L_{SPF}}{r_{s.SPF}} = 6.7 \qquad \lambda_{SPF} := \left(\frac{K \cdot L_{SPF}}{r_{s.SPF} \cdot \pi}\right)^2 \cdot \left(\frac{F_y}{E}\right) \qquad \lambda_{SPF} = 0.008$$

$$F_{cr.SPF} := \begin{cases} F_y \text{ if } \dfrac{K \cdot L_{SPF}}{r_{s.SPF}} \le 25 \\ \text{otherwise} \\ \quad \begin{cases} 0.658^{\lambda_{SPF}} \cdot F_y \text{ if } \lambda_{SPF} \le 2.25 \\ \dfrac{0.877}{\lambda_{SPF}} \cdot F_y \text{ otherwise} \end{cases} \end{cases} \qquad F_{cr.SPF} = 53\text{ksi}$$

Moment About the Work Point:

$b_{i.CHORD} := 18 \cdot in$ $\quad$ $t_{o.CHORD} := 0.875 \cdot in$

$d_{star} := 11.497 \cdot in$ *The value which makes the total moment about the work point zero, is determined!!!*

$$y_{GP} := b_{GP} - b_{i.CHORD} - t_{o.CHORD} - t_{SPF} - d_{star} \qquad y_{GP} = 7.853\,in$$

$$\begin{aligned} M_{WP} := {} & F_{cr.GP} \cdot t_{GP} \cdot (t_{o.CHORD}) \left(\frac{b_{i.CHORD}}{2} + \frac{t_{o.CHORD}}{2} \right) \cdots \\ & + F_{cr.GP} \cdot t_{GP} \cdot (t_{SPF}) \left(\frac{b_{i.CHORD}}{2} + t_{o.CHORD} + \frac{t_{SPF}}{2} \right) \cdots \\ & + F_{cr.GP} \cdot t_{GP} \cdot (d_{star}) \left(\frac{b_{i.CHORD}}{2} + t_{o.CHORD} + t_{SPF} + \frac{d_{star}}{2} \right) \cdots \\ & + F_{y} \cdot t_{GP} \cdot (y_{GP}) \left(b_{GP} - \frac{b_{i.CHORD}}{2} - \frac{y_{GP}}{2} \right) \cdot (-1) \end{aligned}$$

$M_{WP} = -0\,kip \cdot in$

Splice Resistance Calculation:

$$\begin{aligned} P_n := {} & \left(F_{cr.SPF} \cdot A_{SPF} \right) + \left(F_{cr.SPW} \cdot A_{SPW} \right) + \left(F_{cr.GP} \cdot t_{GP} \right) \left(b_{GP} - y_{GP} \right) \cdots \\ & + \left(F_{y} \cdot t_{GP} \right) \left(y_{GP} \right) (-1) \end{aligned}$$

$P_n = 1740\,kip$ *Half of the chord force is carried by one gusset plate, one web splice plate and one of the top/bottom splice plates*

Unity Check:

Maximum chord force at the failure for 0.375 inch gusset plate case is:

$P_{Chord} := 3900 \cdot kip$ $\quad$ $P_{FEA} := \frac{P_{Chord}}{2}$ $\quad$ $P_{FEA} = 1950\,kip$

$\frac{P_{FEA}}{P_n} = 1.12$ *Comparison between the finite element analysis and the nominal buckling resistance*

REFERENCES

AASHTO (2007). AASHTO LRFD Bridge Design Specifications, 4th edition, American Association of State Highway and Transportation Officials, Washington, DC.

AISC (2005). Specification for Structural Steel Building, ANSI/AISC 360-05, American Institute of Steel Construction, Chicago, IL.

ASCE (1967). "Bibliography on Bolted and Riveted Structural Joints", Manuals and Reports in Engineering Practice No. 48, ASCE, New York.

Astaneh-Asl, A. (2008). "Progressive Collapse of Steel Truss Bridges, the Case of I-35W Collapse", Invited Keynote paper, Proceedings , 7th International Conference on Steel Bridges, Guimarães, Portugal, 4-6 June, 2008.

Brown, V. L. S. (1988). "Stability of Gusseted Connections in Steel Structures", Ph.D. dissertation, University of Delaware.

Cai, Q. and Driver, R.G. (2008), "Performance of the Unified Block Shear Equation for Atypical Failure Paths,"6th International Workshop on Connections in Steel Structures", Chicago, IL.

DeJonge, A.E.R. (1945). "Riveted Joints: A Critical Review of the Literature Covering their Development", ASME, New York.

Dowswell, B. (2006), "Effective Length Factors for Gusset Plate Buckling", Engineering Journal, Second Quarter, pp. 91-111.

FHWA (2010). "Guidelines for the Load and Resistance Factor Design and Rating of Riveted and Bolted Gusset-Plate Connections for Steel Bridges", Project No. 12-84, Second Interim Report.

FHWA (2009). "Load Rating Guidance and Examples for Bolted and Riveted Gusset Plates in Truss Bridges", FHWA-IF-09-014.

Fisher, J.W., Kormanik, R., and Allan, R.N. (1966). “Supplement to the Bibliography on Bolted and Riveted Joints”, Report No. 302.1, Fritz Engineering Laboratory, Lehigh University, Bethlehem, PA.

Fisher, J.W., and Beedle, L.S. (1964). ”Bibliography on Bolted and Riveted Structural Joints”, Report No. 302.1, Fritz Engineering Laboratory, Lehigh University, Bethlehem, PA.

Government Board of Engineers (1919). “The Quebec Bridge, Vol. 1”, Department of Railways and Canals, Ottawa.

Holt, R., and Hartmann, J. (2008), “Adequacy of the U10 Gusset Plate Design for the Minnesota Bridge No. 9340 (I-35W Over the Mississippi River)”, Turner-Fairbank Highway Research Center Report.

Iadicola, M. A. (2011). National Institute of Standards and Technology, Gaithersburg, MD.

Kulak, G.L., Fisher, J.W., and Struik, J.H.A. (2001), “Guide to Design Criteria for Bolted and Riveted Joints – 2nd Ed.”, AISC, Chicago, IL.

Munse, W.H. (1976). “Fifty Years of Riveted, Bolted, and Welded Steel Construction”, J. of Construction Division, ASCE, September, 1976, Vol. 102, CO3, pp. 437-447.

Munse, W. H., and Cox, H. L. (1956). "The Static Strength of Rivets Subjected to Combined Tension and Shear", Engineering Experiment Station Bulletin No. 437, University of Illinois, Urbana, IL.

National Transportation Safety Board (2008). “Collapse of I-35W Highway Bridge, Minneapolis, Minnesota, August 1, 2007”, Highway Accident Report NTSB/HAR-08/03, Washington, DC.

Ocel, J. M. and Zobel, R. S. (2010). Turner-Fairbank Highway Research Center, McLean, VA.

Richard, R. M., Rabern, D. A., Hormby, D. E., and Williams, G. C. (1983), “Analytical Models for Steel Connections,” Behavior of Metal Structures, Proceedings of the W.H. Munse Symposium, Edited by W. J. Hall and M. P. Gaus, ASCE.

Roeder, C.W., Leon, R.Y., and Preece, F.R. (1994). “Strength, Stiffness, and Ductility of Older Steel Structures under Seismic Loading”, Report SGEM 94-4, Department of Civil Engineering, University of Washington, Seattle.

Simulia (2010). “Abaqus Analysis User Manual, Version 6.10”, Providence, RI.

Simulia (2009). “Abaqus Analysis User Manual, Version 6.9”, Providence, RI.

Thornton, W. A. and Muir, L. S. (2008). "Vertical Bracing Connections in the Seismic Regime", International Workshop on Connections in Steel Structures VI, Chicago, IL.

Thornton, W. A., and Kane, T. (1999). “Design of Connections for Axial, Moment and Shear Forces”, Chapter 2 in Handbook of Structural Steel Connections Designs and Details (A. Tamboli, ed.), McGraw-Hill, New York, pp. 237-286.

Thornton, W. A. (1984). "Bracing Connections for Heavy Construction", Engineering Journal 21(3): 139-148.

White, D. W., Leon, R. T., Kim, Y. D., Bhuiyan, T., and Mentes, Y. (2011). “Finite Element Evaluation of Steel Truss Bridge Gusset Plate Connections,” Draft Parametric Study Report for NCHRP Project 12-84, School of Civil and Environmental Engineering, Georgia Institute of Technology, Atlanta, GA.

Whitmore, R.E (1952). “Experimental Investigation of Stresses in Gusset Plates”, Bulletin No. 16, Engineering Experiment Station, University of Tennessee.

Wilson, W. M., and Oliver, W. A. (1930). "Tension Tests of Rivets", University of Illinois Engineering Experiment Station, Bulletin No. 210, Urbana, IL.

Wright, W. J. (2009). Department of Civil and Environmental Engineering, Virginia Tech.

VITA

Yavuz Mentes, the son of Hava Mentes and Muzaffer Mentes, was born in Giresun, Turkey on 06 September 1982. He attended Middle East Technical University (METU) where he received his Bachelor of Science in Civil Engineering degree in June 2005. In August 2005, he moved to the United States of America (USA) to attend the School of Civil and Environmental Engineering at Georgia Institute of Technology. Upon receiving his Master of Science in Civil Engineering degree in 2008, Yavuz continued his graduate studies to pursue his Doctor of Philosophy (PhD) in Civil Engineering degree at Georgia Institute of Technology.